ANL/CHM/RP--77160

DE93 002896

SURVEYS OF RESEARCH IN THE CHEMISTRY DIVISION

Argonne National Laboratory

9700 South Cass Avenue

Argonne, Illinois 60439

1992

Brenda M. Grazis, Editor

Leon M. Stock, Division Director

Fred A. Cafasso, Deputy Division Director

The editor wishes to acknowledge the assistance of Anita Bakke, Janet Bergman, Laura Bowers, Kay Foreman, Marlene Gross, Michael Mendoza, Janette Nolan, and Deborah Vervack, whose diligent efforts made this Survey possible.

TABLE OF CONTENTS

THE COVER FIGURE ix

INTRODUCTION xi

I. REACTIVE INTERMEDIATES IN THE CONDENSED PHASE: RADIATION CHEMISTRY AND PHOTOCHEMISTRY 1

A. Chemistry of Ions in the Condensed Phase 2
1. Structure and Reactivity of Condensed-Phase Radical Ions 2
a. Radical Anion Dimers 2
b. Solvent Effects on Radical Ion Reactions: Arene Solvents 4
c. Radical Ions in Alkene Solvents 5
2. Transformations and Reactions of Radical Cations in Zeolites 6
a. Ion-molecule Reactions: TME 7
b. Radical Cation Transformations: Q and NBD 8
3. High-Energy Chemistry 9
4. Ions and Excited States in Radiolysis and Photolysis 13
a. Ion-Recombination in Spurs 13
b. Anion Decay vs. Excited State Formation 15
c. Formation of Aromatic Radical Cations in Alcoholic Solutions; the $SF_5\cdot$ Radical as an Oxidizing Species 16

B. The Role of Solvent in Chemical Reactivity 18
1. Reaction of H Atoms with Benzene in Water 18
2. Mechanism of the $(H)_{aq} \rightleftharpoons (e^-)_{aq}$ Interconversion 21
3. Solvent Relaxation Dynamics 25
a. Ion Solvation and Solvent Structure 25
b. Monte Carlo Simulations of Solvation Energetics 27
c. Solvation Dynamics in Alcohols 28
d. Dynamics in Salt Solutions 29

PUBLICATIONS 31
SUBMISSIONS 32
COLLABORATIONS 33

II. ELECTRON TRANSFER AND ENERGY CONVERSION 35

A. Intramolecular Electron Transfer 35
1. Temperature Dependence of Electron-transfer Rates 35
2. Calculation of Electron Tunneling Pathways 36
3. Internal Reorganization Energies of Rotation 36
4. Effect of Symmetry on Electron-transfer Rates 37
5. Superexchange Through Metal Ions Between Electron Donor and Acceptor Groups 37
6. Salt Effects on Electron-transfer Rates 37

B. Energy Conversion in Microheterogeneous Systems 38
1. Size Control and Surface Modification 39
2. Electron Transfer From Excited Particles 40
3. Electron Transfer to the Particle 40
4. Radicals at the Surface of the Particles 40

PUBLICATIONS 41
SUBMISSIONS 42
COLLABORATIONS 43

III. PHOTOSYNTHESIS AND SOLAR ENERGY CONVERSION 45

A. Studies of Bacterial Photoreaction Centers 45
1. Control of Photochemical Pathways and Assembly of Photosynthetic Structures 45
2. Investigation of Artificial Photosynthesis Using Unnatural Photosynthesis 47
3. Treatments of Excitation and Electron Transfer Using the Redfield Formalism 50
a. General Treatment of Dynamic Solvent Effects in Electron Transfer at High Temperature 50
b. Superexchange and Sequential Electron-Transfer Mechanisms in a Three-site System 51
c. Effects of Fluctuating Electronic Coupling on Electron Transfer 51

B. Structural and Energetic Factors in Photoinduced Charge Separation 52

C. Artificial Photosynthesis 57
1. Background 57
2. Synthetic Photoreaction Centers 59
3 Photophysics and Photochemistry of Photosynthetic Model Systems 59

D. Advances in Instrumentation and Analysis 64
High-Resolution Electron Paramagnetic Resonance 64

E. Synchrotron Investigation of Excited States 66

PUBLICATIONS 68
SUBMISSIONS 71
COLLABORATIONS 72

IV. METAL CLUSTER CHEMISTRY 75

A. The Chemical Reactions of Transition Metal Clusters 75
1. Chemical Probes of Metal Cluster Structure 76
a. The Nitrogen Probe 76
b. Weakly Adsorbing Clusters 77
2. Kinetics of Cluster Reactions 77
a. Reactions of Nickel Clusters with D_2 77
b. Reactions of Cobalt Clusters with D_2 78
3. Physisorption Processes 78
4. Uptake Modeling 79

B. Photoionization and Optical Spectroscopy of Metal Clusters 79
1. Metal Cluster-Rare Gas van der Waals Complexes: A Microscopic Model of Physisorption 80
2. The Optical Response of Niobium Clusters 80
3. Bimetallic Clusters of Aluminum and Cobalt 81

C. Theoretical Studies of Cluster Structure and Dynamics 82
1. Dynamics of Cluster-Molecule Interactions 82
2. Structure, Phases, and Phase Changes of Nickel Clusters from an Embedded-Atom Potential 84
3. The Effective-Medium Approach for Clusters 85

4. Analysis of Molecular Dynamics Schemes 86
5. Cluster Research Within the Theory Institute 86
a. Ab Initio Molecular Dynamics for Metal Clusters 86
b. Structure and Dynamics of Metal Clusters from a Gupta-like Potential 86
c. Configuration Space Sampling and Density of States of Anharmonic Systems 87

PUBLICATIONS 87
SUBMISSIONS 88
COLLABORATIONS 89

V. CHEMICAL DYNAMICS IN THE GAS PHASE 91

A. Theory of Chemical Reactions 92
1. Theoretical Studies of the Energetics of Chemical Reactions 92
a. Ground Potential Energy Surface for CH_2 93
b. Excited Singlet Potential Energy Surfaces for CH_2 94
c. R-Cl Potential Curves 94
2. Theoretical Studies of the Dynamics of Chemical Reactions 95
a. Theoretical Dynamics in the Formation and Dissociation of the Formyl Radical 95
b. Thermal Dissociation of HCN 96
c. Inelastic Scattering on Multiple Surfaces: CH + He 97
d. Inelastic Scattering on Multiple Surfaces: NCO + He 97
e. OH + CO Inelastic Dynamics 98
f. Cl + HCl Reaction Dynamics 98
g. Reaction Kinetics for CH + H and C + H_2 98
h. Quantum Dynamics of $ArI_2 \rightarrow Ar + I_2$ 98
i. Wave Packet Dynamics of Four-Atom Systems 99
j. Hierarchical Analysis of Molecular Spectra 99

B. Computational Chemistry: Energetics and Dynamics of Chemical Reactions 104
1. COLUMBUS Program System 104
a. Maintenance and Developments 104
b. COLUMBUS-related Codes: MCSCF Wave Function Optimization Using Multidimensional Trigonometric Interpolation 105
c. COLUMBUS-related Codes: Analytical Energy Gradients for MRCI Wave Functions 106
2. Full-CI 106
3. New Methods: Electronic Wave Packets 107

C. Kinetics of Chemical Reactions 107
1. Elementary Reaction-Rate Measurements at High Temperature by Tunable-Laser Flash-Absorption 107
2. Flash Photolysis-Shock Tube Studies of Chemical Reactions 109

D. Dynamics of Chemical Reactions 109
1. Crossed-Beam Reaction Dynamics 110
a. Vibronically Inelastic Scattering of NCO + He: Dynamical Renner-Teller Effects 110
b. Angular Correlations in the Collision-Induced Fine-Structure Transition of $O(^3P)$ Atom With Argon 112
2. Fast-Flow Reactor Studies of Radical-Radical Reaction Dynamics 112

PUBLICATIONS 112
SUBMISSIONS 115
COLLABORATIONS 116

VI. PHOTOIONIZATION-PHOTOELECTRON RESEARCH 119

A. Photoionization Studies of CH_3S, CH_2SH, CH_2S, and HCS 120
1. Background 120
2. The Isomeric Transients CH_3S and CH_2SH 120
3. CH_2S and HCS 121
4. The Fragmentation Thresholds of CH_3SSCH_3 122
5. Thermochemistry of the CH_nS Species 122

B. Photoionization Studies of Arsenic Clusters 123
Photoionization Mass Spectrometric Study of As_4 123

C. On s-like Window Resonances 124

D. Three Laws for $D_o(BiF)$ 126

E. Additional Studies of Group V Clusters 127

PUBLICATIONS 127
SUBMISSIONS 128
COLLABORATIONS 128

VII. CHARACTERIZATION AND REACTIVITY OF COAL AND COAL MACERALS 129

A. Separation of Coal Macerals 130
1. Continuous Flow and Centrifugal Sink/Float Separation of Coal Macerals 130
2. Ultraresolution of Coal Macerals and Hyperfine Grinding of Coal 131

B. Characterization of Coals, Other Kerogens, and their Extracts by Thermal Mass Spectrometry 133

C. The Nature and Fate of Natural Resins in the Geosphere. Identification, Classification, and Nomenclature of Resinites 136

D. Laser Desorption/Ionization Mass Spectrometry 139
1. Characterization of Coals by Direct Laser Desorption and Postionization 139
2. DNA and Biopolymer Analysis Using Laser Mass Spectrometry Approaches 141

E. NMR Spectroscopy and Imaging 142
1. Solvent Swelling of Coals Studied by Three-Dimensional NMR Imaging Chemical Microscopy 142
2. Quantitative Solid ^{13}C NMR of Argonne Coals 143

F. XANES Evidence for Selective Organic Sulfur Removal from Illinois No. 6 Coal 146

G. Novel Synthetic Approaches to Catalyst Design 148

PUBLICATIONS 152
SUBMISSIONS 154
COLLABORATIONS 155

VIII. THE PREMIUM COAL SAMPLE PROGRAM 157

A. Program Administration 157

B. Sample Stability 158

PUBLICATIONS 158
SUBMISSION 158
COLLABORATIONS 158

IX. CHEMICAL SEPARATIONS SCIENCE 159

A. Simultaneous Extraction of TRUs, ^{90}Sr, and ^{99}Tc 159

B. Extractant-diluent Interactions: The Influence of Substituents 162

C. Diphonix — A New Ion-Exchange Resin for the Treatment of Industrial Waste Streams, Contaminated Groundwaters, and Mixed Wastes 164

D. The Influence of the Radical Character of Organometallic Reagents on the Direction of Addition to an α,β Unsaturated Phosphoryl Group 167

E. U/TEVA•Spec™: A Novel Extraction Chromatographic Material for the Separation and Preconcentration of Uranium 168

PUBLICATIONS 172
PATENTS 173
SUBMISSIONS 173
COLLABORATIONS 174

X. HEAVY ELEMENTS COORDINATION CHEMISTRY 175

A. Phosphonic Acid Complexes of f Elements 176

B. Europium Phosphonate Complexation Heats and Hydration of the Complexes 177

C. Thermodynamic and Spectroscopic Investigation of Uranyl-MDPA at Elevated pH 178

D. Kinetics of Uranyl-Diphosphonate Complexation in Acidic Solutions 180

E. Molecular Mechanics Calculations for f Element Complexes 181

F. Thermal/Oxidative Instability of Complexants/Complexes 181
1. Nitric Acid Oxidation of Vinylidene-1,1-diphosphonic Acid 181
2. Vanadium-catalyzed Oxidation of 1-Hydroxyethane-1,1-diphosphonic Acid (HEDPA) by Hydrogen Peroxide 182

PUBLICATIONS 183
SUBMISSIONS 183
COLLABORATIONS 184

XI. HEAVY ELEMENTS PHOTOPHYSICS AND PHOTOCHEMISTRY 185

A. Photophysics of 4+ Actinide Ions in CeF_4 185

B. Spectra and Dynamics of Trivalent Actinide Ions in Fluoride Phases 186

PUBLICATIONS 187
SUBMISSION 188
COLLABORATIONS 188

XII. f-ELECTRON INTERACTIONS 189

A. The Electronic Properties of Rare-Earth Ions in High-T_c Superconductors 189

B. The Electronic and Magnetic Properties of RPO_4: $TmPO_4$ 191

PUBLICATIONS 192
SUBMISSIONS 192
COLLABORATIONS 193

XIII. RADIATION CHEMISTRY OF HIGH-LEVEL WASTES
ANL/CHM TASK FORCE ON GAS GENERATION IN WASTE TANKS 195
A. Radiolytic and Thermal Generation of Gases 195
1. Radiolytic Yields 195
2. Radiolytic Degradation of Organics 196
3. The Formaldehyde Reaction 196
4. Mechanisms of N_2O Generation 197
B. Computer Modeling of Simulated Waste Solutions 198
1. Computation of H_2 Yields 198
2. Computation of the NO_x System 198
C. Conclusions 199
PUBLICATIONS 200
SUBMISSIONS 200
XIV. ULTRAFAST MOLECULAR ELECTRONIC DEVICES 201
A. Background 201
B. Concepts and Designs of Molecular Switches 202
C. Development of an Electron Donor-Acceptor-Donor Molecular Switch 203
PUBLICATION 205
SUBMISSION 205
XV. NUCLEAR MEDICINE 207
A. Production of Alpha Emitters for Use in Therapy 207
B. Development of Alpha-Emitting Radiopharmaceuticals for Therapy 208
C. Monoclonal Antibodies for Diagnosis and Therapy 209
D. Hormone Receptor Binding Drugs for Diagnosis and Treatment of Malignancy 210
E. Cyclotron Production of Radionuclides for Research 210
F. Large-scale Production of ^{90}Y for Use in Radionuclide Therapy 211
PUBLICATIONS 212
SUBMISSIONS 213
COLLABORATIONS 214
XVI. ACCELERATOR ACTIVITIES 217
A. 20-MeV Linac 217
B. 3-MeV Van de Graaff Accelerator 217
C. 60-Inch Cyclotron 217
XVII. COMPUTER SYSTEM AND NETWORK SERVICES 219
A. Networking Computers 219
B. Experiment Control and Data Acquisition 219
C. RISC UNIX Computers 220

THE COVER FIGURE

Combustion dynamics in the gas phase is being investigated both theoretically and experimentally at the level of individual elementary reactions. Detailed investigations of key prototypical reactions as well as broader studies of classes of chemical reactions lead to the extensive and varied data base necessary to model practical combustion systems. Equally important, this research reveals the underlying fundamental features of chemical reactivity that are operational in many other areas of chemistry.

The cover figure shows the results of one highly detailed theoretical study of the thermal dissociation of the methyl radical CH_3. This radical is the smallest radical of combustion interest that can dissociate by atomic elimination (CH_2+H products) or molecular elimination (CH+H_2 products). In order to calculate the thermal dissociation rate constant, the minimum energy path to both sets of dissociation products must be known. The cover figure shows the computed minimum energy path for atomic dissociation. The red solid bonds connect the H-C-H fragment in CH_3 that is largely unchanged during the course of the dissociation. The checkered bond indicates the C-H bond in CH_3 that is being broken in the dissociation. The red arrow interrupted by H-atom representations shows minimum energy path for atomic dissociation. The plane in the figure and the two-tone coloring of the atoms emphasize that the reaction path breaks the planar symmetry of the original CH_3 but retains throughout a plane of reflection symmetry.

These results are obtained by multireference configuration interaction electronic structure calculations in which the most highly bound state of all the electrons is determined to a high degree of accuracy as a function of the positions of all the atoms. The positions of the atoms are then varied to find the most energetically favorable reaction path. Such calculations are highly computer intensive. However, they can accurately predict results that are not initially chemically intuitive, such as the out-of-plane nature of the atomic elimination reaction path, a feature not correctly anticipated in all previous theoretical or experimental studies of this reaction.

INTRODUCTION

Surveys of Research, 1992 reviews the research activities of the Argonne National Laboratory's Chemistry Division during the fiscal year that concluded on September 30. Broadly speaking, the Chemistry Division conducts a fundamental research program that addresses scientific problems in the chemical and nuclear sciences that are related to the mission-oriented activities that are elaborated in the strategic plan of the Energy Research Department of the Department of Energy and other national interests of the United States as expressed in the National Energy Strategy.

Currently, the Division has a permanent staff of 70 research chemists and 10 technical support personnel, and a temporary staff of 21 postdoctoral appointees and 15 graduate students. Their activities are aided by six administrative staff members and eight secretaries. Three members of the Chemistry Division hold joint appointments at The University of Chicago. Four chemists from The University of Chicago, Northwestern University, and The University of Illinois-Chicago have joint appointments at Argonne National Laboratory. In addition, about 100 other chemists from academic, government, and industrial laboratories interact with the Division's scientists on a regular basis.

The Radiation Chemistry and Photochemistry Group has made advances in delineating ion-molecule reactions in condensed-phase photoionization. Related studies of radical cations in zeolite matrices reveal that the role of the zeolite matrix is due to more than pore size alone because control of ion-matrix interaction can dramatically influence electronic levels and reactions of absorbed ions. In other studies, new insights were obtained about the structure, energetics, and dynamics of ion solvation in polar liquids. The first measurement of time-dependent yields of both singlet and triplet excited states of solutes makes a significant contribution to the understanding of the role of multiplet ion-pair events in radiolysis.

Work has continued in the Electron Transfer and Energy Conversion Group on basic electron-transfer chemistry. A novel temperature dependence was observed in which the activation energy was substantial at low temperatures and became small at room temperature, and an internal reorganization energy for the twisting motion of biphenyl is responsible for a factor of about five in intramolecular electron transfer to naphthalene. Inert salts (Na^+, Bu_4N^+, etc.) have large effects on ET rates, but, unexpectedly, the larger sized ions have larger effects on the rates. Further advances have been made in the theory of electron transfer. Small basis sets were found to be adequate for calculation of electronic couplings through straight-chain hydrocarbons. Studies on electron transfer from quantized semiconductor particles to molecules bound at their surface revealed significant differences between the absorption spectra, redox potentials, ionization potentials, and lifetimes of the radicals at the surface relative to the free radicals in solution. The rates of electron transfer from radical ions in solution to small chalcogenide particles were also studied as a function of the free energy of the reaction. It was shown that the electrons localize on surface states in these particles and that the transfer is not into the conduction band.

The Photosynthesis Group explores both natural and artificial photosynthesis. Progress in understanding both natural and artificial photosynthesis is advancing rapidly. The complete description of the spin dynamics associated with radical pairs in a charge-separation process has been finished this year. Because of these efforts, CIDEP and CRPP are now complete, powerful, versatile tools for the study of charge separation in natural and artificial photosynthesis. We have developed a Redfield approach for the theoretical calculation of electron transfer to compute three-state electron transfer, which is believed to occur in the primary process of photosynthesis. A method to explore the relationship between rate and energetics in the initial charge-separation step of bacterial photosynthesis has been developed by using genetically altered reaction-center protein in combination with femtosecond spectroscopy. Another highlight this year has been the detection of protein-relaxation processes following quinone reduction in reaction centers of *Rhodobacter capsulatus*. The structure of an **excited**, charge-transfer state has been determined for the first time by using X-rays on light-irradiated cyclopentadienylnickelnitrosyl.

The Metal Cluster Chemistry program has refined its use of the uptake of nitrogen molecules to determine the geometrical structure of small nickel clusters. Chemical reactions are now routinely studied as a function of temperature from -150 to 150 °C. Photoionization studies have focused on metal cluster-van der Waals complexes, and include the first measurements of optical absorption spectra of polyatomic clusters of transition metals. Theoretical studies of cluster dynamics have investigated the dependence of reactivity on cluster-adsorbate binding energy, and have identified for the first time resonance phenomena in cluster-molecule collisions.

In the Chemical Dynamics in the Gas Phase program, several new developments have occurred in both theory and experiment in the last year. In theory, a novel "tree" classification scheme for highly excited spectra of chemically activated molecules has been tested and applied to both experimental and theoretical spectra. A scaleable, highly parallelized full configuration interaction code has been developed and applied to problems in bond strengths on massively parallel computers. On the Touchstone computer with 512 processors, applications that would have taken a month of computer time can now be accomplished in a few hours. In experiment, kinetic studies of the thermal decomposition of chlorinated hydrocarbons have been initiated. The measurements indicate unusually large low-pressure limits. Molecular beam studies on NCO+He offer one of the clearest cases of Hund's case (A) inelastic scattering. The results strongly suggest the different radial extents of the two potential energy surfaces that mediate the scattering.

Studies by the Photoionization-Photoelectron Group of the transient species CH_3S, CH_2S, CH_2SH, and HCS, the latter two performed for the first time, have established the C-H and S-H bond strengths in these molecules, thereby making a significant correction to other recent experimental determinations. The dissociation energy of BiF, a proposed medium for a visible-UV chemical laser, and previously very poorly known, has been determined by three independent methods. Studies of the species Pn_n (Pn = As, Sb, Bi; n = 1-4) are in progress, and have already revealed some systematic behavior in structure, bonding, ionization potentials, and the dynamics of photoionization.

Achievements by the Coal Chemistry program include the discovery of an abundance of molecules with several heteroatoms in lower rank coals, and at least one heteroatom in middle-size molecules in bituminous coals; the presentation of a new, comprehensive classification scheme for resinites that evaluates the extent of coalification; the first 3-D NMR images of a solvent-swollen coal, determination of more accurate f_a values by solid ^{13}C NMR, and quantitation of the selective removal of organic sulfur using synchrotron X-ray spectroscopy. Additionally, new synthetic layered silicate clays have been prepared in the presence of many templating molecules, and the manner in which metal ions are solvated in clays has been elucidated by XAS.

The demand for the Argonne Premium Coal Samples continues to be strong. Total shipments rose to 18,200 ampoules while the number of shipments climbed by 180 to a total of 678. Over 320 research workers are making use of the samples. An additional 82 papers were published on work done with these samples to bring the total to 360.

The Chemical Separations Science Program studies on the design of bifunctional extractions of the carbamoylmethylphosphoryl class have yielded new insight into the influence of the amidic substituents on the solubility of the extraction in hydrocarbons. Basic studies of the strontium extraction (SREX) and transuranic extraction (TRUEX) processes have led to the development of a single combined process that enables one to simultaneously extract and recover strontium-90, technetium-99, americium, plutonium, neptunium, and uranium from acidic nuclear-waste solutions. The combined process enhances our capability to chemically pretreat the high-level nuclear waste presently contained in storage tanks. Adaptation of plant-scale solvent-extraction processes to extraction chromatographic use has led to the development of a uranium/tetravalent actinide-specific resin for use in the monitoring of uranium in bioassay and environmental samples.

The Heavy Elements Coordination Chemistry program on thermally unstable complexants has found that extensive intramolecular hydrogen bonding partly accounts for the unusual strength of f-element-diphosphonate complexes. Unlike typical chelating ligands, differences in complex stability for uranyl-diphosphonates result from variable formation rates, rather than changing dissociation rates. New synthetic pathways to sulfonato and amino derivatives of methanediphosphonates have been found, as has information on the kinetics of peroxide degradation of TUCS.

The Heavy Elements Photophysics and Photochemistry effort is employing photoexcitation to perturb as well as probe actinide ions and their interaction with surrounding ions. Current work has focused on investigation of an unusual phenomenon, excitation line narrowing, in electronic transitions of Cf^{4+} in CeF_4, and on related nonresonant fluorescence line narrowing and spectral hole-burning studies. To provide benchmark spectral data for trivalent actinide ions in fluoride phases, a detailed study of the energy-level structure of Es^{3+} in crystalline LaF_3 has been undertaken.

The f-Electron Interactions Group has used inelastic neutron scattering data to determine the electronic properties of selected rare earths in the RPO_4 matrix. Comparing these results to those obtained by electronic and resonant Raman spectroscopy, we clearly demonstrate that problems in understanding resonant Raman results arise from the treatment of the excited, virtual states.

The Radiation Chemistry of High-Level Wastes program has responded to a problem of national concern that exists in nuclear- and mixed-waste storage tanks at the Hanford site. An interdisciplinary task force was assembled and has been in operation during the last two years. The missions of the task force are to identify the role of radiation in the production of hydrogen and other gases in the waste tanks, and to propose remediation strategies to mitigate the risks involved in the generation of these flammable gases.

The feasibility of building molecular electronic devices based on organic electron donor-acceptor molecules is being investigated by the Ultrafast Molecular Electronic Devices Group. Several new molecules have been synthesized that act as opto-electronic switching components on a picosecond time scale. One particular electron donor-acceptor-donor molecule already characterized undergoes ultrafast optical switching in 10 ps. These new materials may prove useful in developing optical computers.

The Nuclear Medicine Research Group completed several projects in the past year that will have an impact on the field in general. First, they completed the construction and testing of a facility capable of producing clinical quantities of ^{90}Y, which will satisfy the user community for some time. Second, they optimized the production and purification of ^{87}Y. This isotope can be used in preclinical and clinical biodistribution studies of radiopharmaceuticals designed to deliver ^{90}Y for therapy. To date, there has been no satisfactory isotope of Y for this purpose. Finally, several improvements in the technology of labeling with iodine and astatine have been accomplished.

Collaborations between the members of the Chemistry Division and the scientific researchers in other Argonne Divisions have been very rewarding. The collaborative efforts include the Chemical Technology Division, Materials and Components Technology Division, Biological and Medical Research Division, and the Materials Science Division. It is also pertinent to note that the Argonne National Laboratory-Amoco cooperative research program is continuing and that collaborations are also developing with other private companies including NALCO. The collaborative activities of the research groups are noted at the end of each chapter.

Finally, it is an especial pleasure to mention the recognition that has been granted to members of the Division during the past year. Marion Thurnauer and Joe Michael were promoted to Senior Chemist. Karl Vorres received the Distinguished Service Award of the ACS Division of Fuel Chemistry. The work by Jim Norris and Joe Katz on the nature of the primary structure of the photosynthetic apparatus led to receipt of The Rumford Premium awarded by the American Academy of Arts and Sciences. Phil Horwitz was the 1992 recipient of the Glenn T. Seaborg Actinide Separations Award for outstanding and lasting contributions to the development and application of actinide separations processes and methodology. Joseph Gregar received a University of Chicago Outstanding Service Award for his exceptional skill as Argonne's premium glassblower and for his ability to design and fabricate the most complicated and intricate devices in glass or quartz.

I. REACTIVE INTERMEDIATES IN THE CONDENSED PHASE: RADIATION CHEMISTRY AND PHOTOCHEMISTRY

A. D. Trifunac, D. M. Bartels, M. V. Barnabas, K. R. Cromack, C. D. Jonah, Y. Lin, A.-D. Liu, D. M. Loffredo, P. Han, M. C. Sauer, Jr., K. H. Schmidt, D. W. Werst, P. D. Walsh

Outside Collaborators: *R. Cooper, V. V. Krongauz, S. Mezyk, P. W. Percival, E. Roduner, C. Romero*

The research described in this survey represents a multifaceted and comprehensive approach to the study of transient intermediates and chemistry induced by energetic radiation. The goal is to determine the fundamental chemistry that occurs when ionizing or photoionizing radiation interacts with condensed-phase matter. The various short-lived intermediates, radicals, radical ions, electrons, and excited states all play a role in transforming high energy from photons and particles into different stable chemical products.

The simultaneous goals of this research are (1) the understanding of the chemical transformations induced by energetic radiation via the delineation of the overall framework of reactions; (2) the identification and description of reactions of transient species; and (3) the development of novel tools to allow better pursuit of such elusive reaction intermediates. State-of-the-art electron accelerators, ultrafast laser techniques, and novel detection means for the study of ultrafast processes and transient species are continuously being developed and improved.

This survey is presented in two major parts. Part A describes several research efforts in which we study *ions, excited states, and other transients in the condensed phase.* These include studies of radical cations and ion-molecule reactions by the techniques of magnetic resonance, picosecond emission, and picosecond absorption, which probe the role of ions in high-energy chemistry, and studies of ions and their reactivity in specialized matrices such as freons and zeolites.

Part B outlines the work on the *role of solvents in chemical reactivity.* Hydrogen and deuterium atoms have been used as probes of the short-time events in the radiation chemistry of water. The nature of the solvation structure around hydrated electrons has been compared with that of classical monatomic ions by way of thermodynamic and transport properties. In a study in which ions are produced by both laser excitation and pulse radiolysis, we examine the dynamics of solvent reorganization around transient ions.

Highlights of the past year include:

(1) The first observations of aromatic radical anion dimers were made. Dimer formation is hindered by solvation effects, even in nonpolar solvents such as aromatic hydrocarbons.

(2) Significant progress has been made in defining the distribution of spur sizes in the radiolysis of alkane liquids by measuring the time-dependent yields of solute anions, solute triplet states, and solute excited singlet states.

(3) Product studies, including isotopic labeling, and flash photolysis experiments have helped to establish the occurrence of ion-molecule reactions of excited radical ions in photoionization.

(4) The use of zeolite matrices has allowed observation and control of ion-molecule reactions of radical cations.

(5) A combination of experiments, analytical theory, and computer modeling have provided new insights into the structure, energetics, and dynamics of ion solvation in polar liquids.

(6) A careful study of the reaction of H atoms with benzene in water has tested the validity of transition state theory.

(7) Examination of the $(H)_{aq} \rightleftharpoons (e^-)_{aq}$ interconversion reveals that the mechanism is best described as a *proton transfer.* The possibility of proton transfer from Bronsted acids to the solvated electron has implications for other reactions involving this species.

A. Chemistry of Ions in the Condensed Phase

A. D. Trifunac, C. D. Jonah, D. W. Werst, M. C. Sauer, Jr., K. R. Cromack, M. V. Barnabas, D. M. Loffredo, Y. Lin, A.-D. Liu, R. Cooper

1. Structure and Reactivity of Condensed-Phase Radical Ions *A. D. Trifunac, D. W. Werst*

The goals of our radical ion studies are to discover the origins and fates of radical ion intermediates in radiation chemical processes, learn the detailed electronic and structural factors that determine radical ion reactivity, and define the role of the medium in ion chemistry. The combined use of pulse radiolysis and time-resolved magnetic resonance techniques is a major strength in this effort because of the versatility of radiolysis for generating radical cations and radical anions and the excellent structural information obtained via magnetic resonance. Radical ions can be unequivocally identified, and many nuances of structure and intermolecular interactions are revealed to increase our understanding of chemical reactivity beyond what can be learned from kinetic studies alone.

Recent studies have revealed that novel types of intermediates are formed by intermolecular interactions between radical ions and solvent molecules or neutral solute molecules. Such interactions are characterized by the open-shell nature of radical ions and are often bonding interactions, that is, covalent bond formation via electronic orbital mixing. In section a, we discuss the formation of rarely observed dimer radical anions. Although radical cations of olefins and aromatic hydrocarbons readily react with their neutral parent molecules to form dimers, the corresponding dimers of the radical anions have been virtually unreported. We have found strong evidence for dimerization of two fluorinated aromatic radical anions. In section b, we explore solvation effects on radical ion reaction mechanisms, in particular, electron transfer and dimer formation, by comparing results in alkane and aromatic hydrocarbon solvents. Related results of a preliminary nature for radical ions in alkene solvents are discussed in section c.

a. Radical Anion Dimers

The octafluoronaphthalene radical anion ($C_{10}F_8^{-\bullet}$) was observed in electron-irradiated dilute solutions by fluorescence-detected magnetic resonance (FDMR). The spectrum observed in n-hexane containing 10^{-3} M $C_{10}F_8$ is shown in Figure I-1. This spectrum is described by two quintet coupling constants, a_1 = 23 G and a_2 = 20 G, as appropriate for two sets of four equivalent spin one-half ^{19}F nuclei. What appears as a nine-line spectrum at low resolution clearly separates into the 25-line pattern at slightly higher resolution (expanded view of inner three-line groupings, Figure I-1).

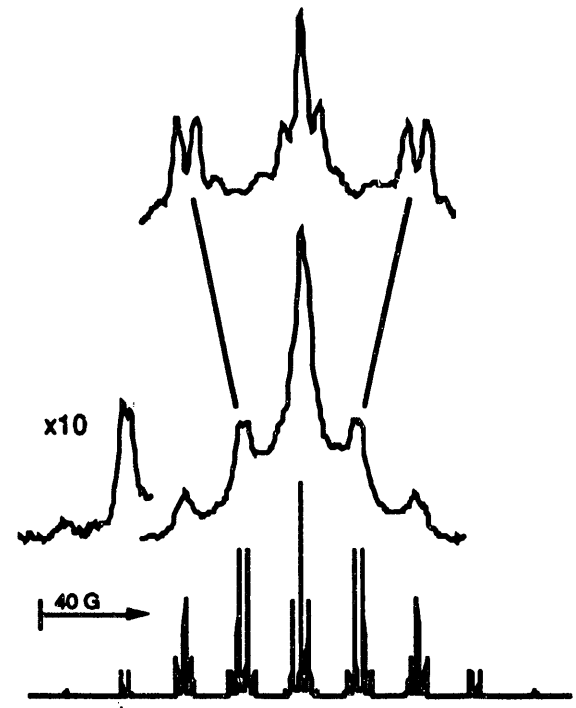

Figure I-1. FDMR spectrum observed at 190 K in n-hexane containing 10^{-3} M $C_{10}F_8$ and 10^{-4} M d_{10}-anthracene (lower experimental trace), no d_{10}-anthracene (upper experimental trace). The upper trace was obtained at higher resolution. The stick spectrum was simulated with the parameters, a(4F) = 23 G, a(4F) = 20 G.

Fluorine substituents have a significant effect on the energies of the unoccupied molecular orbitals of aromatic compounds. In a series of fluorine-substituted benzene and pyridine radical anions, it has been shown that fluorine substitution stabilizes the lowest σ^* orbital, destabilizes the lowest π^* orbital, and gives rise to σ^*-π^* crossover. That is, in heavily fluorinated benzene and pyridine radical anions, the

odd electron occupies a delocalized σ* orbital rather than a π* orbital. The main signature of the σ* ground state anion is that the hyperfine splittings are larger for the radical anion than for the radical cation; this ordering is opposite to the behavior found for lightly or unsubstituted aromatic compounds.

The reported coupling constants for $C_{10}F_8^{\bullet+}$ are 19.0 and 4.8 G. Thus, on this basis alone we would conclude that the LUMO of $C_{10}F_8$ is σ*. The relatively small differences between the coupling constants for the cation and anion, however, leave some room for doubt and suggest that the σ* and π* orbitals are close in energy. This finding may explain the small temperature dependence of the hyperfine splittings, for example, if the mixing of the σ* and π* states has a vibronic component. We cannot rule out a predominantly π* ground state with partial σ character from mixing of a nearby σ* state, which might be sufficient to explain the observed coupling constants.

Figure I-2 shows how the FDMR spectrum changes with increasing $C_{10}F_8$ concentration. The original spectrum is gradually replaced by a spectrum (Figure I-2b) consistent with coupling to 16 nearly equivalent nuclei (a = 7 G). This spectrum is assigned to the dimer radical anion, $(C_{10}F_8)_2^{\bullet-}$, based on the (i) reduced hyperfine splitting, (ii) increased number of equivalent nuclei, (iii) concentration dependence, and (iv) kinetic behavior. By delaying the time window of observation, the ratio of dimer signal to monomer anion signal increases, as monomer anions react with neutral solute molecules to form dimers, equation 1. We propose that $(C_{10}F_8)_2^{\bullet-}$ has a symmetric sandwich-type structure based on the equivalence of the hyperfine couplings.

$$C_{10}F_8^{\bullet-} + C_{10}F_8 \rightleftharpoons (C_{10}F_8)_2^{\bullet-} \qquad (1)$$

Figure I-3 illustrates the concentration dependence of the FDMR spectrum of the radical anion derived from 1,2,4,5-tetrafluorobenzene ($C_6H_2F_4$) in n-hexane. Figure I-3a shows the inner nine lines of the ($C_6H_2F_4^{\bullet-}$) spectrum (a^{4F} = 41 G, a^{2H} = 5.5 G). The unresolved EPR lines of the anthracene radical ions and the toluene solvent radical cation mask the central triplet of $C_6H_2F_4^{\bullet-}$. Analogous to the behavior observed for $C_{10}F_8$, the $C_6H_2F_4^{\bullet-}$ spectrum disappears with increasing solute concentration and is replaced by a narrower spectrum (Figure I-3b). The high-concentration spectrum is not resolved and appears as shoulders on the central, scintillator ion peak. By analogy to the foregoing example, this is also attributed to formation of a dimer anion radical.

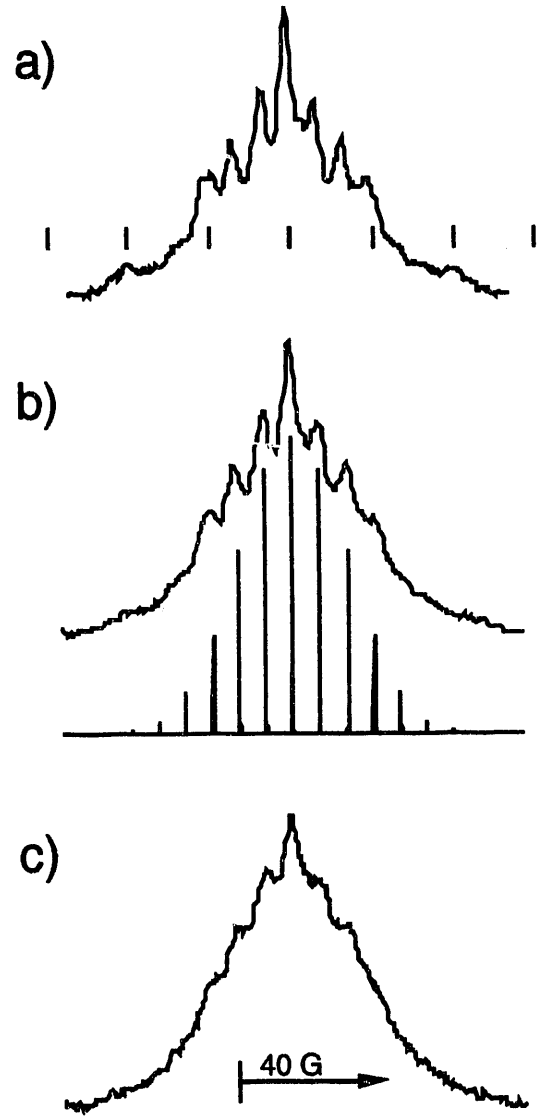

Figure I-2. FDMR spectra observed at 200 K in n-hexane containing a) 3×10^{-3} M, b) 5×10^{-3} M, and c) 10^{-2} M $C_{10}F_8$. The markers in a) locate the average positions of the inner seven groups of lines of the $C_{10}F_8^{\bullet-}$ spectrum. The stick spectrum in b) was simulated with a single coupling constant, a(16H) = 7 G.

The observation of dimer radical anions is interesting in light of the dearth of previous reports of such species, contrasted with the ease of observation of dimers formed from π radical cations. The only previous example of an anion-molecule dimerization reaction that has been studied by EPR is the tetrafluoroethylene radical anion, which undergoes cyclization with a tetrafluoroethylene molecule to give $c\text{-}C_4F_8^{\bullet-}$.

Radical anions of other ethylenes with strong electron-withdrawing groups are thought to react to form dimers based on optical and kinetic evidence.

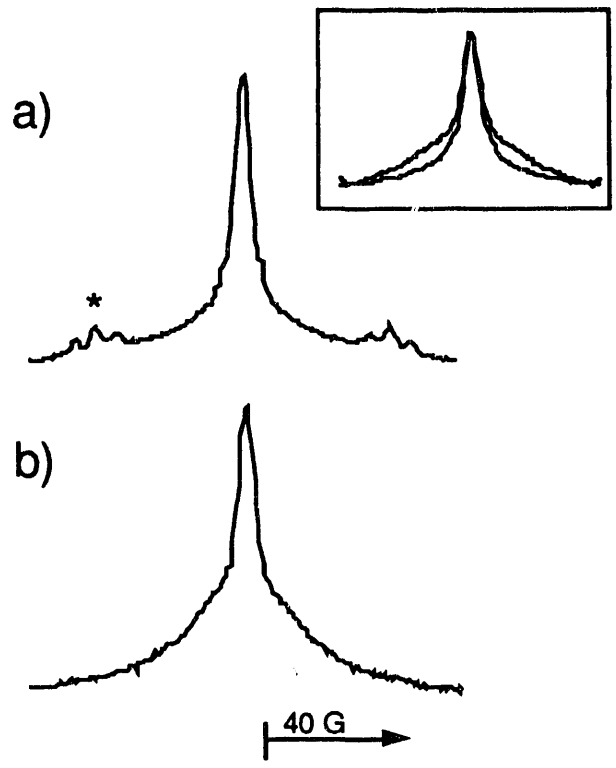

Figure I-3. FDMR spectra observed at 190 K in n-hexane containing 10^{-4} M d_{10}-anthracene and a) 10^{-3} M $C_6H_2F_4$, b) 10^{-2} M $C_6H_2F_4$. The inset shows the superposition of the central portions of the same two spectra.

b. Solvent Effects on Radical Ion Reactions: Arene Solvents

The dimer radical anions, $(C_{10}F_8)_2^{\bullet-}$ and $(C_6H_2F_4)_2^{\bullet-}$, observed in n-hexane are not observed in toluene solvent. At low solute concentration (10^{-3} M), the radical anion FDMR spectra are the same in n-hexane and toluene for both $C_{10}F_8^{\bullet-}$ and $C_6H_2F_4^{\bullet-}$. However, the concentration dependence for both anions in toluene is different from that in n-hexane. In the case of $C_{10}F_8^{\bullet-}$, the spectrum is invariant between 10^{-3} and 10^{-1} M; that is, no dimer is formed. Likewise, in the case of $C_6H_2F_4^{\bullet-}$ in toluene, no dimer is formed, and the dependence of the spectrum on concentration indicates the occurrence of the electron self-exchange reaction, equation 2.

$$C_6H_2F_4^{\bullet-} + C_6H_2F_4 \rightleftharpoons C_6H_2F_4 + C_6H_2F_4^{\bullet-} \quad (2)$$

Figure I-4 shows an expanded view of one of the H_2 triplets (see asterisk in Figure I-3a). As the concentration and exchange rate increase, the lines broaden and the hyperfine splitting decreases. The ^{19}F splitting also decreases. The rate constant for exchange is approximately 10^9 M^{-1} s^{-1}.

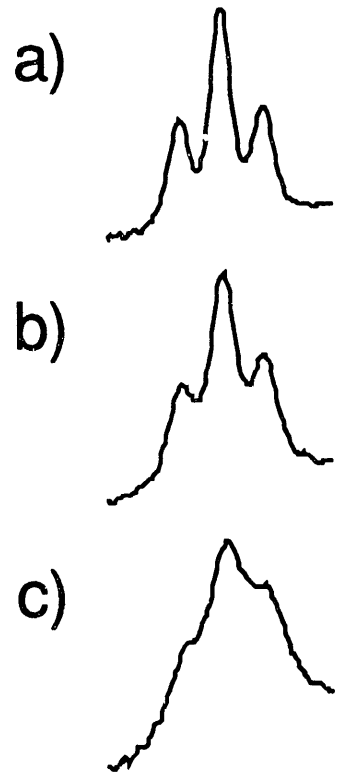

Figure I-4. Exchange effects observed for one H_2 triplet in the FDMR spectrum of $C_6H_2F_4^{\bullet-}$. The solvent is toluene; T = 190 K. The $C_6H_2F_4$ concentration was a) 10^{-2} M, b) 3×10^{-2} M, and c) 10^{-1} M.

We conclude that there is a change of mechanism in the arene solvents compared to alkane solvents. Encounters between the radical anions and neutral solute molecules do not produce dimers in toluene; rather, electron exchange is favored. Although evidence for self exchange is not observed for $C_{10}F_8$, our results do not rule out the possibility of exchange. The spectra only indicate that exchange must be slower than the characteristic EPR timescale. The slower exchange rate for $C_{10}F_8$ compared to $C_6H_2F_4$ is consistent with the more positive electron affinity of $C_{10}F_8$, which should increase the activation barrier for electron transfer.

Any solvent effect that impedes close encounter (orbital overlap) of the anion with neutral solute molecules might impede dimer formation, but what solvent effect can explain the difference between the two nonpolar solvents, n-hexane and toluene? We have previously explained the contrasting behavior of thioether *radical cations* in these two solvents based on electron donor-acceptor interactions between toluene solvent molecules and solute radical cations that lead to the formation of solvent radical cation complexes. The FDMR evidence (changes in hyperfine splittings) of spin and charge transfer between solute radical cations and solvent molecules provides a measure of such orbital interactions. However, charge transfer between radical anions and toluene is unfavorable because the donor/acceptor roles are reversed, and toluene is a poor electron acceptor. Consistent with this fact, we observe no significant differences in the anion coupling constants in toluene compared to n-hexane.

Charge transfer from toluene solvent molecules to the neutral solute molecules is more plausible, as charge-transfer complexes between arene solvents and strong electron acceptors have been observed. Ground-state charge-transfer complexes give rise to new absorption bands shifted to longer wavelengths compared to the parent absorption. However, the minimal red shifts observed in the UV spectra of $C_{10}F_8$ and $C_6H_2F_4$ in toluene show that charge transfer to the neutral solutes is very weak.

On the other hand, nonspecific solvation via ion-dipole and ion-induced-dipole interactions between the anions and solvent molecules is not expected to be significantly different in toluene and n-hexane. The dipole moment of n-hexane is near zero, and that of toluene is negligibly small (0.36 D). The polarizabilities of toluene ($\alpha/4\pi\varepsilon_0$ = 12.3 Å^3) and n-hexane ($\alpha/4\pi\varepsilon_0$ = 11.9 Å^3) are also very similar. Perhaps the strength of the anion-solvent interaction is not accurately predicted from the polarizability derived from the refractive index. Nevertheless, the source of the solvent effect remains a puzzle.

The solvent effects in nonpolar solvents described above are not limited to radical anions. A radical cation example that closely parallels the anion study is the tetramethylethylene radical cation ($TME^{\bullet+}$). Like $C_{10}F_8^{\bullet-}$ and $C_6H_2F_4^{\bullet-}$, $TME^{\bullet+}$ reacts with neutral TME solute molecules to form dimer ions (and higher order aggregates) in n-hexane, but not in toluene. We have also ruled out electron donor-acceptor interactions between $TME^{\bullet+}$ and solvent because the EPR parameters of $TME^{\bullet+}$ are the same in n-hexane and toluene.

c. Radical Ions in Alkene Solvents

Preliminary experiments were also carried out in alkenes to characterize their solvent effects on radical ions and radical ion reactions. For example, FDMR spectra of perfluoronaphthalene in 2-methyl-1-butene reveal the formation of $(C_{10}F_8)_2^{\bullet-}$ as in n-hexane. On the other hand, FDMR spectra of TME in 2-methyl-1-butene and 2-methyl-2-butene exhibit slightly reduced (~16%) hyperfine coupling constants. This result is indicative of orbital interactions between the solute radical cations and solvent molecules and suggests electron donation from solvent HOMOs to the $TME^{\bullet+}$ SOMO; that is, similar to our previous observations of solvent complexation of thioether radical cations in arene solvents.

The effect of solvent interactions on the solvent radical cations is an equally important issue. In alkane liquids, this has been difficult to address because the solvent radical cations are very short-lived. In arene solvents, one observes a single narrow line in the spectrum, attributable to the solvent positive ion. This can be interpreted as delocalization of the hole via aggregate cation formation or via electron hopping. Experimental differentiation between the two processes is lacking. In TME, we have observed, for the first time in a pure liquid, a resolved spectrum indicative of a localized solvent radical cation. As found for TME in other alkene solvents, the hyperfine coupling constant for $TME^{\bullet+}$ in pure TME is reduced (~13%) compared to the value in a noninteracting solvent (e.g., n-hexane).

The observation of a localized hole in pure TME is remarkable in light of the proclivity of olefin radical cations to form delocalized aggregates in dilute solutions, equation 3. One wonders if TME is a special

$$TME^{\bullet+} + (TME)_n \rightleftharpoons (TME)_{n+1}^{\bullet+} \qquad (3)$$

case. We have not found another example among several related alkenes. The high symmetry of TME (only one ^1H coupling constant) is a distinct advantage for EPR detection. We plan future experiments to address the relative stabilities of other alkene radical cations to define their ion-molecule reactions with solvent molecules.

No explanation is available at present for the puzzling concentration dependence of tetramethylethylene radical cations, which shows spin delocalization in small clusters and spin localization in large clusters. The behavior of the solvent holes as dictated by the interactions between the solvent radical cations and neutral solvent molecules has far-reaching implications for condensed-phase radiation chemistry. Solvent interactions with the solvent radical cations influence the lifetime, mobility, and oxidizing strength of the solvent hole. These interactions also change the properties, for example, the oxidation potential, of the solvent.

2. Transformations and Reactions of Radical Cations in Zeolites

A. D. Trifunac, M. V. Barnabas

The study of transient radical ions by time-domain methods is closely coupled to the study of such species by matrix-isolation methods. The ability to stabilize radical ions and to control their reactivity is crucial to obtaining a comprehensive overview of their structure and reactivity. We have recently developed zeolites as the matrix of choice. We have shown that the reactions, structures, and electronic states of radical cations can be influenced by the zeolite matrix and experimental parameters, such as substrate loading and temperature.

Radical cations have been studied extensively in various matrices, where a solution of the molecule of interest is prepared and then frozen, or the solute and solvent are codeposited on a low-temperature surface. Matrices stabilize radical cations by separating the geminate electron or anion and the radical cation and by reducing the probability of recombination. Zeolites have the added advantages that they have unique and constrained frameworks and are rigid over a wide temperature range. Thus, although substrate molecules in most frozen matrices are rigidly trapped except very near the melting point of the solvent (usually considerably below room temperature), adsorbed molecules in zeolites explore an open-pore, interconnected surface, the dimensions of which do not change significantly with temperature and which remains rigid well above room temperature. The fact that the volume available in the adsorption site for translational or rotational motion of solutes does not change with temperature has manifold implications for the study and control of radical cation reactivity.

Much of condensed-phase radical cation chemistry is bimolecular: dimerization reactions, ion-molecule reactions, etc. In order to control radical cation reactivity, it is essential to control encounters between radical cations and neutral reactants, the rate of which is normally determined by the concentration and diffusion rate. Zeolites offer more versatility primarily because of the ability to vary substrate mobility more discretely and selectively, by adjusting the pore sizes and temperature. In the limit that a close match is obtained between the size and shape of a cage or channel structure and the substrate species, radical cations can be virtually immobilized in the zeolite matrix. This can greatly enhance radical cation stability, because ion-molecule reactions can only occur in the presence of smaller reactant molecules that are able to diffuse to the adsorption site.

In addition to size restrictions on diffusion, specific guest-host interactions (e.g., electrostatic interactions between radical cations and metal ions of the lattice) can affect radical cation mobility and stability. Adsorption sites that differ in size, shape, polarity, etc., often exist in the same zeolite. This introduces a heterogeneity in the zeolite matrices that does not normally occur in other matrices, and that can lead to a duality of radical cation reactivity within one matrix due to stabilization of different electronic states or different accessibility of adsorption sites. A benefit of the remarkable synthetic versatility of zeolites is that size, shape, and polarity parameters can be varied, allowing one to "tune" the environment to promote or inhibit reactions.

Pentasil-type zeolites (ZSM-5s) are medium-pore-size zeolites, which allow one to monitor primarily the guest-guest or guest-host interactions over a wide temperature range depending on the substrate concentration. Four pentasil zeolites that have approximately the same channel/pore size, but vary in the Si/Al content, and hence the counterion content, were used in our study. This parameter has a significant effect on the reactions of the radical cations.

Radical cations were produced by γ irradiation of solutes in zeolites at 77 K. The radical cations of tetramethylethylene (TME), quadricyclane (Q), and norbornadiene (NBD) were examined by EPR in the zeolites at different temperatures and concentrations. The chemistry of $TME^{\bullet+}$ involves dimerization and ion-molecule reaction, whereas the radical cations $Q^{\bullet+}$ and $NBD^{\bullet+}$ undergo a variety of rearrangements and transformations. The differences in the zeolite interior

surface topology and composition are invoked to explain the new radical cation chemistry.

a. Ion-molecule Reactions: TME

Figure I-5 shows the EPR spectra for TME in ZSM-5 after γ irradiation at 77 K with observation at 10 K: (a) 0.1%, (b) 1%, and (c) 7% w/w TME. The spectrum of $TME^{\bullet+}$ consists of 13 lines (11 are observable in Figure I-5a) with a hyperfine coupling constant of 17.2 G. When the TME concentration is >5%, the dominant species in the spectrum is the dimer radical cation, $(TME)_2^{\bullet+}$, with a hyperfine coupling constant of 8.3 G. This result is consistent with the formation of dimer radical cations only at higher substrate concentrations. The samples with concentrations between 1 and 5% show that both species are present in different proportions.

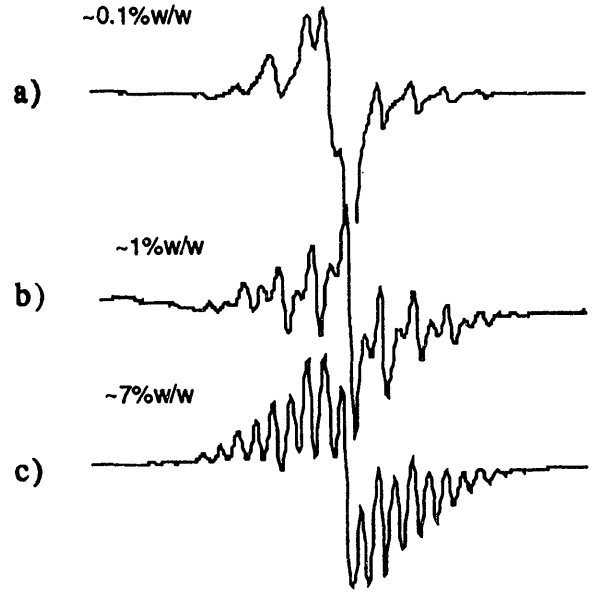

Figure I-5 EPR spectra of TME in ZSM-5 at 10 K a) 0.1%, b) ~1%, and c) 7% w/w TME.

EPR spectra recorded for 5% TME in silicalite S115 at 77 K and 110 K are shown in Figure I-6. The spectrum at 77 K is clearly due to the monomer radical cation. In the temperature range 90-110 K, the spectral change indicates the formation of a neutral radical through an ion-molecule reaction. At 110 K the dominant species in the spectrum is the trimethylallyl radical. Figure I-6c is a simulation of the spectrum of the trimethylallyl radical using the reported hyperfine parameters. Scheme I-1 depicts the probable reaction sequence that connects the three TME radical species observed in zeolites.

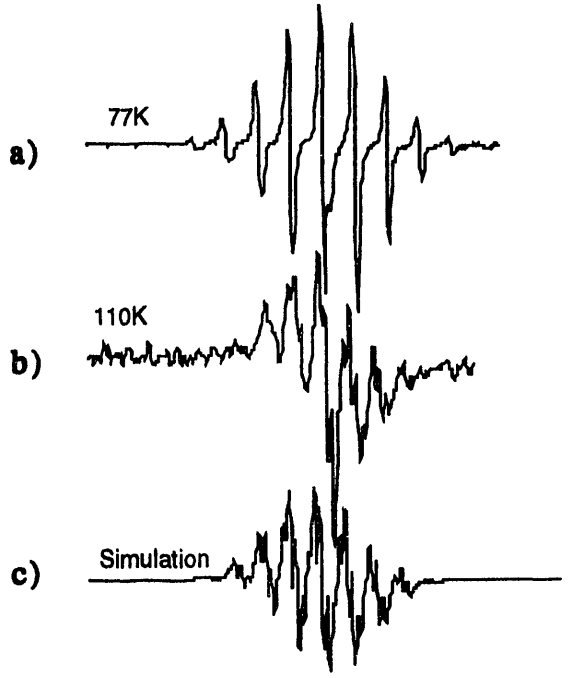

Figure I-6. EPR spectra of 5% w/w TME in silicalite a) at 77 K and b) at 110 K. c) is the simulated spectrum of the trimethylallyl radical.

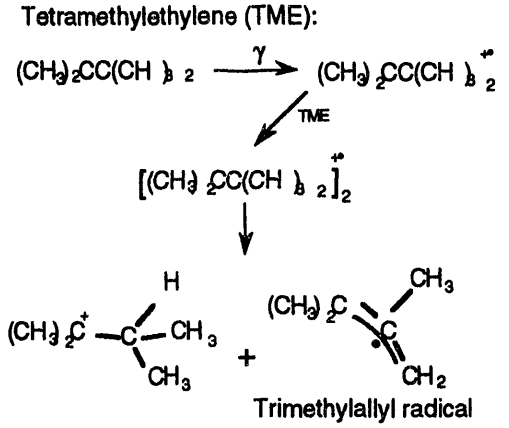

Scheme I-1

Figures I-5 and I-6 offer simple illustrations of the effects of changing the substrate concentration and changing the rate of diffusion via the temperature. However, things can get more complicated. For example, the dimer radical cation formation from the monomer was found to be reversible at low

temperatures. The exact behavior depended on the individual zeolite. Gamma irradiation of TME in Na-ZSM-5 and silicalite S115 gives rise to a dimer radical cation below 50 K, when the concentration of TME is >1% w/w. EPR spectra in the temperature range 50-110 K correspond to the monomer radical cation. Above ~110 K (the exact temperature depending on the TME concentration), only the neutral radical is observed in the case of silicalite, whereas in ZSM-5 both monomer radical cation and neutral radical are observed. EPR spectra in Na-Ω-5 show the coexistence of all three radical species in varying proportions at different temperatures.

Although it is difficult to unravel all of the matrix-specific chemistry, the variations in Si/Al content in these isomorphous zeolites lead to dramatic effects on the radical cation chemistry. These effects include some or all of the following: (1) sites that stabilize $TME^{\bullet+}$ to different extents, (2) different rates of diffusion of TME, (3) different activation barriers for the ion-molecule reaction to form trimethylallyl radical, (4) sites that facilitate dimer cation formation or stabilize $(TME)_2^{\bullet+}$ to different extents. Although it is possible to "tune" radical cation reactivity without a complete understanding of the factors that bear upon the chemistry, greater understanding would allow tuning to be done in a rational and efficient manner.

b. Radical Cation Transformations: Q and NBD

The radical cation chemistry of quadricyclane (Q) and norbornadiene (NBD) is of interest because of the potential utility of this system for energy storage. Previous studies in freon matrices found several conventional and photoinduced radical cation transformations. Scheme I-2 gives some of the transformations possible for the radical cations of Q and NBD. Despite vigorous study by several researchers, the reaction mechanism connecting the isomeric species remains elusive. We have undertaken the study of this system in zeolite matrices.

One barrier to solving the Q/NBD system has been the inability to unambiguously distinguish $Q^{\bullet+}$ and $NBD^{\bullet+}$ by EPR. Fast isomerization of $Q^{\bullet+}$ to $NBD^{\bullet+}$ may render the lifetime of $Q^{\bullet+}$ too short to allow observation. On the other hand, calculations indicate that the hyperfine coupling constants for $Q^{\bullet+}$ and $NBD^{\bullet+}$ should be very similar, and we have assumed this to be the case.

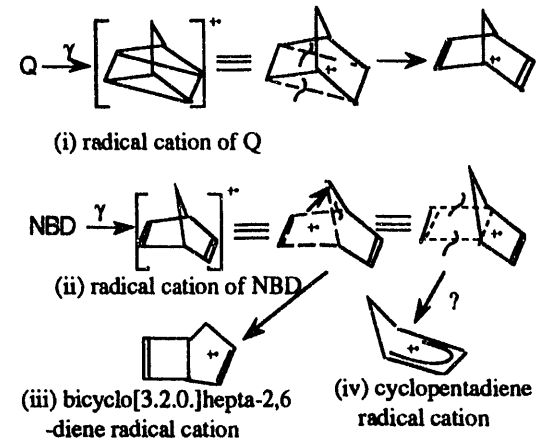

Scheme I-2

The EPR spectra for radical cations of Q and NBD (i and ii in Scheme I-2) were identical in all of the zeolites, with hyperfine coupling constants: a(4H) = 8.0 G and a(2H) = 3.0 G. They are labeled as (i) and (ii) in the central portions of the spectra in Figures I-7 through I-9. Figure I-7 shows the spectrum observed at 240K for Q (0.07% w/w) in silicalite-S115 (which has the same framework as ZSM-5 with Si:Al > 1000:1). The spectrum was unchanged from 77 K to 290 K.

The rearranged radical cation (iii) in Scheme I-2 was not observed in the zeolite with high Al content (Si:Al = 170:1), but it was observed in a narrow temperature range, 100-150 K, in the other three ZSM-5s (Si:Al = 400:1, 980:1, >1000:1) with varying intensity in comparison to the parent radical cation. Figure I-8 shows the EPR spectrum observed at 100 K for NBD (0.07% w/w) in ZSM-5 (400:1).

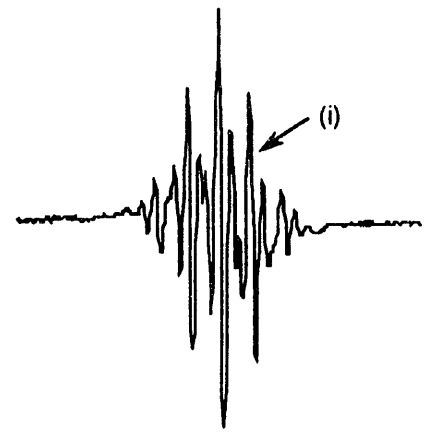

Figure I-7. EPR spectrum of quadricyclane (0.07% w/w) in silicalite at 240 K.

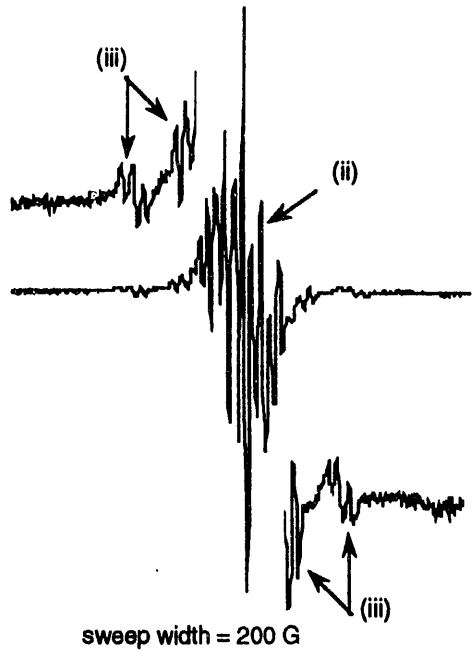

Figure I-8. EPR spectrum of norbornadiene (0.07% w/w) in ZMS-5 (400:1) at 100 K.

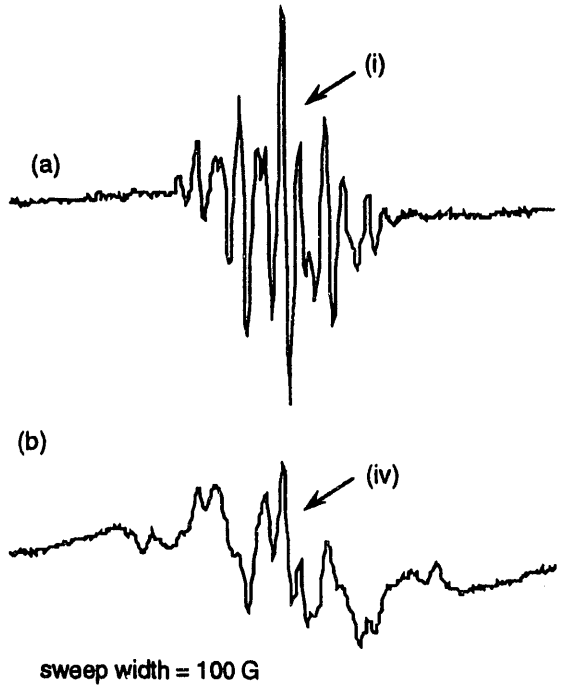

Figure I-9. EPR spectra of quadricyclane in ZSM-5 (170:1) at (a) 130 K and (b) 80 K after being warmed to 200 K.

Other species formed by rearrangement (including photoprocesses) and/or deprotonation of $Q^{\bullet+}$ and $NBD^{\bullet+}$ in freon matrices include the cycloheptatrienyl radical cation, toluene radical cation, 7-norbornadienyl radical, and bicyclo(3.2.0)heptadienyl radical. However, our preliminary results have not revealed any of these species in the zeolites. We have observed an additional species in ZSM-5 (170:1), a cycloreversion product, namely cyclopentadienyl radical cation (iv), at temperatures above 200 K. Figure I-9 shows (a) the spectrum of $Q^{\bullet+}$ and (b) the spectrum corresponding to the cyclopentadienyl radical cation. The persistence of the parent radical cation spectrum at 200 K eliminates the possibility of the formation of cyclopentadiene before the γ irradiation (i.e., by the catalytic effect of zeolite). A thorough study including the determination of the dependence on concentration, temperature, and time of equilibration (i.e., the time between the adsorption of the solute and the irradiation) is underway.

Our preliminary studies indicate that the diversity and variety of quadricyclane/norbornadiene chemistry in zeolite matrices are quite different than in the conventional freon matrices.

3. High-Energy Chemistry

A. D. Trifunac, D. M. Loffredo, A.-D. Liu

The use of intense UV lasers to induce condensed-phase photolysis opens new avenues for the examination of novel photochemistry. When energy input into a condensed-phase system is in excess of that needed to ionize a solute, what happens to the energy excess? Thus far, virtually no work has been done in delineating transient intermediates and products in such "high-energy" regimes. Due to the obvious parallels that can be drawn to radiolysis studies, we have embarked on a comprehensive examination of high-energy chemistry of aromatic molecules in hydrocarbon and alcohol solvents.

Ultraviolet photolysis of an aromatic molecule, AH, in a hydrocarbon or alcohol solvent (RH and ROH) is known to result in ionization, equation 4,

$$AH \xrightarrow{2h\nu} AH^{+}_{\bullet} + e^{-} \qquad (4)$$

but little is known about other chemical processes and the dependence of these processes on the energy input. Two other processes could result from the excess energy input: homolysis, equation 5, where a

$$AH \text{ ~~~> } AH^{**} \rightarrow A\bullet + H\bullet \quad (5)$$

neutral excited state undergoes homolytic cleavage to yield two radicals, and ion-molecule reaction of an excited radical cation, equations 6-8. It is known that ground state ions, $AH^{+}\bullet$, are quite stable in this regard.

$$AH \text{ ~~~> } AH^{*\bullet+} + e^- \quad (6)$$

$$AH^{*\bullet+} + RH \rightarrow A\bullet + RH_2^+ \quad (7)$$

$$AH^{*\bullet+} + ROH \rightarrow A\bullet + ROH_2^+ \quad (8)$$

In either instance, the aromatic radical, A•, is formed. Homolysis also yields hydrogen atoms. We can distinguish between these processes by careful examination of reaction products.

Product analysis. When an aromatic molecule in a hydrocarbon or alcohol solution is irradiated with intense UV photons from a pulsed excimer laser at 248 and 308 nm, the solute is consumed. Several products were observed, and their relative yields were determined. The products reveal the formation of the aryl radical (A•) and its subsequent reactions.

In the appropriately isotopically labeled solute and solvent (hydrocarbon), incorporation of H (or D) atoms in the aromatic molecule was detected. Results are given for naphthalene (Table I-1 and Scheme I-3). These data indicate that the naphthyl radical is formed and that its principal reactions are with the cyclohexane solvent, equation 9, resulting in a series of other

$$A\bullet + RH \rightarrow AH + R\bullet \quad (9)$$

products derived from solvent radicals. All of these products were detected and identified by GC-MS or HPLC-UV methods.

One sees from Table I-1 that the extent of product formation is different for different aromatic compounds. More products are formed with higher energy photons, and the product formation is greater in alcohol solutions (Scheme I-4).

This last observation is consistent with the ion-molecule reaction, equations 7 and 8, but not with neutral excited state homolysis, equation 5, as one would not expect significant solvent polarity and proton affinity influence on neutral excited state homolysis. However, the nature of the solvent should influence the ion-molecule chemistry.

Further evidence that neutral excited state homolysis cannot be important is obtained by examining the H_2 and HD yields. The hydrogen yield following photolysis of various aromatic hydrocarbons in cyclohexane is 20-40% lower than the H_2 yield following photolysis of cyclohexane alone—opposite to the trend predicted from the homolysis mechanism.

The H_2 production in cyclohexane is presumed to involve both neutral state homolysis and the loss of molecular hydrogen from the $c\text{-}C_6H_{12}^{+}\bullet$ radical cation to yield the olefin radical cation. Even though there is considerably more light absorption by the solute molecule, one does not completely eliminate solvent photolysis. Solvent-derived products, such as cyclohexene and bicyclohexyl, are observed with or without an aromatic substrate present. Cyclohexene is always the more abundant product, but the bicyclohexyl yield is considerably increased (Table I-2) when an aromatic solute is present. Previous workers have shown that if only the cyclohexyl radical were involved, then one would obtain a 1:1 ratio of cyclohexene to bicyclohexyl.

Table I-1. Product and isotope distributions after photolysis of perdeuterated polycyclic aromatic hydrocarbons in various solvents at 248 nm.[a]

substrate/solvent	parent ion	isotopic ion	Δ%[b]	% yield of cyclohexyl radicals[c]	% substrate consumed
naphthalene/cyclohexane	$C_{10}H_8$	$C_{10}H_7D$	0.1	10.9	43
naphthalene/cyclohexane(d12)	$C_{10}H_8$	$C_{10}H_7D$	8.0	11.0	41
naphthalene(d8)/cyclohexane	$C_{10}D_8$	$C_{10}HD_7$	7.9	11.4	44
naphthalene(d8)/cyclohexane[d]	$C_{10}D_8$	$C_{10}HD_7$	2.2	3.2	26
naphthalene(d8)/isopropanol	$C_{10}D_8$	$C_{10}HD_7$	8.6	-	-
p-terphenyl(d14)/cyclohexane	$C_{18}D_{14}$	$C_{18}HD_{13}$	4.7	-	-

[a]The samples consisted of 3.0 ml solution in a 1-cm path-length cell, saturated with SF_6. The concentration of each substrate was as follows: naphthalene, 4×10^{-4} M; p-terphenyl, 2×10^{-4} M.
[b]Δ% was determined by subtracting the relative abundance of the isotopic ion before irradiation from the relative abundance of the isotopic ion after irradiation, taking into account the contribution of ^{13}C isotopes.
[c]Determined by multiplying the yield of bicyclohexyl by four, and then dividing by the initial concentration of aromatic substrate (assuming bicyclohexyl yield is representative of the overall radical yield).
[d]Photolysis carried out at 308 nm.

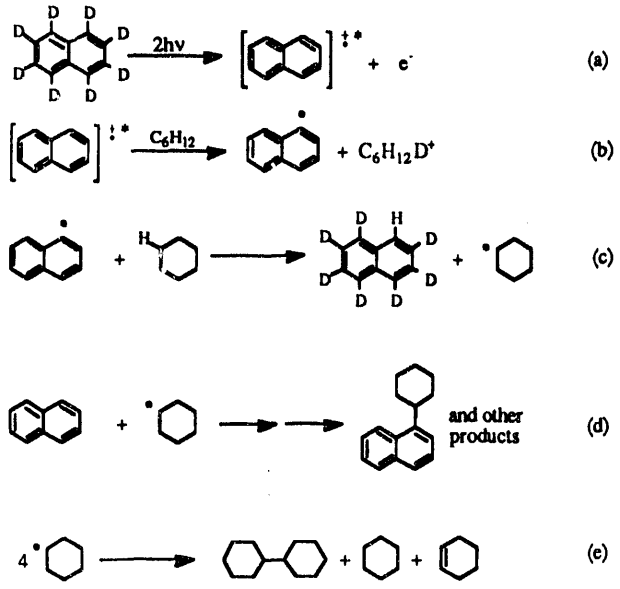

Scheme I-3. Aryl and cyclohexyl radical formation and subsequent reactions with isotopically labeled naphthalene.

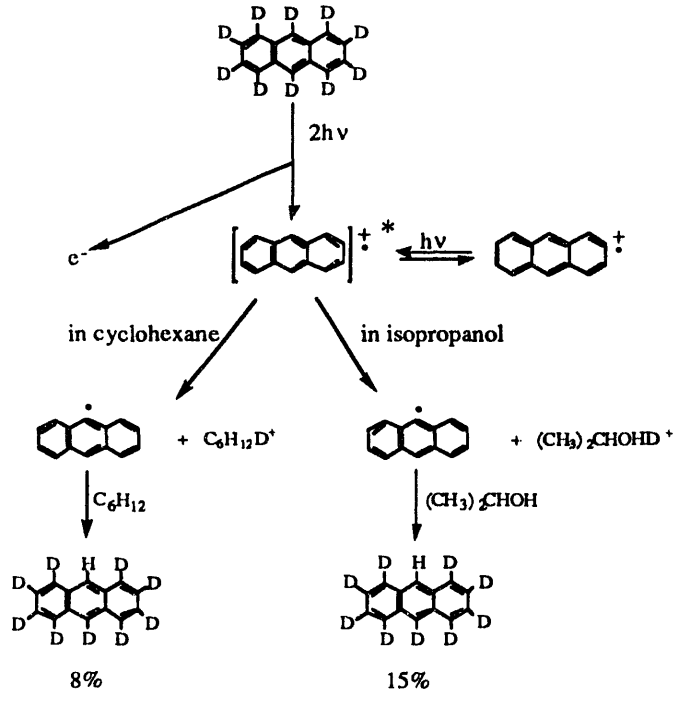

Scheme I-4. Aryl radical formation during flash photolysis (248 nm) of d_{10}-anthracene in cyclohexane or isopropanol.

If homolysis were the only pathway, photolysis of a perdeuterated substrate would result in the formation of a substantial amount of HD. For photolysis of d_{10}-anthracene in cyclohexane, 1.6 mM bicyclohexyl and 7.0 mM cyclohexene were formed. Assuming one product molecule formed per dihydrogen molecule, the maximum relative yield of HD in the H_2 + HD yield would be about 37%. Mass spectral data indicate a much lower value, merely 1.5%.

The effect of SF_6 on product formation is also indicative of an ion reaction, not excited state homolysis. SF_6 increases the yield of radical-derived products. Because electron scavenging reduces ion-electron recombination, it increases the yield of ion-molecule reactions (Table I-2). The effect of SF_6 on excited state homolysis would be exactly opposite; one would expect a decrease in the yield because SF_6 quenches the excited state.

Table I-2. Relative yields of bicyclohexyl from the photolysis of cyclohexane at 248 nm with and without naphthalene and SF_6.

	bicyclohexyl yield during photolysis of cyclohexane only	bicyclohexyl yields during photolysis of cyclohexane in the presence of naphthalene
no SF_6	5.3	4.3
SF_6	1.0	10.0

The degassed samples consisted of 3.0 ml solution in a 1-cm path-length cell. The naphthalene concentration was 1×10^{-3} M. Product yields are relative to the yield of bicyclohexyl in SF_6-saturated solvent alone (actual yield, $\sim 3 \times 10^{-5}$ M).

Flash photolysis and DC-conductivity studies. The transient optical absorption spectrum of $AH^{+}\bullet$ can be measured by nanosecond flash photolysis. The electron yield can be measured by conductivity in hydrocarbon solutions or by optical absorption in alcohols (Figure I-10).

In hydrocarbons, one observes that the yields of $AH^{+}\bullet$ and e^{-} diverge with increasing photon energy; the electron yield increases, but less $AH^{+}\bullet$ is formed at higher photon energies. The experiments in alcohol solutions indicate that, at high light intensities, the ratio, $e^{-}/AH^{+}\bullet$, can be quite large, as illustrated in Figure I-11 for anthracene/2-propanol photolysis.

These observations suggest the emergence of a three-photon process at high intensities. In other words, the initial radical ion formed by biphotonic ionization absorbs another photon to form an excited radical ion ($AH \xrightarrow{2h\nu} AH^{\bullet+} \xrightarrow{h\nu} AH^{*\bullet+}$), leading to even more products. Also, the product yields are qualitatively correlated with the larger $e^{-}_{sol}/AH^{+}\bullet$ ratios at high light intensity.

In conclusion, these studies indicate that multi-photon absorption can induce ion-molecule chemistry in aromatic molecules in hydrocarbon and alcohol solutions. It is not yet clear to what extent two- or three-photon processes are involved, and what the excited states of the aromatic radical cation $AH^{*\bullet+}$ are. What is clear is that a common pathway of chemistry opens with intense UV light for a variety of aromatic compounds in very different solvents, and that this pathway must involve ion-molecule reactions of an excited $AH^{*\bullet+}$ aromatic radical cation.

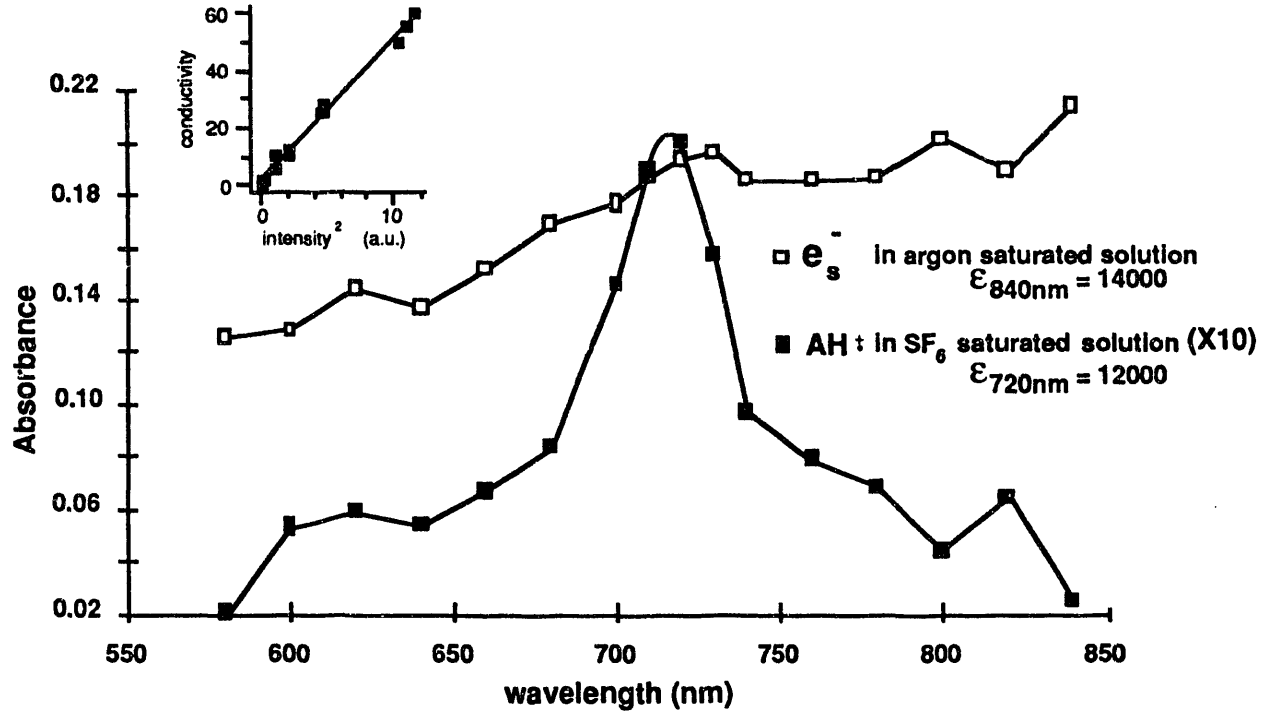

Figure I-10. Spectrum of solvated electrons and anthracene radical cations observed at 50 ns after 248-nm laser flash photolysis of 5×10^{-5} M anthracene in 2-propanol.

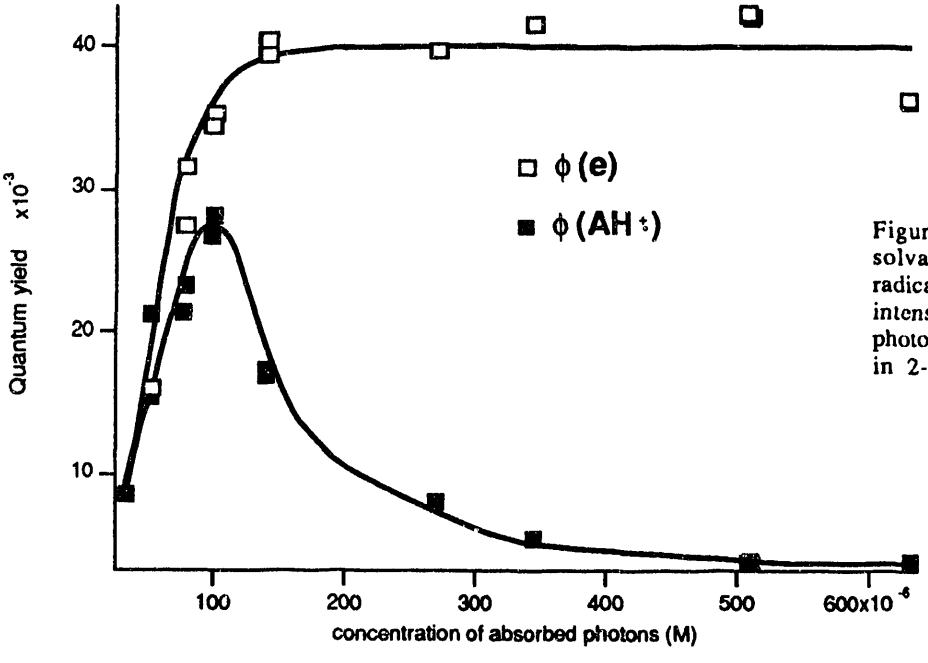

Figure I-11. Quantum yields of solvated electron and anthracene radical cation as a function of laser intensity during 248-nm laser flash photolysis of 5×10^{-5} M anthracene in 2-propanol.

4. Ions and Excited States in Radiolysis and Photolysis

M. C. Sauer, Jr., C. D. Jonah, A.-D. Liu, D. M. Loffredo, A. D. Trifunac

We have carried out experiments on the decay of ions and the formation of excited states in solutions of aromatic molecules in alkane liquids. One objective was to determine the ratio of excited states formed to solute anions recombined; the extent to which this is less than unity tells us the extent of transformation of solvent cations to species that cannot yield excited solutes. Another objective was to determine the ratio of solute triplet states to solute excited singlet states; this gives us a measure of the cross-recombination occurring in multiple-ion-pair spurs and therefore allows a comparison with predictions of the distribution of spur sizes made on the basis of other experimental and theoretical information. Our experiments provide the first determination of the triplet-to-singlet ratio as a function of time.

a. Ion-Recombination in Spurs

The nonhomogeneous kinetics of ion-recombination resulting from the radiolytic ionization of an alkane liquid pertain mainly to the time regime of 0-100 ns. The recombinations occur in single ion pairs and in multiple-ion-pair "spurs". For a single ion pair, the recombination is called "geminate", and will produce a singlet state product (whether electron or positive-ion scavenging has occurred or not) unless spin dephasing has occurred. Spin dephasing/evolution is generally expected to occur after tens of ns. For a multiple-ion-pair spur, cross-recombination events are expected to produce triplet state products 75% of the time. Measurement of the triplet yield in the first 10-20 ns is therefore of prime importance to assess the extent of cross recombinations.

Experiments to address this question have been completed with isooctane, cyclohexane, and n-hexane solutions containing 0.1 M naphthalene or biphenyl. The high concentration is advantageous for three reasons. First, the electrons, positive ions, and solvent excited states are captured by the solute in subnanosecond times, and the rates of triplet and singlet formation from one to tens of nanoseconds represent those from the spur recombinations. Second, more recombinations take place at early times, before spin dephasing is significant; and third, the excited state yields are larger, resulting in a better signal-to-noise ratio.

We measured the time profile of the optical absorbance of triplet naphthalene (^{3}N) following a 30-ps pulse, and converted the results to G values (number per 100 eV absorbed energy) by using the known absorptivity of ^{3}N. The time profile of the fluorescence from the first excited singlet state of biphenyl (^{1}BP) was measured and converted to a ^{1}BP formation curve by a simple mathematical procedure using the known fluorescence lifetime of ^{1}BP. This was converted to G(^{1}BP) on the basis of our previous measurements of G values of aromatic singlets. The derivatives of these G vs. time profiles were then calculated and plotted vs. time. The results are illustrated for isooctane solutions in Figures I-12 and I-13.

Values of d/dt taken from Figures I-12 and I-13, and from similar plots for cyclohexane and n-hexane, were used to calculate the fraction of triplet, $f_{triplet}(t)$ from 1-70 ns. $f_{triplet}(t)$ is the ratio of the rate of triplet formation at time t to the sum of the rates for singlet and triplet. It represents the probability of triplet formation in the ion recombination occurring at time t. The results are shown in Figure I-14.

There are three main features. (1) The formation of the triplet state and formation of the excited singlet state is equally probable when ion recombination occurs in the time regime 1-70 ns, with the following caveat: the values of $f_{triplet}(t)$ depend on the calibration factors used for both the singlet and triplet G-value scales; hence, the vertical scale could have an error of as much as 10-20%. (2) Within the experimental error, there is no tendency of $f_{triplet}(t)$ to increase with time. This finding indicates the absence of an appreciable effect of spin dephasing in the geminate pairs over the time regime 1-70 ns. (3) The values of $f_{triplet}$ for isooctane seem to be significantly higher than for cyclohexane and n-hexane. This result suggests that the known greater average separation between the geminate partners in isooctane is responsible, that is, that greater separation favors cross-recombination in multiple-ion-pair spurs.

Most of the values of $f_{triplet}(t)$ are in the range of 0.5 ± 0.1. This value can be compared with the results from cloud chamber measurements and theoretical calculations of the number of ion pairs per spur, as shown in Table I-3.

In Table I-3, it is assumed that N_s, and hence, $f_{triplet}$, is independent of t. The last two columns give the $f_{triplet}$ values for spurs of various sizes

(numbers of ion pairs) for two different theories (Magee and Brocklehurst). Column 2 gives the fraction of the total ion pairs that are created (by a high-energy electron) in spurs of the size indicated in column 1. The sum of the numbers in the last two columns is the resultant $f_{triplet}$. Our experimental values, 0.5 ± 0.1, are somewhat higher than the values of 0.39 and 0.45 from Table I-3, but are within experimental error.

In view of the possibility that an error in the relative scaling of the ^3N and ^1BP G values could have a significant effect on the value of $f_{triplet}$, another method has been used to derive the value of $f_{triplet}$ from experimental observations. The formation of ^3N has been measured with subnanosecond time resolution (approximately 0.3 ns) from 0.1-1000 ns, and the results have been fitted to a mechanism that takes into account the known reactions, with $f_{triplet}$ as a

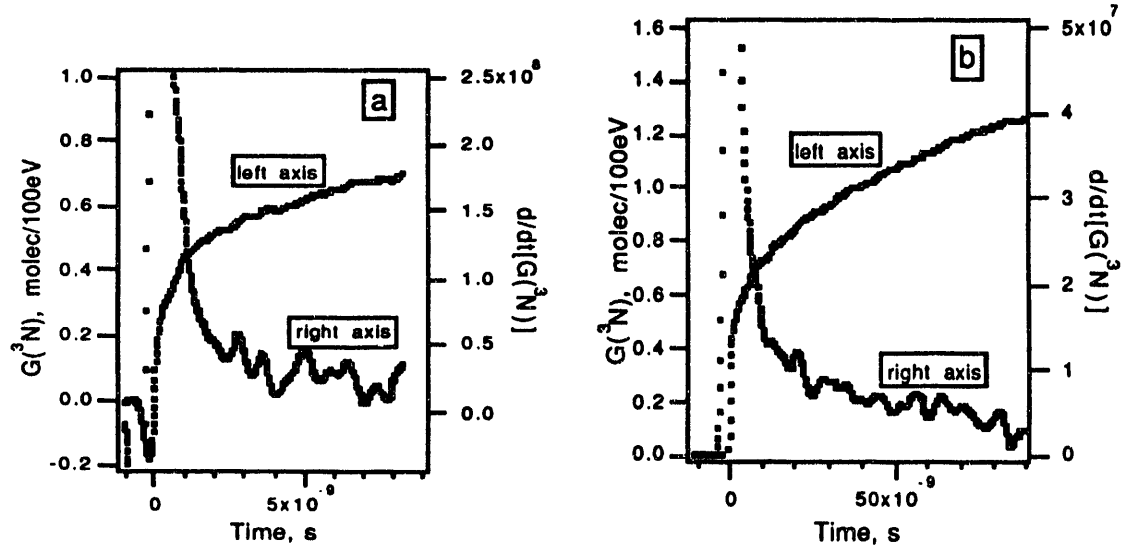

Figure I-12. $G(^3N)$ and d/dt of $G(^3N)$ vs. time for 0.1 M naphthalene in isooctane. Electron pulse: 30 ps, 5.4 krad. (a) 0-9 ns; (b) 0-85 ns.

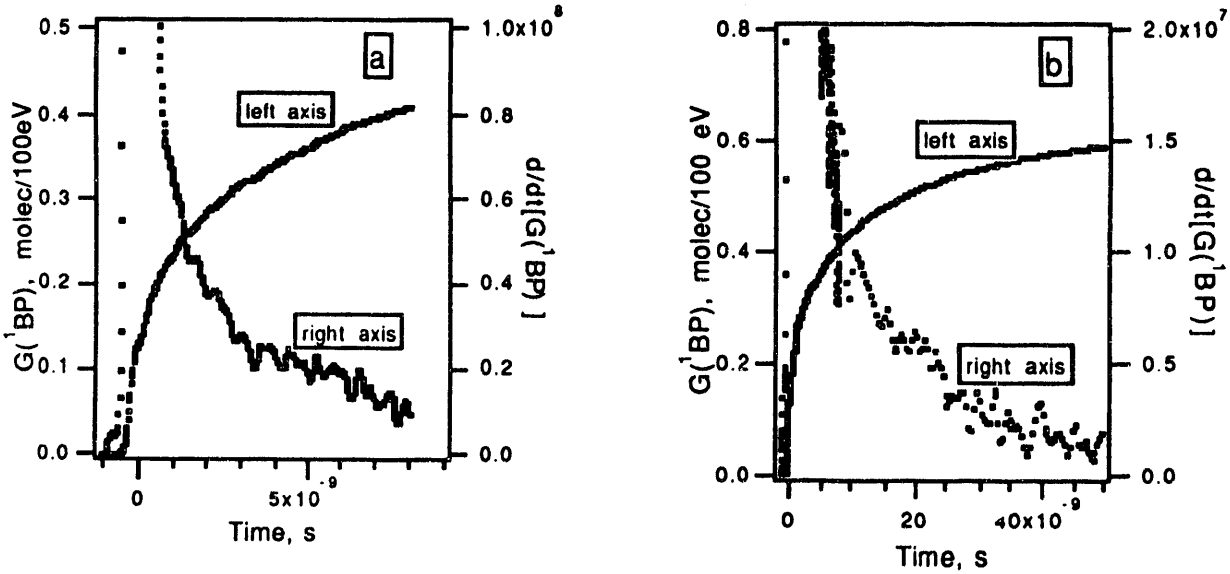

Figure I-13. $G(^1BP)$ and d/dt of $G(^1BP)$ vs. time for 0.1 M biphenyl in isooctane. Electron pulse: 30 ps, 4.0 krad. (a) 0-8 ns; (b) 0-50 ns.

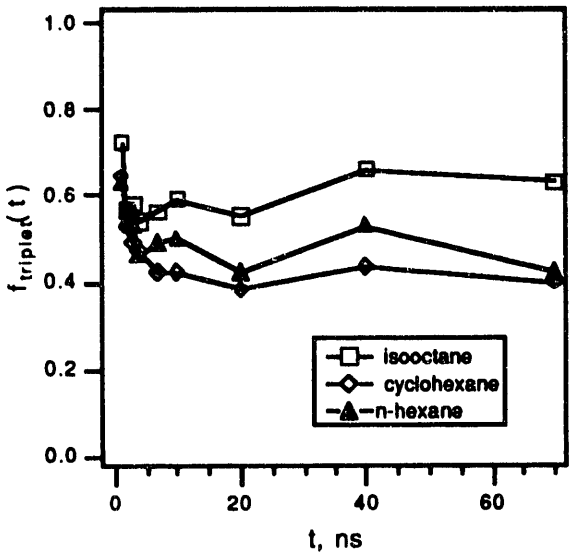

Figure I-14. Fraction of excited states formed at time t that are triplet; 0.1 M solutions of naphthalene or biphenyl in the indicated solvents.

fitted parameter. The experimental $G(BP^-)$ vs. time results are used to specify the rate of ion recombination. The long lifetime of the first excited singlet state of naphthalene (95 ns) makes this solute ideal for this analysis; the triplet observed in the first few tens of nanoseconds must originate mainly from ion recombination (rather than from intersystem-crossing from the singlet). The results for 0.1 M naphthalene in isooctane are shown in Figure I-15. The value of $f_{triplet}$ derived from this method is 0.52 ± 0.05, which is in good agreement with the values from the derivative analysis. Note that the quality of the fit was not improved by allowing $f_{triplet}$ to vary with time, also in agreement with the derivative analysis.

The analysis of $f_{triplet}$ in radiolysis that we have presented here is the most complete and decisive to date, and is the first to examine specifically the time dependence of $f_{triplet}$. The values of $f_{triplet}$ are consistent, within experimental error, with expectations based on analyses of the energy-deposition events in terms of spur-size distribution and cross-recombinations among geminate pairs.

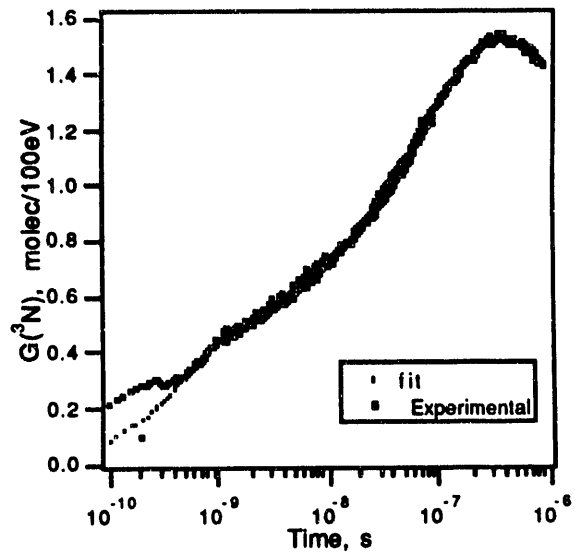

Figure I-15. $G(^3N)$ vs. time for 0.1 M naphthalene in isooctane; experimental and calculated results.

b. Anion Decay vs. Excited State Formation

In conjunction with the measurements of G values of solute excited singlet and triplet states described above, we also measured the G value of the biphenyl anion, BP^-, as a function of time for 0.1 M biphenyl in isooctane, cyclohexane, and n-hexane. Values of d/dt of $G(BP^-)$ were determined in the same

Table I-3. Predicted values of $f_{triplet}$.

n, ion pairs per spur	fraction (F) of ion pairs (Hummel)	singlets per recombin., N_s (Magee)	singlets per recombin., N_s (Brocklehurst)	$f_{triplet} = F \times (1 - N_s)$ (Magee)	$f_{triplet} = F \times (1 - N_s)$ (Brocklehurst)
1	0.30	1.000	1.000	0	0
2	0.17	0.500	0.625	0.085	0.064
3	0.10	0.400	0.500	0.060	0.050
4	0.05	0.357	0.437	0.032	0.028
>4	0.38	≅0.29	≅0.33	≅0.27	≅0.25
				sum = 0.45	sum = 0.39

manner as described for ^3N and ^1BP. Comparison of the rate of BP^- decay with total excited state (^3N + ^1BP) formation rate is shown in Figure I-16, where f_{ex} is the ratio of the sum of the rates of excited state formation divided by the rate of BP^- decay.

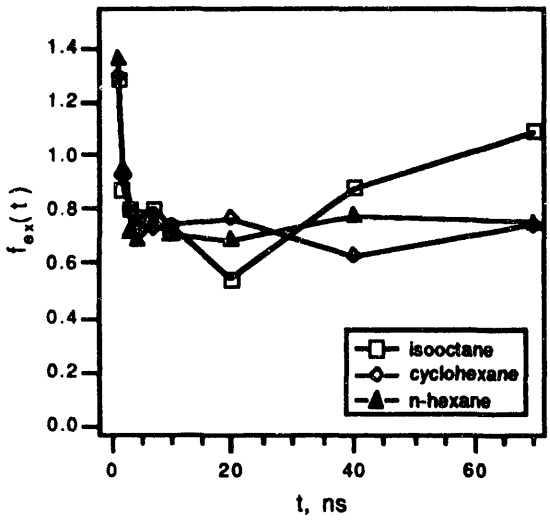

Figure I-16. The ratio of excited state formation to BP^- decay from 1-70 ns.

There are rather large variations in f_{ex} with time. The very high values at 1 ns could be the result of experimental errors, or they could indicate the transformation of solvent radical cations, prior to scavenging by the solute, to species unable to provide excited solute. The variations at later times, and differences between solvents, are most likely due to experimental error. The fact that most f_{ex} values are in the range of 0.7-0.9 means that 70-90% of the solute radical anions recombining in the 1-70 ns regime yield excited states. This finding means that 70-90% of the radical cations that recombine in the specified time regime cannot have been converted to a form that is unable to yield excited solute. Thus, at 0.1 M solute, only a small fraction of the solvent radical cations have undergone ion-molecule reaction with the solvent. This is not surprising, because at 0.1 M solute, transfer of charge from the solvent radical cation to the solute should be very rapid ($t_{1/2} < 0.7$ ns). Therefore, ion-molecule reactions of the solvent radical cation with the solvent to form cations unable to yield excited states, which are about an order of magnitude slower, do not consume a large fraction of the solvent radical cations.

c. Formation of Aromatic Radical Cations in Alcoholic Solutions; the SF_5· Radical as an Oxidizing Species

We have determined that aromatic radical cations are formed in large yields in the pulse radiolysis and laser flash photolysis of SF_6-saturated alcoholic solutions of aromatic molecules. Intense, long-lived absorptions are observed when SF_6 is present. The rate of formation of the absorption is proportional to the concentration of the aromatic molecule. As an example, Figure I-17 shows the spectra, at three times after the laser pulse, observed for SF_6-saturated 5×10^{-4} M anthracene in methanol using 308-nm laser flash photolysis. The 720-nm absorption corresponds to the known absorption maximum for the anthracene radical cation. The spectrum labeled 20 ns (essentially determined during the laser pulse) consists of the first excited singlet state of anthracene (600 nm), the anthracene radical cation (720 nm), and a broad underlying absorption due to the steady-state concentration of solvated electrons.

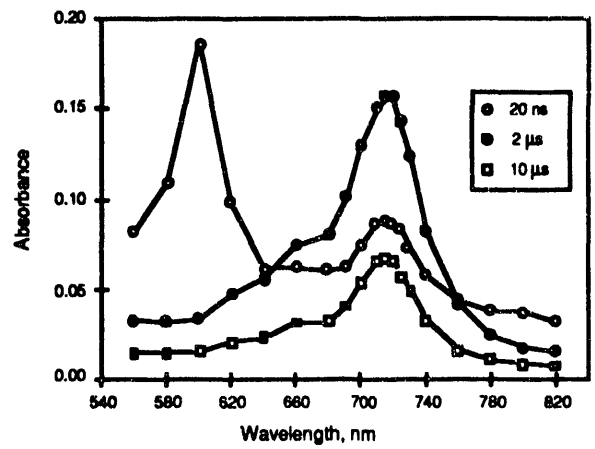

Figure I-17. Absorption spectra for 308-nm laser flash-photolysis of SF_6-saturated 5×10^{-4} M anthracene in methanol.

The slow formation (Figure I-18) occurring over about 800 ns was analyzed; the pseudo-first-order rate constants obtained were linear with [anthracene], yielding a rate constant of 8×10^9 M^{-1} s^{-1} for formation of the anthracene radical cation.

The absorption of the anthracene radical cation in the case of pulse radiolysis of SF_6-saturated 5×10^{-4} M anthracene in 2-propanol is shown in Figures I-19 and I-20.

In pulse radiolysis (Figure I-20), the radical cation is formed only by the "slow" process, which is

thought to be the reaction of $SF_5\cdot$, which results from the dissociative capture of a solvated electron by SF_6, with the aromatic molecule.

The G values and rate constants in Table I-4 indicate that the efficiency of oxidation of the aromatic molecules by $SF_5\cdot$ depends strongly on their ionization potentials and the solvent polarity. $SF_5\cdot$ appears to react with the aromatic molecules via two different pathways, one of which forms the aromatic radical cation and the other of which leads to unidentified products.

Further study will be needed to reveal key details of primary and secondary processes initiated by the UV irradiation or ionizing radiation in the condensed phase. The formation of long-lived aromatic radical cations in alcohols by laser flash photolysis and pulse radiolysis provides a convenient method to generate the aromatic radical cations and enables the study of their properties and reactions in the liquid phase at room temperature. A systematic investigation of the formation of aromatic radical cations by laser flash photolysis and pulse radiolysis with other important aromatic molecules and different electron scavengers in different solvents will make it possible to delineate the energy dependence of these reactions and to assign the role of the solvent in the reactions.

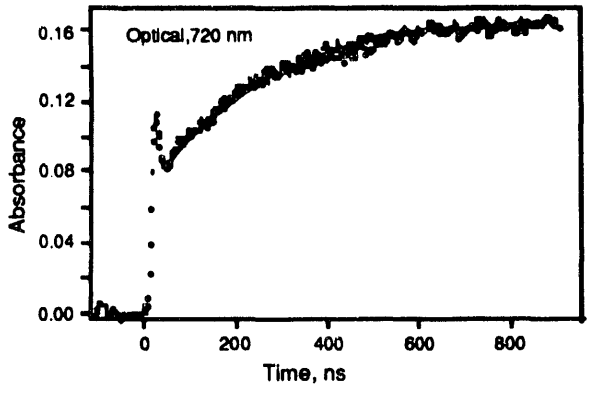

Figure I-18. Absorption at 720 nm vs. time for 308-nm laser flash photolysis of SF_6-saturated 5×10^{-4} M anthracene in methanol.

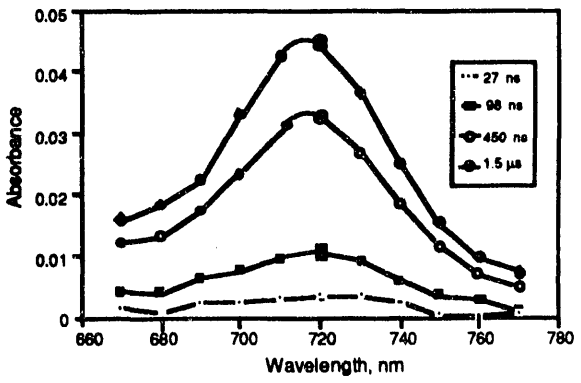

Figure I-19. Absorption spectra at four times following an electron pulse (1.8 krad dose per pulse) in SF_6-saturated 5×10^{-4} M anthracene in 2-propanol.

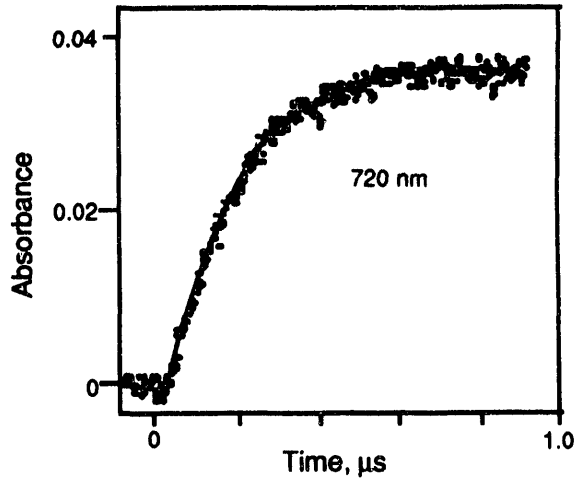

Figure I-20. Time profile at 720 nm following an electron pulse (1.8 krad dose per pulse) in SF_6-saturated 5×10^{-4} M anthracene in 2-propanol.

Table I-4. G-values and rate constants derived from the formation of aromatic radical cations in the pulse radiolysis of SF_6-saturated 2-propanol and methanol solutions.[a]

solute	IP (eV)	λ_{max} (nm)	ε (M^{-1} cm^{-1})	G (per 100 eV) 2-propanol	G (per 100 eV) methanol	10^{-9} k (M^{-1} s^{-1}) 2-propanol	10^{-9} k (M^{-1} s^{-1}) methanol
perylene	7.0	540	3.5×10^4	1.74	—	4	—
anthracene	7.5	720	1.2×10^4	1.72	—	8	8[c]
hexamethylbenzene	7.9	500	2.33×10^3	0.56	4.26	2	1.7
naphthalene	8.1	690	2.70×10^3	<0.1	0.44[b]	—	—

[a]IP is the gas-phase ionization potential of the aromatic molecule from the literature. λ_{max} is the absorption maximum of the solute radical cations. ε is the molar absorptivity of the solute radical cations from the literature. [b]This value was obtained at 0.01 M naphthalene; G is approximately proportional to [N]. [c]Measured by laser flash photolysis.

B. The Role of Solvent in Chemical Reactivity

A. D. Trifunac, D. M. Bartels, C. D. Jonah, Y. Lin, K. H. Schmidt, P. Han, C. Romero, E. Roduner

1. Reaction of H Atoms with Benzene in Water *D. M. Bartels, E. Roduner*

Solvent effects on chemical reaction rates have been investigated in detail for many years and general trends are understood for many reaction types in terms of dielectricity and ionic strength of the medium. The primary interest is the extent to which a given solvent, depending on its dielectric properties and molecular structure, might enhance or retard particular types of reaction. The transition state theory of reaction rates is generally invoked to understand solvent effects, in terms of "stabilization" or "destabilization" of reactants or products or a postulated transition state. A fundamental and largely untested assumption is made in the application of transition state theory to reactions in solution. This is the assumption that equilibrium thermodynamics applies to the transition state as well as to the reactants and products. In view of the highly transient nature of the transition state configuration, it is questionable that a solvent would have time to fully equilibrate about the transition state. In this case, correlation of reaction rates with equilibrium solvent properties may be based on a shaky theoretical foundation.

To investigate this issue, we undertook a study of the addition reaction of hydrogen isotopes to benzene in aqueous solution. Reliable data for this reaction in the gas phase are available, and a study of the analogous light muonium atom ($\mu^+...e^-$) reaction with benzene in several solvents has also been published. In the gas phase, the reaction of H with benzene occurs by addition, with a negligible amount of abstraction at temperatures below 1000 K. The reaction is one of the few simple hydrogen additions that are significantly activated. Addition of the light muonium atom (mass one-ninth of H) has a rate considerably enhanced by tunneling through the barrier, as evidenced by a much lower activation energy and lower frequency factor. Our invention of the EPR-based free induction decay attenuation method makes feasible a study of the H- and D-atom reactions with benzene simultaneously in the same aqueous solvent environment. The results allow a test of the transition state theory assumptions for this system. As we describe below, the results suggest that reactions of H and D may occur with nearly complete hydration of the transition state, but the reaction of Mu must occur too quickly for the water to equilibrate.

ESR measurement of the H-atom reaction rate by the FID attenuation method was chosen because of its simplicity, and the ability to measure H and D reactions simultaneously. Figure I-21 shows a representative example of a scavenging plot of FID attenuation rate vs. benzene concentration. The slope of the plot gives directly the H (or D) atom scavenging rate. The data were obtained with a mixture of 10% H_2O/90% D_2O, so that H and D atoms were both observed in the same experiment. The different slopes show clearly that there is an isotope effect that favors the reaction of H over that of D. Furthermore, there is a small but significant difference in the intercept of the two lines. Inasmuch as H and D data points were obtained alternatingly with the identical solution, the 8.6% larger value of the intercept shows that H is slightly more efficient in second-order spin exchange processes. This fact indicates that diffusion is slightly faster for H than for D.

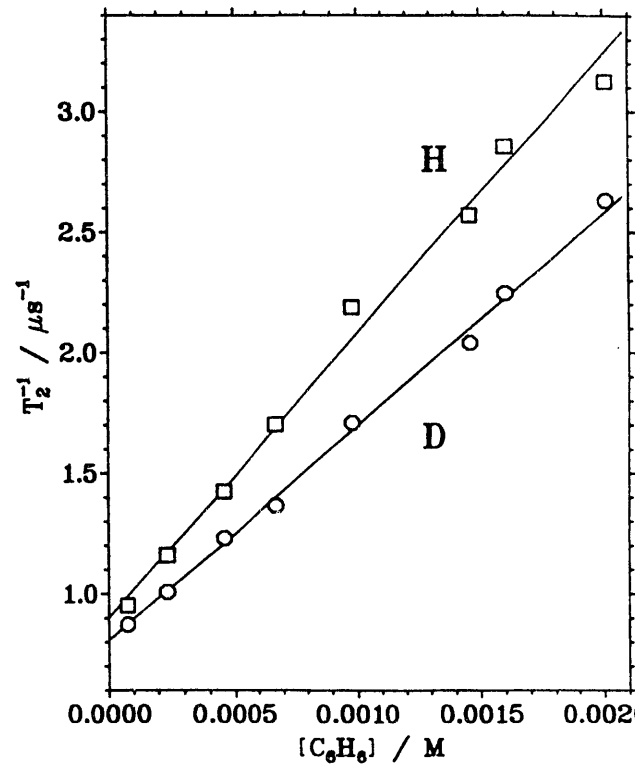

Figure I-21. Inverse relaxation time as a function of benzene concentration for H and D in a mixture of 10% H_2O/90% D_2O at 297.5 K.

The temperature dependence of k_H is displayed in an Arrhenius plot in Figure I-22 (open symbols). There is no systematic deviation between the points obtained in neutral solution with t-butanol scavenger (squares) and those measured in acidic solution with methanol scavenging (crossed squares). The points for H in the H_2O/D_2O mixture lie on the same line, but those representing k_D are clearly lower. There is a slight curvature, but the average Arrhenius parameters are E_a = 19.1 kJ/mole and log (A/sec) = 12.34 (full line in Figure I-22). The activation energy is within error the same in aqueous solution as in the gas phase. The enhanced rate constant in solution is reflected almost entirely by the larger frequency factor, A(aq)/A(g) = 54.

Transition state theory gives the rate constant for bimolecular reactions as equation 10:

$$k = q{\cdot}T{\cdot}\exp\left(\frac{\Delta S^{\neq}}{R}\right){\cdot}\exp\left(\frac{-\Delta H^{\neq}}{RT}\right), \qquad (10)$$

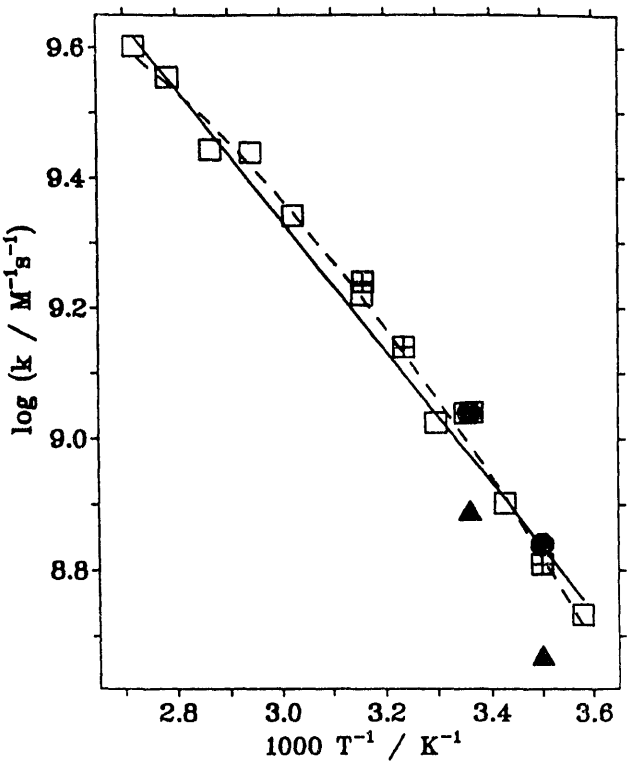

Figure I-22. Arrhenius plot of the rate constant for the reaction with benzene. H in H_2O (open squares, crossed where methanol was used to scavenge hydroxyl radicals), H (filled circles), and D (filled triangles) in a mixture of 10% H_2O/90% D_2O. Normal Arrhenius (full curve), modified with heat capacity term (broken curve, see text).

where q•T includes universal constants and has the units of k. This may lead to a curved Arrhenius plot, in particular when activation entropy and enthalpy are temperature dependent. Assuming a constant heat capacity difference between reactants and transition state and using standard thermodynamics, we obtain equation 11,

$$\ln k(T) = \ln(q{\cdot}T_o) + \frac{\Delta S_o^{\neq}}{R} + \left(\frac{\Delta C_p^{\neq}}{R} + 1\right)\ln\left(\frac{T}{T_o}\right) - \frac{\Delta H_o^{\neq} + \Delta C_p^{\neq}(T-T_o)}{RT}, \qquad (11)$$

where $\ln(q{\cdot}T) + \frac{\Delta S_o^{\neq}}{R}$ is the natural logarithm of the Arrhenius frequency factor at T_o. The broken line in Figure I-22, a fit of the experimental data to equation 11, is clearly a better representation of the experimental points than the straight line.

For interpretation of the solvent effects on the reaction rate we compare the reaction in the gas phase with that in solution as in Scheme I-5:

$$\begin{array}{lccccc} \text{Gas:} & H & + & C_6H_6 & \xrightarrow{k_H(g)} & [C_6H_6{\cdots}H]^{\neq} \\ & \downarrow\Delta G^{H}_{solv} & & \downarrow\Delta G^{C_6H_6}_{solv} & & \downarrow\Delta G^{\neq}_{solv} \\ \text{Solution:} & H & + & C_6H_6 & \xrightarrow{k_H(aq)} & [C_6H_6{\cdots}H]^{\neq} \end{array}$$

Scheme I-5

Based on transition state theory, equation 10, the enhancement due to solvation is given by equation 12:

$$\frac{k_{(aq)}}{k_{(g)}} = \frac{K^{\neq}_{(aq)}}{K^{\neq}_{(g)}} = \exp\left(\frac{-\Delta G^{\neq}_{solv} + \Delta G^{C_6H_6}_{solv} + \Delta G^{H}_{solv}}{RT}\right) \qquad (12)$$

The solubility of benzene in water is well established as a function of temperature, and has been critically reviewed. The solvation properties of the transition state are, of course, not known, but may be estimated by averaging the results for benzene and for 1,4-cyclohexadiene. Previously, the solvation property of the hydrogen atom has been estimated by averaging the free energy of solvation of H_2 and of He. We propose to use the values of H_2 alone for the reason outlined here. The solvation enthalpy is governed largely by dispersion forces and is therefore a strong function of solute polarizability. The polarizability of

H atoms (alpha = 8.7×10^{-31} m^3) is much closer to that of H_2 (7.9×10^{-31} m^3) than to that of He (2×10^{-31} m^3). The entropy of solvation is a large negative number for all noble gas atoms and small molecules (46.7 J/mol•deg for H_2 at 298 K, nearly the same number as for benzene and cyclohexadiene). Assuming that the entropy of solvation is the same for H as for H_2, we conclude that the free energy of solvation of atomic hydrogen is approximated well by that of molecular hydrogen.

The predicted values of k(aq)/k(g) based on equation 12 and the strategy outlined above are compared with experiment (squares) in Figure I-23 (solid line). The agreement is striking in that the experimental points fall only about 10% short of the prediction. Also shown (broken curve) is the predicted behavior based on the approximation (found to apply to muonium reactions in previous studies) that the benzene molecule and the transition state are sufficiently similar with respect to solvation so that the corresponding free energies cancel. In that case, the enhancement factor is given solely by the free energy of solvation of the hydrogen atom, equation 13:

$$\frac{k_{(aq)}}{k_{(g)}} \equiv \exp\left(\frac{-\Delta G^{H}_{solv}}{RT}\right) = L^{-1} \qquad (13)$$

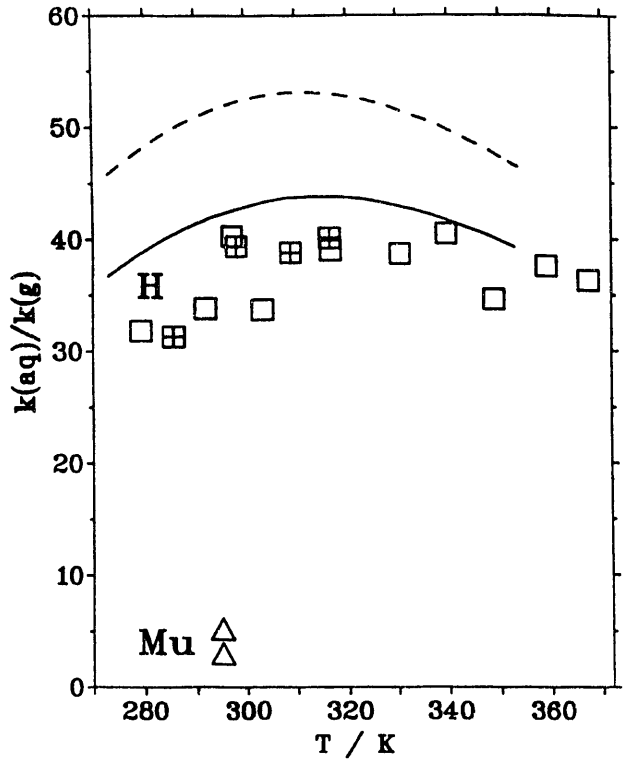

Figure I-23. Enhancement factor of the rate constant in aqueous solution over the corresponding gas-phase value. The broken line gives the predicted curve based on ΔG_{hyd} of H_2 alone, equation 13, and the solid curve represents the full equation 12.

Comparison of the two lines in Figure I-25 demonstrates that 80% of the enhancement effect can be ascribed to solvation of the H atom. The remaining deviation between the best prediction and the experiment can easily be ascribed to experimental error and the approximations made in estimating the solubility of H and of the transition state. It should be noted, however, that the curve is shifted to much higher values and thus far from our experimental data for k(aq)/k(g) when H solvation is approximated by He instead of by H_2.

The preceding analysis suggests that essentially the full solvent enhancement effect for the reaction of H with benzene in water is explained in terms of equilibrium solubility of reactants and transition state. The same conclusion has been reached previously for the reaction of benzene with muonium in methanol and in hydrocarbon solution where the enhancement was less drastic. This implies that the transition state is also fully equilibrated for the muonium addition in these less polar solvents. However, the muonium reaction in water is different, as indicated by the points in Figure I-23. The solvent enhancement is only a factor of four rather than the predicted factor of 40. The question then arises, why is the muonium reaction rate enhanced less than the rate for H and D in aqueous solution?

The negative solvation entropies indicate that both the hydrogen atom and the benzene molecule reside in "clathratelike" hydrophobic cages. The two cages must merge prior to the reaction. In order that advantage can be taken of the full free enthalpy of solvation, there has to be complete relaxation of the solvent around the transition state on the time scale of barrier crossing. Comparison between the experimental and predicted values in Figure I-23 indicates that this is the case for H but suggests that it may not be so for the light muonium atom (atomic mass 0.11). Because the addition reaction is exothermic and the transition state early, the effective mass moving along the reaction coordinate will essentially be that of the adding hydrogen isotope. Based on the mass dependence of the imaginary frequency that describes the degree of freedom corresponding to the reaction coordinate, the light Mu atom is expected to move

over or through the barrier about three times faster than H. This motion is effectively a low-frequency vibration that occurs on a time scale similar to the libration of the water molecules. It is thus conceivable that we have a borderline case in water, where relaxation of the cage, involving reorientation of water dipoles, is nearly complete for H but too slow for Mu. Only the high-frequency (electronic) part of the solvent polarizability would then be able to follow Mu through the transition state. Because in water this is only a fraction of the total dielectric response, solvation of the transition state would be incomplete and the assumption of equilibrium between reactants and transition state not appropriate.

2. Mechanism of the $(H)_{aq} \rightleftharpoons (e^-)_{aq}$ Interconversion *D. M. Bartels and P. Han*

The hydrated electron is arguably the most important transient species in the radiolysis of water, and is certainly the most interesting and unusual. In years past, investigations in this group have focused on the dynamics of electron energy loss as the electron becomes trapped and then fully solvated. More recently, we have addressed the equilibrium thermodynamic and transport properties of the fully solvated species, to contrast the prototypical quantum ion with more common classical species. The thermodynamic properties of the hydrated electron were deduced from the highly unusual reaction of H or D with OH^-/OD^-, equation 14, in mixtures of light and heavy water.

$$H\,(D) + OH^-\,(OD^-) \underset{k_{-14}}{\overset{k_{14}}{\rightleftharpoons}} (e^-)_{aq} + H_2O\,(D_2O) \quad (14)$$

A very old, but still unresolved, important question concerns the mechanism of this $(H)_{aq} \rightleftharpoons (e^-)_{aq}$ interconversion. Is the reaction (particularly the back reaction) an electron transfer similar to most other reactions involving $(e^-)_{solv}$, or does the equilibrium involve a proton transfer? If it involves proton transfer, ideas about the mechanism of other hydrated electron reactions may need to be modified. Our goal in the further investigation of equilibrium 14 has been to resolve this question.

In Figure I-24 we display new results for the H + OH^- reaction in light water that were obtained with improved methodology and equipment. Superimposed is the least-squares Arrhenius fit obtained in our *previous* work. Clearly, the average result has not changed significantly, but there is a significant improvement in the precision. Least-squares analysis of the new FID attenuation data gives $A = 1.32 \pm 0.17 \times 10^{14}\ M^{-1}\ sec^{-1}$, and $E_a = 38.36 \pm 0.32$ kJ/mole.

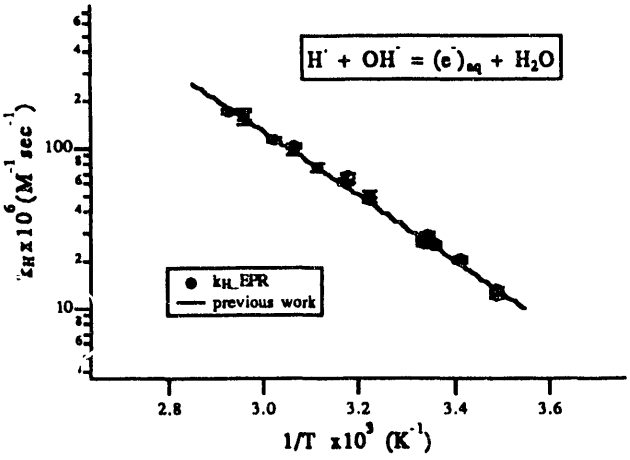

Figure I-24. Arrhenius plot for reaction 14 (light water), as measured by the FID attenuation method. The solid line is the least-squares result reported in previous work.

In a recent publication dealing with the hydrated electron thermodynamics, Schwarz raised the possibility that the FID attenuation method may overestimate the rate of reaction 14 if there is also a "base-catalyzed" chemical exchange process occurring. That is to say, H atoms may combine with OH^- to form an intermediate H_2O^-, which dissociates rather than proceeding to the $(e^-)_{aq}$ product. If the "other" proton can emerge from the intermediate to reform the H atom, the proton-exchange event would be indistinguishable from a forward reaction event, so far as FID attenuation is concerned. To examine this possibility, we performed optical transient absorption experiments to measure the rise of $(e^-)_{aq}$ absorption due to reaction 14.

Figure I-25 displays a sample of the data for a 0.0467 M NaOH solution at 49.6 °C. The absorption increase seen in the first microsecond(s) of Figure I-25 is the signal of interest. The second-order decay of the signal was slow (half-life at least 10 times longer than $1/k_1[OH^-]$), but not negligible on the timescale of reaction 14. We approximate the important kinetic processes as in Scheme I-6.

$$(e^-)_{aq} \xrightarrow{k_d} \text{products}$$

$$(H)_{aq} \xrightarrow{k_d} \text{products}$$

$$(H)_{aq} \xrightarrow{k_g} (e^-)_{aq}$$

Scheme I-6

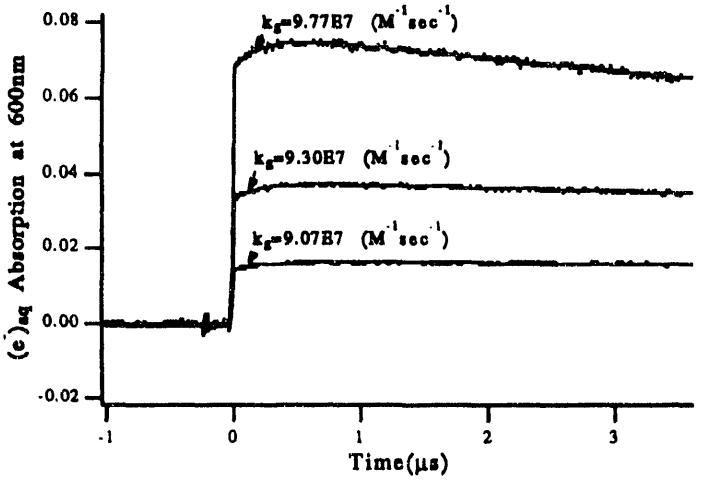

Figure I-25. Hydrated electron absorption following pulse radiolysis of 0.01 M Na_2SO_3, 0.046 M NaOH solution at 49.6 °C in triply distilled heavy water. Three different radiolysis doses of ca. 400, 200, and 100 rads to the same solution are shown.

The initial slow rise and roughly the first one-quarter to one-third of the subsequent decay were fit to the corresponding first-order growth/first-order decay function, equation 15,

$$A(t) = A_0 [(C+1) \exp(-k_d t) - C \exp(-k_g t)]$$

$$C = f_H \, k_d/(k_d + k_g) , \qquad (15)$$

where k_g is the rate of growth, k_d is the rate of decay, f_H is the ratio of yields $G(H)/[G(H) + G(e^-_{aq})]$ immediately after the pulse, and A_0 is the initial absorption. As indicated in Figure I-25, the values of k_g extracted from this analysis proved to be slightly dose-dependent, and 5-15% larger than the k_{12} rate constants derived in the EPR experiments. The values of k_g were plotted vs. A_0, and the (zero dose) intercept of the plot was taken for the "best" experimental estimate of k_{12}.

Results of the optical absorption experiment for light water are plotted in Figure I-26 together with the least-squares result of the EPR experiments. The good agreement of the two methods makes it clear that a correct result has been obtained, and *no chemical-exchange process contributes to the FID decay.* This conclusion is significant in the following discussion of the reaction mechanism.

EPR and optical experiments were carried out in heavy water, and the combined results are plotted in Figure I-27. The FID attenuation experiment in heavy water was far more difficult because of the roughly four times smaller initial CIDEP signal of D atoms in D_2O. This required larger radiolysis pulses and much longer signal averaging to achieve equivalent results. On the other hand, the optical experiment was no more difficult in heavy water. As is obvious from Figure I-27, both methods agree to within their signal-to-noise limitations. The global least-squares fit gives $A = 1.19 \pm 0.22 \times 10^{14}$ M^{-1} sec^{-1}, and $E_a = 38.16 \pm 0.47$ kJ/mole for the $D + OD^-$ reaction. The global least-squares result for the *light water* $H + OH^-$ reaction is also superimposed as a solid line in Figure I-27. It is clear from this comparison that

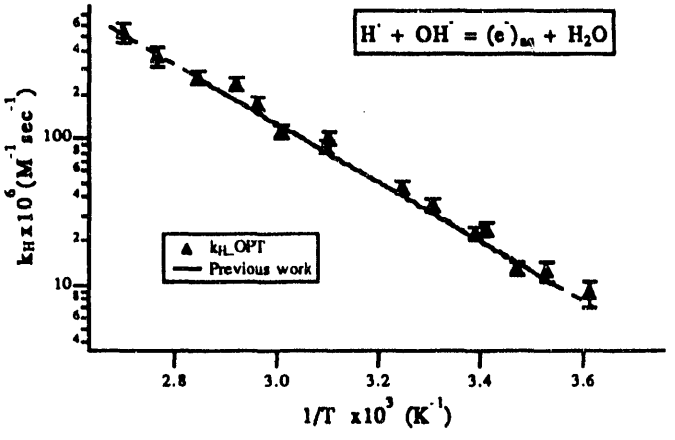

Figure I-26. Arrhenius plot for reaction 14 (light water), as determined optically by the rise of $(e^-)_{aq}$ absorption. The solid line is the least-squares result obtained by the FID attenuation method.

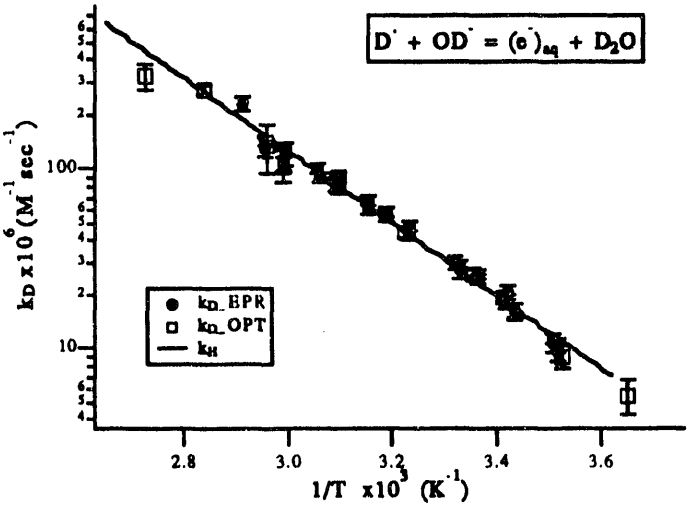

Figure I-27. Arrhenius plot for reaction 14 (heavy water). Both FID attenuation and optical experiments are indicated. The solid line is the least-squares result obtained in the *light water* reaction, for purposes of comparison.

there is very little H/D isotope effect on the rate of reaction 14, and within the precision of our measurements, we are unable to clearly define any differences in activation energy and pre-exponential factors. This result contrasts with the order-of-magnitude isotope effect favoring H_2O over D_2O in reaction -14.

With these experimental results in hand, we proceed now to consideration of the reaction mechanism. The encounter of the H atom and hydroxide ion can most easily be envisioned in terms of hydroxide diffusion by proton transfer to a hydrophobic H-atom cavity. The proton-transfer diffusion mechanism will bring the hydroxide into a configuration where the central oxygen and its three strong H bonds form a side of the H-atom cavity. At this point, a sufficiently high-energy collision of the H atom and the oxygen of the hydroxide ion, together with appropriate solvent rearrangement, can form a water molecule and liberate an electron.

The question we wish to address is how this interconversion of $(H)_{aq}$ and $(e^-)_{aq}$ is accomplished, or in other words, what is the nature of the transition state in equilibrium 14? The simplest postulate considers a discrete, H_2O^-, intermediate as shown in equation 16.

$$(H)_{aq} + (OH^-)_{aq} \rightleftharpoons (H_2O^-)_{aq}^{\dagger} \rightleftharpoons H_2O + (e^-)_{aq} \quad (16)$$

Starting from the left side of the equilibrium, one envisions a H atom in a hydrophobic cavity, with the OH^- ion strongly hydrated and incorporated into the hydrogen-bond network. The encounter occurs when the OH^- diffuses to become part of the wall around the H atom. One postulates that the H atom adds to the OH^- ion, forming a transient H_2O^- ion, which then ionizes to give H_2O and an electron that becomes solvated. Starting from the right side of the equilibrium, the electron must somehow become localized on a single H_2O molecule, giving the H_2O^-, which then fragments to give the H and OH^- product.

The simple picture can be rejected based on the results obtained in this study. Any transition state or intermediate that suggests an equivalence of protons, for example, the $(H_2O^-)^{\dagger}$ formulation, is incompatible with the observation that the overall forward rate (measured optically) is exactly equal to the (EPR) rate of FID attenuation. Modern theories of reaction rates in solution emphasize the diffusive quality of reactive trajectories near the transition-state barrier. The reactants may often cross over the free-energy barrier and then cross back again without ever reaching the final product state. If the transition state in reaction 14 were symmetric or near-symmetric with respect to the two protons, then an exchange of protons between the H atom and the OH^- ion should often occur in those encounters that fail to proceed to product. The FID attenuation rate would be the sum of the forward reaction rate and one-half the proton exchange rate. The experiments indicate that no "base-catalyzed" proton exchange occurs. Therefore, the transition state should more properly be formulated $(H\cdots OH)^-$, with the location of the "excess" charge still to be specified.

In fact, the transition state of equilibrium 14 should be inherently asymmetric by virtue of the solvent cavity or void occupied by either the H atom (left side of equilibrium 14) or by the electron (right side). In terms of the picture we have described for the encounter of H and OH^-, a water molecule will likely form at the *boundary* of the cavity, which defines the asymmetry. The key is to ask where the excess electron can most easily localize. It makes no sense energetically that the H-atom solvation cavity should fully collapse, followed by the creation of a new solvent cavity for the electron. By analogy with the presolvated electron problem, electron localization can most easily occur in a "pre-existing" region of low solvent density: the H-atom cavity. Similar considerations apply to the reverse reaction. Simulations indicate that electrons are solvated on average with one OH bond of each solvating water molecule pointing in toward the negative charge, and the other forming a hydrogen bond to the next solvation shell. In the reaction -14 of an electron with one of these H_2O molecules, an OH bond near the electron charge center can dissociate, leaving a proton to combine with the unpaired electron and to form a hydrogen atom within the pre-existing cavity. This formulation avoids some of the work needed to create a new void in the solution, and requires only rearrangement of the walls of the solvent cage. When these complementary pictures are connected by a common transition state, it becomes clear that in the $(H)_{aq} \rightleftharpoons (e^-)_{aq}$ equilibrium, the unpaired electron does not "move" from the solvent cavity; rather, the transformation is effectively accomplished by *proton transfer* between a water molecule and the nucleophilic electron charge center within the cavity. The energetics and primary isotope effects in the forward and reverse reactions are most easily explained in these terms. A two-dimensional representation of the overall process is shown in Figure I-28.

$$H + OH^- \rightleftharpoons (e^-)_{aq} + H_2O$$

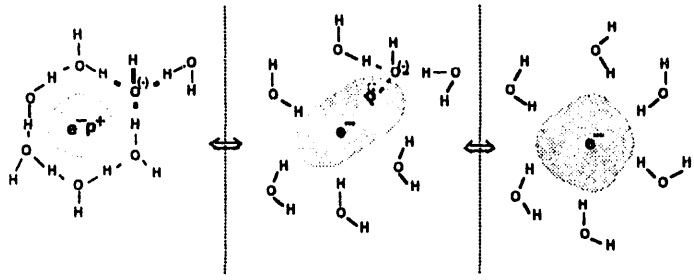

Figure I-28. Proton-transfer mechanism envisioned for equilibrium 14.

If proton transfer from water to the solvated electron is possible in the case of reaction -14, there is no reason to think that similar proton-transfer reactions from stronger Bronsted acids should not occur. The most obvious example is the well-known reaction of $(e^-)_{aq}$ with hydronium ion, equation 17.

$$(e^-)_{aq} + (H_3O^+)_{aq} \rightleftharpoons (H)_{aq} + H_2O \qquad (17)$$

Reaction 17 is very fast ($k_{17} = 2.3 \times 10^{10}$ M^{-1} sec^{-1}), but five to 10 times less than diffusion limited. The hydronium ion is an exceptionally poor scavenger of presolvated electrons. Thus, like water itself, it has no tendency to act as an excess electron acceptor in an electron-transfer reaction. The properties of reaction 17 can readily be explained in terms of a proton transfer from hydronium to the weak base $(e^-)_{aq}$, but are hard to reconcile with an electron-transfer mechanism.

A number of moderately slow $(e^-)_{aq}$ reactions with Bronsted acids that give H atoms as products can be correlated by a Bronsted plot of reaction rate vs. pK_a. An updated version of this Bronsted plot for hydrated electron reaction with aqueous acids appears in Figure I-29. One can probably conclude that all Bronsted acids that are poor electron acceptors will react by proton transfer to $(e^-)_{aq}$ at the minimum rate suggested in this Bronsted correlation.

The possibility of proton transfer to the weak base $(e^-)_{aq}$ may have further interesting implications for the unique bimolecular recombination reaction of two hydrated electrons. Evidence suggests that this reaction occurs by a two-step mechanism, very possibly involving a dielectron, as in equation 18.

$$(e^-)_{aq} + (e^-)_{aq} \rightleftharpoons (e^-)^2_{aq} \rightarrow H_2 + 2OH^- \qquad (18)$$

No H atoms are produced in this reaction, which means that spin pairing must occur prior to or in concert with the actual creation of the singlet H_2 molecule. When the spin factor of 1/4 is included in the Debye-Smoluchowski rate expression for diffusion-limited reaction of charged species, one deduces a reaction distance for the hydrated electron pair of approximately 10 Å. This would seem to imply a long-range electron-transfer process, and it is difficult to imagine any "acceptor" site other than the existing hydration cavity of one of the electrons. The isotopic enrichment favoring H over D in the H_2, D_2, and HD product mixture is quite large, suggesting an intermediate that lives long enough (picoseconds?) to thermally equilibrate with protons and deuterons of the solvent. The second-order electron recombination proceeds at a rate that is nearly diffusion limited, below ca. 150 °C. At higher temperatures, the disappearance rate actually decreases, which suggests that the activation energy for the reverse step of the pre-equilibration is much higher than the forward reaction step, and at a sufficiently high temperature the dielectron dissociation competes kinetically with the next step in the reaction. What is the next step? If proton transfer limits the lifetime of the hydrated electron, it may well also limit the (much shorter) lifetime of the hydrated dielectron. Thus, we suggest that a water molecule reacts by proton transfer to the dielectron, forming H^-.

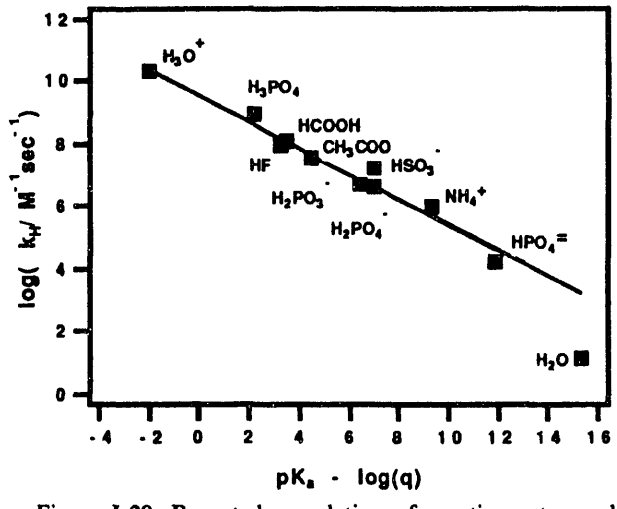

Figure I-29. Bronsted correlation of reaction rates and acid/base equilibrium constants for acids that transfer protons to hydrated electrons. The variable q is the number of equivalent proton-accepting sites on the conjugate base. In the case of acetic acid, the rate is corrected to separate the competing electron-attachment and proton-transfer rates.

$$(e^-)^2_{aq} + H_2O \rightarrow H^- + OH^- \quad (19)$$

$$H^- + H_2O \rightarrow H_2 + OH^- \quad (20)$$

The hydride ion then reacts immediately with another water molecule to form H_2, as in the generally accepted "hydride" mechanism for the $H + (e^-)_{aq}$ reaction.

3. Solvent Relaxation Dynamics

Y. Lin, C. D. Jonah

The effects of solvation and solvent dynamics on chemical reactions and, especially, on charge-transfer processes, have long been a subject of great importance in radiation chemistry. In the past, attention was focused primarily on equilibrium solvent effects, such as the effect of solvent polarity on the reaction. Two questions that have only recently come to the forefront in this area of research are, (1) how do solvent molecules react to the sudden creation of a charged species? and (2) how is this response controlled by microscopic factors in the molecular structure of the charged molecule and in the solvent structure. In the past decade, a number of researchers have employed picosecond time-resolved absorption and emission spectroscopy to probe the dynamics of electron solvation or the solvation of a large molecular dipole created in a polar liquid. However, until we began our studies, the solvation dynamics of anions in room-temperature liquids had not been measured. This is a major deficiency because many chemical processes that occur in the condensed phase involve ions or ionic intermediates. The solvation of these charged species can greatly affect chemical events. In fact, prior to our studies, the only information that has been obtained about the anion solvation dynamics has come from trying to understand chemical reactivity in different solvents by using models for the role of solvation on the total reactivity—thus deriving the effect from the consequences. The studies described here focus on the structural and dynamical properties of ion solvation.

a. Ion Solvation and Solvent Structure

Experimental studies of solvation dynamics are usually carried out by instantaneously creating a dipole or charged species in a polar solvent and subsequently monitoring the emission or absorption spectrum of this species. As solvation of this species progresses, the solvent structure rearranges, leading to a change in the energy of the probe molecule or ion that changes the emission or absorption spectrum. We selected the benzophenone anion as the microscopic probe for the following reasons: (1) The anion spectrum is separated from that of the triplet and excited state, and is strongly shifted by a polar solvent. (2) The anion can be produced very quickly by a reaction with the "dry electron", which can conveniently be produced by electron beam radiolysis.

How do the structures of the solvent molecules determine the dynamics and energetics of solvation? We studied the transient absorption spectra of benzophenone anion in linear alcohols, branched alcohols, and acetonitrile. Our results demonstrate that solvent reorganization strongly affects the electronic structure of the solute ions, and changes the absorption spectrum of the ions. Figure I-30 shows the benzophenone anion absorption spectrum in n-octanol at 50 ps, 300 ps, and 3 ns after the electron beam pulse. The blue shift of the spectrum is quite obvious. The time-dependent behavior in other alcohols is similar, albeit faster for the smaller alcohols. The absorption maximum of the benzophenone anion spectrum shifts from 675 nm to 635 nm and then to 625 nm for the three different times. The final broad absorption band has been assigned to the relaxed benzophenone anion in alcohol, whereas the spectra at early times are assigned to the anion before solvent rearrangement. As shown in Figure I-31, the final absorption peak position and width are practically the same throughout the linear alcohol series. Only the timescale for the blue shift depends on the chain length of the alcohol.

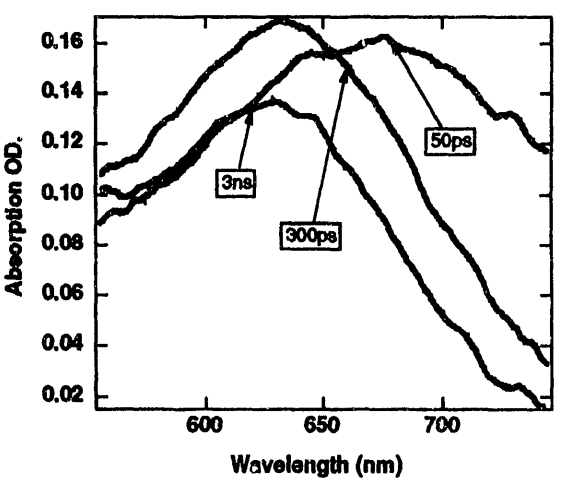

Figure I-30. Benzophenone anion absorption at 50 ps, 300 ps, and 3 ns after the electron pulse in n-octanol.

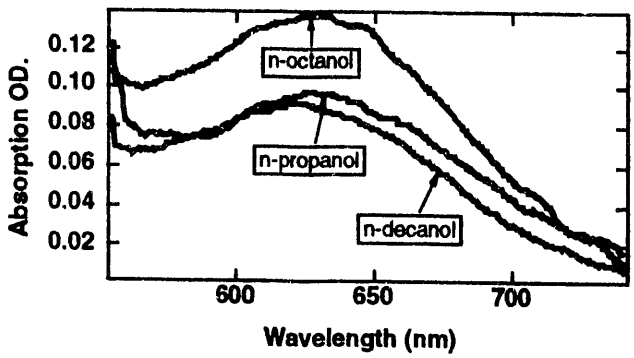

Figure I-31. Transient absorption spectra of benzophenone anion in three different linear alcohol solvents (n-propanol, n-octanol, and n-decanol) at 3 ns after the electron pulse.

The situation is very different when the solvent is changed from a linear to a branched alcohol. Figure I-32 plots the absorption of the benzophenone anion in n-octanol and 2-octanol. As shown in Figure I-32 (top), the absorption spectra are very similar for the primary and secondary alcohols at very early times, times prior to solvation. Both reflect newly created ion species in random (unrelaxed) solvent configurations. The absorption spectra are very different for the fully solvated species in linear and branched alcohols. The shift of the spectrum of the benzophenone anion in 2-octanol is smaller than in n-octanol, and the final spectral position is about 35-nm red-shifted from what is observed in the normal alcohol. Similar solvation behavior was also observed in other branched alcohol systems such as 2-butanol and 2-propanol.

The transient absorption spectra of the benzophenone anion in acetonitrile are shown in Figure I-33. The absorption maxima at 50 ps, 300 ps, and 3 ns are the same; unfortunately, the time-dependent solvation process in this system is too fast for us to observe. However, the final position of the anion absorption shows that the equilibrium local solvent structure and energetics in acetonitrile are significantly different from those in linear alcohols. The absorption spectrum at 3 ns is 90-nm red-shifted compared to the linear alcohols and 55-nm red-shifted compared to the branched alcohols. The red shift of the probe absorption spectra in going from linear alcohols to branched alcohols and to acetonitrile was also observed for the solvated electron.

The differences between the primary and secondary alcohols cannot be explained by the concentration of dipoles because the dipole concentrations of n-octanol and 2-octanol are the same. The difference, can,

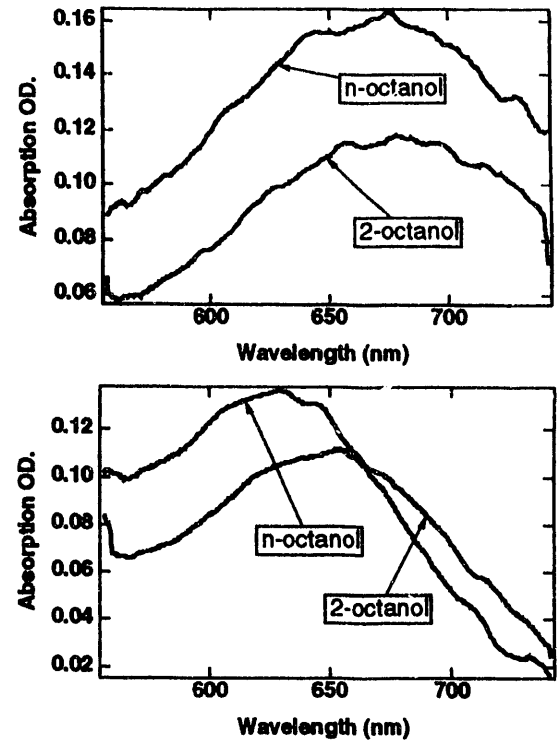

Figure I-32. The transient absorption spectra of benzophenone anion in n-octanol and 2-octanol solution at 50 ps (top) and 3 ns (bottom) after the electron pulse.

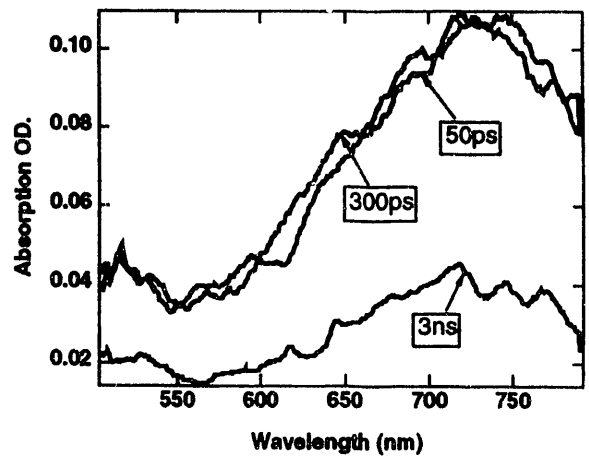

Figure I-33. The transient absorption spectra of benzophenone anion in acetonitrile. The center of the absorption peak is at 720 nm.

however, be explained by the steric factors that will prevent a close packing of secondary alcohols around an anion. For a primary alcohol, there is only a single carbon chain attached to the carbon atom bonded to the OH dipole. The OH dipole can point towards the anion and the carbon chain extend in the opposite direction. There will thus be little interference

between alcohol molecules. However, for the secondary alcohol, there are two carbon chains attached to the carbon atom bonded to the OH dipole. The second carbon chain (in the experiments described here, a methyl group) will interfere with a neighboring alcohol molecule, and thus the OH moieties will not be as near to the anion for a secondary alcohol as for a primary alcohol. Modeling studies in support of these ideas are given in the next section.

b. Monte Carlo Simulations of Solvation Energetics

We have used Monte Carlo (MC) simulations to evaluate our hypothesis that the difference between primary and secondary alcohols is due to the differences in the packing of the solvent molecules around an anion. In this simulation, we have used a simplified model that encompasses the linear and branched chain alcohols and acetonitrile within a simple framework and mapped the energetics of the system as a function of the relevant solvent properties.

We have explored the equilibrium properties of the anion solvation process in a model dipolar cluster. The model consists of N solvent molecules around a central charged entity (anion). Studies were done as a function of N ($N \leq 342$), and no significant differences were found. The solvent molecules are assumed to have the shape of three linearly connected hard spheres. Three different dipole distributions of the solvent molecules were used. In the first case, the solvating dipole is at the end of the molecule with its positive charge at the exposed end. This describes the linear alcohols. The second case corresponds to the situation in acetonitrile, where the dipole is at the end of the molecule, and the exposed end is negatively charged. The third case simulates the situation in the branched alcohols, where the dipole is located in the center of the molecule (center ball in our model) and is perpendicular to the axis of the molecule.

The degrees of freedom that are involved in the calculation of the energetics are the position and orientation of the solvent molecules as well as the position and orientation of the solvent dipole moments. All electrostatic interactions among the solvent and solute molecules are considered explicitly. Other molecular interactions are simply replaced by hard-sphere repulsive potentials that keep molecules from overlapping.

The process of "relaxation to equilibrium" was monitored through the calculation of the solvation energy V_s, which is the electrical potential at the solute site. This was done as a function of the number of configurations for several different initial configurations. After the system has reached equilibrium, the values of solvation energy obtained from different initial configurations are within the statistical fluctuation. The influence of the initial configuration disappeared after 30,000 configurations. These calculations have been done for a series of cluster sizes from 26 to 342, and the results were found to be independent of cluster size.

The potential well arising from the arrangement of the solvent molecules around the anion was calculated. The results of these calculations are shown in Figure I-34. The differences in the potentials are evident for the three different placements of the dipole group in the model solvent molecule. In these calculations, the central charge is assumed to be the anion. As can be seen in Figure I-34, curve 1 (primary alcohols) shows the deepest and narrowest potential well; hence, the absorption of the anion in this kind of solvent would occur at higher energy. This indeed is what we observed experimentally. Curve 2 (acetonitrile) displays a relatively shallow and wide potential well. Curve 3 (branched alcohols) shows a deeper potential than for acetonitrile but the potential is not as narrow nor as deep as curve 1. From Figure I-34, red shift is expected to occur on going from linear alcohols to branched alcohols to acetonitrile.

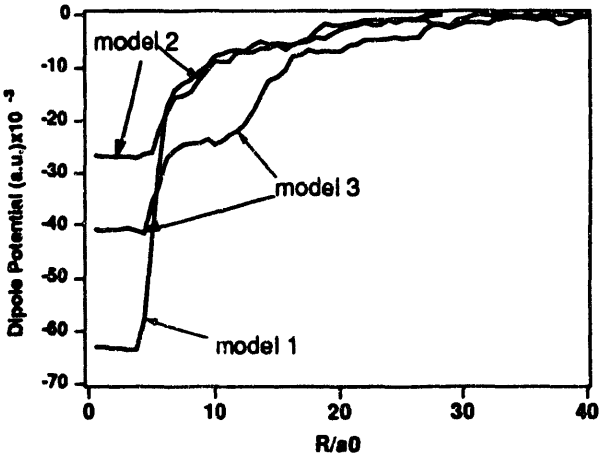

Figure I-34. Monte Carlo simulation of the distance dependence of the dipole potential energy for three different model fluids. The parameters used in these calculations are q_0 = -1 (a.u.), p_1 = 1.5 D, T = 300 K, and N = 124.

Our simulation qualitatively explains the observed spectral shift as a function of solvent, and demonstrates that the charge distribution of the solvent molecules determines the structure and energetics of the solvation process.

c. Solvation Dynamics in Alcohols

To compare the experimental solvation times of the anion and the electron in the same solution, or to relate the solvation times to the solvent dielectric relaxation times, it is necessary to develop an approach to extract solvation parameters from the experimental data. This cannot be done by fitting the decay curve at a given wavelength, because the time dependence of the absorptions are different at different wavelengths. To obtain the desired information, a more complete analytical method for obtaining the solvation time has been developed.

To find the solvation time τ_s, we assume that the anion ground state relaxes exponentially with the characteristic time τ_s. During the solvent reorganization process, the center and width of the anion absorption spectrum can be described by equations 21 and 22,

$$\lambda(t) = \lambda_\infty + (\lambda_0 - \lambda_\infty)e^{-t/\tau_s} \qquad (21)$$

$$\Delta(t) = \Delta_\infty + (\Delta_0 - \Delta_\infty)e^{-t/\tau_s}, \qquad (22)$$

where λ_0 and λ_∞ are the anion absorption maxima for the initial unsolvated species and final solvated species, respectively, and Δ_0 and Δ_∞ are the corresponding absorption band widths. The expressions given in (21) and (22) allow the time- and wavelength-dependent anion absorption to be written as equation 23,

$$I(\lambda,t) = \frac{1}{\sqrt{2\pi}\Delta(t)} e^{-\frac{(\lambda-\lambda(t))^2}{2\Delta^2(t)}} e^{-k_r t}, \qquad (23)$$

where k_r is the rate for the subsequent chemical process, such as charge recombination. To accurately obtain the solvation time τ_s, the magnitude of k_r should be small compared to the rate of solvation.

For comparison with the experimental data, equation 23 must be convolved with the instrument response function. The parameters λ_0 and Δ_0 in equation 23 are independently obtained from the absorption of the benzophenone anion in nonpolar solvents (λ_0 = 790 nm, Δ_0 = 105 nm in n-hexane). The value of λ_∞ is obtained from the long time limit of the anion absorption. The parameters left to be determined are Δ_∞, τ_s, and k_r. Because of the early formation of benzophenone triplet and ketyl radical product, Δ_∞ cannot be accurately determined from the final spectrum, so it appears as an adjustable parameter. Figure I-35 shows the results of the calculation for the transient absorption data of the benzophenone anion in n-octanol. The parameters, τ_s, Δ_∞, and k_r are listed in Table I-5. The Δ_∞ values for three different linear alcohols are very similar. The value of τ_r ($1/k_r$) is ≈3 ns, which is two orders of magnitude longer than the characteristic solvation time (τ_s) in the same solvent. Therefore, the solvation processes we are studying are not influenced by subsequent chemical processes.

It is interesting to compare and contrast the dynamics measured here with those found for electron solvation. The initial solvent arrangement around a benzophenone ion should be favorable for the neutral

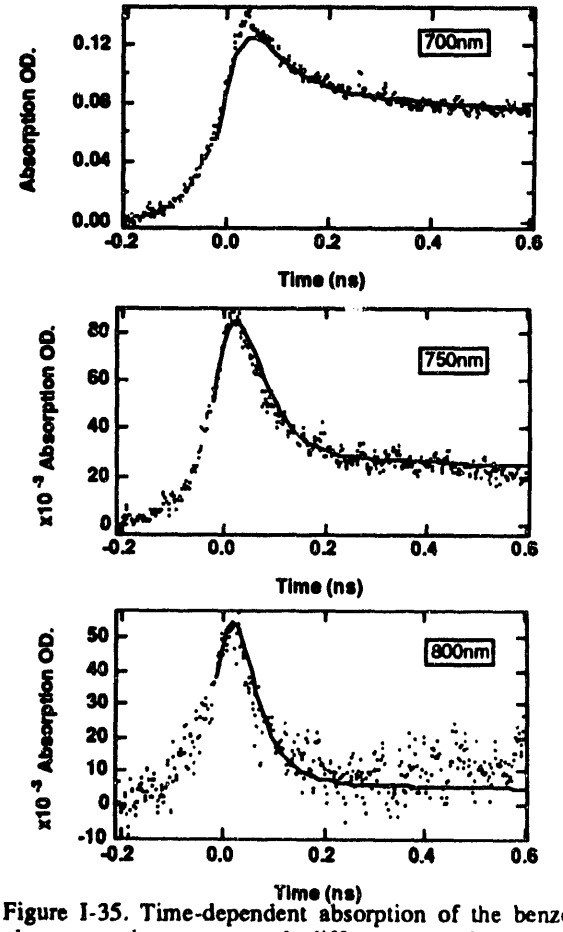

Figure I-35. Time-dependent absorption of the benzophenone anion at several different wavelengths in n-octanol. The lines correspond to the calculations from equation 23, and the dots are the experimental data. In these calculations τ_s = 55 ± 5 ps, Δ_∞ = 68 ± 2 nm, and ($1/k_r$) = 2.8 ± 0.3 ns.

Table I-5. The characteristic benzophenone anion solvation time τ_s and final spectral bandwidth Δ_∞ in several linear alcohols. The rates for the subsequent chemical reaction are also given for comparison.

Solvents	τ_s(ps)	Δ_∞ (nm)	$\frac{1}{k_r}$ (ns)
n-butanol	35	66	2.0
n-octanol	55	70	2.8
n-decanol	90	70	3.0

benzophenone molecule, whereas the electron solvation begins from a configuration that is particularly favorable for the electron (otherwise the electron would not be trapped in that particular location). To assess these effects and to give an idea of the kind of solvation mechanism that may be operating, we have prepared Table I-6 to summarize (1) the benzophenone anion solvation times obtained from this study; (2) the electron solvation times; and (3) solvent dielectric relaxation times. The results indicate that anion solvation is slower than electron solvation. For example, the solvation time for the benzophenone anion in n-decanol is approximately 90 ps, whereas the electron solvation time is 55 ps. These values can be compared to the dielectric relaxation times for n-decanol for τ_1-τ_3 of 2 ns, 48 ps, and 3.3 ps. The three Debye relaxation times τ_1, τ_2, and τ_3 are associated with the time scales of hydrogen-bonding dynamics in molecular aggregates, the molecular rotation, and rotation about the terminal C—OH bond, respectively. For both dipole solvation and electron solvation, the solvation time correlates best with τ_2, the monomer dielectric rotation time of the alcohol.

A more rigorous description can be given by using the longitudinal relaxation time τ_L, which is defined as $(\varepsilon_\infty/\varepsilon_0)\tau_D$, where ε_∞ and ε_0 are the infinite frequency and static dielectric constants, and τ_D is the Debye dielectric relaxation time. Because of the complicated dispersion behavior in alcohols, a single value of τ_L does not exist. The experimentally measured solvation times in alcohol solutions are faster than τ_{L1}, but are slower than τ_{L2}. The observed solvation time is a blend of several solvent motions and a combination of different dielectric relaxation times. Because it takes longer to move an alcohol molecule if a hydrogen bond must be broken, the longer time for the anion solvation suggests that the initial structure around the anion requires a greater rearrangement of the solvent molecules than the structure near an electron, and that part of the reorganization will require the breaking of hydrogen bonds.

d. Dynamics in Salt Solutions

The experiments described above probe the solvation of ions in dipolar, nonconducting solutions. However, in many chemical systems, counterions play an important role in the chemistry. Although ionic effects are well known in chemistry, the quantitative understanding of the role of ions at high concentrations is still fragmentary. This section represents an extension of our studies on solvation dynamics into the realm of ionic solutions. In some ways, ionic solutions might be viewed as simply more polar versions of the pure solvent counterparts. They could, therefore, be expected to influence reactions in a similar manner. Dynamically, however, ionic solutions are very different from pure polar solvents. Whereas dynamics in a pure solvent involves primarily the reorientation of solvent molecules, the time dependence of salt-solute interactions arises from the translational motion of ions.

We have used both picosecond and nanosecond pulse radiolysis techniques to examine the behavior of benzophenone anion in several ionic solutions with Li^+, Na^+, and Ba^{2+} in acetonitrile. Transient absorption spectra of the benzophenone anion in the presence of 0.5 M $NaClO_4$ in acetonitrile are shown in Figure I-36. In the absence of salt, the solvation dynamics of the benzophenone anion in acetonitrile are too fast to be observed, and the absorption maximum of the final solvated species is 720 nm. In the

Table I-6. The benzophenone anion solvation times obtained from this experiment and electron solvation times in several linear alcohol systems. Dielectric data are given for comparison.

solvents	τ_s (ion) (ps)	τ_s (electron) (ps)	dielectric relaxation times (ps) τ_1	τ_2	τ_3	$\tau_{L1} = \tau_1\left(\frac{\varepsilon_{\infty 1}}{\varepsilon_{01}}\right)$ (ps)	τ_{L2} (ps)
n-butanol	35	30	670	27	2.4	127	21
n-octanol	55	45	1780	39	3.2	406	30
n-decanol	90	51	2020	48	3.3	565	42

presence of 0.5 M $NaClO_4$, the absorption maximum of the radical anion of benzophenone is blue-shifted from 720 nm to 650 nm, and the dynamics are considerably slower. As in the pure solvent, the spectral dynamics cannot be described by a "two-state" kinetic model; instead, the spectral change appears to be continuous as the environment around the benzophenone rapidly alters from the original unstable state to the final state. Figure I-37 shows that solvation is a nanosecond process. The solvation dynamics observed are strongly affected by the identity and the concentration of the cation. The different relaxation times for different cation solutions may indicate strong coupling between the benzophenone anion and a cation, or may indicate the formation of contact ion pairs: benzophenone radical anion-cation.

Two other research groups have recently studied dipole solvation in salt solutions. These experiments show, consistent with our results, that solvation is much slower in ionic solutions and depends on the salts and their concentration in the solution. They have interpreted their results by using two different models, one based on the Debye-Falkenhagen (DF) theory and the second based on specific ionic interactions. Both models appear to be unsatisfactory to explain their observation. The solvent times calculated from DF theory are about an order of magnitude faster than the experimental measurements, whereas the concentration dependence expected from the ionic interactions is not in agreement with the experimental data. We believe that our findings provide a better guide for the interpretation of this family of observations, and we are now studying this important issue.

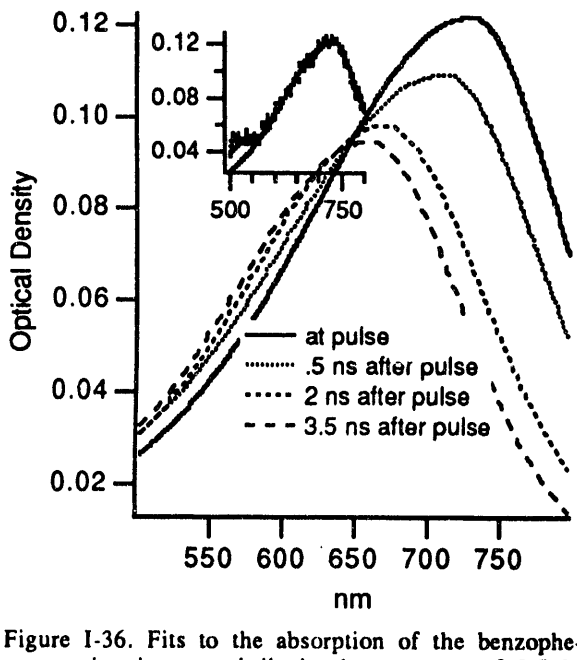

Figure I-36. Fits to the absorption of the benzophenone anion in acetonitrile in the presence of 0.5 M $NaClO_4$. The inset shows the experimental data at the pulse end and the fitted absorption. The peak at 550 nm is assigned to the ketyl radical.

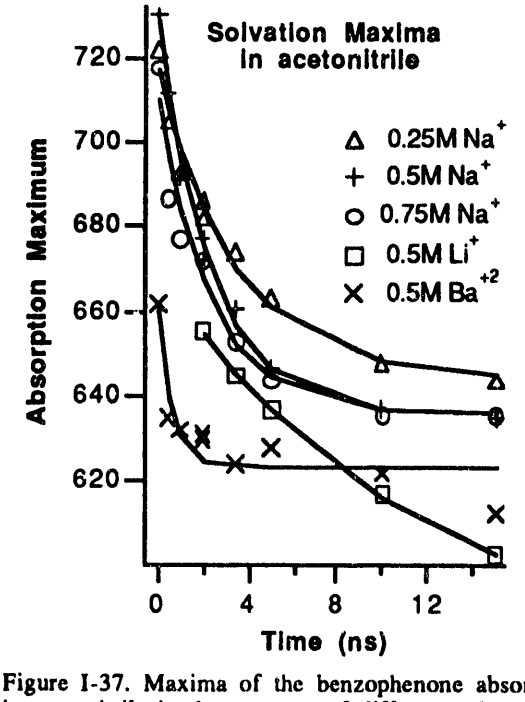

Figure I-37. Maxima of the benzophenone absorption in acetonitrile in the presence of different salts at various salt concentrations. Lines are least-squares fits to an exponential decay.

PUBLICATIONS

ELECTRONIC STATES OF CIS- AND TRANS-DECALIN RADICAL CATIONS IN ZEOLITES
M. V. Barnabas* and A. D. Trifunac
Chem. Phys. Lett. 187, 565-570 (1991)

H/D ISOTOPE EFFECTS IN WATER RADIOLYSIS. 3. ATOMIC HYDROGEN IN ACIDIC H_2O/D_2O MIXTURES
P. Han* and D. M. Bartels
J. Phys. Chem. 95, 9370-9374 (1991)

SOLVENT EFFECTS ON THE PHOTOCHEMISTRY OF A KETOCYANINE DYE AND ITS FUNCTIONAL ANALOGUE, MICHLER'S KETONE
M. V. Barnabas*, A. D. Liu*, A. D. Trifunac, V. V. Krongauz*, and C .T. Chang*
J. Phys. Chem. 96, 212-217 (1992)

CONDENSED PHASE STUDIES OF RADICAL IONS IN PHOTOIONIZATION AND RADIOLYSIS
A. D. Trifunac, A.-D. Liu*, and D. M. Loffredo*
Dynamics and Mechanisms of Photoinduced Transfer and Relate Phenomena, N. Mataga et al., Eds.; Elsevier Science Publishers, 1992, pp. 259-274

PHOTOIONIZATION OF POLYCYCLIC AROMATIC HYDROCARBONS IN ALKANE SOLUTIONS: "HIGH ENERGY" CHEMICAL PATHWAYS
D. M. Loffredo*, A.-D. Liu*, and A. D. Trifunac
Rad. Phys. Chem. 40, 255-262 (1992)

PHOTODISSOCIATION OF HEXAARYLBIIMIDAZOLE. II. DIRECT AND SENSITIZED DISSOCIATION
A.-D. Liu*, A. D. Trifunac, and V. V. Krongauz*
J. Phys. Chem. 96, 207-212 (1992)

ION-MOLECULE REACTIONS OF TETRAMETHYLETHYLENE RADICAL CATIONS IN ZEOLITES
M. V. Barnabas* and A. D. Trifunac
Chem. Phys. Lett., 193, 298-304 (1992)

FLUORESCENCE-DETECTED MAGNETIC RESONANCE
D. W. Werst and A. D. Trifunac
A Specialist Periodical Report, Electron Spin Resonance, Royal Society of Chemistry, M. C. S. Symons, Ed., 1992, pp. 161-186

STUDIES OF ION SOLVATION USING PULSE RADIOLYSIS
C. D. Jonah and Y. Lin
Proceedings, 9 ICRR: A Twentieth-Century Perspective, Vol. II, 1992, pp. 63-68

PULSE RADIOLYSIS OF DEXTRAN-WATER SOLUTIONS
M. M. Gleizen*, A. C. Chernovitz*, and C. D. Jonah
J. Phys. Chem. 96, 5180-5183 (1992)

EXPERIMENTAL INVESTIGATION OF THE DYNAMICS OF BENZOPHENONE ANION SOLVATION
C. D. Jonah and Y. Lin
Chem. Phys. Lett. 191, 357-361 (1992)

*Not affiliated with the Chemistry Division or affiliated on a temporary basis.

RADIOLYTIC AND RADIOLYTICALLY INDUCED GENERATION OF GASES IN SIMULATED WASTE SOLUTIONS
D. Meisel, M. C. Sauer, Jr., C. D. Jonah, H. Diamond, M. S. Matheson*, F. Barnabas*, E. Cerny*, and Y. Cheng*
Proceedings, Waste Management '92 "Working Towards A Cleaner Environment", March 1-5, 1992, Tucson, AZ, pp. 859-865

H/D ISOTOPE EFFECTS IN WATER RADIOLYSIS IV. THE MECHANISM OF $(H)_{aq} \rightleftharpoons (e^-)_{aq}$ INTERCONVERSION
P. Han* and D. Bartels
J. Phys. Chem. 96, 4899-4906 (1992)

TEMPERATURE DEPENDENCE OF SOLVATED ELECTRON DIFFUSION IN H_2O AND D_2O
K. H. Schmidt, P. Han*, and D. Bartels
J. Phys. Chem. 96, 198-206 (1992)

RADICAL-CATION COMPLEXES FORMED BY π-LONE PAIR INTERACTIONS
D. W. Werst
J. Phys. Chem. 96, 3640-3646 (1992)

ELECTRON TRANSFER FROM CO_2^- TO PERYLENE IN CYCLOHEXANE
M. C. Sauer, Jr. and C. D. Jonah
J. Phys. Chem. 96, 5872-5875 (1992)

DIFFUSION AND CIDEP OF H AND D ATOMS IN SOLID H_2O, D_2O AND ISOTOPIC MIXTURES
D. M. Bartels, P. Han*, and P. W. Percival*
Chem. Phys. 164, 421 (1992)

SUBMISSIONS

EARLY EVENTS IN RADIATION CHEMISTRY AND IN PHOTOIONIZATION
A. D. Trifunac, D. M. Loffredo*, and A. D. Liu*
J. Rad. Phys. Chem. (1992)

OBSERVATION OF AN AROMATIC RADICAL ANION DIMER: $(C_{10}F_8)_2^{\bullet -}$
D. W. Werst
J. Am. Chem. Soc. (1992)

INVESTIGATION OF ELECTRON TRANSFER BETWEEN THE HEXAARYLBIIMIDAZOLE AND VISIBLE SENSITIZER
Y. Lin, A.-D. Liu*, A. D. Trifunac, and V. V. Krongauz*
Chem. Phys. Lett. (1991)

EARLY EVENTS FOLLOWING RADIOLYTIC AND PHOTOGENERATION OF RADICAL CATIONS IN HYDROCARBONS
D. W. Werst and A. D. Trifunac
Radiat. Phys. Chem. (1992)

---

*Not affiliated with the Chemistry Division or affiliated on a temporary basis.

TRANSIENT ABSORPTION SPECTRA OF AROMATIC RADICAL CATIONS IN HYDROCARBON SOLUTIONS
A-D. Liu*, M. C. Sauer, Jr., D. M. Loffredo*, and A. D. Trifunac
J. Photochem. Photobiol. (1991)

A NOVEL MECHANISM OF FORMATION OF TRANSIENT AROMATIC RADICAL CATIONS IN ALCOHOLS: LASER FLASH PHOTOLYSIS AND PULSE RADIOLYSIS STUDIES
A.-D. Liu*, M. C. Sauer, Jr., C. D. Jonah, and A. D. Trifunac
J. Phys. Chem. (1992)

SUBEXCITATION ELECTRON INTERACTIONS IN RARE GASES: PRODUCTION OF ELECTRONIC EXCITED STATES IN HELIUM OR NEON MIXTURES WITH ARGON, KRYPTON, OR XENON
R. Cooper* and M. C. Sauer, Jr.
Phys. Rev. A (1992)

THE DEPENDENCE OF THE BENZOPHENONE-ANION SOLVATION ON SOLVENT STRUCTURE
Y. Lin and C. D. Jonah
J. Phys. Chem. (1992)

PICOSECOND DYNAMICS OF BENZOPHENONE ANION SOLVATION
Y. Lin and C. D. Jonah
J. Phys. Chem. (1992)

SOLVENT AND ISOTOPE EFFECTS ON ADDITION OF ATOMIC HYDROGEN TO BENZENE IN AQUEOUS SOLUTION
E. Roduner* and D. M. Bartels
Ber. Bunsenges. Phys. Chem. (1992)

SOLVENT EFFECTS IN NONPOLAR SOLVENTS: RADICAL ANION REACTIONS
D. W. Werst
Chem. Phys. Lett. (1992)

COLLABORATIONS

R. Cooper, University of Melbourne, Australia
Studies of transient species created in gases, liquids, and solids are being carried out. Recent efforts have concentrated on the spectra and dynamics of excited species created in solids, such as sapphire, which are investigated via time-resolved measurements of emitted light using the techniques of pulse radiolysis and laser flash photolysis. Sapphire is a prime contender for a lining material of the containment vessel in fusion reactors, and these studies are useful in understanding radiation effects.

V. V. Krongauz, DuPont de Nemours Company, Inc., Wilmington, DE
Several related efforts using laser flash photolysis, EPR, and picosecond laser techniques are being carried out to study the photochemistry of photopolymer initiation. Emphasis has been on the dissociation mechanism of the free-radical initiator HABI (hexaarylbiimidizole) and the role of dye sensitizers.

S. Mezyk, Atomic Energy of Canada, Ltd., Pinawa
Reaction rates of H atoms with I^- and other iodine-containing solutes are being measured for the purpose of predicting the spread of radioactive iodine in potential nuclear accidents.

---

*Not affiliated with the Chemistry Division or affiliated on a temporary basis.

P. W. Percival, Simon Fraser University and TRIUMF, Burnaby, British Columbia, Canada
Investigation of H and D atoms in ice by time-resolved EPR has allowed determination of diffusion rates, and the development of a model H atom-H_2O interaction potential. The aim of the collaboration is improved understanding of H-atom transport and reactivity in solid lattices.

E. Roduner, Physical Chemistry Institute, Zurich University, Switzerland
Reaction of H atoms with benzene in water has been investigated in a test of the validity of transition state theory for reactions in aqueous solution. Precision measurements of the hyperfine coupling of H and D atoms in water have been made to elucidate the nature of hydrophobic hydration, and effects of water "structure" on reaction rates.

C. Romero, University of Santiago, Chile
The properties of the hydrated electron are being studied via molecular dynamics simulations. A computational program has been developed to simulate aqueous LiCl solutions, and the results are compared to the experimental optical absorption spectrum. Water molecules are treated classically, and the electron is given a full quantum treatment. This is an important step towards simulating chemical reactions in ionic solutions.

II. ELECTRON TRANSFER AND ENERGY CONVERSION

*J. R. Miller, D. Meisel, T. Iyoda, N. Liang, C. Luangdilok, P. Piotrowiak, D. Yogev, M. S. Matheson, A. F. Wagner**

Outside Collaborators: *G. L. Closs, I. I. Creaser, L. A. Curtiss, P. Eaton, F. Grieser, J. M. Harrowfield, D. Lawless, G. A. Lawrance, P. Mulvaney, C. A. Naleway, B. Paulson, A. M. Sargeson, N. Serpone*

This program explores fundamental questions of electron-transfer (ET) reactions and redox catalysis that could lay foundations for new energy technologies. Electron transfer is studied with a close coupling of experiment and theory. Special experimental tools enable measurements of how rates of electron transfer between molecules depend on distance, energy, polarity, angular orientation, and temperature. These measurements are unusual in their ability to investigate the effect of each of these critical variables without interference from the others in a quantitative way that enables fundamental examination and development of theory, as exemplified in the recent striking success of theory in predicting temperature dependence. Redox catalysis by small semiconductor particles is being studied in a fundamental way by the development of new knowledge of the electronic and surface properties of the particles. Recent advances allow production of particles of controlled sizes. Careful measurements of particle sizes, their absorption and emission spectra, and the dynamics of charge transfer in these particles allow insights into present, rudimentary theories that relate size to band-gap. Recent efforts focus on electron transfer at the surface of the particles.

A. Intramolecular Electron Transfer

J. R. Miller, N. Liang, P. Piotrowiak, G. L. Closs, P. Eaton, B. Paulson

1. Temperature Dependence of Electron-transfer Rates *J. R. Miller, N. Liang, G. L. Closs*

Weakly exoergic electron-transfer reactions in polar solvents are expected to have a substantial temperature dependence of the Arrhenius form. Our earlier results for weakly exoergic electron-transfer reactions have supported these expectations: the activation energies were substantial and constant. A contrary example has now been found in cis-2-(4-biphenylyl)-7-(2-naphthyl)transdecalin (cis-2,7BDN) in which both substituents occupy axial (ax) positions.

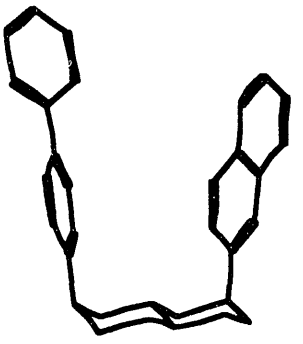

cis-2,7BDN

The temperature dependence of ET in the anion of this molecule was of interest because a small solvent reorganization energy was expected due to the proximity of the biphenyl and naphthyl groups, which are in a nearly parallel conformation. The observed temperature dependence was surprising: the Arrhenius plot was strongly curved. The activation energy is large at temperatures approaching -100 °C but becomes small at room temperature. These results were obtained in 2-methyltetrahydrofuran from -100 to 28 °C. Nothing in electron-transfer theory led us to expect this behavior. Two general explanations seem conceivable. One is that the electronic coupling is not constant, but changes with temperature due to direct interactions between the biphenyl and naphthyl groups. The other is that the solvent reorganization energy is strongly temperature dependent due to serious failures of the

*Collaborator from another ANL Chemistry Division group.

dielectric continuum model of solvent reorganization, which neglects the molecular size and shape of the solvent molecules. To obtain more information we will measure temperature dependence to higher temperatures and use molecular modeling to examine the questions of whether one solvent molecule can fit between the biphenyl and naphthyl groups and of whether thermal ejection of that solvent molecule might be responsible for the unusual temperature dependence.

2. Calculation of Electron Tunneling Pathways *J. R. Miller, L. A. Curtiss, C. A. Naleway, A. F. Wagner*

Calculations of electronic couplings for long-distance electron transfer require knowledge of the tails of molecular wavefunctions. Important questions of how to adequately calculate long-range interactions must be clearly resolved to approach experimental puzzles such as those outlined in sections below. Last year, application of a new method for ab initio calculation of pathways for transmission of electronic couplings through molecular material led to the conclusion that long-range interactions are important due to pathways that "skip" over one or more bonds. Because the tails of wavefunctions affect most molecular properties only weakly, they are not well determined in present electronic structure calculations.

One approach to this problem is to study the effect of the size of the basis set used in the electronic structure calculations. We have performed ab initio HF-SCF calculations to determine the electronic couplings between two CH_2• radicals connected by planar zig-zag (extended) saturated hydrocarbon chains from butane to octane. Increasing the basis set from STO-3G to 3-21G, 6-31G, 6-31G*, 6-31G**++ showed that the increasing sophistication of the basis sets did not have any substantial effects on the computed electronic couplings past the 3-21G level. Although the basis sets may not be similarly adequate in all cases, our results do imply that potentially serious errors are not being made in the present application. The methodology for calculations of superexchange pathways from the Hartree-Fock results has been examined. Comparisons of two different types of localized orbitals, the NBO (natural bond orbitals) and NLMO (natural localized molecular orbitals), indicated that the pathways constructed from the NBOs gave somewhat better agreement with the SCF calculations than did the NLMOs.

3. Internal Reorganization Energies of Rotation *J. R. Miller, B. Paulson, G. L. Closs*

Molecular orbital calculations have provided estimates of internal reorganization energies for several donor/acceptor molecules. For biphenylyl, which has been our favorite electron-donor group because its anion is a strong electron donor and has excellent spectral features, the calculations have suggested the presence of an internal twist. The dihedral angle between the two rings in the biphenyl group is about 40° for the neutral molecule, but only about 15° for the radical anion. This structural change gives rise to an internal reorganization energy that could have a substantial effect on the energetics controlling electron transfer. We, therefore, replaced the biphenyl group with its planar analog, the 9,9'-dimethyl-2-fluorenyl (2F) group, in molecules that have naphthalene as the acceptor and either 1,4-cyclohexane (C) or the steroid 3,16-androstane (S) as the spacers. For the 2F group, the interring angle is 0° for both the neutral molecule and the anion, so no reorganization energy of twisting is expected.

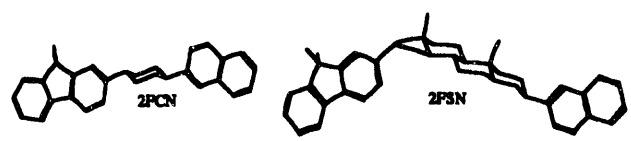

The electron-transfer rates to naphthalene for anions of the molecules 2FCN and 2FSN in tetrahydrofuran (THF) were increased by a factor of about five relative to rates in the corresponding biphenyl (B) derivatives. Inasmuch as this change is not expected to affect the electronic coupling, the increased electron-transfer rates imply an internal reorganization energy of twisting in biphenyl of 0.1-0.15 eV. This result is in very good agreement with the amount calculated by semiempirical molecular orbital theory using the AM1 Hamiltonian. The internal reorganization energy of twisting in the biphenylyl group is then predicted by theory and verified by experiment to have a substantial effect on ET rates. Previous interpretations of rate vs. $\Delta G°$ data for a series of compounds containing the biphenylyl group were fitted without consideration of such a reorganization energy, and it will be necessary to correct the previous solvent reorganization energies.

4. Effect of Symmetry on Electron-transfer Rates *J. R. Miller, B. Paulson, G. L. Closs*

The highly symmetric anionic 9-fluorenyl group participates in fast electron-transfer reactions. Unlike the anion, the wavefunction for the cation is anti-symmetric about the point of attachment to the cyclohexane: for every MO coefficient in the upper half of the 9-fluorenyl (9F) group in the picture, a symmetrically related atom in the lower half of the 9F group has an equal and opposite MO coefficient.

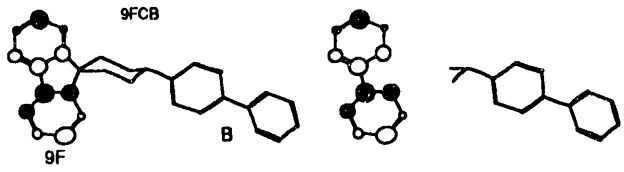

Therefore, in the positive ion of the molecule 9FCB containing a spiro 9F group bound via the 1,4-cyclohexyl spacer to a biphenylyl (B) group, the carbon atoms in the left half of the spacer group should, by symmetry, have no interaction with the 9F group, so through-bond interactions would have to occur without the help of those atoms, as is schematically indicated in the right half of the picture where those atoms are omitted. In the strict through-bond picture in which coupling interactions pass between adjacent bonds, the electronic coupling would be zero. The observed rate, however, is not reduced. We believe that the electronic coupling that keeps this rate high will be understood in terms of the kinds of "skipping" pathways discussed last year, although it seems very surprising that no reduction in rate can be detected. We intend to explore this quantitatively with pathway calculations in FY1993.

5. Superexchange Through Metal Ions Between Electron Donor and Acceptor Groups *J. R. Miller, T. Iyoda*

In the molecule shown, a biphenylyl group and a nitrobenzene group are attached to a [2,2] crown ether.

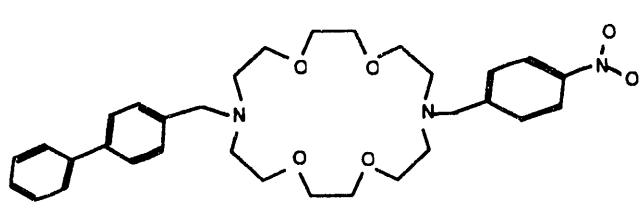

When pulse radiolysis was used to attach an electron to the biphenyl group, the observed electron-transfer rate (preliminary result) is about 2×10^9 s^{-1}. This molecule has the unique ability to complex an ion between the donor and acceptor group. With a Na^+ ion complexed inside the crown, the electron-transfer rate increases to greater than 10^{10} s^{-1}. Although the structure has conformational flexibility, which enhances the rates, its importance is not clearly understood at this time. Our preliminary interpretation of the result is that the sodium ion does not substantially promote electronic coupling by superexchange.

6. Salt Effects on Electron-transfer Rates *J. R. Miller, P. Piotrowiak*

Electron-transfer reactions in synthetic chemistry, electrochemistry, or in energy conversion often occur in ion pairs, in which an inert counterion neighbors a radical ion. It is clear that in salt-free solutions the pulse radiolysis technique produces free ions. Our approach has been to study first the simpler process of electron transfer in free ions, and to use the information that can be obtained in this way as a basis for understanding more complex systems. We anticipated that ion pairing might have substantial effects on the rates of weakly exoergic intramolecular electron-transfer reactions because motion of the cation would be required for electron transfer to occur. Accordingly, we have measured the effects of salts on the rate constants for intramolecular electron transfer in the biphenyl-cyclohexane-naphthalene structure.

Current measurements show that inert salts can decrease the electron-transfer rate constant by as much as a factor of 1000 for this weakly exoergic ($\Delta G°$ = -0.06 eV) electron-transfer reaction. The cations used ranged from Li^+ (0.6 Å) to tetraoctylammonium (4.4 Å). Cations that have larger radii caused larger decreases in the rate (see Figure II-1). The effect of cation size is contrary to our expectations. Smaller cations such as Li^+ would be expected to bind more strongly to the aromatic radical anions of biphenyl or naphthalene due to the stronger Coulomb force of the more concentrated charge in small ions. Consequently, the smaller ions would be expected to cause larger decreases in the ET rates.

That the opposite occurs may be rationalized, in part, as a consequence of a competition between solvation of the cations and ion pairing with the aromatic anions. Small cations may be very strongly solvated by the THF solvent molecules so that they pair less strongly with anions.

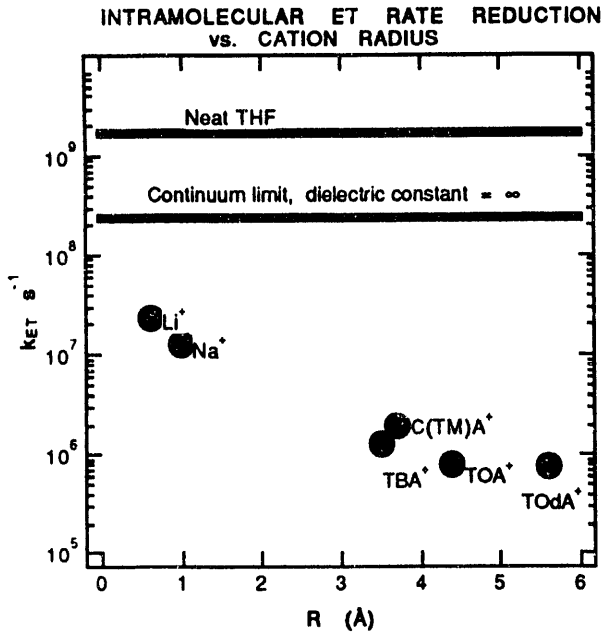

Figure II-1. Intramolecular electron-transfer rate as a function of cation radius.

To help understand salt effects on ET rates, optical electron-transfer (OET) spectra were observed for the anion of the symmetric difunctional molecule, dihydropentacene.

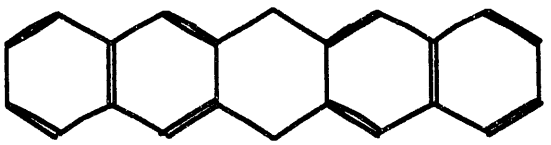

These spectra contain transitions for transfer of an electron from one naphthyl group to the other. The maximum of the OET band is in the infrared region with a maximum at a wavelength longer than 2000 nm in THF. When the naphthalene anion (N^-) in this molecule is paired with a Na^+ or a tetrabutylammonium$^+$ ion (NB_4^+), the optical electron-transfer band shifts to the blue, because ion pairing stabilizes the N^-. The much larger shift in the case of the sodium indicates that Na^+ pairs more strongly with N^- than does NB_4^+. This is opposite to the trend observed in the ET rates, in which sodium caused a smaller decrease in ET rate than did NB_4^+. This new information tells us that the larger reduction of ET rates caused by ion pairing with NB_4^+ is not due to a stronger ion pairing with NB_4^+ than with Na^+, which might have been understood as strong solvation of Na^+ by THF, so that it is effectively the larger ion. The observation that large cations reduce the ET rates more than small ones is still a mystery.

B. Energy Conversion in Microheterogeneous Systems

D. Meisel, C. Luangdilok, D. Yogev, M. S. Matheson, P. Mulvaney, F. Grieser, D. Lawless, N. Serpone

The design of a system to use light energy to produce fuels or other valuable chemicals will require some microorganization of a large number of functionalities. These functionalities will include light-harvesting antenna, cascading unidirectional charge-transfer moieties, and catalytic entities all prearranged in an optimal microenvironment similar in principle to the organization in the natural photosynthetic apparatus. Our program investigates the potential application of microheterogeneous assemblies in the design of photochemical energy conversion systems. In recent years, the program focused on solid particles and the solid/liquid interface of colloidal aggregates. These particles were shown to be effective in many of the stages required for energy conversion, but the parameters that govern the physical properties of such systems and the rate and efficiency of charge transfer to/from these particles are not well understood. We, therefore, study the detailed mechanisms that control these processes in an effort to provide a rational basis for the design of energy-conversion devices. The techniques utilized in this program include the linac facility in conjunction with laser flash photolysis and time-correlated single photon counting techniques for the study of charge transfer and photophysical dynamics in these systems. Electron microscopy, electron diffraction, and a variety of colloid chemistry techniques are used to characterize the microheterogeneous systems and the interfaces involved.

This year, the program focused on the photophysical properties of size-controlled, capped, small chalcogenide semiconductor particles. In the past, we have shown that the evolution of chalcogenide particles can be initiated by using radiation chemistry techniques that allow control of the resultant particles over a broad range of particle sizes. This year, the same methodology was applied to several transition metal chalcogenides with a variety of capping thiols at the surface of the latter particles. In an effort to understand the mechanism by which band-gap excitation of transition metal oxides leads to efficient oxidations, we were able to show that direct hole scavenging by water molecules or organic substrates is a major pathway in these light-induced oxidations.

1. Size Control and Surface Modification

In previous years, we developed techniques to synthesize chalcogenide particles, primarily CdS, of well-defined and a priori controlled sizes. The size control is achieved via a competition between H_2S and thiols (RSH) for cadmium ions at the surface of the growing particles. The effort this year focused on modification of the surface of these particles with various functionalities. Several long alkyl chain thiols were tested for their ability to control the growth of the particles. It was found that the alkyl chain length, in the range of C_3-C_{12}, is not important in this regard. Yet the resultant particles are now coated with a highly hydrophobic layer. These particles can be separated from the colloidal solution as solid powders and can be redissolved in nonpolar solvents. Despite the extensive manipulation involved in the coagulation of these particles, their absorption and fluorescence spectra and their size and size distribution are maintained. In addition to their growth-controlling effects, the thiols also stabilize the particles against anodic photocorrosion. Removal of the caps by extensive dialysis and replacement with inert stabilizers (e.g., hexametaphosphate) lead to rapid deterioration of the sol during photolysis. Organic electron donor/acceptors (e.g., nitrothiophenol, thioquinoline) as well as inorganic functionalities (e.g., Cd^{2+} or Ni^{2+} bis-dithiolates) could easily be attached to the particles. All of these substances are able to control the size, in a similar way to the inert thiols.

Two distinct modes of attachment of the functionalized thiolates to the particles were discovered: covalent binding and physical adsorption. The latter dominates when inert thiols occupy the majority of binding sites. The different absorption spectra of nitrothiophenol bound to CdS in these two modes is shown in Figure II-2. The ratio between the two modes of binding can be controlled by manipulating the ratio of the two thiols, the inert thiol (RSH in Figure II-2) and the functionalized thiol (NTP in Figure II-2), during the particle synthesis. In both cases, electron-transfer quenching of the particle fluorescence was observed as described below.

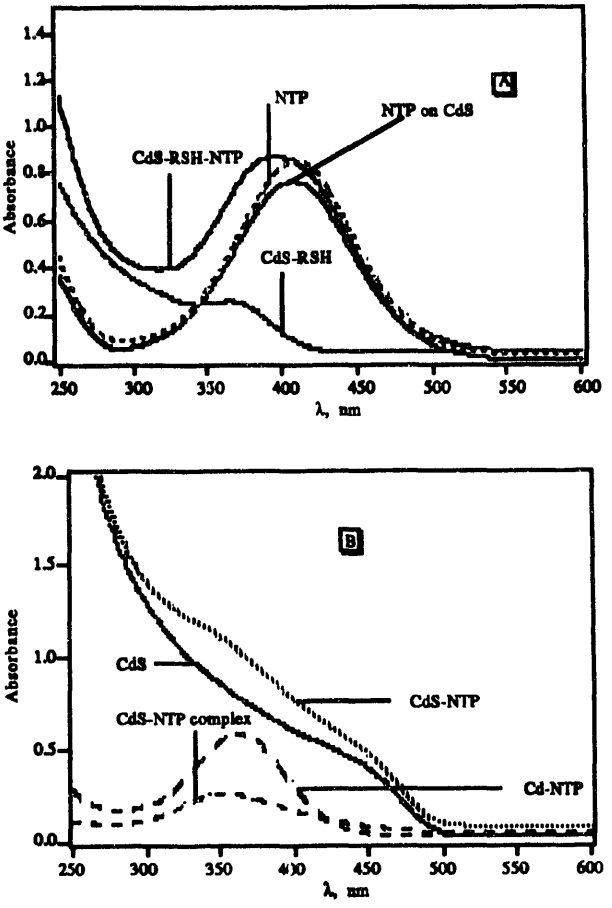

Figure II-2. Two modes of size control and surface modification. A (top): Absorption spectra of CdS, size controlled by 1-hexanethiol (RSH) and surface modified by nitrothiophenol (NTP). The absorption spectrum of CdS-RSH-NTP minus CdS-RSH is identical to that of NTP. B (bottom): Absorption spectra of CdS, size controlled and surface modified by NTP. The absorption spectrum of CdS-NTP minus CdS is identical to that of the Cd(II)-NTP complex.

2. Electron Transfer From Excited Particles

The organic acceptors such as nitrothiophenol efficiently quench emission from the particles. Much of the quenching occurs on time scales faster than the resolution of our present equipment. This process is believed to involve transfer of the electron prior to its trapping in defect sites and in competition with the trapping process. Fluorescence quenching via the transfer of trapped carriers is also observable and its dynamics could be studied. The rate of transfer of the trapped electron to the acceptor was found to depend on its energy level. Electrons in shallower traps are transferred faster than those in deeper traps. The formation of the radical ion that results from this quenching has been verified by flash photolytic observation of its spectrum, which was essentially identical to the spectrum obtained from the pulse radiolytic reaction of e^-_{aq} with the acceptor. In those cases where neither charge nor energy transfer is possible, that is, when inert thiols are used to control the size, the quantum yield of fluorescence from the particles increases substantially. This was shown to arise from a decrease in the rate of nonradiative decay modes in the particles. Because these nonradiative decay modes involve recombination of charge carriers trapped in various defect sites (in particular, surface states), it is believed that the bound thiols contribute electronic charge to some of these traps. Once these traps are filled, trapping at these sites is prevented and the quantum yield increases.

3. Electron Transfer to the Particle

Nanometer-size CdS particles were prepared in THF by the method described above and were allowed to react with a series of organic radical ions. The redox potentials of these radical ions span the range of -2.10 to -0.1 V, from well above the conduction band edge to deep within the band gap of the particles, as illustrated in Figure II-3. Surprisingly, in all these cases the rate of electron transfer from the radical ions to the particles was at the diffusion-controlled limit ($1.7\text{-}5.0) \times 10^{-11}$ M^{-1} s^{-1}). This observation indicates that the Fermi level of the particles must be located at least 0.8 eV below the conduction band. For the intrinsic semiconductor, the Fermi level is at mid-gap, ca. 1.0 eV below the conduction band. The particles are, therefore, essentially free of impurity donors. Nonetheless, traps for carriers do exist in particles as evidenced by the red emission that we invariably observe from these particles.

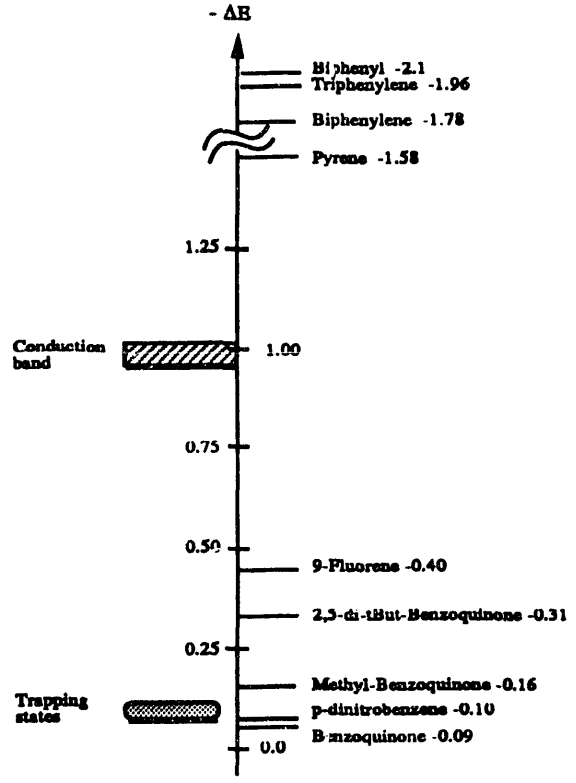

Figure II-3. Redox potentials of organic radical ions (against NHE) and the position of the energy levels of the CdS particles. Values for the radical ions (shown in figure) are corrected for the Nernst factor.

4. Radicals at the Surface of the Particles

The radical ions of the functionalized thiols could be generated by either pulse radiolysis or flash photolysis as described above. The chemical properties of these radicals, however, are notably altered from those in the solution. Figure II-4 illustrates the effect of surface binding on the lifetime of the radical anion of nitrothiophenol (NTP). Clearly, the lifetime at the surface is much longer than for the free radicals. Two main causes were identified for the increased stability of the radicals on the surface. First, the availability of radicals and parent NTP molecules close to one another at the surface inhibits their disappearance. The radicals in solution disappear by dimerization with the parent molecule (reaction 1) followed by disproportionation (reaction 2). The scarcity of mobile molecules and radicals at the surface inhibits these

reactions substantially. Second, the surface potential changes the local pH by approximately two units. Consequently, proton transfer to radical ions (reaction 3) is reduced significantly. Because disproportionation of the radicals proceeds faster for the neutral species, their stability increases. Changes in the acidity of the radical ions and their redox potentials also impact this chemistry.

$$NTP^- + NTP \rightleftharpoons (NTP)_2^- \quad (1)$$

$$2NTP^- \rightarrow P \quad (2)$$

$$NTP^- + H^+ \rightleftharpoons NTPH \quad (3)$$

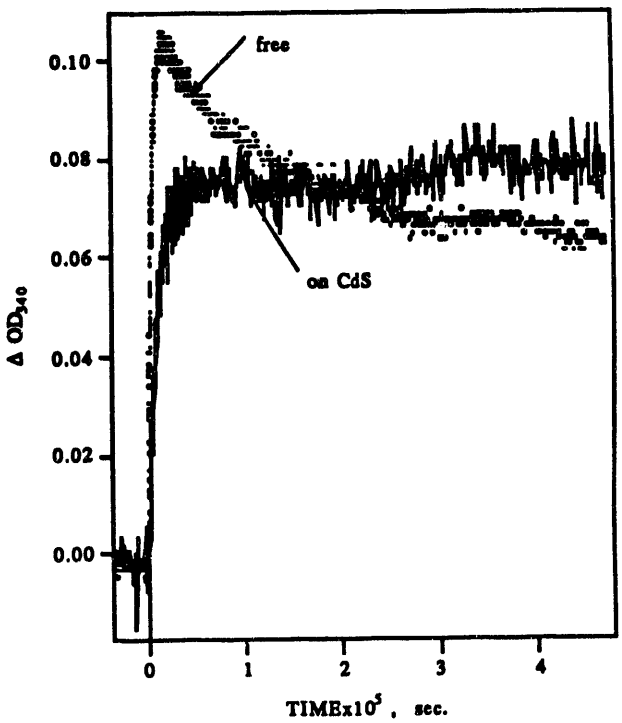

Figure II-4. Effect of surface binding on the stability of the radical ion of nitrothiophenol. Dotted curve - free radical ion in solution. Solid curve - radical ion at the surface of CdS.

PUBLICATIONS

SPECTRA AND REACTIVITY OF THE SOLVATED ELECTRON IN THE PRESENCE OF SODIUM CATION IN TETRAHYDROFURAN AND IN ITS α, α'-METHYLATED DERIVATIVES
P. Piotrowiak* and J. R. Miller
J. Am. Chem. Soc. 113, 5086-5087 (1991)

SUPEREXCHANGE-PATHWAY MODEL FOR LONG-DISTANCE ELECTRONIC COUPLINGS
C. A. Naleway*, L. A. Curtiss*, and J. R. Miller
J. Phys. Chem. 95, 8434-8437 (1991)

KINETIC EFFECTS OF ZETA POTENTIAL ON INTERFACIAL ELECTRON TRANSFER
P. Mulvaney*, F. Grieser*, and D. Meisel
Electrochemistry in Colloids and Dispersions, R. A. Mackay and J. Texter, Eds. VCH Publishers, New York, 1992, 467-473

OXIDATION KINETICS OF ULTRA SMALL COLLOIDAL CHALCOPYRITE WITH ONE ELECTRON OXIDANTS
E. J. Silvester*, F. Grieser*, D. Meisel, and T. W. Healy*
J. Phys. Chem. 96, 4382-4388 (1992)

*Not affiliated with the Chemistry Division or affiliated on a temporary basis.

RADIATION INDUCED GROWTH OF MICRO CRYSTALLITES
D. Meisel
Radiation Research, Vol. 2, W. C. Dewey et al., Eds., Academic Press, 1992, pp. 121-126

ELECTRICAL DOUBLE LAYER EFFECTS ON ELECTRON TRANSFER REACTIONS AT COLLOIDAL METAL OXIDE-AQUEOUS SOLUTION INTERFACES
P. C. Mulvaney*, F. Grieser*, and D. Meisel
Radiation Research, Vol. 2, W. C. Dewey et al., Eds., Academic Press, 1992, pp. 127-132

COMMON THREADS IN PHOTOCATALYSIS AND IMAGING: SILVER, SILVER HALIDES AND SEMICONDUCTORS
D. Meisel
Proceedings, Symposium on "Electronic and Ionic Properties of Silver Halides", 44th Annual Conference of the Society of Photographic Science and Engineering (SPSE), May 12-17, 1991, St. Paul, Minnesota, B. Levy, Ed., Society of Imaging Science and Technology Publication, 1991, pp. 208-215

ELECTRON TRANSFER REACTIONS OF TECHNETIUM AND RHENIUM COMPLEXES. 3. PULSE RADIOLYSIS STUDIES ON TRANS-$[M(III)X_2(DMPE)_2]^+$ AND $[M(I)(DMPE)_3]^+$ COMPLEXES IN AQUEOUS AND AQUEOUS SURFACTANT MEDIA (WHERE M = Tc OR Re, X = Cl OR Br, AND DMPE = 1,2-BIS(DIMETHYLPHOSPHINO)ETHANE)
A. Roodt*, J. C. Sullivan, D. Meisel, and E. Deutsch*
Inorg. Chem. 30, 4545-45549 (1991)

OXIDATIVE HOMOLYSIS REACTIONS BETWEEN ORGANOCHROMIUM MACROCYCLES AND DIHALIDE RADICAL ANIONS
S. Shi*, J. H. Espenson*, D. Meyerstein*, and D. Meisel
Inorg. Chem. 30, 4468-4470 (1991)

REDOX MECHANISMS IN HETEROGENEOUS PHOTOCATALYSIS. HOLE VS. OH RADICAL OXIDATION AND FREE VS. SURFACE-BOUND OH RADICAL OXIDATION PROCESSES
N. Serpone*, D. Lawless*, R. Terzian*, and D. Meisel
Electrochemistry in Colloids and Dispersions, R. A. Mackay and J. Texter, Eds., VCH Publishers, New York, 1992, pp. 399-416

SUBMISSIONS

KINETICS OF URANIUM (VI) REDUCTION IN AQUEOUS POLYELECTROLYTE SYSTEMS
C. G. Pippin*, J. C. Sullivan*, D. Meisel, and R. G. Choppin*
Radiochim. Acta (1992)

SIZE CONTROL AND SURFACE MODIFICATION OF COLLOIDAL SEMICONDUCTOR PARTICLES
C. H. Luangdilok* and D. Meisel
Isr. J. Chem. (Special Issue on Quantum Size Particles) (1992)

ON THE GENERATION OF H_2 FROM FORMALDEHYDE IN BASIC AQUEOUS SOLUTIONS
S. Kapoor*, F. Barnabas*, C. D. Jonah, M. C. Sauer, Jr., and D. Meisel
J. Am. Chem. Soc. (1992)

---

*Not affiliated with the Chemistry Division or affiliated on a temporary basis.

COLLABORATIONS

N. Serpone, Concordia University, Montreal, Canada
Our collaboration with Serpone and his students focuses on two aspects of the oxidative cycles in photoinduced redox processes in colloidal semiconductors: identifying the mechanisms of photooxidation metal-oxide colloidal particles and control of the spectral response and charge-carrier recombination rates in TiO_2 particles. We utilize the linac facility and laser flash photolysis/single-photon counting techniques in these mechanistic studies.

F. Grieser and T. Healy, University of Melbourne, Australia
In this collaboration with the University of Melbourne group, the pulse radiolysis technique is utilized to quantitatively delineate general mechanisms of charge transfer to/from transition metal-oxide colloidal particles of well-defined crystal structure, morphology, and surface compositions. The interaction of electron donors with the surface of the particles is studied using pulse-radiolytically generated radicals in an effort to understand the parameters that control their rate of reaction with the particles.

E. Pelizzetti, University of Turin, Italy
E. Borgarello, Eni Research Center, Eniricerche, Milan, Italy
This three-pronged collaboration concentrates on the growth of noble-metal and metal-oxide particles initiated by radiation chemical techniques. The growth is studied by conductivity, absorption and emission spectroscopies, and light scattering. The reactivity of the small clusters, during the growth process, is studied by a linac-laser synchronized system. The mechanistic aspects of their application in photoredox systems, primarily in photodegradation of pollutants, is explored using flash photolysis.

D. Meyerstein, Ben Gurion University, Israel
J. Espenson, Iowa State University, Ames
The role of metal-carbon bonds in catalytic processes has been recognized for a long time, yet only a few of the reactive intermediates involved in the formation and dissociation of such bonds are known. In this collaboration, the formation of carbon-transition metal (primarily Cr(III)) bonds is studied using pulse radiolysis.

S. Isied, Rutgers University, New Brunswick, NJ
We will attempt to measure rates of electron transfer in binuclear metal complexes separated by amino acid spacers.

C. A. Naleway, American Dental Association Laboratory, Chicago, IL
Methods are being developed to calculate long-distance electronic-coupling interactions for electron-transfer reactions.

III. PHOTOSYNTHESIS AND SOLAR ENERGY CONVERSION

J. R. Norris, M. K. Bowman, L. Chen, H. L. Crespi, J. Tang, M. C. Thurnauer, D. M. Tiede, M. R. Wasielewski, M. P. O'Neil, U. H. Smith, P. Thiyagarajan, H. Levanon, F. Lytle, S. Snyder, W. A. Svec, A. M. Wagner, G. P. Wiederrecht, Y. Zhang, T. J. DiMagno, A. L. Morris, Z. Wang, S. Bondeson, A. Barkoff

Outside Collaborators: *A. Angerhofer, L. Belford, J. Biggins, S. A. Dikanov, P. L. Dutton, G. R. Fleming, Govindjee, R. Griffin, M. Gunner, D. Gust, D. Hanson, P. Höfer, G. Jones, L. Kispert, G. Kothe, O. Micić, P. Montano, T. Moore, M. P. Niemczyk, T. Schaafsma, M. Schiffer, M. Seibert, Yu. D. Tsvetkov, N. C. Yang*

The Photosynthesis and Solar Energy Conversion Group seeks to understand the ingredients that control rapid, efficient, long-lived photoinduced charge separation. Our investigations emphasize a quantitative, molecular-level understanding of natural and artificial photosynthesis, associated electron-transfer reactions, and photochemistry. The crucial foundation for the proper understanding of photo-induced electron transfer rests on our detailed three-dimensional structure of the reaction center. Ultrafast photochemistry is experimentally explored by femtosecond optical spectroscopy and time domain EPR. Various synthetic chemical models, including special and unique systems mimicking artificial photosynthesis, have been synthesized and also probed by femtosecond spectroscopy and time domain EPR. The details of photon-driven charge separation have been examined in bacteria as well as in green-plant systems. A rather complete theoretical understanding of spin dynamics and associated spectroscopy has emerged from our studies of radical pairs generated in the bacterial reaction center. Finally, a recipe for understanding the initial act of photosynthesis is suggested through the studies of bacterial reaction centers modified by site-directed mutagenesis. These focused projects of the photosynthesis group have resulted in working artificial systems as well as in a more detailed understanding of charge separation.

A. Studies of Bacterial Photoreaction Centers

J. R. Norris, M. K. Bowman, L. Chen, H. L. Crespi, J. Tang, M. C. Thurnauer, D. M. Tiede, M. R. Wasielewski, U. H. Smith, D. Hanson, P. Thiyagarajan, M. Schiffer, T. DiMagno, Z. Wang

1. Control of Photochemical Pathways and Assembly of Photosynthetic Structures

D. M. Tiede, P. Thiyagarajan, J. R. Norris

This project examines the mechanisms for control of reaction pathways in bacterial photosynthesis by protein environments. One highlight this year has been the detection of protein relaxation processes following quinone reduction in reaction centers of *Rhodobacter capsulatus*. The thermally activated, microsecond-time-scale electron transfers between the two reaction-center quinones, designated Q_A and Q_B, provide a useful contrast to the activationless, picosecond-time-scale primary reactions. The quinone electron-transfer reactions are being studied to examine the role of the protein in the reorganization reactions that are required to activate this reaction.

The formation of the Q_A and Q_B anions produces distinctive optical absorption shifts of the reaction-center bacteriochlorophyll and bacteriopheophytin molecules in static, photochemically trapped PQ^- states. These shifts can be understood as a through-space electrostatic interaction between the transition moments of these molecules and the electric fields associated with the quinone anions. One intriguing feature is that Q_A^- and Q_B^- induce characteristic but different absorbance changes despite the structural symmetry of the reaction center.

In this work, we have measured the time-resolved electrochromic shifts of the bacteriochlorophyll and

bacteriopheophytin molecules associated with the formation of the quinone anions in the reaction center. These experiments provide a vehicle for measuring the electric field propagation through the reaction-center protein, and identify reorganization processes that affect this propagation.

The optical absorbance changes associated with the formation of the static PQ_A^- and PQ_B^- states in *Rb. capsulatus* reaction centers are shown in the top portion of Figure III-1. The most prominent change produced by the formation of Q_A^- is a red-shift of a transition centered around 760 nm. This can be assigned to the bacteriopheophytin, designated Bph_A, that functions as an electron acceptor during the primary reactions. Additional shifts are also seen for a bacteriochlorophyll transition, centered around 815 nm, and for the special pair in the 850-900-nm region. In contrast, the most prominent change produced by the formation of Q_B^- is a red-shift centered at 750 nm that can be assigned to the photochemically inactive bacteriopheophytin, Bph_B. Q_B^- is seen to cause only minor perturbations of the other chromophores.

The stronger perturbation of Bph_A by Q_A^- and Bph_B by Q_B^- makes intuitive sense because the crystal structures show that each quinone is closely associated with a single bacteriopheophytin. However, there is no obvious structural feature to explain the difference in perturbation of the bacteriochlorophyll absorptions by Q_A^- and Q_B^- in light of the nearly equivalent positions of the quinones with respect to the bacteriochlorophylls. In this project we have found an explanation for these anomalies by measuring the time-resolved spectra associated with the quinone anions.

The static spectra shown in Figure III-1 predict that electron transfer from Q_A^- to Q_B should be accompanied by absorption changes shown by the difference spectrum in the lower portion of this figure. Difference spectra recorded during the Q_A^- to Q_B electron transfer are shown in Figure III-2. The Q_B^--Q_A^- difference spectrum measured 100 μs following excitation differs markedly from that predicted in Figure III-1.

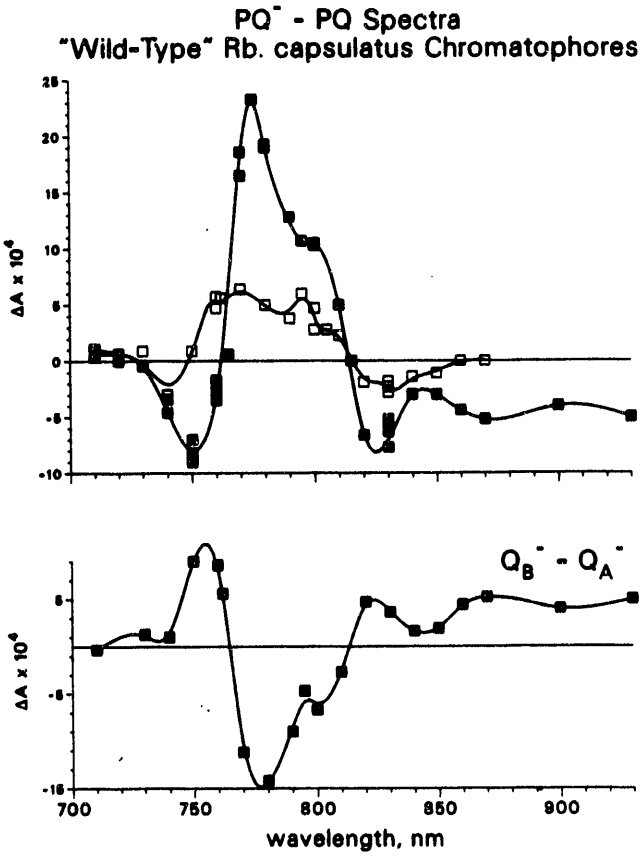

Figure III-1. Difference spectra associated with quinone reduction in *Rb. capsulatus*. The top portion of the figure shows the absorbance changes measured upon the static reduction of Q_A, ■, and Q_B, □. The lower portion of the figure shows the difference between these two spectra. This is the predicted spectrum of the absorbance changes expected to accompany Q_A^- to Q_B electron transfer.

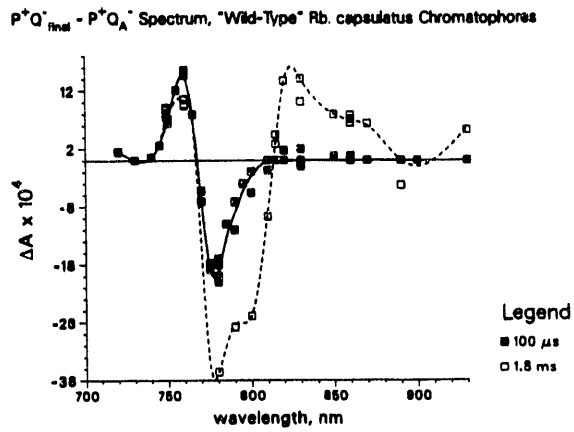

Figure III-2. Transient $Q_AQ_B^-$-$Q_A^-Q_B$ difference spectra in chromatophores of *Rb. capsulatus*. The spectrum marked by the filled squares is the difference between the absorbance of the $P^+Q_AQ_B^-$ state measured at 100 μs following laser excitation and the initial $P^+Q_A^-Q_B$ state, measured at 2 μs. The unfilled squares mark the absorption difference between the $P^+Q_AQ_B^-$ state measured 1.8 ms after laser excitation, minus that of the initial $P^+Q_A^-Q_B$ state.

Only the bacteriopheophytin absorption bands are seen to respond promptly to the electron transfer from Q_A^- to Q_B. This is also illustrated by the absorption transients measured at single wavelengths, shown in Figure III-3.

In contrast to the prompt response of the bacteriopheophytin absorption bands, the electrochromic shifts of the bacteriochlorophylls are initially unaffected by the electron transfer from Q_A^- to Q_B. These results suggest that initially both quinone anions produce equivalent absorption shifts on the bacteriochlorophylls, as expected from the reaction-center structure. However, following the formation of the $P^+Q_AQ_B^-$ state, relaxation processes with a response time of about 400 μs are found to attenuate the electrochromic shifts in the bacteriochlorophyll-band region. A similar relaxation is seen for the $P^+Q_A^-$ state when its lifetime is extended by blocking electron transfer to Q_B. However, the quenching of the electrochromic shift is found to be greater for Q_B^- than Q_A^-.

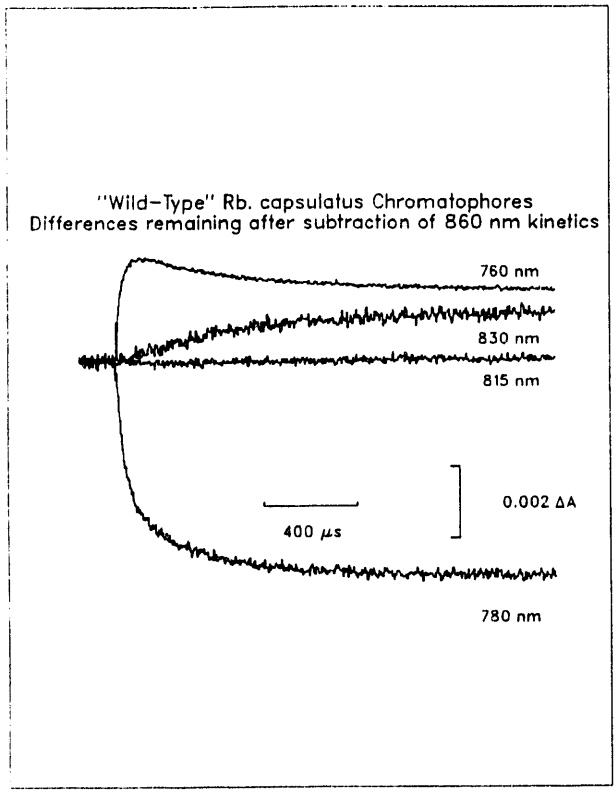

Figure III-3. Absorbance transients remaining after subtraction of the decay kinetics for P^+, measured at 860 nm. These traces show the kinetic components that are present at selected wavelengths, but absent in the 860-nm transients.

The time evolution in these spectra can be interpreted as due to a charge reorganization in the vicinity of quinone anions that leads to a stabilization of charge and attenuation of the electric field propagation through the protein. The pH dependence of the relaxation kinetics in the bacteriopheophytin bands implies that at least part of the quenching mechanism involves proton transfer. In addition, variations in this relaxation phenomena in reaction centers containing mutations at single amino acid sites suggest it may be possible to identify the involvement of specific residues in the relaxation process.

2. Investigation of Artificial Photosynthesis Using Unnatural Photosynthesis

J. R. Norris, L. Chen, H. L. Crespi, G. R. Fleming, T. DiMagno, D. Hanson, M. Schiffer, U. H. Smith, A. Wagner

Recently, we have addressed two major issues of the primary events of photosynthesis: Why is only a single side (the A-side) of the highly C2 symmetrical reaction center active? How does the electron get from the special pair donor (P) to the bacteriopheophytin acceptor (H_A)? To probe these questions we have explored the correlation between the reduction potential of the primary donor and the initial charge-separation rate measured by femtosecond spectroscopy in a series of mutated reaction centers from *Rb. capsulatus.*

A usual method for determining the rate of photoinduced electron transfer in the primary events of photosynthesis is via the lifetime of the excited, singlet state of the primary donor, P*. Most determinations of this lifetime are based on stimulated emission, and are interpreted with a single exponential process. In this survey, using improved signal-to-noise, the lifetime of P* as measured by monitoring either stimulated emission or spontaneous emission is never characterized by a single exponential process.

That the decay of P* is not a single exponential process complicates the interpretation of the primary events of bacterial photosynthesis. Is the data bi-exponential, multiexponential, stretched-exponential, or another possibility? Here we treat the decay of P* as a biexponential process. Additionally, the possible origins of the nonsingle exponential decay must be contemplated. At least four following possibilities exist: (1) incomplete vibrational relaxation after excitation, (2) sample heterogeneity, (3) intrinsic nonsingle exponential decay, and (4) undoubtedly, to some

extent, coexistence of the three previous classifications.

Currently, differentiating among the various possibilities is premature. Instead, in this survey the consequences of assuming that the observed decay of P* is an intrinsic biexponential process arising from homogeneous reaction centers, that is, case (3) above, is discussed. Additionally, the correlation between reduction potential of the primary donor and the reaction rate of the primary event is explored.

To examine the nonsingle exponential decay, we have investigated a series of symmetry-related mutants of *Rb. capsulatus* by assuming that the wild-type *Rb. sphaeroides* R-26 reaction-center structure is an accurate model for the mutated, reaction-center proteins of *Rb. capsulatus*. The manipulations of the amino acid sites L181 and M208, related by C2 symmetry as shown in Figure III-4, produce modified chemical kinetics for the initial charge-separation event. Because the L181 group, located primarily on the inactive B side, has almost the same effect in altering the chemistry as does the M208 moiety on the active A side, we have also assumed that the dominant role of these two sites is via the special pair. Finally, we assume that the mutations create no significant structural modifications for influencing the electron-transfer rates.

In order to explain the kinetic differences produced by these mutations, we have correlated electron-transfer rate with the free energy of the initial chemistry by measuring the reduction potential of the primary donor in the dark. In wild-type and mutant reaction centers, the free-energy gaps G(WT) and G(Mutant), respectively, between P* and the initial product, perhaps P^+BH_A, can be approximated by the following equations:

$$G(WT) = -E_D(WT) + E_A(WT) + E_C(WT) + G_{P^*}(WT) \quad (1a)$$

$$G(Mutant) = E_D(Mutant) + E_A(Mutant) + E_C(Mutant) + C_{P^*}(Mutant), \quad (1b)$$

where, in equation 1a, $E_D(WT)$ is the reduction potential of the donor, $E_A(WT)$ is the reduction potential of the relevant acceptor, $E_C(WT)$ is a Coulombic correction factor and $G_{P^*}(WT)$ is the free-energy offset from P*. Because the optical spectrum of P is virtually unchanged by the mutations, the relative energy of P* is assumed not to be changing with the mutation. Equation 1b, the same as equation 1a, is written explicitly for mutated reaction centers.

Previously, we have documented that the major effect of the M208 and L181 amino acids is not on the acceptors but, by default, on the special pair. Consequently, the effect of both the M208 and the L181 sites on B_A and H_A will be neglected such that only the reduction potential of the donor changes (i.e., $E_A(WT) \equiv E_A(Mutant)$) and $E_C(WT) \equiv E_C(Mutant)$). By subtracting equation 1b from equation 1a, the free energy can be expressed solely in terms of the reduction potential of the donor and the energy offset from P*, G_{P^*}, as described in equation 2b,

$$\Delta G(Mutant) \equiv G(WT) - G(Mutant) = -E_D(WT) + E_D(Mutant) + G_{P^*}(Mutant) - G_{P^*}(WT) \quad (2a)$$

or

$$\Delta G(Mutant = -E_D(WT) + E_D(Mutant) + G_0, \quad (2b)$$

where $G_0 \equiv G_{P^*}(Mutant) - G_{P^*}(WT)$ is a reference free energy. In other words, the absolute free energy for either wild-type or a particular mutant reaction center is not needed, only the difference in the reduction potential between the donor in wild-type and the donor in mutated reaction centers. Finally, by assuming that the reorganization energy, λ, and the electronic matrix element for electron transfer, V, are independent of mutation, a Marcus parabola correlates reduction potential to the log of the rate based on equation 3. Inasmuch as the experimental data accurately fits a parabola the assumptions appear to be reasonable.

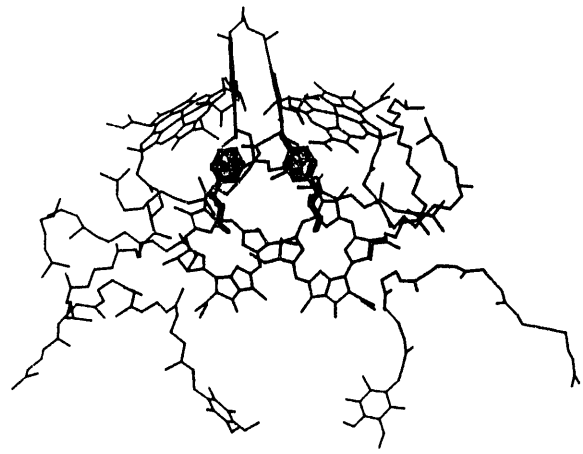

Figure III-4. *Rb. sphaeroides* R26 reaction-center structure with the C_2 related residues phenylalanine L181 (left) and tyrosine M208 (right) along with the other chromophores. The active A side is on the right.

$$k = \frac{2\pi}{\hbar(4\pi k_B T)^{1/2}} V^2 \exp\left[\frac{\{\Delta G(WT \text{ or Mutant}) - \lambda\}^2}{4 k_B T \lambda}\right] \quad (3)$$

Ten different reaction centers have been constructed and measured. Thus, we have 10 equations to determine only four parameters (G(WT), G_0, λ, and V). Given these four parameters and the measured difference in reduction potential, the rate of any reaction-center mutant can be estimated. By definition, G_0 will represent the offset in free energy between the putative intermediate state and P* in wild-type reaction centers.

Rate constants and redox potentials for 10 reaction centers, including wild-type *Rb. capsulatus*, are presented in Table III-1. In most cases that have been probed by both stimulated and spontaneous emission, the fast component of the spontaneous emission agrees with the single rate constant by stimulated emission reported in the past. The redox potentials were determined chemically with a potassium ferricyanide/ferrocyanide redox couple. The state of oxidation of the special pair was monitored by optical absorption spectroscopy. The reference potential for Table III-1 is the standard hydrogen reaction. Typically, reproducibility was better than ±5 mV and the value determined for wild type is in reasonably good agreement with other laboratories. Experiments are in progress to establish the accuracy of the reduction potentials reported in Table III-1.

As shown in Figure III-5, the logarithm of the rate versus the measured reduction potential of the "dark" donor special pair can be described rather accurately by a parabola. A variety of theoretical approaches will result in such a parabolic relationship. For simplicity of interpretation, we have used the simple, nonadiabatic electron-transfer theory of Marcus.

The correlation in Figure III-5 when described by Marcus theory gives a G(WT) for wild-type reaction centers of *Rb. capsulatus* of approximately 50 cm^{-1}. Not as evident, but perhaps more important, the apparent low-frequency reorganization energy, λ, is

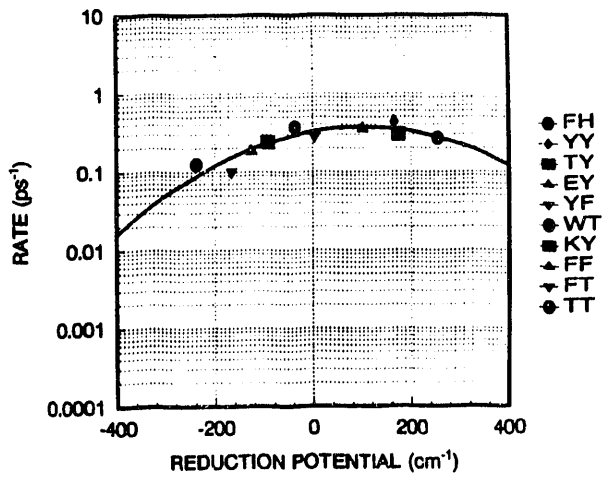

Figure III-5. Experimental rate versus reduction potential for reaction centers from *Rb. capsulatus*. Left letter = L181. Right letter = M208. WT = wild type.

Table III-1. Kinetic and redox properties of mutated reaction centers.

mutation inactive-active	lifetime ps (fast)	%	lifetime ps (long)	%	redox potential (mV)
Phe-His	3.7*				466
Tyr-Tyr	2.3$^{\tau}$	84.4	10.5	15.6	477
Thr-Tyr	3.2*				476
Glu-Tyr	2.8*				485
Tyr-Phe	3.5$^{\tau}$	59.5	24.2	40.5	497
Phe-Tyr (WT)	2.7$^{\tau}$	72.3	11.1	27.7	502
^{1}H sphaeroides	2.7$^{\tau}$	80.8	12.1	19.2	530
^{2}H sphaeroides	3.2$^{\tau}$	82.6	16.5	17.4	---
Lys-Tyr	4.2*				509
Phe-Phe	5.4$^{\tau}$	53.3	40.0	46.7	513
Phe-Thr	10.0$^{\tau}$	38.0	70.0	62.0	518
Thr-Thr	8.0*	51.8	56.3	48.2	527

*Measured by stimulated emission.
$^{\tau}$Measured by spontaneous emission.

$\cong 100\ cm^{-1}$ or less, that is, extremely small. Within the confines of our assumptions, the small reorganization energy suggests that an explanation other than simple Marcus theory may be needed. As one alternative, the electron-transfer process may involve a nearly degenerate intermediate charge-separation state in resonance with P*. For example, if the intermediate is operating partially via the superexchange mechanism, then the relevant superexchange energy gap is close to zero. Consequently, the maximum of the parabolic relationship shown in Figure III-6 would be enhanced by a resonance phenomenon associated with the three-level degeneracy (initial state, intermediate state, and final state). In such a case, the steepness of the rate versus reduction potential arises from the resonance and not from a small reorganization energy.

The homogeneous kinetics of Figure III-6 previously invoked for the reaction center results in biphasic kinetics with the assumption that $k_1/k_{-1} = \exp\{-G(WT)/(k_BT)\}$. Previous interpretations of the kinetics were based on a dominant, single exponential process of P*, where $k_2 > k_1$, and the energy level of the intermediate state P^+BH_A is more than k_BT away from the energy level of P*. But if the intermediate state is nearly within k_BT of the energy of P*, then the amplitude of the second component should become experimentally determinable as shown in Table III-1. For the relative amplitudes of the two components in Table III-1, k_2 for wild-type reaction center is required to be smaller than k_1, that is, $k_2 < k_1$. In other words, the electron-transfer chemistry becomes dominated by the superexchange process where P^+BH_A (or whatever the intermediate state is) serves as a superexchange coupling state and as a "parking state". However, one alternative explanation is the more conventional view with $k_2 > k_1$. In this description of the observations, the observed biphasic or multiphasic decay of P* is the result of reaction-center heterogeneity and/or incomplete vibrational relaxation.

3. Treatments of Excitation and Electron Transfer Using the Redfield Formalism

J. R. Norris, J. Tang, Z. Wang

Electron-transfer reactions play an essential role in chemical and biological processes such as oxidation-reduction and photosynthesis. To improve our understanding of these processes we have developed a more general theoretical approach to tackle problems such as the effects of solvent dynamics on electron transfer, the competing superexchange and sequential electron-transfer mechanisms in photosynthesis, and the effects of fluctuating electronic coupling on electron transfer for a nonrigid system.

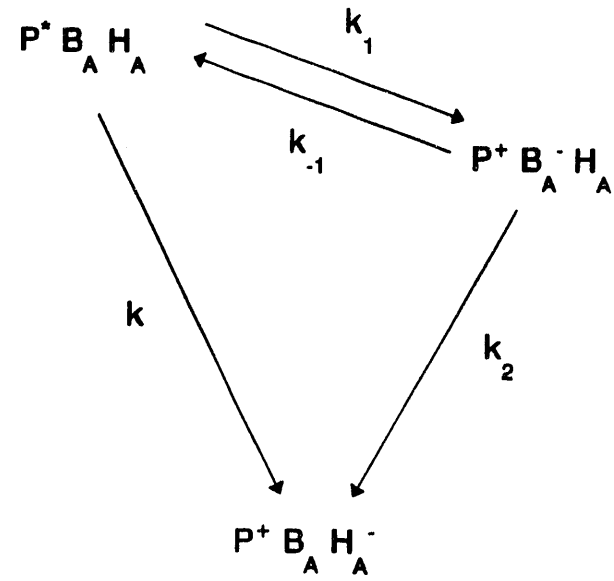

Figure III-6. Kinetic scheme incorporating an intermediate state to produce the complex biexponential kinetics observed in the fluorescence spectra.

a. General Treatment of Dynamic Solvent Effects in Electron Transfer at High Temperature

To improve our understanding of electron-transfer reactions we have developed a theoretical approach for the treatment of the solvent effects on the electron transfer at high temperature. Unlike earlier work of others, the treatment is general and covers the whole span of the solvent relaxation time. In our approach, we have employed the nonperturbative Zusman equation. In the hybrid equation there is a classical Smoluchowski diffusion operator describing the effects of over-damped solvent on the electron, and a quantum mechanical part describing the mixing of the donor and the acceptor via the electronic coupling. We have performed numerical solutions for such an equation using various time scales for the solvent relaxation. In the normal nonadiabatic limit when the solvent relaxation is fast, our result confirms the prediction of the famous Marcus equation. In the adiabatic regime in which the solvent friction slows down the electron-transfer process, our calculation agrees well

with Jortner's results, which include an adiabaticity factor in the Marcus rate expression. In addition, we have identified an interesting new regime of ultrafast nonadiabatic solvent relaxation in which the electron-transfer rate is enhanced with an inverse dependence on solvent relaxation time different from Kramer's classical results of chemical reaction rate in the small viscosity limit. The enhanced electron-transfer rate in our calculation results from extensively induced energy-level overlap by the uncertainty broadening due to a short solvent relaxation time.

b. Superexchange and Sequential Electron-Transfer Mechanisms in a Three-site System

We have extended our approach using the Zusman equation to investigate the mechanisms of superexchange versus sequential electron transfer in a three-site system involving reactant, intermediate, and product. Unlike many previous works using the second-order perturbation theory, which assumed the direct vertical energy gap between the donor and the intermediate is much larger than the electronic couplings, our approach is nonperturbative and the contributions from all higher order terms of the electronic coupling are included inherently. Thus, it allows us to examine a wider range of conditions from nonadiabatic to adiabatic cases as well as from nondegenerate to degenerate cases when all three Marcus parabolas cross at the same point so that the direct vertical energy gap vanishes. We have identified a new "resonance-shaped" effect on superexchange electron-transfer rate (shown in Figure III-7) that results from energy-level crossing. Our calculations also indicated that the sharp curvature in the Marcus plot of the observed electron-transfer rates versus free energy for photosynthetic reaction centers of *Rhodobacter capsulatus* wild type and mutants may be related primarily to the "resonance" effect of the superexchange, and may not directly reflect the true reorganization energy. The observed mild temperature dependence for the electron-transfer rate is also consistent with the activationless superexchange mechanism.

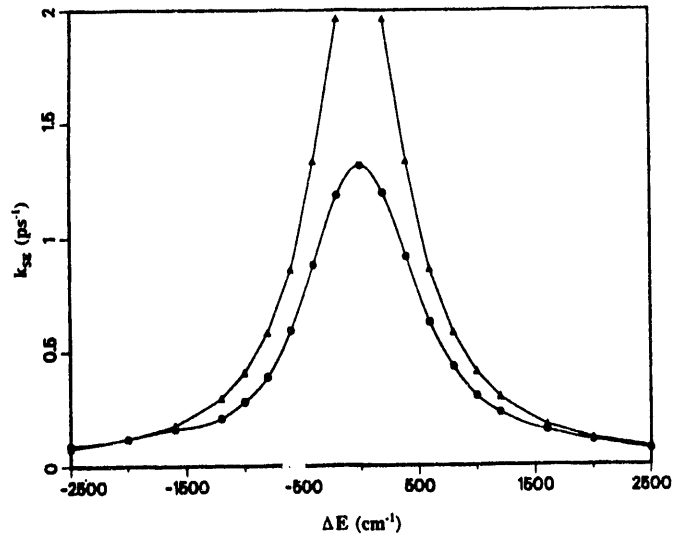

Figure III-7. Calculated superexchange electron-transfer rate vs. the direct vertical energy gap ΔE as shown by the bottom curve. The top curve using the second-order perturbation theory shows a divergence at the center.

c. Effects of Fluctuating Electronic Coupling on Electron Transfer

In most theoretical treatments of electron transfer, the Condon approximation is usually made assuming that the electronic coupling is not affected by the solvent dynamics. It is a good approximation if the electron transfer involved is in a rigid system. However, for long-distance intermolecular electron transfer in liquid solution or intramolecular electron transfer involving a highly flexible molecular frame, the electronic coupling can be modulated in time and, thus, the ordinary Condon approximation to factor out the electronic coupling from the Frank-Condon factor may not be valid. We have developed a model to describe the effects of fluctuating electronic coupling on electron transfer. Our calculations indicate a diminished electron-transfer rate in the limits of a very short correlation time for the electronic coupling. However, under certain favorable conditions, depending on the correlation time, the reorganization energy, and the free-energy gap, the electron-transfer rate can be enhanced by the fluctuating electronic coupling.

B. Structural and Energetic Factors in Photoinduced Charge Separation

M. C. Thurnauer, J. R. Norris, S. W. Snyder, A. L. Morris, U. H. Smith, H. L. Crespi, Y. Zhang, S. Bondeson, A. Barkoff

Our work focuses on understanding the structural and energetic features that are required for a system to undergo efficient photoinduced charge separation, that is, the conversion of light energy into electrochemical potential. This process typically occurs by the sequential electron-transfer steps shown schematically in Figure III-8. A so-called donor (D) is excited by light, and from its excited state, D*, rapidly transfers an electron down an energy cascade of electron acceptors until the distance between the electron and hole is such that recombination is prevented for hundreds of microseconds to milliseconds. The efficiency of this process is determined, in large part, by the energetic and structural properties of the system. The natural photosynthetic systems carry out charge separation very efficiently. By studying and comparing the charge-separation process in several photosynthetic systems, we expect to determine the critical structural and energetic features required for high-yield charge separation.

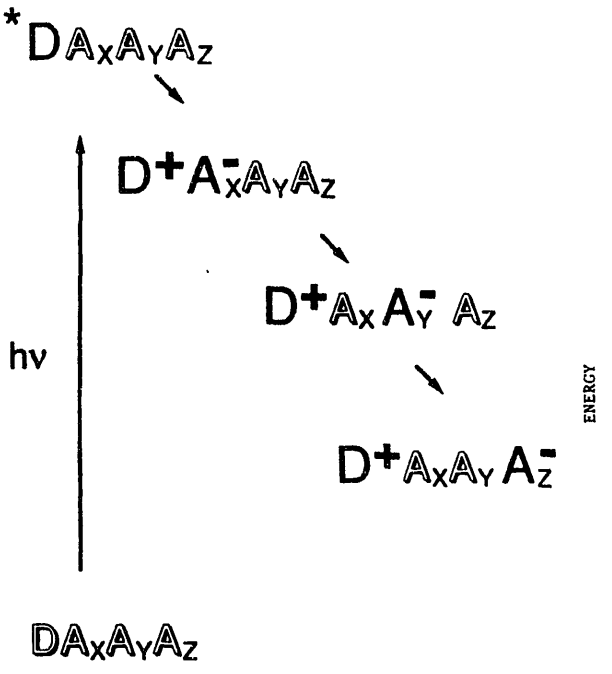

Figure III-8. General description of photoinduced electron transfer leading to stabilized charge separation.

Purple Bacteria	P $BChl_2$	B BChl	I BPh	Q_A Quinone	Fe Q_B
PSII	P Chl_2		I Ph	Q_A Quinone	Fe Q_B
PSI	P (Chl)		A_0 Chl	A_1 Quinone	$[F_XF_aF_b]$ Fe-S centers
Green Bacteria	P (BChl)		A_0 BChl	A_1 Quinone	$[F_XF_aF_b]$ Fe-S centers

Figure III-9. Comparison of the reactants that participate in the initial charge-separation steps in four natural photosynthetic systems.

Figure III-9 shows the reactants that participate in initial charge separation in two different photosynthetic bacteria and the two photosystems of plants. The sequence of events leading to successful energy conversion is well defined in the case of the purple photosynthetic bacteria. The primary electron donor (P) is composed of a pair of bacteriochlorophyll molecules. Electron transfer proceeds through a series of acceptors, including a bridging, monomeric bacteriochlorophyll, a bacteriopheophytin (I), and a quinone (Q_A), which interacts magnetically with a nonheme iron (Fe^{2+}). The reduced quinone is considered to be the first "stabilized" acceptor. Comparisons between photosystems reveal that the electron-transfer sequence is highly conserved in terms of types of species involved in formation of the stabilized charge-separated state. However, speculation increases in descending order for the photosystems presented in Figure III-9. For example, there is no definitive proof that A_1 is involved in electron transfer along the same pathway as A_0 and F_X in PSI. In green-sulfur bacteria, the electron-transfer sequence is primarily based upon analogy with PSI. By applying time-resolved EPR techniques to study these systems, we are working to verify the identity of the donors and acceptors, and concurrently, to study the significance of the similarities and differences in structure and function in these photosystems.

The purple photosynthetic bacteria are best defined because the crystal structure of the reaction-center protein (the site of charge separation) has been determined. Therefore, this system provides a basis

for comparison of the natural photosystems. Because the initial "stabilized" charge separation takes place between P and Q_A, the purple bacterial reaction centers show that at least two electron-transfer steps are needed for efficient charge separation. The critical structural factors required to produce this charge separation also confer unique magnetic resonance properties that develop on the transient paramagnetic species produced in these early energy conversion steps. In particular, the charge-separated state exhibits a characteristic electron spin polarization (ESP) when studied by time-resolved electron paramagnetic resonance techniques. In fact, one measure of successful replication of charge separation in artificial photosynthetic systems is duplication of the ESP behavior. Therefore, a major goal of this research is to follow and characterize the ESP developed in the early electron-transfer steps of photosynthesis. A complete understanding of the phenomenon will make it possible to further define these reactions in several of the photosynthetic systems that are poorly characterized, and to develop an understanding of artificial photosynthetic systems.

We have formulated a theoretical model that describes how ESP evolves in a system undergoing sequential electron transfer. Application of the model to the electron-transfer reactions that take place in purple photosynthetic bacteria makes it possible to test the model and demonstrate its sensitivity to structural and kinetic variations. The reactions under consideration are shown in Figure III-10.

Our model considers ESP development on radical pair 1 (RP_1) that is then projected onto radical pair 2 (RP_2), the state that is observed by EPR. It differs from other models that only consider ESP development on either RP_1 or RP_2. The model clearly demonstrates that the extent to which RP_1 or RP_2 contributes to the ESP observed on RP_2 depends on the relative magnitudes of the magnetic interactions on RP_1 compared to the lifetime of RP_1. This point is illustrated in Figure III-11, which shows how the EPR spectrum of the charge-separated state in purple bacterial reaction centers ($P^+Q_A^-$) depends on the lifetime of RP_1 for both Fe^{2+}-depleted (Figure III-11a) and Fe^{2+}-containing (Figure III-11b) reaction centers.

Several illuminating conclusions can be drawn from the calculated spectra of Figure III-11. For the relatively "broad" linewidths of the radicals found in the photosynthetic systems, when the ESP from RP_1 dominates (lifetime of RP_1 > 2 ns), the spectrum is

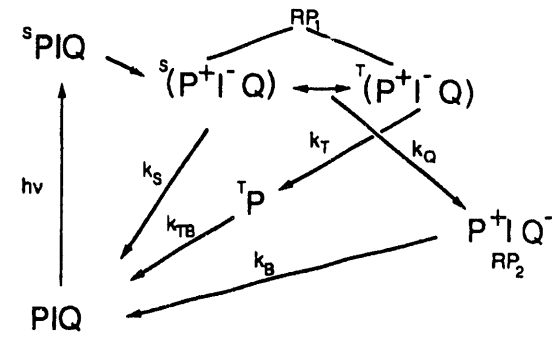

Figure III-10. Schematic of the reactions which lead to stabiiized charge separation ($P^+IQ_A^-$) in purple bacterial reaction centers. The model of ESP in sequential electron transfer includes all decay routes of RP_1.

more intense than when the ESP from RP_2 dominates (lifetime of RP_1 < 700 ps). In the latter case, systems with relatively broad linewidths, such as protonated samples compared to deuterated samples, will have strongly attenuated ESP signals. In other words, if the lifetime of RP_1 is slightly lengthened from what it is in intact, native reaction centers (200 ps), the spectrum strongly resembles the case where ESP is developed solely on RP_1. This point, and the smooth transition of the spectrum as a function of the lifetime of RP_1, would not have been evident without our complete model for ESP in sequential electron transfer.

Previously, we have studied the ESP found in iron-depleted purple bacterial reaction centers (Figure III-11a). In these systems, we have varied either the lifetime of RP_1 or its magnetic interactions by isotopic substitution (P^+, Q_A^- either both deuterated, protonated, or one deuterated and the other protonated), obtaining spectra at more than one microwave frequency, and substituting the Fe^{2+} with diamagnetic Zn^{2+}. In summary, the complete model is required because all the results cannot be explained with ESP development solely on RP_1 or RP_2. Our recent results on iron-containing purple bacterial reaction centers demonstrate clearly that our complete model is necessary in order to fully understand the ESP in purple bacterial reaction centers.

The lifetime of RP_1 can be changed by replacing the native ubiquinone-10 with quinones that have different redox potentials, thereby changing the free energy of the electron transfer from RP_1 to RP_2. In collaboration with Gunner (City College of New York) and Dutton (University of Pennsylvania), we have studied the ESP in purple bacterial reaction

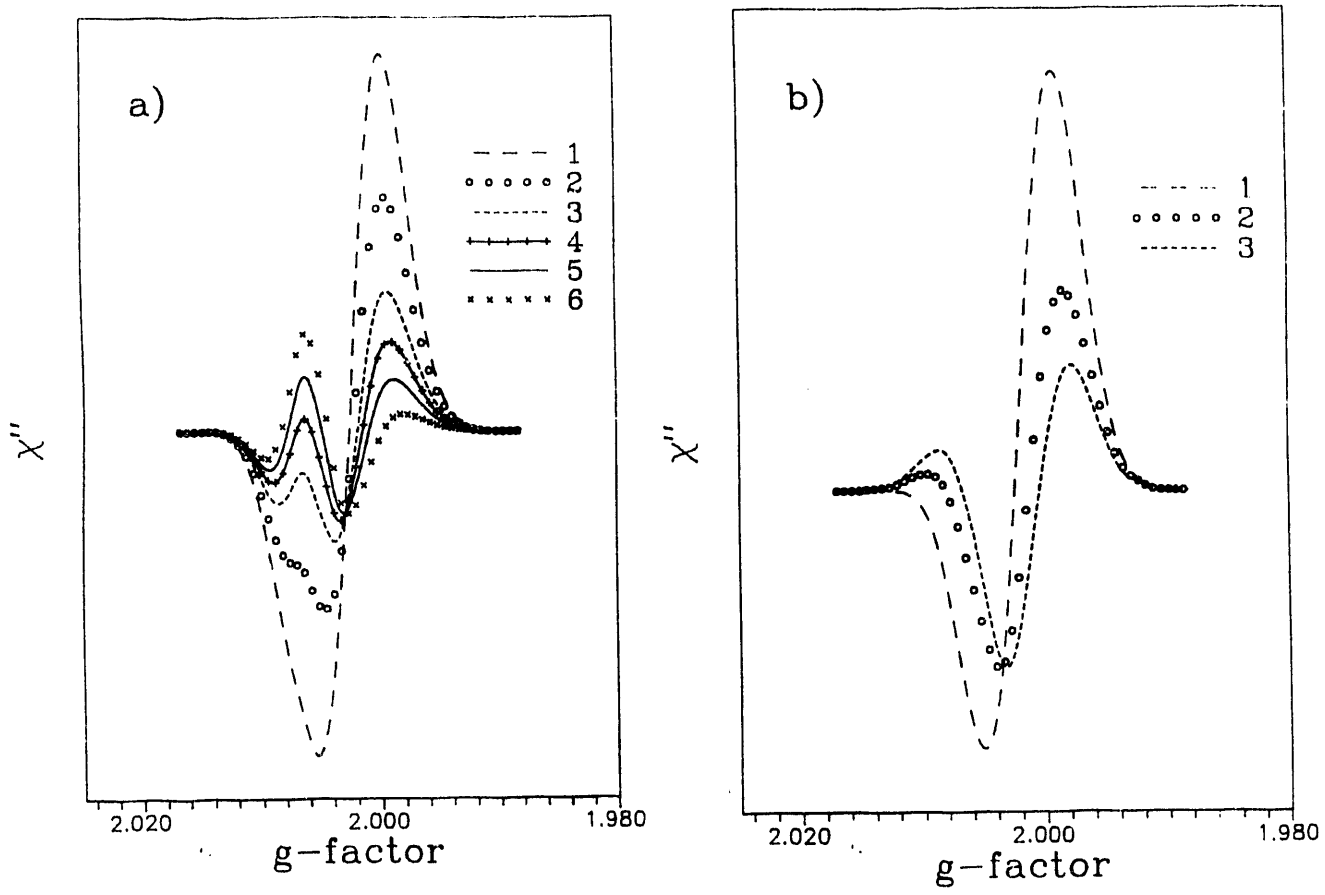

Figure III-11. Calculated dependence of the ESP-EPR spectra from the charge-separated state $P^+Q_A^-$ in (a) iron-depleted reaction centers of purple photosynthetic bacteria (protonated samples, X-band microwave frequency). Signal due to overlapping P^+ and Q_A^-. D_{PI} = -8.5G; D_{PQ} = -2G; J_{PI} = 7G; J_{PQ} = 0; k_S = $3e6s^{-1}$; k_T - $4e8s^{-1}$; 1) k_Q = $1e8s^{-1}$; 2) k_Q = $3e8s^{-1}$; 3) k_Q = $5e8s^{-1}$; 4) k_Q = $7e8s^{-1}$; 5) k_Q = $1e9s^{-1}$; 6) k_Q = $2e9s^{-1}$. (b) Iron-containing reaction centers from purple photosynthetic bacteria (protonated, X-band). D_{PI} = -4.5G; D_{PQ} = -1.5G; J_{PI} = 7.0G; J_{PQ} = 0; k_S = 1e6; k_T = 6e8; 1) k_Q = 5e9; 2) k_Q = 2e9; 3) k_Q = 1.0e9; 4) Signal due to P^+ only. The $Q_A^-Fe^{2+}$ signal is broad and is not observed in the spectral range of the figure.

centers containing a variety of quinones. Several examples of the spectra obtained are shown in Figure III-12. The spectra and plots of spectral intensity vs. yield of $P^+"Q_A^-"$ (related to lifetime of RP_1) can be simulated with the assumption that ESP develops solely on RP_1 (P^+I^-), and with no magnetic interactions on the observed charge-separated state (with the exception of the samples that have high $P^+"Q_A^-"$ yield and give very weak signals). This result is surprising because, from the crystal structure of the reaction-center protein, the distance between P and Q_A is known, and a small dipolar coupling is expected. The result, however, is only understood in the context of our complete model. As discussed above and shown in Figure III-11b, when the lifetime of RP_1 is 600 ps or longer, the ESP spectrum of P^+ looks very much like that of the one that would be obtained for ESP development solely on RP_1.

Recently, we have obtained ESP-EPR spectra from native iron-containing purple bacterial reaction centers. The spectra found in both protonated and deuterated reaction centers are shown in Figure III-13a,b. The distinct ESP pattern clearly resembles the pattern predicted for a 200 ps lifetime of RP_1 and magnetic interactions between P^+ and Q_A^- (Figure III-11b). Note also the weak signal in the high-yield sample (Figure III-12) shows the same pattern as predicted. Thus, we can accommodate all the results with one model.

Another test of the model is to compare spectra at more than one microwave frequency. Figure III-14a,b shows the spectra for the case of reaction

centers reconstituted with 2,7-dimethyl anthraquinone obtained at 9.5 (Figure III-14a) and 35 GHz (Figure III-14b). Although the change in ESP going from low- to high-frequency (shift to more absorptive) can be interpreted by ESP development solely on RP_1, the good fits shown in Figure III-14 are obtained with our complete model.

Now that we are confident that we understand ESP in sequential electron transfer we are beginning to apply this understanding to study photosynthetic systems other than the purple photosynthetic bacteria. Examples from plant PSI, the green-sulfur bacteria, and site-directed mutants of the purple bacterium *Rb. capsulatus* are presented here.

In the case of PSI, we have shown recently (in collaboration with Biggins, Brown University) that the charge-separated state that exhibits ESP is due to $P^+A_1^-$ (Figure III-9), and that A_1 is phylloquinone or vitamin K_1. The characterization of the signal

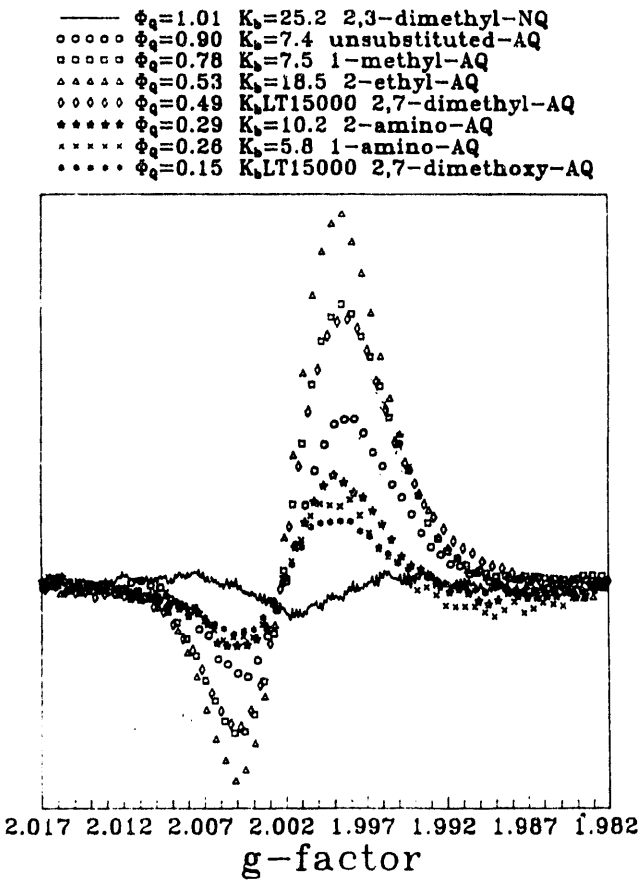

Figure III-12. Examples of ESP-EPR spectra of P^+ in iron-containing, quinone-replaced reaction centers of *Rb. sphaeroides*. The yields ϕ_Q of $P^+Q_A^-$ are related to k_Q.

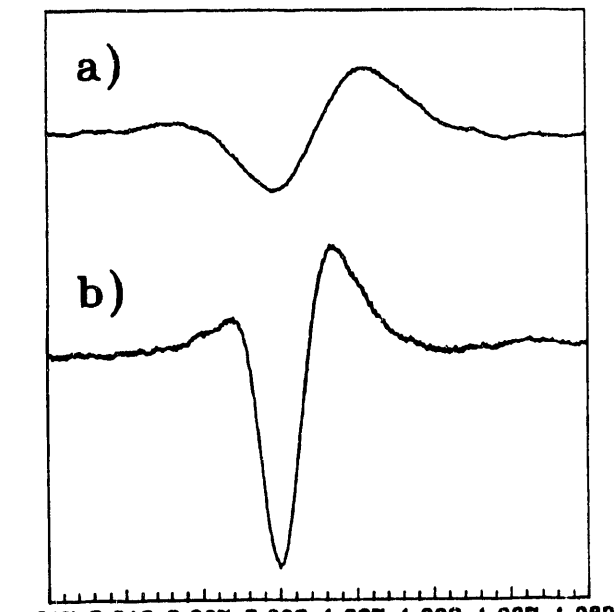

Figure III-13. Electron spin polarization of $P^+[QFe^{2+}]^-$ in native iron-containing reaction centers of *Rb. sphaeroides*. a) protonated sample, b) deuterated sample.

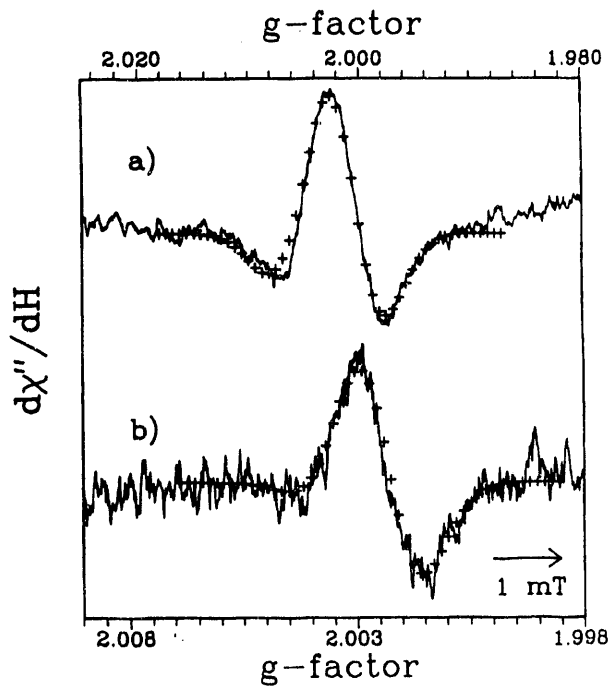

Figure III-14. ESP-EPR spectrum of P^+ in iron-containing reaction centers of *Rb. sphaeroides* R26 in which the native ubiquinone-10 has been replaced with 2,7-dimethylanthraquinone. (Note: spectra obtained with light-modulation EPR technique and therefore are the derivative of absorption mode.) (a) X-band (9.5 GHz) spectrum. (b) Q-band (35 GHz) spectrum. The fits are obtained using the general model of ESP in sequential electron transfer with the following relevant parameters. $k_T = 4e8s^{-1}$, $k_S = 3e6s^{-1}$, $k_Q = 6e7s^{-1}$, $D_{PQ} = -2$ G.

involved experiments in which the native quinone was extracted from the reaction center with organic solvents and reconstituted with deuterated phylloquinone. Recently, we have demonstrated that the native quinone is labile in that it will exchange with deuterated phylloquinone without an initial extraction of the native quinone. Figure III-15 gives an example of a fully deuterated PSI sample in which the "native" deuterated phylloquinone has been exchanged with protonated phylloquinone. As expected (see above), the intensity of the protonated quinone signal is severely attenuated. This is verified by the preliminary fits to the data using the sequential electron-transfer ESP model. Thus, we can study intact reaction centers of mixed isotopic composition.

Although the PSI reaction center has been crystallized, its crystal structure is not available. In addition, the kinetics of electron transfer is not well defined in PSI. The availability of the protonated, deuterated, and the mixed isotopic cases for $P^+A_1^-$ in basically intact reaction centers should make it possible to obtain the structural features of A_1^- in its binding pocket in PSI reaction centers.

A general analogy between the electron-acceptor pathways in green-sulfur bacteria and PSI is believed to exist. Although ESP behavior is readily observed in a variety of PSI samples, ESP is much more difficult to observe in green-sulfur bacteria. We have observed ESP in membrane fractions of the green-sulfur bacterium *Chlorobium vibrioforme* under reducing conditions. The observed ESP behavior more closely resembles the ESP observed in the quinone-replaced, iron-containing purple bacterial reaction centers than that found with PSI (Figure III-16). We are investigating the meaning of this similarity in terms of the nature and role of the electron acceptors in green-sulfur bacteria.

Another interesting application of ESP in sequential electron transfer is to the understanding of kinetics and structure in site-directed mutants of purple photosynthetic bacteria. In collaboration with Hanson and Schiffer, BIM Division, Argonne, we are studying chromatophores and reaction centers from the bacterium *R. capsulatus* that have been modified around the quinone binding sites (see Table III-2). In some of these mutants, the Q_A binding site is

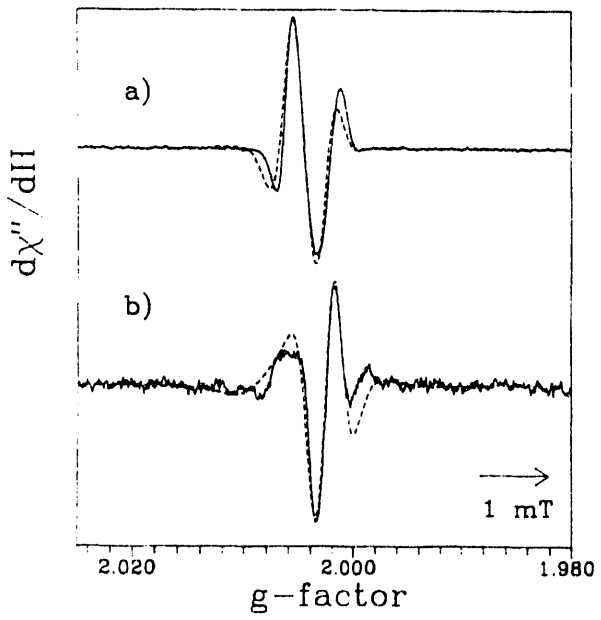

Figure III-15. Top: ESP-EPR spectrum of $P^+A_1^-$ in fully deuterated PSI particles. Bottom: ESP-EPR spectrum of $P^+A_1^-$ in PSI particles as above except that the "native" deuterated A_1 has exchanged with a protonated phylloquinone. The preliminary fits (circles) were obtained with our ESP model assuming that an intermediary pair does not contribute to the ESP.

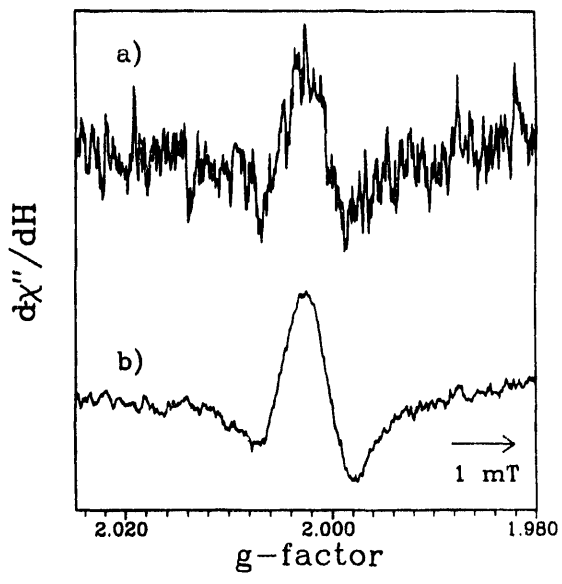

Figure III-16. Comparison between the ESP-EPR spectrum obtained in (a) green-sulfur bacteria under reducing conditions and that found in (b) iron-containing purple photosynthetic bacteria that have the native ubiquinone-10 replaced with 2-tert-butyl-anthraquinone.

modified so that it has an amino acid sequence like the native Q_B binding site. (In a completely active reaction center, the electron moves from Q_A to Q_B (see Figure III-9)). After two excitation events, Q_B is doubly reduced and leaves its binding site to be replaced by another quinone from a quinone/hydroquinone pool. Thus, Q_B is considered labile in its completely reduced state.) Table III-3 describes how we assay for the effects of modifying these sites by observing the EPR spectra of the oxidized P^+ and the triplet state of P^+. High-yield P^+ is obtained when k_Q (Figure III-10) is fast as in native reaction centers. Triplet is obtained when k_Q slows down and k_T can compete with k_Q, or when Q_A is reduced or absent from the reaction center. We are examining the ESP of the charge-separated state in these mutants in order to determine if k_Q is modified or if Q_A is missing from the mutant reaction centers. This aspect of our work is also related to understanding the quinone exchange process (labile quinone) that we have discovered in PSI.

Table III-2. Quinone binding-site mutants of *Rb. capsulatus*

wild type	BP_M	Fe	BP_L
Q_BQ_A	Q_B		Q_A
	L213 Asp		Ala M247
	L212 Glu		Ala M246
	BP_M		BP_L
"212"	Q_B	Fe	Q_A
"Q_AQ_A"	L213 Ala		Ala M247
	L212 Ala		Ala M246
	BP_M		BP_L
"246"	Q_B	Fe	Q_A
"Q_BQ_B"	L213 Asp		Asp M247
	L212 Glu		Glu M246
	BP_M		BP_L
"RQ"	Q_B	Fe	Q_A
"Q_AQ_B"	L213 Ala		Asp M247
	L212 Ala		Glu M246
	BP_M		BP_L
"1L"	Q_B	Fe	Q_A
"$Q_BQ_{A/B}$"	L213 Asp		Asp M247
	L212 Glu		Ala M246
	BP_M		BP_L
"5P"	Q_B	Fe	Q_A
"$Q_BQ_{X/B}$"	L213 Asp		Asp M247
	L212 Glu		Gly M246

Alanine	$-CH_3$
Aspartic acid	$-CH_2CO_2H$
Glutamic acid	$-CH_2CH_2CO_2H$
Glycine	-H

Table III-3. Summary of results of EPR assay of chromatophores of mutants of *Rb. capsulatus*

	no additions		reduced		BQ added		UQ_0 added	
	P^+	triplet	P^+	triplet	P^+	triplet	P^+	triplet
WT	s., rev.	v.w.	n.s.	s.	s., rev.	v.w.	s., rev.	n.s.
212	s., rev.	n.s.	n.s.	s.	s., rev.	v.w.		
246	var. n.s.-m.	var. m.-s.	n.s.	s.	m., l.rev	s.	n.s.	s.
RQ	s., rev.	m.	n.s.	s.	m., rev.	s.	s., rev.	w.
1L	s., rev.	w.	n.s.	s.	s., rev.	n.s.		
5P	s., rev.	n.s.	n.s.	s.	s., rev.	n.s.	s., rev.	n.s.

s. = strong; w. = weak; v.w. = very weak; m. = medium; n.s. = no signal; rev. = reversible; l. rev. = less reversible; var. = variable

C. Artificial Photosynthesis

M. R. Wasielewski, W. A. Svec, M. P. O'Neil, G. P. Wiederrecht, M. P. Niemczyk

1. Background

The primary step of natural photosynthesis is a rapid, photoinduced charge separation that is followed by a series of nonphotochemical electron-transfer steps that store chemical energy. The principle goals of our research in artificial photosynthesis are, first, to understand the molecular details of how energy- and electron-transfer reactions are carried out in nature, and, second, to use this understanding to develop donor-acceptor molecules that improve upon the natural system. These improvements focus on the ability of donor-acceptor molecules to efficiently separate charge and maintain their chemical integrity over extended periods of time. Our approach to this problem is to synthesize biomimetic models that possess multiple donors and acceptors within a well-defined overall molecular structure. These molecules are used

to study the physics of excitation energy transfer and the chemistry of photoinduced electron-transfer reactions in the context of molecular structure.

The chlorophyll and quinone electron donors and acceptors in photosynthetic reaction centers are positioned at precise distances and orientations to promote efficient charge separation and to impede charge recombination. Moreover, the nature of the medium that lies between the donor and acceptor is thought to have a large influence on the observed rates of electron transfer. We have studied extensively covalently linked porphyrin-quinone molecules as models for the light-initiated charge separation in photosynthesis. Studies performed to date have been concerned primarily with the dependence of the electron-transfer reactions on free energy, distance, and solvent.

Recent interest in the role of the solvent in electron-transfer reactions has focused on ultrafast photoinduced electron transfers, highlighted by investigations into the primary events of bacterial photosynthesis. In contrast to photosynthesis, which exhibits a quantum yield of primary charge separation near unity at cryogenic temperatures, most photosynthetic model systems based on chlorophyll or porphyrin electron donors exhibit significantly reduced efficiencies of light-initiated, singlet state electron transfer whenever they are dissolved in rigid glass media. This occurs because solvent dipoles reorient around an ion pair in a polar liquid, decreasing the energy of the ion pair, whereas solvent dipoles cannot reorient around an ion pair produced within a frozen solvent, and thus, provide little stabilization of the ion pair. As a result, the energy level of the ion pair is much higher in the rigid glass than in the liquid. In fact, the ion-pair state energy may be so high that it lies above the energy of the excited state, in which case photoinduced electron transfer cannot occur. We recently reported that the ion-pair states in a series of 14 structurally related porphyrin-triptycene-acceptor molecules are destabilized by 0.8 eV in going from a polar liquid to a rigid glass. This quantitative study gives us the information that we need to design molecules that undergo efficient photoinduced charge separation in rigid media.

It is very important to develop electron donor-acceptor systems that photochemically separate charge in the solid state because the integration of molecules that carry out charge separation into complete systems for energy storage will require environments wherein molecular motion is restricted. The photosynthetic reaction center is a good example of vectorial electron transport in a system wherein the motions of the donors, the acceptors, and the surrounding medium are restricted. Thus, a critical design criterion for any such system is the achievement of a high quantum yield of photochemical charge separation that is independent of the surrounding medium.

One of the principal goals of our modeling work is to increase the lifetime of the charge-separated ion pair, while maintaining an overall high quantum efficiency for the reaction. For ion pairs to be long-lived, the electronic coupling between the individual ions needs to be very small. To achieve this in nature, charge separation in bacterial photosynthetic reaction centers proceeds in three steps from the lowest excited singlet state of the dimeric bacteriochlorophyll electron donor to yield a weakly interacting dimer cation-quinone anion radical pair, P^+-Q^-, separated by 28 Å. The chromophores within the reaction center are positioned at precise distances and orientations to insure that the electronic coupling between P^+ and Q^- is sufficiently weak to allow P^+-Q^- to live for about 100 ms. Thus, an important focus of our research is the design of molecules that minimize the electronic interaction between the oxidized donor and reduced acceptor. This minimization can be attained by careful design of the spacer groups linking the donor and acceptor, and by using more than a single electron-transfer step to increase the distance between the separated charges as is done in natural photosynthesis.

Semiclassical electron-transfer theory predicts that the rate constant for charge recombination, k_{cr}, depends both on the electronic coupling matrix element, V, between the radicals within the ion pair, and the Franck-Condon weighted density of states, FCWD. The FCWD term depends on the free energy of the recombination reaction, as originally given by Marcus:

$$k_{cr} = (2\pi/\hbar)V^2 \cdot FCWD \qquad (4)$$

For an optimized free energy of reaction, equation 4 predicts that a radical ion pair that lives for milliseconds should possess $V < 0.001$ cm^{-1}. Under these conditions, the electron-electron exchange interaction between the radicals, $2J$, which is on the same order of magnitude as V, is sufficiently weak that differences in local magnetic fields surrounding each radical result in singlet-triplet mixing of the radical pair spin sublevels. This mixing produces a non-Boltzmann population of the spin sublevels of the radical pair

and may result in the appearance of spin-polarized EPR spectra. Achieving high quantum yield charge separation in low-temperature solids is a prerequisite for observing structure-dependent, anisotropic spin-spin interactions, such as the dipolar interaction, *D*, in radical pairs. We have recently reported the observation of such spectra for the first time using a molecular triad in the solid state. This work has been extended by the preparation of 1 and 2, Figure III-17, the first molecules based on a chlorophyll electron donor to exhibit spin-polarized EPR spectra analogous to those observed in photosynthetic reaction centers from both green plants and purple bacteria in the solid state in a low-temperature glass.

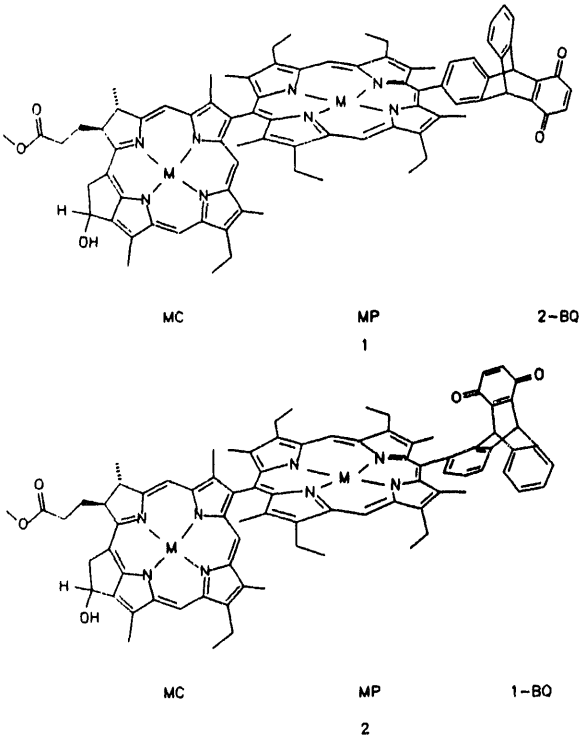

Figure III-17. Structures of ZC-ZP-2-BQ, 1, and ZC-ZP-1-BQ, 2, M = Zn.

2. Synthetic Photoreaction Centers

M. R. Wasielewski, W. A. Svec, M. P. Niemczyk

We have prepared a new series of chlorophyll-porphyrin-quinone model systems for the study of photoinduced charge separation across long distances. The strategy that we have used in designing these molecules is to place the electron donors and acceptors at fixed distances relative to one another to promote long-lived, unidirectional electron transfer. We have developed synthetic methods to rigidly fix a chlorophyll chromophore such that its π system is perpendicular to that of an adjacent porphyrin. This limits the electronic interaction between these low-lying orbitals. In addition, we are able to selectively position a quinone molecule at a fixed orientation relative to the porphyrin. Moreover, this quinone is electronically decoupled from the π system of the porphyrin by using a rigid hydrocarbon spacer molecule between the porphyrin and the quinone.

Compounds **1** and **2** were prepared as shown in Figures III-18a and III-18b. Diels-Alder reaction of benzoquinone with the appropriate substituted anthraldehyde results in the adducts shown. The adduct is rearranged and the resulting hydroquinone is protected as the diacetate by treatment with acetic anhydride in pyridine. The resultant protected quinone aldehyde is condensed with one mole of methyl pyropheophorbide *d* and two moles of 3,3'-diethyl-4,4'-dimethyldipyrrylmethane in CH_2Cl_2 using BF_3-Et_2O catalyst to yield the statistical mixture of porphyrinogens. The porphyrinogens are oxidized to porphyrins with chloranil at room temperature and separated on silica gel. The 9-keto groups of the resultant chlorophyll-porphyrin-protected quinones were reduced selectively with $NaBH_4$; the hydroquinone was unmasked with acid, and oxidized to the quinone with chloranil. Metalation of the macrocycles with Zn proceeds readily to yield the final products shown in Figure III-17.

3. Photophysics and Photochemistry of Photosynthetic Model Systems

M. R. Wasielewski, M. P. O'Neil, G. P. Wiederrecht

Recent interest in the role of the solvent in electron-transfer reactions has focused on ultrafast photoinduced electron transfers and theoretical modeling of solvation. The vast majority of work in this area involves donor-acceptor systems in which the donor and acceptor either freely diffuse in solution to form a complex following excitation, or are already complexed in their ground state prior to excitation. Many difficulties in the analysis of electron-transfer rates as a function of reaction free energy arise due to translational degrees of freedom within such complexes. A particularly controversial aspect of this work for many years was the theoretical prediction derived

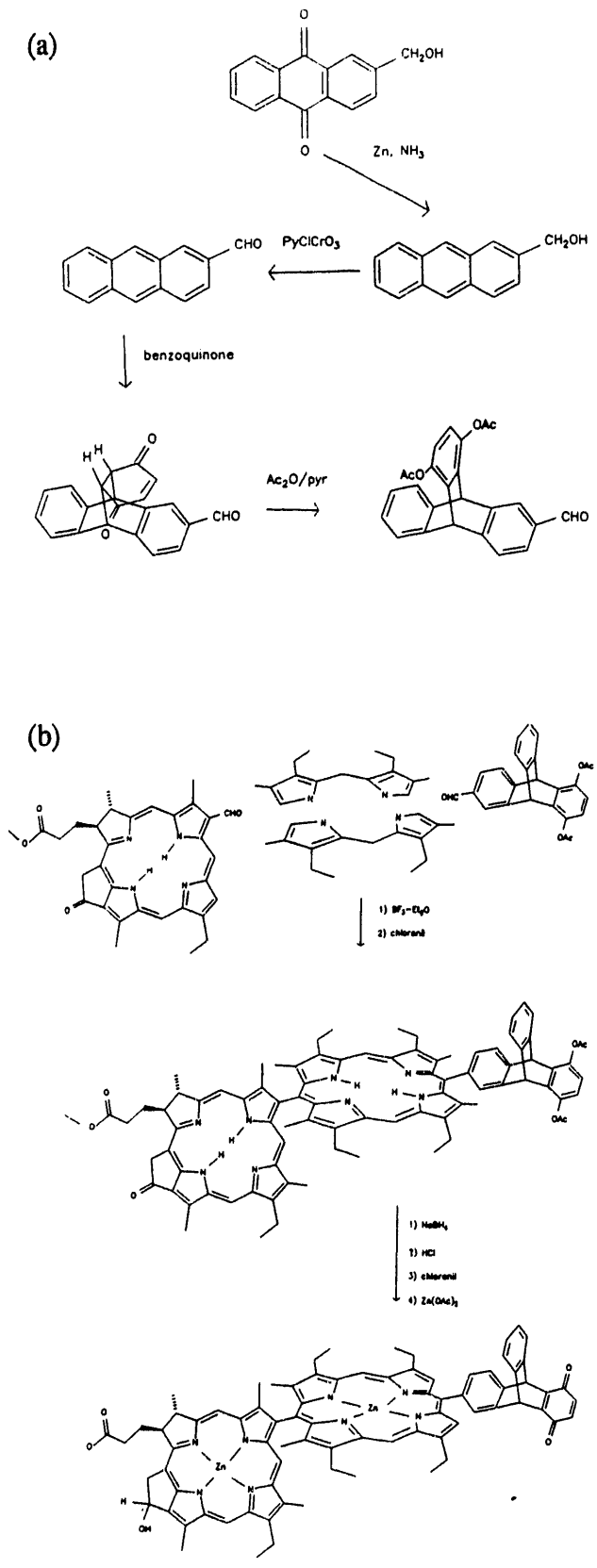

Figure III-18. (a): Synthetic pathway for compounds **1** and **2**. (b): Synthetic pathway for compounds **1** and **2**.

from the work of Marcus and amplified by the work of many others that a decrease in rate constant should occur when the free energy of reaction became very large. This is the so-called "inverted region" in the rate vs. free-energy relationship. Recently, Kakitani and Mataga have proposed an alternative view in which selective solvation of the donor-acceptor pair influences the rate vs. free-energy dependence as a function of whether ion pairs are created or destroyed in the reaction, or whether charge is merely shifted from the donor to the acceptor in the reaction. Experimental studies designed to test these theoretical models have, to date, involved mostly noncovalent donor-acceptor complexes. Our recent work focuses on the use of fixed-distance, covalent donor-acceptor molecules to study the influence of solvent polarity both in liquid and solid solution on the free-energy dependence of photochemical charge-separation reactions.

In polar liquids the free energies of charge separation in a donor-acceptor molecule, $\Delta G'_{cs}$, can be estimated with reasonable accuracy using the one-electron oxidation, E_{ox}, and reduction, E_{red}, potentials of the donor and acceptor, respectively, and the Coulomb stabilization of the ion pair:

$$\Delta G'_{cs} = E_{ox} - E_{red} - e_0^2/\varepsilon_s r_{12} - E_s , \qquad (5)$$

where e_0 is the charge of the electron, ε_s is the static dielectric constant of the high-polarity medium, r_{12} is the center-to-center distance between the ions, and E_s is the energy of the lowest excited singlet state of the porphyrin donor determined from the frequency of the (0,0) band of its fluorescence spectrum. We determined $\Delta G'_{cs}$ for the 36 compounds presented in Figure III-19 in benzonitrile at 295 K containing 0.1 M tetra-n-butylammonium perchlorate.

Rate constants for electron transfer in benzonitrile, chlorobenzene, and toluene were determined using picosecond transient absorption and emission spectroscopy along with fluorescence-quenching measurements. The ion-pair transient absorption spectra closely match those reported for the various porphyrin cation radicals. The rate constants for electron transfer from the lowest excited singlet state of the porphyrin to the acceptor are plotted as a function of free energy in Figure III-20. Note that equation 5 is adequate for estimating the free energy of the ion pair in polar liquids like benzonitrile. In this case, the electrochemical determination of $\Delta G'_{cs}$ and the rate constant measurements are both performed in the same solvent.

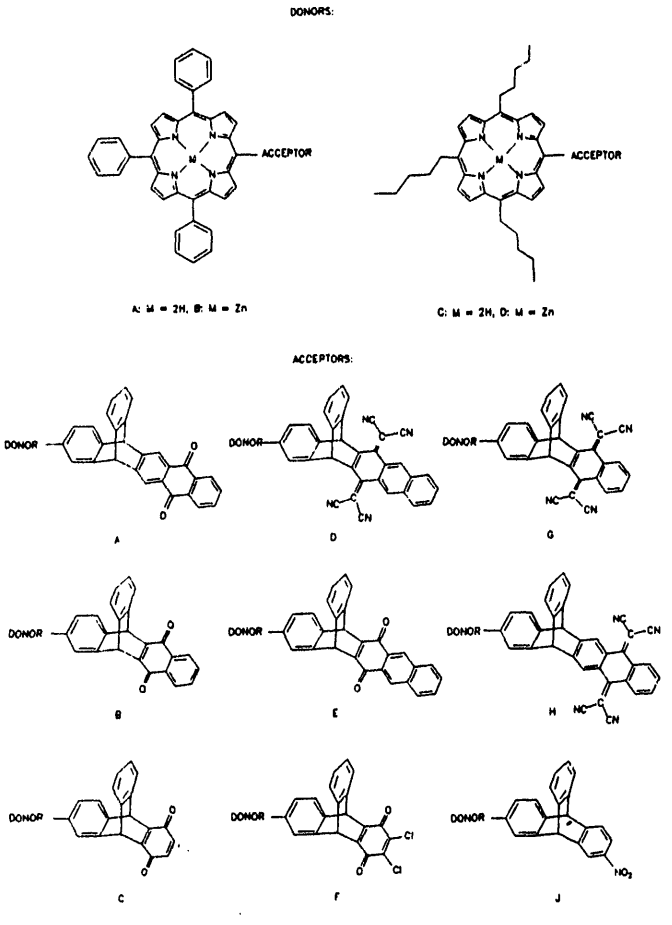

Figure III-19. Thirty-six different donor-acceptor combinations using one each of four donors (A-D) and nine acceptors (A-J).

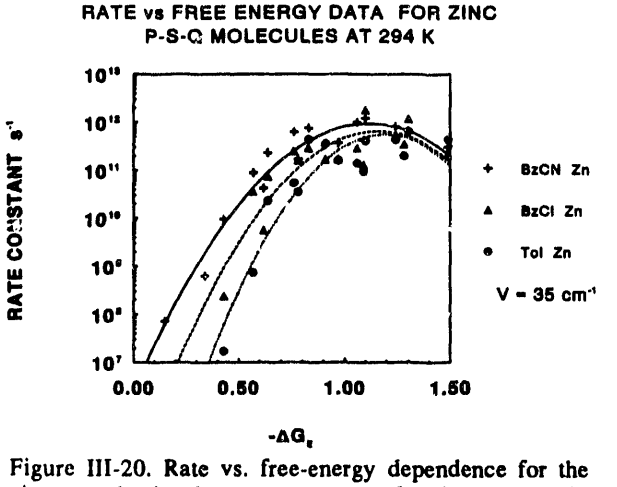

Figure III-20. Rate vs. free-energy dependence for the zinc porphyrin donor-acceptor molecules shown in Figure III-19.

However, our earlier results showed that the free energy of a charge-separation reaction determined from electrochemical redox potentials of the donor and acceptor in a high-static dielectric constant medium is not accurate in the solid state or even in other solvents, for that matter. We need to relate the change in free energy measured in polar media to that in other media such as nonpolar solvents and solids. In classical Marcus electron-transfer theory the activation energy for the charge-separation reaction is given by equation 6,

$$E_a = (\Delta G_{cs} + \lambda)^2/4\lambda \,, \qquad (6)$$

where λ is the total nuclear reorganization energy of the reaction. The true value of ΔG_{cs} in a particular medium can be given as

$$\Delta G_{cs} = E_{ox} - E_{red} - E_s + \Delta G_d \,, \qquad (7)$$

where ΔG_d is the energy by which the ion pair is destabilized when it is taken from a medium with high ε_s to one in which ε_s is low.

Using the Born dielectric continuum model of the solvent, Weller derived equation 8 to calculate the ion-pair destabilization energy, ΔG_d, in a solvent with an arbitrary value of ε_s and high-frequency dielectric constant ε_o, if the redox potentials of the donor and acceptor are measured in a medium with a high dielectric constant, ε_s':

$$\Delta G_d = e_o^2[(1/2r_1) + (1/2r_2) - (1/r_{12})]/\varepsilon_s - e_o^2[(1/2r_1) + (1/2r_2)]/\varepsilon_s' \,, \qquad (8)$$

where r_1 and r_2 are the radii of the two ions, and the remaining parameters are defined above.

Marcus dissected the total nuclear reorganization energy for electron transfer into two terms: λ_s, the change in energy due to nuclear motion of the solvent, and λ_i, the change in energy due to nuclear motion within the donor and acceptor. Thus,

$$\lambda = \lambda_s + \lambda_i \,. \qquad (9)$$

Later, Marcus used the same Born model of the solvent to derive an expression for λ_s:

$$\lambda_s = e_o^2[(1/2r_1) + (1/2r_2) - (1/r_{12})][1/\varepsilon_o) - (1/\varepsilon_s)] \,. \qquad (10)$$

If we define $\Delta G_E = E_{ox} - E_{red} - E_s$ and $C = e_o^2[(1/2r_1)+(1/2r_2)-(1/r_{12})]$, equations 6-10 can be combined to yield equation 11:

$$E_a = [\Delta G_E + (C/\varepsilon_o) + \lambda_i]^2/4[C[1/\varepsilon_o] - [1/\varepsilon_s] + \lambda_i] \quad (11)$$

Each term that comprises ΔG_E can be measured experimentally, whereas C can be estimated reasonably well from the molecular structure of the donor-acceptor system. Equation 11 predicts that plots of ln k_{cs} vs. $-\Delta G_E$ in a series of structurally related compounds will possess maxima at the *same value of* $-\Delta G_E$ *independent of the static dielectric constant of the medium in which* k_{cs} *is measured.* This occurs because ε_o is always about 2 for typical organic media, and C and λ_i are values that are approximately constant for a given structural type. Moreover, since the denominator depends both on ε_o and ε_s, changing ε_s will generate a series of nested rate vs. free-energy curves with widths that depend on the static dielectric constant of the solvent.

Figure III-20 shows that the rates of charge separation within the porphyrin-triptycene-acceptor series increase dramatically with increasing free energy of reaction and remain very fast throughout the high-driving-force regime. The experimental rate constants remain above 10^{11} s^{-1} all the way out to $-\Delta G_{cs}$ = 1.5 eV, which is 75% of the total energy available from excitation of the porphyrin to its lowest excited singlet state. Equation 11 predicts that changing the static dielectric constant of the solvent should not result in a change in the maximum of the rate vs. free-energy profile if the data is plotted against $-\Delta G_E$. In addition, equation 11 predicts that a series of nested curves will result if the rate constants are measured in solvents wherein ε_s is varied. Although the data set that we have obtained thus far is incomplete, the data in Figure III-20 show that the maxima of ln k_{cs} vs $-\Delta G_E$ curves for data obtained in toluene, chlorobenzene, and benzonitrile are approximately the same. This behavior is predicted by equation 11. Moreover, the plot clearly reveals the nesting of the rate vs. free-energy curves that is predicted by the treatment derived above.

Our studies on photoinduced charge separation within fixed-distance donor-acceptor molecules as a function of solvent polarity show that the rate constants for charge separation remain large well into the inverted region of the rate vs. free-energy profile. Although the rate vs. free-energy dependence can be modeled by semiclassical electron-transfer theory, a more thorough look into the theoretical models that can be used to describe this phenomenon will await completion of measurements on all 36 molecules in six different solvents. Inasmuch as the energy level of the ion pair is strongly modulated by the solvent polarity, this modulation can be used to further examine the rate vs. free-energy dependence of these reactions.

Current work in our laboratory has focused on the influence of solvent motion on the rates and energetics of photochemical charge separation in glassy solids. The efficiencies of many nonadiabatic electron-transfer reactions involving photochemical electron donors with relatively low excited state energies, such as porphyrins and chlorophylls, are poor in the solid state. Recent work has shown that placing a porphyrin-acceptor system in a glassy solid at low temperature significantly raises the energy of its ion-pair state. This destabilization can be as much as 0.8 eV relative to the ion-pair state energy in a polar liquid. This contrasts sharply with photosynthetic reaction centers, which maintain medium-independent electron-transfer rates with relatively small free energies of charge separation. Using this information we have designed chlorophyll-porphyrin-quinone molecules **1** and **2** that produce long-lived radical ion pairs in glassy solids with high quantum efficiency. These systems maintain their efficiency when placed in other glassy matrices, such as polymers.

The EPR spectra of the radical ion pairs produced within **1** and **2** can be used to examine how the electronic coupling matrix element, V, changes with molecular structure, and how the surrounding medium influences the FCWD term in equation 1. The π system of the chlorophyll electron donor, ZC, in compounds **1** and **2** is rigidly positioned 90° to that of the adjacent porphyrin, ZP. The methyl groups surrounding the attachment positions in both macrocycles serve to fix the geometry by providing steric constraints. This serves to electronically decouple the π systems of these two macrocycles. In addition, the ring E keto group is reduced to a hydroxy in ZC. This produces two changes that combine to greatly increase the free energy available for charge separation in this molecule. First, the lowest excited singlet state of ZC increases to 2.00 eV from the usual 1.86 eV in the keto-containing molecule. Second, reduction of the ketone to a hydroxy makes the macrocycle 0.24 V easier to oxidize. Thus, the total free energy available for photoinduced charge separation increases by 0.38 eV by simple reduction of the ring E keto group.

The triptycene benzoquinone moiety is also spatially fixed relative to the porphyrin. In **1** this

results in about a 60° angle between the O-O axis of the benzoquinone and the porphyrin macrocyclic plane, whereas in **2** the O-O axis is parallel to the plane of the porphyrin. The benzoquinone reduces at -0.47 V vs. SCE in butyronitrile. Thus, the total free energy available for the charge separation ^{1*}ZC-ZP-BQ → ZC^+-ZP-BQ^- is 1.13 eV in polar solvents. In a low-temperature glass such as 2-methyltetrahydrofuran (MTHF), this value should decrease to about 0.3 eV. Thus, both **1** and **2** should readily undergo charge separation in the low-temperature glass.

Femtosecond transient absorption and emission measurements with no applied magnetic field show that **1** and **2** undergo a single-step photoinduced electron-transfer reaction, ^{1*}ZC-ZP-BQ → ZC^+-ZP-BQ^-, in τ = 10 and 3 ps, respectively, at 77 K. The faster rate of reaction for **2** relative to **1** suggests that V for the charge-separation reaction in **2** is somewhat larger than dhat in **1**. There is no evidence for participation of a distinct chemical intermediate of the porphyrin. Thus, the porphyrin functions to promote a superexchange interaction between ZC^+ and BQ^-. This behavior is consistent with the fact that the energy level of ZC^+-ZP^--BQ in the glassy solid is significantly higher than that of ^{1*}ZC-ZP-BQ. The recombination reaction, ZC^+-ZP-BQ^- → ZC-ZP-BQ, for both **1** and **2** occurs with about a 1-ms time constant at 77 K.

The time-resolved EPR spectrum of ZC^+-ZP-BQ^- in **1** is given in Figure III-21, whereas that of the corresponding isomer **2** is shown in Figure III-22. The spectrum is displayed in the first derivative mode. It is readily seen that irradiation of **1** and **2** produces an intense EPR signal that consists of an emissive, **E**, low field line and an absorptive, **A**, high field line. At 30 K the ZC^+ and BQ^- free radicals display gaussian lines: ZC^+, g_{iso} = 2.0028, FWHM = 10 G; BQ^-, g_{iso} = 2.0047, FWHM = 5 G. Replacement of either ZC or BQ in **1** or **2** by a p-tolyl group results in no observed EPR signals. The solid curves in Figures III-17 and III-18 show the simulation of the spin-polarized spectrum. Using the known structures of **1** and **2**, the gross features of the spectra can be simulated reasonably well. Thus, as expected, the anisotropic spin-spin interactions within the radical pair are a sensitive probe of structure. Spin polarization in ZC^+-ZP-BQ^- results from the fact that the radical pair retains a memory of the photoexcited singlet state from which it was born, that is, the spins within the radical pair remain correlated. In this case,

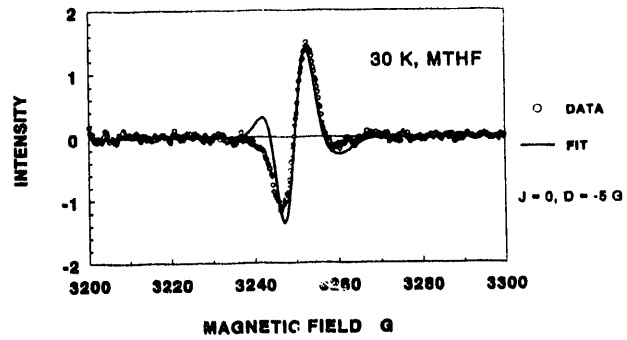

Figure III-21. Spin-polarized EPR spectrum of ZC^+-ZP-BQ^- from **1**.

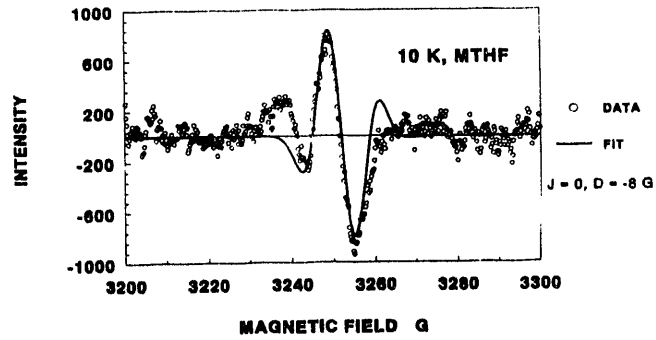

Figure III-22. Spin-polarized EPR spectrum of ZC^+-ZP-BQ^- from **2**.

S-T_0 mixing within ZC^+-ZP-BQ^- produces polarized spectra. If ZC^+-ZP-BQ^- is a correlated radical pair, a pair of partially overlapping antiphase doublets is expected. The polarization pattern observed, **E A E**, is similar to that observed for $P700^+$-A_1^- in PSI of green plants, and $P865^+$-Q^- in bacterial reaction centers. Recently, theoretical models have been developed to simulate these spectra. These models focus on the influence of *J*, *D*, and *g* anisotropy on the EPR spectra of radical pairs. In addition, some models consider the kinetics of radical-pair formation. The dipolar coupling, *D*, between the two radicals is strictly analogous to a classical dipole-dipole interaction, and, thus, depends on the distance and orientation of the radicals relative to one another. Moreover, these theories explicitly include the anisotropies of the *g* tensors of each radical.

In ZC^+-ZP-BQ^-, the *g* tensor of BQ^-, is quite anisotropic because about 80% of the spin density in BQ^- is centered on the oxygen atoms. The *g* tensor for ZC^+ is much less anisotropic. The key parameters that were included in the simulation are *J* = 0 G,

D = -5 G for **1**, and J = 0, D = -8 G for **2**, and the orientation of ZC relative to BQ in both **1** and **2**. The dipolar coupling, D, for ZC^+-ZP-BQ^- was calculated using the classical expression for the magnetic dipole-dipole interaction, the ZC^+-BQ^- distance and orientation, and the spin distributions of ZC^+ and BQ^-. It is important to note that the distances and orientations between the BQ^- π system relative to that of ZC^+ used in the simulations were determined independently from the known structures of **1** and **2**. The simulations fit the observed spectra reasonably well except for the wings of the spectra. The discrepancy between experiment and simulation in these regions of the spectra could be due to neglect of kinetic modeling in the simulation, or to the fact that an isotropic g value was used for ZC^+, because the g tensor for ZC^+ is unknown. Nevertheless, the rotation of the quinone relative to the primary electron donor ZC is shown to cause a predictable change in the overall shape of the EPR spectrum. This agreement gives us confidence that such theoretical descriptions of the anisotropic spin-spin interactions can be used to determine the structure of radical pairs for which independent detailed structural information is lacking. Further comparisons of the EPR signals from our supramolecular arrays with those from the donor-acceptor arrays within photosynthetic reaction-center proteins for which no X-ray structures are known will yield information concerning the distances and orientations of the donors and acceptors within these proteins.

Our observation of spin-polarized EPR spectra in **1** and **2** depends on achieving a delicate balance of structure-dependent electronic interactions between the donors and acceptors within the supramolecular array. This strongly suggests that we now know how to precisely mimic the weak radical pair interactions found only in natural photosynthesis. With this knowledge, we will be able to design efficient biomimetic supermolecules that can be used to probe the influence of the surrounding medium on the charge-separation process.

D. Advances in Instrumentation and Analysis

J. R. Norris, M. K. Bowman, J. Tang, M. C. Thurnauer, H. Levanon, P. Höfer, S. A. Dikanov, Yu. D. Tsvetkov

High-Resolution Electron Paramagnetic Resonance

M. K. Bowman, M. C. Thurnauer, H. Levanon, J. R. Norris, P. Höfer, S. A. Dikanov, Yu. D. Tsvetkov

We have used a variety of high-resolution electron paramagnetic resonance (EPR) techniques to identify and characterize the reduced A_1 electron acceptor in green-plant photosystem I (PSI). The A_1 acceptor was previously shown to be vitamin K_1 but the chemical nature of A_1 in its reduced state has been the subject of considerable controversy. The reduced A_1 has been assigned to the radical anion of vitamin K_1, the neutral radical of vitamin K_1, as well as free-radical rearrangement products of vitamin K_1. We have used high-resolution EPR spectroscopy in the 2-mm band to accurately measure the anisotropic g factors of several free radicals from vitamin K_1 and its analog vitamin K_3 (also known as menadione or 2-methyl naphthoquinone) (Figure III-23).

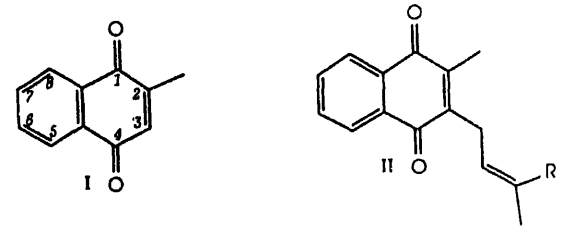

Figure III-23. Molecular structure of vitamin K_3 (I) and vitamin K_1 (II), which is the acceptor A_1 in PSI.

EPR in the 2-mm band uses much higher microwave frequencies and larger magnetic fields than the usual X-band EPR. As a consequence of the higher dispersion from larger magnetic fields, the 2-mm band EPR spectra have much greater resolution for the g factors than conventional EPR spectra. The anisotropic components of the g factor were measured for most of these radicals for the first time, although the average or isotropic g factors had been measured previously at X-band or Q-band. We found that even with the increased resolution of 2-mm EPR, the isotropic g factors are not sufficiently different to discriminate between the different free radicals and to identify the reduced form of A_1.

When the full, anisotropic g-factor matrices are examined (Table III-4), these free radicals can be

Table III-4. Principal values of the g-factor matrix

	g_x	g_y	g_z	g_{iso}
vitamin $K_1^{+\cdot}$	2.00439	2.00376	2.00227	2.00347
vitamin $K_1^{0\cdot}$	2.00528	2.00528	2.00251	2.00343
vitamin $K_1^{-\cdot}$	2.00588	2.00496	2.00225	2.00436
reduced $A_1^{\cdot}$	2.0055	2.0046	≅2.0023	2.0038-2.0047

distinguished from each other. In particular, the reduced A_1 found in vivo has an anisotropic g-factor matrix that agrees with the values measured here for the radical anion of the quinone form of vitamin K_1. The agreement is even better if one corrects for an apparent systematic shift of the g factors of reduced A_1 by 0.0003, which is comparable to the absolute accuracy of the g-factor standards used for calibration.

We also characterized the same radical anion sample using electron nuclear double resonance (ENDOR) and electron spin echo envelope modulation (ESEEM) spectroscopies to verify its identity. The ENDOR spectrum in liquid solution showed several sharp lines that could be assigned to individual protons of the vitamin K_1 radical anion. The hyperfine coupling constants from this ENDOR spectrum agree with couplings obtained by both EPR and ENDOR in other laboratories. The ENDOR spectrum was also recorded from a frozen solution of the radical anion of vitamin K_1. A small, very anisotropic coupling was found to one or more protons that did not correspond to any of the couplings measured in the liquid phase spectra. We also observed this coupling in ESEEM measurements on a sample in deuterated solvent. Here, the coupled nucleus is a deuteron, indicating that it is an exchangeable proton. The ESEEM spectrum is more easily quantifiable than the ENDOR spectrum, and the coupling involves a single proton (or deuteron) in the radical anion of vitamin K_1 and two protons in the radical anion of vitamin K_3.

Similar hyperfine couplings are found in the radical anions of other quinones, and are assigned to solvent protons that are hydrogen bonded to the oxygens of the quinone. This indicates that, in solution, the radical anion of vitamin K_1 has one oxygen atom hydrogen bonded to the solvent whereas the radical anion of vitamin K_3 has hydrogen bonds on both oxygens. The reason for this difference in these two closely related free radicals may reflect steric crowding at the C4 oxygens in vitamin K_1 by the adjacent hydrocarbon chain that vitamin K_3 lacks.

These high-resolution EPR experiments have identified the reduced form of the A_1 acceptor as the radical anion of vitamin K_1. These experiments also demonstrated that 2-mm or similar high-frequency EPR measurements can distinguish between very similar free-radical species. In this respect, the anisotropic g-factor matrix is much more powerful than the average or isotropic value of the g factor. In addition, these experiments measured the three principal values of the anisotropic g-factor matrix for reduced A_1 that are necessary for modeling of the electron spin polarization (ESP) patterns in PSI particles.

We made significant advances in understanding coherent Raman beats (CRB) in EPR spectroscopy. We observed CRBs in an EPR experiment a few years ago, and showed that it contained the same sort of information as an ESEEM experiment but with better spectral resolution. However, we did not understand how to generate CRBs efficiently for quantitative measurements. The CRBs originate from coherences in free radicals. The coherences can involve either nuclei (which we originally observed) or electrons in free radicals, triplets, and biradicals (which had not been observed).

We now understand quantitatively how nuclear coherences can be generated by microwave pulses for CRB detection in an EPR experiment. The CRBs manifest themselves as a modulation of the conventional EPR signal caused by a quantum beating phenomenon between eigenstates of nuclei coupled to the unpaired electron spin. The generation of CRBs is similar to the generation of ESEEM. We have proposed methods for duplicating many of the popular ESEEM experiments with CRBs. The use of CRBs for the detection of ESEEM has two important advantages with respect to conventional detection of ESEEM: (1) the CRBs produce spectra with higher resolution because their modulation decays with a time constant unaffected by spectral diffusion, which limits the ESEEM resolution in many cases; and (2) the CRBs can be generated and detected efficiently without using coherent microwave pulses, which will make experiments at very high EPR frequencies easier.

Recently, we have verified experimentally several of our predicted methods for generating CRBs from nuclear coherences. We are able to duplicate stimulated echo ESEEM (Figure III-24) and HYSCORE (hyperfine sublevel correlation spectroscopy)

experiments and have shown that the CRB technique is applicable to nuclei with I > 1/2. Another important experimental observation was made: CRBs from an electron spin coherence. We had previously predicted these electron spin CRBs but they had never been observed. These CRBs may offer a better way of detecting quantum beats in both natural and artificial photosynthetic systems.

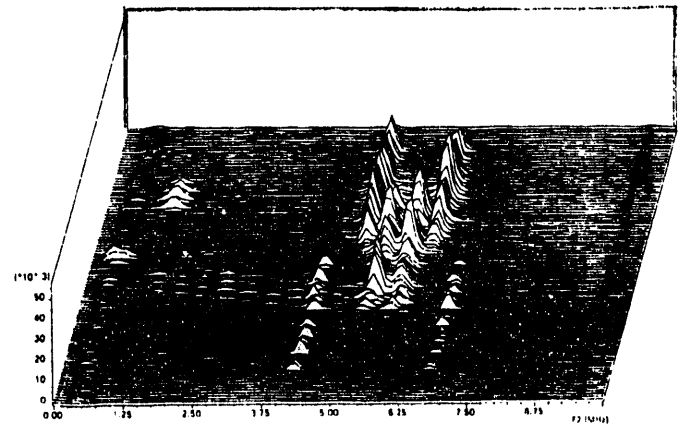

Figure III-24. A two-dimensional spectrum from CRBs in crystalline SiO_2. Peaks arise from ^7Li in three paramagnetic centers. Highly resolved pairs of lines are obtained from each center.

B. Synchrotron Investigation of Excited States

J. R. Norris, L. Chen, M. C. Thurnauer, M. K. Bowman, P. Montano, J. Tang, H. Levanon, Z. Wang, F. Lytle

One of the major unresolved questions in both chemistry and photosynthesis concerns the specific role that structural changes in photoexcited molecules and their surrounding solvent play in chemical processes. Intense pulsed X-rays from synchrotrons will allow direct measurement of excited-state molecular structures and dynamics. We have started to develop methods to determine molecular structures with a time resolution of ultimately 50 ps. Our research activities on time-domain X-ray spectroscopy have focused on development of an X-ray shutter and on extended X-ray absorption fine structure (EXAFS) experiments on excited states of compounds. Our goal is picosecond time-domain structure determination with X-ray absorption spectroscopies (i.e., EXAFS and X-ray absorption near-edge structure (XANES)) and picosecond time-resolved X-ray diffraction (e.g., single crystal, powder, or membrane).

Our work is directly addressing two major aspects of this goal:

(1) Methods to generate a single X-ray pulse. Third-generation synchrotrons, such as the Advanced Photon Source (APS) now under construction at Argonne, provide about six million pulses per second. However, time-domain experiments typically require a single X-ray pulse or pulses at a much lower rate, perhaps 100 per second. For many experiments, these X-ray pulses must be slaved to light pulses provided by a laser. Thus, a major problem is the development of a suitable X-ray shutter that can be slaved to a pulsed laser.

(2) *Exploration of excited state EXAFS.* The ultimate experiment requires the short, brilliant X-ray pulses that can only be produced by the third-generation synchrotrons becoming available in 1996. In order to determine the types of experiments that will be feasible, we are measuring structures of molecules in excited states with available synchrotron facilities. The main difficulty in these experiments is to find those few molecules that have excited states that can be fruitfully studied using the limited capabilities of existing synchrotrons. EXAFS spectra have been obtained from two excited states and show some significant structural changes.

The first problem was discussed extensively last year. Structural changes can be mapped stroboscopically by setting different time delays between a "pump" pulse (perhaps a laser) to generate an excited state and the synchrotron "probe", a standard technique of time-domain spectroscopy. The time resolution of this "pump-probe" experiment is independent of the detection device, depending only on the pulse width of the radiation source, about 50 ps for APS. For such experiments to work, the system for study must undergo reversible changes with relaxation times less than the interval before the next "pump-probe" cycle.

No synchrotron facility can control the time interval between single radiation bunches, and very few excited states can utilize the pulsed nature of synchrotron radiation. Modifying the repetition rate of the X-ray pulses is the key to a general method for measuring structural changes in excited molecules.

We have proposed a shutter consisting of a rotating mirror with its rotation locked to a multiple of the synchrotron interpulse period. The synchrotron X-ray pulses will be reflected to a 0.5-mm slit in front of the sample located 2 m from the mirror. We have designed a shutter with a 4-in. diameter mirror rotating at 15,000 rpm. Using a multilayer mirror, we will select a single X-ray pulse with a bandwidth of up to 10% from an Undulator A beamline. A slower mechanical chopper placed before the shutter will be used for a dual purpose: to reduce the energy from the X-ray pulse train absorbed by the mirror when a pulse is not being selected; and to further reduce the pulse repetition rate below the 250 Hz that the shutter will produce. The shutter design is nearly complete and will be constructed this year for testing at existing synchrotron facilities.

Our first attempts at excited-state EXAFS involved the photoexcited triplet of metalloporphyrins in solid-state solutions. These experiments were not very successful because of the large mismatch between the X-ray cross section (needed for EXAFS) and the optical cross section (needed for excited-state production). In our first attempts, we required such a high concentration of ZnTPP (zinc tetraphenylporphyrin) for good absorption of the X-rays that our light was unable to penetrate the sample and excite a large fraction of the molecules, even with its relatively long triplet-state lifetime (e.g., 15-20 ms at 77K) and high quantum yield. As a consequence, we have switched to two other molecules with excellent results.

Our first success came with cyclopentadienyl nickel nitrosyl (CpNiNO). This is a molecule with a simple, symmetric structure in the ground state. When it absorbs light near 365 nm, an electron is transferred from the nickel atom to the NO group, which then bends from its initial end-on configuration with the nickel (Figure III-25). This charge-separated, excited state has a long lifetime that depends strongly on temperature, exceeding two hours at 8 K.

We have measured the structure of CpNiNO in its ground state at both room temperature and 8 K. Our results (Table III-5) for the nickel-carbon, the nickel-nitrogen and the nickel-oxygen distances agree with those from microwave spectroscopy. In particular, the EXAFS spectra gave strong indications that the nickel-nitrogen-oxygen atoms were arranged in a straight line. We were able to maintain 57% of the molecules in the excited state at 8 K and measured EXAFS spectra (Figure III-26). The excited state EXAFS spectra show a lengthening of the nickel-nitrogen bond by about 0.12 Å and a rotation of the NO group by an angle of about 30°. These are large changes in structure that produce obvious changes in the EXAFS spectrum. In order to prove that these changes were due to excited state formation and not to sample decomposition, we pumped the system back and forth between the excited and ground states using 365-nm radiation (to produce the excited state) and white light (to produce the ground state). The EXAFS spectra followed this cycle quantitatively, and we were able, reversibly, to generate the excited state and its spectrum or to generate the ground state and its spectrum over half a dozen complete cycles. This is important proof that "pump-probe" experiments are feasible on reversible systems.

We have also examined an iron complex that undergoes transitions between high-spin and low-spin forms with long-lived states at low temperatures. We have obtained EXAFS spectra from the ground-state, low-spin form and from the excited, high-spin form generated either by light or thermally. The EXAFS spectra appear to show some reversible differences but they are still undergoing analysis.

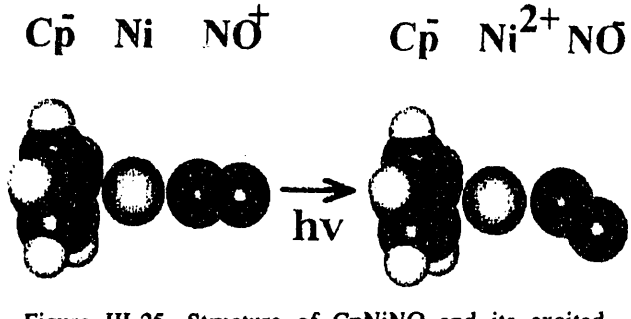

Figure III-25. Structure of CpNiNO and its excited state.

Table III-5. Interatomic distances in CpNiNO in the ground and excited states

	Ni-C	Ni-N	Ni-O
ground state	2.15±0.02Å	1.65±0.03Å	2.78±0.04Å
excited state	2.15±0.02Å	1.77±0.03Å	2.82±0.04Å

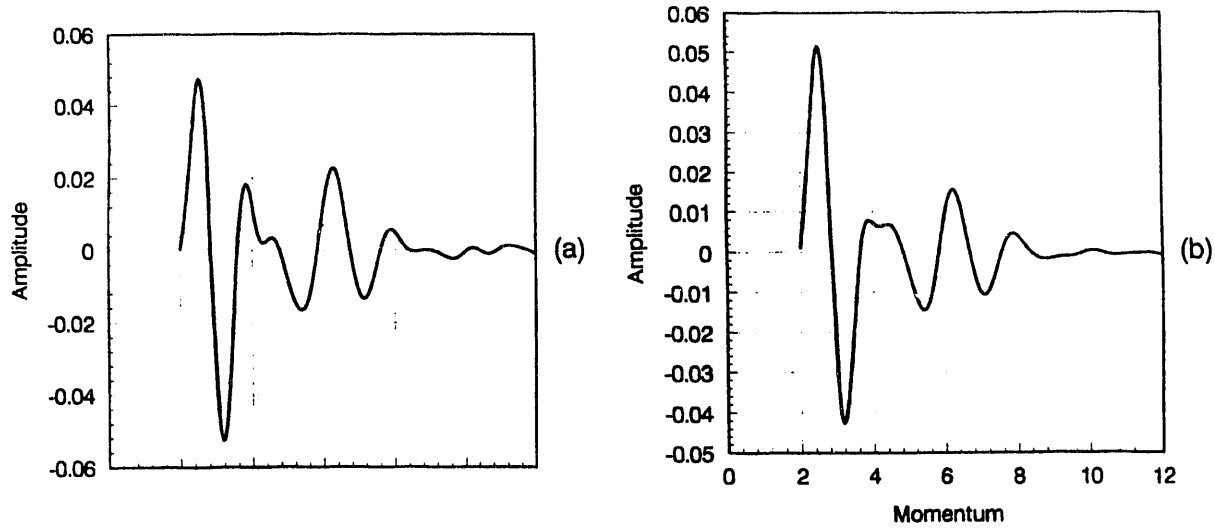

Figure III-26. EXAFS spectra of CpNiNO (a) in the ground state and (b) in the excited state.

PUBLICATIONS

PRIMARY CHARGE SEPARATION IN PHOTOSYNTHETIC BACTERIAL REACTION CENTERS AND FEMTOSECOND SOLVATION DYNAMICS

C.-K. Chan*, S. J. Rosenthal*, T. J. DiMagno*, L. X-Q. Chen, X. Xie*, J. R. Norris, and G. R. Fleming*
Dynamics and Mechanisms of Photoinduced Electron Transfer and Related Phenomena, N. Mataga et al., Eds., Elsevier, 1992, pp. 105-122

THE TIME DEVELOPMENT OF THE MAGNETIC MOMENT OF CORRELATED RADICAL PAIRS

Z. Wang*, J. Tang, and J. R. Norris
J. Magn. Reson. 97, 322-334 (1992)

A SHUTTER DESIGN FOR TIME DOMAIN STUDIES USING SYNCHROTRON RADIATION AT THE ADVANCED PHOTON SOURCE

J. R. Norris, M. K. Bowman, L. Chen, J. Tang, M. C. Thurnauer, G. S. Knapp*, and P. A. Montano*
Rev. Sci. Instrum. 63, 1172-1175 (1992)

CHARACTERIZATION OF CHARGE SEPARATION IN MEMBRANE SPANNING PROTEIN REACTION CENTERS OF BACTERIAL PHOTOSYNTHESIS

T. J. DiMagno*, C-K. Chan*, D. K. Hanson*, M. Schiffer*, G. R. Fleming*, and J. R. Norris
Charge and Field Effects in Biosystems - III, M. Allen, Ed., Birkhauser, Boston, 1992

PHOTOPHYSICS AND PHOTOINDUCED-ELECTRON-TRANSFER REACTIONS OF ZINC AND FREE-BASE OCTAETHYLPORPHYCENES

A. Berman*, A. Michaeli*, J. Feitelson*, M. K. Bowman, J. R. Norris, H. Levanon*, E. Vogel*, and P. Koch*
J. Phys. Chem. 96, 3041-3047 (1992)

PHOTOSYNTHETIC ELECTRON TRANSFER REACTIONS IN THE GREEN SULFUR BACTERIUM *CHLOROBIUM VIBRIOFORME*: EVIDENCE FOR THE FUNCTIONAL INVOLVEMENT OF IRON-SULFUR REDOX CENTERS ON THE ACCEPTOR SIDE OF THE REACTION CENTER

M. T. Miller*, X. Liu*, S. W. Snyder*, M. C. Thurnauer, and J. Biggins*
Biochem. 31, 4354-4363 (1992)

*Not affiliated with the Chemistry Division or affiliated on a temporary basis.

PHOTOINDUCED ELECTRON TRANSFER REACTIONS OF ROSE BENGAL AND SELECTED ELECTRON DONORS

T. Sarna*, J. Zajac*, M. K. Bowman, and T. G. Truscott*
J. Photochem. Photobiol. A 60, 295-310 (1991)

MECHANISM OF THE INITIAL CHARGE SEPARATION IN PHOTOSYNTHETIC BACTERIAL REACTION CENTERS

C.-K. Chan*, T. J. DiMagno*, L. X-Q. Chen, J. R. Norris, and G. R. Fleming*
Proc. Natl. Acad. Sci., USA 88, 11202-11206 (1991)

THE ROLE OF SPIN CHEMISTRY IN THE PRIMARY EVENTS OF PHOTOSYNTHESIS

G. Kothe*, S. Weber*, R. Bittl*, J. R. Norris, S. W. Snyder*, J. Tang, M. C. Thurnauer, A. L. Morris*, R. R. Rustandi*, and Z. Wang*
Spin Chemistry, Y. J. I'Haya, Ed., The Oji International Conference on Spin Chemistry, 1991, pp. 420-434

RECONSTITUTION AND EXCHANGE OF QUINONES IN THE A_1 SITE OF PHOTOSYSTEM I. AN ELECTRON SPIN POLARIZATION ELECTRON PARAMAGNETIC RESONANCE STUDY

R. R. Rustandi*, S. W. Snyder*, J. Biggins*, J. R. Norris, and M. C. Thurnauer
Biochim. Biophys. Acta 1101, 311-320 (1992)

DIRECT ASSIGNMENT OF VITAMIN K_1 AS THE SECONDARY ACCEPTOR A_1 IN PHOTOSYSTEM I

S. W. Snyder*, R. R. Rustandi*, J. Biggins*, J. R. Norris, and M. C. Thurnauer
Proc. Natl. Acad. Sci., USA 88, 9895-9896 (1991)

TRANSIENT EPR OF LIGHT-INDUCED RADICAL PAIRS IN PLANT PHOTOSYSTEM I: OBSERVATION OF QUANTUM BEATS

G. Kothe*, S. Weber*, R. Bittl*, E. Ohmes*, M. C. Thurnauer, and J. R. Norris
Chem. Phys. Lett. 186, 474-480 (1991)

SPIN-POLARIZED RADICAL ION PAIR FORMATION RESULTING FROM TWO-STEP ELECTRON TRANSFER FROM THE LOWEST EXCITED SINGLET STATE OF A FIXED-DISTANCE PHOTOSYNTHETIC MODEL SYSTEM AT 5 K

M. R. Wasielewski, G. L. Gaines*, M. P. O'Neil*, W. A. Svec, and M. P. Niemczyk*
Mol. Cryst. Liq. Cryst. 194, 201-207 (1991)

PHOTOINDUCED ELECTRON TRANSFER REACTIONS IN THE SOLID STATE: RATE vs. FREE ENERGY DEPENDENCE IN FIXED-DISTANCE PORPHYRIN-ACCEPTOR MOLECULES

G. L. Gaines, III*, M. P. O'Neil*, W. A. Svec, M. P. Niemczyk*, and M. R. Wasielewski
J. Am. Chem. Soc. 113, 719-721 (1991)

SPECTROMETRIC CHARACTERIZATION OF PURIFIED C_{60} AND C_{70}

K. R. Lykke, M. J. Pellin, P. Wurz*, D. M. Gruen, J. E. Hunt, and M. R. Wasielewski
Proceedings, Materials Research Society Symposium 206, 679-686, 1991

ENERGY AND ELECTRON TRANSFER IN COVALENTLY-LINKED CHLOROPHYLL CONTAINING DONOR-ACCEPTOR MOLECULES

M. R. Wasielewski
Chlorophylls, H. Scheer, Ed., CRC Press, Boca Raton, 1991, pp. 269-286

MODELLING THE PRIMARY ELECTRON TRANSFER EVENTS OF PHOTOSYNTHESIS

M. R. Wasielewski
Metal Ions in Biological Systems, H. Sigel, Ed., Marcel Dekker, New York, Vol. 27, 1990, pp. 361-430

---

*Not affiliated with the Chemistry Division or affiliated on a temporary basis.

SOLVENT DEPENDENT PHOTOPHYSICS OF FIXED-DISTANCE CHLOROPHYLL-PORPHYRIN MOLECULES: THE POSSIBLE ROLE OF LOW-LYING CHARGE TRANSFER STATES.
M. R. Wasielewski, G. L. Gaines*, M. P. O'Neil*, W. A. Svec, and M. P. Niemczyk*
Electron Transfer in Inorganic, Organic, and Biological Systems, G. McLendon et al., Eds., ACS Symposium Series, 1991, pp. 134-148

TRIPLET STATES OF FULLERENES C_{60} AND C_{70}: EPR SPECTRA, PHOTOPHYSICS, AND ELECTRONIC STRUCTURES
M. R. Wasielewski, M. P. O'Neil*, K. R. Lykke, M. J. Pellin, and D. M. Gruen
J. Am. Chem. Soc. 113, 2774-2776 (1991)

SUB-PICOSECOND PHOTOINDUCED ELECTRON TRANSFER IN WATER SOLUBLE PORPHYRIN DIMERS
F. J. Vergeldt*, R. B. M. Koehorst*, T. J. Schaafsma*, J.-C. Lambry*, J.-L. Martin*, D. G. Johnson*, and M. R. Wasielewski
Chem. Phys. Lett. 182, 107-113 (1991)

SOLVENT AND TEMPERATURE DEPENDENCE OF THE LOWEST EXCITED SINGLET STATE LIFETIME OF 7',7'-DICYANO-7'-β-APOCAROTENE
M. P. O'Neil*, M. R. Wasielewski, M. M. Khaled*, and L. D. Kispert*
J. Chem. Phys. 95, 7212-7218 (1991)

SOLVENT EFFECTS ON THE RATE vs FREE ENERGY DEPENDENCE OF PHOTOINDUCED CHARGE SEPARATION IN FIXED-DISTANCE DONOR-ACCEPTOR MOLECULES
M. R. Wasielewski, G. L. Gaines, III*, M. P. O'Neil*, W. A. Svec, M. P. Niemczyk*, L. Prodi*, and D. Gosztola
Dynamics and Mechanisms of Photoinduced Electron Transfer and Related Phenomena, N. Mataga et al., Eds., Elsevier, Amsterdam, 1992, pp. 87-103

FOURIER-TRANSFORM ESR ON MODEL SYSTEMS OF THE PRIMARY CHARGE SEPARATION IN PHOTOSYNTHESIS
A. Angerhofer*, M. R. Wasielewski, G. L. Gaines, III*, M. P. O'Neil*, W. A. Svec, and M. P. Niemczyk*
Z. Phys. Chem. 172, 17-30 (1991)

PHOTOINDUCED ELECTRON TRANSFER IN SUPRAMOLECULAR SYSTEMS FOR ARTIFICIAL PHOTOSYNTHESIS
M. R. Wasielewski
Chem. Rev. 92, 435-461 (1992)

SUPRAMOLECULAR ARRAYS FOR THE EFFICIENT CONVERSION OF LIGHT INTO CHEMICAL ENERGY IN THE SOLID STATE
M. R. Wasielewski, G. L. Gaines, III*, M. P. O'Neil*, M. P. Niemczyk*, and W. A. Svec
Supramolecular Chemistry, V. Balzani and L. DeCola, Eds., Kluwer, The Netherlands, 1992, pp. 201-218

COHERENT RAMAN BEATS IN ELECTRON PARAMAGNETIC RESONANCE SPECTROSCOPY
M. K. Bowman, R. J. Massoth*, and C. S. Yannoni*
Pulsed Magnetic Resonance: NMR, ESR, and Optics, D. M. S. Bagguley, Ed., Oxford Science Publications, Oxford, Chapter 19, 1992, pp. 423-445

COHERENT RAMAN BEAT DETECTION OF NUCLEAR COHERENCES: AN ALTERNATIVE TO ELECTRON SPIN ECHO ENVELOPE MODULATION
M. K. Bowman
Israel J. Chem. 32, 31-40 (1992)

---

*Not affiliated with the Chemistry Division or affiliated on a temporary basis.

CHARACTERIZATION OF FREE RADICALS FROM VITAMIN K_1 AND MENADIONE BY 2 mm-BAND EPR, ENDOR AND ESEEM
M. K. Bowman, M. C. Thurnauer, J. R. Norris, S. A. Dikanov*, V. I. Gulin*, A. M. Tyryshkin*, R. I. Samoilova*, and Yu. D. Tsvetkov*
Appl. Magn. Res. 3, 353-368 (1992)

SUBMISSIONS

THE GENERAL TREATMENT OF DYNAMIC SOLVENT EFFECTS IN ELECTRON TRANSFER AT HIGH TEMPERATURE
Z. Wang*, J. Tang, and J. R. Norris
J. Chem. Phys. (in press)

STRUCTURE AND FUNCTION OF THE PHOTOSYNTHETIC REACTION CENTER FROM RHODOBACTER SPHAEROIDES
M. Schiffer* and J. R. Norris
The Photosynthetic Reaction Center, J. Deisenhofer and J. R. Norris, Eds., Academic Press, New York (in press)

GENERAL FEATURES OF ISOTROPIC RAMAN SPECTRA FOR DISORDERED PEPTIDES
L. X.-Q. Chen and R. G. Snyder*
Biopolymers (in press)

STRUCTURAL REARRANGEMENT AND HYDROGEN BINDING IN AMORPHOUS n-ALKYLACETAMIDES
L. X.-Q. Chen, R. G. Snyder*, and H. L. Strauss*
Biopolymers (in press)

ELECTRON TRANSFER BETWEEN BACTERIAL REACTION CENTERS AND MOBILE C-TYPE CYTOCHROMES
D. M. Tiede and P. L. Dutton*
The Photosynthetic Reaction Center, J. Deisenhofer and J. R. Norris, Eds., Academic Press, New York (in press)

BACTERIAL REACTION CENTERS PROTONS CAN DIFFUSE TO THE SECONDARY QUINONE BY ALTERNATIVE PATHWAYS
D. K. Hanson*, L. Baciou*, D. M. Tiede, S. L. Nance*, M. Schiffer*, and P. Sebban*
BBA (in press)

STUDY OF REACTION CENTER FUNCTION BY ANALYSIS OF THE EFFECTS OF SITE-SPECIFIC AND COMPENSATORY MUTATIONS
M. Schiffer*, C.-K. Chan*, C-H. Chang*, T. J. DiMagno*, G. R. Fleming*, S. Nance*, J. Norris, S. Snyder*, M. Thurnauer, D. M. Tiede, and D. K. Hanson*
The Photosynthetic Bacterial Reaction Center: Structure, Spectroscopy, and Dynamics, J. Breton and A. Vergmelio, Eds., Plenum Press, London, NATO ASI Series (in press)

RECENT EXPERIMENTAL RESULTS FOR THE INITIAL STEP OF BACTERIAL PHOTOSYNTHESIS
T. J. DiMagno*, S. J. Rosenthal*, X. Xie*, M. Du*, C.-K. Chan*, D. Hanson*, M. Schiffer*, J. R. Norris, and G. R. Fleming*
The Photosynthetic Bacterial Reaction Center: Structure, Spectroscopy, and Dynamics, J. Breton and A. Vergmelio, Eds., Plenum Press, London, NATO ASI Series (in press)

---

*Not affiliated with the Chemistry Division or affiliated on a temporary basis.

PROTEIN RELAXATION FOLLOWING QUINONE REDUCTION IN *RHODOBACTER CAPSULATUS*: DETECTION OF LIKELY PROTONATION-LINKED OPTICAL ABSORBANCE CHANGES OF THE CHROMOPHORES

D. M. Tiede and D. K. Hanson*

The Photosynthetic Bacterial Reaction Center: Structure, Spectroscopy, and Dynamics, J. Breton and A. Vergmelio, Eds., Plenum Press, London, NATO ASI Series (in press)

MEASUREMENT OF THE g-TENSOR OF THE $P700^+$ SIGNAL FROM DEUTERATED CYANOBACTERIAL PS-I PARTICLES

T. F. Prisner*, A. E. McDermott*, S. Un*, J. R. Norris, M. C. Thurnauer, and R. G. Griffin*

Proc. Natl. Acad. Sci., USA (in press)

MODELING PRIMARY ELECTRON TRANSFER EVENTS IN PHOTOSYNTHESIS USING SUPRAMOLECULAR STRUCTURES

M. R. Wasielewski

The Photosynthetic Reaction Center, J. Deisenhofer and J. R. Norris, Eds. Academic, New York, 1992 (in press)

ULTRAFAST PHOTOINDUCED ELECTRON TRANSFER REACTIONS IN SUPRAMOLECULAR ARRAYS: FROM CHARGE SEPARATION AND STORAGE TO MOLECULAR SWITCHES

M. R. Wasielewski, M. P. O'Neil*, D. Gosztola, M. P. Niemczyk*, and W. A. Svec

Pure and Applied Chemistry (in press)

MEASUREMENT OF ELECTRON DIPOLAR FIELDS AND DYNAMICS IN SOLIDS

M. K. Bowman

Techniques in Magnetic Resonance for Carbonaceous Solids, R. Botto and Y. Sanada, Eds., American Chemical Society Advances in Chemistry Series (in press)

STRATEGIES FOR MEASUREMENT OF ELECTRON SPIN RELAXATION

M. K. Bowman

Techniques in Magnetic Resonance for Carbonaceous Solids, R. Botto and Y. Sanada, Eds., American Chemical Society Advances in Chemistry Series (in press)

MOLECULAR STRUCTURE OF NICKELCYCLOPENTADIENYLNITROSYL IN CONDENSED PHASES STUDIED BY EXAFS

L. X. Chen, M. K. Bowman, M. C. Thurnauer, F. W. Lytle*, and J. R. Norris

Chem. Phys. Lett. (in press)

FEMTOSECOND SPONTANEOUS EMISSION STUDIES OF REACTION CENTERS FROM PHOTOSYNTHETIC BACTERIA

M. Du*, S. J. Rosenthal*, X. Xie*, T. J. DiMagno*, M. Schmidt*, J. R. Norris, and G. R. Fleming*

Proc. Natl. Acad. Sci., USA (in press)

COLLABORATIONS

M. Gunner, City College of New York
P. L. Dutton, University of Pennsylvania
ESP in iron-containing, quinone-replaced purple photosynthetic reaction centers.

J. Biggins, Brown University
Reconstitution and exchange of quinones in PSI, green-sulfur bacteria.

G. Kothe, University of Stuttgart
Time-resolved EPR (high time resolution).

R. Griffin, MIT
High-frequency EPR of oxidized donor in PSI and purple photosynthetic bacteria.

L. Belford, University of Illinois, Urbana
High-frequency EPR of oxidized donor in purple photosynthetic bacteria.

D. Hanson and M. Schiffer, Biological and Medical Research Division, ANL
EPR assay and ESP in quinone-site mutants of purple photosynthetic bacteria.

O. Mićić, Boris Kidric Institute, Belgrade, Yugoslavia
Photoinduced charge separation in semiconductor colloids studied by EPR.

Govindjee, University of Illinois, Urbana
Primary photochemistry of PSI reaction centers.

G. Jones, Boston University
Photochemistry of dyes bound to polymers, and electron transfer across peptides.

H. Levanon, Hebrew University
EPR of radical-pair states.

A. Angerhofer, University of Stuttgart
EPR of radical-pair states.

L. Kispert, University of Alabama, Tuscaloosa
Carotenoid excited states.

T. Moore and D. Gust, Arizona State University, Tempe
Carotenoid energy-transfer studies.

T. Schaafsma, Agricultural University, Wageningen, The Netherlands
Electron transfer in porphyrin-quinone donor-acceptor molecules.

M. Seibert, NREL
Primary photochemistry of PSII reaction centers.

N. C. Yang, University of Chicago
Exciplex-induced electron-transfer processes.

IV. METAL CLUSTER CHEMISTRY

S. J. Riley, E. K. Parks, J. Jellinek, M. B. Knickelbein, E. A. Kemereit, Z. B. Güvenç
W. J. C. Menezes, M. J. Lopez, L. Zhu, J. Ho

Outside Collaborators: *V. Bonačić-Koutecký, P. Fantucci, S. F. Chekmarev, I. L. Garzon, G. Lacueva, A. F. Voter, F. W. Dech*

The Metal Cluster Chemistry Group has three programs studying the fundamental properties of isolated clusters of catalytically active metals. Such chemical properties as cluster reactivity and binding capacity, the nature and thermodynamics of adsorbate binding, and cluster geometrical structure are studied in one experimental program. Studies of the reactions of first-row transition metal clusters with small molecules such as nitrogen, hydrogen, ammonia, and water provide information about cluster structure and changes in structure with cluster size, with adsorbate coverage, and with temperature. The most significant recent development in these studies has been the refinement of the nitrogen probe for the determination of small-cluster structure. A second experimental effort studies physical properties of metal clusters. These include the formation of cluster-rare gas van der Waals complexes and the measurement of cluster ionization potentials. For the first time, the optical absorption spectra of polyatomic clusters of transition metals have been measured. A third, theoretical, program is focused on dynamical simulations of clusters and cluster chemical reactions. These studies are the first to identify resonance phenomena in cluster-molecule collisions.

A. The Chemical Reactions of Transition Metal Clusters

S. J. Riley, E. K. Parks, E. A. Kemereit, L. Zhu, J. Ho

Clusters are generated in a laser vaporization source that is coupled to a continuous-flow-tube reactor (FTR). Reagents can be introduced into the flowing gas stream at two ports located different distances from the end of the FTR. This allows the time dependence of a reaction to be determined, which is important in identifying whether the reaction is at equilibrium or is kinetically controlled. Also, the use of two ports allows the study of two-reagent reactions. The entire cluster source and FTR can be heated (to 200 °C) or cooled (to -150 °C). From the temperature dependence of a reaction at equilibrium, thermodynamic parameters such as reaction enthalpy and entropy can be determined. If a reaction is kinetically controlled, a measurement of rate constants as a function of temperature allows a determination of any activation barriers. Continuous gas flows provide carefully controllable and characterizable reaction conditions, a situation essential for the quantitative studies we do and one not found in the more common pulsed-valve cluster sources.

The clusters and their reaction products expand out of a nozzle at the end of the FTR, and are formed into a molecular beam. The beam is ionized by a pulsed excimer laser in the ion extraction region of a time-of-flight (TOF) mass spectrometer. In a typical experiment, FTR conditions such as reagent pressure, temperature, and interaction time are systematically varied, and the resulting changes in the mass spectra are recorded.

In the past year, we have concentrated on studying the reactions of cobalt and nickel clusters with hydrogen and nitrogen. Both kinetics and saturation experiments have been done. The most significant development has been optimization of the cluster source so that low temperatures can be routinely and reliably attained. Kinetics experiments at low temperatures have shown that temperature-dependent sticking probabilities can greatly affect reaction rates. Variable-temperature saturation experiments have provided new and important information about cluster structure, and also suggest that physisorption processes can be used

to probe structure. In fact, these results, together with the correlation of chemical reactivity with cluster-van der Waals complex formation described in section B, have supported an emerging realization that trapping an adsorbed molecule into a physisorbed precursor may play a crucial role in determining cluster reactivity.

1. Chemical Probes of Metal Cluster Structure *E. K. Parks, S. J. Riley, L. Zhu, J. Ho*

Studies of metal cluster chemistry are increasingly revealing the importance of cluster structure (i.e., the way the atoms are packed together) in determining chemical reactivity. Unfortunately, there are few experimental techniques for determining cluster structure. Most probes, such as electron microscopy and X-ray diffraction, require solid and/or high-density samples and cannot be applied to transition metal cluster beams. A traditional beam-based structural probe, the appearance of stability-induced "magic numbers" in cluster mass spectra, does not work for clusters made in a laser vaporization source, because cluster growth is kinetically controlled and the amount produced of a given cluster does not depend on the stability of that cluster. We were the first to show that systematic variations in cluster chemical properties can point to certain structural motifs. For example, the extent of an equilibrium reaction with weakly bound reagents such as water is dependent on cluster-adsorbate binding energies. Substantial cluster-size dependence of these binding energies can occur and can be explained on the basis of particular cluster structures. Saturation of clusters with such reagents as ammonia and nitrogen provides a count of the number of binding sites on cluster surfaces. Again, patterns of these numbers occur that can point to specific packing schemes. In the past year we have done extensive saturation studies of nitrogen on small nickel and cobalt clusters, and have accumulated considerable insight into the structure of these clusters.

a. The Nitrogen Probe

The adsorption of N_2 molecules has proven to be a particularly useful probe of cluster structure. The cluster-N_2 adsorption energy is relatively small, so that N_2 adsorption usually causes little change in the metal cluster structure. The N_2-N_2 interaction is extremely weak, so that the determination of N_2 saturation levels is not obscured by multilayer N_2 adsorption. This is illustrated in Figure IV-1, which shows N_2 uptake plots ($\bar{m}$ vs. the logarithm of the N_2 pressure, where $\bar{m}$ is the average value of m) for $Ni_n(N_2)_m$, n = 13, 14, and 19. Uptake plots generally show three regions of behavior. At low reagent pressure, the reaction is kinetically controlled and uptake is fairly rapid. At intermediate pressures, the rate of uptake decreases as the reaction enters an equilibrium regime. At higher pressures, a plateau in the data may appear, indicating saturation of the cluster. Such saturation is evident at N_2 pressures above 100 mTorr in Figure IV-1, and indicates that Ni_{13}, Ni_{14}, and Ni_{19} saturate with 12, 14, and 17 N_2 molecules, respectively.

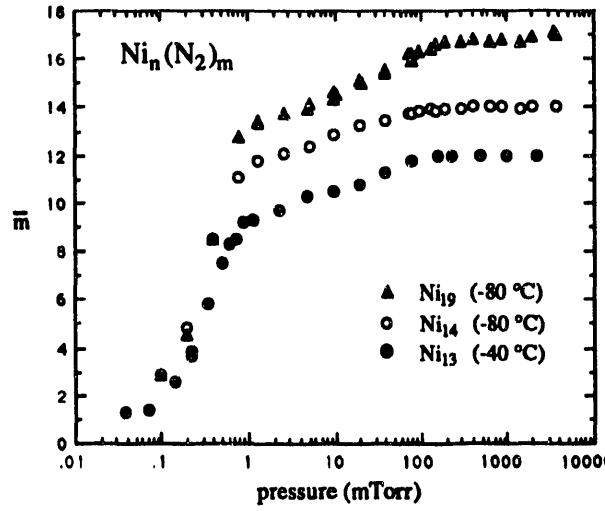

Figure IV-1. Uptake plots for nitrogen reaction with Ni_{13}, Ni_{14}, and Ni_{19}.

The data in Figure IV-1 are representative of extensive studies that we have carried out on the reactions of small nickel and cobalt clusters with nitrogen over a wide temperature range. The composition of $Ni_n(N_2)_m$ clusters saturated with nitrogen has been determined for $4 \le n \le 20$, and similar studies on cobalt clusters have been completed. Small nickel clusters tend to adsorb more than one N_2 molecule per metal atom. For example, Ni_4 has two levels of N_2 adsorption. Four N_2 molecules are adsorbed at low N_2 pressures with cluster-N_2 adsorption energies of ~0.5 eV, whereas at higher N_2 pressures four more molecules (with weaker bonds) are added, so that the cluster saturates at $Ni_4(N_2)_8$. The adsorption energies

can be estimated by modeling the uptake plots (see below). As cluster size increases, the saturation level becomes one N_2 molecule adsorbed for each surface metal atom in the cluster. This is an important observation, because a determination of the number of surface atoms allows us to choose between different possible structures. Several clusters have noteworthy features in their uptake plots. $Ni_7(N_2)_m$, for example, has a plateau at m = 1, indicating that there is one unique nickel atom that has the highest binding energy for a N_2 molecule. This suggests that the structure of Ni_7 is not the most likely pentagonal bipyramid (which might show a plateau at m = 2, but not 1). Although Ni_{13} and Co_{13} saturate with the adsorption of 12 N_2 molecules, as expected for several possible structures having one central atom, Ni_{14} saturates at m = 14, consistent with a tetrahedral structure in which all atoms are exposed. Co_{14}, on the other hand, saturates at m = 13, indicating that 14-atom clusters of the two metals, when saturated with nitrogen, have different structures. Ni_{19} saturates at m = 17, consistent with a double icosahedral structure, whereas $Co_{19}(N_2)_m$ shows a more complex behavior, suggesting several structural isomers based on fcc packing. Clearly, cluster structure is a complex function of cluster size as well as metal. The identification of cluster isomers will be important to our future attempts to understand structure-reactivity relationships.

b. Weakly Adsorbing Clusters

Nickel clusters in the 20- to 50-atom size range show significant variations in the strength of their binding of adsorbate molecules. Because the ionization potentials of these clusters also show variations in this size range, it is possible that the clusters are adopting a variety of structures. It is found, however, that those cluster sizes that show weak adsorption for nitrogen generally also have weak adsorption for other reagents. One example of this behavior is Ni_{28}. This cluster shows a distinct minimum in the adsorption of Ar atoms, Kr atoms, N_2 molecules, and H_2O. There is emerging evidence that clusters that show such weak adsorption may have close-packed fcc structures that have only (111) type faces, i.e., faces where n-fold sites are limited to $n \leq 3$. Such clusters might be expected to bind rare gases more weakly and may in fact bind most reagents more weakly. There are two 28-atom clusters having only (111) faces. One is made of interpenetrating 19-atom octahedra and the other of twinned 20-atom tetrahedra with the two apex atoms along the C_3 axis of the cluster removed. Ammonia saturation data for clusters in this size region, which count the number of apex atom sites, show exactly the behavior expected for either of these two structures. To distinguish the structure, we will attempt to saturate the cluster with nitrogen. Because the number of surface atoms is different for the two clusters (26 for one and 27 for the other), saturation, if it can be achieved, will tell one structure from the other. We will also attempt to saturate these clusters with rare gases. If this can be done, important structural information could result, because rare gases should not alter cluster structures significantly.

2. Kinetics of Cluster Reactions *L. Zhu, J. Ho, E. K. Parks, S. J. Riley*

a. Reactions of Nickel Clusters with D_2

The temperature dependence of the reaction kinetics of Ni_n clusters with deuterium has been determined in the range 133-413 K for cluster sizes n = 9-14. Except for Ni_9, the reaction rate constants are found to be nearly gas-kinetic and to be independent of temperature over the entire temperature range studied, suggesting that dissociative chemisorption of D_2 on nickel clusters is a direct process and proceeds without an activation barrier. Ni_9, on the other hand, exhibits a room temperature reaction rate constant that is roughly an order of magnitude smaller than the other clusters. Although the temperature dependence for Ni_9 is similar to that of the other clusters above 213 K, its reaction rate constants exhibit a significant increase with decreasing temperature below 213 K. The absence of a temperature dependence and the low reactivity of Ni_9 with D_2 above 213 K can be rationalized in terms of a direct dissociative chemisorption mechanism that is limited by the number of available active reaction sites or proper reagent orientation rather than by the presence of an activation barrier towards reaction. Because the same mechanism should also apply in the low-temperature range, the increase in rates observed below 213 K must be due to an additional reaction mechanism that operates only at low temperatures. This mechanism apparently involves an increase in the sticking probability of D_2 on Ni_9 at low temperatures, which then mediates the dissociative chemisorption.

b. Reactions of Cobalt Clusters with D_2

The kinetics of the reactions of bare cobalt clusters with deuterium have been studied in the past year. Absolute reaction rate constants for the addition of the first D_2 molecule to Co_n have been carefully measured at room temperature in the cluster size range n = 7-68. The rate constants are found to be a strong function of cluster size, varying by nearly three orders of magnitude over this size range. The size dependence is particularly evident in the n = 7-25 range, where Co_{15} is the most reactive cluster, and Co_{7-9}, Co_{19}, and Co_{20} are particularly unreactive compared to the others. Abrupt changes in the rate constants from one cluster to the next, such as from Co_9 to Co_{10}, Co_{14} to Co_{15}, and Co_{18} to Co_{19}, are observed. Between Co_9 and Co_{10}, the rate constant increases by more than one order of magnitude. For clusters above n = 25, the rate constants show several less prominent maxima and minima superimposed on a slow, nearly monotonic increase with cluster size. The rate constants roughly scale with $n^{2/3}$ in this size region, which is consistent with a model of a spherical cluster having a constant reaction rate per unit surface area (or number of surface metal atoms).

Temperature dependences of the reactivities have been studied in the range from -100 °C to 100 °C for the unreactive clusters Co_{14}, Co_{19}, Co_{20}, and Co_{21}. Certain patterns are observed. The reactivity of Co_{14} increases slightly with increasing temperature. Because the temperature dependence is so weak, it provides no definite evidence for a reaction barrier in the Co_{14}-D_2 system. The rate constant for Co_{20} is nearly temperature-independent above 293 K, but suddenly increases when the temperature approaches 173 K. This suggests that another adsorption mechanism emerges at low temperature, as was seen for $Ni_9 + D_2$. The behaviors of Co_{19} and Co_{21} are even more interesting. At low temperature (213-173 K), the kinetic depletion plots (plots of the logarithmic intensity of the bare cluster ions vs. D_2 density in the FTR) are not linear, suggesting that there is more then one cluster structure present for Co_{19} and Co_{21} and that the structures have different reactivities. This result is consistent with the N_2 saturation experiments described above, which also point to isomers for cobalt clusters above n = 18. These results again demonstrate the importance of identifying structural isomers to help explain cluster chemical properties.

3. Physisorption Processes *L. Zhu, J. Ho, E. K. Parks, S. J. Riley*

When D_2 is dissociatively chemisorbed on small nickel clusters, the cluster ionization potentials (IPs) increase monotonically with coverage, to the point where one-photon ionization by an ArF excimer laser is not possible. Yet at sufficiently low FTR temperatures, we see peaks in the ArF laser-generated mass spectra corresponding to Ni_nD_m species having m values larger than the known chemisorption saturation values. This is clearly illustrated in Figure IV-2, which shows that two groups of product peaks are seen following the reaction of D_2 with Ni_{13} at 133 K. One group of peaks with m_{max} values smaller than the chemisorption saturation comes from dissociative chemisorption of D_2 on nickel clusters. This group dies out in intensity because the ArF laser cannot ionize the saturated species. The second group is apparently due to species having D_2 molecules physisorbed on clusters already saturated with chemisorbed D atoms. The physisorbed molecules lower cluster IPs sufficiently that they can be ionized by the ArF laser. This is the first time that molecular physisorption of this type has been clearly identified in gas-phase metal cluster studies.

We can also quantify the physisorption saturation of the clusters. By subtracting the corresponding chemisorption contribution (determined in a separate experiment using F_2 laser ionization), the level of physisorption can be determined. For example, Ni_{13}

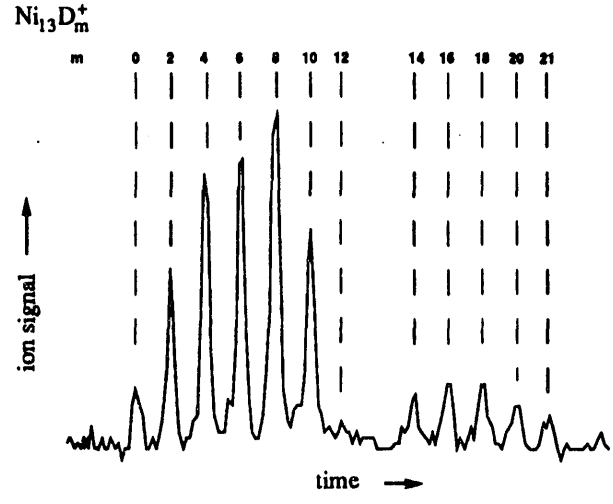

Figure IV-2. Portion of the mass spectrum recorded at an FTR temperature of 133 K and a D_2 pressure of 1 mTorr.

saturates with 14 chemisorbed D atoms, and ultimately saturates with a total of 38 deuteriums. We thus conclude that 12 physisorbed D_2 molecules can bind to Ni_{13}, the same as for N_2. We believe that such detailed physisorption studies, combined with our well-established chemisorption studies, will provide more insight into cluster structure and structure-reactivity relationships.

4. Uptake Modeling *E. K. Parks*

The uptake of a chemical reagent by a cluster is analogous to an adsorption isotherm measured in surface science studies, and can be analyzed to obtain absorption cross sections and cluster-adsorbate binding energies as a function of coverage. The rate of adsorption is modeled by assuming a cross section, and the rate of desorption with an RRK-type formalism. In our calculations the actual sequence of reagent molecule adsorptions and desorptions for an individual cluster is followed statistically for a time period corresponding to the time that reagents interact with the clusters in the FTR. The calculation starts with a bare cluster at the beginning of the FTR, and at the end of the reaction time the number of reagent molecules adsorbed on the cluster is determined. The calculation is repeated for roughly 1000 clusters in order to obtain statistically significant values for the reagent uptake. A fitting of the calculated results to the measured adsorbate uptake in the kinetics region determines the adsorption cross sections. Fitting in the equilibrium region determines the adsorption bond energies, which govern the desorption rates through the RRK model.

This analysis has been applied to the reaction of ammonia with the six polyicosahedral clusters $Fe_{19,23,26,29,32,34}$. Our earlier studies have demonstrated that these polyicosahedral clusters all saturate with the adsorption of 12 NH_3 molecules. Figure IV-3 shows uptake plots for Fe_{23} reacting with ammonia. The solid lines are the calculated uptake data for four FTR temperatures, and the points are the experimental data. The cluster-NH_3 bond energies are found in this case to decrease linearly with coverage from roughly 0.95 eV at low coverage to 0.50 eV at saturation. The model shows a similar linear decrease in the adsorption bond strength with coverage for the other clusters in the polyicosahedral series, with the extent of the decrease larger for smaller clusters. These results imply, in contrast to what was expected, that steric interactions between the NH_3 molecules do not seem to play a significant role in the relationship between bond strength and coverage. Such modeling calculations will be of great utility in extracting kinetic and thermodynamic information from adsorbate uptake data.

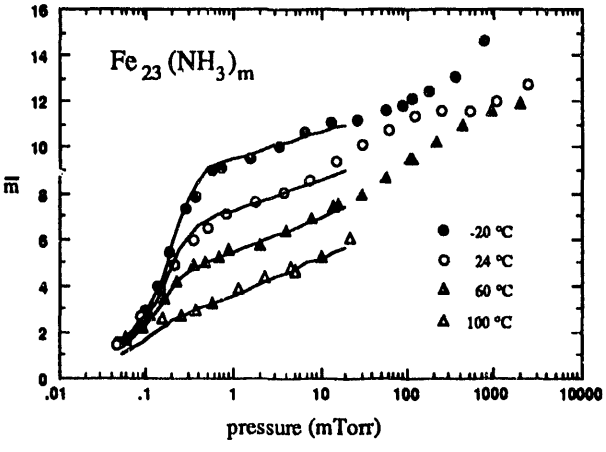

Figure IV-3. Calculated (solid curves) and measured (data points) uptake of ammonia by Fe_{23}.

B. Photoionization and Optical Spectroscopy of Metal Clusters

M. B. Knickelbein, W. J. C. Menezes

Over the past year we have refined and extended our laser photoionization mass spectrometry studies that probe the physical nature of metal clusters and cluster-adsorbate systems. The apparatus used in these studies is similar to that described in the previous section, except that a tunable ultraviolet laser is available for cluster photoionization. In addition, we have added an ArF excimer laser that enables us to do two-color pump-probe photodepletion spectroscopy experiments. These have yielded the first optical absorption spectra recorded for transition metal clusters.

1. Metal Cluster-Rare Gas van der Waals Complexes: A Microscopic Model of Physisorption *M. B. Knickelbein, W. J. C. Menezes*

We have investigated several systems of rare gas van der Waals (vdW) complexes of transition metal clusters, M_nR_m. These novel species are produced by seeding a few percent of argon or krypton into the helium carrier gas of our cluster source and cooling the nozzle to 77 K. As shown in Figure IV-4, the relative probability F_{vdW} for Fe_n, Co_n, and Ni_n clusters to form vdW complexes with rare gases is strongly dependent on cluster size. For example, Ni_9 is relatively "inert" toward vdW complex formation, whereas Ni_{13} forms complexes with high probability. Moreover, the nonmonotonic variations in F_{vdW} are strongly correlated with the variations observed in the *chemical* reactivity of these clusters with molecular deuterium, shown along with F_{vdW} in Figure IV-4. It is likely that these variations in complex formation efficiency result from size-dependent variations in the surface structure of the clusters: those clusters with surface sites capable of binding rare gas atoms strongly will form complexes with greater efficiency than topologically "smooth" clusters that lack such sites. The correlation between F_{vdW} and deuterium reactivity may mean that those surface sites that most readily bind a rare gas atom are the most reactive sites for a direct (i.e., concerted) reaction with hydrogen. Another possibility is that these $M_n + D_2$ reactions proceed through a long-lived intermediate $M_n\cdots D_2$ van der Waals species, in which the hydrogen molecule is trapped into a physisorbed precursor state prior to undergoing dissociative chemisorption:

$$M_n + D_2 \rightleftharpoons M_n\cdots D_2$$

$$M_n\cdots D_2 \rightarrow M_nDD\ .$$

In such a two-step mechanism, the overall reaction rate will be proportional to the steady state concentration of the $M_n\cdots D_2$ intermediate, so that those clusters that readily form these intermediates will be more reactive than those that do not. It is reasonable to expect that those clusters that most easily form rare gas complexes will also form $M_n\cdots D_2$ van der Waals complexes with the greatest probability.

The F_{vdW}-reactivity correlations in Figure IV-4 are not perfect for the first-row transition metals, and are entirely absent for niobium clusters. This indicates that other factors such as cluster electronic structure cannot be neglected. A fuller delineation of the interplay between electronic and geometric effects will be essential to our understanding of cluster chemistry.

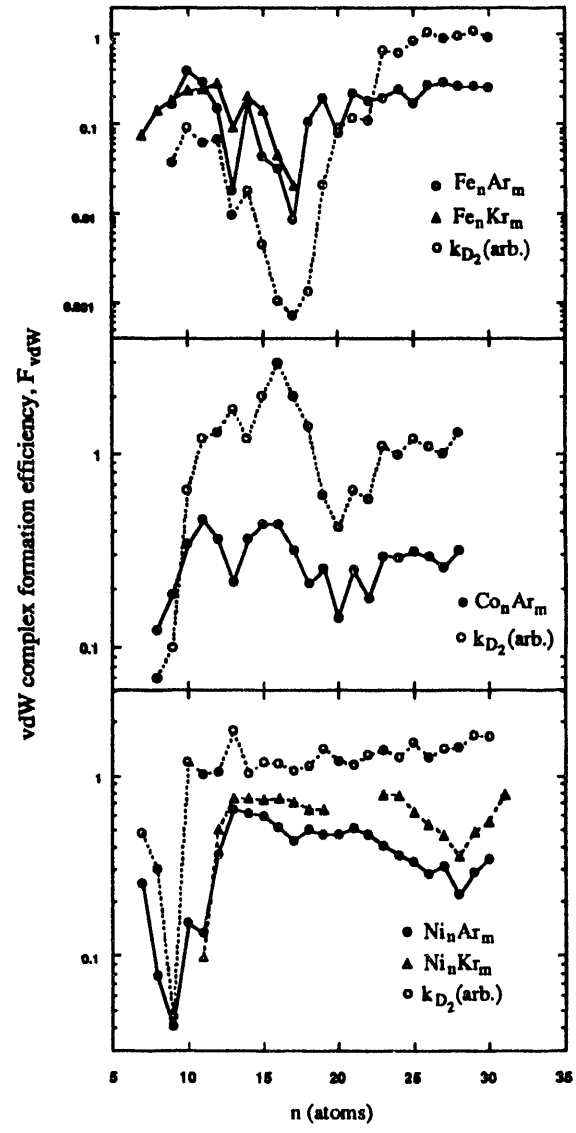

Figure IV-4. Relative probability F_{vdW} of rare gas van der Waals complex formation for Fe_n, Co_n, and Ni_n clusters (left scale, filled symbols) and rate constants for reactions with D_2 (open symbols).

2. The Optical Response of Niobium Clusters *M. B. Knickelbein, W. J. C. Menezes*

The ability to convert a relatively large fraction of metal clusters to rare gas van der Waals complexes has led to the development of a new technique for determining metal cluster optical absorption spectra. Because these transition metal clusters are produced in

very small amounts and with a wide distribution of sizes, the traditional techniques of optical absorption spectroscopy are not usable. However, we have found that photon absorption by metal clusters can be followed with high sensitivity by monitoring the loss of rare gas atoms from metal cluster-rare gas complexes following photoabsorption: $M_nR_m + h\nu \rightarrow M_n + mR$. Absorption spectra can be measured using the fractional depletion of M_nR_m species in the molecular beam as a function of laser wavelength. By concurrently measuring laser fluence, we can obtain absolute absorption cross sections, enabling comparison with theories such as the Mie model of metal particle optical response. The first photodepletion measurements on Nb_nAr_m complexes, from n = 7-20, have been completed, spanning the 336-614 nm wavelength range. Spectra for Nb_7Ar and $Nb_{20}Ar$ are shown in Figure IV-5. Our results indicate that niobium clusters in this size range have broad, apparently featureless absorption spectra, with oscillator strengths that increase steadily into the ultraviolet, in qualitative agreement with the predictions of the Mie model (also shown in Figure IV-5). These results represent the first size-specific optical absorption spectra ever recorded for polyatomic transition metal clusters. Such measurements are essential to a fuller understanding of cluster electronic properties and as input to theoretical treatments of cluster electronic states. We plan to extend these studies to larger niobium clusters and to clusters of other transition and coinage metals.

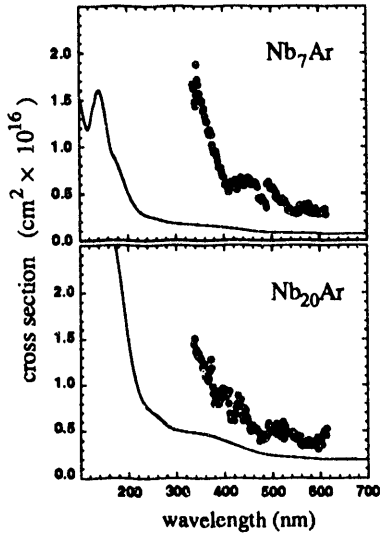

Figure IV-5. Photodissociation action spectra for Nb_7Ar and $Nb_{20}Ar$ from 336-614 nm. Solid curves are the theoretical spectra from Mie theory.

3. Bimetallic Clusters of Aluminum and Cobalt *W. J. C. Menezes, M. B. Knickelbein*

There are now many cases where electronic shell effects are seen in the properties of clusters of nearly free electron metals. These effects appear as sudden discontinuities in size-dependent properties for clusters containing certain magic numbers of atoms. These effects are predicted by simple shell models in which delocalized electrons, confined to a spherical potential, cause the clusters to display quantum level structure characterized by shells composed of degenerate levels, similar to those shown by electrons in atoms and by protons and neutrons in nuclei. For the spherical-square-well potential, electronic shell closings are predicted to occur when the number of electrons n_e equals one of the magic numbers of 2, 8, 18, 20, 34, 40, 58.... Such shell closings have been observed in the IPs of alkali and coinage metal clusters, where sudden IP decreases follow the predicted shell closings. Deviations from the predicted shell-filling pattern are sometimes observed, however, pointing to the limitations of simple "structureless" potential models that neglect the discrete nature of the nuclear charge distribution.

It is a significant observation that electronic shell effects are observed only in clusters of metals that should, by simple valence considerations, contribute an integral number of electrons to the collection of delocalized electrons comprising the "conduction" band of a cluster. For example, the IPs of aluminum clusters, Al_n, show many of the sudden jumps displayed by clusters of monovalent nearly free electron metals, with $n_e = 3n$. Interestingly, as our studies have shown, transition metal clusters do not display such magic-number behavior in their ionization potentials. This is presumably because the valence electrons of transition metals, in particular the d electrons, are more involved in localized bonding than the outermost s electrons of the alkali and coinage metals. As a test of these ideas, we have measured ionization potentials of bimetallic aluminum/cobalt clusters Al_nCo_m with n > m in order to determine the effective valency of cobalt atoms in small aluminum clusters. The IPs of Al_nCo_m for m = 0-3 are shown in Figure IV-6. The electronic shell structure that has been seen for aluminum clusters (three electrons per atom) is seen to be perturbed by the presence of the cobalt atoms, and the perturbation is consistent with cobalt contributing one electron to the clusters'

conduction band, such that $n_e = 3n_{Al} + n_{Co}$. This can be seen most clearly by comparing the IPs of "pure" aluminum clusters to those of clusters in which a single cobalt atom is present: the large IP decrease from $Al_{13}Co$ ($n_e = 40$) to $Al_{14}Co$ ($n_e = 41$) remains, but there is a reversal of the odd-even alternation pattern for n = 15-20. Although some of these shell-closing features are seen for Al_nCo_2 and Al_nCo_3, any recognizable vestiges of the aluminum cluster shell structure disappear for clusters containing four or more cobalt atoms.

Further studies of similar bimetallic clusters should prove to be useful in elucidating the nature of bonding in clusters containing transition metal atoms.

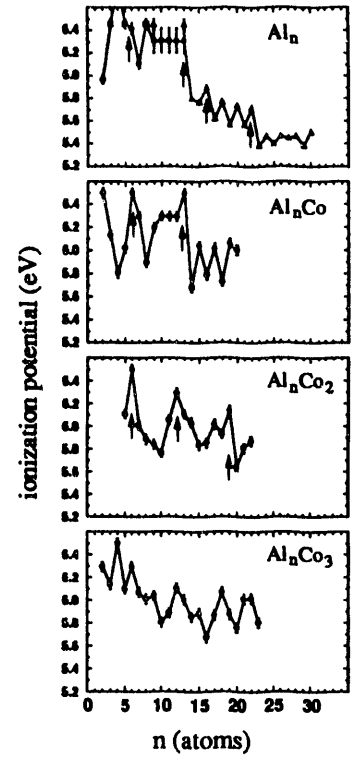

Figure IV-6. Vertical ionization potentials for Al_nCo_m, m = 0-3. Apparent electronic shell closings are denoted by arrows.

C. Theoretical Studies of Cluster Structure and Dynamics

J. Jellinek, Z. B. Güvenç, M. J. Lopez, V. Bonačić-Koutecký, S. F. Chekmarev, F. W. Dech, P. Fantucci, I. L. Garzon, G. Lacueva, A. F. Voter

The theoretical program focuses on studies of the fundamental structural and dynamical properties of clusters that include isomers (stable and metastable), interconversion and coexistence of these isomers, phases and phase changes (e.g., solidlike to liquidlike) in clusters, mechanisms of cluster-molecule interactions, and evolution of these properties with cluster size. Because these properties are ultimately determined by the nature of the interatomic interactions, one of the major goals of our studies is to develop an adequate modeling of these interactions. We concentrate primarily on metal clusters—the subject of the experimental research in the group. The presence of a theoretical and an experimental component within the group provides a continued challenging and stimulating interaction between theory and experiment.

The traditional concepts, approaches, and tools of theoretical chemistry and physics were developed to study the gaseous, liquid, and condensed states of matter. The "microscopic" nature of clusters as intermediates between isolated atoms and molecules, on the one hand, and solids/liquids, on the other, requires a critical reevaluation and modification of the existing theoretical arsenal in order to use it in cluster-related problems. Moreover, the newness of the cluster field calls for new theoretical methodologies. Our work involves general conceptual (analytical) developments, code development and optimization specifically tailored to systems with a moderate-to-large number of degrees of freedom, and large-scale numerical simulations that yield information on a broad variety of physico-chemical properties characteristic of clusters.

1. Dynamics of Cluster-Molecule Interactions *J. Jellinek, Z. B. Güvenç*

In the past year we have continued our detailed investigation of cluster-molecule interactions using the $D_2 + Ni_{13}$ collision system as a paradigm. We utilize the technique of quasiclassical trajectory simulations to study the reactive (dissociative adsorption of the molecule on the cluster) and inelastic (scattering of the molecule from the cluster) channels of the interaction. These are characterized as functions of such parameters as the initial (quantized) rovibrational

state of the molecule, the collision energy, and the structure and temperature of the cluster. The interaction between the Ni atoms is modeled by an embedded atom potential, whereas those between D-D and D-Ni are represented by a LEPS (London-Eyring-Polanyi-Sato) function. The quantitative analysis is carried out in terms of a variety of physico-chemical characteristics, which range from detailed probabilities through cross sections to rate constants and activation energies.

Our results clearly indicate, for the first time in the context of cluster studies, that both the molecule's dissociative adsorption and its scattering can be direct or indirect. The indirect processes involve formation of transient cluster-molecule complexes, i.e., resonances. We have formulated a new resonance analysis scheme that allows one to calculate, in the course of trajectory simulations, resonance formation probabilities and cross sections, their lifetimes, and the branching ratios between the direct and indirect processes. Typical results in terms of probabilities for the reactive interaction of D_2 with Ni_{13} are shown in Table IV-1; the resonance lifetimes should be compared to the zero-point vibrational period of D_2, which is ~0.01 ps. It is clear that as the collision energy increases, the lifetime decreases, and the fraction of the direct reaction increases. With increasing impact parameter, the resonance lifetime decreases (not shown). The analysis of the cross-section data, which includes the contribution from all impact parameters, indicates that in the reactive channel the molecular sticking probability is a decreasing function of the collision energy.

We have also examined the effect of cluster temperature on its reactivity. In Figure IV-7, the dissociative adsorption cross sections are plotted as functions

Table IV-1. Probabilities of the direct (P^{DR}) and indirect (P^{IR}) reactions, fractional contribution of the direct reaction (f^{DR}), and reactive resonance lifetimes (τ) for the case of a D_2 molecule initially in the $v_i = 1$ vibrational and the $j_i = 0$ rotational state colliding with a zero-temperature cuboctahedral Ni_{13}. The impact parameter b = 0.25 Å.

E_{tr}^i (eV)	0.038	0.30	0.50	0.90
p^{DR}	0.06	0.11	0.13	0.20
p^{IR}	0.44	0.39	0.52	0.57
f^{DR}(%)	12	22	19	26
τ(ps)	0.07	0.03	0.02	0.01

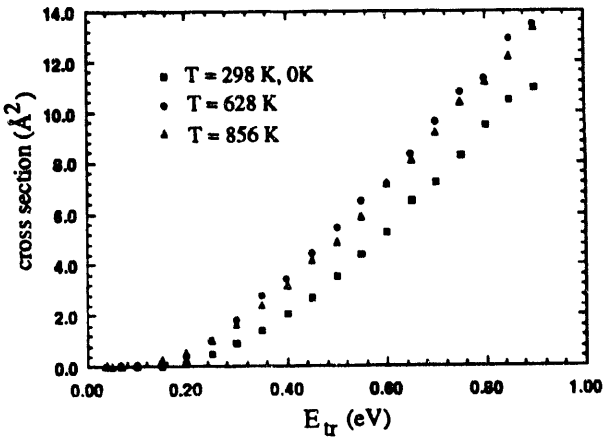

Figure IV-7. Cross section of the dissociative adsorption of D_2 ($v_i = 0$, $j_i = 3$) on an icosahedral Ni_{13} as a function of the collision energy for different initial temperatures T of the cluster.

of the collision energy for different initial temperatures of an icosahedral Ni_{13}. The results show that the cluster reactivity remains constant in the temperature range T = 0-298 K. It increases somewhat at T = 628 K, and remains essentially unchanged (or possibly even shows a slight tendency to decrease) at T = 856 K. It should be noted that at these temperatures the cluster is below the isomerization threshold. Its thermal motion, however, causes deformation of the initially (at T = 0 K) perfect icosahedral structure. The qualitative features of the temperature dependence of the reactivity reflect an intricate interplay of the cluster energetic and topological factors. Work is in progress on extending these studies to higher temperatures.

The resonance mechanism of cluster reactivity as an alternative to the direct reaction, as well as the relative independence of the reactivity on temperature discussed above, have recently been confirmed, at least partially, by experiments in our group (see sections A and B).

The cluster-molecule reaction mechanism(s) are largely defined by the topology of the cluster-molecule interaction potential. To gain information about this topology, we have mapped out the minimum energy LEPS interaction as a function of the cluster center-of-mass (c.m.)—D_2 (c.m.) distance and the D-D distance. The contour plot of the map for icosahedral Ni_{13} is shown in Figure IV-8. Six low-energy "lakes" separated by "ridges" can be clearly identified. The lake corresponding to the smallest D-D distances represents the energies and location of the

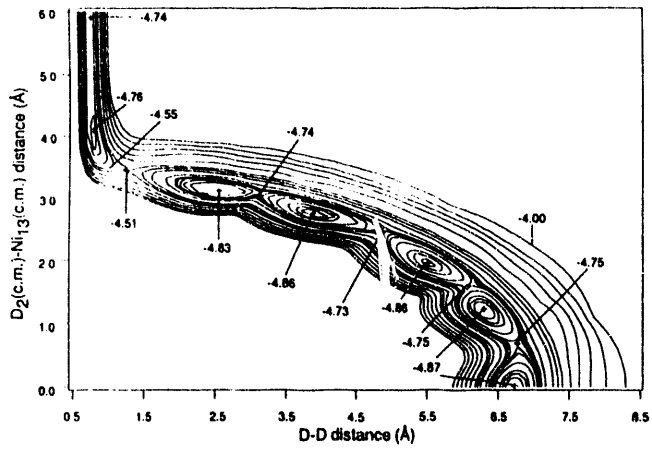

Figure IV-8. Contour plots of the minimized LEPS interaction energy of a D_2 molecule with an icosahedral Ni_{13} cluster as a function of the D_2 (c.m.)—Ni_{13} (c.m.) and the D-D distances. The numbers indicate the well depths and the barrier heights in eV.

molecular adsorption potential well. The other five represent the topologically different pairs of sites and corresponding energies of the dissociative (atomic) adsorption of D_2. The ridges are potential barriers. One notices that there is no barrier to molecular adsorption, and that the highest barrier is for breaking the D-D bond.

It turns out that the reaction rate constant(s) and exothermicity calculated from the original LEPS potential (DePristo and co-workers) do not reproduce quantitatively the values deduced from the experimental measurements made in our group. We examined how sensitively the calculated results depend on the parameters of the potential and found quite a strong sensitivity. We have shown that a 10% increase of the D-Ni bond strength in the LEPS potential produces agreement between theory and experiment. Our future work will further explore the delicate problem of fine tuning the cluster-molecule interaction potentials. Questions such as dependence of the mechanisms of cluster interactions, especially reactions, on the cluster size, effect of the cluster temperature on the resonance phenomena, etc. will be addressed.

2. Structure, Phases, and Phase Changes of Nickel Clusters from an Embedded-Atom Potential *J. Jellinek, Z. B. Güvenç*

The structure and specificity of phases and phase changes in small metal (especially transition metal) clusters persist as a challenging aspect of cluster research. We have extended our earlier investigation of these properties in Ni_n clusters, based on an embedded-atom potential (EAP) for modeling the interatomic cohesion, from n = 12-14 to n = 9, 15, 18-20, 55. The different isomeric forms of these clusters were determined by the technique of simulated thermal quenching. As an example, we find that the lowest energy structure for Ni_9 determined by the electronic structure calculations of Siegbahn et al. is only the second most stable among the isomers we obtain from the EAP approach. The EAP lowest energy structure is only ~0.09 eV more stable than the next isomer, but it has a very different geometry.

As their internal energy increases, the clusters undergo a characteristic solid-to-liquidlike transition. The nature and the different stages of the transition, as well as the energies (or temperatures) corresponding to these stages, are identified through the analysis of a variety of characteristic physical quantities such as the short-time-averaged kinetic energy, the caloric curve, root-mean-square (rms) bond length fluctuations, and mean-square displacements. Clusters of all the sizes studied exhibit a so-called "coexistence" (or isomerization) stage over a finite range of energies (temperatures). The time evolution of a cluster in this stage is characterized by intermittent spontaneous isomerization transitions, with each isomer surviving long enough between the transitions to be identifiable. The Ni_{20} cluster, the most stable isomer of which is a double icosahedron with an additional atom decorating a threefold face, "melts" in two stages. The isomerization stage ($T \approx 1100$-1300 K) is preceded by a lower temperature "premelting" stage ($T \approx 400$-700 K) similar to that found by us earlier for Ni_{14}. Premelting is a local melting of the cluster involving the "extra" atom and atoms in its vicinity. It is caused by the locally destabilizing effect of this extra atom on the underlying and otherwise very stable icosahedral Ni_{19}. We conjecture that the premelting phenomenon is characteristic of nickel (or, more generally, transition metal) clusters of those sizes that form complete icosahedra with one (or, for larger clusters, possibly a few) extra decorating atom(s).

An interesting feature of the melting mechanism in Ni_{55} is the distinguishable stage of surface melting. In Figure IV-9, the rms bond-length fluctuations, averaged over the bonds between (a) all the 55 atoms, (b) the 42 surface atoms, and (c) the 13 core atoms, are plotted as functions of the cluster temperature. It

is clear that the melting transition, the signature of which is the abrupt rise in the value of the rms bond-length fluctuations, starts between T = 800 K and 900 K and is caused by the increased mobility of the surface atoms. The icosahedral 13-atom core resists melting up to T ≈ 1100 K. "Snapshots" of the cluster and of its core (Figure IV-10) taken from simulation runs at different energies (temperatures) clearly illustrate the solidlike, the surface-melted, and the liquidlike phases.

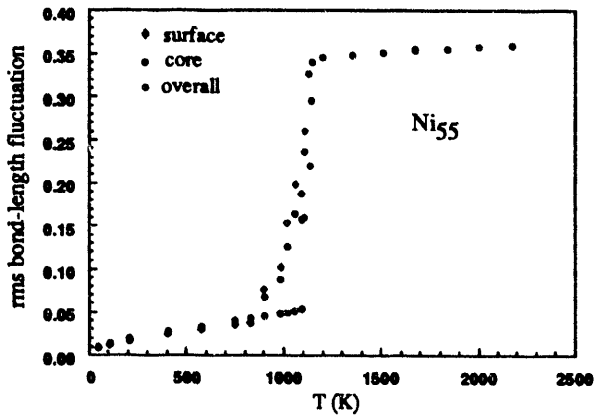

Figure IV-9. Rms bond-length fluctuations averaged over the bonds between all the 55 atoms, the 42 surface atoms, and the 13 core atoms, respectively, as functions of the cluster temperatures.

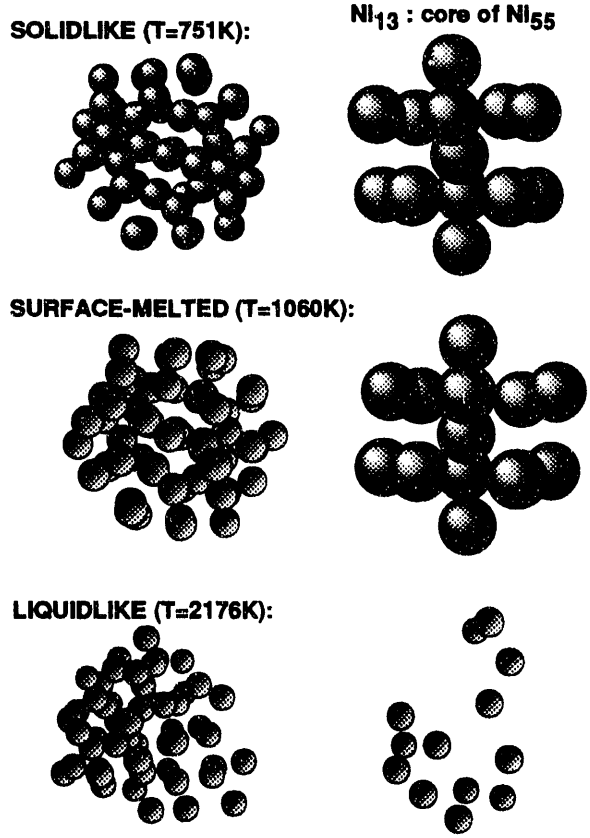

Figure IV-10. Snapshots of the initially icosahedral Ni_{55} and of its 13-atom core at different temperatures of the cluster.

3. The Effective-Medium Approach for Clusters *J. Jellinek, M. J. Lopez*

One of the most important and most difficult aspects of theoretical studies of metal clusters is the problem of an accurate description or, alternatively, adequate modeling of the interatomic interactions. The so-called effective-medium approach is one of the more fundamental schemes for calculating the cohesive energy and other bulk and surface properties of metals. Unlike the embedded-atom method, the effective-medium approach explicitly identifies the different interactions contributing to the total energy and, in principle, avoids fitting of parameters. In practical implementations, however, approximations and fittings were introduced. An important feature of the original effective-medium scheme that makes it virtually inapplicable to clusters is the built-in assumption of a lattice structure. Some modifications have been considered, but they introduce further questionable approximations, and the entire method remains extremely demanding computationally.

We have initiated a new project, the goal of which is to formulate an effective-medium-like approach that is internally consistent, computationally efficient, and applicable to the bulk as well as to clusters. To achieve this flexibility, an optimal compromise between the fundamental and fitted components of the method must be introduced. In our scheme, the lattice bias is totally eliminated. The scheme still correctly reproduces not only the equilibrium cohesive energy of the bulk but also the change of the cohesive energy with the lattice constant. The energy of the diatomic molecule is mimicked exactly as well. We have derived and utilized a number of new fundamental relationships. One of these is the correlation between the average electronic densities that any two atoms contribute to each other's environment. We expect to complete the conceptual development of the new method in the near future. The emphasis then will shift to numerical implementations and applications.

4. Analysis of Molecular Dynamics Schemes *J. Jellinek, G. Lacueva*

When studying clusters, which are systems far from the thermodynamic limit, the constant-energy (microcanonical) and the constant-temperature (canonical) molecular dynamics (MD) simulations may be inequivalent. In fact, in many cases the canonical MD may be more appropriate because it is the temperature, rather than the total energy, of a cluster that is under control in experiments.

About eight years ago, Nosé introduced an ingenious constant-temperature MD in which the thermal bath, to which the physical system is coupled, is mimicked by a single degree of freedom. It was claimed that this was the only way in which a canonical ensemble could be simulated by a continuous deterministic dynamics. About five years ago, we generalized Nosé's approach and proved that there are infinitely many such ways. In order for the dynamics to produce thermally averaged properties of the physical system, the dynamics of the extended system (which includes the extra "bath" degree of freedom) has to be ergodic. It turned out that it may be problematic to satisfy this requirement for systems with only a few degrees of freedom. In fact, the original Nosé dynamics cannot thermalize a one-dimensional harmonic oscillator, which is an illustration of its limitations. Doubt has been cast in the literature as to whether coupling to a single additional degree of freedom can ever "mix up" a one-dimensional harmonic oscillator. We have analyzed many different canonical MDs generated within our generalization of Nosé's scheme and have shown that they thermalize the harmonic oscillator very efficiently. The implication of this is that these dynamics are more efficient in sampling the phase space of the physical system than the Nosé MD. Our current work focuses on attempts to identify the factors that govern the sampling efficiency of the different dynamics. Identification of these factors will allow for a more judicious selection of the dynamics that are optimized to the specific systems and problems under study.

5. Cluster Research Within the Theory Institute *J. Jellinek, V. Bonačić-Koutecký, P. Fantucci, I. L. Garzon, S. F. Chekmarev*

The primary goal of our activity within the Theory Institute is to facilitate an expansion of theoretical cluster research at Argonne by fostering long-term collaborations with theoretical cluster research groups around the world. The mechanism of collaboration includes visits to Argonne of theorists from different institutions for periods of a few months. The resulting collaborations then continue in the respective home institutions, with possible repeated periods of joint work.

a. Ab Initio Molecular Dynamics for Metal Clusters *J. Jellinek, V. Bonačić-Koutecký, P. Fantucci*

The goal of this collaboration is to produce an ab initio (as understood by chemists) molecular dynamics scheme for studying metal clusters and cluster-molecule systems. The scheme is based on combining an ab initio quantum chemical calculation of the electronic energies for a set of fixed nuclei with the classical dynamics of the nuclei. The latter evolve under the forces defined as the derivatives of the energy of the electronic ground state with respect to the nuclear coordinates. A major problem is to achieve a level of computational efficiency that will allow for carrying out simulation runs long enough for a meaningful dynamical analysis. A large effort has been invested in optimization of the code. This involved speeding up the calculation of the integrals, vectorization, using stored precomputed quantities, etc. The codes were ported to the massively parallel Touchstone DELTA machine and successfully tested for the Li_6 cluster. The efficiency of the runs, as a function of the number of processors used, has been mapped out, and it was found that for the particular case of Li_6 the optimum is provided by 128 processors. The test runs unambiguously proved that the task is feasible, although further optimizations are needed. Work on these is in progress.

b. Structure and Dynamics of Metal Clusters from a Gupta-like Potential *J. Jellinek, I. L. Garzon*

We continued exploration of the structural and dynamical properties of nickel and gold clusters of various sizes using a Gupta-like potential. This is a many-body potential that depends on five parameters. Two of these parameters can be viewed, respectively, as an energy-scaling and a length-scaling unit, and we interpret them as depending not only on the material

(element) but also on the cluster size. The other three parameters are material-dependent only. The goal of this study is to contribute to a global comparison of the different potentials for metal clusters through a comparison of the structural and dynamical features derived from them.

It is reassuring, although somewhat surprising, that virtually all the predictions for nickel clusters derived from the Gupta-like potential are the same as from the embedded-atom approach (section C.2). This includes size-specific features such as premelting in Ni_{14} and Ni_{20}, and surface melting in Ni_{55}.

The structural features of gold clusters are quite different from those of nickel clusters. The most stable geometries are usually of lower symmetry, and there are many more isomers within a specified energy range. Some of the gold clusters, e.g., Au_{14}, exhibit quite peculiar features in their isomerization dynamics. Work is in progress on the analysis of these.

c. Configuration Space Sampling and Density of States of Anharmonic Systems *J. Jellinek, S. F. Chekmarev*

The fundamental role of the density of states of any physical system stems from the fact that the knowledge of this quantity allows one to calculate both equilibrium (thermodynamic) and nonequilibrium (kinetic) characteristics of the system. Often one has to know the absolute (normalized) density of states. This quantity can be calculated analytically only for harmonic systems. Until recently, no efficient way of obtaining this quantity for arbitrary anharmonic systems has been known.

We have implemented two of the three different ways of calculating the absolute density of states in numerical simulations that we had suggested earlier. One implementation is based on molecular dynamics, the other on a novel so-called microcanonical Monte Carlo (MC) sampling technique. The microcanonical MC proved a very efficient technique of sampling the configuration space of a system with a fixed total energy. (The traditional canonical Monte Carlo is a sample technique for a system with a fixed temperature.) We have tested our implementations on argon clusters. This choice was dictated by the computational simplicity of the Lennard-Jones potential describing these clusters and by the abundance of data on these clusters that can be used as a basis for comparison and evaluation. The tests proved the reliability and efficiency of the new techniques. We intend to use them broadly in our future studies.

Future plans for the Theory Institute include expansion of the effort to more projects and more participants.

PUBLICATIONS

CHEMICAL DETERMINATION OF THE GEOMETRICAL STRUCTURE OF ISOLATED TRANSITION METAL CLUSTERS
S. J. Riley
Nanostruc. Mater. 1, 155-159 (1992)

ICOSAHEDRAL STRUCTURE IN HYDROGENATED COBALT AND NICKEL CLUSTERS
T. D. Klots*, B. J. Winter*, E. K. Parks, and S. J. Riley
J. Chem. Phys. 95, 8919-8930 (1991)

EVIDENCE FOR POLYICOSAHEDRAL STRUCTURE IN AMMONIATED IRON, COBALT, AND NICKEL CLUSTERS
E. K. Parks, B. J. Winter*, T. D. Klots*, and S. J. Riley
J. Chem. Phys. 96, 8267-8274 (1992)

ATOMIC STRUCTURE OF CLUSTERS THROUGH CHEMICAL REACTIONS
S. J. Riley and E. K. Parks
Physics and Chemistry of Finite Systems: From Clusters to Crystals, Vol. I, P. Jena et al., Eds., Kluwer, Dordrecht, The Netherlands, 1992, pp. 19-28

*Not affiliated with the Chemistry Division or affiliated on a temporary basis.

THE CHEMISTRY OF TRANSITION METAL CLUSTERS
S. J. Riley
Metal-Ligand Interactions: From Atoms, to Clusters, to Surfaces, D. R. Salahub and N. Russo, Eds., Kluwer, Dordrecht, The Netherlands, 1992, pp. 17-36

ELECTRONIC SHELL STRUCTURE IN THE IONIZATION POTENTIALS OF COPPER CLUSTERS
M. B. Knickelbein
Chem. Phys. Lett. 192, 129-134 (1992)

METAL CLUSTER-RARE GAS VAN DER WAALS COMPLEXES: PHYSISORPTION ON A MICROSCOPIC SCALE
M. B. Knickelbein and W. J. C. Menezes*
J. Phys. Chem. 96, 6611-6616 (1992)

THE OPTICAL RESPONSE OF SMALL NIOBIUM CLUSTERS
M. B. Knickelbein and W. J. C. Menezes*
Phys. Rev. Lett. 69, 1046-1049 (1992)

MODE SELECTIVITY IN CLUSTER-MOLECULE INTERACTIONS: $Ni_{13} + D_2$
J. Jellinek and Z. B. Güvenç*
Mode Selective Chemistry, J. Jortner et al., Eds., Kluwer, Dordrecht, The Netherlands, 1991, pp. 153-164

PHASE CHANGES IN NICKEL CLUSTERS FROM AN EMBEDDED-ATOM POTENTIAL
Z. B. Güvenç*, J. Jellinek, and A. F. Voter*
Physics and Chemistry of Finite Systems: From Clusters to Crystals, Vol. I, P. Jena et al., Eds., Kluwer, Dordrecht, The Netherlands, 1992, pp. 411-416

THE $D_2 + Ni_{13}$ REACTION: MODE-SPECIFIC AND STRUCTURE-SPECIFIC FEATURES
J. Jellinek and Z. B. Güvenç*
Physics and Chemistry of Finite Systems: From Clusters to Crystals, Vol. II, P. Jena et al., Eds., Kluwer, Dordrecht, The Netherlands, 1992, pp. 1047-1056

MELTING OF NICKEL CLUSTERS
I. L. Garzon* and J. Jellinek
Physics and Chemistry of Finite Systems: From Clusters to Crystals, Vol. I, P. Jena et al., Eds., Kluwer, Dordrecht, The Netherlands, 1992, pp. 405-410

SUBMISSIONS

CHEMISTRY WITH NEUTRAL METAL CLUSTERS
S. J. Riley
Clusters of Atoms and Molecules, H. Haberland, Ed., Springer (in press)

GAS PHASE REACTIONS OF TRANSITION METAL CLUSTERS
S. J. Riley
Ber. Bunsen-Ges. Phys. Chem. (in press)

TEMPERATURE DEPENDENCE OF THE REACTION OF NICKEL CLUSTERS WITH DEUTERIUM
L. Zhu*, J. Ho*, E. K. Parks, and S. J. Riley
J. Chem. Phys. (1992)

*Not affiliated with the Chemistry Division or affiliated on a temporary basis.

REACTIONS OF COBALT CLUSTERS WITH DEUTERIUM
J. Ho*, L. Zhu*, E. K. Parks, and S. J. Riley
Z. Phys. D (1992)

CHEMICAL PROBES OF METAL CLUSTER STRUCTURE - Fe, Co, Ni, AND Cu
E. K. Parks, L. Zhu*, J. Ho*, and S. J. Riley
Z. Phys. D (1992)

PHYSISORPTION OF DEUTERIUM ON DEUTERATED NICKEL CLUSTERS
L. Zhu*, J. Ho*, E. K. Parks, and S. J. Riley
Z. Phys. D (1992)

PHOTODISSOCIATION SPECTROSCOPY OF Nb_nAr_m VAN DER WAALS COMPLEXES
W. J. C. Menezes* and M. B. Knickelbein
J. Chem. Phys. (1992)

THE EVOLUTION OF ELECTRONIC STRUCTURE IN Al_nCo_m CLUSTERS
W. J. C. Menezes* and M. B. Knickelbein
Z. Phys. D (1992)

MOLECULE-CLUSTER COLLISIONS: REACTION OF D_2 WITH Ni_{13}
J. Jellinek and Z. B. Güvenç*
Nuclear Physics Concepts in Atomic Cluster Physics, Lecture Notes in Physics, H. O. Lutz et al., Eds., Springer-Verlag, Heidelberg, 1992 (in press)

CLUSTER-MOLECULE SYSTEMS: ANALYSIS AND TUNING OF THE INTERACTION POTENTIAL
J. Jellinek and Z. B. Güvenç*
Z. Phys. D (1992)

SURFACE MELTING IN Ni_{55}
Z. B. Güvenç* and J. Jellinek
Z. Phys. D (1992)

PECULIARITIES OF STRUCTURES AND MELTINGLIKE TRANSITION IN GOLD CLUSTERS
I. L. Garzon* and J. Jellinek
Z. Phys. D (1992)

COLLABORATIONS

V. Bonačić-Koutecký, Institute of Physical and Theoretical Chemistry, Free University, Berlin, Germany
P. Fantucci, University of Milan, Italy
Development of an ab initio molecular dynamics scheme for metal clusters and cluster-molecule systems.

S. F. Chekmarev, Institute of Thermophysics of the Siberian Branch of the Russian Academy of Sciences, Novosibirsk
New conceptual developments for phase-space sampling and for calculation of the absolute densities of states in cluster systems.

I. L. Garzon, Institute of Physics of the National Autonomous University of Mexico, Ensenada
Molecular dynamics studies of melting behavior of nickel and gold clusters using a size-dependent Gupta-like potential.

---

*Not affiliated with the Chemistry Division or affiliated on a temporary basis.

G. Lacueva, John Carroll University, University Heights, OH
Analysis of efficiency of different constant-temperature molecular dynamics.

A. F. Voter, Los Alamos National Laboratory
Implementation of the embedded-atom potential for nickel.

F. W. Dech, Computing and Telecommunications Division, Argonne National Laboratory
Work on visualization of dynamical processes in cluster systems, including cluster-molecule interactions and melting of clusters.

V. CHEMICAL DYNAMICS IN THE GAS PHASE

A. F. Wagner, M. J. Davis, L. B. Harding, R. J. Harrison, J. P. Hessler, K. Liu, R. G. Macdonald, J. V. Michael, R. L. Shepard, S. K. Gray, J. H. Kiefer, G. C. Schatz, S.-W. Cho, H. Du, F. LeQuere, K. P. Lim, J. Nicholas

Outside Collaborators: *M. H. Alexander, R. Ahlrichs, J. M. Bowman, M. Ernzerhof, E. Goldfield, M. F. Guest, R. Kendall, T. Kovar, H. Lischka, P. J. Ogren, R. M. Pitzer, I. Shavitt, E. Stahlberg, P. Szalay*

A knowledge of chemical dynamics provides the foundation for understanding and controlling such complex chemical phenomena as the combustion of hydrocarbon fuels, the chemistry of the atmosphere, and the development of new materials. Research carried out over the past 20 years has led to rapid advances in both the fundamental and applied aspects of chemical dynamics.

The combination of advanced experimental studies and modern theory can be an effective means of obtaining important insights into the mechanisms, energetics, and dynamics on that most fundamental of chemical processes, the elementary chemical reaction. Our program in CHEMICAL DYNAMICS IN THE GAS PHASE provides just such a close collaboration between experimental and theoretical efforts in the study of chemical reactivity. The emphasis of the program is on investigations of molecular systems with four to 10 atoms. Such systems are beginning to become amenable to detailed experimental and theoretical studies. The reactions of systems involving four to 10 atoms are significantly more challenging than the triatomic systems for which a large number of detailed and elegant studies have been reported in the past decade. However, the diversity of chemical behavior evinced in polyatomic systems will greatly enlarge our overall understanding of fundamental factors that influence chemical change.

Research in the THEORY OF CHEMICAL REACTIONS involves studies of both the energetics and kinetics/dynamics of chemical reactions. An important thrust is the calculation and use of realistic potential energy surfaces rather than the simplistic surfaces that have formed the basis for most earlier studies of chemical reactions. Our activity in COMPUTATIONAL CHEMISTRY provides the computational tools needed to model chemical reactions theoretically; special emphasis is placed on the development of codes for modern minisupercomputers and supercomputers with parallel architectures. The theoretical program is a unique combination of expertise in the calculation of the energetics of molecular processes, the calculation of the dynamics of chemical reactions, and the application of computers to large-scale chemical computations.

Two major experimental efforts are included in the program. The effort in the KINETICS OF CHEMICAL REACTIONS involves the use of shock tubes to measure reaction rates and branching ratios from below 1000 K to over 5000 K, including measurement of the elusive hydrogen atom produced in many important dissociative processes. The effort in the DYNAMICS OF CHEMICAL REACTIONS involves use of a crossed supersonic molecular beam machine to measure both angle- and state-resolved cross sections for polyatomic reactions. By using pulsed molecular beams, we are able to take full advantage of the sensitivity, resolution, and versatility of pulsed laser spectroscopic techniques.

A. Theory of Chemical Reactions

A. F. Wagner, M. J. Davis, L. B. Harding, R. J. Harrison, R. L. Shepard, S. K. Gray, G. C. Schatz, S.-W. Cho, F. LeQuere, M. H. Alexander, J. M. Bowman, J. Kiefer, E. Goldfield, J. Nicholas

A detailed description of the dynamics of chemical reactions requires the calculation of potential energy surfaces, which accurately represent the interactions between the species involved in the reaction, followed by solution of the equations describing the motion of the nuclei on these surfaces. During the past decade, great strides have been taken in the development of theoretical models and computational algorithms for describing the energetics and dynamics of chemical reactions. Accurate theoretical techniques can now be used to characterize the potential energy surfaces for three-, four- and five-body systems. Methods are available for locating transition states and for calculating the reaction paths for chemical reactions. For selected reactions complete potential energy surfaces can even be determined. Once the potential energy surface has been specified, the detailed dynamics of elementary chemical reactions can be calculated, providing information on cross sections, angular distributions, energy consumption and disposal, etc. If only portions of the potential surface have been characterized, it is still possible to calculate the thermal rate reliably by using statistical theories.

1. Theoretical Studies of the Energetics of Chemical Reactions *L. B. Harding, R. J. Harrison, R. L. Shepard*

To calculate the energetics of chemical reactions we must solve the electronic Schrödinger equation for all molecular conformations sampled by the reactive encounter. Substantial changes occur in the electronic structure of a molecular system as the reaction progresses from reactants through the transition state to products. To describe these changes, our approach includes the following three elements:

(i) the use of multiconfiguration self-consistent-field wave functions to provide a consistent zero-order description of the electronic structure of the reactants, transition state, and products;

(ii) the use of configuration interaction techniques to describe electron correlation effects needed to provide quantitative predictions of the reaction energetics; and

(iii) the use of large, optimized basis sets to provide the flexibility needed to describe the variations in the electronic distributions.

With this approach we are able to study reactions involving as many as five to six atoms with errors of just a few kcal/mol in the predicted reaction energetics. Predictions to chemical accuracy, that is, to 1 kcal/mol or less, are beginning to be feasible, although not routine, for small polyatomic species if advanced theoretical methodology and computer technology are employed.

Most of the multiconfiguration self-consistent-field (MCSCF) methods in use today were formulated in the 1970s. (The advances since that time that have been in the development of exceedingly fast algorithms to implement these methods.) We have found the Generalized Valence Bond (GVB; Goddard and co-workers), Fully Optimized Reaction Space (FORS; Ruedenberg and co-workers), and Complete Active Space Self-Consistent-Field (CASSCF; Siegbahn, Roos and co-workers) methods to be most useful. The GVB is the simplest MCSCF wave function that provides a consistent theoretical description of the association and dissociation of atoms and molecules. The FORS and CASSCF wave functions eliminate many of the deficiencies of the GVB wave function but are linear MCSCF expansions that grow rapidly in length as the number of correlated electrons increases.

Although multiconfiguration wave functions provide a qualitatively useful description of chemical reactions, to obtain quantitative results electron correlation effects neglected in these wave functions must be taken into account. These effects can be included in the calculations by using configuration interaction (CI) techniques. In the CI approach, we have found the GVB+1+2, FORS+1+2 and CASSCF+1+2 wave functions, which include all single and double excitations relative to the above multireference wave functions (MRSDCI), provide useful predictions of the energetics of a broad range of chemical reactions. This approach has been developed by us and others in a robust, portable set of computer codes called COLUMBUS Program System.

We have also developed advanced approaches that go beyond MRSDCI. The first is a full-CI technique that efficiently includes all configurations for small basis sets. The second is a selected CI combined with a perturbation treatment (CI+PT) of unselected configurations. Both of these methods are now being applied in our applications research.

The number of configurations that must be included in the CI and CC calculations increases rapidly with the size of the basis set. One goal is to minimize the number of basis functions required to achieve a given level of accuracy. This problem has been addressed by Ahlrichs and co-workers (1985), Almlöf and Taylor (1987), and, more recently, Dunning (1989). All of these methods use compact contracted basis sets of primitive Gaussian functions optimized by correlated atomic calculations. Such basis sets are called correlation consistent because their construction is such that an increase in the basis-set size systematically decreases the correlation error.

Application of the electronic structure techniques described above to a particular molecular system produces the energies and other properties of the system at the selected molecular geometries. This is not the same as a potential energy surface (PES), which is a continuous global function of the internal coordinates. In other words, the electronic structure calculations do not yield a continuous representation of the potential energy surface but rather a pointwise representation of the surface. For describing restricted regions of the potential energy surface, for example, the regions around the minima or saddle points, the calculated energies can be adequately represented by a local expansion of the energy in either a Dunham (1934) or Simons-Parr-Finlan (1973) series. With such information, it is in fact possible to estimate the rates of reactions by using transition-state theory methods. However, for more detailed dynamical studies, such as classical trajectory or quantum dynamics calculations, a global representation of the discretized potential energy surface must be determined. The fitting of a PES, which requires a large number of electronic structure calculations, has proven to be a challenging problem.

An alternative approach to determining a global representation of the PES involves the calculation of reaction paths and valleys for chemical reactions. The concept of a reaction path, which describes the continuous transformation of reactants to products, is firmly embedded in the lore of chemistry. The reaction path has been rigorously defined by Fukui (1970) as the path of steepest descent from the saddle point to reactants in one direction and to products in the other direction. Miller, Handy, and Adams (1980) have put forward a theory of reaction dynamics that involves a description of the system in terms of motion along the reaction path coupled with harmonic motion in the degrees of freedom perpendicular to the path, a reaction valley approach. Detailed information on the mechanism, energetics, and dynamics of a chemical reaction can be obtained by fully characterizing the reaction valley.

In the molecular systems discussed below, several of the electronic structure techniques described above have been applied to produce representations of either critical regions, reactions paths, or the entire global potential energy surface. Several of these representations, or those developed in past years, are used in the following parts of this section to calculate the corresponding reaction dynamics.

a. Ground Potential Energy Surface for CH_2 *L. B. Harding*

Atomic carbon, CH, and CH_2 are all important reactive species in hydrocarbon flames. It has been postulated that reaction (1),

$$CH(^2\Pi) + H(^2S) \rightarrow [CH_2] \rightarrow C(^3P) + H_2 , \quad (1)$$

is an important source of atomic carbon in fuel-rich hydrocarbon flames.

To aid in the detailed modeling of the dynamics of this reaction, we have constructed a global, ground state PES for methylene based on accurate ab initio calculations. The calculations consist of a CASSCF+1+2 wavefunction with a polarized valence triple zeta, (4s,3p,2d,1f/3s,2p,1d), basis set. The calculations predict that decomposition of $CH_2(^3B_1)$ to form $C(^3P) + H_2$ is 78.3 kcal/mole endothermic whereas decomposition to form $CH(^2\Pi) + H(^2S)$ is 105.2 kcal/mole endothermic. These results are in good agreement with experimental estimates of 80.3 ± 0.5 and 105.9 ± 0.8 kcal/mole, respectively.

These calculations have been carried out at over 6000 geometries in order to accurately characterize all energetically accessible regions of this PES. The points were then fit to a modified, many-body expansion designed to accurately describe the cusps in the ground state PES resulting from intersections between low-lying electronic states.

The calculations show a very broad, attractive entrance channel for the addition of CH to H with the only orientations leading to repulsive interactions being those very close to linear. Even the colinear orientations are not predicted to be very repulsive. The barrier to linear addition, which occurs at a $^3\Sigma^-$-$^3\Pi$ surface crossing, is predicted to be 2.1 kcal/mole and

the barrier to direct linear abstraction is predicted to be 2.7 kcal/mole. The dissociation of CH_2 forming C + H_2 is predicted to occur with no barrier in the reverse direction via a pathway that involves crossing from the $^3B_1$ PES onto the $^3A_2$ PES as the R(C-H_2) increases. This crossing leads to a cusp in the ground state PES that appears to form the dynamical bottleneck controlling the dissociation. The $^3A_2$ PES is predicted to have a shallow (4.7 kcal/mole) minimum at long range resulting from a dative bonding interaction between an empty carbon p orbital and the H_2. A plot of the C_{2v} portion of this PES is shown in Figure V-1. In this plot the cusp dividing the $^3B_1$ and $^3A_2$ regions of the PES can be seen between R(C-H_2) = 1.5 and 2.5 au. Trajectory studies of reaction 1 in both the forward and reverse directions are now in progress in collaboration with Schatz.

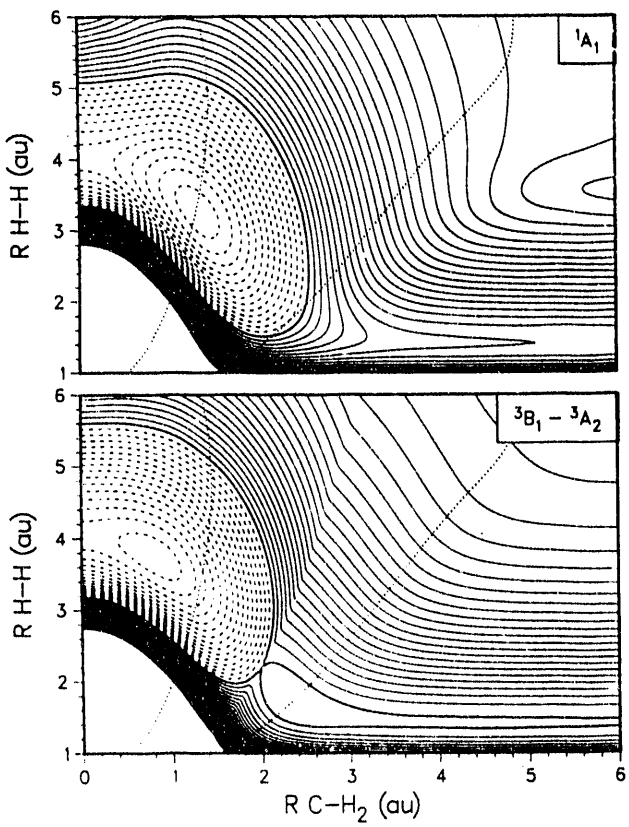

Figure V-1: The ground state, singlet and triplet, C + H_2, interaction potentials. The orientation is fixed at C_{2v}. The contour increment is 5 kcal/mole. Solid lines denote energies higher than that of the C(^{3}P) + H_2 asymptote, dashed lines denote lower energies. The dotted lines show the locations of the intersections between the two surfaces.

b. Excited Singlet Potential Energy Surfaces for CH_2 *L. B. Harding*

The C_{2v} portions of the three lowest singlet surfaces correlating with C(^{1}D) + H_2 have also been examined using the same theoretical methods as for the triplet surface. The calculations show no barrier to insertion on the $^1A_1$ PES. In fact this PES is sufficiently attractive that it crosses the triplet PES close to the long-range, $^3A_2$, minimum (see Figure V-1). The energy at the lowest crossing point is ≅5 kcal/mole below that of C(^{3}P) + H_2. The $^1B_1$ and $^1A_2$ surfaces are similar to the corresponding triplet surfaces except that the $^1A_2$ surface is significantly more attractive than the $^3A_2$ surface. The net effect is that the lowest energy crossing between the $^1B_1$ and $^1A_2$ surfaces occurs at an energy well below the C(^{1}D) + H_2 asymptote, whereas the lowest crossing between the $^3B_1$ and $^3A_2$ surfaces was found to be nearly degenerate with the C(^{3}P) + H_2 asymptote. These results support the conclusion of Riesler et al. who have reported evidence that the C(^{1}D) + H_2 → CH + H reaction proceeds on more than one electronic surface.

c. R-Cl Potential Curves *L. B. Harding*

The first step in the pyrolysis of chlorocarbons is C-Cl bond cleavage. One factor that affects the rate of bond cleavage is the long-range C-Cl interaction potential. We have now characterized C-Cl interaction potentials for the series, C-Cl, HC-Cl, H_2C-Cl, and H_3C-Cl. The calculations were carried out with both polarized double zeta and polarized triple zeta basis sets. The only C-Cl bond energy in this series known accurately from experiment is the last one, H_3C-Cl. Here, the double zeta, triple zeta, and experimental D_0's are 73.4, 78.6, and 82.0 ± 0.2 kcal/mole, respectively. The calculations predict the C-Cl bond energies of the radical species are all significantly stronger than that of H_3CCl, with the diatomic molecule CCl having the strongest bond, 94.0 kcal/mole. The trend here is the opposite to that found for CH bonds where the diatomic molecule has the weakest bond energy. The R-Cl long-range interaction potentials are now being used to estimate the high-pressure-limiting rate constant for R+Cl addition.

2. Theoretical Studies of the Dynamics of Chemical Reactions

A. F. Wagner, M. J. Davis, S. K. Gray, G. C. Schatz, S.-W. Cho, F. LeQuere, M. H. Alexander, J. M. Bowman, E. Goldfield, J. Nicholas

The most commonly used theories for the dynamics of chemical reactions are transition state theory (TST) for direct reactions, statistical theories (ST) for loose, complex-forming or dissociative reactions, and Rice-Ramsberger-Kassel-Marcus theory (RRKM) for tight, complex-forming or dissociative reactions. As conventionally applied, these theories require only minimal information about the potential energy surface, namely, the structures, vibrational frequencies, and energies of the reactants and transition states. Powerful extensions of TST developed in recent years incorporate potential energy surface information either along the minimum energy path (variational TST [Truhlar and Garrett, 1979]) or within a reduced set of dimensions (reduced dimensionality TST [Bowman and co-workers, 1981]; reaction path and reaction surface Hamiltonian methods [Miller and co-workers, 1980s]). These extensions incorporate dynamics calculations on the included portions of the surface to arrive at generally more accurate descriptions of direct reactions. Variational extensions for RRKM theories are also available and are more accurate. Similar reduced dimensionality and reaction path variants of RRKM theory are possible.

Both conventional and variational forms of these theories invoke two approximations. First, once the reactants have reached the transition state, the reaction proceeds with unit probability, that is, there is no recrossing of the transition state back to reactants. Second, all of phase space that is accessible to the reactants during the course of the collision up to the transition state is uniformly occupied. This implies that the true transition state occurs at vibrationally adiabatic barriers on the potential energy surface. It also implies for ST and RRKM theories that metastable dissociating molecules randomly explore all of phase space until they find that small portion of it that is at the transition state. Reduced dimensionality or reaction path variants of these theories allow for either exact dynamics for a restricted number of degrees of freedom or dynamics on approximate potentials for all degrees of freedom.

To go beyond these approximations, the entire potential energy surface must be explored by either quasiclassical trajectories (QCT) or exact quantum (EQ) methods. Although, in principle, EQ methods provide the exact results, including tunneling effects, in practice these methods have been in the past computationally feasible only for systems with very few degrees of freedom (≤3). In addition to expense, many EQ methods have limited regions of numerical stability. However, recent work in both close-coupled hyperspherical (CCH) methods and L^2 variational methods have largely overcome these problems for systems with a few degrees of freedom. Nonreactive EQ approaches have been developed for problems involving multiple surfaces, for example, fine-structure and lambda-doublet transitions in the collisions of radicals. Although not yet extended to reactions, such extensions are feasible.

QCT remains the most frequently used method for detailed studies of reaction dynamics. However, for complex-forming reactions, the long-lived nature of the complex makes the trajectories both time consuming and inaccurate. Furthermore, because trajectories are deterministic, the statistical approximations of uniform occupation of phase space mentioned above are not directly examined by each trajectory. Nonetheless, with appropriate formulation, trajectories can be used to probe statistical behavior in detail. In particular, they can locate bottlenecks to the flow of flux in phase space. If statistical theories apply, passage through these bottlenecks gives the rate for both intramolecular energy transfer and intermolecular particle transfer (i.e., dissociation and reaction). A modification to RRKM theory (Gray and Davis, 1986) exploits such trajectory calculations.

In the reactions discussed below, the variety of dynamics methods just mentioned are applied according to the specifics of each reaction. Most of the potential energy surfaces used in these applications are provided by accurate calculations such as those discussed in the previous section.

a. Theoretical Dynamics in the Formation and Dissociation of the Formyl Radical

S. K. Gray, A. F. Wagner, S-W. Cho, J. M. Bowman, E. Goldfield

Theoretical studies begun here several years ago on the ground state dynamics and kinetics of

$$H + CO \underset{}{\overset{M}{\rightleftharpoons}} HCO^* \rightleftharpoons HCO\,, \qquad (2)$$

where M is a buffer gas, have continued and been expanded to include photodissociation on the first excited surface.

In studies on the ground state PES in collaboration with Bowman (Emory University), a nearly complete survey of the 27 lowest isolated resonances for total angular momentum J=1 has been completed using the LBH potential energy surface calculated in our group several years ago. These 27 resonances are composed of nine families of three resonances that emerge out of the nine lowest resonances for J=0. Like the case for J=0, the J=1 resonances have been characterized by the stabilization calculations and time-independent scattering calculations described in previous years. Significant basis set problems were encountered when either method was extended to J=1. These problems were resolved with the realization that J=1 cases display greater sensitivity to CO vibrations that require an expansion of this part of the basis set. Results indicate that HCO resonances have a largely symmetric top pattern with modest, but measureable, distortions in the pattern occurring for resonances with large amounts of HCO bend. All the resonances were found to have lifetimes lower than, but within a factor of two of, the lifetimes for the corresponding J=0 resonances. For each family of three resonances, there is a pair of very closely separated resonances that can be assigned by $K = \pm 1$, where K is the projection of J on the symmetric top axis. Despite their similar widths and locations, the product distributions of these pairs of resonances are found to be clearly distinct.

Work begun last year on the time-dependent wave packet dynamics of the decay of resonances on the ground PES of HCO was completed. This project led to both the development of novel theoretical methods that should be applicable to a wide variety of problems, and to mechanistic insights into the specific problem of the decay (to H + CO) of resonances in the HCO radical. In terms of methodology, a novel and efficient wave packet propagation scheme of general utility was developed. Also, the Prony method of spectral analysis was shown to be a particularly useful approach for inferring resonance energies and decay widths out of wave packet propagations. In particular, with appropriate initial condition selection, it was shown that wave packet propagations as short as 2 ps could yield resonance decay widths consistent with lifetimes as long as 1000 ps. In terms of the specific decay mechanism for HCO radicals, it was shown that the wave packet density associated with product formation crosses the transition state region in a localized but asymmetric manner (due to potential anisotropy). It is this localization of the density that leads to very distinct patterns in the rotational product distributions.

Studies were begun last year to understand the lifetimes and product distributions that result when HCO is excited to its first excited PES, as in recent experiments out of Houston's group at Cornell. The excited PES has a linear equilibrium geometry, and is exactly degenerate with the ground PES at linear geometries. The H + CO products correlate with the ground electronic state and result via predissociation in the excited state via the Renner-Teller effect. The Renner-Teller effect is a breakdown in the Born-Oppenheimer approximation that results from the interaction of electronic orbital angular momentum and the bending vibration. We have developed a time-dependent theoretical formalism capable of describing this process accurately. The wave packet propagation technique developed for the study of the ground electronic state resonances in HCO, and the Prony method of spectral analysis, were also employed in these calculations. An ab initio based excited state potential surface was developed to complement the ground electronic state surface that was already available. Extensive wave packet propagations have been performed, corresponding to a variety of vibrational excitations in the excited state (and several values of total angular momentum and its projection on the linear HCO axis). Our calculated lifetimes are in very good accord with experiment, but the calculated CO rotational product distributions tend to be somewhat narrower than the available experimental results. This may point to the necessity of refinements in the potential surfaces for HCO, particularly at and near the collinear geometries. We have also predicted that certain excitations in HCO should lead to distinct bimodal product distributions.

b. Thermal Dissociation of HCN

A. F. Wagner, J. H. Kiefer

A standard derivation of the bond energy from the measured thermal dissociation rate constant of HCN,

$$HCN \xrightarrow{M} H + CN, \qquad (3)$$

is more than 5 kcal/mole lower than the known thermodynamic value. The standard derivation ignores the hindered rotation of H about CN from the usual H-

CN isomer to the less stable CN-H isomer. The barrier for this isomerization is quite high (>40 kcal/mole). However, in collaboration with Kiefer (UIC), we performed an approximate rigid bender calculation of the complete spectrum of hindered rotor states and showed that the density of these states dramatically increased the A factor, allowing the derivation of the correct bond energy. The importance of the hindered rotation is enhanced by the fact that: (1) the vibrationally adiabatic barrier to hindered rotation decreases as the internal vibrational energy in the CN and H-CN bonds increases, and (2) the moment of inertia for the hindered rotation increases with the same increase in internal vibrational energy. This dynamics is a simpler version of what is inferred in the dissociation of acetylene and other small unsaturated molecules.

c. Inelastic Scattering on Multiple Surfaces: CH + He *A. F. Wagner, M. H. Alexander*

The inelastic process

$$CH(^2\Pi,v,N,F_i,\lambda)+He \rightarrow CH(^2\Pi,v',N',F_i',\lambda')+He \quad (4)$$

requires both the A' and A" PESs in the exact close-coupled quantum dynamics calculations of its inelastic cross sections. As described in previous years, such calculations carried out on a variety of computed PESs revealed systematic, quantitative theoretical overestimates of the dynamic threshold for excitation into the higher N states as compared to experiments done in this group several years ago. This year, in collaboration with M. Alexander (University of Maryland), final tests of changes in the van der Waals regions of the PESs were carried out. This part of the PESs is known to be too shallow because the basis sets used in the calculation of the surfaces did not include the diffuse functions necessary for an accurate description. However, the well depth is computed to be very small (on the average surface [the sum of the A' and A' PESs] it varies from 0.015 to 0.045 kcal/mole depending on the He angle of approach). Full quantum dynamics calculations on modified surfaces with completely absent van der Waals minima were carried out and do not improve the agreement between theory and experiment. Further model quantum dynamics calculations were carried out that treat the CH+He as a closed-shell system but allow a survey of alterations to the van der Waals region of the average PES. These studies indicate that the van der Waals minima increase the inelastic cross sections only over an energy range approximately three times the well depth above threshold. This would imply that even doubling the computed van der Waals well depth (probably the limiting size of the error, given what is know experimentally about analogous systems) would only marginally improve the agreement between theory and experiment. The conclusion from all the calculations on CH+He is that systematic disagreements still exist between theory and experiment with angular and radial variations in the spin-orbit coupling elements being the most likely cause of any deficiency from the side of theory.

d. Inelastic Scattering on Multiple Surfaces: NCO + He *A. F. Wagner*

The inelastic process

$$NCO(^2\Pi,N,F_i,\lambda)+He \rightarrow NCO(^2\Pi,N',F_i',\lambda')+He \quad (5)$$

has recently been measured by Liu and Macdonald (see later sections of this survey). Though superficially similar to CH+He, NCO is a Hund's case a molecule while CH is Hund's case b. In Hund's case a, it is known that spin-orbit changing collisions can only come about through the difference PES formed by subtracting the A' and A" PESs that are sampled by the collision). In the case of NCO, this PES should be of much smaller range than that for the average PES. A simplifying hypothesis to describe the overall rotational scattering would be that the average PES controls the overall rotational distribution whereas the difference PES controls the branching of the distribution into different spin-orbit manifolds. The first part of this model was tested by: (1) constructing a simple parameterized average PES from the known surface for $He+CO_2$, (2) calculating the rotationally inelastic cross section within the Infinite Order Sudden Approximation to closed shell quantum dynamics on the average PES, and (3) comparing the results to the experimental rotational distribution (with the distributions from different spin-orbit manifolds combined). Excellent agreement between theory and experiment at five different collision energies was obtained with modest modifications in the initial $He+CO_2$ PES. The most important modification was to off-set the center of mass of the molecule from the center of symmetry by the experimental amount found in NCO.

e. OH + CO Inelastic Dynamics *G. C. Schatz*

The rotational inelastic process

$$OH + CO \rightarrow HO(j') + CO \qquad (6)$$

has been studied by classical trajectories using newly developed A' and A" PESs (discussed last year) that are based on extensive ab initio calculations that cover geometries that are important to rotational excitation. The results are in good agreement with beam experiments of Sonnenfroh, Liu, and MacDonald in our group. They show that chemical interactions are important in nonreactive rotational excitation only when the final OH is highly rotationally excited and the collision energy is relatively low. This confirms an experimental conjecture based on the fact that OH+CO and OH+N_2 (where no reaction is possible) have very similar inelastic cross sections.

f. Cl + HCl Reaction Dynamics *G.C. Schatz*

Using the enhanced version of the CCH code that includes two or more coupled electronic potential energy surfaces, we have studied

$$Cl' + HCl \rightarrow Cl+HCl' \qquad (7)$$

including for all three PESs that correlate with the ground states of the reagents and products. With these results we have rigorously determined how electronic fine structure influences the reactive rate constants. All previous work has treated electronic fine structure through a statistical factor that is based on transition state theory. The validity of this approximation has never been rigorously tested, but it is possible that errors associated with it could account for significant errors in theoretical predictions of thermal rate constants. Our results indicate that the validity of this approximation varies with the size of the spin-orbit splitting, with errors of 50% possible for Cl atoms. A more signficant influence of spin-orbit splitting is found in the rate constant for reaction from specific fine-structure states. Here the rate constant can vary by orders of magnitude even for relatively small splittings (<100 cm^{-1}).

g. Reaction Kinetics for CH + H and C + H_2 *G. C. Schatz*

The PES for the triplet CH_2 radical discussed earlier has been used to calculate thermal rate constants for the reaction 1 in both directions. This reaction is important in soot production in the pyrolysis of hydrocarbons. Experimental studies of CH+H are in conflict with one measurement indicating no temperature dependence above 1500 K, and another indicating substantial temperature dependence at lower temperatures down to 300 K. Our results indicate no significant temperature dependence over the entire range 300-2000 K, and the magnitudes of the rate constants are in good agreement with two previous high-temperature measurements. Our results for C + $H_2 \rightarrow CH_2$ are also in good agreement with experiment.

h. Quantum Dynamics of $ArI_2 \rightarrow Ar + I_2$ *S. K. Gray*

The ArI_2 system is computationally challenging from a quantum dynamical viewpoint because of the many I_2 vibration-rotation states that must be included and the heavy Ar mass. Also, despite being a van der Waals complex, its dynamics is particularly complex owing to the presence of complicated resonances. Nonetheless, with the aid of techniques developed for our HCO resonance decay work, we were able to carry out a numerically accurate quantum dynamics study of the vibrational predissociation

$$ArI_2(v') \rightarrow Ar + I_2(v \leq v' - 3) \qquad (8)$$

in three dimensions. These results therefore represent excellent benchmarks for testing out and developing more approximate theories of resonance and unimolecular decay. Recent real-time experiments out of Zewail's group on this reaction provide additional motivation for this work and, indeed, our results were found to be consistent with these experiments. In addition, we found that closely spaced resonances, for example, resonance states just 1 cm^{-1} apart in energy, are important in determining the overall dynamics in this system, as shown in Figure V-2. These resonances lead to a two- or three-level IVR (intramolecular vibrational relaxation) phenomenon, similar in spirit to that recently seen in calculations by Halberstadt and co-workers on $ArCl_2$. Experimental implications of such resonances include the potential of observing quantum beats in real-time experiments and complicated, structured product distributions in energy-resolved experiments.

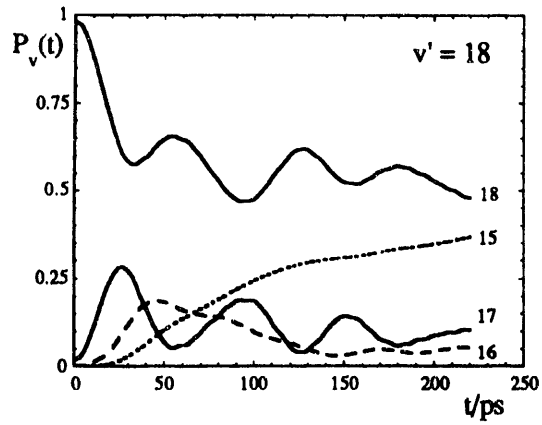

Figure V-2. The probability of being in various internal I_2 vibrational states as a function of time for a wave packet prepared at t = 0 to be consistent with a v' = 18 excitation in $ArI_2(v')$. Energy conservation requirements imply that Ar + $I_2(v)$ products form predominantly for $v \leq v'-3 = 15$ in this case (final rotational states are averaged over). Although one sees monotonic growth in the v = 15 product channel, a quantum beating phenomenon is evident in the v = 18 and 17 channels, and this is consistent with the presence of at least two closely spaced resonances.

i. Wave Packet Dynamics of Four-Atom Systems *S. K. Gray, F. Le Quéré*

The dynamics of four-atom systems can be considerably more complicated and computationally challenging than triatomic dynamics, particularly when one wishes to describe the dynamics at the highest level of theory (numerically accurate quantum dynamics). We have completed an initial project on the dynamics of the fragmentation of van der Waals clusters of the form X_2BC, where X = Ne or He, and BC = a diatomic halogen molecule. The process of interest is $X_2BC \rightarrow 2X + BC$ via vibrational predissociation. Although it was necessary to freeze some degrees of freedom, our model included features, such as multiple continua, that can make four-atom dynamics particularly difficult. We developed a formalism for estimating product distributions from our finite time and finite grid-size wave packet propagations. Our estimated lifetimes and BC product distributions were in reasonable accord with experimental results from Janda's group on Ne_2Cl_2 and He_2Cl_2. The relative importance of "sequential" $X_2BC \rightarrow X + XBC \rightarrow 2X + BC$ vs. direct $X_2BC \rightarrow 2X + BC$ decay mechanisms was explicitly addressed by detailed inspection of the wave packet as a function of time. In several cases we found that the nonlocal nature of quantum mechanics prevents a clear assignment of the mechanism. We also found one instance of closely spaced resonances (as in the ArI_2 study) complicating the theoretical dynamics. Interestingly, recent real-time experiments from Zewail's group on X_2BC systems also point to the role of such resonances.

The methodology developed for these van der Waals clusters directly applies to chemically activated adducts formed in addition reactions. In the same way that HCO studies (see section a.) provided a methodology for studying triatomic van der Waals molecules (see section h.), so we are currently applying the four-atom methodology most easily developed here to chemically activated HOCO and HOOH.

j. Hierarchical Analysis of Molecular Spectra *M. J. Davis*

Over the last decade, it has become possible to experimentally generate highly excited vibration-rotation spectra of high resolution. The purpose of the project has been to develop methodology to characterize, visualize, and understand the complexity of such molecular spectra. The hierarchical analysis gives information concerning energy transfer in the particular molecule studied, through, for example, statistics that estimate the number of time scales inherent in a molecule in the range of energy sampled by a particular spectrum. When a theoretical model of a spectrum is available, one can also generate information concerning energy-transfer pathways and unambiguous assignments of smooth spectral features, if these exist. An interesting aspect of this type of analysis is that the assignments may be quite different than standard spectroscopic assignments (see below).

Figure V-3 summarizes some of the spectra we have analyzed to establish the utility of the hierarchical analysis. The top row shows hierarchical trees generated for three experimental spectra and the bottom row three theoretical spectra. The C_2H_2 spectrum is a SEP (stimulated emission pumping) spectrum, the first NO_2 spectrum is an electronic excitation spectrum, and the second NO_2 spectrum is a microwave-optical double resonance spectrum. The first NO_2 spectrum is vibronic, being generated from the vibronic band origins, and the second is rovibronic but a pure sequence (single J). The first theoretical spectrum is a photodetachment spectrum (lower left), the second theoretical spectrum is a vibrational spectrum for a model potential that exhibits classical chaos,

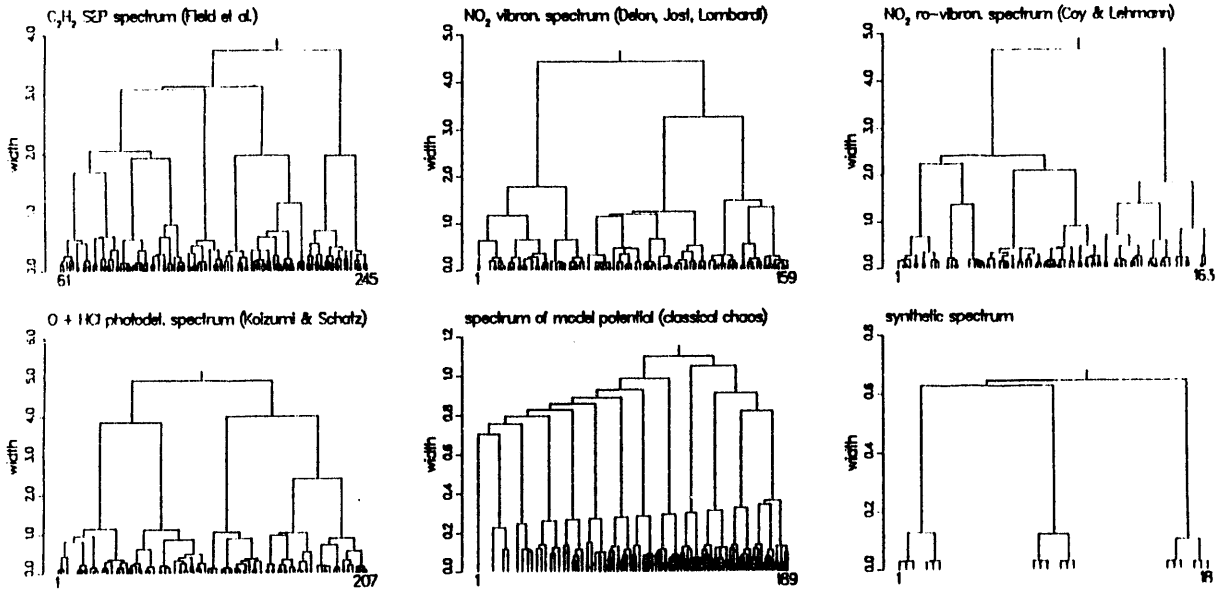

Figure V-3. Trees for several systems for which hierarchical analysis has been undertaken.

and the final theoretical spectrum is synthetic and is meant to test the various measures we have used to analyze the trees.

The type of information contained in the hierarchical analysis is summarized in Figure V-4. The left hand column shows either smooth features of a model spectrum (first three rows) or portions of the model spectrum (bottom two rows). This spectrum was used to generate the tree on the middle bottom of Figure V-3. The middle column shows portions of the same tree (i.e., subtrees), and the third column shows states associated with the smooth features. The final two states are eigenstates of the system, and it can be observed that these are complicated. However, the smooth states in the top three rows of the third column are easy to assign, because the nodes can be counted. The top and middle states have nine nodes along the y-direction and no nodes in the x-direction, whereas the second state has eight nodes in the y-direction and one along the x-direction. The appearance of energy transfer can be observed in the states of column three by comparing the middle and bottom states. Although the bottom state has a preponderance of density along the y-direction as does the middle state, there is now clearly density in the x-direction and this extra density represents energy transfer.

One can discern energy-transfer pathways by following specific paths down the same tree as was used to generate Figure V-4. This is done in Figure V-5 These are plots of quantum phase space and the

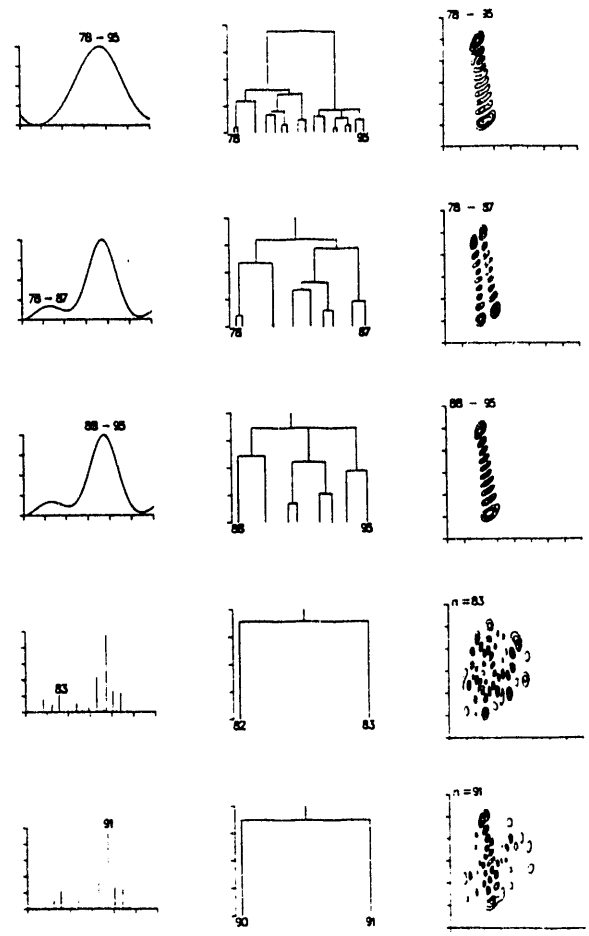

Figure V-4. An overview of the nature of the trees and smoothed eigenstates generated from a hierarchical analysis. See text for further details.

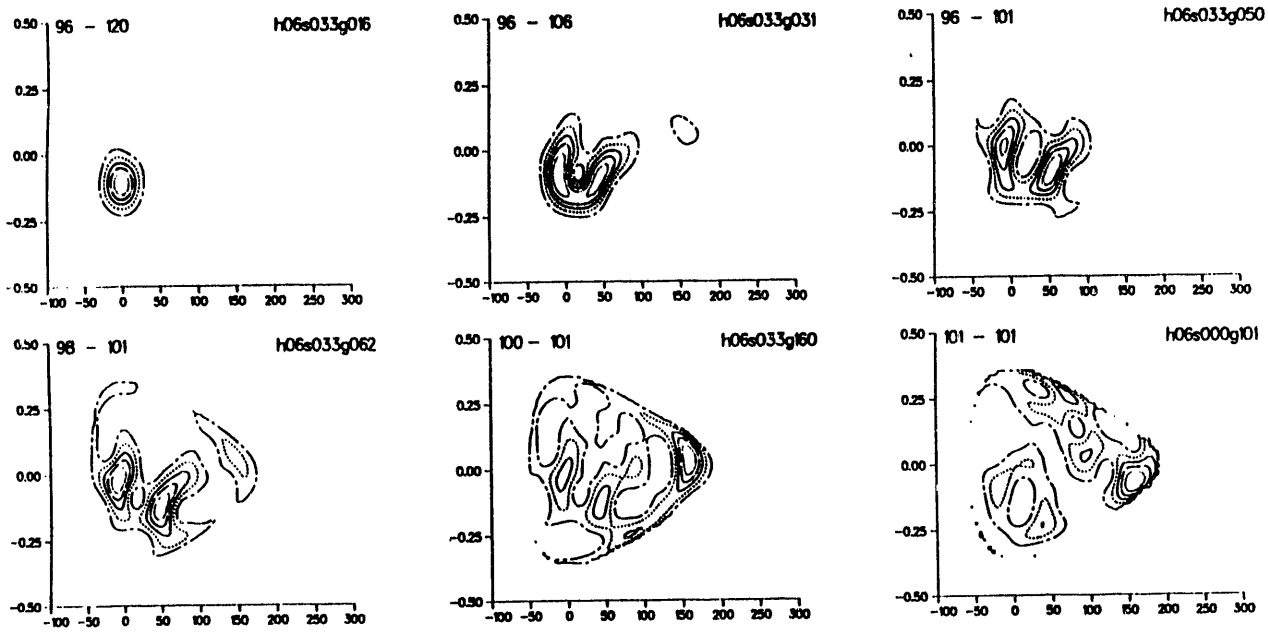

Figure V-5. These plots demonstrate that the hierarchical analysis can discern energy-transfer pathways. In the plot on the upper left, density starts in a localized region and spreads. The plots are generated by following a path down a tree and should be read from left to right, with the top being read first.

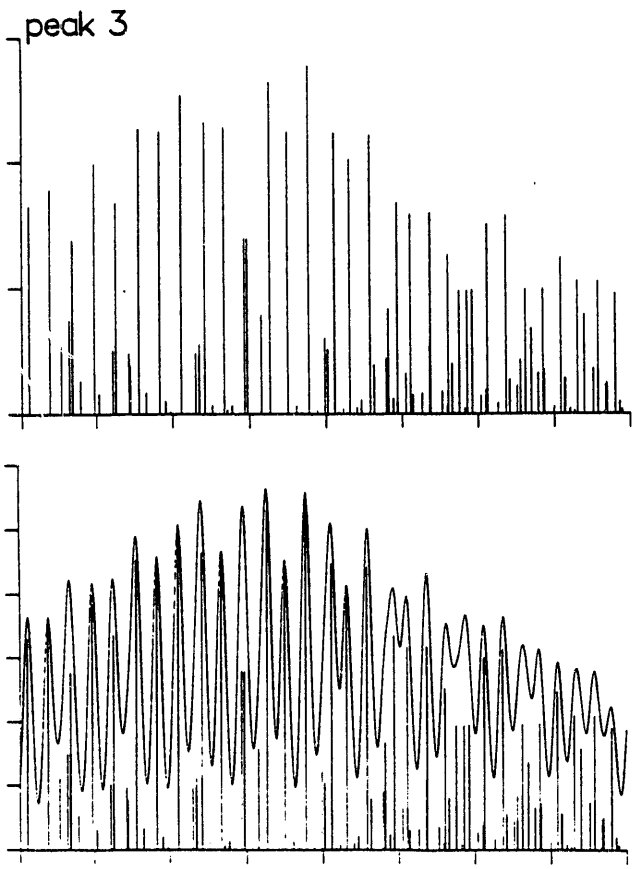

Figure V-6. An example of a spectrum (top) that does not give a simple smooth spectrum (bottom).

contours are ordered from low to high as: chain-dashed, dashed, solid, chain-dot, and dotted. The path down the tree is followed from left to right on the top and continued from left to right on the bottom. One can observe that the peak of the density that is centered in the first picture spreads out in the next two along the top, forming two peaks in the process, and eventually spreads further in the bottom three pictures, with this being most evident in the last two pictures.

As noted above, the assignment of smooth spectral features is an important aspect of the hierarchical analysis. The previous case, Figure V-4, was straightforward, but Figures V-6 and V-7 show a case which is much more difficult. The spectrum at the top of Figure V-6 shows a spectrum generated for the same system as Figures V-4 and V-5, but with a different initial excitation. The spectrum has many lines of nearly equal intensity, and a smoothed version of the spectrum in the lower plot of Figure V-6 shows no apparent pattern. However, if one plots the states associated with the smooth features, a pattern emerges in Figure V-7, though a single state in the figure does not appear to be simple. It should be noted that these states are assignable, but lie on curvilinear coordinates that cross themselves.

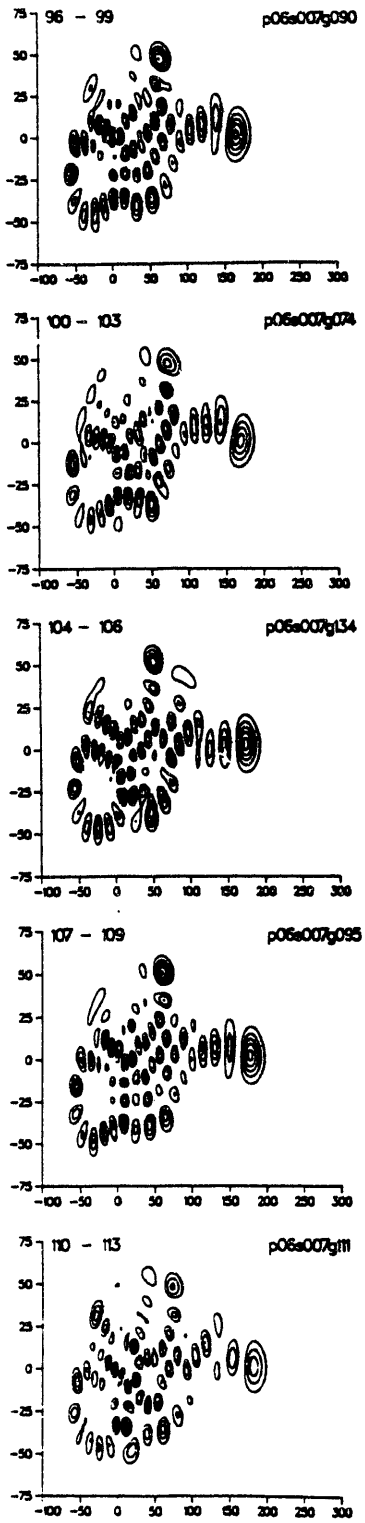

Figure V-7. Although the smoothed spectrum at the bottom of Figure V-6 is complicated, the states associated with the smooth structure display a pattern. The smooth states presented here, although complicated, can be assigned quantum numbers based on a curvilinear coordinate that crosses itself.

Figures V-8-V-11 show results for one of the NO_2 cases plotted in Figure V-3, the vibronic spectrum. Figure V-8a shows the full tree and Figures V-8b-V-8f show subtrees cut from the full tree. One can observe in the plots that there are several distinct time scales present in this system as evidenced by the range of heights of the nodes of the trees. Figure V-9 quantifies this by plotting a statistic that measures the range of time scales. Two important aspects of the plots in this figure are the overall range of the x-axis of each plot and the shape of each curve, particularly any sudden drops. The ranges of the curves indicate that there is probably not complete energy transfer for NO_2 and the sudden drops signal the presence of distinct bottlenecks to energy transfer. We can quantify the lack of complete energy transfer by comparing statistics for the NO_2 tree with those of the tree for the model system previously presented. This is done in Figure V-10. In both cases, the statistics demonstrate that the NO_2 spectrum (the solid line) shows more localization than the model system (dashed line) as evidenced by a lower value in V-10a and a higher value in V-10b. The hierarchical analysis also points to important aspects of smooth features of the NO_2 spectrum, and this is presented in Figure V-11. The top plot shows a three-peak case that can be assigned to motion on an electronically excited state of NO_2 and points to a bend/stretch excitation, whereas the bottom plot shows a very distinct feature (as judged by the hierarchical analysis), but this latter plot almost certainly corresponds to a time scale where there is coupling between two electronic surfaces. What energy-transfer property causes such a distinct structure represents an interesting, but unresolved aspect of our analysis.

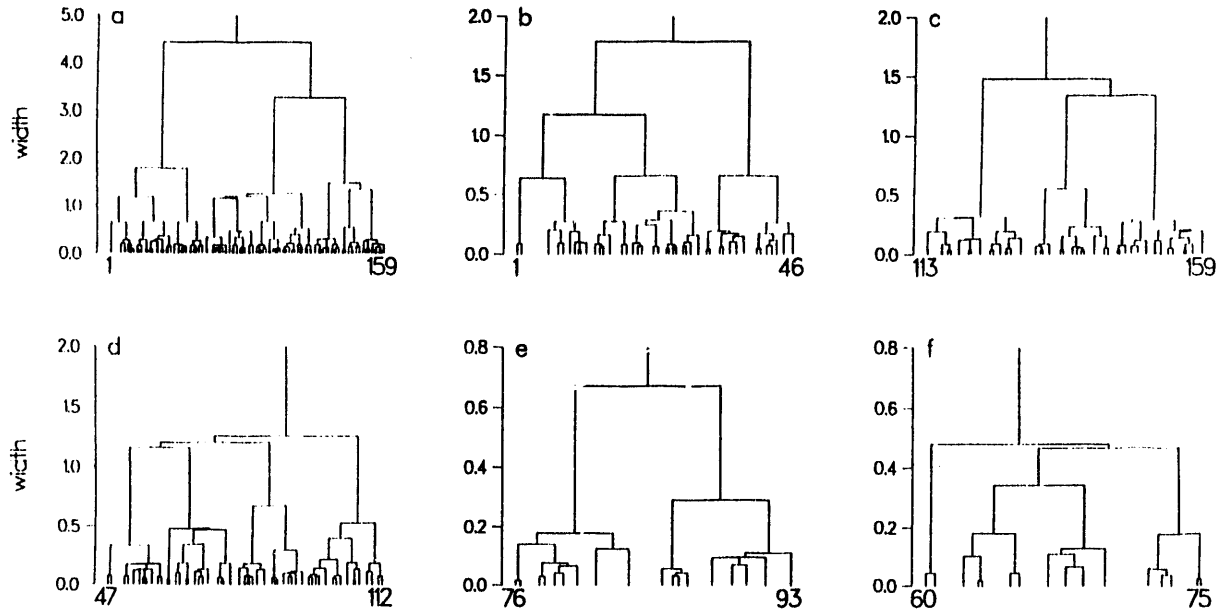

Figure V-8. A full tree (a) and some subtrees (b-f) for an NO_2 excitation spectrum.

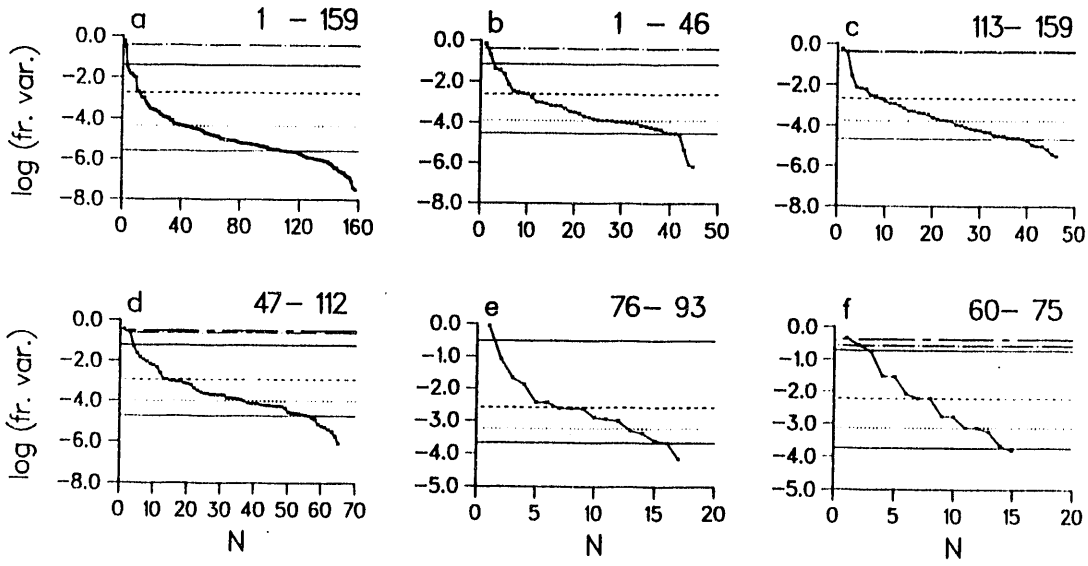

Figure V-9. Statistics for the tree and subtrees of Figure V-8.

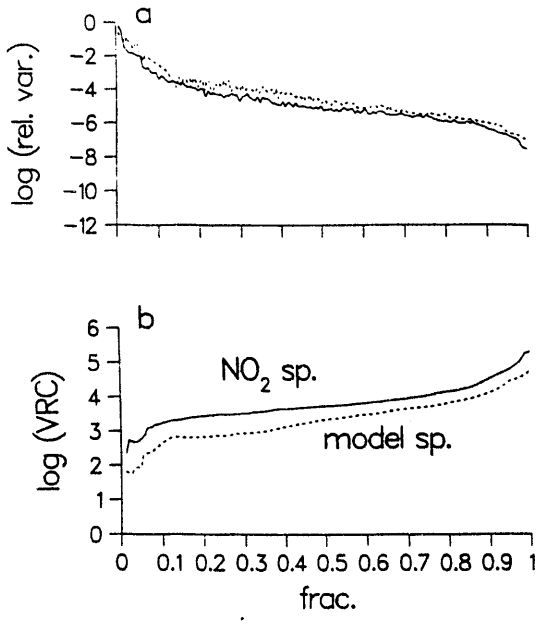

Figure V-10. These plots compare statistics for the NO_2 spectrum with that of a model system and demonstrate, for example, that the NO_2 spectrum possesses more clustering than the model system.

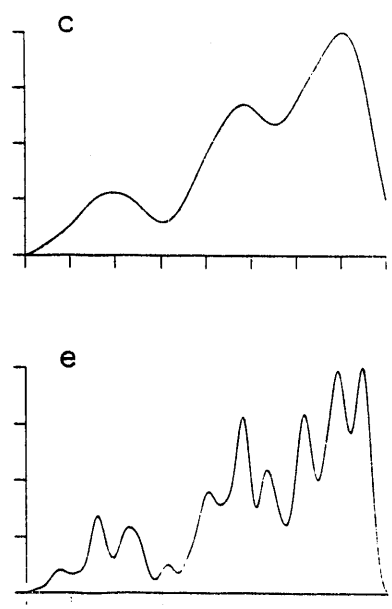

Figure V-11. The hierarchical analysis points to some strong features in the smoothed spectra of NO_2. These plots show two cases that are described more fully in the text.

B. Computational Chemistry: Energetics and Dynamics of Chemical Reactions

R. L. Shepard, R. J. Harrison, R. Ahlrichs, M. F. Guest, H. Lischka, R. M. Pitzer, I. Shavitt, P. Szalay, E. Stahlberg, T. Kovar, M. Ernzerhof

The work described in this section provides the computational tools needed to address the applications-oriented work described in the preceding section. The work outlined there often strains the capabilities of modern computers for calculating the energetics and dynamics of chemical reactions. Considerable effort must be devoted to the development and upgrading of techniques and codes for chemical computations, to the optimization of these codes on modern vector-oriented computers, and to the development of efficient and effective interfaces to the large code systems, such as the COLUMBUS package in use in this effort.

The group also attempts to take advantage of advances in computer technology, especially parallel computing architecture, to address important computational problems; a considerable amount of work is, however, often required to adapt this technology to the problems of interest. In particular, the development of efficient, portable implementations of our ab initio electronic structure programs for parallel computers requires a substantial effort in the formulation of effective parallel algorithms.

There are four major sets of electronic structure codes used by the group: the MRSDCI program system called COLUMBUS, a full-CI code, a selected CI plus perturbation theory (CI+PT) program, and a coupled-cluster (CC) program. Improvements in two programs have occurred in the last year. In addition, exploration of other methods were carried out.

1. COLUMBUS Program System

a. Maintenance and Developments

R. L. Shepard, R. Ahlrichs, M. Ernzerhof, T. Kovar, H. Lischka, R. M. Pitzer, I. Shavitt, P. Szalay

The COLUMBUS program system of electronic structure codes has been maintained on the various machines used for production calculations by the Theoretical Chemistry Group, including the Sun workstations, the Kubota (Stardent) Titans, the Alliant FX/2800, the Cray Y-MP at SCRI at Florida State University, and on the Cray Y-MP and two Cray 2 machines at NERSC at Livermore National

Laboratory. The COLUMBUS program system is maintained and developed collaboratively with several researchers including Shavitt and Pitzer (Ohio State University), Lischka (University of Vienna, Austria), and Ahlrichs (University of Karlsruhe, Germany).

A standard integral file structure (SIFS) has been developed, and has been incorporated into the complete electronic structure code system. This integral file structure includes self-defining header records and allows efficient vectorization of the processing of the integral file records, variable index packing methods, the flexible inclusion of various new integral types (including, for example, dipole moment and spin-orbit integrals), and the definition of low-level record-processing support routines that will promote portability. A supporting library, consisting of approximately 3500 lines of FORTRAN, has been developed, and is distributed with the COLUMBUS program system (see below). This library may also be used within other electronic structure codes, for example, as an interchange format.

Two new utility programs have been developed based on the SIFS. These programs, IRFMT and IWFMT, convert between binary and text-only representations of integral and density matrix files. When combined with the remote shell capabilities of UNIX workstations, these utility programs allow integral files to be transferred from the binary representation of one machine to the binary representation of another machine without explicitly storing the intermediate text-only representation. These utility programs are included in the COLUMBUS distribution files (see below) as an illustration of the usefulness of the SIFS.

An initial version of program CIPC has been developed in order to allow interactive analysis of large-scale multireference CI wave functions computed with the COLUMBUS program system. This program reads complete or partial lists of expansion coefficients, and allows them to be sorted and viewed in various ways. CSFs may be viewed as (unitary group approach) step-vectors and, optionally, as combinations of Slater determinants.

The initial parallel version of the CI diagonalization program CIUDG developed in the last two years has been ported to several parallel machines, including our Alliant FX2800 to the Intel iPSC/i860. Using the TCGMSG library, this program also runs on networks of workstations. This version is based on a partitioning of the Hamiltonian matrix, trial vector, and matrix-vector product, and uses a distributed-memory, message-passing programming model. Each CPU is responsible for only a subset of the possible combinations of segment pairs. In the original implementation, each CPU processed the entire list of coupling coefficients over the internal orbitals and the complete list of integrals each iteration. In the current version, only the required coupling coefficients are generated by each CPU as needed during the diagonalization procedure, eliminating the associated I/O, and increasing the efficiency significantly in highly segmented cases. In collaboration with Lischka, ongoing work is directed towards eliminating the integral I/O inefficiencies displayed in the current version of the program.

The COLUMBUS program system is now available using the *anonymous ftp* facility of the internet from the server ftp.tcg.anl.gov. The announcement of the availability of the program system on various electronic bulletin boards coincided with Columbus Day, October 14, 1991. In addition to the source code, the complete online documentation, installation scripts, sample calculations, and numerous other utilities are included in the distribution. The entire program system can be downloaded in *tar* format (optionally compressed), or individual files may be obtained from within the directory structure. The codes have been distributed to over 30 outside testers, along with the ongoing maintenance and testing being performed by the programmers at approximately another dozen sites. Statistics of *anonymous ftp* connections have been kept since May 1992, and since that time the COLUMBUS codes have been accessed roughly 50 times per week. Initial responses from these early users of the COLUMBUS program system have been both positive and constructive.

b. COLUMBUS-related Codes: MCSCF Wave Function Optimization Using Multidimensional Trigonometric Interpolation *R. L. Shepard*

A new method of MCSCF wave function optimization was developed in previous years. This method is based on a nonlinear transformation of the wave function variation coordinates along with the construction of a global interpolating function. This interpolating function is constructed for each MCSCF iteration in such a way that it reproduces exactly the energy, gradient, and hessian at the expansion point,

at an infinite number of isolated points, and at points on the surfaces of an infinite number of nested multi-dimensional balls within the wave function variational space. Current work is directed towards the efficient computation of the orbital corrections from the interpolating function. Using the known periodic behavior of this interpolating function, new iterative methods are being developed in order to reduce the number of expensive matrix-vector products that must be formed. This new wave function optimization method is being included into the production-level MCSCF code used by the group, and eventually into the COLUMBUS program system.

c. COLUMBUS-related Codes: Analytical Energy Gradients for MRCI Wave Functions *R. L. Shepard*

A new formalism has been developed over the last few years for computing analytical energy derivatives and energy-response properties for general MRCI wave function. This formalism is based on successive orbital transformations in which the transformation matrix from one intermediate orbital set to the next depends only on a single orbital condition or constraint. Lagrange multipliers are thereby eliminated entirely from the formalism. This formalism allows a subset of the doubly occupied orbitals to be frozen in the MRCI wave function, it allows different invariant-active-orbital subspaces to be resolved independently, and it allows arbitrary successive energy-optimized orbital transformations to be applied. The MRCI energy gradient contributions from all such orbital transformations are transformed back to the AO basis in a displacement-independent manner. This allows the gradient elements to be computed with computationally efficient trace operations without the explicit storage (or further manipulation) of the derivative integrals. An initial implementation of this method has been completed

The multireference CI energy gradient method outlined above allows the computation of all 3N components of the gradient with very little additional effort beyond the CI wave function evaluation itself. The most computationally demanding step is the evaluation of the CI one- and two-particle density matrices. This requires approximately the effort of one additional iteration of the iterative CI diagonalization procedure. The successive orbital transformation approach outlined above allows any required orbital resolution terms to be treated naturally in the most convenient orbital basis. The only coordinate-dependent quantities required in the above approach are the derivative integrals, and they are used only in trace operations in the AO basis. This allows the entire gradient vector to be computed in such a way that the computational effort required is independent of the number of geometrical degrees of freedom This is the first time that all of these features have been incorporated into a general multireference CI energy gradient method.

In addition to the computation of analytic energy gradients, the new formalism lends itself to the computation of energy-response properties. These are properties that may be written in the form $dE/d\lambda|_{\lambda=0}$ where λ is a measure of a perturbation to the standard electronic Hamiltonian operator. These properties include the dipole moment of a molecule (e.g., $\mu_x=dE/d\varepsilon_x$, where ε_x is the strength of the x component of an external electric field ε) and the dipole moment derivatives (e.g., $d\mu_x/dR$, where R is some internal coordinate). Examples of both of these properties have been demonstrated with the new method.

Current work on this program includes the incorporation of the SIFS described above, and other modifications in order to smoothly integrate this program into the rest of the COLUMBUS program system. Several shortcomings of the current implementation, including the limitation to *s*-, *p*-, and *d*-type basis functions and the inefficient treatment of generally contracted basis functions will require replacement of the derivative integral program, and several candidate codes are being examined for this purpose.

2. Full-CI *R. J. Harrison, E. Stahlberg*

Our full-CI program has been modified to be more effective on massively parallel machines, in particular the Intel Touchstone Delta Field Prototype. The program explicitly recognizes data local or non-local to a given processor, a feature found critical to effective implementation on distributed memory, massively-parallel computers like the Touchstone. This code on large problems can achieve sustained production rates in excess of 4 GFLOP/s on the full 512 processors of the Touchstone. This amounts to about 20% of the peak rate and is one of the highest sustained rates ever achieved for a production code. An improved diagonalization procedure and data compression techniques minimize I/O.

The code was applied to benchmark calculations on Ne, CH_3, and CH_4. These calculations provide the measure of error for the incompleteness of other electronic structure methods employing truncated configuration or perturbation expansions. The CH_4 calculation is the largest CI calculation ever performed. In Figure V-12, the importance of a parallel implementation of the code in making the CH_4 calculation feasible is indicated.

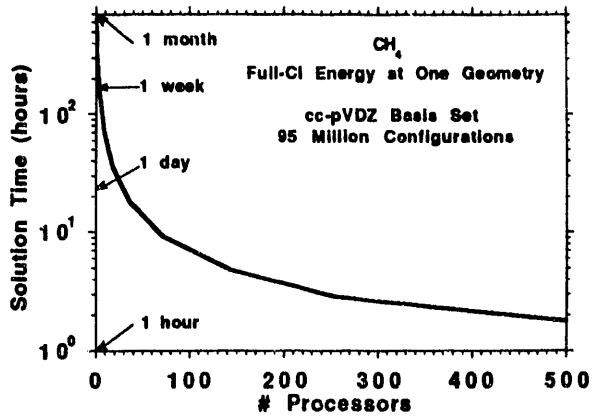

Figure V-12. The full-CI calculation of the energy of CH_4 at one geometry point as a function of the number of processors used in the Touchstone Delta computer.

3. New Methods: Electronic Wave Packets

S. K. Gray, R. J. Harrison

A new time-dependent approach to directly solving the Schroedinger equation has been developed. Relatively minor modifications of existing configuration interaction electronic structure codes allow one to construct directly electronic wave packets, that is, the behavior in time of certain nonstationary electronic excitations. One can create "interesting" electronic states -- as might be prepared with short, intense laser pulses, for example -- and simply monitor the behavior of the electronic density. The major use of this whole approach is to explore the short time dynamics of various high-energy, nonstationary excitations in atoms or small molecules. Calculations on the four-electron Be atom have been carried out with both a white light initial excitation and an initial state preparation that strongly mixes only two states. Both cases produce autocorrelation functions that show recurrences, or beats, on the subfemtosecond time scale. Other initial preparations are being examined that should lead to recurrences observeable by femtosecond spectroscopy.

C. Kinetics of Chemical Reactions

J. P. Hessler, J. V. Michael, H. Du, K. P. Lim, P. J. Ogren

The objective of this program is to measure thermal rate coefficients and branching ratios of elementary reactions that are important in combustion. However, the work may also be applied to the chemistry of the atmosphere and to the development of new materials, as many of the reactions are the same.

To provide detailed information on molecular interactions, it is necessary to measure the rate of chemical reactions over a wide range of temperature and pressure. At the present time, there are competent researchers who are continually presenting absolute rate data in the temperature region between 200-800 K. There is much less activity in the higher temperature range that is typical of combustion. Hence, the programs at Argonne concentrate on the higher temperature region. Two approaches, both utilizing shock-tube techniques, are employed. In the first, state-of-the-art laser techniques are used to measure the kinetic properties of atomic and diatomic species involved in simple reacting systems at high temperatures, 1000-5000 K. In the second, flash photolysis is used to produce reactive species in the temperature range between 800-2000 K; the time-dependent behavior of these species is monitored by resonant-absorption methods.

These programs blend a unique combination of expertise in chemical kinetics and kinetic modeling with molecular dynamics, quantum electronics, analytical chemistry, and laboratory computer applications for data collection and analysis.

1. Elementary Reaction-Rate Measurements at High Temperature by Tunable-Laser Flash-Absorption

J. P. Hessler, H. Du, P. J. Ogren

For over three decades, kineticists have known of the deleterious effects correlated reactions produce on the accuracy of rate-coefficient measurements. To help

minimize the effects of this dilemma we developed the "correlation analysis" procedure for designing and evaluating kinetic experiments on complex chemical systems. This procedure uses the temporal integral of products of sensitivity coefficients to (1) calculate the relative importance of reactions that affect the kinetic behavior of a specific observable over a given interval, (2) evaluate the correlation between any of the above reactions, and (3) determine how the uncertainties in the rate coefficients of correlated reactions propagate in an analysis of experimental data. The advantages of this procedure are that it is directly related to the analysis of experimental data, conceptually simple, easy to implement, and provides a quantitative means for assessing the relative accuracy of different experiments. In addition, it provides a new, efficient, and systematic method for calculating the correlation between reactions.

Briefly, the procedure was derived by expanding the chi-squared function about an initial set of rate coefficients, $\{a_1^*, ..., a_M^*\}$. The relative importance of a reaction, that is, its weight, is determined by the curvature of the $\Delta\chi^2$ surface in the M-dimension hyperspace that defines changes in the rate coefficients of the reactions. The correlation between reactions is determined by the orientation of the principal axis of the ellipsoids of constant $\Delta\chi^2$. If we measure a physical observable Z, for example, the hydroxyl concentration, as a function of a running variable, for example, time, over an increment $\Delta t = t_N - t_1$, the ellipsoids of constant $\Delta\chi^2$ may be described by a discrimination matrix, $[D(Z,\Delta t)]$. The matrix elements of this matrix are given by

$$D_{j,k}(Z,\Delta t) = \sum_{i=1}^{N} \frac{a_j^* a_k^*}{Z_{max}^2} S_{Zj}(t_i;a^*) S_{Zk}(t_i;a^*) , \quad (9)$$

where $S_{Zj}(t_i;a^*)$ is the sensitivity coefficient at t_i for the observable Z with respect to the rate coefficient a_j, and Z_{max} is the maximum value of the observable in the interval Δt. The weights, $w(a_j)$, of the reactions are given by the diagonal elements of the normalized discrimination matrix,

$$w(a_j) = \frac{D_{j,j}(Z,\Delta t)}{Tr[D(Z,\Delta t)]} . \quad (10)$$

The correlation between two reactions is given by the orientation of the semimajor axis, θ_{kj}(major), of the ellipsoids of constant $\Delta\chi^2$ in the plane that defines changes in the two rate coefficients. If we assume $D_{jj} \le D_{kk} \le D_{MM}$, this angle is given by

$$\theta_{kj}(\text{major}) = .5*\tan^{-1}[2D_{jk}/(D_{kk}-D_{jj})] \pm \pi/2 . \quad (11)$$

For the reactions j and k to be considered uncorrelated, it is a necessary, but not sufficient, condition that $\theta_{kj}(\text{major}) = \pi/2$, that is, $D_{jk} = 0$.

We have applied the correlation analysis procedure to the oxidation of the methyl radical:

$$CH_3+O_2 \rightarrow H_2CO + OH \quad (12a)$$
$$\rightarrow H_3CO+O \rightarrow H_2CO+O+H . \quad (12b)$$

The second channel is important at high temperatures, T > 2000 K, and its rate is fairly well established. Measurements designed to monitor the first channel produced rate coefficients that range from immeasurably slow to 4×10^{12} cm^3/molecule-sec at 2000 K. Using the correlation analysis procedure, we designed experiments to measure the formaldehyde plus hydroxyl channel. The analysis shows that, if the temporal behavior of the hydroxyl radical is monitored, the rate of the formaldehyde plus hydroxyl channels may be determined without interference from other reactions if (1) we use a fast source for the methyl radical, for example, azomethane, and (2) the initial concentration of oxygen is large enough to assure that oxidation of methyl proceeds much more rapidly than methyl-methyl recombination. Our preliminary results for the rate of the formaldehyde plus hydroxyl channel give

$$k_{12}(T) = (8.86\pm0.88)\times10^{-10} \exp[-48321/T(K)]$$
$$\text{cm}^3 \text{ molec}^{-1} \text{ s}^{-1} \quad [13]$$

from 3450 to 5300 K.

In addition, we have used correlation analysis to show that measurements on stoichiometric systems are most sensitive to the rate of $H + O_2 \rightarrow OH + O$. Also, measurements of CO in systems with a small amount of azomethane in pure oxygen are hindered by four highly correlated reactions. The reaction of formaldehyde with the hydroxyl radical to produce the formyl radical plus water, and the reactions of the formyl radical with molecular oxygen to produce either HO_2 plus carbon monoxide or the hydroxyl radical plus carbon dioxide are highly correlated with the reaction that produces formaldehyde plus the hydroxyl radical. The fact that these four reactions are highly

correlated precludes drawing any conclusions about the rate of the formaldehyde plus hydroxyl radical channel from measurements of the temporal dependence of CO.

2. Flash Photolysis-Shock Tube Studies of Chemical Reactions *J. V. Michael, K. P. Lim*

During the past year, the flash or laser photolysis-shock tube (FP- or LP-ST) apparatus has been used to measure the temperature dependence of the thermal rate constants for two bimolecular reaction. Unlike the lower temperature classical methods of gas-phase chemical kinetics, this method allows absolute thermal rate constants to be determined at combustion temperatures. It can also be extended to relatively low temperatures so that results, in favorable cases, can be obtained over the large temperature range, 650-2500 K. Hence, the method allows for overlap between the classical lower temperature methods and the usual high-temperature shock-tube methods. In addition, the thermal decomposition of N_2O has been studied by the atomic resonance absorption spectroscopic (ARAS) method. The LP-ST method has been extended to include Cl-atom reactions, and the thermal decomposition of CH_3Cl has also been studied by the ARAS method. The thermal decomposition of CH_3Cl has then served as a source of CH_3 radicals for an additional study of the O + CH_3 reaction. Because this is a delayed photolysis experiment, the method has been named the pyrolysis photolysis-shock tube technique.

Rate constants for the reaction,

$$O + CH_3Cl \rightarrow OH + CH_2Cl, \qquad (14)$$

have been measured by the O-atom ARAS technique, and the results of 45 experiments can be represented by the Arrhenius expression, $k_{14} = 4.82 \times 10^{-10}$ exp(-6574 K/T) cm^3 $molecule^{-1}$ s^{-1} over the temperature range, 916-1485 K. These results have been combined with lower temperature results from Rensselaer Polytechnic Institute (Ko and Fontijn), and the results are best given by a three-parameter expression of the form $k = AT^n exp(-B/T)$ as $k_{14} = 2.57 \times 10^{-11}$ $T^{0.31}$ exp(-5633 K/T) cm^3 $molecule^{-1}$ s^{-1} over the combined temperature range, 556-1485 K.

The ARAS method has been extended to monitor N atoms at $\lambda = 119.9$ nm, and the rate constants for

$$N + NO \rightarrow N_2 + O, \qquad (15)$$

have been measured by the LP-ST technique between 1251-3152 K. The results are best represented by the temperature-independent expression, $k_{15} = (3.7 \pm 0.8) \times 10^{-11}$ cm^3 $molecule^{-1}$ s^{-1}.

The thermal decomposition of N_2O has been studied by observing initial O-atom formation with the ARAS technique. This decomposition was also used to calibrate two resonance lamp configurations, thereby allowing for the determination of absolute O-atom concentrations under shock wave heating conditions. The results for the process

$$N_2O + M \rightarrow N_2 + O + M, \qquad (16)$$

where M is either Ar or Kr, can be represented by the Arrhenius expression, $k_{16} = 5.25 \times 10^{-10}$ exp(-27921 K/T) cm^3 $molecule^{-1}$ s^{-1}.

Utilizing the Cl-atom ARAS technique, rate constants for the thermal decomposition of CH_3Cl,

$$CH_3Cl \rightarrow CH_3 + Cl, \qquad (17)$$

have been measured, and the results from initial rate analysis can be expressed in first-order by the Arrhenius expression, $k_{17} = 1.21 \times 10^{10}$ exp(-27838 K/T) s^{-1}. This measurement has motivated the R-Cl PES and dynamics calculations discussed above.

CH_3 radicals from reaction (17) serve as a source for a subsequent study of the reaction,

$$O + CH_3 \rightarrow H_2CO + H. \qquad (18)$$

Oxygen atoms for the reaction 18 study were prepared by the delayed photolysis of SO_2. These were then monitored in real time by the O-atom ARAS technique. The results between 1609-2002 K showed that there was no temperature dependence. The temperature-independent rate constant is $k_{18} = (1.4 \pm 0.5) \times 10^{-10}$ cm^3 $molecule^{-1}$ s^{-1}.

D. Dynamics of Chemical Reactions *K. Liu, R. G. Macdonald, Z. Ma*

The goal of the experimental program in chemical dynamics is to characterize the detailed dynamics of chemical reactions in a comprehensive fashion. This requires production of the radicals of interest, control

of the reactant translational, rotational, and vibrational energies, measurement of the product state and angular distributions, etc. This is a considerable challenge. However, recent advances in experimental techniques now make it possible to begin to address these questions in detail.

To meet this challenge, a state-of-the-art crossed molecular beam apparatus has been constructed for the studies of radical-molecule reactions, and a fast-flow reactor is currently under construction for the studies of radical-radical reactions. Both apparatus use extensive laser-based techniques for the generation of radicals and for the state-resolved detection of reaction products.

1. Crossed-Beam Reaction Dynamics

K. Liu, R. G. Macdonald, Z. Ma

The objective of this program is to investigate the dynamics of radical-molecule collisions under single-collision conditions at the state-to-state level of detail. The radical beam is created by UV laser photolysis of a suitable precursor in a strong pulsed molecular beam expansion. Both the reactants and products are probed in a state-specific manner using either laser-induced-fluorescence (LIF) or resonance-enhanced multiphoton ionization (REMPI) detection techniques. A unique feature of this crossed-beam machine is that the state-specific detector remains fixed while both beam sources can be rotated independently about the scattering center. Thus, two types of experiments may be performed for the integral cross section measurements: (1) the beam intersection angle is fixed and the product state distribution probed by varying the laser wavelength; this provides state distributions at a selected initial energy; and (2) the laser wavelength is fixed and the beam intersection angle is varied; this measures state-resolved integral cross sections as a function of initial translational energy. In addition, the implementation of Doppler-shift technique during the past year allows state-to-state differential cross section to be determined. By exploiting the polarization aspects of this technique, it is demonstrated that the azimuthal dependence of the angular distributions can also be revealed.

a. Vibronically Inelastic Scattering of NCO + He: Dynamical Renner-Teller Effects *K. Liu, R. G. Macdonald*

As a continuing effort to understand the inelastic scattering of polyatomic free radicals, an extensive investigation of the title process has been undertaken. Reported here is a new type of energy-transfer process, a collision-induced inter-Renner-Teller component transition. The results for all the rovibronic energy-transfer processes between NCO($X^2\Pi$) + He measured in this work are summarized in Figure V-13. In this figure, the relative cross sections are plotted in terms of an energy-gap law expression. The insert indicates the energy-level diagram and the rovibronic energy-transfer processes considered. Several interesting features are noted. First, the six collisional processes shown in the figure appear to be divided into two classes, 1, 2, 4, and 6 being one class and 3 and 5 the other, characterized by the energy-gap law with nearly the same slopes, as indicated by the dashed and dotted lines, respectively. However, the processes where $(00^10)\ ^2\Delta_{5/2}$ is the final product state appear to be 5-10 times less efficient than the others having similar energy gaps. Second, although the T-V energy-transfer processes (2 and 4) are less efficient than the T-R ones (not shown), this deficiency appears in accord with energetic considerations. In other words, even though

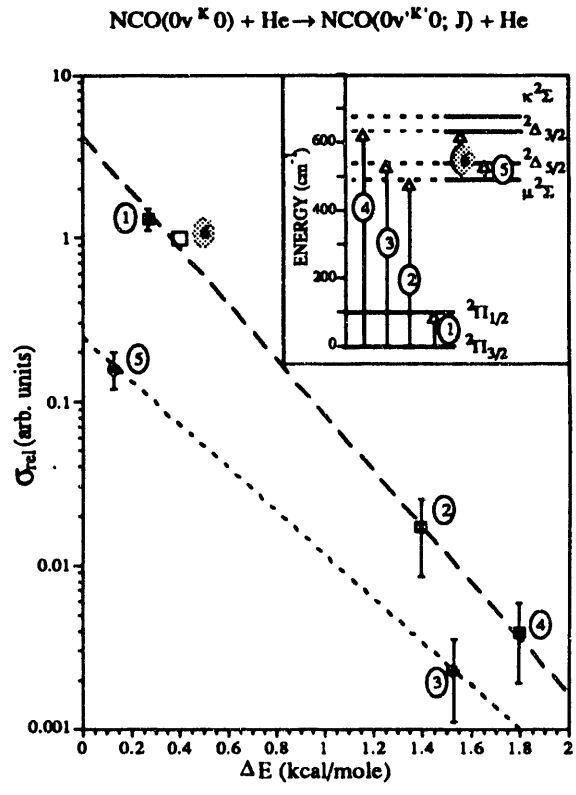

Figure V-13. Semilog plot of cross sections for various energy-transfer processes vs. energy gap between reactant and product vibronic manifolds. All cross sections have been measured at E_o = 3.81 kcal mol^{-1}. The insert illustrates the collisional processes studied.

processes 2 and 4 represent T-V energy transfer, process 6 an inter-Renner-Teller transfer, and process 1 a spin-orbit changing collision with rotational excitation, all these cross sections can be correlated with the energetics of the process regardless of its nature. Third, processes 5 and 6 are energy transfer between the Renner-Teller components with the former being energetically favorable. Yet, process 6 is found to be six times more efficient, indicating a strong propensity for this inter-Renner-Teller pathway.

Work is in progress to extend the exact quantum scattering formalism developed by Alexander for diatomic $^2\Pi$ radicals + ^1S atoms to the linear $^2\Pi$ polyatomic case by considering the bending excitation explicitly. Here, a simpler, yet intuitive, argument will be presented to rationalize some of the findings of this work. In particular, let us focus on the propensity observed for the inter-Renner-Teller pathways, process 5 vs. 6.

Considerable insight into the nature and underlying mechanism for these inter-Renner-Teller component processes can be gained by considering the wavefunctions of the vibronic states involved. These are listed in Table V-1 as unsymmetrized basis set, $|\Lambda,l,\Sigma>$. An examination of the basis functions shows that the collision-induced vibronic transitions, $(01^10)m^2\Sigma \rightarrow (01^20)^2\Delta_{3/2}$ and $(01^10)m^2\Sigma \rightarrow (01^20)^2\Delta_{5/2}$ can be distinguished by whether Λ (for the $(01^20)^2\Delta_{3/2}$ product state) or l (for $(01^20)^2\Delta_{5/2}$) change sign as a result of the interaction with He. The sign change of the angular momentum projection along the bond axis corresponds physically to a change in orientation of the angular momentum. In the case of rotationally inelastic collisions of a $^2\Sigma$ diatomic radical, an e → e and f → f spin-doublet state propensity has been well-established. From the formal theoretical analysis, Alexander et al. were able to show that the observed propensity toward conservation of the e/f symmetry label is a manifestation of a collisional propensity to retain the initial orientation of the nuclear angular momentum. Analogous to this $^2\Sigma$ diatomic radical case, one could anticipate that a collision resulting in a change of the initial orientation of nuclear angular momentum (i.e., the vibrational angular momentum in the present case) would be less probable. As is evident from Figure V-13, this is indeed the case: the collision-induced inter-Renner-Teller component transition for $(01^10)\mu^2\Sigma \rightarrow (01^20)^2\Delta_{3/2}$ is more efficient than that for $(01^10)m^2\Sigma \rightarrow (01^20)^2\Delta_{5/2}$ despite their energetic difference. This intuitive argument for the conservation of vibrational angular momentum orientation is nicely borne out from our formal theoretical analysis.

Furthermore, it is conjectured that the inter-Renner-Teller component process $(01^10)\mu^2\Sigma \rightarrow (01^20)^2\Delta_{3/2}$ or $(01^20)^2\Delta_{5/2} \rightarrow (01^10)\kappa^2\Sigma$, occurring in the (010) vibronic manifold, is in fact analogous to the spin-orbit changing process, $(00^10)^2\Pi_{3/2} \rightarrow (00^10)^2\Pi_{1/2}$, occurring in the ground vibronic manifold. This arises because this inter-Renner-Teller process involves only changes in Λ (and of course J), not in l, similar to the case of a spin-orbit changing process, $^2\Pi_{3/2} \rightarrow {}^2\Pi_{1/2}$, in the vibronic ground state (00^10). Hence, like the latter case, the collision-induced transitions $(01^10)\mu^2\Sigma \rightarrow (01^20)^2\Delta_{3/2}$ and $(01^20)^2\Delta_{5/2} \rightarrow (01^10)\kappa^2\Sigma$ should also be induced by the difference potential between the two adiabatic PESs $V_{A''}$ and $V_{A'}$. Again, the formal theoretical analysis has confirmed this notion. In this regard, it is interesting to note that from a spectroscopic point of view the splitting of the $(01^20)^2\Delta_{5/2}$ and $(01^20)^2\Delta_{3/2}$ vibronic manifolds is mainly determined by the spin-orbit interaction. On the other hand, from a collisional point of view, the $(01^10)\mu^2\Sigma$ and $(01^20)^2\Delta_{3/2}$ vibronic manifolds (similarly $(01^20)^2\Delta_{5/2}$ and $(01^10)\kappa^2\Sigma$) behave more like a "pair of spin-orbit manifolds", because the transition between them is induced by the difference potential similar to the transition between $(00^10)^2\Pi_{3/2}$ and $(00^10)^2\Pi_{1/2}$ in the ground vibronic manifold. Previously, a term *dynamical Renner-Teller effect* has been coined to represent many of the major findings from the studies on the *rotationally* inelastic collisions of $^2\Pi$ radicals. Within the context of the proposed interpretations, the findings in this work about *vibrationally excited* $^2\Pi$ radicals can be viewed as another dynamical manifestation of the Renner-Teller effect.

Table V-1. Unsymmetrized basis set wavefunctions, $|\Lambda,l,\Sigma>$, for describing the vibronic states for a $^2\Pi$ triatomic radical.

vibronic level	basis set $\|\Lambda,l,\Sigma>$
$(01^10)k^2\Sigma$	|-1,1,1/2>
$(01^20)^2\Delta_{3/2}$	|-1,-1,1/2>
$(01^20)^2\Delta_{5/2}$	|1,1,1/2>
$(01^10)\mu^2\Sigma$	|1,-1,1/2>
$(00^10)^2\Pi_{1/2}$	|-1,0,1/2>
$(00^10)^2\Pi_{3/22}$	|1,0,1/2>

b. Angular Correlations in the Collision-Induced Fine-Structure Transition of $O(^3P)$ Atom With Argon *K. Liu, Z. Ma*

The collision-induced fine-structure transition is the simplest nonadiabatic process among all possible radical reactions. The title process also plays a significant role in the development of excimer chemical lasers. Yet, its detailed dynamics is still not fully understood. By implementing a (2+1) REMPI technique for the state-resolved detection of O atom, the process of $O(^3P_2 \rightarrow {}^3P_{1,0})$ with Ar was investigated experimentally for the first time. The angular distributions of scattered products $O(^3P_{1,0})$ were measured by Doppler-shift technique. By exploiting the polarization of the probe laser, the m_j-dependent angular distributions were deduced. Preliminary data analysis clearly indicated that all three (j,m_j) distributions were quite similar in the forward direction, exhibiting a rainbow-like peak, whereas at larger angles, a strong dependence on m_j was found. This m_j-resolved differential cross-section measurement represents one of the few cases in which the collision-induced angular-angular correlations were investigated.

2. Fast-Flow Reactor Studies of Radical-Radical Reaction Dynamics
R. G. Macdonald

The molecular beam chemistry project involves the elucidation of the detailed dynamics of radical + molecule interactions; however, there is very sparse information available about the dynamics of radical + radical interactions. These processes are very important in combustion, being chain-termination steps as well as generating new molecular species. A new experimental apparatus has been constructed to investigate radical-radical dynamics. In this new apparatus, one radical or atomic species will be produced with a known concentration in a microwave discharge flow system. The other radical or atom will be produced by pulsed laser photolysis of a suitable photolyte. The time dependence of the state-selected products will be followed by absorption of a continuous infrared laser. This approach will allow the reaction of interest to be differentiated from other radical reactions occurring simultaneously. The experimental approach will be highly versatile, being able to detect a number of molecular species of particular interest to combustion processes, such as water, methane, acetylene, etc., at the state-specific level. State-specific infrared absorption coefficients of radicals can be measured in situ, allowing for the determination of the absolute concentrations and, hence, branching ratios for reactions having multiple reaction pathways.

As an initial test of the capabilities of this new apparatus the dynamics of one of the most important reactions in combustion chemistry $H + O_2 \rightarrow OH(v,J) + O$ will be investigated. Although this reaction has been extensively studied in the past, a complete product-state distribution by a single experimental technique has not been carried out; thus, this study will be a good test of the time-dependent infrared absorption method as well as furthering our understanding of the dynamics of this reaction.

PUBLICATIONS

A QUASICLASSICAL TRAJECTORY STUDY OF OH ROTATIONAL EXCITATION IN OH+CO COLLISIONS USING AB INITIO POTENTIAL SURFACES
K. Kudla*, A. G. Koures*, L. B. Harding, and G. C. Schatz*
J. Chem. Phys. 96, 7465-7473 (1992)

THE HOMOGENEOUS PYROLYSIS OF ACETYLENE II: THE HIGH TEMPERATURE RADICAL CHAIN MECHANISM
J. H. Kiefer*, S. S. Sidhu*, R. D. Kern*, K. Xie*, H. Chen*, and L. B. Harding
Combust. Sci. Tech. 82, 101-130 (1992)

REMPI MASS SPECTRUM OF THE OH RADICAL IN THE GAS PHASE
R. Forster*, H. Hippler*, K. Hoyermann*, G. Rohde*, and L. B. Harding
Chem. Phys. Lett. 183, 465-470 (1991)

*Not affiliated with the Chemistry Division or affiliated on a temporary basis.

THEORETICAL STUDIES OF THE HYDROGEN PEROXIDE POTENTIAL SURFACE. 2. AN AB INITIO, LONG-RANGE, $OH(^2P)+OH(^2P)$ POTENTIAL
L. B. Harding
J. Phys. Chem. 95, 8653-8660 (1991)

THEORETICAL STUDIES OF THE REACTIVITY AND SPECTROSCOPY OF H+CO⇌HCO. I. STABILIZATION AND SCATTERING STUDIES OF RESONANCES FOR J=0 ON THE LBH AB INITIO SURFACE
S.-W. Cho*, A. F. Wagner, B. Gazdy*, and J. M. Bowman*
J. Chem. Phys. 96, 2799-2811 (1992)

ISOLATED RESONANCE DECOMPOSITION OF A MULTI-CHANNEL S MATRIX: A TEST FROM THE SCATTERING OF H+CO⇌HCO
S.-W. Cho*, A. F. Wagner, B. Gazdy*, and J. M. Bowman*
J. Chem. Phys. 96, 2812-2818 (1992)

THE ADDITION AND DISSOCIATION REACTION H+CO⇌HCO. 3. IMPLEMENTATION OF ISOLATED RESONANCE RRKM THEORY WITH EXACT QUANTUM STUDIES FOR J=0
S.-W. Cho*, A. F. Wagner, B. Gazdy*, and J. M. Bowman*
J. Phys. Chem. 95, 9897-9900 (1991)

AN ANALYTICAL REPRESENTATION OF THE LOWEST POTENTIAL ENERGY SURFACE FOR THE REACTION O + HCL → OH + Cl
H. Koizumi*, G. C. Schatz*, and M. S. Gordon*
J. Chem. Phys. 95, 6421-6428 (1991)

THREE DIMENSIONAL QUANTUM SCATTERING STUDIES OF TRANSITION STATE RESONANCES: RESULTS FOR O + HCl → OH + Cl
H. Koizumi* and G. C. Schatz*
Advances in Molecular Vibrations, J. M. Bowman and M. A. Ratner, Eds., JAI Press (1991), pp. 139-164

RESONANCES IN HEAVY+LIGHT-HEAVY ATOM REACTIONS: INFLUENCE OF DIFFERENTIAL AND INTEGRAL CROSS SECTIONS ON TRANSITION STATE PHOTODETACHMENT SPECTRA
G. C. Schatz*, D. Sokolovski*, and J. N. L.Connor*
Far. Disc. Chem. Soc., 86, 1729-1738 (1991)

THE NATURE AND DECAY OF METASTABLE VIBRATIONS: CLASSICAL AND QUANTUM STUDIES OF VAN DER WAALS MOLECULES
S. K. Gray
Advances in Molecular Vibrations and Collision Dynamics, Vol. 1A, J. M. Bowman and M. A. Ratner, Eds., JAI Press, Greenwich, Connecticut, 1991, pp. 47-82

WAVE PACKET DYNAMICS OF RESONANCE DECAY: AN ITERATIVE EQUATION APPROACH WITH APPLICATION TO HCO → H + CO
S. K. Gray
J. Chem. Phys. 96, 6543-6554 (1992)

MARKOV SHIFTS IN THE HENON FAMILY
M. J. Davis, R. S. MacKay*, and A. Sannami*
Physica D 52, 171-178 (1991)

---

*Not affiliated with the Chemistry Division or affiliated on a temporary basis.

CLASSICAL DYNAMICS AND THE NATURE OF HIGHLY EXCITED STATES
M. J. Davis, C. C. Martens*, R. G. Littlejohn*, and J. S. Pehling*
Advances in Molecular Vibrations, J. M. Bowman, Ed., JAI Press, 1991, pp. 1-47

CHEMICAL REACTIONS AS PROBLEMS IN NONLINEAR DYNAMICS: A REVIEW OF STATISTICAL AND ADIABATIC APPROXIMATIONS FROM A PHASE SPACE PROSPECTIVE
M. J. Davis and R. T. Skodje*
Advances in Classical Trajectory Methods, W. L. Hase, Ed., JAI Press, 1992, pp. 77-164

SMOOTHED EIGENSTATES FROM MOLECULAR SPECTRA
M. J. Davis
Chem. Phys. Lett. 192, 479-485 (1992)

PROCEEDINGS OF THE ARGONNE INTEGRAL EVALUATION WORKSHOP
J. Almlöf*, R. Shepard, and R. J. Harrison, Eds.
Int. J. Quantum Chem. 40 (1991)

THE COLUMBUS STANDARD INTEGRAL FILE STRUCTURE: A PROPOSED INTERCHANGE FORMAT
R. Shepard
Int. J. Quantum Chem. 40, 865-887 (1991)

A GENERAL MRCI GRADIENT PROGRAM
R. Shepard, H. Lischka*, P. G. Szalay*, T. Kovar*, and M. Ernzerhof*
J. Chem. Phys. 96, 2085-2098 (1992)

PORTABLE TOOLS AND APPLICATIONS FOR PARALLEL COMPUTERS
R. J. Harrison
International J. Quant. Chem. 40, 847-863 (1991)

ANALYTICAL CALCULATION OF FULL CONFIGURATION INTERACTION RESPONSE PROPERTIES: APPLICATION TO Be
H. Koch* and R. J. Harrison
J. Chem. Phys. 95, 7479-7485 (1991)

RATE COEFFICIENT FOR THE REACTION $H+O_2 \rightarrow OH+O$; RESULTS AT HIGH TEMPERATURES, 2000 TO 5300 K.
H. Du* and J. P. Hessler
J. Chem. Phys. 96, 1077-1092 (1992)

MEASUREMENT OF THERMAL RATE CONSTANTS BY FLASH OR LASER PHOTOLYSIS IN SHOCK TUBES: OXIDATIONS OF H_2 AND D_2
J. V. Michael
Prog. Energy Combust. Sci. 18, 327-347 (1992)

INELASTIC SCATTERING OF $NCO(^2\Pi)$ + HE: PROTOTYPICAL ROTATIONAL STATE DISTRIBUTIONS FOR HUND'S CASE (a) RADICALS?
R. G. Macdonald and K. Liu
J. Phys. Chem. 95, 9630-9633 (1991)

STATE-TO-STATE COLLISION DYNAMICS OF MOLECULAR FREE RADICALS
R. G. Macdonald and K. Liu
Optical Methods for Time- and State-Resolved Chemistry, SPIE Proceedings Series,Vol. 1638, C.-Y. Ng, Ed., 1992, pp. 416-422

---

*Not affiliated with the Chemistry Division or affiliated on a temporary basis.

THE DYNAMICAL RENNER-TELLER EFFECT II: ROTATIONALLY INELASTIC SCATTERING OF $NCO(X^2\Pi,00^10)$ + He
R. G. Macdonald and K. Liu
J. Chem. Phys. 97, 978-990 (1992)

SUBMISSIONS

ISOTOPE EFFECTS IN ADDITION REACTIONS OF IMPORTANCE IN COMBUSTION: THEORETICAL STUDIES OF THE REACTIONS CH + H_2 ⇌ CH_3* ⇌ CH_2+H
A. F. Wagner and L. B. Harding
ACS Symposium Series (in press)

THE IMPORTANCE OF HINDERED ROTATIONS AND OTHER ANHARMONIC EFFECTS IN THERMAL DISSOCIATION OF SMALL UNSATURATED MOLECULES: APPLICATION TO HCN
A. F. Wagner, J. H. Kiefer*, and S. S. Kumaran*
24th Symp. (Int.) on Combustion (in press)

COMPARSION OF QUASICLASSICAL AND QUANTUM DYNAMICS FOR RESONANCE SCATTERING IN THE Cl + HCl → ClH + Cl REACTION
W. Jakubetz*, D. Sokolovski*, J. N. L. Connor*, and G. C. Schatz*
J. Chem. Phys. (in press)

AB INITIO ELECTRONIC STRUCTURE CALCULATIONS OF STATIONARY POINTS AND BARRIER HEIGHTS FOR THE ClHCl AND HCl_2 SYSTEMS
M. A. Vincent*, J. N. L. Connor*, M. S. Fordon*, and G. C. Schatz*
Chem. Phys. Lett. (1992)

QUANTUM DYNAMICS OF ArI_2 → Ar + I_2
S. K. Gray,
Chem. Phys. Lett. (in press)

HIERARCHICAL ANALYSIS OF MOLECULAR SPECTRA
M. J. Davis
J. Chem. Phys. (1992)

ON THE GLOBAL CONVERGENCE OF MCSCF WAVE FUNCTION OPTIMIZATION: THE METHOD OF TRIGONOMETRIC INTERPOLATION
R. Shepard
Theoretica Chimica Acta (in press)

ELIMINATION OF THE DIAGONALIZATION BOTTLENECK IN PARALLEL DIRECT-SCT CALCULATIONS
R. Shepard
Theoretica Chimica Acta (in press)

A PARALLEL IMPLEMENTATION OF THE COLUMBUS MULTIREFERENCE CONFIGURATION INTERACTION PROGRAM
M. Schüler, T. Kovar*, H. Lischka*, R. Shepard, and R. J. Harrison
Theoretica Chimica Acta (in press)

---

*Not affiliated with the Chemistry Division or affiliated on a temporary basis.

MASSIVELY PARALLEL FULL CONFIGURATION INTERACTION. BENCHMARK ELECTRONIC STRUCTURE CALCULATIONS ON THE INTEL TOUCHSTONE DELTA
R. J. Harrison and E. A. Stahlberg*
J. Parallel Dist. Comp. (1992)

CORRELATION ANALYSIS OF COMPLEX KINETIC SYSTEMS; A NEW SCHEME FOR UTILIZING SENSITIVITY COEFFICIENTS
J. P. Hessler and P. J. Ogren*
J. Chem. Phys. (in press)

THE MEASUREMENT OF THERMAL BIMOLECULAR RATE CONSTANTS BY THE FLASH PHOTOLYSIS-SHOCK TUBE (FP-ST) TECHNIQUE: COMPARISON OF EXPERIMENT TO THEORY
J. V. Michael
Advances in Chemical Kinetics and Dynamics (in press)

ISOTOPE EFFECT STUDIES AT HIGH TEMPERATURES BY THE FLASH OR LASER PHOTOLYSIS (FP OR LP-ST) TECHNIQUE
J. V. Michael
ACS Symp. Series, Isotope Effects in Chemical Reactions and Photodissociation Processes, J. G. Kaye, Ed. (in press)

RATE CONSTANTS FOR THE N_2O REACTION SYSTEM: THERMAL DECOMPOSITION OF N_2O; $N + NO \rightarrow N_2 + O$; AND IMPLICATIONS FOR $O + N_2 \rightarrow N + NO$
J. V. Michael and K. P. Lim*
J. Chem. Phys. (in press)

A KINETICS STUDY OF THE $O(^3P) + CH_3Cl$ REACTION OVER THE 556-1485 K RANGE BY THE HTP AND LP-ST TECHNIQUES
T. Ko*, A. Fontijn*, K. P. Lim*, and J. V. Michael
24th Symp. (Int.) on Combustion (in press)

COLLABORATIONS

M. H. Alexander, University of Maryland, College Park
A collaborative study on the inelastic scattering of CH off of He was completed. This study uses ab initio potential energy surfaces and a coupled-surface quantum dynamics scattering program to produce inelastic cross sections for comparison to measurements done by Liu and Macdonald in our program.

J. M. Bowman, Emory University, Atlanta, GA
A collaborative study on HCO unimolecular dissociation continues. Stabilization calculations and time-independent scattering calculations are being used to describe isolated resonances and to modify the potential energy surface so as to obtain better agreement with experiment.

E. Goldfield, Cornell University, Ithaca, NY
Time-dependent quantum and classical mechanics is being used to examine the photodissociation of HCO* in the first excited state. This dissociation involves Renner-Teller coupling with the first excited and ground state potential energy surfaces. Comparisons are being made with experiment.

---

*Not affiliated with the Chemistry Division or affiliated on a temporary basis.

I. Shavitt and R. M. Pitzer, Ohio State University
H. Lischka, University of Vienna, Austria
R. Ahlrichs, University of Karlsruhe, Germany
R. Kendall, Pacific Northwest Laboratory
The COLUMBUS program system is a collection of Fortran programs for performing general multireference single- and double-excitation configuration interaction (MRSDCI) wave function optimization based on the graphical unitary group approach. Since the original development effort (1980-1981), the program has been maintained and enhanced separately at various sites by the different research groups of the original developers. During the past two years, these various versions have been merged into a single version that combines all of the important features of the various separate versions. The source code is maintained in such a way that the code for any of the supported computers may be generated automatically from the code corresponding to another computer by using a conversion utility included in the program system. The program was made publicly available this year via the "anonymous ftp" facility of internet. Over 500 ftp requests for programs of the COLUMBUS suite have been logged in the first six months of distribution.

H. Lischka, T. Kovar, and P. Szalay, University of Vienna, Austria
M. Emzerhof, University of Bonn, Germany
Energy derivatives for MRCI wave functions. The theory of analytic energy gradient evaluation has made remarkable progress in the past few years for MCSCF and CI wave functions. This progress has resulted in a new formulation of energy gradients for MRCI wave functions that possesses several advantages over previous formulations. During the past year, this formulation has been extended into a very general approach that may also be used in the future for other wave function simplifications such as orbital localization. This method has been implemented in the COLUMBUS program system and timings of this portion of the code clearly demonstrate the efficiency of this approach.
Parallel implementation of the MRSDCI method. Using the portable message-passing tools developed in the Theoretical Chemistry Group by Harrison, the MRSDCI diagonalization program CIUDG of the COLUMBUS program system has been modified using a distributed-memory programming model to run efficiently on a wide range of parallel computers. A production version of this code is available.

M. F. Guest, S.E.R.C. Daresbury Laboratory, U.K.
Development of the UK version of the GAMESS ab initio chemistry package. The UK version of GAMESS is a very powerful and efficient package, maintained by Guest, and used by a very large community worldwide. The program is working on most of our group's computers. Guest and Harrison collaborate in porting GAMESS to relevant new machines, including new functionality within the package (e.g., the full-CI program).
Development of algorithms for parallel computers. Guest heads the Advanced Computing Research Group at Daresbury, where he has many parallel machines, including a large hypercube. We have mutual interest in the development of algorithms, particularly for post-Hartree-Fock models, which are suitable for massively parallel machines.

R. A. Kendall, Molecular Science Research Center, PNL
We are collaborating on the development of parallel computer programs, focusing presently on integrals and SCF and selected-CI. This has resulted in two papers submitted for publication.

P. J. Ogren, Earlham College, Richmond, IN
Ogren prepares samples that are not commercially available, for example, azomethane and azoethane. In addition, he assists with calculations on kinetic models used in analyzing the shock-tube measurements made in the group. These include the sensitivity analysis of the reactions selected for study via the new technique of "correlation analysis" developed by Hessler. Hessler is collaborating with Ogren on the development of a tunable-laser system to measure the absolute intensity of opto-galvanic signals generated in a uranium hollow cathode lamp in research funded by the National Science Foundation.

VI. PHOTOIONIZATION-PHOTOELECTRON RESEARCH

J. Berkowitz, B. Ruščić, R. Yoo

Outside Collaborators: *L. A. Curtiss, J. A. Pople*

Our photoionization research program is aimed at understanding the basic processes of interaction of VUV light with atoms and molecules. Our emphasis in the last several years has been the generation and investigation of transient species, both atoms and free radicals. Various techniques have been used to generate these species, including sublimation, pyrolysis, microwave discharge, and chemical reaction. The chemical reaction method, in which H or F atoms produced in a discharge flow into a reaction chamber, has proven to be particularly fruitful for generating several transient species by successive abstraction reactions, e.g., CH_2SH, CH_3S, CH_2S, and HCS from F + CH_3SH. The experimental results impact upon thermochemistry, geometric and electronic structure of neutral and ionic species, and dynamics.

Our molecular studies have recently emphasized free radicals. Here, in addition to autoionization structure, we obtain precise adiabatic ionization potentials (IP) and fragment appearance potentials (AP), from which we extract bond energies and heats of formation. These experimental results are of utmost importance in testing the most sophisticated current ab initio molecular calculations (e.g., fourth-order Møller-Plesset perturbation theory and its improvements), which claim accuracies of ±2 kcal/mol for heats of formation and ±0.1 eV for IPs. The synergistic interplay of ab initio theory and experiment has enabled us to arrive at unusual molecular structures and the systematics of molecular bonding.

This is underscored in our recent studies of the Si_2H_n transient species and the corresponding cations. For example, the structure of Si_2H_2 is inferred to be cyclic, and that of $Si_2H_3^+$ tribridged, both very different from their carbon analogs.

In the past year, *inter alia*, we have focused our experimental effort on two controversial issues:

1. The heats of formation of the important isomeric transient species CH_2SH and CH_3S, and their cations. Recent experimental results and ab initio calculations differ substantially. Our results, which include the first experimental study of CH_2SH, are in agreement with the ab initio calculations. As a follow-up to this study, we have also examined the transients CH_2S and HCS, and determined their thermochemical properties.

2. The molecule BiF has been of considerable interest for many years, because it has seemed to be among the most promising candidates for a visible-UV chemical laser. Vital to its use is the value of D_o(BiF). Early work favored a value around 3 eV, whereas two recent experimental studies provide evidence for D_o(BiF) near 5 eV. We have obtained three independent values for this quantity, utilizing photoionization mass spectrometry and the three laws of thermodynamics, to arrive at D_o(BiF) = 3.76 ± 0.13 eV.

In addition, we have embarked on a detailed study of the Group V molecular species As_n, Sb_n, and Bi_n. These species are of practical interest for CVD preparation of microelectronics devices, and of fundamental interest in cluster studies. In addition to precise spectroscopic and thermochemical values, these studies have already provided two important insights.

1. Unlike the linear N_3, the heavier analogs are triangular, nearly equilateral.

2. Excitations from the inner s orbitals of the atoms give rise to window resonances. The diatomic molecules P_2, As_2, and probably Sb_2 and Bi_2, upon excitation from their $s\sigma_u$ orbitals, also manifest window resonances. This general behavior is not yet fully understood.

Our photoionization studies on each of the Bi_n (n = 1-4) species, not yet completed, are already immensely superior to recently published synchrotron studies of these species.

Most of our research is of a fundamental nature, but the processes and species we study are implicated in a wide range of chemical reactions, including combustion of carbon and sulfur compounds and halogen-containing substances, atmospheric and interstellar chemistry, and plasma chemical vapor deposition of silicon, germanium, gallium arsenide, and indium phosphide materials.

A. Photoionization Studies of CH_3S, CH_2SH, CH_2S, and HCS

1. Background

Recently there has been an upsurge of interest in simple organosulfur species, focusing primarily on the determination of their thermochemical properties. These activities have been in part motivated by the need to shed more light on the combustion of sulfur-containing fuels and subsequent pollution-related atmospheric chemistry.

The transient species CH_3S, CH_2SH, CH_2S, and HCS are believed to play important roles as intermediates in the above processes. We have studied all of these transients by photoionization mass spectrometry. The species were prepared in situ by H abstraction with F atoms from CH_3SH. In addition, CH_2S was prepared by pyrolysis of CH_3SCl and CH_3SSCH_3, whereas HCS was also prepared by an abstraction/pyrolysis combination ($F+CH_2S$). Our studies of CH_2SH and HCS represent the first direct photoionization measurements of these species, whereas those on CH_3S and CH_2S are improvements on prior measurements.

2. The Isomeric Transients CH_3S and CH_2SH

The species CH_3S and CH_2SH are isomeric, and both are formed during the $F+CH_3SH$ reaction. In photoionization mass spectrometric measurements, both appear at the same m/e=47 channel (Figure VI-1). The long-wavelength end of the photoion yield curve corresponds to ionization from CH_2SH. In the threshold region, a few steplike features appear, which are attributable to a vibrational progression of 1020± 40 cm^{-1} in the cation. There is also a hint of another progression of 600^{+80}_{-40} cm^{-1}. The half-rise of the first step occurs at 1645.3± 0.7 Å ≡ 7.536 ± 0.003 eV and corresponds to the adiabatic IP of CH_2SH. At ~1340 Å another series of steps appears, corresponding to ionization from the isomeric species CH_3S. The spacing between the steps indicates that the active vibration in CH_3S^+ has a frequency of 700± 60 cm^{-1}. The half-rise point of the first step occurs at 1338.6 ± 0.7 Å ≡ 9.262 ± 0.005 eV, and corresponds to the adiabatic IP of CH_3S.

The two species in question can be further distinguished by selective isotopic studies. Thus, the reaction of $F+CD_3SH$ generates CD_2SH (which appears at m/e = 49) and CD_3S (m/e=50). Figure VI-2

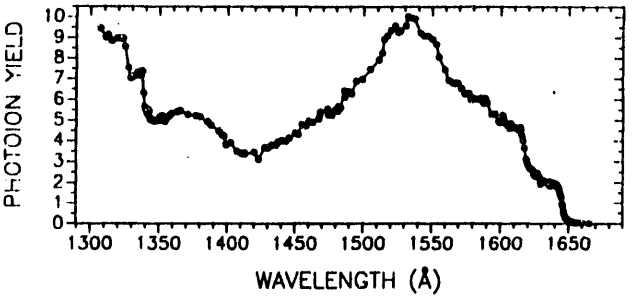

Figure VI-1. The photoion yield curve of m/e = 47 monitored during the reaction of F atoms with CH_3SH. The region ~1340-1660 Å is attributable to $CH_2SH + h\upsilon \rightarrow CH_2SH^+ + e$, whereas the growth in the region below ~1340 Å is primarily attributable to $CH_3S + h\upsilon \rightarrow CH_3S^+ + e$.

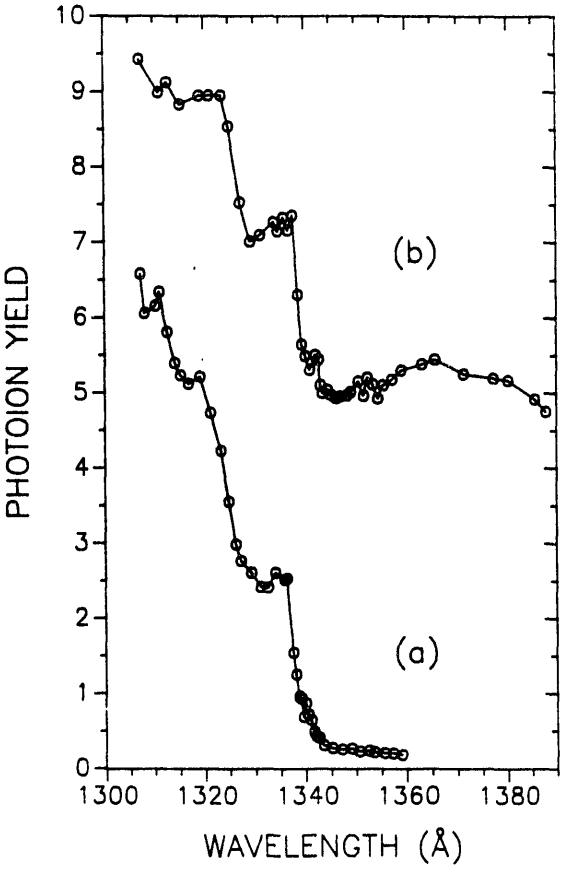

Figure VI-2. (a) The photoion yield curve at m/e = 50 (CD_3S^+), monitored during the reaction of F atoms with CD_3SH. (b) An expanded portion of Figure VI-1, attributed to $CH_3S + h\upsilon \rightarrow CH_3S^+ + e$. Note the similarity in structure between curves (a) and (b), and the much lower "background" above 1340 Å in curve (a).

compares the photoion yield curve of CD_3S with the region of the m/e = 47 curve obtained during the $F+CH_3SH$ experiments and attributed to CH_3S. The two curves are very similar, hence confirming the initial inference. The adiabatic IP of CD_3S is 9.268± 0.005 eV (≡1337.8±0.7 Å), whereas the Franck-Condon active frequency in CD_3S^+ has a value of 730±60 cm^{-1}. Figure VI-3 depicts the photoion yield curve of CD_2SH, also obtained by starting from the deuterated sample. This curve does not have any steplike growth in the shorter wavelength region, again confirming the earlier inference. Apart from this difference, its shape is very similar to that of its nondeuterated counterpart, CH_2SH. The adiabatic IP of CD_2SH is 7.522 ± 0.003 eV (≡1648.3 ± 0.7 Å), and the active frequencies have magnitudes of 900 ± 40 cm^{-1} and 490 ± 40 cm^{-1}.

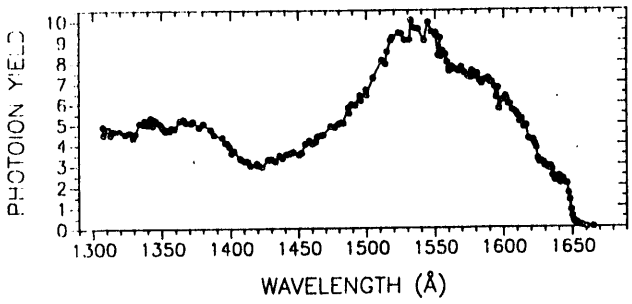

Figure VI-3. The photoion yield curve of m/e = 49, monitored during the reaction of F atoms with CD_3SH. This curve is attributed to the process $CD_2SH + h\upsilon \rightarrow CD_2SH^+ + e$.

3. CH_2S and HCS

The photoion yield curve of CH_2S (Figure VI-4a) has a very abrupt threshold, indicating very little change in geometry upon ionization. The adiabatic IP of CH_2S is 9.376 ± 0.003 eV (≡1322.3 ± 0.4 Å). The prominent steplike onset of the 0 → 0 transition is followed by a much smaller step, corresponding to the 0→ 1 transition. Their energy separation, ~1050 ± 80 cm^{-1}, indicates that the C-S stretch in CH_2S^+ has essentially the same value as in CH_2S, whereas the ratio of their intensities indicates (by Franck-Condon analysis) that the C-S bond length changes by only 0.03 Å upon ionization. Above the threshold, the photoion yield curve displays a smooth plateau that at shorter wavelength starts displaying autoionizing peaks. These peaks correspond to vibrational components of nd and/or ns and np Rydberg members converging to the $\tilde{A}$ and $\tilde{B}$ states of CH_2S^+.

Figure VI-4b shows the HCS^+ fragment yield curve from CH_2S. The AP of this fragment, important in determining the related thermochemistry, is ≤11.533 ± 0.021 eV (at 0 K).

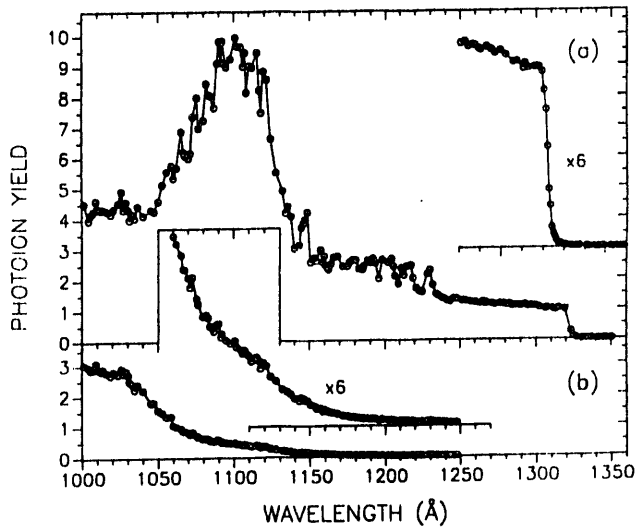

Figure VI-4. Photoion yield curves of CH_2S obtained by pyrolysis of CH_3SCl at 370 °C. (a) Parent CH_2S^+. (b) Fragment HCS^+. The magnified inset in (b) shows two linear regions (1060-1085 Å and 1085-1120 Å) and a long exponential tail.

Unlike the abrupt threshold of CH_2S, the photoion yield curve of HCS (Figure VI-5) has a very broad Franck-Condon region, consistent with a transition from bent HCS to linear HCS^+. The underlying staircase structure, complicated by the presence of autoionizing peaks, indicates that the bending frequency in HCS^+ is 700 ± 30 cm^{-1}. When the Franck-Condon envelope is as expanded as in this case, it is quite possible that the probability of the 0 → 0 transition is vanishingly small and thus virtually unmeasurable. Rather than relying on the apparent threshold in the experimental curve, we undertook a careful analysis of the measured Franck-Condon distribution and concluded that IP(HCS) is ≤7.499 ± 0.005 eV, and possibly one vibrational quantum lower, 7.412 ± 0.007 eV. The analysis also indicates that the bond angle in HCS is ~130°-135°.

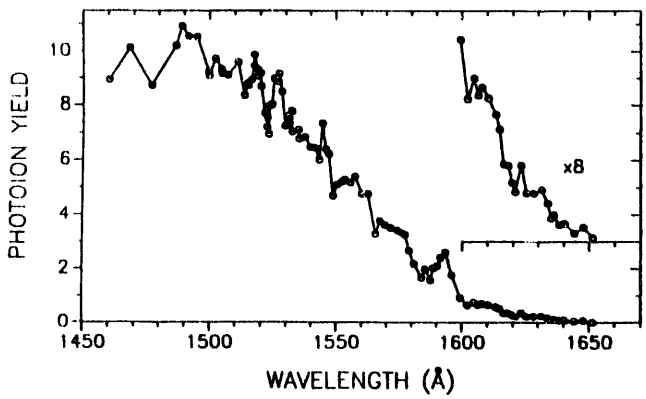

Figure VI-5. Photoion yield curve of HCS^+ from HCS, obtained during F + CH_3SH reactions, presumably by sequential H abstraction.

4. The Fragmentation Thresholds of CH_3SSCH_3

In order to provide independent data that would enable us to determine the pertinent thermodynamic quantities just discussed, we examined the photodissociative ionization of CH_3SSCH_3. In a narrow energy region, four new fragmentation channels become possible, each having a different m/e as signature: $CH_2S^+ + CH_3SH$ (m/e = 46), $CH_2SH^+ + CH_3S$ (m/e = 47), $CH_3SH^+ + CH_2S$ (m/e = 48), and $CH_3SH_2^+ + HCS$ (m/e = 49). The related photoion yield curves display pronounced curvature near their respective thresholds and are subject to substantial kinetic shifts, which make their APs unreliable for use in thermochemical determinations. However, measuring the *relative* energy differences, by shifting one fragment curve along the wavelength axis until it is superposed on another, circumvents this limitation, and provides valuable thermodynamic relations. Thus, for example, the hypothetical reaction $CH_2S + CH_3SH^+ \rightarrow CH_3S + CH_2SH^+$ is found to be (at 0 K) thermoneutral (0.0 ± 0.7 kcal/mol), whereas $CH_2S^+ + CH_3SH \rightarrow CH_2S + CH_3SH^+$ is found to be endothermic by 1.3 ± 0.6 kcal/mol. The latter is a charge transfer reaction, whose enthalpy can be readily calculated from IP(CH_3SH) and our IP(CH_2S) to be 1.48 ± 0.08 kcal/mol, in very good agreement with the above measurement.

5. Thermochemistry of the CH_nS Species

From the adiabatic IPs of CH_3S and CH_2SH and auxiliary data (AP of CH_2SH^+ from CH_3SH measured previously in this laboratory, and an independent ΔH_f° of CH_3S), we have determined the heats of formation of these species and of their cations. We find that CH_3S is more stable than CH_2SH by 6.3 ± 2.0 kcal/mol, and hence $D_o(H\text{-}CH_2SH)$ = 92.4 ± 2.0 kcal/mol (≤94.0 ± 0.1 kcal/mol) is stronger than $D_o(H_3CS\text{-}H)$ = 86.1 ± 0.6 kcal/mol by the same quantity. However, CH_2SH^+ is more stable than CH_3S^+ by 33.5 ± 2.0 kcal/mol. This latter value is in agreement with a recent ab initio calculation, but in strong disagreement with other recently published experiments. A careful analysis of the latter experiments shows that they have been seriously flawed; $\Delta H_{f_o}^\circ$ (CH_3S) and $\Delta H_{f_o}^\circ$ (CH_3S^+) were placed too high by ~3-4 kcal/mol, whereas $\Delta H_{f_o}^\circ$ (CH_2SH^+) was placed too low by 5-7 kcal/mol.

The measurements performed on CH_2S and HCS, together with those on CH_3SSCH_3, enable us to determine $\Delta H_{f_o}^\circ$ (CH_2S) = 28.3 ± 2.0 kcal/mol (≤29.9 ± 0.9 kcal/mol) and $\Delta H_{f_o}^\circ$ (HCS) = 71.7 ± 2.0 kcal/mol (≤73.3 ± 1.0 kcal/mol, ≥69.7 ± 2.0 kcal/mol), as well as the heats of formation of CH_2S^+ and HCS^+.

Our heats of formation of the CH_nS species, together with auxiliary data, enable us to calculate most of the C-H, S-H, and C-S bond energies within this system and observe some interesting trends. For example, the values of C-S bond energies indicate that this is a single bond in CH_3SH, CH_3S, and CH_2SH (with a bond order slightly higher than one in the latter case), it becomes double in CH_2S and HCS, and corresponds to a triple bond in CS. Also, starting from CH_3SH, the successive C-H (and S-H) bond energies oscillate between a high and a low value, because every second dissociation is accompanied by the strengthening of the C-S bond.

All of the heats of formation and IPs of the CH_nS transient species determined by us experimentally are in excellent agreement with recent ab initio calculations.

B. Photoionization Studies of Arsenic Clusters

A major problem in studies of clusters of neutral species is the preparation of a specific cluster, in the absence of other clusters. This can be very important if detection is performed by ionization, because fragmentation of a cluster ensemble could make the desired cluster appear at a lower mass-to-charge ratio (m/e), whereas a higher cluster may appear at the anticipated m/e. Certain strongly bound clusters are naturally occurring, particularly those of Group IV (C_n, Si_n, Ge_n), Group V (P_n, As_n, Sb_n), and Group VI (S_n, Se_n, Te_n). By adjusting thermochemical activities of precursors, it is possible to make a specific cluster dominant in the vapor. We have undertaken such a study of the Group V species. In addition to their intrinsic interest, such studies may have practical benefits. For example, it has been found that higher quality crystals of GaAs are formed when the arsenic vapor contains As_2, rather than As_4.

Our initial studies, with the arsenic species, are outlined below.

Photoionization Mass Spectrometric Study of As_4

When solid arsenic is sublimed, the dominant vapor species is As_4. This species, like its isovalent analog P_4, has tetrahedral structure. The uppermost occupied orbitals, $(a_1)^2(t_2)^6(e)^4$, represent the molecular interaction of three p-type electrons per atom. Ionization from either of the two uppermost occupied orbitals subjects the molecular ion to Jahn-Teller distortion from the tetrahedral structure. This, in turn, is expected to lead to an extended Franck-Condon distribution.

The photoion yield curve of As_4 is shown in Figure VI-6. Three broad autoionizing bands can be seen near threshold. These are attributed to Rydberg members of a series converging to the second excited state ($\tilde{B}\ ^2A_1$) of As_4^+, which does not suffer Jahn-Teller distortion. The photoion yield curve of As_4^+ (As_4) approaches the background level gradually, at ~1440-1460 Å. At the extreme, this implies an *apparent* adiabatic threshold of ~8.49 eV. Analysis of the photoelectron spectrum of As_4, by Jahn-Teller modeling, has led others to predict that the true (but unobserved) adiabatic threshold is 7.83 eV. Our result is a rigorous upper limit; determination of the "true" adiabatic IP awaits a different type of experiment, such as charge exchange bracketing.

In Figure VI-6, the photoion yield curves of the various As_n^+ (n = 1-3) fragments are also shown. Of these, the lowest energy and most thermochemically reliable one is that of As_3^+ (As_4). The threshold, reduced to 0 K, gives an AP of ≤11.23 eV, from which we calculate $\Delta H^\circ_{f_0}(As_3^+)$ ≤228.7 ± 1.3 kcal/mol.

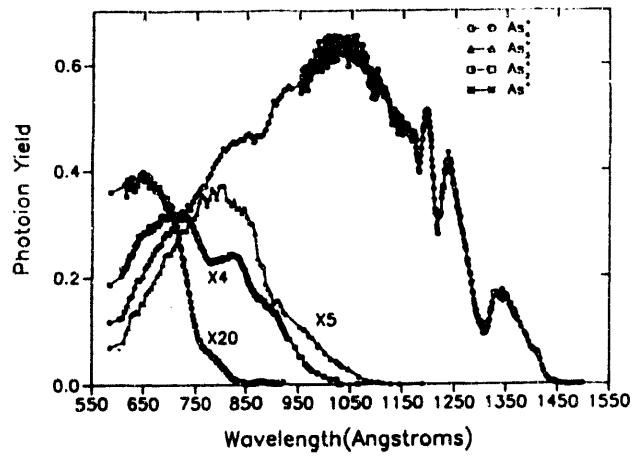

Figure VI-6. An overview of the photoion yield curves of As_4^+, As_3^+, As_2^+, and As^+ from As_4. The ordinate is in arbitrary units, but the relative intensities are significant.

By volatilizing the compound InAs, we can shift the equilibrium among the As_n species so that As_2 dominates. The valence electronic configuration of As_2 is $(\sigma_g 4s)^2(\sigma_u 4s)^2(\sigma_g 4p)^2(\pi_u 4p)^4$. This is identical to that of P_2, and similar to that of N_2, except that the order of $\sigma_g 4p$ and $\pi_u 4p$ is reversed. The photoion yield curve of As_2 (Figure VI-7) displays two autoionizing Rydberg series (one about twice as intense as the other), both converging to the excited ($A^2\Sigma_g^+$) state of As_2. From the Rydberg formula, we can deduce a precise value for this IP, 10.238 ± 0.002 eV. An analysis of the threshold region leads to an adiabatic IP, corresponding to formation of $X^2\Pi_{u,3/2}$ of As_2^+, of 9.69 ± 0.02 eV. Finally, a deeper lying window resonance series (see section C., below) enables us to establish the IP of the second excited state, $B^2\Sigma_u^+$, to be 15.37 eV.

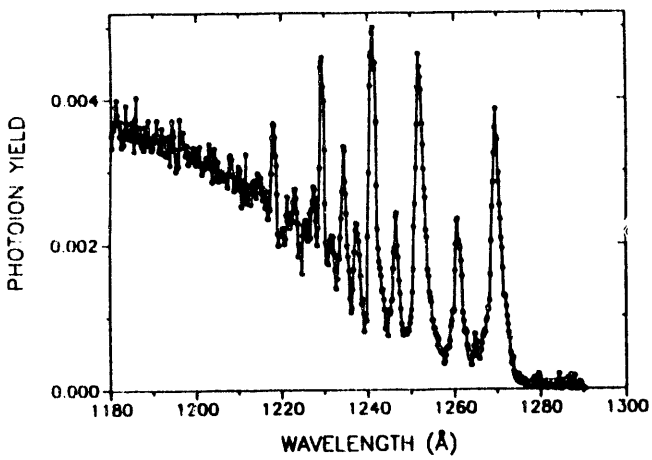

Figure VI-7. The photoion yield curve of $As_2^+(As_2)$ in the region near threshold. Two autoionizing Rydberg series ("short" and "tall") are observed, converging to the excited $A^2\Sigma_g^+$ state of As_2^+.

The heats of formation of As_2 and As_4 are well established by prior measurements. However, evidence for As_3 is ephemeral. We did not observe convincing evidence for its presence in the vapor, under various conditions. However, we were able to establish a lower limit to $\Delta H^\circ_{f_0}(As_3)$. Consider the hypothetical reaction in the gas phase

$$As_2 + As_4 \rightarrow 2As_3 .$$

By determining the photoionization intensity of $As_2^+(As_2)$ and $As_4^+(As_4)$ in the equilibrium vapor, and an upper limit to $As_3^+(As_3)$, we can determine an upper limit to the equilibrium constant,

$$K_{eq} = \frac{(As_3)^2}{(As_2)(As_4)} ,$$

and hence a lower limit to ΔF° for this reaction. This value, together with the entropy change (or equivalently, the change in free-energy function), leads to a lower limit for $\Delta H^\circ_{f_0}(As_3)$. The entropies of As_2 and As_4 are readily calculated, but that for As_3 is problematic. The structure of the isovalent N_3 is linear, and prior workers had assumed that P_3, As_3, etc., are also linear. However, recent ab initio calculations had indicated that these latter species had triangular structures, deviating from equilateral by (weak) Jahn-Teller distortion. We assumed such a structure, and used scaled internuclear distances and vibrational frequencies to deduce $S^\circ(As_3)$. After completion of our work, we learned that Balasubramanian et al. [J. Chem. Phys. 95, 3494 (1991)] had calculated spectroscopic parameters similar to our assumed ones. The results of our analysis lead to $\Delta H^\circ_{f_0}(As_3) \geq 60.0$ kcal/mol, and (from another analysis) $\Delta H^\circ_{f_0}(As_3) \approx 63$ kcal/mol. This, in turn, leads to an atomization energy for As_3 of 143.4 kcal/mol, substantially larger than the ab initio value of Balasubramanian et al., 122 kcal/mol. For these heavy systems, one expects that geometrical structures may be calculated fairly well, but bond energies, reflecting small differences in large quantities, are less reliable.

From our limit $\Delta H^\circ_{f_0}(As_3^+) \leq 228.7$ kcal/mol and the deduced value for $\Delta H^\circ_{f_0}(As_3)$, we can arrive at IP $(As_3) < 7.32$ eV and ≤ 7.19 eV. The ab initio calculated value of Balasubramanian et al. is 7.1 eV. Thus, although we were unable to detect As_3 directly, we have arrived at very useful thermochemical values for this species. The combined results of this study have enabled us to make constructive criticisms of recent work on the clusters of As_n, Sb_n, and Bi_n that were performed by supersonic expansion and photoionization with laser or synchrotron radiation.

C. On s-like Window Resonances

Usually, resonances in photoionization are observed as peaks superposed upon a continuum, heralding a new channel. The interaction of this new channel with the underlying continuum can occasionally result in a *diminution* in the continuum intensity at the resonance, which is referred to as a window resonance. In our recent studies of As_2 (section B), we observed such a window resonance series, attributed to the transitions

$$...(4s\sigma_g)^2(4s\sigma_u)^2(4p\sigma_g)^2(4p\pi_u)^4\ As_2 + h\upsilon \rightarrow$$
$$...(4s\sigma_g)^2 4s\sigma_u(4p\sigma_g)^2(4p\pi_u)^4\ ns .$$

Earlier, we had observed window resonances in the photoionization of atomic As. Both series of window resonances are displayed in Figure VI-8. In atomic As, the window resonances can be identified with the transitions

$$(core)(4s)^2(4p)^3 + h\upsilon \rightarrow (core)4s(4p)^3mp.$$

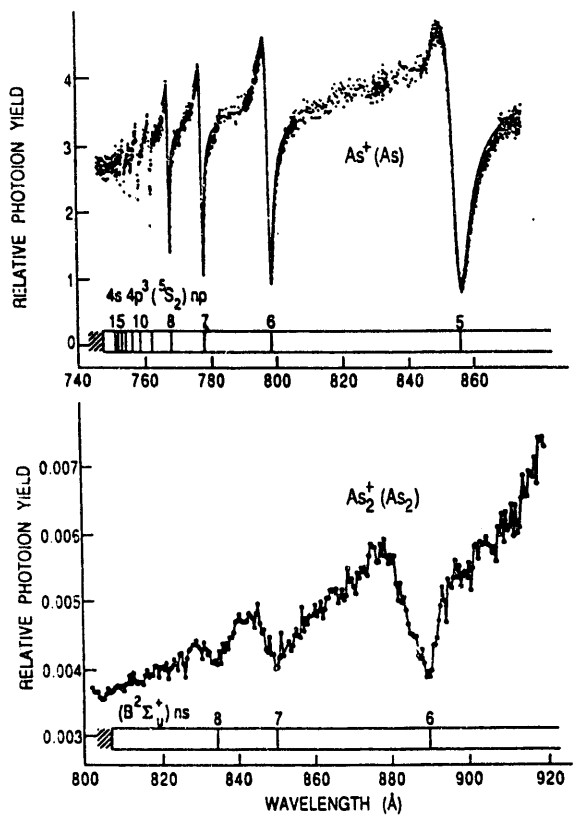

Figure VI-8. Upper panel: window resonances corresponding to the transitions $...(4s)^2(4p)^3 + h\upsilon \rightarrow ...4s(4p)^3mp$ in atomic As. Lower panel: window resonances corresponding to the transitions $...(4s\sigma_u)^2(4p\sigma_g)^2(4p\pi_u)^4 + h\upsilon \rightarrow ...4s\sigma_u(4p\sigma_g)^2(4p\pi_u)^4ns$ in As_2.

Thus, in both As, where excitation from a 4s orbital is implicated, and in As_2, where the ns electron has been excited from a $4s\sigma_u$ orbital, the less frequently encountered window resonance appears to have a similar origin. Upon further research, this behavior was seen to be systematic. Thus, the corresponding spectra of P and P_2, previously studied, also display these window resonances. Similar resonances emanating from the uppermost s-like occupied orbitals are known in the noble gases, the halogen and chalcogen atoms.

Fano has parameterized the interaction of excited, quasidiscrete states with the underlying continuum by the equation

$$q = \frac{\langle \Phi | T | i \rangle}{\pi V_E^* \langle \phi_E | T | i \rangle},$$

where $\langle \Phi | T | i \rangle$ describes the transition from the initial state i to the quasidiscrete state Φ (T is a transition operator, which for the present purposes is the electric dipole operation), $\langle \phi_E | T | i \rangle$ describes the transition to a nearby continuum ϕ_E, and V_E^* is the configuration interaction matrix element between quasidiscrete state and continuum. The condition for a window resonance is that $q \approx 0$. For $|q| \approx 1$, an asymmetric profile results, dipping below the continuum level on one side, and enhancing the continuum on the other. For $|q| > 2$, autoionization manifests itself as a peak surmounting the continuum.

Our observations on P, P_2, As, As_2, etc., correspond to q near zero. From the definition of q, a plausible inference is that the numerator, which is related to the oscillator strength (f) for the transition, is very small. In a Rydberg series of transitions, the average oscillator strength, $\Delta f/\Delta E$, merges smoothly into the corresponding continuum, df/dE. In the present case of window resonances, the implication is that ionization from such an s-like orbital also has a low probability. Photoelectron spectroscopic studies bear this out. The summed oscillator strength (excitations plus ionization) is considerably less than what might be expected for a partial sum rule. For an ns shell that is doubly occupied, the f sum would be expected to be 2; for Ne, as a known example, it is ~0.75. Rather complex calculations of a many-body variety have attributed these window resonances in Ne, Ar, and Kr to a strong shielding effect from the outer p shell. This intershell correlation can influence the partial oscillator strength, shifting some of the ns oscillator strength into other shells.

The alkali and alkaline earth elements have no outer p shell, and manifest large oscillator strengths for the first (i.e., intrashell) transition. For example, the well-known Na D line (3s → 3p) has an oscillator strength of 0.97.

The large oscillator strength for this transition in the alkali and alkaline earth elements implies much smaller values for the higher members of the respective series, i.e., 2s → 3p, 4p ... and 3s → 4p, 5p ... This, in turn, can be attributed to the presence of a Cooper minimum somewhere in the region of higher series members, or in the near continuum. The Cooper minimum is a consequence of the cancellation of positive and negative contributions to the dipole matrix element. If this pattern persists in the p-block elements, it could partially explain the low values of the dipole matrix elements implied by the window resonances.

In summary, two effects appear to be operative in the photoexcitation and photoionization of ns subshells. For the noble gases, with complete outer p subshells, there is a shielding effect, which gives rise to asymmetric and/or window resonances, and shifts some of the oscillator strength into other channels. For the alkali and alkaline earth elements, with no outer p subshells, there tends to be a shifting of the oscillator strength into the first ns → np transition. The available experimental data support the view that both effects are present for the intermediate cases. As the outer p shell fills, its shielding of the ns orbital increases (greater intershell correlation) and the strength of the intershell transition decreases.

Similar arguments can be given for the behavior of $ns\sigma_u$ molecular orbitals. An interesting distinction exists between the behavior of first full-row elements (N, O, F, Ne) and their heavier analogs, both atoms and molecules. The former display asymmetric resonance profiles ($|q| = 1$-2) whereas the latter are closer to pure windows ($q \sim 0$). We attribute this distinction to the fact that 2s and 2p orbitals are close in energy, and occupy similar regions of space, more so than the 3s-3p and 4s-4p combinations. Presumably, this makes the shielding not quite as effective in the first row elements.

D. Three Laws for $D_o(BiF)$

In 1984, Herbelin and Klingberg reacted $NF(a^1\Delta)$ with bismuth atoms, in a search for an efficient pathway for converting the stored electronic energy of NF into laser light. During the course of these studies, they observed an intense blue flame that was identified as the BiF (A → X) emission system. They developed a kinetic model for the processes leading to light emission, which "... appears to approach 100% efficiency in converting the electronic energy stored in NF ($a^1\Delta$) into a blue-green (A-X) emission," making this system an interesting candidate as a basis for developing a visible chemical laser."

The feasibility of utilizing BiF for this purpose depends upon its stability. Most early work up to 1981 favored a value of $D_o(BiF)$ hovering around 3 eV, whereas two recent experimental studies provide evidence for $D_o(BiF)$ near 5 eV. Another recent experimental study infers $D_o(BiF) \leq 3.14$ eV, whereas an ab initio calculated value by Balasubramanian yields 2.63 eV.

We have applied the three laws of thermodynamics in independent experiments to determine $D_o(BiF)$. They are as follows:

1. Conservation of Energy. We prepare BiF in the gas phase, and determine the AP of Bi^+ from BiF by photoionization mass spectrometry. Because the IP of atomic Bi is well known, we can subtract this quantity (7.28562 ± 0.00004 eV) from the AP ($\leq 10.98_2 \pm 0.05$ eV) to deduce $D_o(BiF) \leq 3.84 \pm 0.05$ eV.

2. The Equilibrium Constant, and its Variation with Temperature. We prepare BiF in the vapor phase by volatilizing a mixture of Bi and BiF_3. In the vapor, we can detect Bi, BiF, and BiF_3 by photoionization mass spectrometry. The wavelengths for photoionization are so chosen that the ions observed can only be attributable to parent (rather than fragment) ions. A minor exception is that BiF_2^+ is chosen as the diagnostic for BiF_3, because it is a much more abundant ion, but no confusion can result from this choice. We then formulate the equilibrium reaction

$$2Bi_{(g)} + BiF_{3(g)} \rightarrow 3BiF_{(g)} \ .$$

The equilibrium constant for this reaction is independent of pressure. It is proportional to the ion intensities $(BiF^+)^3/(Bi^+)^2(BiF_2^+)$. We determine the value of this quantity as a function of temperature, and then plot ln K_{eq} vs. 1/T. From the slope of this function, we obtain a value of $\Delta H_T = 10.1 \pm 5$ kcal/mol for the above reaction at the mean experimental temperature, or $\Delta H_o = 11.4 \pm 5$ kcal/mol. Then, with known values for $\Delta H^\circ_{f_o}(Bi)$ and $\Delta H^\circ_{f_o}(BiF_3)$, we deduce $D_o(BiF) = 3.76 \pm 0.13$ eV.

3. The Third Law: Absolute Equilibrium Constant, Absolute Entropy. The photoionization cross section is dependent upon wavelength. In particular, it is a rapidly varying function in the vicinity of resonances. In the present work, we eschew these resonances. The cross section is also related to the size of the atom (or molecule), because it is connected to the total integrated oscillator strength (equal to the number of electrons), and also to the polarizability, which increases with the size of the species. The form of the equilibrium constant discussed above tends to

cancel these variations. The number of molecules appearing in the numerator is the same as in the denominator. Therefore, only relative cross sections are important. The smallest and largest species appear in the denominator, the intermediate sized one in the numerator, thus allowing for the possibility of further compensation in error. More detailed arguments can be given. If we nevertheless allow for an uncertainty of a factor 100 in the equilibrium constant (roughly equivalent to an uncertainty of a factor 3 in the relative cross section of BiF, compounded with an uncertainty of a factor 2 for Bi), the uncertainty in $\Delta F^\circ = -RT\ln K_{eq}$ is only ±0.13 eV. When the value of ΔF° (5.77 kcal/mol) is combined with the absolute free energy functions for Bi, BiF, and BiF_3, we obtain ΔH_0 = 12.39 kcal/mol for the equilibrium reaction, or $D_0(BiF) = 3.76 \pm 0.13$ eV.

Thus, all three laws of thermodynamics yield very nearly the same result in our measurements. The flaws in prior measurements are discussed in our paper. In particular, various Birge-Sponer extrapolations have been attempted, with widely varying results. However, a modification that has been proposed that allows for the degree of ionicity in the molecule yields a result in good agreement with the present value when applied to BiF.

We have also succeeded in determining a value for $\Delta H^\circ_{f_0}(BiF_2)$ from a study of the equilibrium reaction $Bi_{(g)} + BiF_{2(g)} \rightarrow 2BiF_{(g)}$. Thus, we conclude that $D_0(FBi\text{-}F) = 3.50 \pm 0.15$ eV and $D_0(F_2Bi\text{-}F) = 4.5_1 \pm 0.2$ eV.

During the above measurements, we also obtained $IP(BiF) = 8.658 \pm 0.012$ eV, and $IP(BiF_2) = 8.05 \pm 0.05$ eV. No prior values are known.

E. Additional Studies of Group V Clusters

Studies of the Sb_n and Bi_n (n = 1-4) species are in progress. One of the purposes is to test some of the patterns predicted from studies of other related systems. For example, we want to look for window resonances in Sb, Sb_2, Bi, and Bi_2. Bismuth is interesting because it is heavy enough to manifest some departures from the lighter elements of Group V, possibly due to relativistic effects, and also because an L-S description of coupling is less likely to be valid. The ground state of all Group V atoms is ^4S. For the corresponding atomic ions with a p^2 configuration, the possible L-S states are ^3P, ^1D, and ^1S. Rydberg states formed by adding a Rydberg electron to the latter ion cores can give rise to quartet (from ^3P) and doublet (from ^1D and ^1S) states. In the atoms N, P, and As, no evidence is observed for quartet → doublet transitions. In Bi, it may be possible. A photoabsorption measurement claims to observe these transitions. We now have preliminary information in the window resonance region, demonstrating the presence of more than one series, and peak profiles that look more like asymmetric resonances than "pure" windows.

The vaporization behavior of Bi differs from that of P, As, and Sb. The tetramer species, dominant in the latter, is very weak in Bi. Instead, Bi and Bi_2 are approximately equally abundant, with Bi_3 and Bi_4 about two orders of magnitude weaker. Other methods have consequently provided little information on Bi_3 and Bi_4. A recent synchrotron radiation study of these species observed almost no signal above the noise level. By contrast, we have obtained preliminary photoion yield curves for both Bi_3 and Bi_4. We believe this to be the first direct photoionization study of any of the triangular Group V trimers.

PUBLICATIONS

PHOTOIONIZATION MASS SPECTROMETRIC STUDIES OF THE COMBUSTION INTERMEDIATES CH_2OH AND CH_3O

B. Ruščić and J. Berkowitz

Preprints of Papers, Division of Fuel Chemistry, 202nd American Chemical Society National Meeting, New York City, August 25-30, 1991, Vol. 36, pp. 1571-1575

PHOTOIONIZATION MASS SPECTROMETRIC STUDY OF CH_3OF

B. Ruščić, E. H. Appelman, and J. Berkowitz

J. Chem. Phys. 95, 7957-7961 (1991)

VACUUM ULTRAVIOLET PHOTOIONIZATION MASS SPECTROMETRIC STUDY OF C_{60}
R. K. Yoo*, B. Ruščić, and J. Berkowitz
J. Chem. Phys. 96, 911-918 (1992)

PHOTOIONIZATION OF As_2 AND As_4: IMPLICATIONS FOR GROUP V CLUSTERS
R. K. Yoo*, B. Ruščić, and J. Berkowitz
J. Chem. Phys. 96, 6696-6709 (1992)

PHOTOIONIZATION MASS SPECTROMETRIC STUDIES OF THE ISOMERIC TRANSIENT SPECIES CH_2SH AND CH_3S
B. Ruščić and J. Berkowitz
J. Chem. Phys. 97, 1818-1823 (1992)

SUBMISSIONS

ON s-LIKE WINDOW RESONANCES IN SOME ATOMS AND HOMONUCLEAR DIATOMIC MOLECULES
J. Berkowitz, B. Ruščic, and R. K. Yoo*
Comments on Atomic and Molecular Physics (1991)

THREE LAWS FOR D_0 (BiF)
R. K. Yoo*, B. Ruščic, and J. Berkowitz
Chem. Phys. (1992)

PHOTOIONIZATION MASS SPECTROMETRY OF CH_2S AND HCS
B. Ruščic and J. Berkowitz
J. Chem. Phys. (1992)

PHOTOION PAIR FORMATION
J. Berkowitz
VUV and Soft X-Ray Photoionization Studies, U. Becker and D. A. Shirley, Eds., Plenum Press

VALENCE IONIZATION PROCESSES IN THE VUV REGION
J. Berkowitz
VUV and Soft X-Ray Photoionization Studies, U. Becker and D. A. Shirley, Eds., Plenum Press

---

COLLABORATIONS

J. A. Pople, Carnegie-Mellon University, Pittsburgh, PA
L. A. Curtiss, Chemical Technology Division, Argonne National Laboratory
K. Balasubramanian, Arizona State University, Tempe
D. Yarkony, Johns Hopkins University, Baltimore, MD
Our collaboration with Pople and Curtiss continues to be mutually beneficial. In the past year, they have calculated by G2 theory the properties of the CH_nS species that we have investigated experimentally. Balasubramanian has the capability of calculating the properties of heavy atoms and molecules, including relativistic effects. He calculated the properties of the Group V trimers coincidentally at the time we were performing some experiments. Now, he has decided to examine the dimers and tetramers more extensively, to compare with our experimental results. Yarkony is continuing to examine the peculiar case of CH_3O^+, which is unstable on our experimental time scale although CD_3O^+ is stable.

---

*Not affiliated with the Chemistry Division or affiliated on a temporary basis.

VII. CHARACTERIZATION AND REACTIVITY OF COAL AND COAL MACERALS

R. E. Winans, K. B. Anderson, C. A. A. Bloomquist, R. E. Botto, K. A. Carrado, K. Chatterjee, D. E. Drinkwater, G. R. Dyrkacz, D. L. French, R. Hayatsu, J. E. Hunt, R. L. McBeth, P. E. Melnikov, J. V. Muntean, J. Nicholas, L. Ruscic, R. G. Scott, L. M. Stock, P. Thiyagarajan, S. R. Wasserman

Outside Collaborators: *S. L. Dieckman, N. Gopalsami, M. L. Gorbaty, J. T. Joseph, G. Keldsen*

Our research in the physical separation, chemical degradation, and instrumental characterization of coal provides new insights into its molecular structure. Coal's heterogeneous structure adversely influences its reactivity, thereby complicating processing technologies for the production of usable, high-quality fuels and chemical feedstocks. Therefore, we have been systematically studying physical methods for the separation of coal into its fundamental organic constituents (macerals) to reduce heterogeneity. Furthermore, chemical degradation methods are coupled with structural and spectroscopic measurements, such as synchrotron radiation, solid-state NMR spectroscopy and imaging, laser desorption time-of-flight mass spectrometry, and high-resolution tandem mass spectrometry, to probe coal structural elements, in particular large molecular building blocks. Research on the synthesis and characterization of large-pore, layered-clay catalysts for heavy hydrocarbon upgrading is also underway with specific information being gained from neutron and X-ray scattering. All the coal work focuses on the Argonne Premium Coal Samples, whose characteristics are given in Table VII-1.

Major achievements during the past year include the discovery that a vast majority of middle-size molecules in bituminous coals contain at least one heteroatom, and that molecules with several heteroatoms are very abundant in the lower rank coals. A new, comprehensive classification system for resinites that evaluates the extent of coalification is presented. New insights about coal structures have been gained through laser mass spectrometric techniques. The first 3-D NMR images of a solvent-swollen coal have been obtained. More accurate f_a values have been determined by solid ^{13}C NMR. Selective removal of organic sulfur has been quantitated using synchrotron X-ray spectroscopy (XAS) in collaboration with Gorbaty. Finally, new synthetic layered silicate clays have been prepared in the presence of many templating molecules, including transition-metal complexes and organic dyes, and the manner in which metal ions are solvated in clays has been elucidated by XAS.

Table VII-1. Elemental analyses for the coal samples.

		% C	per 100 carbons			
sample	name	(dmmf)	H	N	S	O
8	Beulah-Zap lignite	74.1	79.5	1.35	0.36	20.9
2	Wyodak-Anderson subB	76.0	85.6	1.28	0.23	18.0
3	Herrin hvCB	80.7	77.2	1.51	1.15	13.0
6	Blind Canyon hvBB	81.3	85.7	1.67	0.17	10.8
4	Pittsburgh hvAB	85.0	76.7	1.69	0.40	7.96
7	Lewiston-Stockton hvAB	85.5	76.3	1.62	0.30	8.93
1	Upper Freeport mvB	88.1	66.0	1.55	0.32	6.59
5	Pocahontas lvB	91.8	58.5	1.25	0.21	2.04

A. Separation of Coal Macerals

G. R. Dyrkacz, C. A. A. Bloomquist, L. Ruscic

Despite a long history, efforts to understand coal structure continue to be hampered by its physical and chemical heterogeneity. Coal exhibits physical variations on a submicron scale. Furthermore, the relationship between this physical complexity and the chemical complexity is unclear. One of our major research goals is to develop reliable methods to separate coal into its fundamental constituents. These constituents can then be used in studies of the fundamental chemical and physical structure of coal to yield more detailed and less ambiguous information.

Many factors influence the heterogeneity of coal, including the variety of organic plant materials that were present in the original swamp, the manner in which the materials were degraded and subsequently buried, and variations in metamorphosis. Our primary interest has been the organic components. All of the organic material is present in macerals, which are the analog of minerals in rocks. They represent the primary level of organic heterogeneity, and are characterized by their color, reflectance, and morphology. Each of the three major groups of macerals is subdivided into several individual types. The liptinite maceral group consists of organic material derived from aliphatic materials such as algae, spores, and resins. The vitrinites, which are derived from degraded woody tissues, are the most common macerals in U.S. coals, and are widely used for structural studies of coals. The third maceral group is the inertinites.

Developing efficient methods for separations of these macerals has been one of our primary goals. Our early work pioneered the development of density gradient centrifugation (DGC) techniques. Through our efforts and others who have followed our lead, DGC has become almost a standard for high-resolution maceral separations from coal and oil shale. Recently, we have used DGC techniques to evaluate the more traditional centrifugal sink/float method and the newer continuous flow centrifugation method.

1. Continuous Flow and Centrifugal Sink/Float Separation of Coal Macerals

Density gradient techniques are unequaled in their ability to produce high-resolution separations of coal macerals. In addition, they provide a direct visualization of the density distribution of the coal sample. Unfortunately, DGC techniques are batch methods and usually only small amounts of pure material can be obtained from each separation. Thus, it would be useful to have other separations methods to bypass this problem. The two readily available techniques are traditional centrifugal sink/float (S/F) and continuous flow centrifugation (CFC). The former technique is a batch method, but it can produce a large amount of material in each float/sink operation. Continuous flow centrifugation separations allow large volumes of liquid slurry to be easily processed, and both the float and sink fractions can be continuously separated.

Our experimental studies on these separations methods were reported in previous surveys. This year we have compiled and analyzed the results and contributed four large manuscripts. Our efforts in this area are now complete.

Many of the protocols needed for routine separations of micronized coals have been established. One major contribution centers on the ability to quantitatively understand the course of these separations. We have shown mathematically how sink/float separation intimately depends on the density chosen for the separation and the density distribution of the sample. In addition, we have recognized that both the number of fractionations and size of the density interval between successive separations can have a profound influence on the purity of fractions. The work on CFC separation has been particularly gratifying; this system is very effective for large laboratory-scale separations. However, several subtle elements that are important in the separations are still not fully understood.

In summary, the research at Argonne has established that greater than 85% pure sink or float fractions can be easily achieved. Second, the traditional media used for density separations all cause agglomeration of the particles, and consequently result in inefficient separations, but two media, which are discussed in this study, provided excellent separations — CsCl/Brij-35 and $Ca(NO_3)_2$/Brij-35. There is little doubt that the Brij-35 surfactant plays a major role in the wetting and maintaining of coal-particle dispersions, but the salt also plays a complex role. Third, fine float phase particles were discovered to mix into the sink phase in centrifugal S/F separations. This behavior results from minor variations in temperature and force fields during centrifugation. Particles that

are larger than 10 μm do not exhibit this problem. Fourth, in the continuous flow centrifuge, the centrifugal and flow dynamics of the fluid within the rotor are very complex; some zones in the rotor have little axial flow, while others are not spinning at the nominal rotor speed. Finally, in agglomerating media, different density particles agglomerate in constant proportions. Consequently, recycling only marginally improves the purity of a fraction.

To complete the study, we investigated large particle separations (~30 μm). Large particles should separate more efficiently by virtue of their size and smaller surface-area-to volume ratio. However, S/F and CFC separations of float phases showed purities similar to the much finer micronized coals. These results conflicted with our intuition and the analytical density gradients of float-phase materials. We reasoned that the problem was due to the density gradient monitoring system, which influenced the position of the large particles. Two methods were studied to circumvent this problem. First, we did a preparative-level separation and directly measured the amount of material in each density fraction. The results showed that our intuition was correct: much less contaminating material was observed. Unfortunately, the absolute purity was still uncertain. Therefore, a different approach was tried. The gradient in the centrifuge was photographed, and the gray scale of the negative read using a microphotometer. The results seemed to support the original analytical density gradient data. However, distortions in the photographs may impact this interpretation. Thus, the absolute purity of the large particles is still an open question.

2. Ultraresolution of Coal Macerals and Hyperfine Grinding of Coal

Work has also progressed on a new project to define limits on the heterogeneity of coal. Coal extracts contain hundreds of chemical species, but the complexity of the insoluble macromolecular structure of coal is not clear. The extractable material can be derived from many complex reactions during the metamorphic process, and may not faithfully reflect an underlying regular structure of the macromolecules. In many coals, lignin is the predominant chemical species that is transformed into vitrinite. Lignin itself is a fairly complex three-dimensional macromolecule that is formed by random polymerization from, at most, three simple phenolic starting materials. Even so, the pyrolysis of lignin produces many compounds, a result that masks its underlying simplicity. Because vitrinite is derived mainly from lignin, it is possible that its structure may be more regular than most coal scientists now believe.

There is little doubt that the chemical structure of vitrinite must be more complex than lignin. Some of the lignin must have undergone degradation reactions before burial. The existence of humic acids is good evidence for this. However, vitrinites in coal often show distinct residual cellular structures. This fact suggests that the transformation of lignin to vitrinite occurred by modification of the lignin polymer directly, without extensive macromolecular degradation and repolymerization. One way to phrase the question of the chemical structure of coal is: Does coal contain high-molecular-weight macromolecules, each composed of many different subunits, or does it contain a small set of macromolecules, each with a small set of different subunits? The former case suggests that separation of the microscopic macerals is about the best resolution that could be achieved. The latter case suggests that further liberation and separation of coal macerals may lead to further delineation of coal structure. This question may be difficult to answer under any circumstances, but finer separations of the macerals is an essential first step.

To accomplish higher resolution of coal material, it is necessary to liberate the different macromolecules from each other. Initially we tried to break down the solid coal particles. Starting with a fluid energy mill (FEM) product, we ground the coal to submicron particle sizes, using a high-speed planetary ball mill. Two coals, PSOC-732 from the Pennsylvania State University Coal Bank and APCS 7 from the Argonne Premium Coal Sample program, were studied. Both are high-volatile bituminous coals and both contain all three maceral groups.

We found that large grinding media, such as 1-cm balls, were completely inappropriate. However, 3.2-mm chrome steel balls reduced FEM ground coal to submicron particles within a few hours. As a material is mechanically ground in the impact type mill, curious and complicating phenomena can occur. Particles may agglomerate by a process called cold welding. They may become plastic and no longer shatter on grinding. Chemical changes in the structure may occur, resulting in the formation of new chemical species. Crystalline materials can change to amorphous or different crystal forms. Particles can undergo

densification, either by the elimination of pores or by the formation of new physical structures. All of these processes may occur with coal. All are undesirable side effects.

The quantitation of submicron coal particles is not straightforward. Although we intend to use SEM techniques to quantify the particle-size distribution in the future, for the initial experiments we used an optical microscope to measure relative fineness and found that the particles do become progressively finer with longer grinding time.

If, upon ultrafine grinding, any of the undesirable phenomena noted above were occurring, either the density or surface area would change. Thus, we monitored the density distribution to detect changes in the particles. The initial grinding experiments suggested that the density progressively shifted to higher values with increased time. The shift was discovered to correlate with the introduction of air into the mill. If the samples were simply batch ground without intermittent opening of the grinding bowl, the progressive shift to higher density ceased. All subsequent grinding was performed with degassed solvents in a sealed bowl. We then found that grinding caused a rapid initial shift of the density distribution to a lower density, which then remained nearly constant. At present, we are not certain why the density of the coal decreases. One possible reason is that some pores have become sealed during the grinding process.

Grinding also caused an initial rapid narrowing of the density distribution. However, further grinding showed little subsequent change. Such a change may be indicative of particle accretion (cold welding). For example, Figure VII-1 displays an idealized monodisperse system where each particle can accrete with any other particle in the system. Each cycle represents a perfect inelastic collision between two particles to generate a third particle that will not accrete. The result is a new particle-size distribution, which is then allowed to further accrete in the next cycle. As the number of collision cycles increases there is a narrowing of the original density band, and a shifting of the distribution to the point representing the density of the coal sample. Both coals experimentally exhibited a similar phenomenon in that both the liptinite and inertinite bands were rapidly lost. Surface-area measurements are currently in progress to determine other physical changes.

FTIR work was carried out to detect chemical changes. Both diffuse reflectance and transmission

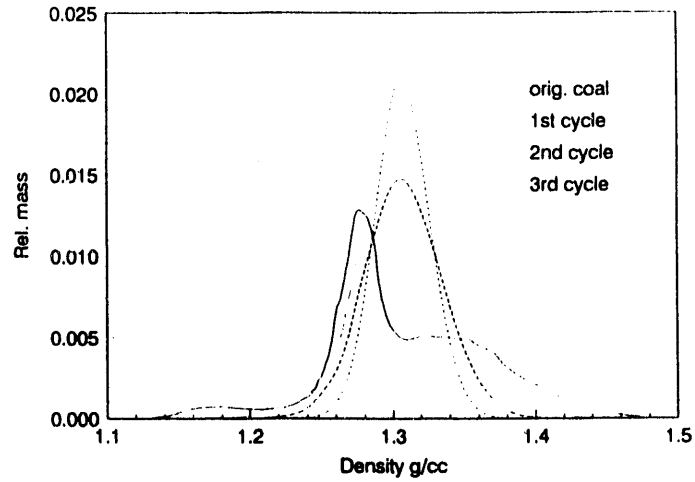

Figure VII-1. Calculation of particle accretion caused by perfect plastic collision of monodisperse particles to form a new composite particle. Each cycle represents single collisions of each particle.

spectroscopy were used. Unfortunately, there were large differences in the baselines between FEM and hyperfine ground material. Diffuse reflectance measurements were less affected by this baseline problem, which is undoubtedly due to particle scattering. When water was used as the grinding medium, there was a definite increase in hydroxyl-group concentration even when the grinding was done in nitrogen. When the coal was ground in heptane, there was no increase in the hydroxyl band. The results suggest that water is reacting with the coal. Such oxidation reactions may be catalyzed by the mill components. Along with the increase in -OH in aqueous media, there were decreases in bands at 1600 cm^{-1}, and in the aromatic deformation modes in the 900-700 cm^{-1} region. The band at 1600 cm^{-1} is believed to be due to C=C stretching bands, enhanced by oxygen substitution. What the significance of these decreased absorptions is in the ground coals is not clear. We are not certain whether the changes constitute some real loss of aromatic character, or are due to changes in the physical structure.

Another interesting finding was that there were few spectral differences between samples ground in air or in nitrogen. This result contrasts with the density information. It may be that the density changes parallel changes in surface properties, or contamination by iron species (from the mill).

Although the particles are becoming smaller, particle accretion is occurring. We are now investigating methods to circumvent this undesirable feature.

B. Characterization of Coals, Other Kerogens, and their Extracts by Thermal Mass Spectrometry

R. E. Winans, P. E. Melnikov, R. L. McBeth, R. E. Botto

The objective of this study is to elucidate the nature of medium-size molecules (250-2000 daltons) derived from coals in extractions of different severity. The Argonne Premium Coals have been extracted with pyridine at reflux and with KOH/ethylene glycol at 250 °C. The results from these extractions and vacuum pyrolysis are given in Table VII-2. Details on how the coals were treated are shown in Scheme VII-1. Thermal desorption and pyrolysis mass spectrometry were the major approaches chosen to provide detailed information on structure and heteroatom composition. Soft ionization techniques, including desorption chemical ionization (DCI) and fast atom bombardment (FAB), were combined with high-resolution and tandem MS techniques. The DCIMS studies were performed on a Kratos MS 50 triple analyzer with isobutane as the reagent gas. The solids and extracts were heated directly in the source of the mass spectrometer on a small platinum wire coil. In addition to the three-sector MS 50, tandem MS data have been obtained on a four-sector instrument located at the University of Manchester, Institute of Science and Technology (UMIST). The four-sector (MS1-MS2) spectrometer is a combination of two Kratos Concept-Hs, each with a 10,000 mass range. The sensitivity in MS-2, where the daughter spectra are obtained, is enhanced by using an array detector.

In this report we shall emphasize the differences in the nature of the unextracted coal, its pyridine extract, and the extracted coal residue. With this approach, the desorption-pyrolysis yields of the extracts and residues combined were greater than the yields from pyrolysis of the starting material. Although molecular-weight distributions exhibited only a minor dependence on rank, the nature of molecules with the same nominal mass varied greatly with rank.

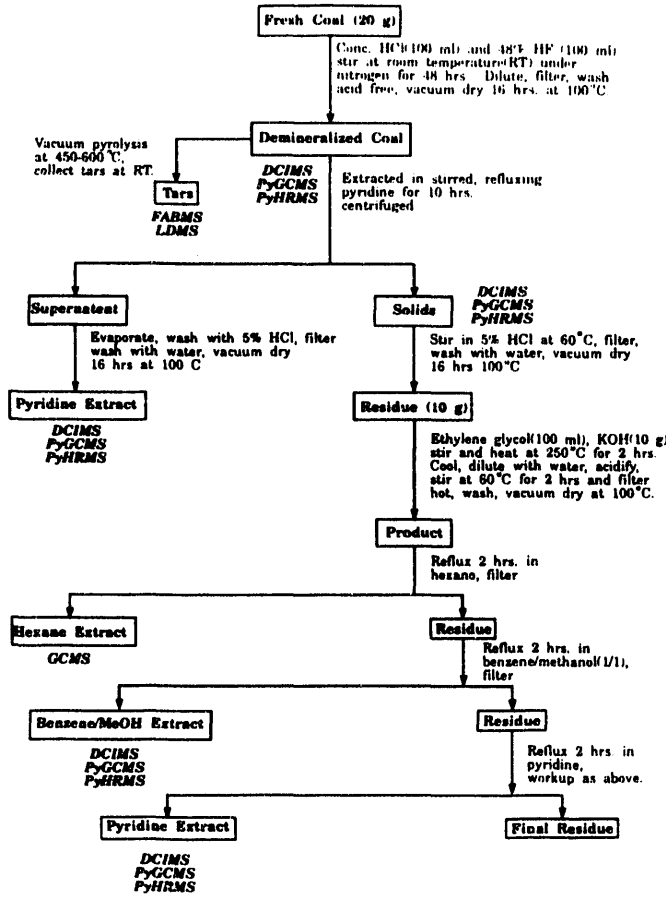

Scheme VII-1

Table VII-2. Yields for the coal samples.

sample	name	yields (wt%, dmmf*) pyridine pyrolysis	pyridine extract	KOH/glycol solubles
8	Beulah-Zap lignite	23.6	17.9	89
2	Wyodak-Anderson SubB	39.3	29.3	88
3	Illinois No. 6	36.8	29.0	77
6	Blind Canyon hvBB	50.2	25.0	73
4	Pittsburgh hvAB	16.2	24.4	39
7	Lewiston-Stockton hvAB	22.9	16.9	32
1	Upper Freeport mvB	14.3	3.6	22
5	Pocahontas lvB	12.1	2.6	4

*Dry-mineral-matter free.

Pyrolysis combined with a variety of mass spectrometric techniques has been used extensively to study coals and separated coal macerals. High-resolution mass spectrometry elucidated the distribution of heteroatoms in vacuum pyrolysis products, and resulted in the discovery of a large number of products containing multiple heteroatoms. Initial results with the DCIMS approach on demineralized and extracted Argonne coals have also been presented.

This study has now been extended to include the pyridine extracts, and tandem MS techniques have been used to elucidate the structure of larger molecules. The secondary reactions that often occur in the pyrolysis have been minimized by focusing on extracts. Most of the Argonne coals contain abundant heteroatoms, which are going to play an important role in their chemistry. The number of aromatic carbon atoms per heteroatom is shown in Figure VII-2. The four lowest rank coals contain more than one heteroatom per six-member ring. Except for the highest rank coal, heteroatom species must be present in most middle-size coal molecules. The current research on the extracts demonstrates this feature.

The results, Table VII-2, indicate that the batch pyrolysis yields and the pyridine extract yields are parallel, except for the Blind Canyon coal (APCS 6). The fact that this coal is rich in liptinites may account for the greater pyrolysis yield. However, the yields of products observed in the DCIMS experiments as a function of time and temperature for the coal and the extract differed significantly. This is shown for the Blind Canyon coal in Figure VII-3. The extract exhibits a much more bimodal character with a significant yield of volatiles at the lower temperatures. This is a general phenomena for all the coals but becomes more pronounced with the higher rank coals. These data suggest that the thermally extractable material may be a subset of the potentially extractable material. In addition, the extracts appear to be more thermally stable than the solids. This may be due to a transport problem because the volatiles in the solid move through the pore structure and can experience secondary reactions. Also, it may be that there is more donatable hydrogen available in the extracts.

In some cases, the extracts yielded higher molecular weight products and a different set of compounds than the whole coal. Figure VII-4 illustrates an example of this result for the Lewiston-Stockton coal (APCS 7). The whole-coal spectrum shows well-defined series at m/z < 250, whereas the extract contains two sets of series of peaks at m/z = 250-400 and m/z = 500-600. The high-mass set is expanded in Figure VII-4b. There are pairs of peaks separated by two mass units and repeating every 14 units (methylene). What is even more interesting is that these products appear across the whole temperature range as is shown in Figure VII-5. Initially, it was thought that these peaks could be a series of M+1 ions resulting from porphyrins, but their unusual nature prompted

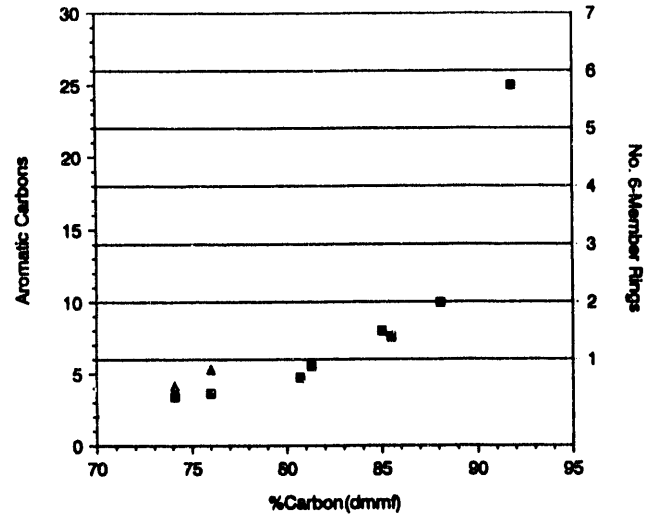

Figure VII-2. Aromatic carbons per heteroatom for the Argonne Premium Coal Samples using the aromaticity values from Table VII-1. Carboxylic oxygens have been substrated for the two low-rank coals (▲).

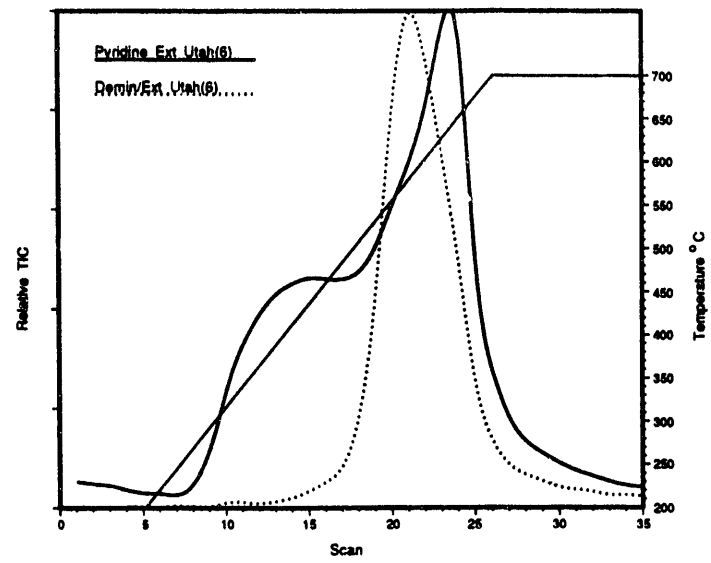

Figure VII-3. Total ion pyrograms for DCIMS of Blind Canyon (APCS 6) pyridine extract and demineralized/ extracted residue.

further investigation by tandem MS. The daughter spectrum of m/z = 535 is shown in Figure VII-6. This fairly complicated spectrum exhibits a large number of aliphatic fragments. It is not a porphyrin or a large polycyclic aromatic compound. There is the possibility that it could be an aromatized terpenoid with the partial structure shown in Figure VII-6 for the fragment at m/z = 255. A very different daughter spectrum is observed for parent ion m/z = 533,

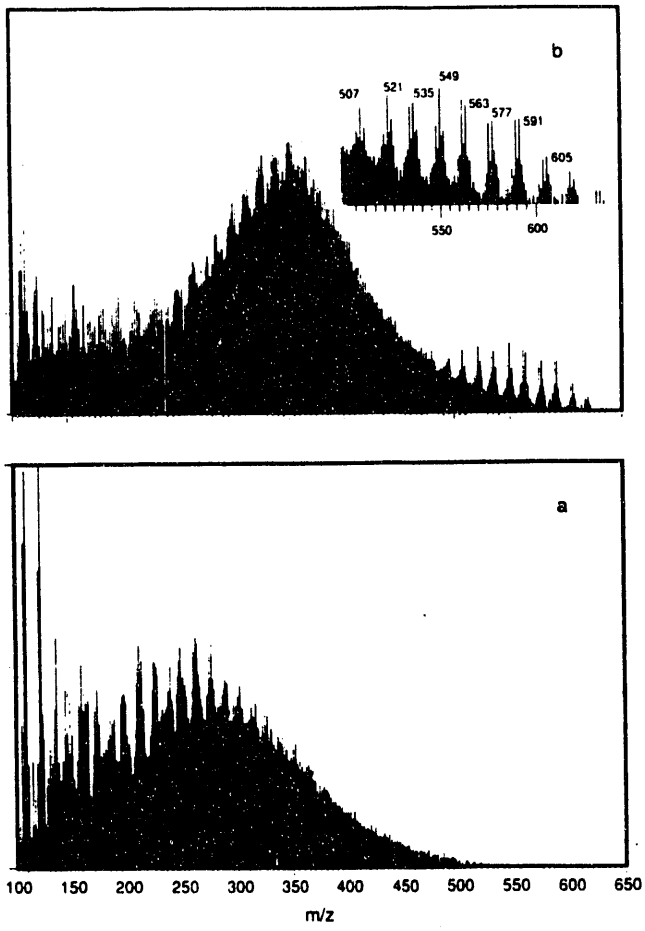

Figure VII-4. Averaged DCI mass spectra for (a) demineralized Lewiston-Stockton coal (APCS 7) and (b) pyridine extract of the same coal.

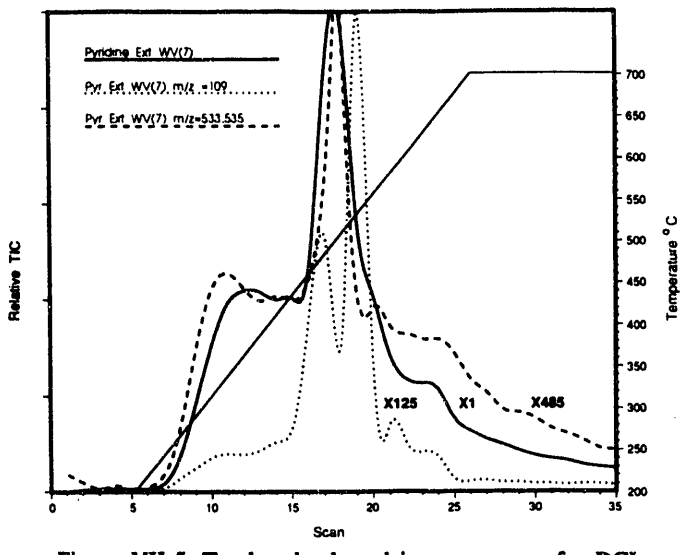

Figure VII-5. Total and selected-ion pyrograms for DCI MS of pyridine extract of Lewiston-Stockton coal (APCS 7): solid - total ion, dotted - m/z = 109, and dashed - sum of m/z = 533, 535.

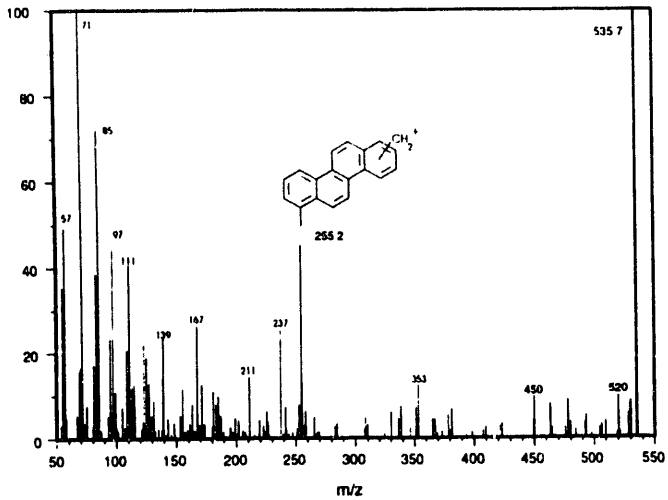

Figure VII-6. Daughter spectrum from parent m/z = 535 from CIMS of pyridine extract from Lewiston-Stockton (APCS 7) taken on UMIST four-sector instrument.

demonstrating that these pairs of peaks are apparently not related. This is the first example of this class of terpenoid biomarker molecules being observed in bituminous coals. Another example of where biomarkers are observed in the extract but not in the pyrolysis of the whole coal is found for the subbituminous coal. In the extract, long-chain fatty acids were observed, but not in the whole coal.

Obviously, the most abundant heteroatom is oxygen. A majority of the molecules identified in the low-rank coals, lignite and subbituminous, contain one or more oxygens. Many of the molecules are similar to the original lignin precursors. The scheme below illustrates the progression in the types of oxygen-containing molecules observed as a function of rank. At the very highest rank coal, the small amount of oxygen that occurs is found in annelated furans. This is observed in tandem MS experiments and is verified by solid ^{13}C NMR results. In Figure VII-7 is shown

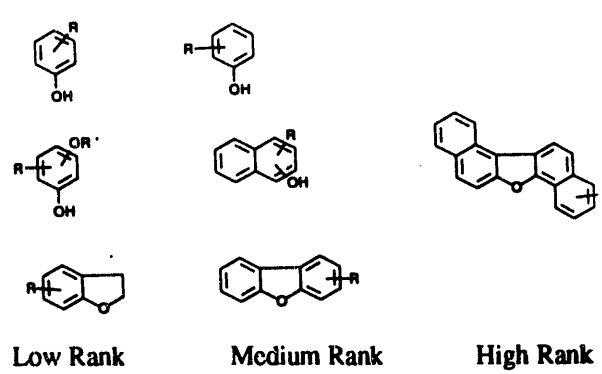

the spectrum for the low-volatile Pocahontas coal (APCS 5). The resonances for furan structure are clearly seen in a fairly simple spectrum.

Another important result is the suggestion from the extract data that large molecules derived from lignin sources are soluble in pyridine. In Figure VII-5, the selected ion (m/z = 109) curve is shown, which represents alkylphenol fragments. The yield at low temperature is small, but as soon as high-temperature pyrolysis begins, these fragments are observed. Initial experiments with the base-solubilized material revealed that the most abundant products in the low-rank coals were C_2 and C_3 alkylphenols derived from lignin. This demonstrates that coals are not simple two-phase systems, rather they contain a continuum of increasing molecular weight species.

These data suggest that future work should place emphasis on the extracts and mild degradation products. Thermally extractable molecules and solvent extractable molecules are almost certain to be different. The discovery of large lignin-derived fragments existing in the pyridine extractables suggests that these extracts may be quite representative of the vitrinite in whole coal.

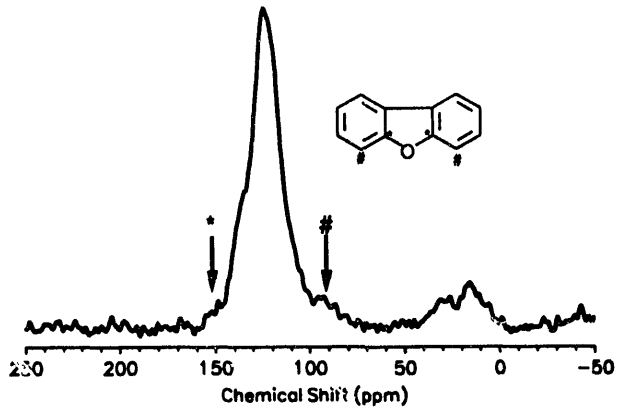

Figure VII-7. ^{13}C solid NMR spectrum of the lv bituminous coal (APCS 5).

C. The Nature and Fate of Natural Resins in the Geosphere. Identification, Classification, and Nomenclature of Resinites

K. B. Anderson, R. E. Winans, R. E. Botto

Sedimentary organic matter derived from the resins of higher plants is normally referred to as resinite by the general petrographic community, or by the common name for these materials, "amber". Most resinites may be classified, on the basis of structural characteristics, into one of four classes. In order to exclude the effects of structural changes that reflect differences in the relative maturity of different samples, classifications are based on the structural character of the original resin from which the resinite was derived. In all samples characterized to date, this may be reasonably inferred from analytical data concerning the structure and composition of the individual sample.

The classification system herein proposed is intended to recognize and delineate the existence of a number of discrete forms of resinite in the geosphere, and to provide a basis for uniform nomenclature of structurally related resinites. The proposed classification system is summarized in Table VII-3. Class I resinites, which are by far the most abundant form of resinite in the geosphere, are derived from resins based primarily on polymers of labdatriene (diterpenoid) carboxylic acids, especially communic or ozic acids. Class II resinites are derived from resins based on polymers of sesquiterpenoid hydrocarbons, especially various isomers of cadinene. Class III resinites are natural polystyrenes. Figure VII-8 is a comparison of total ion chromatograms obtained by pyrolysis of samples of Class Ia, Class II, and Class III resinites, demonstrating the ease of differentiation of these different classes of resinite by Py-GC-MS. No reliable samples of Class IV resinite were available for comparison. Class IV resinites are the least well characterized of the four resinites, but appear to be largely nonpolymeric materials, dominated by sesquiterpenoids based on the cedrane carbon skeleton. Resinites belonging to Class I are further subdivided into three subclasses on the basis of their detailed composition. Class Ia resinites, which include succinite and related "Baltic ambers", are derived from resins based primarily on communic acid and incorporate significant amounts of succinic acid into their macromolecular structure. Class Ib resinites are also derived from resins based primarily on communic acid, but do not contain succinic acid. Class Ic resinites are derived from resins based primarily on labdatrienoic acids of the *enantio* series, especially ozic and/or zanzibaric acids.

Table VII-3. Proposed classification system for resinites.

CLASS I.	**All Class I resinites are derived from resins based on polymers primarily of labdatriene carboxylic acids.**
Class Ia	Derived from resins based primarily on polymers of communic acid (I), partially copolymerized with communol. Significant incorporation of succinic acid, probably as a cross-linking agent is characteristic.
	Examples: succinite (Baltic Amber) and many other (primarily) European ambers.
Class Ib	Derived from resins based primarily on polymers of communic acid (I), with varying degrees of copolymerization with communol. Succinic acid is absent.
	Examples: New Zealand resinites, Victorian Brown Coal resinites, and many others.
Class Ic	Derived from resins based primarily on polymers of ozic acid (IIa) and/or zanzibaric acid (IIb).
	Examples: resinites from Mexico and Dominican Republic, some African resinites (Zanzibar, Kenya).
CLASS II.	**Derived from resins based on polymers of bicyclic sesquiterpenoid hydrocarbons, especially cadinene. Triterpenoid, including disesquiterpenoid component, may also be present, probably mostly as occluded materials.**
	Examples: Utah resinites, some Indonesian resinites.
CLASS III.	**Basic structural character is polystyrene.**
	Examples: some New Jersey resinites, some German resinites (Siegburgite).
CLASS IV.	**Basic structural character is sesquiterpenoid, especially based on the cedrane (IX) skeleton. Apparently nonpolymeric.**
	Examples: Bovey-Tracy retinilite, Ionite, Moravian resinites.

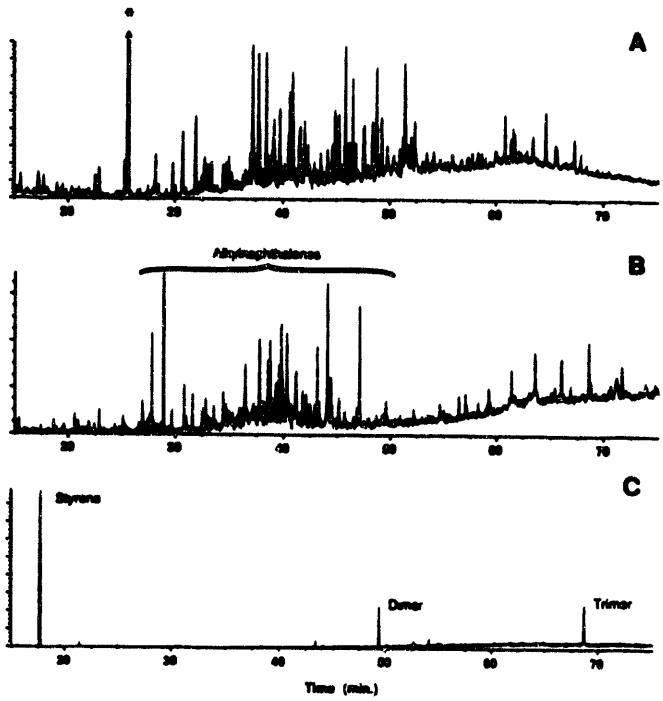

Figure VII-8. Total ion chromatograms. Samples: (A) Class I(a), Bitterfeldite (Germany), T_{py}= 480 °C. * = dimethyl succinate; (B) Class II, Utah resinite (showing abundant alkylnaphthalene isomers, including especially cadinene-derived and related structures); (C) Class III, Sayerville resinite (New Jersey). Data were obtained by using a 60-m DB-1701 capillary GC column at T_{Py} = 540 °C for Utah and Sayerville resinites.

Like all other forms of sedimentary organic matter, the resinites undergo structural systematic changes over the course of geologic time. The rates at which these processes proceed are almost certainly strongly temperature dependent, and, therefore, the structure and composition of any given resinite will depend on: (i) the structure and composition of the original resin from which the resinite is derived; and (ii) the age *and* thermal history of the sample. For this reason, it is inappropriate to describe structural changes in resinites as a function of the "age" of the sample. Rather, it is more appropriate to describe changes in the structure and composition of these materials as a function of their "maturity", which reflects *both* age and thermal history, as is usual in discussions of the structural changes that occur in other types of sedimentary organic matter.

As a consequence of changes in the structures and compositions of resinites due to the effects of maturational "forces", it is not reasonable to develop a classification system for resinites that is based solely on structural or compositional characteristics as they presently occur, as such differences may reflect nothing more than differences in the level of maturity of samples of closely similar origin. We have found however, that even up to quite high levels of maturity, the degree of structural character retained by resinites is sufficient to reasonably establish the

nature of the original resins from which distinct classes of resinites have developed. The classification system described in Table VII-3 is, therefore, based on the principal structural character of the original resin from which any given resinite has been derived.

The most readily apparent effect of maturation on the structure of Class I resinites is loss (by isomerization) of exomethylene functionality. This type of structure is readily identified by solid-state ^{13}C NMR and IR spectroscopy and, hence, labdatriene-based resins and immature Class I resinites may readily be recognized and identified by these spectroscopic analyses. Carbon-13 resonances at 108 ppm and 148 ppm, and IR absorbance at 887 cm^{-1} are highly specific for exomethylene structures. (See, for example, Figure VII-9.) On the basis of presently available data, it appears that the occurrence of detectable levels of these structures in sedimentary organic matter is unique to Class I resinites, and, therefore, evidence for such structural character strongly indicates a Class I resinite. With increasing maturity, however, exomethylene structure is progressively "lost" due to isomerization to more thermodynamically favorable isomers. This effect is illustrated in Figure VII-9, which shows the solid-state ^{13}C spectra of four Class Ib resinites from New Zealand coal fields. Loss of exomethylene resonances (108 ppm and 148 ppm) with increasing maturity (measured here in terms of the rank of the coals from which these samples were obtained) is clearly apparent in these spectra. However, the total relative abundance of olefinic carbon observed in the spectra illustrated in Figure VII-9 is approximately equal for all samples, which indicates that the observed loss of intensity from exomethylene resonances is predominantly due to isomerization to more stable, olefinic structures, as illustrated in Scheme VII-2. Hence, although evidence for exomethylene functionality is highly characteristic of immature Class I resinites, the absence of such evidence does not necessarily indicate an alternative classification, because these structures are progressively lost as a function of increasing maturity and are virtually absent in "mature" samples of Class I resinites.

Scheme VII-2

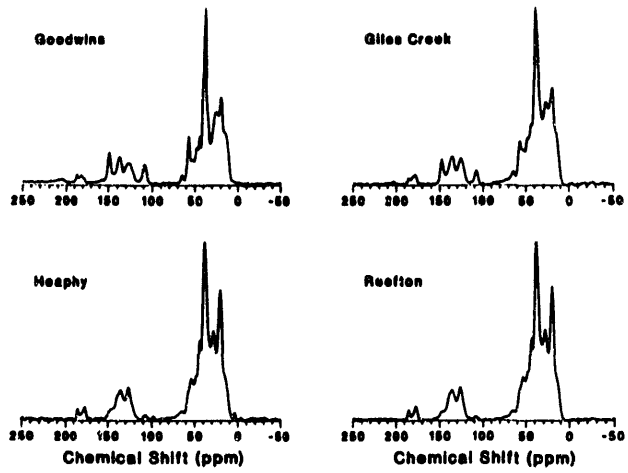

Figure VII-9. Cross polarization/magic-angle spinning solid-state ^{13}C NMR spectra of four Class Ib resinites obtained from coal fields in New Zealand. Spectra are plotted in order of increasing maturity (based on coal rank): Goodwins (lignite A) < Giles Creek (lignite B) < Heaphy (subbituminous) ≈ Reefton (subbituminous).

Additional evidence concerning the nature of the effects of increasing maturation on the structure and composition of Class I resinites can be obtained from the composition of their pyrolysates and suggests that in addition to isomerization of exomethylene functionality, maturation of Class I resinites also involves isomerization of the trisubstituted olefin located in the side chain of polycommunic acid (and other polylabdatrienes) to the adjacent, more thermodynamically stable, tetrasubstituted position, (illustrated in Scheme VII-2). This effect is crudely illustrated by the ratio of three characteristic bicyclic acids derived from the A/B ring system of polycommunic acid (III, IV, and V) by cleavage of the side-chain. (Note: in Class Ic resinites, the corresponding *enantio*-compounds VI, VII, and VIII are observed.) The ratio of these acids in the pyrolysates of Class I resinites is apparently controlled, at least in part, by the position of the olefinic structure located in the monomer side-chain, by pyrolytic β-bond scission. It is also likely that formation of these acids will be affected by location of the isomerized exomethylene group; studies aimed at clarifying this issue are in progress. The ratio of these compounds is illustrated in Figure VII-10. The formation of these acids is clearly maturity dependent, and therefore reflects changes in the structural nature of the resinite as a function of increasing maturity.

Understanding of the nature of sedimentary organic matter derived from the resins of higher plants has now evolved to a point where a number of chemically distinct forms of these materials have been recognized. In petrographic studies, the general classification "resinite" is still essential. However, in geochemical studies of resinites, it is desirable to indicate the basic structural character of the resinite(s) being described, in order to facilitate correlation with data obtained from comparable resinites from other sites. It is our intention that the classification system described above will provide a convenient nomenclature for the description of the fundamental structural character of resinites. It is to be hoped that this will enhance recognition of the generally limited structural diversity of resinites.

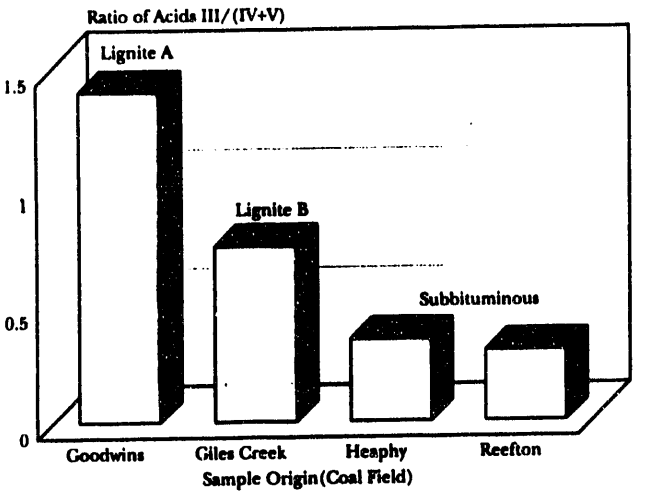

Figure VII-10. Ratio of characteristic trimethyl/tetramethyl bicyclic acids (III/(IV + V)), determined as their corresponding methyl esters, in the pyrolysates (Py-GC-MS) of four New Zealand resinites. Samples are identical to those described in Figure VII-9.

D. Laser Desorption/Ionization Mass Spectrometry

J. E. Hunt, D. E. Drinkwater, R. E. Winans

The objective of our research is to develop, improve, and apply laser-assisted mass spectrometric methods for the analysis of large molecules. A key process for successful mass analysis of large nonvolatile molecules is, of course, to produce gas-phase ions. The more established methods of thermal desorption and ion bombardment are limited for molecular analysis by thermal decomposition and fragmentation. Laser techniques with variations in wavelength, pulse length, and power density have the potential to overcome these limitations. Our early work established time-of-flight (TOF) mass spectrometry as the most flexible and viable method. Accordingly, we have continued our study of this approach. An improvement in resolution in our linear TOF by a factor of three over our previous work has been achieved, resulting in a resolution of 3400 at mass 260. Resolution enhancements are a result of the production of stable, well-behaved, low translational energy ions and carefully optimized ion optics, including acceleration conditions and laser focusing. This high resolution can be achieved for a large range of species and we are using time-of-flight mass spectrometry for analysis of raw coal, extracted coal, coal-related model systems, polymers, and biopolymers.

1. Characterization of Coals by Direct Laser Desorption and Postionization

J. E. Hunt, D. E. Drinkwater, R. E. Winans

Our investigation of the molecular structure of coal using laser desorption mass spectrometry continues. Our goal is to desorb ions that are characteristic of the molecular species present in the coal sample rather than to pyrolytically ablate material from the coal surface. To achieve this goal, the desorption laser is intentionally operated near the threshold for production of ions to minimize the fragmentation of the desorbing material or below ionization threshold to produce intact neutral species for subsequent laser ionization (postionization). Previous work has established laser desorption as a method for obtaining the relative molecular-weight distributions of physically separated coal macerals. We have obtained results for demineralized Lewiston-Stockton coal (APCS 7) and a pyridine extract of the same coal that are in agreement with those found in DCI (see section VII-B1). In accord with the DCI results, the LDMS of the pyridine extract not only shows a higher average molecular distribution (hereinafter referred to as AMW), but also shows mass peaks not observed in

the demineralized coal. In continuation of this work on coals and coal extracts, we now have established the chemical identity of some major components from the toluene-soluble liquefaction products of the liptinite and vitrinite from APCS 7. The coals were separated into maceral groups by a continuous flow centrifugation technique, and subjected to small-scale liquefaction in tetralin. The structural assignments are summarized in Table VII-4. These suggestions are based on complementary results from high-resolution (40,000) electron impact ionization mass spectrometry. All major species contain one or more oxygen atoms. Furthermore, they exhibit more oxygen-containing heteroatom species per carbon in the higher AMW vitrinite as compared to the lower AMW liptinite. These oxygen-containing species are products from the liquefaction. However, the efficacy of LDMS for mass analysis of these coal extracts is clearly established.

Although laser desorption of coals produces useful and unique information, more work is needed to clarify the chemistry and physics of the laser desorption of high-molecular-weight species. To this end, we have studied some model systems related to coal and other selected pure compounds. One example is the model synthetic coal molecule shown in Figure VII-11. The mass spectrum produced at low laser power (top panel), shows a base peak at m/z 368, with smaller peaks at higher mass, including a possible covalent dimer ion at m/z 734. The resolution at mass 734 is in excess of 2000. At higher laser powers, the spectrum, Figure VII-11 (lower panel), takes on a different appearance. Although the resolution is

Table VII-4. Possible assignments for series seen in laser desorption and EI HRMS.

LIPTINITE Series	Formula	Structure
208, 222, 236, 250	$C_{15}H_{12}O$	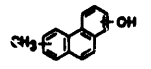
234, 248, 262, 276, 290, 304	$C_{16}H_{10}O_2$	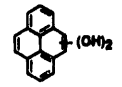
VITRINITE Series	**Formula**	**Structure**
210, 224, 238, 252, 266, 280	$C_{14}H_{10}O_2$	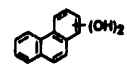
250, 264, 278, 292, 306, 320, 334	$C_{16}H_{10}O_3$	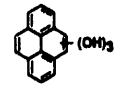
HRMS 40,000		

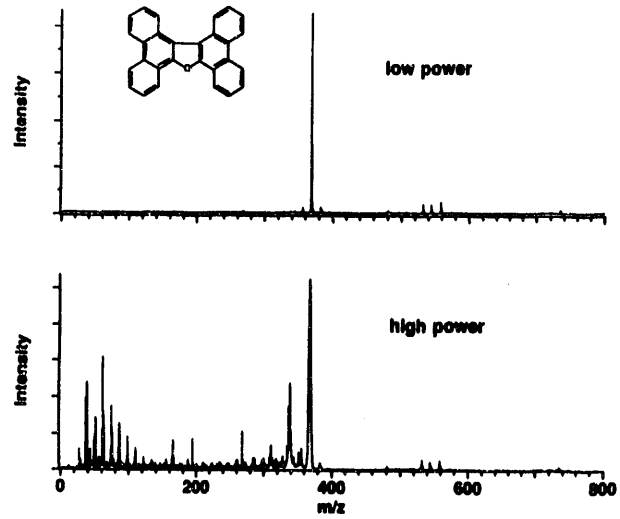

Figure VII-11. Laser desorption mass spectra of synthetic (9-phenanthrol based) coal-model compound. The upper panel is low laser power (1×10^6 W/cm^2). The lower panel is high laser power (5×10^7 W/cm^2). Note fragmentation in the lower panel.

lower (1100 at m/z 734) as a result of higher initial kinetic energy effects at the sample surface, there are additional peaks in the spectrum. These peaks are fragment ions of the parent molecule and serve to structurally define the molecule.

All of the studies mentioned thus far depend on *prompt ion production*, that is, detection of ions produced directly by the laser desorption process itself. This technique is useful in many instances, but it suffers from matrix effects due to the strong dependence on surface ionization and surface neutralization on both substrate chemistry and the nature of the desorbate. Using pure compounds, we have sought to alleviate some of the inherent matrix effects by selectively analyzing *neutral species* that are desorbed by the laser. This is accomplished by a second laser beam of variable wavelength and intensity. Model systems are pure aromatic compounds embedded in a cross-linked polyisoprene backbone: poly-(2,2,4-trimethyl)-1,2-dihydroquinoline (MW = 346) and N-(1,3-dimethylbutyl)-N'-phenyl-p-phenylenediamine (MW = 268).

These compounds are polar, contain heteroatoms, are chemically complex, are present as complex mixtures, and are present in minor concentrations (in usually <1%). Our goal is to selectively ionize these specific compounds using a second laser beam focused into the plume of neutral species created by the first

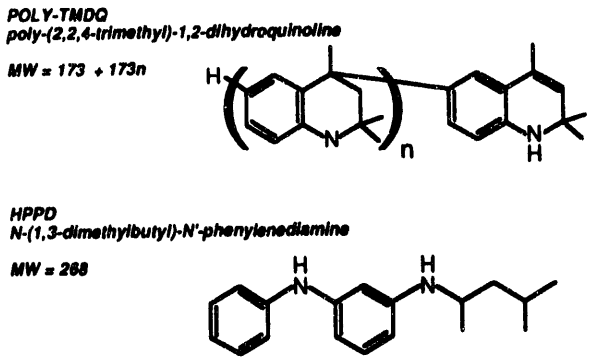

desorption laser. An example is given in Figure VII-12 for the two compounds in the model system. Four different ionization wavelengths are used to accentuate different characteristic species in the sample. Laser radiation at 355 nm selectively ionizes aromatic compounds, whereas 212 nm tends to ionize almost everything except for low-molecular-weight species (<100 amu). Parent peaks and some simple fragmentation-loss peaks for both compounds are observed in the 355-nm spectrum, whereas 308-nm and 266-nm light selectively ionize only the diamine (MW = 268).

As a result of our studies with model compounds, a clearer, more well-defined picture of effects in laser desorption mass spectrometry of higher molecular weight species and mixtures of species is emerging. These results provide the basis for applications of this technique to the complex systems found in coals and coal extracts.

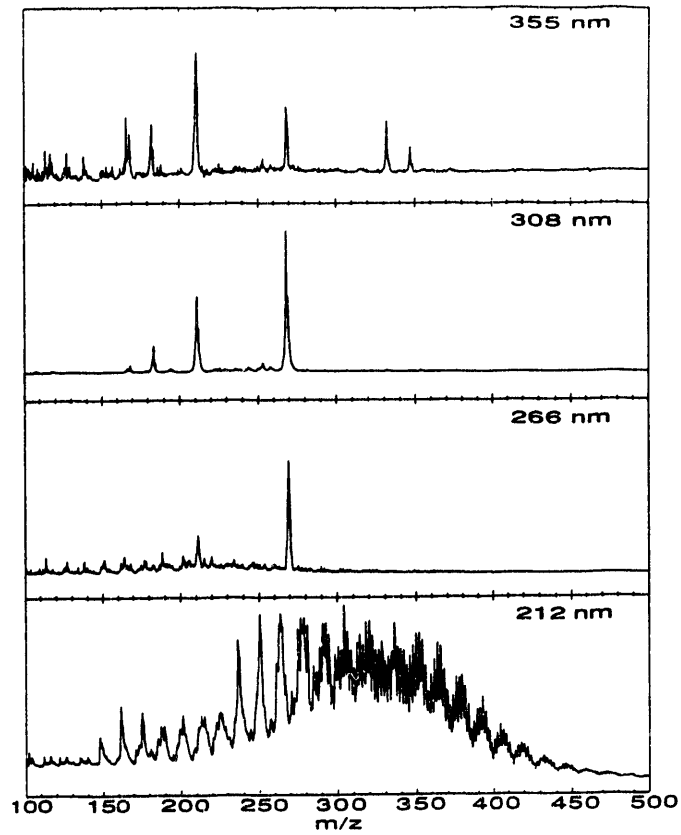

Figure VII-12. Laser desorption/laser ionization spectrum of model compounds, poly-2(2,2,4-trimethyl)-1,2-dihydroquinoline (MW = 346) and N-(1,3-dimethylbutyl)-N'-phenyl-p-phenylene diamine (MW = 268), at four different ionization wavelengths. Each of the wavelengths accentuates different characteristic species in the sample.

2. DNA and Biopolymer Analysis Using Laser Mass Spectrometry Approaches

J. E. Hunt, D. E. Drinkwater, R. E. Winans

We have begun an investigation into laser-based mass spectrometric methods to improve DNA-sequence analyses. This research, which is supported by LDRD funds, bears on the Human Genome Project to sequence the human genome in a timely and cost-effective manner. Traditional sequencing technologies for biopolymers are tedious and time-consuming. As an alternative sequencing technology, mass spectrometry offers speed, sensitivity, and, recently, the mass range for the analysis of large nucleic acid fragments. In our approach, the mass spectrometer would directly analyze the ionized components in an unfractionated mixture of sequencing reactions, bypassing the need for electrophoretic separation. We are studying matrix-assisted laser desorption ionization (MALDI) mass spectrometry to provide faster sequencing methodologies than traditional chemical and gel separation methods. At present, matrix-assisted laser desorption is an evolving technique, the potential of which has not been fully explored.

A first step in this direction was to produce positive and negative TOF spectra of a molecular weight 5733, bovine insulin. Figure VII-13 is the positive ion mass spectrum of a caffeic acid matrix/insulin sample generated by 30 shots of a 337-nm nitrogen-laser desorption. For calibration accuracy, a small-molecular-weight peptide, luteinizing hormone releasing hormone (LHRH) (MW 1182) was added to the sample. Clearly visible in Figure VII-13 are the molecular ion of insulin, the LHRH spike, and an insulin dimer ion of molecular weight 11466. Polynucleotide fragments in the mass region of 12000 would correspond to approximately 40-bases, a useful mass range for the proposed sequencing method.

We obtained samples of oligodeoxynucleotide 10-mers having each of the four bases at either end of the chain, in other words, the inner eight bases are capped with A, T, C, or G on the 5' and 3' ends. This results in 16 possible sequences with 10 different molecular-weight species. Using 337-nm radiation and 3,5-dinitrobenzoic acid as a matrix, we have successfully detected negative molecular ions of this range of base compositions of oligodeoxynucleotide 10-mers. A remarkably strong signal was obtained for the singly charged parent molecules. The resolution was less than that achieved for proteins, although the maximum in the peak corresponded well to the actual average mass of the 10-mers. The molecular weight of the average of the 16 possible sequence combinations of this sample is 3009.5. To fully resolve the species in this sample, a resolution of better than 1 part in 3000 is needed. For a low-resolution mass spectrum the mass distribution alone without isotopic contributions corresponds to a peak that is 80 mass units wide. In the lower mass region, strong ion signals of all the nucleotide bases are observed, indicating some fragmentation of the oligonucleotide. Wavelength and matrix variations can reasonably be expected to ameliorate this complication and improve the ion yield as well as the quality of the spectrum. These data suggest that future work should be directed to improving mass resolution. This will be done by changing sample preparation conditions, ion optics and detection, and laser conditions.

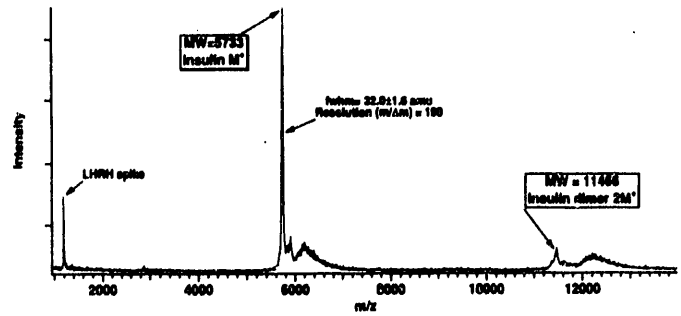

Figure VII-13. Matrix-assisted laser desorption of bovine insulin using 337-nm N_2 laser and caffeic acid as matrix. The molecular ion and dimer ion are observed at a resolution of ~190 (m/Δm).

E. NMR Spectroscopy and Imaging

D. C. French, S. L. Dieckman, R. E. Botto

1. Solvent Swelling of Coals Studied by Three-Dimensional NMR Imaging Chemical Microscopy *D. C. French, S. L. Dieckman, R. E. Botto*

Coal is a complex, heterogeneous, macromolecular solid that is primarily comprised of microscopically discernible substances, termed macerals, which are derived from different chemically transformed plant materials. The macerals in coal exhibit highly diverse chemical behavior, and thus their characterization is important for the development of future coal-processing technologies. One method of coal characterization is the investigation of the solvent-swelling phenomenon.

In previous studies, we reported the first application of ^1H NMRI techniques for spatially resolving the individual microlithotypes within a solid coal. Two-dimensional (2-D) NMRI proved to be a promising tool for the characterization of maceral domains in a dried specimen of Utah Blind Canyon coal (APCS 6). We also developed a three-dimensional (3-D) method that was utilized to spatially map macerals within a solid coal specimen, and image the distribution of mobile macromolecular phases created by swelling the coal with pyridine-d_5. Rather than imaging the coal itself, important information concerning the solvent accessibility to the macerals and other microlithotypes can be obtained by imaging a good swelling solvent, such as pyridine, in the coal. Our approach now uses 3-D NMRI for spatially mapping the solvent distribution in coals that have been swollen with protic pyridine. The technique is based on a 3-D gradient recalled echo (GRE) pulse sequence for data acquisition and image reconstruction by 3-D Fourier Transform (FT). Images with a resolution of 40 to 50 μm show the presence of microlithotypes and microfractures, in addition to the distribution of regions that differ with regard to pyridine accessibility.

The 3-D surface-rendered GRE images of the Utah (APCS 6) and Lewiston-Stockton (APCS 7) pyridine-swollen coals are shown in Figure VII-14. Here, image contrast results from acquiring only the spin-echo from mobile protons with long spin-spin relaxation times (T_2). Therefore, bright features result

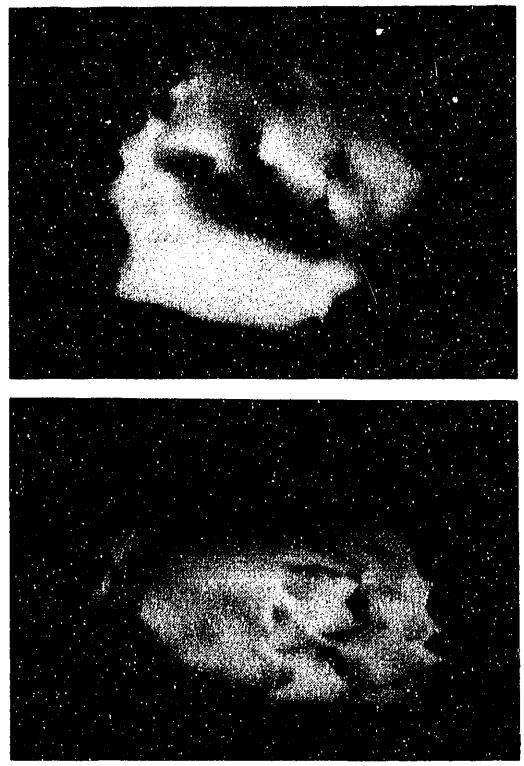

Figure VII-14. 3-D surface renderings of the (a) Utah (APCS 6) and (b) Lewiston-Stockton coals (APCS 7).

from regions in the coals that contain a high density of pyridine, and the dark areas result from regions that are inaccessible to the solvent. The artifacts visible in the images arise from a local commercial FM broadcast near the spectrometer-operating frequency. Features devoid of pyridine, such as pits, cracks, and gouges, appear magnified in the image of the Utah specimen. The vertical feature on the front face of the 3-D surface rendering of the Lewiston-Stockton specimen shows a microscopic structure contiguous with the surface of the specimen that is inaccessible to pyridine.

Transaxial slices of the interior *x-y* planes of the Utah and Lewiston-Stockton coals obtained with the GRE pulse sequence are shown in Figures VII-15 and VII-16. The geometry of these slices shows a good correspondence with the 3-D surface renderings. Figure VII-15 shows sequential transaxial 40-μm slices of the Utah coal. The dark feature at the top center of Figure VII-15d is known to result from a microscopic fracture. Bright features in the slices show areas of high-pyridine density. Dark features result from areas of low pyridine penetration, microfractures, and void spaces.

The dark feature, inaccessible to pyridine, toward the center of the *x-y* projections (Figure VII-15) is known, from X-ray data, to be a mineral nodule buried in the interior of the Utah specimen. Figure VII-16 shows sequential transaxial 50-μm slices of the interior of the Lewiston-Stockton coal. The images show the presence of contrasting horizontal bands in the *x-y* plane. When the coal was swollen with pyridine, the secondary interactions binding strata within the specimen were relaxed. Contrasting bands in the images show that differential swelling in the bedding plane has produced microfractures and regions with greater or lesser pyridine accessibility. The dark vertical feature corresponds to the same that appears as a void in the 3-D surface rendering indicating that this interior structure runs through the object to its surface. The dark structure in the images is a region of low pyridine accessibility.

The heterogeneity of the coal matrix produces variations in the magnetic susceptibility throughout the specimen. Diffusion of pyridine through areas with susceptibility differences, particularly at organic-mineral interfaces and at the surface of microfractures, substantially shortens the proton T_2. Image contrast resulting from susceptibility effects is enhanced by utilizing the GRE pulse sequence because magnetization that is dephased by susceptibility differences is not refocused by the readout gradient. Mineral deposits may contain metal atoms with unpaired electrons, which also enhance T_1 and T_2 contrast due to the paramagnetic susceptibility of these environments. Also, these dark features appear larger than the corresponding physical structures due to the susceptibility difference and the concomitant increase in the proton-relaxation rate.

2. Quantitative Solid ^{13}C NMR of Argonne Coals *R. E. Botto*

Work carried out in our laboratory over the past several years has clearly demonstrated that complications associated with cross-polarization (CP) measurements cause signal distortion in ^{13}C NMR, and pose a problem in the accuracy of measurements on coal. It was estimated that CP experiments underestimate the carbon aromaticity of coal by as much as 10-15%. These findings prompted us to investigate single-pulse (SP) techniques combined with pretreatment of coals to enhance relaxation, for improving the reliability of the solid NMR measurements.

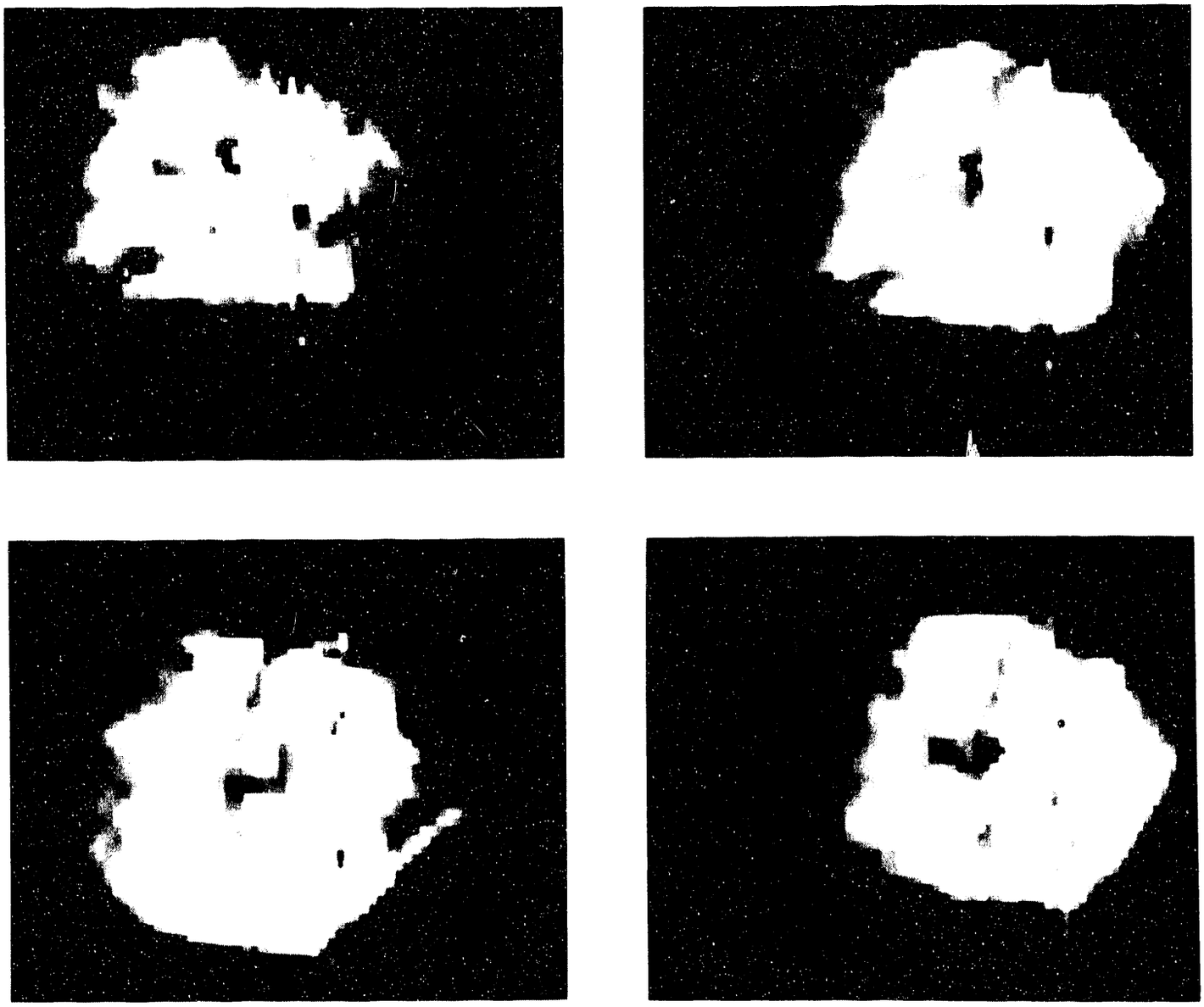

Figure VII-15. *X-y* slices of the Utah coal (APCS 6) swollen with pyridine (*a-d* clockwise from upper left). The in-plane resolution is 40 μm.

Initial studies focused on measurement of the spin-lattice relaxation times (T_1) for the entire suite of eight Argonne Premium coals, so that optimum pulse recycle delay times ($5 \times T_1$) could be determined for the analysis of each coal. Pretreatment of coal samples having long relaxation times (>20 s) prior to NMR analysis was found to be an effective means of shortening T_1, thereby reducing the total accumulation time by a factor of four or greater.

A solid-state NMR version of the ring-down elimination (RIDE) pulse sequence was developed to reduce severe baseline distortion typically found in SP experiments carried out at low frequencies and with high-Q probes (see Figure VII-17). SP-RIDE spectra of selected Argonne Premium coals is shown in Figure VII-18. Analysis of these spectra allows accurate analysis of the different functional groups and carbon aromaticities for the Argonne Premium coals. Fraction of aromaticity values (f_a) are tabulated in Table VII-5. In general, carbon aromaticity values determined by SP-RIDE techniques are higher than the mean values from several laboratories (eleven) determined by CP, and can be as great as 15% higher in the case of the Beulah-Zap lignite (APCS 8) and Wyodak subbituminous (APCS 2) coals.

Figure VII-16. *X-y* slices of the Lewiston-Stockton coal (APCS 7) swollen with pyridine (*a* top; *b* bottom). The in-plane resolution is 50 μm.

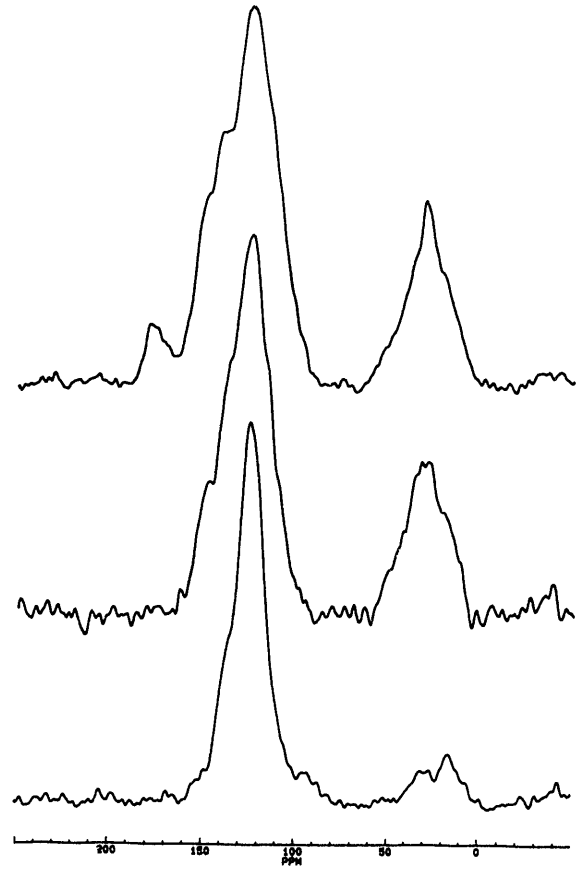

Figure VII-18. SP-RIDE spectra of (top) Wyodak subbituminous (APCS 2), (middle) Illinois bituminous (APCS 3), and (bottom) Pocahontas bituminous (APCS 5) coals.

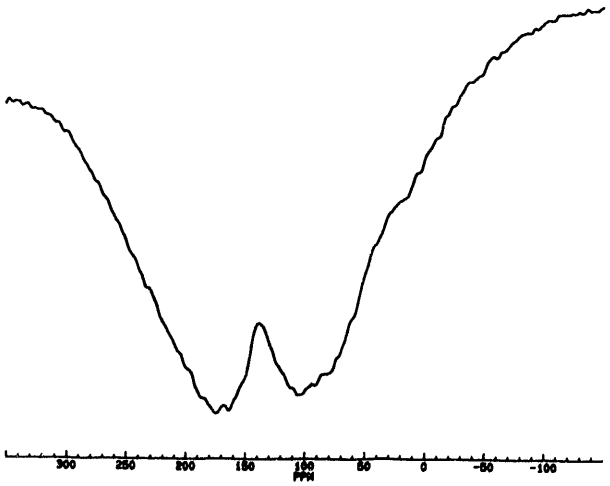

Figure VII-17. SP-NMR spectrum of Pittsburgh #8 coal (APCS 4).

Table VII-5. Carbon aromaticities of Argonne Premium Coal Samples

coal name	APCS sample no.	f_a (SP-RIDE)[a]	f_a (CP)[b]
POC	5	0.89	0.85 _ 0.01
UF	1	0.84	0.80 ± 0.02
LS	7	0.82	0.75 ± 0.02
BC	6	0.70	0.63 ± 0.03
PITT	4	0.78	0.72 ± 0.03
ILL	3	0.74	0.71 ± 0.02
W	2	0.71	0.62 ± 0.04
		6% CO_2H	
BZ	8	0.77	0.69 ± 0.05
		4% CO_2H	

[a]Single-pulse ring-down elimination pulse sequence.
[b]Mean values of carbon aromaticity and standard deviations.

F. XANES Evidence for Selective Organic Sulfur Removal from Illinois No. 6 Coal

K. Chatterjee, M. L. Gorbaty, L. M. Stock

In continuing our investigation of new combined chemical and spectroscopic methods for the investigation of coal, we turned our attention to the use of selective chemical reactions and XANES spectroscopic analysis to distinguish between two different classes of organically bound sulfur forms in Illinois No. 6 coal, APCS 3.

The Illinois No. 6 coal was freed of pyrite by treatment with lithium aluminum hydride. The product contained 1.8% S (mf), 8.5% ash, and only 0.09% iron. There were no reflections for pyrite in the powder diffraction X-ray spectrum.

Several reactions for selective organic desulfurization were investigated, but we soon began to focus on single electron-transfer (SET) reactions, equation (1), for selective sulfur removal.

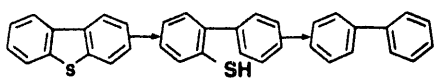

(1)

SET reaction: potassium, naphthalene, tetrahydrofuran, 67 °C, 24 hours.

This approach seemed most appropriate because the method, in principle, could be made catalytic or photochemical and, therefore, practical. Subsequently, strongly basic reagents, equation (2), were studied in an attempt to eliminate sulfidic sulfur compounds. Lochmann's base (BASE), which is a mixture of an organometallic compound and an alkoxide, proved to be suitable.

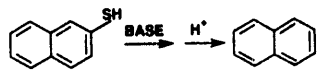

(2)

BASE reaction: n-butyllithium, potassium t-butoxide, heptane, 98 °C, 6 hours.

The reaction of the Illinois coal with the SET reagent reduced the organic sulfur content from 1.8% to 1.1% (mf). In a separate experiment, the pyrite-free material was treated with BASE in heptane. Hydrolysis of the reaction product with dilute aqueous acid gave a coal with 1.2% S (mf). The results are summarized in Figure VII-19.

Working in collaboration with Gorbaty and his associates, we studied the sulfur species in the pyrite-free starting material and the products of the SET and BASE reactions by X-ray absorption near edge structure (XANES) spectroscopy at the National Synchrotron Light Source at Brookhaven National Laboratory. Gorbaty's previous work had already established that useful information about the forms of organically bound sulfur in coals could be obtained by XANES spectroscopy. The XANES spectrum of the pyrite-free coal is shown in Figure VII-20.

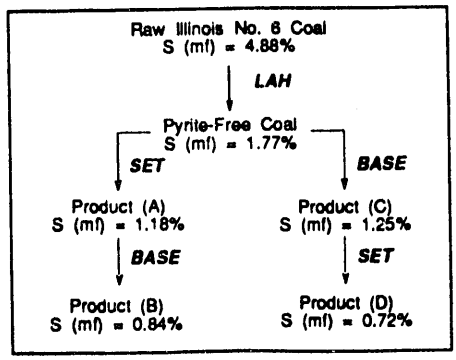

Figure VII-19. Desulfurization of Illinois No. 6 coal through a combination of LAH, SET, and BASE reactions.

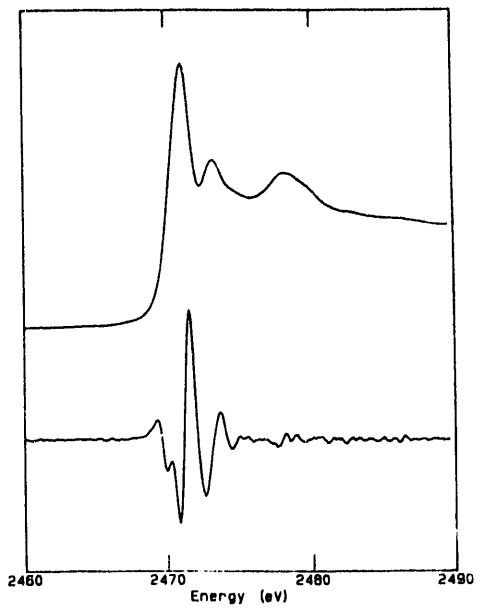

Figure VII-20. XANES spectra (top) and the third derivative (bottom) of the pyrite-free Illinois No. 6 coal (APCS 3).

The XANES spectrum and the third derivative of this sample showed no evidence for the presence of pyritic sulfur, and reconstruction of the third derivative indicated that about 65% of the organically bound sulfur compounds have heterocyclic or aromatic character and about 35% sulfidic character. These values are comparable to the values for the starting coal, indicating that the LAH treatment does not alter the organically bound sulfur forms. The third derivatives of the absorption spectra of the pyrite-free sample and the two different reaction products are displayed in Figure VII-21.

The third derivatives of the XANES spectrum exhibit two key features near 2469.6 and 2470.5 eV. The feature at 2469.6 eV arises from sulfidic sulfur compounds and includes aromatic and aliphatic thiols, aliphatic sulfides, and aryl alkyl sulfides. The feature near 2470.5 eV is dominated by sulfur bound to sp^2-hybridized carbon atoms such as thiophene and its derivatives including benzothiophene, dibenzothiophene, and other sulfur-containing heterocycles, and diaryl sulfides.

Comparison of the third derivatives of the spectra of the reaction products with that of the starting coal reveals that, depending on the chemistry used, features are selectively diminished. The SET reagent removes sulfur compounds that contribute to the feature near 2470.5 eV, whereas BASE removes the forms that give rise to the feature at 2469.6 eV. The results are exactly in accord with the chemical expectation that the SET reagent should be especially effective for the removal of heterocyclic sulfur compounds, whereas BASE should selectively react with the sulfidic sulfur compounds. To test this interpretation in another way, we treated the SET reaction product with BASE and the product of BASE reaction with the SET reagent. The sulfur contents decreased significantly after the second reaction; the values are 0.8% in the former case and 0.7% in the latter case. The spectroscopic results are shown in Figure VII-22.

These experiments establish several important general points. First, selective organic reagents can be designed to surgically remove different organic sulfur compounds from coals. Second, the XANES methods of Gorbaty and Huffman are capable of the speciation of sulfidic and aromatic and heterocyclic sulfur compounds. In addition, these experiments confirm several independent suggestions that Illinois Basin coals contain appreciable amounts of sulfidic sulfur compounds as well as the normally abundant heterocyclic substances, and further that mild and selective chemical strategies can accomplish appreciable organic desulfurization in this coal. In this connection, it should be noted that the mass balances and heat

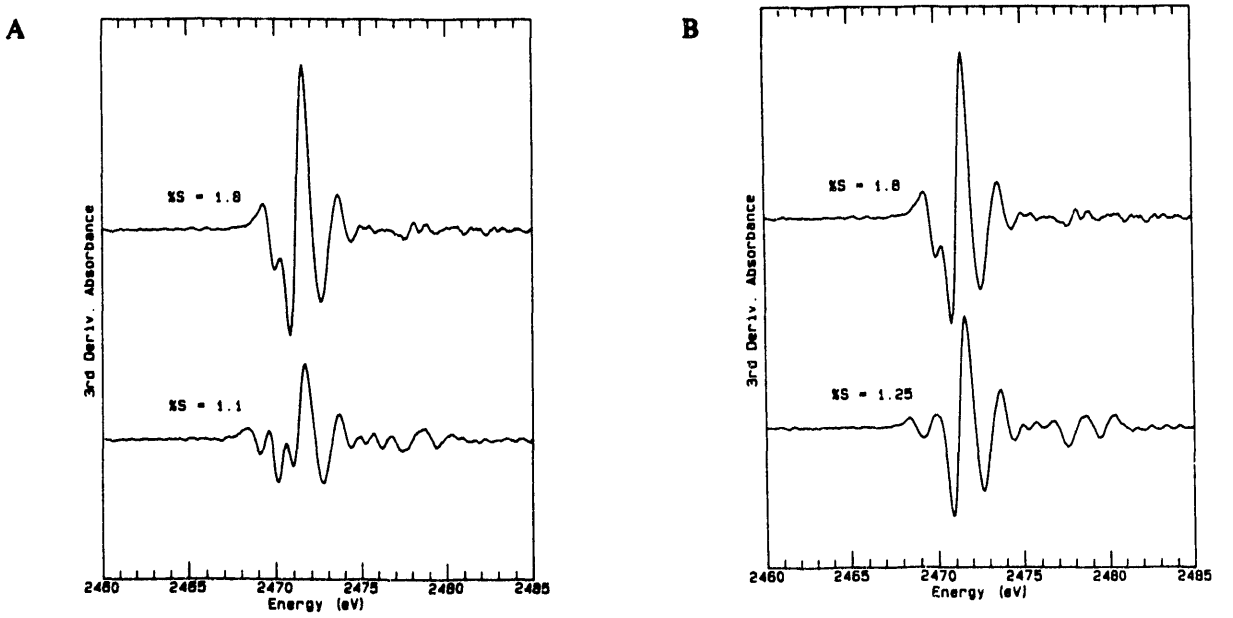

Figure VII-21. (A) Third-derivative XANES spectra of the pyrite-free Illinois No. 6 coal (upper) and the SET-treated coal (lower). Numbers on the left-hand side of the traces are % sulfur (mf). (B) Third-derivative XANES spectra of the pyrite-free Illinois No. 6 coal (upper) and the BASE-treated coal (lower). Numbers on the left-hand side of the traces are % sulfur (mf).

balances are very favorable. Worthy goals for future research center on improving the resolution of the noninvasive spectroscopic techniques and on finding practical reaction systems to accomplish organic desulfurization.

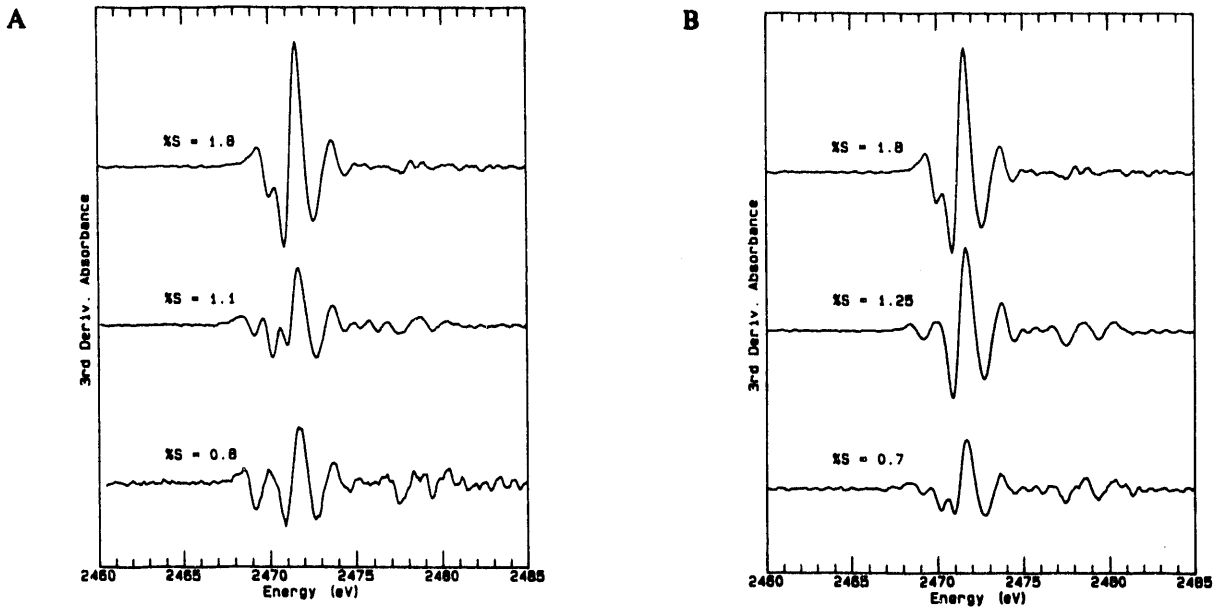

Figure VII-22. (A) From top to bottom: third-derivatives XANES spectra of the pyrite-free Illinois No. 6 coal, the SET-treated coal, and the product obtained on BASE treatment on the SET-treated coal. Numbers on the left-hand side of the traces are % sulfur (mf). (B) From top to bottom: third-derivatives XANES spectra of the pyrite-free Illinois No. 6 coal, the BASE-treated coal, and the product obtained on SET treatment on the BASE-treated coal. Numbers on the left-hand side of the traces are % sulfur (mf).

G. Novel Synthetic Approaches to Catalyst Design

K. A. Carrado, R. E. Winans, P. Thiyagarajan, J. B. Nicholas, G. L. Keldsen, S. R. Wasserman

This phase of our research evolved from the investigation of the role of clays in coalification. It became apparent that many natural clays promoted the conversion of complex coal molecules. Consequently, we undertook a program to investigate this chemistry systematically in an attempt to prepare clay catalysts designed to upgrade low-quality petroleum residues and coal-derived heavy liquids. Novel chemical approaches are being developed for synthesizing these crystalline microporous catalysts, which are based on layered silicate or other porous oxide frameworks. In general, metal oxide gels are prepared hydrothermally in the presence of large organic or organometallic templating molecules. Major objectives of this fundamental program are (1) preparing layered inorganic frameworks that possess large pore sizes for catalytic applications, (2) establishing a better understanding of the gel chemistry involved, (3) continuing to build a theoretical understanding of the surface chemistry of clays based on molecular modeling techniques, and (4) obtaining precise structural information concerning such phenomena as solvation and diffusion within a clay, because such understanding is critical to clay-surface chemistry in such applications as catalysis and environmental transport.

Smectite clay minerals are two-dimensional layered silicates that constitute a naturally occurring class of inorganic catalysts and supports. Two tetrahedral silicate sheets sandwiching a central sheet of octahedral sites form a 2:1 smectite clay layer. The octahedral sites are occupied by aluminum ions in montmorillonite and by magnesium ions in hectorite. The (001) reflection along the c-axis as measured by X-ray powder diffraction (XRD) gives the distance

between clay layers, and is a function of the type of interlayer cation present. These interlayer cations are easily exchangeable. When bulky inorganic complexes such as the Keggin-type Al_{13}-oxohydroxy cluster are exchanged into the interlayer region, a so-called pillared clay results because, upon heating, a thermally stable oxide pillar holds the layers apart, thus affording an appreciable microporous volume. Our synthetic strategy is to prepare pillared clays in situ; in other words, to crystallize clay layers from a gel in the presence of a pillaring species to place new structure types with different compositions and pore volumes directly in the clay. The feasibility of this method was demonstrated previously in our group by using hydrothermal crystallization conditions to synthesize porphyrin-containing hectorites. The reactions can be carried out in aqueous media by refluxing a gel that contains a silica sol, freshly precipitated magnesium hydroxide, lithium fluoride, and an organic template (such as a porphyrin).

This general method has now proven to be amenable to a remarkable variety of templates, including transition-metal complexes and organic-dye molecules. Necessary criteria for a successful template include water solubility, positive charge, and thermochemical stability under reaction conditions. Porphyrins were the initial template of choice because they are large planar molecules that were thought to help induce the layered-silicate formation. Further tests have shown that planarity is unnecessary. Templates have ranged from nearly planar porphyrins and phthalocyanines to somewhat bulkier aromatic organic dyes, to spherical transition-metal complexes. Such synthetic diversity is encouraging as work progresses with larger and more complicated molecular templates. Our objective is to form materials with extra-large (>15 Å) pore sizes or gallery heights.

In the previous year, several synthetic hectorites were prepared and characterized via microanalysis and XRD. A much more comprehensive examination of the materials has now been completed, including a comparison of their properties to natural hectorites ion-exchanged with the corresponding templates. For example, both a higher surface area and lower overall uptake of template for synthetic vs. ion-exchanged clays result from excess silica present in the synthetic product (this is, in fact, the only impurity). Orientations of templates within the clay galleries were also assigned from XRD and, in some cases, UV-visible diffuse reflectance (DR) data (see Table VII-6). Thermal gravimetric analysis was also performed for all systems, in both oxygen and nitrogen atmospheres, in order to determine thermal stabilities of the clay-organic complexes.

Truly desirable templates must have a high thermal stability. One approach is to derivatize an organic template with an inorganic functionality. In such a system, calcination would oxidize the organic portion to leave the inorganic structural unit behind in a newly formed pillared clay. Toward this goal, we have synthesized a porphyrin that contains peripheral siloxane units. The specific molecule is tetrapyridyl porphyrin (propyltrimethoxysilane) bromide, $TPyP(silane)_xBr_x$, where x = 3-4 (see Figure VII-23). Because the trimethoxysilane functionality would be easily hydrolyzed in the aqueous hectorite sol gel, a test hectorite crystallization reaction of *tetrakis*(N-methyl pyridyl)porphyrin in a 50% ethanol gel was first carried out. A large excess of magnesium hydroxide was found to be necessary in order for an organohectorite to crystallize under these solvent conditions. The next step will be to try the $TPyP(silane)_x$ as a template in the 50% ethanol gel.

Table VII-6. XRD data for synthetic hectorite clays.

template	size of template[1] (Å)	Δd(001)* Å	orientation[2]
ethyl violet	15.9 × 15.3 × 6.1	11.9	tilted oligomers or parallel dimers[3]
methyl green	14.3 × 13.8 × 5.3	6.3	parallel
alcian blue (AB)	19.2 × 16.6 × 5.0	4.4	parallel
AB, pyridine variant	18.2 × 15.6 × 5.0	6.1	parallel
Ru(II)(o-phen)3	ca. 9.5 × 9.5 × 9.5	9.0	spherical template
Co(III)sepulchrate	7.9 × 4.2 × 4.2	4.5	parallel

[1]As calculated using *Alchemy III*.
*d(001) minus clay layer of 9.6 Å to give gallery height alone.
[2]Orientation of template within clay gallery.
[3]Also supported by UV-vis DR data.

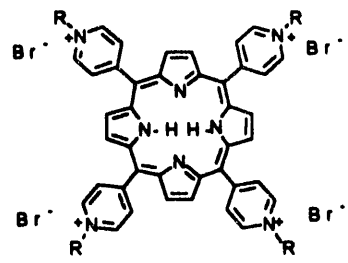

R = $-CH_2CH_2CH_2SiO(CH_3)_3$

Figure VII-23. Structure of $T_{py}P(silane)_{3-4}Br_{3-4}$.

Crystallization mechanisms and organic-inorganic interactions in gel systems such as those of concern here are in general not well understood. Small-angle neutron scattering (SANS) provides a unique method for examining how the silica sol and magnesium hydroxide particles interact in the presence of organic templating molecules to form a layered magnesium-silicate structure. SANS measurements of a crystallizing hectorite gel were made using the small-angle diffractometer at the Intense Pulsed Neutron Source of Argonne National Laboratory. One experiment was carried out to assure that layered-silicate products, for example, magaadite, $NaSi_7O_{13}(OH)_3 \cdot 3H_2O$, do not crystallize from a hectorite gel. Specifically, hectorite clay gels were prepared in aqueous solution with and *without* magnesium hydroxide. When the gel contained only tetramethylammonium hydroxide, lithium fluoride, and silica sol, no layered products were detected either by XRD or by SANS. Under the same conditions, crystallization can be obtained by both methods when magnesium hydroxide is present.

The scattering from unreacted magnesium hydroxide (the layered mineral is called brucite) is so dominant that finer details in the scattering profile cannot be observed. This component therefore needs to be contrast-matched, or made "invisible" in the neutron scattering profile. This is done by adjusting mixtures of heavy and light water to precisely match the scattering power of a specific component. Previously, a contrast match value of 55% D_2O was experimentally determined for magnesium hydroxide. A solvent of this composition was then used to crystallize hectorite from a precursor gel. Aliquots were taken from the hydrothermal crystallization reaction after two, four, eight, and 22 hours. These were also subsequently dialyzed in 55% D_2O to assure comparable solvents in each case. The SANS data have not yet been analyzed, although a cursory analysis does show that strong scattering from layered magnesium hydroxide is absent. XRD spectra of each aliquot (as dried films) show that the magnesium hydroxide content decreases as a shoulder in the d(001) region of hectorite increases, as expected.

Theoretical chemistry methods have also been applied to the study of silicate clays. Properties that can be modeled in this way include the structure and dynamics of the clay itself, interactions of adsorbed molecules with the clay surface, and acidic and reactive properties of catalytic sites. An understanding of these properties is fundamental in the development of new catalysts. In a continuation of work first reported last year, the enthalpies of adsorption of 13 hydrocarbons with five to 10 carbon atoms on the clay mineral montmorillonite were further investigated by computer simulation using energy minimization (EM) and molecular dynamics (MD) techniques. The disordered nature of successive 2:1 layers in montmorillonites precludes definitive structure determination; consequently, atomic coordinates for this clay mineral were adapted from a model that had been proposed for a closely related, but somewhat more ordered, Ascan smectite. As in our previous work, a $6 \times 4 \times 3$ grouping of these unit cells with periodic boundary conditions was used as the basis for the clay surface.

Molecular dynamics equilibration was readily achieved when ensemble-average MD calculations involving a minimum of 12 hydrocarbon molecules were carried out (under conditions of infinite dilution). Calculated heats of adsorption gave excellent correlations with experimental values based on gas chromatography retention data not only for the six non-branched alkanes ($R^2 = 0.9992$), but also for the entire 13 hydrocarbon set, which included branched and cyclic members ($R^2 = 0.9658$), see Figure VII-24. As in our earlier work, Hopfinger Lennard-Jones potentials (rather than the more repulsive MM2 Lennard-Jones potentials) were used to model the hydrocarbon-montmorillonite interactions.

In order to design new clay catalysts for the processing of coal-derived heavy liquids, an understanding of the nature of the interaction between these fluids and the clay is required. In addition, because clays are major components of the earth's surface, the elucidation of the structure of clays and the interactions of

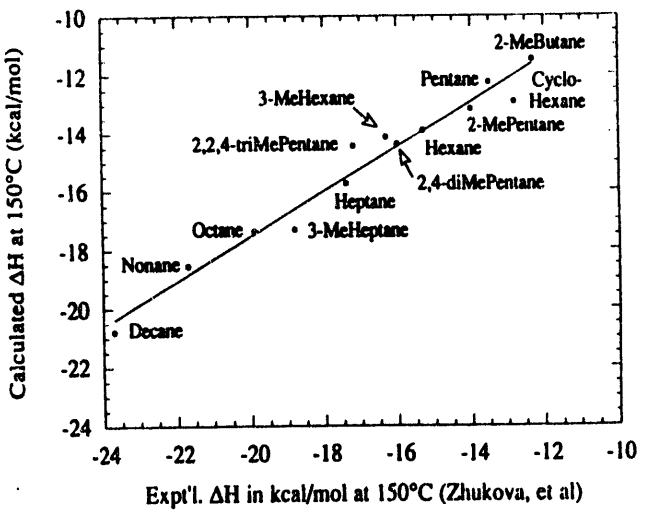

Figure VII-24. Heats of adsorption (ΔH) of hydrocarbons on montmorillonite.

organic and inorganic compounds with these minerals is of fundamental importance in understanding the hazards that such compounds can present to the environment. Unfortunately, the lack of long-range order within a clay prevents the use of techniques such as X-ray diffraction to analyze these interactions. However, X-ray absorption spectroscopy (XAS) can be used to probe the local coordination environment (<5 Å) of transition metals within a clay.

In smectite clays, the 2:1 inorganic lattice layers are separated by a layer of water and charge-compensating cations. These ions can be exchanged with transition metals to function as a probe of the interlayer environment in the clay. In this research, XAS was used to monitor the interaction of protic solvents with copper-bentonite. Figure VII-25a shows the X-ray absorption near edge structure (XANES) before and after penetration of water into this clay. The sharp feature at 8979 eV, which corresponds to the 1s-4p electronic transition, becomes merely an inflection point for the solvated material. This change is indicative of a transition from square-planar to pseudo-octahedral coordination as the solvent enters the clay. Figure VII-25b also shows the Fourier-filtered inverse-transform for the first coordination sphere about the copper atom. The change in phase corresponds to an increase of approximately .03 Å as the copper atom encounters the solvent. Similar results are observed for methanol, ethanol, and ethylene glycol. Because of the different steric requirements of these four solvents, the similarity in results for each solvent probably indicates that the copper

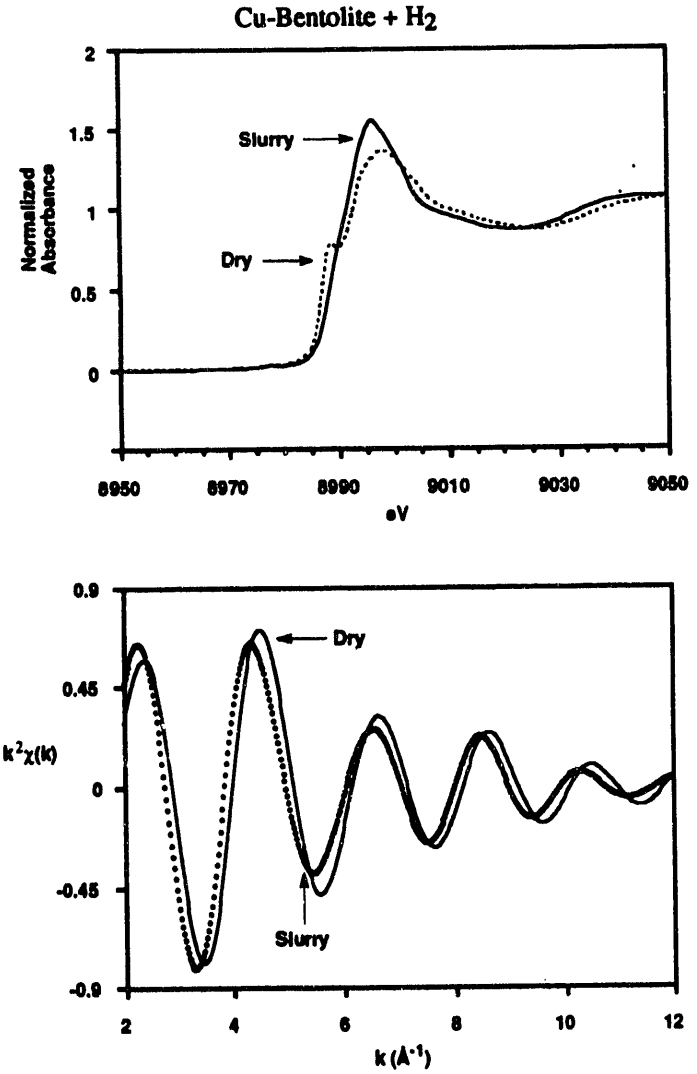

Figure VII-25. Top: X-ray absorption near edge spectra (XANES) of Cu(II) in Bentolite: air-dried and slurry in water. Bottom: Fourier-filtered EXAFS spectra of the first coordination sphere of Cu(II) in Bentolite: air-dried and slurry in water.

atom is effectively in solution within the solvated clay. It cannot leave the clay, however, because of Coulombic forces. This clay system is one of the few that has been examined by XAS in both the solid and liquid state.

X-ray absorption spectroscopy has also been used to determine whether sequential addition of copper and a water-soluble porphyrin to a clay yields the same material as the direct introduction of a copper-porphyrin. Figure VII-26 shows the XANES spectra for the copper-porphyrin both as the salt and in the clay interlayers, and a copper-clay subsequently exchanged with free-base porphyrin. Figure VII-26

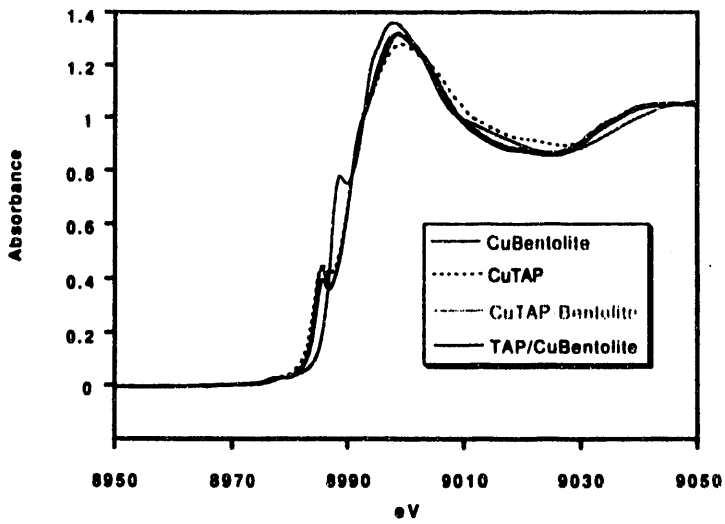

Figure VII-26. X-ray absorption near edge spectra (XANES) of copper(II)-tetrakis(n,N,N-trimethyl-4-aniliniumyl)porphyrin complexes in Bentolite.

also includes the absorption spectrum for the intermediate copper-clay in which the transition metal has aqueous coordination. These spectra demonstrate that placing the copper-porphyrin in the clay does not alter the copper-porphyrin interaction. In addition, the sequential treatment with copper and porphyrin also yields the expected copper-porphyrin. These results are promising because they illustrate how XAS can be used to probe the chemistry that occurs within a clay.

Various transition-metal thioether complexes were also explored as possible templates for hectorite crystallization because metal sulfide particles could provide remarkable props with unusual catalytic activity. Unfortunately, the metal complexes, for example Ni(II)(trithiacylononane)$_2$, are not stable to basic conditions (hectorite gel pH = 9-10). Nevertheless, nickel, copper, and iron thioether complexes were successfully ion-exchanged into natural hectorites and montmorillonites, and their XRD, surface areas, and thermal behavior were recorded. It will be necessary to observe how these species decompose within the clay layers, in the interest of potential formation of metal-sulfide particles. In the future, clay preparations that do not require a basic pH (the silicon source is tetraethoxysilane instead of silica sol) will be optimized for use with organometallic templates, especially the transition metal thioethers.

The Co(III) sepulchrate-clays displayed unique behavior among all the various clays described in this project, and were thus examined in further detail. For example, the ion-exchanged Co(III) sepulchrate-hectorite was highly ordered (intense and sharp (001) diffraction peak). In contrast to the synthetic sample, the d-spacing of 17.1 Å indicates that the molecule is intercalated perpendicular to the clay layers rather than parallel (see Table VII-6). In addition, the surface area is more than double that of the other samples. The synthetic sample also appears to be more crystalline and pure for the sepulchrate than for any other template examined, as evidenced by XRD, surface area, and template uptake. The most intriguing property of these samples is a color change that occurs upon either exposure to nitrogen or to slight heating. For example, samples change reversibly from orange in air to purple in nitrogen, and back again. These species await further study by both EPR and UV-vis DR spectroscopy.

PUBLICATIONS

MASS SPECTROMETRIC STUDIES OF COALS AND COAL MACERALS
R. E. Winans
Advances in Coal Spectroscopy, H. L. C. Meuzelaar, Ed., Plenum Press, New York, 1992, pp. 255-274

CHARACTERIZATION OF COALS, OTHER KEROGENS, AND THEIR EXTRACTS BY THERMAL MASS SPECTROMETRY
R. E. Winans, P. E. Melnikov, and R. L. McBeth
Preprints, Division of Fuel Chemistry, American Chemical Society, 37, 693-698 (1992)

STRUCTURE AND STRUCTURAL DIVERSITY IN RESINITES AS DETERMINED BY PYROLYSIS-GAS CHROMATOGRAPHY-MASS SPECTROMETRY
K. B. Anderson* and R. E. Winans
Preprints, Division of Fuel Chemistry, American Chemical Society, 36, 765-773 (1991)

*Not affiliated with the Chemistry Division or affiliated on a temporary basis.

THE NATURE AND FATE OF NATURAL RESINS IN THE GEOSPHERE. I. EVALUATION OF PYROLYSIS-GAS CHROMATOGRAPHY-MASS SPECTROMETRY FOR THE ANALYSIS OF PLANT RESINS AND RESINITES

K. B. Anderson* and R. E. Winans

Anal. Chem. 63, 2901-2908 (1991)

USE OF CONTINUOUS FLOW CENTRIFUGATION TECHNIQUES FOR COAL MACERAL SEPARATION. PART I. FUNDAMENTALS

G. R. Dyrkacz and C. A. A. Bloomquist

Energy & Fuels 6, 357-374 (1992)

THE SEPARATION OF MACERALS BY CONTINUOUS FLOW CENTRIFUGATION. PART II. MULTIPLE DENSITY FRACTIONATION OF COALS.

G. R. Dyrkacz and C. A. A. Bloomquist

Energy & Fuels 6, 374-386 (1992)

THREE-DIMENSIONAL MICROSCOPIC ^{1}H NMR IMAGING OF RIGID POLYMERS

S. L. Dieckman*, P. Rizo*, N. Gopalsami*, J. P. Heeschen*, and R. E. Botto

J. Am. Chem. Soc. 114, 2717-2719 (1992)

LASER DESORPTION/PHOTOIONIZATION TIME-OF-FLIGHT MASS SPECTROMETRY OF POLYMER ADDITIVES

J. E. Hunt, K. R. Lykke, and M. J. Pellin

NATO ASI Ser., Ser. B 269 (Methods Mech. Prod. Ions Large Mol.), 309-314 (1991)

HIGH-YIELD SYNTHESIS, SEPARATION, AND MASS-SPECTROMETRIC CHARACTERIZATION OF FULLERENES C_{60} TO C_{266}

D. H. Parker*, P. Wurz*, K. Chatterjee*, K. R. Lykke, J. E. Hunt, M. J. Pellin, J. C. Hemminger*, D. M. Gruen, and L. M. Stock

J. Am. Chem. Soc. 113, 7499-7503 (1991)

DEPENDENCE OF SECONDARY ION EMISSION FROM ORGANIC MATERIAL ON THE ENERGY LOSS OF THE IMPACTING HEAVY ION

J. E. Hunt and K. Wien*

Proceedings, Latin American Summer School on Physics 1991, Caxambu, MG, Brazil, World Scientific, New Jersey, 1991, pp. 214-229

THERMAL ANALYSIS OF PORPHYRIN-CLAY COMPLEXES

K. A. Carrado, K. B. Anderson*, and P. S. Grutkoski*

Supramolecular Architecture: Synthetic Control in Thin Films and Solids, ACS Symp. Ser. #499; T. Bein, Ed.; ACS, Washington, D.C., 1992, pp. 155-165

PREPARATION OF HECTORITE CLAYS UTILIZING ORGANIC AND ORGANOMETALLIC COMPLEXES DURING HYDROTHERMAL CRYSTALLIZATION

K. A. Carrado

Industrial and Engineering Chemistry Research, 31, 1654-1659 (1992)

BLOCH DECAY SOLID-STATE ^{13}C NMR SPECTROSCOPY OF SAMARIUM IODIDE TREATED ARGONNE PREMIUM COALS

J. V. Muntean* and L. M. Stock

Energy & Fuels, 5, 765-767 (1991)

---

*Not affiliated with the Chemistry Division or affiliated on a temporary basis.

SOLID STATE ^{13}C NMR SPECTROSCOPY OF A POCAHONTAS NO. 3 COAL
L. M. Stock and J. V. Muntean*
Energy & Fuels, 5, 767-769 (1991)

XANES EVIDENCE FOR SELECTIVE ORGANIC SULFUR REMOVAL FROM ILLINOIS NO. 6 COAL
L. M. Stock, K. Chatterjee*, M. L. Gorbaty*, G. N. George*, and S. R. Keleman*
Energy & Fuels, 5, 771-773 (1991)

TOWARD ORGANIC DESULFURIZATION
L. M. Stock
Energia, 3, 1 (1992)

SUBMISSIONS

AB INITIO MOLECULAR ORBITAL STUDY OF THE EFFECTS OF BASIS SET SIZE ON THE CALCULATED STRUCTURE AND ACIDITY OF HYDROXYL GROUPS IN FRAMEWORK MOLECULAR SIEVES
J. B. Nicholas*, R. E. Winans, R. J. Harrison*, L. E. Iton*, L. A. Curtiss*, and A. J. Hopfinger*
J. Phys. Chem. (accepted)

THE NATURE AND FATE OF NATURAL RESINS IN THE GEOSPHERE. III. RE-EVALUATION OF THE STRUCTURE AND COMPOSITION OF *HIGHGATE COPALITE* AND *GLESSITE*
K. B. Anderson* and R. E. Botto
Org. Geochem. (submitted)

DISCRETE LAYERS OF ORDERED C_{60} MOLECULES IN THE COCRYSTAL $C_{60}{\cdot}CH_2I_2{\cdot}C_6H_6$: SYNTHESIS, CRYSTAL STRUCTURE, AND ^{13}C NMR PROPERTIES
U. Geiser, S. K. Kumar*, B. M. Savall*, S. S. Harried*, K. D. Carlson, P. R. Mobley*, H. H. Wang, J. M. Williams, and R. E. Botto
Chem. Mat. (in press)

THE NATURE AND FATE OF NATURAL RESINS IN THE GEOSPHERE. II. IDENTIFICATION, CLASSIFICATION AND NOMENCLATURE OF RESINITES
K. B. Anderson*, R. E. Winans, and R. E. Botto
Org. Geochem. (in press)

MEASUREMENT OF SPIN-LATTICE RELAXATION IN ARGONNE PREMIUM COAL SAMPLES
C. Tsiao* and R. E. Botto
Techniques in Magnetic Resonance for Carbonaceous Solids, ACS Advances in Chemistry Series No. 229, R. E. Botto and Y. Sanada, Eds. (in press)

QUANTITATION IN CARBON NMR SPECTROSCOPY OF CARBONACEOUS SOLIDS
R. A. Wind*, G. E. Maciel*, and R. E. Botto
Techniques in Magnetic Resonance for Carbonaceous Solids, ACS Advances in Chemistry Series No. 229, R. E. Botto and Y. Sanada, Eds. (in press)

CONCLUDING REMARKS: APPLICATION OF ADVANCED MAGNETIC RESONANCE TECHNIQUES TO ARGONNE PREMIUM COALS
B. G. Silbernagel* and R. E. Botto
Techniques in Magnetic Resonance for Carbonaceous Solids, ACS Advanced in Chemistry Series No. 229, R. E. Botto and Y. Sanada, Eds. (in press)

---

*Not affiliated with the Chemistry Division or affiliated on a temporary basis.

MASS SPECTROMETRIC ANALYSIS OF RUBBER VULCANIZATES BY LASER DESORPTION/LASER IONIZATION
K. R. Lykke, D. H. Parker*, P. Wurz*, J. E. Hunt, M. J. Pellin, and D. M. Gruen
Anal. Chem. (accepted) (1992)

AN INVESTIGATION INTO THE PROCESS OF CENTRIFUGAL SINK/FLOAT SEPARATION OF MICRONIZED COALS. PART I. SOME INFERENCES FOR COAL MACERAL SEPARATIONS
G. R. Dyrkacz, L. Ruscic*, and J. Fredericks*
Energy & Fuels (in press)

AN INVESTIGATION INTO THE PROCESS OF CENTRIFUGAL SINK/FLOAT SEPARATION OF MICRONIZED COALS. PART II. MULTIPLE FRACTIONATION OF SINGLE COAL SAMPLES
G. R. Dyrkacz and L. Ruscic*
Energy & Fuels (in press)

FAST, ONE-STEP SEPARATION AND PURIFICATION OF BUCKMINSTERFULLERENE, C_{60}, FROM CARBON SOOT
L. M. Stock and K. Chatterjee*
J. Org. Chem. (accepted)

THREE-DIMENSIONAL NMR MICROSCOPIC IMAGING OF COAL SWELLING IN PYRIDINE
D. C. French*, S. L. Dieckman*, and R. E. Botto
Energy & Fuels (1992)

COLLABORATIONS

S. Cebulak, Sileasia University Katowice, Poland
Investigation of the thermal properties of separated macerals.

J. De Leeuw, Delft University, The Netherlands
Analysis of pyrolysis products of separated macerals.

B. Johns, University of Melbourne, Australia
Examination of the pyrolysis products of separated Australian macerals by FTIR, NMR and GC/MS.

T. Vassalo and M. Wilson, CSIRO, Australia
Examination of the pyrolysis products of separated Australian macerals by FTIR, NMR, and GC/MS.

A. Cohen, University of South Carolina
Separation of peat by density-gradient centrifugation methods.

M. Gorbaty, Exxon Research and Engineering, Annandale, NJ
Sulfur compounds in synthetic coals and separated macerals are being investigated by using XANES and XAFS.

G. L. Keldsen, Purdue University North Central, Westville, IN
Interactions between clays and hydrocarbons are being studied by means of molecular mechanics. Our initial efforts have focused on reproducing observed trends in heats of absorption.

C. Venier, Pennzoil Products Company, The Woodlands, TX
Very pure high-molecular-weight hydrocarbons are being characterized by high-resolution mass spectrometry. These materials have potential for use as the matrix for fast atom bombardment MS analysis of coal-derived materials.

*Not affiliated with the Chemistry Division or affiliated on a temporary basis.

T. G. Squires, Associated Western Universities, Inc., Salt Lake City, UT
In this collaborative effort, we study chemical and thermal reactivities of polymers designed to model structural features in coals. Techniques used to characterize coals have been applied to polymers synthesized by Squires. The results have enabled us to better understand coal structure and reactivity.

R. B. Johns, University of Melbourne, Australia
The density gradient separation technique is being used to study Australian brown coals. Initial results have shown that this approach works very well for these coals. Separate studies on solid ^{31}P NMR of derivatized wools have elucidated sites of phosphorylation leading to flame-retardant properties.

J. Carnahan, Northern Illinois University, DeKalb
Microwave-induced plasma emission spectrometric techniques are being developed to characterize large organic coal-derived molecules.

E. Quinga, Amoco Oil Company, Naperville, IL
Structure and reactivity relationships in the liquefaction of Argonne Premium Coal Samples and separated macerals are being studied in a very broad-based effort.

G. W. Zajac and J. Z. Shyu, Amoco Oil Company, Naperville, IL
Surface analysis of catalytic materials.

R. Ollendorff, Amoco Oil Company, Naperville, IL
The Amoco-Argonne Coal Chemistry Seminar Series is bringing in a number of well-known researchers in the field. The seminars alternate between Argonne and Amoco and occur about once a month.

D. Fishel, Kent State University, Kent, OH
Large model compounds are being designed and synthesized for reactivity studies and evaluation of new mass spectrometric approaches.

M. Melchior, Exxon Research and Engineering, Annandale, NJ
NMR spin-diffusion measurements are being utilized to probe domain structures in coals.

J. Boon, FOM-Institute of Atomic and Molecular Physics, Amsterdam, The Netherlands
Solid-state ^{13}C NMR spectroscopy and PyMS analyses of charred crusts from Late Iron Age pottery samples have revealed information on the diet and food gathering of prehistoric peoples of northern Europe.

VIII. THE PREMIUM COAL SAMPLE PROGRAM

K. S. Vorres

Outside Collaborators: *C. Kruse, B. Farris*

A. Program Administration

The objectives of the Premium Coal Sample Program are to make the best coal samples available for basic coal research, and to encourage their use by the basic coal science community. These samples have been used for comparison, correlation, and generation of new knowledge for the five to seven years since they first became available. Earlier *Surveys of Research* described the activities involved in sample selection, collection, transport, processing, packaging, and distribution. The term "premium" in the name refers to the extreme care taken in each step from selection through distribution, including the minimal exposure to oxygen, thorough mixing, and extensive inventory of ampoules for long-term supplies.

As a result of a strong effort to rebuild the sample inventory in the previous fiscal year, the inventory is expected to meet normal demands for samples for 15-20 years for the most popular samples (Illinois #6 and Wyodak) and for longer periods for the others.

An additional 180 shipments were made to raise the total to 678 shipments to over 320 coal researchers around the world. The growth in the use of the samples is shown in Figure VIII-1. The more than 2,200 ampoules shipped raised the total over 18,200.

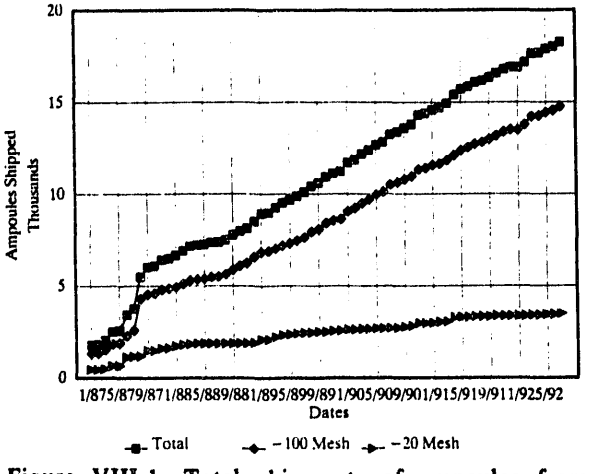

Figure VIII-1. Total shipments of ampoules from January 1987 through July 1992

The acceptance of the samples is strong and growing, with 20 new users replacing some who are no longer active. The rate of ampoule shipments has continued relatively constant despite generally decreased levels of support for fossil fuel research. The number of shipments is increasing while the average size of the shipment is decreasing.

An additional 82 papers were published to raise the total to 360 reporting work done with the Argonne Premium Coal Samples. The Users Handbook has been continually expanded to incorporate additional bibliographic information. Another edition is planned for early 1993. The information growth will approximately double the size of the Handbook. Separate chapters provide a description of the program and each sample; analytical data; references to literature dealing with the use of the samples; summaries of the research reported in the references; and other generally useful information. This document contributes substantially to the uniqueness and value of the Program. This Handbook is periodically distributed to all recipients of samples and to others who request it.

The Quarterly Newsletter updates the bibliographic information with new references. Selected individuals are undertaking a summary of the work done in one of 17 different categories of research in which the papers have been published. It is planned to incorporate this summary into the Handbook and to publish it in Energy & Fuels.

Symposia on Research with Argonne Premium Coal Samples will no longer be held as part of the program of the Fuel Chemistry Division in conjunction with American Chemical Society meetings. The use of the samples is now so widespread that papers describing research with them fit naturally in symposia related to topics of research, such as coal liquefaction.

The processing facility equipment is operated on a weekly basis to confirm the operability of the components. This operation also helps maintain the oxygen at a low level in the processing facility, which is now used to store special samples.

B. Sample Stability

Sample stability is monitored by annual analysis of the gas inside of the ampoules. The new mass spectrometer now being used by the ANL Analytical Chemistry Laboratory has achieved better limits of detection for the gases analyzed. Oxygen was found to be in concentrations either at or below the limit of detection (10 ppm) and argon at constant concentrations. These results indicate the integrity of the seals. Gradual changes in methane, carbon dioxide, and hydrogen contents have been measured consistent with earlier observations. The changes are attributed to diffusion of dissolved gas from the interior of the particles into the void space of the ampoule. A summary of recent results was presented at the August 1992 American Chemical Society meeting in Washington, D.C.

PUBLICATIONS

GAS EVOLUTION FROM COAL IN SEALED GLASS AMPOULES
K. S. Vorres
Proceedings of 1991 International Conference on Coal Science, 147-150 (1991)

DRYING OF BEULAH ZAP LIGNITE. PRETREATMENT WITH SOLVENTS AND REHYDRATION
K. S. Vorres
Preprints, Fuel Chemistry Division, American Chemical Society 37, 988-1005 (1992)

GAS EVOLUTION FROM COAL IN SEALED GLASS AMPOULES
K. S. Vorres
Preprints, Fuel Chemistry Division, American Chemical Society 37, 1945-1950 (1992)

SUBMISSION

Coal
K. S. Vorres
Kirk-Othmer Encyclopedia of Chemical Technology, Fourth Edition, J. Wiley & Sons, Inc., 60 pp

COLLABORATIONS

C. Kruse, Illinois State Geological Survey, Champaign
The Illinois Basin Coal Sample Program is headquartered at the Illinois State Geological Survey. Kruse administers this program for the Survey, and Vorres is serving as the chairman of the advisory committee for the IBCSP.

B. Farris, Columbia Academy, Columbia, TN
Farris participated in data reduction for studies of the rate of drying of the lignite coal in dry and humid nitrogen. This work included correlations of drying rate with gas-flow rate, temperature, and sample weight.

IX. CHEMICAL SEPARATIONS SCIENCE

E. P. Horwitz, H. Diamond, M. L. Dietz, R. C. Gatrone, R. Chiarizia

Outside Collaborators: *S. Alexandratos, R. A. Leonard, D. Nelson, R. D. Rogers*

Our program has as its objectives the development of new and/or improved separation methods based on new biphasic systems and new organic extractants, and the elucidation of the basic chemistry involved in these systems. Our studies are directed towards fundamental problems in separations science. Solutions to these problems may be of importance to environmental restoration (ER) and waste management (WM). Separations science is perhaps the one technology that will likely have the greatest role in achieving final solutions to many of the most difficult and costly ER and WM problems at DOE facilities. Liquid-liquid and solid-liquid partitioning processes, in particular, promise to play a lead role in main areas of ER and WM.

Although partitioning processes are widely used throughout the world, the need for new extractants, new reagents to modify and enhance the efficiency of separation processes, and new routes to synthesize these reagents is greater today than at any time in the past. Our program on chemical separations science addresses a number of the above areas. The major subdivisions of the program are:

1. *Extractant-diluent interactions.* Extractant-diluent interactions are studied to achieve major alterations in extractant behavior with respect to third-phase formation or to eliminate the need for cation and/or anion dehydration to achieve extraction.

2. *New classes of aqueous metal-ion complexants.* New classes of ion-exchange resins and non-phosphorus-based aqueous-soluble complexing agents are under investigation because they have unique properties with respect to their ability to complex metal ions in highly acidic media.

3. *New concepts for the preparation of organophosphorus extractants and complexants.* New methods are developed for synthesizing sterically hindered organophosphorus extractants and for converting directly phosphorus-oxygen bonds into phosphorus-carbon or phosphorus-hydrogen bonds.

4. *Separation potential of new extractant systems.* New extractants and new complexant combinations are evaluated to demonstrate the achievement of separation and to identify potential applications. Emphasis is placed on new methods for nuclear-waste processing, by-product recovery from high-level waste, and the recovery of critical and strategic materials.

A. Simultaneous Extraction of TRUs, ^{90}Sr, and ^{99}Tc

E. P. Horwitz, H. Diamond, M. L. Dietz, R. D. Rogers

The chemical pretreatment of stored high-level nuclear waste for waste minimization is a major technological challenge. In all likelihood, this pretreatment will involve one or more solvent extraction (SX) processes. The popularity of SX in the nuclear industry stems from its ability to operate in a continuous mode, to achieve high throughputs and high decontamination factors of product streams, and to utilize relatively small quantities of very selective chemical compounds (extractants) as metal-ion complexants. Because of the diversity and complexity of nuclear wastes, especially those wastes contained in single-shell tanks at the Hanford site, the demands on any separation process are great. Perhaps the greatest difficulty for the separations chemist is to develop processes that remove not only actinides (the most toxic radionuclides in nuclear waste) but also selected heat-producing and long-lived fission products, for example, ^{90}Sr and ^{99}Tc, in a single process.

The basic problem in designing an SX process, or any other partitioning process, to achieve multi-element extraction is that no single ligand is capable of coordinating selectively to elements with such widely differing chemical properties as, for example, transuranic elements (Np, Pu, Am) and Sr. In the mid-1980s, members of the Chemical Separations Science

Group developed a stand-alone acid-side SX process (TRUEX) for the removal and recovery of uranium and transuranic elements (TRUs) from nuclear waste. Recently, we have developed an acid-side SX process (SREX) to extract and recover ^{90}Sr from high-level nuclear waste. Both TRUEX and SREX processes extract Tc to a significant extent, although not as efficiently as they extract TRUs and Sr. A possible solution to the multicomponent extraction is to mix the extractants used in TRUEX and SREX.

In order to mix two different extractants and achieve the behaviors of each individually, both extractants must be essentially the same type, either neutral, liquid cationic, or liquid anionic. The first two types are not compatible because neutral extractants contain basic donor groups that form hydrogen bonds with liquid cationic (acidic) extractants. On the other hand, neutral and anionic extractants are compatible because there is very little opportunity for interaction. The key extractants in TRUEX and SREX process solvents are octyl(phenyl)-N,N-diisobutylcarbamoylmethyl-phosphine oxide (CMPO) and 4,4'(5')bis-tertiary-butylcyclohexano-18-crown-6 (DtBuCH18C6), respectively. Both compounds are neutral extractants. However, DtBuCH18C6 is dissolved in 1-octanol in the SREX process solvent formulation, and alcohols strongly hydrogen-bond to phosphine oxides, which drastically reduces their effectiveness.

Another major problem that arises when extractants are mixed is the onset of third-phase formation. Third-phase formation, or the formation of a second organic phase, is due to the greater attraction that extractant molecules have for one another than they have for the diluent. This cohesive attraction between extractant molecules causes them to aggregate and form a separate (usually heavy) organic phase.

Both problems, that is, the replacement of octanol as the diluent for the crown ether and the minimization of third-phase formation, were solved as a result of basic research studies on extractant-diluent interactions. These studies showed the importance of utilizing high concentrations of a second moderately polar molecule, for example, tri-n-butyl phosphate (TBP), to reduce dipole-dipole or dipole-induced-dipole interactions between extractant molecules that cause aggregation and third-phase formation. The presence of a large ratio of TBP to crown ether and/or CMPO effectively eliminated any solubility problems and enhanced the extraction of Sr nitrate by the crown ether to practical levels. Of equal importance is the fact that when CMPO and DtBuCH18C6 are dissolved in TBP their extraction efficiencies, as measured by the distribution ratio, D_{Am} and D_{Sr}, are unchanged, whether present individually or as a mixture.

Unfortunately, undiluted TBP is too soluble in aqueous solutions and is too viscous to be useful in SX processes unless it is mixed with a hydrocarbon diluent. However, polar extractants in hydrocarbon diluents are prone to third-phase formation. Again, our basic research studies in the area of extractant-diluent interactions showed the importance of creating cavities in hydrocarbon media to reduce third-phase formation. Cavities are created by utilizing branched-chain hydrocarbons. The creation of cavities or holes in the organic phase reduces the energy required by large polar molecules to fit between diluent molecules. The extraction of uranyl nitrate was chosen to induce third-phase formation in mixtures of CMPO-DtBuCH18C6-TBP-hydrocarbon because uranium is the most abundant extractable constituent in dissolved sludge waste from single-shell storage tanks at Hanford. Table IX-1 shows the influence of carbon chain length and flash point on the loading of uranyl nitrate in 0.2 M CMPO-0.2 M DtBuCh18C6-TBP mixtures. The data in Table IX-1 show the maximum concentration of uranyl nitrate that can be extracted into the combined solvent without the formation of a

Table IX-1. Maximum loading of process solvent (process solvent 0.2 M CMPO—0.2 M DtBuCH18C6) (aqueous phase 3M HNO_3 - uranyl nitrate, 25 °C)

diluent	no. of carbons	flash point	[U]org,M*
1.2 M TBP - Dodecane	12.0	71	0.021
1.2 M TBP - Norpar™-12	11.5	69	0.038
1.2 M TBP - Isopar™-L	12.0	61	0.140
1.2 M TBP - Isopar™-M	13.5	80	0.029
1.2 M DA[AP] - Isopar™-M	13.5	80	0.20

*Maximum concentration of uranium in the process solvent without third-phase formation

third-phase. Norpar™-12 is a normal paraffinic hydrocarbon, whereas Isopar™-L and -M are isoparaffinic hydrocarbons. The data show that for a given chain length, isoparaffinic hydrocarbons are more effective than normal paraffinic hydrocarbons at suppressing third-phase formation.

Although the combination of TBP phase modifier and Isopar™-M diluent appears adequate for a combined TRUEX-SREX solvent formulation, the formation of a third-phase at 0.04 M U in the solvent puts severe restriction on the flowsheet design. The volume of organic to aqueous phase (O/A) in the extraction cycle cannot be much below one without overloading the solvent. However, again our basic research studies in the area of extractant-diluent interactions have shown the importance of the polarity of the phase modifier, as well as diluent structure, in reducing the third-phase formation. Earlier studies performed during the development of the TRUEX process showed that the substitution of the more basic dibutyl butylphosphonate DB[BP] for TBP reduced the tendency for third-phase formation. Based on these earlier studies, we replaced TBP with diamyl amylphosphonate, DA[AP]. (DB[BP] was not used because of its solubility.) Table IX-1 shows the substantial increase in the concentration of U that can be extracted without the formation of a third-phase. Similar results are obtained with Bi and Fe, both of which will be present in large concentrations in dissolved sludge waste from storage tanks.

Figure IX-1 shows the nitric acid dependency distribution ratios of Sr, Tc, and Am using a solution 0.2 M in DtBuCH18C6 - 0.2 M CMPO-1.2 M Da[AP] in Isopar™-M. All three elements are sufficiently extractable from 3 M HNO_3 (the most likely concentration of a feed solution) using the new formulation to warrant its use in a combined TRUEX-SREX process. Of even greater importance is the influence of macro concentrations of U and Bi on D_{Sr}, D_{Tc}, and D_U, shown in Figure IX-2. These data show that increasing concentrations of U and Bi in the solvent have very little effect on D_{Sr} because neither U or Bi is complexed by the crown ether. On the other hand, D_{Am} is significantly affected by high concentrations of U and Bi because both of these elements are extracted as their nitrate salts by CMPO. Fortunately, the decrease in D_{Am} is not as large as expected based on a $Am(NO_3)_3$•3CMPO stoichiometry. A possible reason for the lower dependency of D_{Am} is that DA[AP] is also coordinating to $UO_2(NO_3)_2$ for a mixed $UO_2(NO_3)_2$ •CMPO•DA[AP] complex. The net effect is that less CMPO is being consumed as U is extracted. A similar explanation applies to the extraction of Bi although the mixed complex may have the following stoichiometry: $Bi(NO_3)_3$•2CMPO•DA[AP], which accounts for the greater decrease in D_{Am} with Bi than with U. The D_{Tc} value increases with both U and Bi extraction due to the tendency of TcO_4^- to complex with extracted metal ions. Thus, the combined TRUEX-SREX

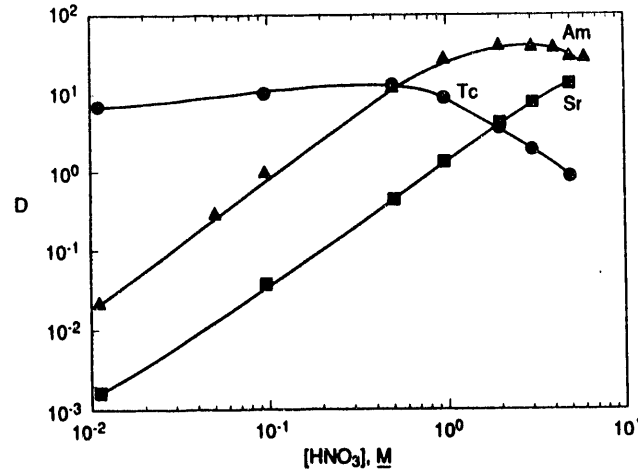

Figure IX-1. Distribution ratios of Sr, Am, and Tc vs. aqueous HNO_3 concentration for combined process solvent (0.2 M DtBuCH18C6—0.2 M CMPO—1.2 M Da[AP] in Isopar™-M.)

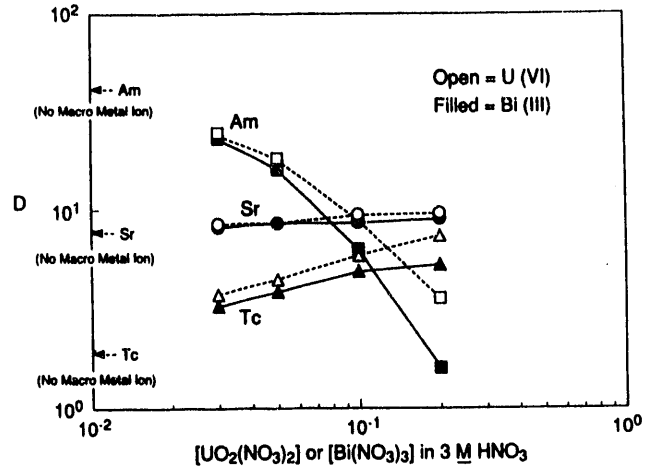

Figure IX-2. The influence of loading on the extraction of Sr, Am, and Tc using combined process solvent (given in Figure IX-1). Aqueous phase = 3.0 M HNO_3.

process solvent formulation is effective even in the most likely situation where macro concentrations of U and Bi will be present.

Work is in progress on testing the new combined solvent formulation in dissolved sludge waste simulant and on developing and testing flowsheets. A combined TRUEX-SREX process will make a major impact on the economics of chemical pretreatment of nuclear waste because the combined process would require less space and equipment and would be easier to control compared to individual TRUEX and SREX processses carried out in tandem.

B. Extractant-diluent Interactions: The Influence of Substituents

R. C. Gatrone, E. P. Horwitz, M. L. Dietz

To achieve separation by means of partitioning processes, for example, liquid-liquid or solvent extraction (SX), extraction chromatography (EXC), or ion exchange (IX), one must exploit the inherent physical and chemical factors involved in the transport of metal ions from an aqueous to a nonaqueous environment. Although many of the chemical and physical principles of SX, EXC, and IX are well understood, the interactions occurring between extractants and diluents and the role of water in the nonaqueous phase are two of the least understood aspects of the three separations techniques. Frequently, the utilization of extractant-diluent effects can bring about profound (and oftentimes beneficial) changes in the behavior of extractants. For example, the change in the behavior of octyl(phenyl)-N,N-diisobutylcarbamoylmethylphosphine oxide (CMPO) when mixed with an excess of tributylphosphate (TBP) was tantamount to the preparation of a new extractant. This discovery led to the formulation of the TRUEX process solvent.

Recently, our studies on extractant-diluent interactions have concentrated on how changes in the structure of the amidic substituent of the carbamoylmethylphosphine oxide extractants influence solubility of the extracted complex in normal paraffinic hydrocarbon solvents. Earlier studies have shown that the solubility of the CMPO-complex, as manifested by the lack of third-phase formation on metal-ion loading, is influenced by the substituents attached to the amidic nitrogen. Our modeling efforts using the computer program *Alchemy*™ have suggested that an increase in the steric hindrance around the amidic nitrogen improves the solubility of the extracted complex by shielding the effective positive charge on the nitrogen atom. Shielding the positive charge interferes with aggregation of the molecule through dipole-dipole interaction. Figure IX-3 shows the modeling results for the N,N-diethyl and N,N-diisobutylacetamide portion of the n-octyl (phenyl)-N,N-dialkylcarbamoylmethylphosphine oxide obtained from the program. We have qualitatively proposed that a decrease in the visible portion of the nitrogen atom in the space-filling representation due to an increase in steric hindrance corresponds to a decrease in the dipole-dipole interactions and in third-phase formation.

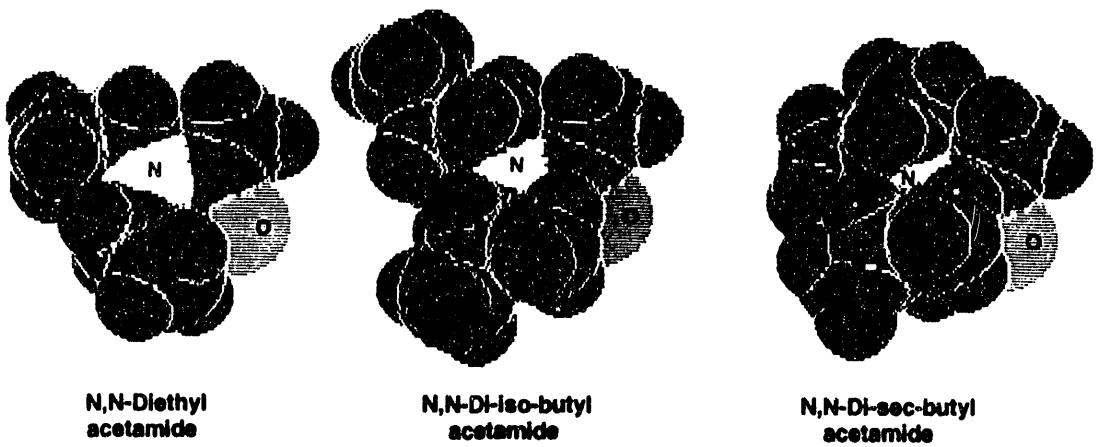

Figure IX-3. Conformations of selected N,N-dialkylacetamides as computed by *Alchemy*™ molecular modeling program.

To more quantitatively determine the effect of steric hindrance on the formation of a third-phase in a nonpolar diluent, we synthesized a series of octyl(phenyl)-N,N-dialkylcarbamoylmethylphosphine oxides in which the degree of steric hindrance around the nitrogen atom was systematically varied. The compounds prepared and yields obtained are listed in Table IX-2. The most sterically hindered compound we wished to prepare was the carbamoylmethylphosphine oxide derived from 2,2,4,4-tetramethylpiperdinylacetamide, which is comparable to the bis-tert-butyl derivative. We prepared the requisite 2-chloroacetamide by reacting 2,2,4,4-tetramethylpiperdine with 2-chloroacetyl chloride. Unfortunately, this particular acetamide is unreactive toward nucleophilic (S_N2) substitution and does not react with the magnesium salt of octyl(phenyl)phosphine oxide, nor with iodide, thiocyanate, or sulfide anions; thus we were unable to include a bis-tert-butyl species in our study. We may explain the unreactive nature of the 2,2,4,4-tetramethylpiperdinylacetamide toward nucleophilic substitution using the molecular models from *Alchemy*™. If we examine the pathway by which a nucleophile must approach the carbon bearing the chloride-leaving group, we see a significant increase in the interaction between the aromatic group on the phosphoryl anion and the methyl groups on the piperdinyl ring. This apparent increase in energy in the ground state of the displacement reaction causes the addition reaction to fail. It is interesting to note that the bis-sec-butyl acetamide, although still significantly hindered, does undergo displacement in refluxing benzene, albeit more slowly than the less hindered amides.

Despite our inability to prepare a bis-tertiary-butyl derivative, we felt that varying the series compounds from diethyl to di-secondary butyl would clearly demonstrate the effect that increasing the steric requirements would have upon third-phase formation. Our preliminary experiments were confined to third-phase formation during the extraction of nitric acid. It is well known that the basic phosphine oxide can extract significant quantities of nitric acid and that, frequently, the extracted nitrate complex is insoluble in normal paraffinic hydrocarbon diluents. Because tributylphosphate was added to the TRUEX process solvent to increase the observed solubility of the OϕD(iB)CMPO·HNO_3 and the OϕD(iB)CMPO·$Am(NO_3)_3$ complexes, the preliminary examination of the CMPO derivatives listed in Table IX-2 was done under conditions where the formation of a third-phase would be favored. After determination of the minimum nitrate concentration where third-phase formation would not occur, the derivatives would be reexamined using uranium ion to determine the maximum loading prior to third-phase formation.

We examined the third-phase formation of the newly prepared CMPO derivatives by contacting dodecane solutions with various nitric acid concentrations followed by the addition of a tracer-scale amount of americium-241. We carefully counted the organic and aqueous phases to ascertain the mass balance of Am-241. The nitric acid concentration where the mass balance was poor due to the formation of an almost invisible quantity of heavy organic phase located at the organic/aqueous interface is recorded in Table IX-3 as $[HNO_3]_{max}$.

The results from Table IX-2 clearly confirm the trends expected from our molecular modeling data, as third-phase formation decreases with increasing steric hindrance around the nitrogen atom. Furthermore, the molecular modeling data for N,N-di•sec-butyl

Table IX-2. CMPO derivatives synthesized.

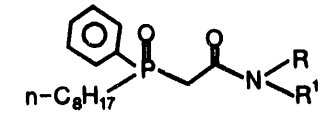

R	R^1	% yield	purity (%)
Et	Et	38*	98
Et	n-Bu	40*	99.6
n-Bu	n-Bu	25*	97.5
i-Bu	i-Bu	66	99
t-Bu	t-Bu	?	—

Table IX-3. Effect of amidic nitrogen substitution on third-phase formation.

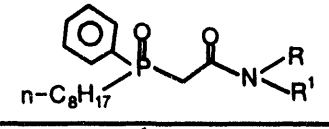

R	R^1	$[HNO_3]_{max}$ M*
Et	Et	0.02
Et	N-Bu	0.02
n-Bu	n-Bu	0.51
i-Bu	i-Bu	0.62
sec-Bu	Sec-Bu	3.07

acetamide confirm that the octyl (phenyl)-N,N-di-sec-butylcarbamoylmethylphosphine oxide is the most sterically hindered of the substituted amidic derivatives. This is shown in Figure IX-3 where the most sterically hindered amidic groups have the least visible nitrogen. As expected, it provides the best phase-compatibility data on contact with nitric acid. Studies to determine the maximum loading of uranium and/or neptunium are currently in progress.

The preliminary results obtained for the third-phase formation during the extraction of nitric acid by these CMPO derivatives, which parallel the third-phase formation that occurs under high metal-ion loading conditions, suggest that the most hindered derivative, octyl(phenyl)-N,N-di-sec-butylcarbamoyl-methylphosphine oxide, would be a viable candidate to replace the commercially available diisobutyl derivative. Collaborative studies to determine the optimum method of purifying the sec-butyl CMPO are being considered.

C. Diphonix — A New Ion-Exchange Resin for the Treatment of Industrial Waste Streams, Contaminated Groundwaters, and Mixed Wastes

E. P. Horwitz, R. C. Gatrone, R. Chiarizia, S. Alexandratos

Interest in the removal and recovery of heavy (toxic) metal ions from contaminated groundwater, mixed wastes, industrial waste streams, and contaminated drinking water continues to increase as environmental laws become more stringent and permissible discharge limits are lowered. Treatment of contaminated water or industrial waste streams has frequently utilized precipitation and ion-exchange technologies. However, precipitation will not meet the lower limits and requires excessive quantities of chemicals, and commercially available ion-exchange resins do not have high affinities for many of the toxic metals relative to Ca and Mg.

We have synthesized and characterized a new ion-exchange resin that shows considerable potential for environmental restoration, for the treatment of industrial waste streams, and for the treatment of alpha-active mixed waste. The new resin contains geminally substituted diphosphonic acid functional groups. The resin is called Diphonix for diphosphonic ion exchange. Alkyl-1,1-diphosphonic acids are among the most powerful complexing agents for polyvalent metal ions in aqueous solution, particularly at pH < 2. But heretofore, it has not been possible to synthesize resins containing diphosphonic acid groups because of the difficulty of introducing this group into a preformed polymer matrix. The synthesis of Diphonix was accomplished by the copolymerization of tetraalkylvinylidene diphosphonate with styrene, divinylbenzene, and acrylonitrile followed by deesterification of the resultant resin by refluxing with concentrated HCl. During the latter step, the nitrile group is hydrolyzed to a carboxylic acid. Essentially 100% of the vinylidene diphosphonate ester is incorporated into the polymer matrix. The copolymerization of the vinylidene diphosphonate ester is a major achievement because of the steric hindrance imposed on the vinylidene group by the diphosphonic group. This difficulty was obviated by using another relatively small monomer (acrylonitrile in our case) as a "carrier" to induce polymerization of the vinylidene diphosphonate. However, the resultant diphosphonic acid resin had rather slow metal ion-exchange rates because of its hydrophobicity. We discovered that by sulfonation of the diphosphonic acid resin, the hydrophilicity of the resin is increased significantly and the metal ion-exchange rates are now comparable to the commercially available macroporous strong acid cation-exchange resins (e.g., BioRad AGMP-50).

The structure of a segment of the polymer matrix of Diphonix is shown in Figure IX-4. The resin is actually trifunctional, that is, it contains three functional groups, a gem-diphosphonic group, a carboxylic acid group, and a sulfonic acid group.

Early experiments showed definitively that the diphosphonic acid functionality dominates the behavior of the resin towards metal ions. Figure IX-5 shows

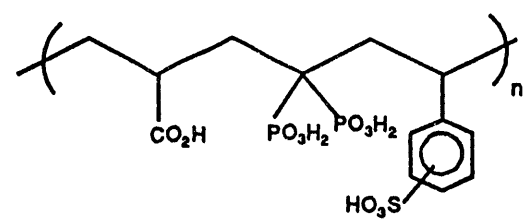

Figure IX-4. Diphonix polymer matrix.

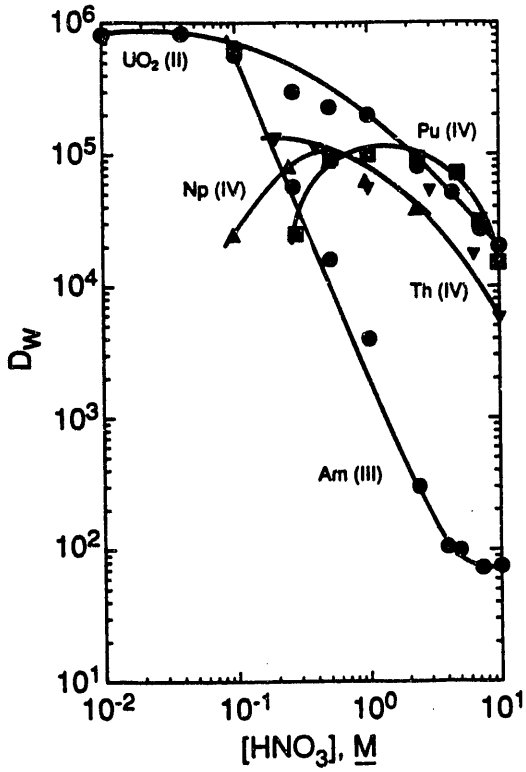

Figure IX-5. Uptake of actinide ions by Diphonix.

the distribution ratio (the amount of activity per gram of resin/amount of activity per mL of solution) of actinides in the tri-, tetra-, and hexavalent oxidation states as a function of the nitric acid concentration. The data show that Diphonix has extraordinarily strong affinities for the actinides in II, IV, and VI oxidation states, even in 10 M HNO_3. Equally impressive is the ability of Diphonix to extract actinides from high-salt concentrations. Table IX-4 compares the distribution ratios U (VI), Pu (IV), and Am (III) for Diphonix, a commercially available sulfonic acid resin (BioRad AGMP-50), and a monophosphonic-sulfonic acid resin analogous to Diphonix except that a monophosphonic acid functional group replaces the diphosphonic acid group. The aqueous phase is 4 M $NaNO_3$-0.1 M HNO_3. The data in Table IX-4 show that Diphonix is superior in its ability to sorb actinides from salt solution. These data translated to a column run would mean that 100 to 1000 more displacement volumes could flow through a Diphonix column before breakthrough occurs than would be the case with the other two resins. The strong retention of actinides even at high acidity and high-salt concentrations is consistent with the behavior of a gem-diphosphonic acid functionality. Conditions for stripping the actinides from Diphonix involve the use of a solution containing either hydroxethane-1,1-diphosphonic acid or preferably the more easily destroyed vinylidene-1,1-diphosphonic acid. It is noteworthy that the only efficient stripping agents for Diphonix involve another equally strong complexing agent containing the gem-diphosphonic acid functionality.

An important property of an ion-exchange resin is its ability to remove heavy (toxic) metals in the presence of high concentrations of Na^+, Mg^{2+}, and Ca^{2+} ions. Sodium, magnesium, and calcium salts are usually the major constituents of groundwater and industrial waste aside from the toxic metals. Figures IX-6 and IX-7 compare the uptake of a number of metal ions from pH 5 to 8 with Diphonix and BioRad AGMP-50. Both resins were in their Ca^{2+} form. In almost every case the distribution ratio is at least 100 times higher with Diphonix than on the commercial sulfonic resin. Table IX-5 compares the selectivity of Diphonix and IRC-718 relative to Ca for a number of toxic metal ions. (Rohm & Haas IRC-718 is the only commercially available all-purpose chelating ion-

Table IX-4. Comparison of the sorption of U, Pu, and Am by sulfonic, monophosphonic, and diphosphonic acid ion-exchange resins.

	4 M $NaNO_3$ - 0.1 M HNO_3		
	sulfonic	monophosphonic	diphosphonic
U	2.9×10^2	2.9×10^3	2.2×10^4
Pu	2.6×10^2	1.3×10^3	2.9×10^3
Am	4.8×10^1	2.4×10^1	5.7×10^3

Table IX-5. Comparison of the relative selectivities of Diphonix and of an iminodiacetic chelating resin.

	iminodiacetic acid (Amberlite IRC-718) pH 4	Diphonix pH 5
Ca	1.0	1.0
Mn	1.2	4.1×10^3
Co	6.7	4.5×10^2
Ni	57	2.7×10^2
Cu	2.3×10^3	$> 10^3$
Zn	17	1.4×10^4
Cd	15	1.2×10^3
Hg	2.8×10^3	3.5×10^3
Pb	1.2×10^3	9.9×10^3
U	4.4×10^2	1.3×10^4

exchange resin.) The superiority of Diphonix is again apparent.

Diphonix resin can be readily regenerated by stripping with either moderate concentrations of acid, for example, H_2SO_4 or HCl, or in the case of actinides with strong complexing agents. The resin appears to be quite stable chemically and has essentially the same physical characteristics as commercially available ion-exchange resins.

A patent application on Diphonix has been filed by the ARCH Development Corporation and licensed to EIChroM Industries, Darien, IL, and EIChroM has made plans for the commercial production of the new ion-exchange resin.

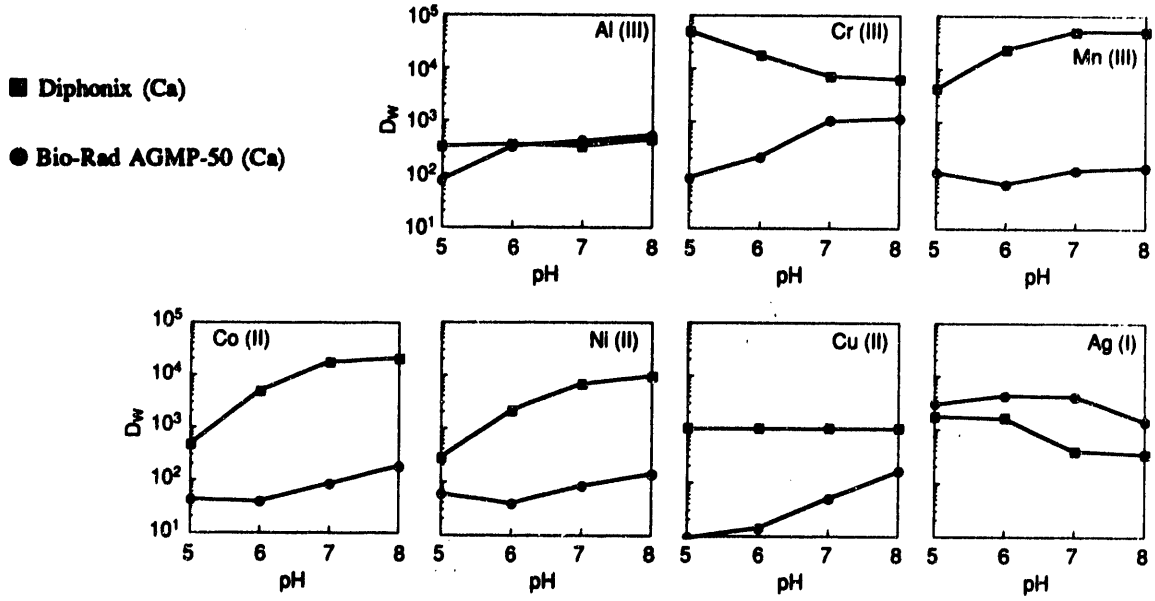

Figure IX-6. Weight-distribution ratios of selected metal ions using Ca-Diphonix resin (25 °C).

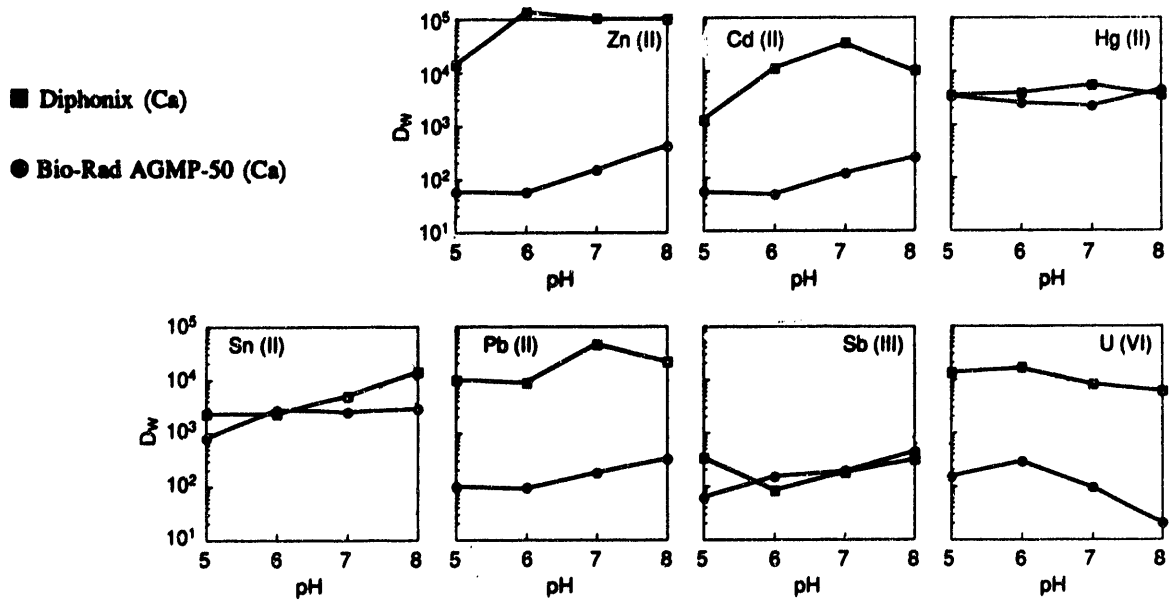

Figure IX-7. Weight-distribution ratios of selected metal ions using Ca-Diphonix resin (25 °C).

D. The Influence of the Radical Character of Organometallic Reagents on the Direction of Addition to an α,β Unsaturated Phosphoryl Group

R. C. Gatrone

The principal objectives of our research are the preparation of starting materials that are prerequisites for the facile syntheses of a variety of potential extractants, for example, unsymmetrically bis-substituted phosphine oxides, the development of methods that will permit stereoselective control of such reactions, and the understanding of the basic organic chemistry of these syntheses.

Difficulties encountered in the synthesis of new classes of extractants frequently hinder the study of the relationship between extractant behavior and extractant structure. Often, many months may be required to prepare a single example of a class of compounds with a unique combination of substituents and properties.

The addition of a Grignard reagent to a phosphoryl (P=O) containing compound is an extremely versatile method for preparing unsymmetrically substituted phosphine oxides. Preliminary results obtained on the addition of octylmagnesium bromide to ethyl phenylphosphinate suggested that this reaction, like its carbonyl counterpart, proceeds via a metal-ion-stabilized radicallike intermediate species. We wished to determine whether or not this intermediate, if made more stable either by stabilizing the radical or by solvation, would to react to generate products from the 1,4 or 1,6 mode of addition (Figure IX-8). Furthermore, if a degree of control over the alternate addition reaction were attainable, this reaction would offer a single-step preparation of alkyl-substituted arylphosphinic acids. Currently, these compounds are only made by the direct addition of hypophosphorous acid to an aromatic or olefinic center or by the hydrolysis of an aryl phosphonous dihalide, which may be prepared by the addition of an organometallic reagent to phosphorus trichloride. Neither of these methods is completely satisfactory for a general synthesis of this class of compounds because the reactions are multistep procedures involving difficult separation to isolate the product.

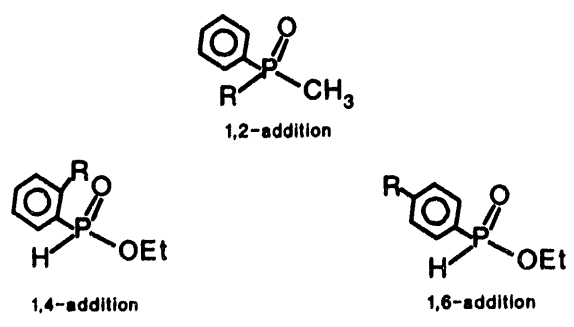

Figure IX-8. Expected products from the Grignard reaction.

The mechanism of the Grignard reaction with ketones has been suggested to proceed via a single electron-transfer (SET) mechanism. As a SET mechanism is favored by stable radicals, good coordinating solvents, and traces of transition-metal impurities in the magnesium used to prepare the reagent, we felt that a series of increasingly more stable alkyl radicals used to prepare the Grignard reagent should promote a corresponding increase in the yield of the alternate addition product.

If a SET mechanism is operating in this reaction, the first step in the addition of a Grignard reagent to ethyl phenylphosphinate (Figure IX-8) must be proton abstraction. Addition to phosphorus occurs via a SET from the σ-complex formed by the addition of a second equivalent of the Grignard reagent. This transfer occurs to an anionic phosphorus center. Earlier, Hays and Hamilton have shown that the sodium or magnesium salts of dialkylphosphites readily react with Grignard reagents, although they did not investigate the nature of the mechanism of addition.

We have shown that the addition of one equivalent of methylmagnesium iodide to an ether solution of ethyl phenylphosphinate at room temperature initially abstracts the phosphorus proton.

The organometallic reagents we examined are listed in Table IX-6 with the isolated yields of the 1,2, and 1,4 (or 1,6) addition products. The yield of the product from addition to the aromatic ring increased with the corresponding increase in the stability of the radical that would be derived from the Grignard reagent. That is, we observe a significant increase in the yield of aromatic addition according to the series: neo-pentyl > t-butyl > iso-propyl > primary radicals. In addition, we observe nearly a doubling of the yield (neo-pentyl: ≅ 4% aromatic addition, t-butyl: ≅ 3% aromatic addition) with more coordinating solvents such as tetrahydrofuran.

Although we cannot suggest that the reaction will be useful synthetically for the preparation of the aromatic-substituted phosphinic acids, the yields observed corroborate the proposed mechanism for the generation of traces of acidic impurities during the preparation of (alkyl)phenyl phosphine oxides.

Table IX-6. Yields of alternate addition products.

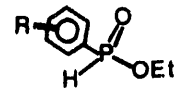

R	M + 1 *	^{31}P (ppm) **	% yield
Me	185	39.9	0.2
Et	199	-	-
n-Pr	213	41.8	0.3
i-Pr	213	41	0.8
n-Bu	227	-	-
s-Bu	227	40.7	0.3
i-Bu	227	-	-
t-Bu	227	41.1	1.2
neo-Pe	241	41.0	2.0

*Solid probe, chemical ionization. **300 MHz GE GN Omega, 5 mm broadband probe, $CDCl_3$.

E. U/TEVA•Spec™: A Novel Extraction Chromatographic Material for the Separation and Preconcentration of Uranium

E. P. Horwitz, M. L. Dietz, R. Chiarizia, H. Diamond

Numerous methods have been described for the determination of uranium in a variety of environmental, geological, or biological matrices. In many instances, the low concentrations of uranium encountered and the presence of high levels of potential interferents preclude its direct determination. As a consequence, various separation and preconcentration techniques must often be employed prior to analysis. Uranium separation is also required for the characterization of certain uranium-rich samples, among them various minerals, waste solutions, and uranium metal itself, because high uranium levels can interfere with the accurate quantitation of various trace elements.

Many methods have been described for effecting the separation of uranium from mixtures of cations. Liquid-liquid extraction, for example, has been widely applied. Extraction procedures, however, are time-consuming, generate considerable volumes of organic waste, and have limited effectiveness in removing certain common matrix constituents. These shortcomings make liquid-liquid extraction unattractive for routine use on large numbers of samples. A variety of procedures based on ion exchange have also been described. The lack of specificity of conventional ion-exchange resins, however, often complicates sample treatment.

Extraction chromatography (EC) provides a simple and effective means by which the separation and preconcentration of various cations can be accomplished. In extraction chromatography, an inert support is impregnated with an organic extractant, either alone or in combination with a suitable diluent, to produce a solid sorbent capable of selectively removing certain metal ions from aqueous solution. In effect, EC combines the selectivity of liquid-liquid extraction with the multistage character of a chromatographic process and the ease of handling and convenience of an ion-exchange resin.

Earlier studies in this laboratory designed to identify the structural features governing the uranium selectivity of various neutral organophosphorus extractants have shown that dipentyl pentylphosphonate (DP[PP]), also called diamyl amylphosphonate (DA[AP]), dissolved in dodecane (Figure IX-9), is an efficient and selective reagent for the extraction of uranium from acidic nitrate media. We have investigated the application of an extraction chromatographic material comprised of this extractant supported on an inert polymeric substrate, to the isolation of uranium from various environmental samples for subsequent quantitation. This is appropriate because many procedures for the determination of uranium in such samples involve a digestion or leaching of the sample with nitric acid.

After preliminary studies demonstrated that an extraction chromatographic resin consisting of 40% (w/w) diamyl amyl phosphonate DA[AP] sorbed on Amberlite XAD-7 (henceforth referred to as

Extractant:

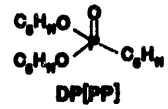

DP[PP]

Diluent: None

Extraction Equilibria:

$$UO_2^{2+} + 2NO_3^- + \overline{2E} \rightleftharpoons \overline{UO_2(NO_3)_2 \cdot E_2}$$

$$Th^{4+} + 4NO_3^- + \overline{3E} \rightleftharpoons \overline{Th(NO_3)_4 \cdot E_3}$$

Figure IX-9. Extractant and extraction equlibria for U/TEVA•Spec™.

U/TEVA•Spec™ resin) could retain uranium from solutions containing high nitric acid concentrations and that retained uranium could be readily eluted from the resin with either water or dilute nitric acid (as anticipated from earlier liquid-liquid extraction studies), a systematic examination of the uptake of uranium and various other actinide elements was undertaken. Figure IX-10 summarizes the results of this study, expressed as the capacity factor, k', for each element on the U/TEVA•Spec™ column versus nitric acid concentration. (k' represents the number of free column volumes to peak maximum and is related to the distribution ratio of the metal ion in the corresponding liquid-liquid system by the following equation: $k' = DV_s/V_m$, where V_s and V_m are the stationary and mobile phase volumes, respectively.) Several features of the data are noteworthy. First, k' for uranium reaches a maximum (of ~300) at ~6 M nitric acid, then levels off. Equally significant from the point of view of chromatographic performance is the fact that k' is substantial (~70) even at 1 M acid. Thus, the resin will efficiently sorb uranium from any of a wide range of nitric acid concentrations. This ability to load a sample containing any of a variety of acid concentrations and to strip sorbed uranium using only dilute nitric acid, it should be noted, makes uranium separation using the U/TEVA•Spec™ resin considerably simpler than with many previously described methods. Moreover, U/TEVA•Spec™ offers obvious advantages in terms of minimizing reagent consumption and waste generation.

Figure IX-10 also indicates that several other actinide ions show significant affinity for the U/TEVA•Spec™ resin. The k' values for tetravalent plutonium, for example, actually exceed those of ura

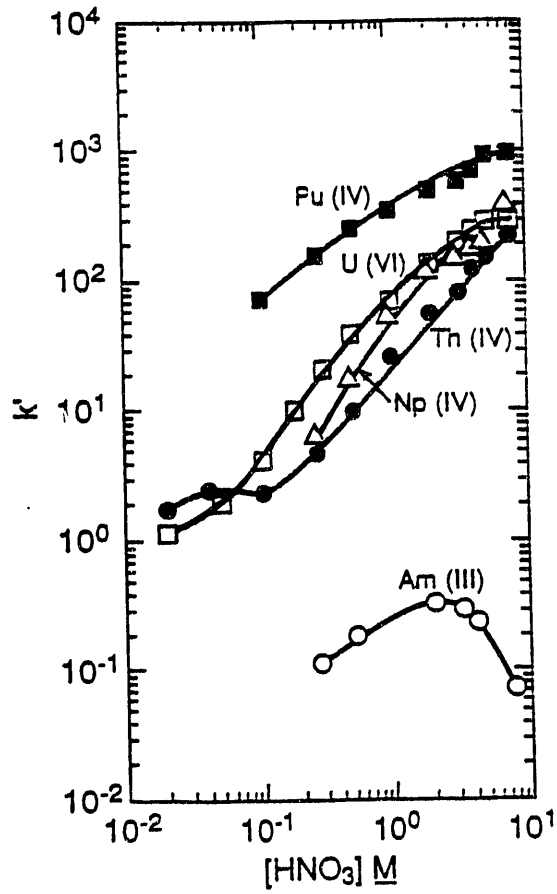

Figure IX-10. Nitric acid dependency of k' for selected actinides.

nium by a substantial margin over the entire range of acidities considered. The behavior of both thorium (IV) and neptunium(IV) roughly parallels that of uranium(VI), although at any given acidity, k' for thorium is typically a factor of 2-5 less than that of uranium. This difference in k' is sufficient to provide for a clean separation of the two ions.

Unlike U/Th separation, U/Np separation cannot be conveniently effected using only nitric acid, because at concentrations yielding adequate uranium retention, the k' values of uranium and neptunium are very similar. Addition of an appropriate aqueous complexing agent (e.g., oxalic acid) to the eluent, however, reduces the sorption of neptunium (as well as that of thorium and plutonium) by more than an order of magnitude, while producing only a slight decrease in uranium retention.

Figure IX-11 demonstrates that the utility of the U/TEVA•Spec™ resin is not confined to acidic nitrate media, depicting the dependence of k' for uranium and

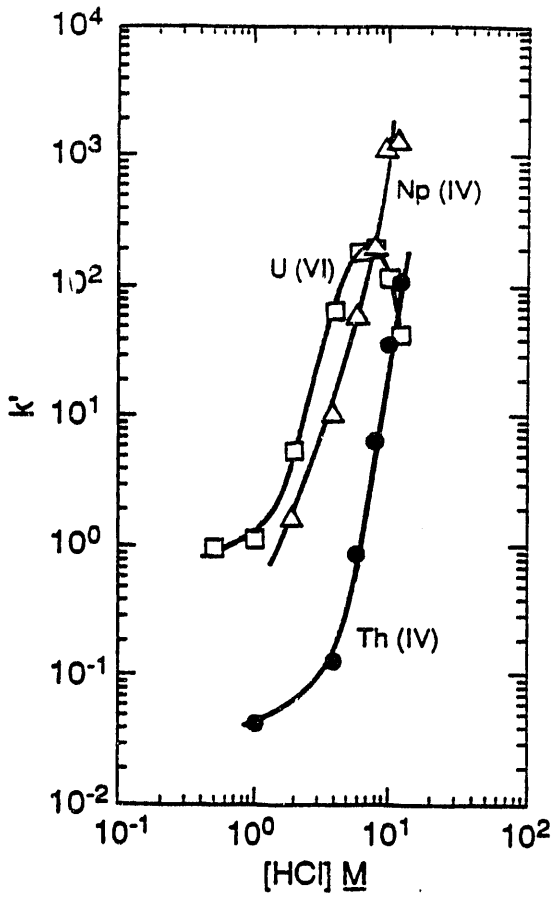

Figure IX-11. Hydrochloric acid dependency of k' for selected actinides.

several other actinides on hydrochloric acid concentration. Several similarities between the behavior of the various ions in hydrochloric acid and that described in nitric acid are apparent. The k' value for uranium, for example, reaches a maximum at ~7 M acid. Moreover, this value is quite close to that seen in nitric acid, ~300. Also, Am(III) (not shown in Figure IX-11) is poorly retained, as was the case in nitric acid. There are, however, important differences between the capacity factor data in the two acids. For example, k' for uranium declines more steeply from its maximum in hydrochloric acid as the acid concentration falls than it does in nitric acid. Thus, while k'_U does not fall below 100 until ~1.2 M nitric acid, it reaches this value by 4 M in hydrochloric acid. As a result, the range of acidities suitable for sample loading is narrower in the latter (ca. 4-6 M). Both the U/Np and U/Th separation factors are somewhat better in hydrochloric acid, however. At 4 M nitric acid, for example, k'_U and k'_{Np} differ by less than a factor of 2. In 4 M hydrochloric acid, however, this difference is nearly a factor of 5. Such results suggest that elution sequences involving a crossover from nitric acid to hydrochloric acid (or vice versa) may offer a means to isolate and sequentially elute several actinides in a single run, further increasing the utility of the U/TEVA•Spec™ resin.

The large values of k' possible for uranium in nitric acid media and the low retention anticipated for many mono-, di-, and trivalent metal ions indicate that it should be possible to elute off many of the commonly encountered constituents of various samples (e.g., transition metals, alkali and alkaline earth elements) from the U/TEVA•Spec™ column prior to uranium breakthrough. Table IX-7 summarizes the elution behavior of nearly three dozen elements using 2 M nitric acid as the eluent. As can be seen, nearly all of the test elements can be removed with only 10 FCV of 2 M nitric acid. (Zr and Ru each require ~15 FCV.) As expected from Figure IX-7, no trace of uranium is observed even after 30 FCV of the acid.

Table IX-7. Elution behavior of selected elements on a U/TEVA•Spec™ (fine particle) column[a]

elution volume (FCV)[b]	elements
≤5	Li, Mg, K, Co, Rb, Sr, Ag, Cs, La, Pr, Nd, Sm, Eu
≤10	Na, Al, Ca, Cr, Mn, Fe, Ni, Cu, Zn, Y, Rh, Cd, Ba, Ce, Pb
≤15	Zr, Ru
>100	U

[a]Column parameters: Resin particle diameter = 50-100 microns; bed volume = 1 mL; bed height = 5.0 cm; 1 FCV = 0.60 mL.

[b]Element is 2 M nitric acid. "Elution volume" refers to the volume, in FCV, required to elute ca. 99% of the indicated element.

The results presented in Figures IX-10 and IX-11 and in Table IX-7 suggest that the U/TEVA•Spec™ resin should be well suited to the separation and preconcentration of uranium from environmental or geological samples. The performance of the resin in such applications was evaluated by examining the suitability of material for the isolation of a highly pure uranium fraction from several water, sediment, or soil samples for subsequent isotopic analysis by thermal ionization mass spectrometry (TIMS). This represents a particularly demanding application of the resin because of the low-uranium concentrations typically

present, the variability and complexity of the sample matrices, and the need for an extremely pure uranium fraction. Table IX-8 summarizes the results of trials designed to determine the recovery of uranium typically achieved using the U/TEVA•Spec™ resin. As can be seen, recoveries are both high (averaging 95%) and remarkably consistent, despite the different sample compositions and the substantial sample mass processed in some cases. In every instance, the uranium product obtained was extremely clean, leaving no visible residue in either the collection beaker or on the mass spectrometer filament. Table IX-9 summarizes the results of TIMS analyses of 14 samples of a National Bureau of Standards standard reference soil. Measured isotopic abundances were found to be in excellent agreement with the certified values for ^{234}U and ^{238}U. (The disagreement between the values for ^{235}U suggests nonuniform distribution of this isotope in the sample, not incomplete recovery of this isotope.)

U/TEVA•Spec™, then, provides a simple and effective method for the separation and preconcentration of uranium from a wide range of environmental and geological sample types. Application of the resin is, in fact, limited only by the need to convert the sample to a nitric or hydrochloric acid solution for loading. Although work to date has focused largely on its environmental applications, the excellent uranium selectivity of U/TEVA•Spec™ should make it suitable for use in a number of other situations, including bioassays, analysis of nuclear wastes and reprocessing solutions, and the elimination of uranium interference in various trace-element determinations in uranium-rich samples. Work addressing some of these opportunities is currently underway.

Table IX-8. Uranium recovery from actual and standard environmental samples.

sample description	weight or volume analyzed	uranium present, μg before column	uranium present, μg after column	recovery (%)
water-NBS 950a	5.0 mL	26.1	24.8	95.3
limestone gravel and sediment	3.12 g	18.3	17.6	95.9
limestone gravel and sediment	2.32 g	25.2	23.8	94.6
surface soil	1.03 g	23.5	22.3	95.1
glassblasting residue	1.49 g	35.1	33.8	96.2
				Mean: 95.4

Table IX-9. Uranium isotopic distribution in a standard soil sample (NBS-SRM 4353).

isotope	activity[a] (Bq/g)	concentration[b] (μg/g)	isotopic abundance (wt.%) calculated	isotopic abundance (wt.%) experimental
U-234	0.0391±0.0014	0.000170±0.000006	0.0054±0.0002	0.0055±0.0003
U-235	0.0019[c]	0.024[c]	0.76[c]	0.719±0.018
U-238	0.0389±0.0020	3.13±0.16	99.23[c]	99.275±0.018
Total uranium (μg/g): 3.15±0.16 (NBS certificate)				
3.04±0.15 (experimental)				

[a]From NBS certificate.
[b]Calculated by converting activities to masses via specific activities.
[c]No uncertainty available from NBS certificate.

PUBLICATIONS

TUCS: A NEW CLASS OF AQUEOUS COMPLEXING AGENTS FOR USE IN SOLVENT EXTRACTION PROCESSES
E. P. Horwitz, H. Diamond, R. C. Gatrone, K. L. Nash, and P. G. Rickert
Solvent Extraction, T. Sekine, Ed., Elsevier Science Publishers B.V., 1990, pp. 357-362

THE TRUEX PROCESS: A VITAL TOOL FOR DISPOSAL OF U. S. DEFENSE NUCLEAR WASTE
E. P. Horwitz and W. W. Schulz*
New Separation Chemistry Techniques for Radioactive Waste and Other Specific Applications, Elsevier Applied Science, 1991, pp. 21-29

THE SYNTHESIS AND DECOMPOSITION OF NOVEL ORGANOPHOSPHORUS COMPLEXANTS
R. C. Gatrone, E. P. Horwitz, P. G. Rickert, and K. L. Nash
Separation Sci. Tech. 25, 1607-1627 (1990)

APPLICATION OF SUPPORTED LIQUID MEMBRANES FOR REMOVAL OF URANIUM FROM GROUNDWATER
R. Chiarizia*, E. P. Horwitz, P. G. Rickert, and K. M. Hodgson*
Separation Sci. Tech. 25, 1571-1585 (1990)

NEW FORMULATIONS FOR IRON OXIDE DISSOLUTION
R. Chiarizia* and E. P. Horwitz
Hydrometallurgy 27, 339-360 (1991)

SREX: A NEW PROCESS FOR THE EXTRACTION AND RECOVERY OF STRONTIUM FROM ACIDIC NUCLEAR WASTE STREAMS
E. P. Horwitz, M. L. Dietz, and D. E. Fisher*
Solvent Extr. Ion Exch. 9, 1-25 (1991)

SEPARATION AND PRECONCENTRATION OF STRONTIUM FROM BIOLOGICAL AND ENVIRONMENTAL SAMPLES BY EXTRACTION CHROMATOGRAPHY USING A CROWN ETHER
E. P. Horwitz, M. L. Dietz, and D. E. Fisher*
Anal. Chem. 63, 522-525 (1991)

THE APPLICATION OF NOVEL EXTRACTION CHROMATOGRAPHIC MATERIALS TO THE REDUCTION AND REMOVAL OF RADIONUCLIDES FROM WASTE SOLUTIONS
E. P. Horwitz, M. L. Dietz, S. B. Rajkovich*, and D. M. Einolf*
Radioact. Radiochem. 2, 10-12 (1991)

AN IMPROVED METHOD FOR THE DETERMINATION OF ^{89}Sr AND ^{90}Sr IN URINE
M. L. Dietz, E. P. Horwitz, D. M. Nelson*, and M. Wahlgren*
Health Physics 61, 871-877 (1991)

DILUENT EFFECTS IN THE EXTRACTION OF Am(III) FROM NITRIC ACID SOLUTIONS BY SELECTED CARBAMOYLPHOSPHORYL EXTRACTANTS AND RELATED MONOFUNCTIONAL COMPOUNDS
R. Chiarizia* and E. P. Horwitz
Solvent Extr. Ion Exch. 10, 101-118 (1992)

A NOVEL STRONTIUM SELECTIVE EXTRACTION CHROMATOGRAPHIC RESIN
E. P. Horwitz, R. Chiarizia*, and M. L. Dietz
Solvent Extr. Ion Exch. 10, 313-336 (1992)

---

*Not affiliated with the Chemistry Division or affiliated on a temporary basis.

CESIUM FLUOROXYSULFATE, $CsSO_4F$: A NOVEL REAGENT FOR THE RAPID OXIDATION OF AMERICIUM AT AMBIENT TEMPERATURE AND ITS SEPARATION FROM CURIUM
E. H. Appelman, H. Diamond, E. P. Horwitz, and J. C. Sullivan
Radiochim. Acta 55, 61-64 (1991)

ACID DEPENDENCY OF SELECTED METAL ION EXTRACTION BY A STRONTIUM SELECTIVE EXTRACTION CHROMATOGRAPHIC RESIN: CALCULATED VS EXPERIMENTAL CURVES
R. Chiarizia*, E. P. Horwitz, and M. L. Dietz
Solvent Extr. Ion Exch. 10, 337-362 (1992)

IMPROVED CHEMISTRY FOR THE PRODUCTION OF YTTRIUM-90 FOR MEDICAL APPLICATIONS
M. L. Dietz and E.P. Horwitz
Apppl. Radiat. Isot. 43, 1093-1101 (1992)

PATENTS (Granted)

NEW FORMULATIONS FOR IRON OXIDE DISSOLUTION
E. P. Horwitz and R. Chiarizia*
U. S. Patent No. 5,078,894 (January 7, 1992)

NEW STRONTIUM EXTRACTION/RECOVERY PROCESS
E. P. Horwitz and M. L. Dietz
U. S. Patent No. 5,100,585 (March, 1992)

METHOD FOR THE SEPARATION OF STRONTIUM FROM BIOLOGICAL AND ENVIRONMENTAL SAMPLES
E. P. Horwitz and M. L. Dietz
(Granted)

SUBMISSIONS

THE APPLICATION OF NOVEL EXTRACTION CHROMATOGRAPHIC MATERIALS TO THE CHARACTERIZATION OF RADIOACTIVE WASTE SOLUTIONS
E. P. Horwitz, M. L. Dietz, and R. Chiarizia*
J. Radioanal. Nucl. Chem. (in press)

SEPARATION AND PRECONCENTRATION OF URANIUM FROM ACIDIC MEDIA BY EXTRACTION CHROMATOGRAPHY
E. P. Horwitz, M. L. Dietz, R. Chiarizia*, H. Diamond, A. M. Essling*, and D. Graczyk*
Analyt. Chim. Acta (in press)

COMBINING EXTRACTANT SYSTEMS FOR THE SIMULTANEOUS EXTRACTION OF TRANSURANIC ELEMENTS AND SELECTED FISSION PRODUCTS
E. P. Horwitz
Proceedings, 1st Hanford Separations Science Workshop, Battelle, Pacific Northwest Laboratory, Richland, WA, July 23-25, 1991 (in press)

NOVEL EXTRACTION CHROMATOGRAPHIC FROM NUCLEAR WASTE CHEMISTRY
M. L. Dietz and E. P. Horwitz
LC & GC (1992)

---

*Not affiliated with the Chemistry Division or affiliated on a temporary basis.

SEPARATION AND PRECONCENTRATION OF Th, U, AND TRUs FROM ACIDIC MEDIA BY EXTRACTION CHROMATOGRAPHY

E. P. Horwitz, R. Chiarizia*, M. L. Dietz, H. Diamond, and D. M. Nelson*

Analyt. Chim. Acta (1992)

COLLABORATIONS

S. D. Alexandratos, University of Tennessee, Knoxville

The feasibility of incorporating the geminally substituted diphosphonic acid moiety into a polymer matrix to form a new class of ion-exchange resins is being investigated. Ion-exchange resins containing the gem-diphosphonic acid functional group should possess properties vastly superior to commercially available cation-exchange resins and should find wide-scale applications in environmental restoration and in waste management.

D. Nelson, Environmental Safety and Health Division, Argonne National Laboratory

New highly efficient methods are being developed for the separation of actinides and ^{90}Sr from urine, feces, and environmental samples. Such methods will enable the ESH and ACL Divisions to reduce the cost considerably and to increase the frequency of performing analyses.

R. D. Rogers, Northern Illinois University, De Kalb

New types of biphasic systems are being developed by chemically bonding or sorbing complexing agents onto solid supports. These new biphasic systems should possess unique properties for the separations of hydrated cations and anions.

*Not affiliated with the Chemistry Division or affiliated on a temporary basis.

X. HEAVY ELEMENTS COORDINATION CHEMISTRY

K. L. Nash, E. H. Appelman, L. R. Morss, P. G. Rickert, J. C. Sullivan, E. P. Horwitz, M. L. Dietz*, R. C. Gatrone**

Outside Collaborators: G. R. Choppin, E. Lisic, D. D. Ensor, A. Jache, E. N. Rizkalla, L. F. Rao, J. L. Kim, C. Lierse

The broad aim of this program is to understand those characteristics of chelating agents (steric, electrostatic, and structural) that are associated with the formation of the strongest and most soluble complexes with heavy metals. Our focus is on the bonding and reactivity of f elements in metal complexes in solutions, and the relationship between the coordination geometries of solvated complexes and solid compounds. We are examining the thermodynamics and kinetics of metal complexation reactions, the solvation of complexes, coordination numbers and modes, and spectral properties of f-element complexes to better understand the relationship between the structural features of such complexes and their behavior in solution. Our ultimate goal is to achieve a fundamental understanding of this chemistry to facilitate the design of complexing agents and ligands tailored to specific metal ions, or classes of metal ions. To the extent that such thermodynamic and kinetic data can be used to predict their behavior, we are also interested in acquiring the data necessary for accurate modeling of metal-ion complexation reactions under process, environmental, or even biological conditions.

In addition to their commercial utility in nuclear energy (including a central role in waste disposal and waste processing), materials science, and nuclear medicine, the 4f and 5f series of elements possess a unique mix of properties useful for the evaluation of the most important aspects of ligand design. The constricting radii of the trivalent lanthanides and actinides are ideally suited to the evaluation of size-exclusion (e.g., crown ether) type ligands. Structural details (e.g., interatomic distances) of complexes in solution can also be derived from lanthanide-induced paramagnetic shifts in NMR spectroscopy. Diamagnetic ^{139}La NMR provides a direct probe of the inner coordination sphere of lanthanide complexes. The multiple oxidation states of the light actinides are ideally suited to testing of electrostatic bonding models of metal-ion coordination. The existence of the upper oxidation states of the light actinides as linear dioxocations in aqueous solutions creates a unique opportunity to investigate the effect of geometric restrictions in design of chelating agents. The small difference in the strength of the interaction of 4f- and 5f-metal ions with soft-donor atoms (like sulfur) allows us to investigate the involvement of these highly shielded electrons in covalent bonding. Finally, the intrinsic radioactivity of the actinides, and the readily induced radioactivity of several lanthanides, permit study of the coordination chemistry of ligands and complexes with very low solubility.

Coordination chemistry of heavy metal complexes pervades many areas of practical interest. For example, in chemical separations, the use of water-soluble complexing agents can make possible metal-ion partitioning that would not work without the complexant. In nuclear medicine, chelating agents are essential for the delivery of the radiotherapeutic agent to the target organ. The relative effectiveness of such reagents is governed by the thermodynamics and kinetics of the complexation reaction, and competing reagents are typically evaluated on this basis. An enhanced understanding of the chemistry and the structural details of metal complexes can have major impact in designing new reagents for separations, nuclear medicine, water treatment chemistry, homogeneous catalysis, and bioinorganic chemistry, to name a few.

The third aspect of this program is aimed at reconciling the continued need for metal chelating agents with current demands by society for environmental responsibility. It is vital to recognize that the most efficient reagent (e.g., EDTA) may not be acceptable from an environmental or toxicity perspective. Our approach is to design effective complexing agents that

*Collaborator from another ANL Chemistry Division group.

incorporate a degree of thermal/oxidative instability to ameliorate waste-disposal problems associated with the use of chelating agents. These organic compounds retain their ability as complexants under normal conditions, but are readily decomposed to inorganic materials upon relatively mild subsequent treatment. We call such compounds Thermally Unstable Complexants or simply TUCS. It is also our objective to elucidate the mechanisms of oxidation of chelating agents in order to effectively "design-in" the appropriate degree of instability, and to examine the basic chemistry of homogeneous destruction of chelating agents in order to determine their environmental acceptability.

Our personnel and facilities provide the opportunity to investigate the interaction of heavy metal ions with organic chelating agents from many experimental perspectives. We combine expertise in solution thermodynamics and kinetics, solid state structure determination and thermochemistry, NMR spectroscopy, and radiochemical methods with the ability and facilities to handle macroscopic concentrations of actinides, to prepare compounds containing the transamericium actinides by microchemical synthetic methods, to handle powerful oxidants and peroxidizing agents, and, in collaboration with outside researchers, to synthesize organic ligands.

A. Phosphonic Acid Complexes of f Elements

K. L. Nash, L. R. Morss, P. G. Rickert, J. C. Sullivan, G. R. Choppin, L. F. Rao

The most widely studied class of chelating ligands for the f elements are those possessing carboxylic acid functional groups as the primary binding site for the metal ion. The wide variety of structures of polycarboxylic and aminopolycarboxylic acid complexants provides a number of favorable coordination geometries that lead to the formation of complexes of moderate stability. However, carboxylate functional groups also have a moderately strong affinity for hydrogen ions. For most metal ions, the net free energy for protonation of these ligands exceeds that for complexation (see, for example, Figure X-1). As a result, most carboxylate ligands do not form metal complexes in solutions below pH ≡ 2.

Literature reports indicate that phosphonic acid groups ($-PO_3H_2$) can be readily substituted for carboxylate groups in structures of known chelating agents. There is also evidence that certain ligand geometries that are unstable as carboxylates can be stabilized by the substitution of phosphonate groups. The carboxylate and phosphonate groups differ in three principal characteristics:

1. the geometry of the functional group (planar for $-CO_2H$, O-C-O bond angle 120°, trigonal for $-PO_3H_2$ with O-P-O bond angle 109°),
2. an extra oxygen-donor atom in $-PO_3H_2$,
3. an additional ionizable proton in $-PO_3H_2$ ($pK_1 \equiv 2.0$, $pK_2 \equiv 7.0$ for phosphonate vs. $pK \equiv 4$-6 for carboxylate).

This combination of factors leads to the formation of complexes of moderate stability in acidic solutions.

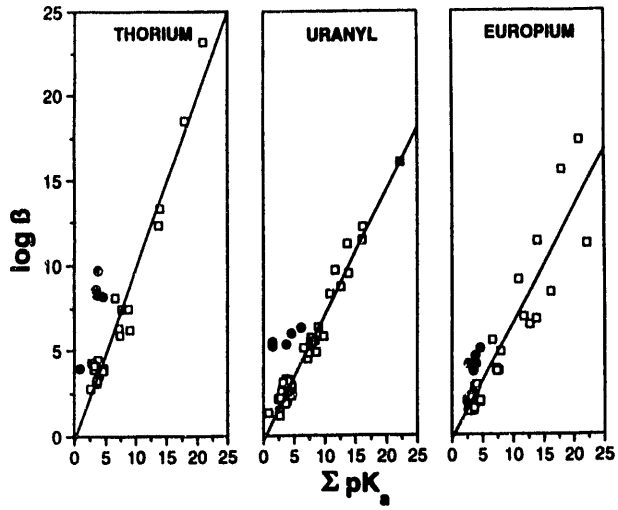

Figure X-1. Stability constants (log β) for 1:1 thorium, uranyl, and europium complexes with a variety of carboxylate and aminopolycarboxylate (□), and phosphonate (•) ligands vs. the total hydrogen-ion affinity (Σ pK_a) for the ligands.

Our earlier studies of the complexation of europium, thorium, and uranyl (representing the tri-, tetra-, and hexavalent oxidation states of the actinides), and correlation of those data with existing data for carboxylate and aminopolycarboxylate ligands, have established that the complexes between these metal ions and 1,1-diphosphonic acids are stronger than all known carboxylate and aminopolycarboxylate complexes in acidic solutions. This relationship is illustrated in Figure X-1. In this figure, the free energy for

complexation (represented by log β) and the total protonation free energy (Σ pK_a) for a large sampling of carboxylate and aminopolycarboxylate ligands (open symbols) and phosphonic acid ligands (closed symbols) are compared. The linear correlation indicates the predominantly electrostatic nature of the interaction between the f elements and hard-base donor ligands. For a given free energy of protonation, the phosphonate ligands are two (europium(III)) to five (thorium (IV)) orders of magnitude stronger than the carboxylate ligands. We previously suggested the existence of a correlation between the strength of the complexes and the number of oxygen-donor atoms in the ligand.

The combination of strong metal-ion affinity and low proton affinity accounts, at least superficially, for the enhanced complexing ability of the phosphonates (as compared with carboxylates). But, because f-element complexation is governed almost exclusively by electrostatic considerations, this combination of characteristics represents a dichotomy. How can the phosphonate group have such low hydrogen-ion affinity while maintaining a strong attraction for polyvalent metal ions? We have attempted to reconcile these observations through a series of experiments designed to probe the inner coordination sphere of the complexed metal ions.

B. Europium Phosphonate Complexation Heats and Hydration of the Complexes

K. L. Nash, G. R. Choppin, L. F. Rao

We have recently investigated the heats of complexation of europium diphosphonate complexes and its fluorescence decay rate (2.0 M $NaClO_4$, 25.0 °C). The former experiments address the energetics of the complexation reactions, whereas the latter assess the degree of innersphere dehydration of Eu(III) upon complex formation.

Europium complexes with each of the three diphosphonate ligands studied, methanediphosphonic acid (MDPA, I), vinylidene-1,1-diphosphonic acid (VDPA, II), and 1-hydroxyethane-1,1-diphosphonic acid (HEDPA, III) are characterized by very similar thermodynamic parameters and residual hydration values. As is typical of most f-element complexes, stability of the 1:1 complex is derived from a favorable complexation entropy, though opposed by an endothermic heat. The equilibrium for the addition of the second H_3L^- ligand is favored by both an exothermic heat and a slightly positive entropy. The degree of innersphere hydration of the metal ion in the complexes, derived from the results of the fluorescence decay experiments, is indicated in equations 1 and 2.

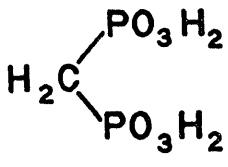

(I)

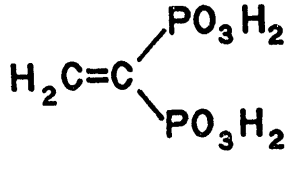

(II)

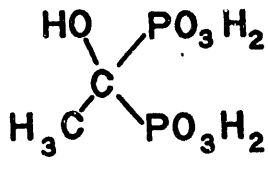

(III)

$$Eu(H_2O)_9^{3+} + H_3L^- \rightleftharpoons Eu(H_3L)(H_2O)_7^{2+} + 2H_2O \quad (1)$$

$$Eu(H_3L)(H_2O)_7^{3+} + H_3L^- \rightleftharpoons Eu(H_3L)_2(H_2O)_3^{2+} + 4H_2O \quad (2)$$

The result in equation 1 is consistent with the formation of a bidentate chelate complex that displaces two water molecules. Addition of the second ligand results in apparent excess dehydration of the metal ion.

The thermodynamic data for the formation of $Eu(H_3MDP)^{2+}$ are ΔH = +9.56 kJ/mol, ΔS = +102 J/mol-K, which compare favorably with analogous data for the nominally isostructural Eu-malonate complex ($Eu(mal)^{2+}$ ΔH = +13 kJ/mol, ΔS = +113 J/mol-K). The degree of dehydration reported earlier for the complexation reaction of europium by

malonate is nearly identical to that for $Eu(H_3MDP)^{2+}$. These data are consistent with similar bond strengths for the europium-oxygen bonds in carboxylates and phosphonates, and are strongly suggestive of similar coordination geometries.

Comparison of the thermodynamic data for the addition of the second ligand to the Eu-MDP and Eu-malonate complexes indicates that the complex structures are profoundly different. Though no fluorescence data are available for the $Eu(mal)_2^-$ complex (to indicate residual hydration), the thermodynamic data (ΔH = +7 kJ/mol, ΔS = +75 J/mol-K) for the addition of the second ligand to $Eu(mal)^+$ indicate a lower net enthalpy and smaller entropy contribution than for formation of the 1:1 complex. For the addition of the second H_3MDP^- ligand to $Eu(H_3MDP)^{2+}$, the net enthalpy is much lower than for addition of the first ligand (ΔH = -7.1 kJ/mol), whereas the entropy change is nearly zero (ΔS = +16 J/mol-K), despite the apparent displacement of four water molecules. One should expect a large positive entropy for reaction 2 as the cratic contribution (related to the change in the number of species in the net reaction) to the entropy must be large. The exothermic heat is also consistent with a net increase in bond strength, despite the loss of four water molecules (and their implicit bond energies). To reconcile this expectation with the observed small entropy, the 1:2 complex must adopt a highly ordered geometry. One possible explanation for this observation is the formation of a 1:2 complex possessing substantial intramolecular hydrogen bonding. A possible structure for this complex is IV:

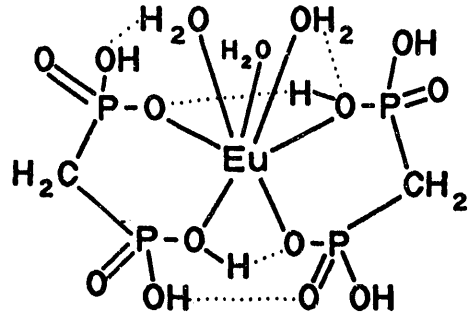

(IV)

This subtle additional favorable contribution to complex strength may account for the exceptional stability of protonated complexes of the type described here, and may be a general feature of diphosphonate complexants.

C. Thermodynamic and Spectroscopic Investigation of Uranyl-MDPA at Elevated pH

K. L. Nash, L. R. Morss, P. G. Rickert

Literature data are not consistent in their prediction of the relative stability of phosphonate and carboxylate complexes at elevated pH. Some data indicate continued enhancement with increased ionization of the phosphonate ligands, whereas other results suggest that phosphonate ligands are actually weaker at high pH. The intramolecular hydrogen bonding postulate is impacted by this argument. To examine this question and to elucidate details about the molecularity of phosphonate bonding, the complexes of uranyl by MDPA at elevated pH have been studied by potentiometric titration, ^{31}P and ^{23}Na NMR spectrometry, and by titration calorimetry. Though the analysis of the data is not yet complete, the three sets of data appear consistent with the following discussion.

Potentiometric titrations of 0.005 M MDPA solutions containing 0 to 0.0025 M uranyl were conducted at 0.1 M ionic strength and 25.0 °C. The titration results were analyzed using the program BEST (Martell and Motekaitis). The titration results are shown in Figure X-2. Analysis is not yet complete,

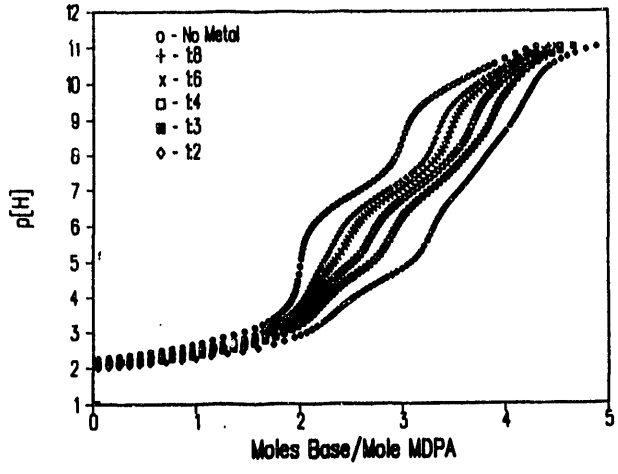

Figure X-2. Potentiometric titration results for the uranyl-MDPA system at 0.005 M total ligand.

but complementary distribution and NMR studies indicate the following equilibria are most important at pH above 3:

$$UO_2^{2+} + 3H^+ + 2L^{4-} = UO_2H_3L_2^{3-}, \quad \log \beta_{132} = 40.9 ; \quad (3)$$

$$UO_2^{2+} + 2H^+ + 2\,L^{4-} = UO_2H_2L_2^{4-}, \quad \log \beta_{122} = 35.6 ; \quad (4)$$

$$UO_2^{2+} + 2L^{4-} = UO_2L_2^{6-}, \quad \log \beta_{102} = 21.3 ; \quad (5)$$

$$2UO_2^{2+} + 2L^{4-} = (UO_2)_2L_2^{4-}, \quad \log \beta_{202} = 35.9 ; \quad (6)$$

$$2UO_2^{2+} + H^+ + 3L^{4-} = (UO_2)_2HL_3^{7-}, \quad \log \beta_{213} = 48.8 . \quad (7)$$

One or two additional, as yet not firmly identified, species are required to completely reconcile the potentiometric data.

To help identify the uranyl-MDPA complexes, a series of ^{31}P and ^{23}Na NMR spectra were run. In the ^{31}P spectra, a discrete singlet resonance for the free ligand (17.0 ppm vs. 85% H_3PO_4), and two distinct singlet resonances associated with the formation of uranyl complexes (23.0 ppm and 27.2 ppm) were observed. At pH below 5, the 23.0 resonance indicates the presence of 1:2 complexes only. As the pH is increased above 4-5, the integrated area of the 23.0 resonance decreases with a concomitant increase in the free-ligand resonance and the appearance of the second metal complex resonance at 27.2 ppm. Good solubility is observed throughout the pH range 2-11, implying that all of the uranyl ion must be bound in diphosphonate complexes. The integrated area of the 27.2 peak is maximized at pH 7-7.5 under all conditions. Above this pH, the areas of both the free ligand and the 27.2 ppm complex decrease whereas the 23.0 peak again becomes more intense. At pH 11, the 27.2-ppm resonance is not observed except at the highest total metal-ion concentration. Selected spectra run at 0 °C indicate splitting of the complex resonances consistent with four to six slightly different phosphorus environments in the metal complexes. Line broadening of ^{23}Na spectra suggests the binding of sodium ions by the uranyl-MDPA complexes (many of which have high formal negative charges).

An example of the changes in the integrated areas of the peaks is shown in Figure X-3. Calculated $\bar{n}$ (average ligand number) values (assuming all uranyl is bound) change from 2.0 at pH < 4 to a minimum of 1.0 at pH 7, then increase to 1.5-2.0 at higher pH (dependent on the total metal-ion concentration).

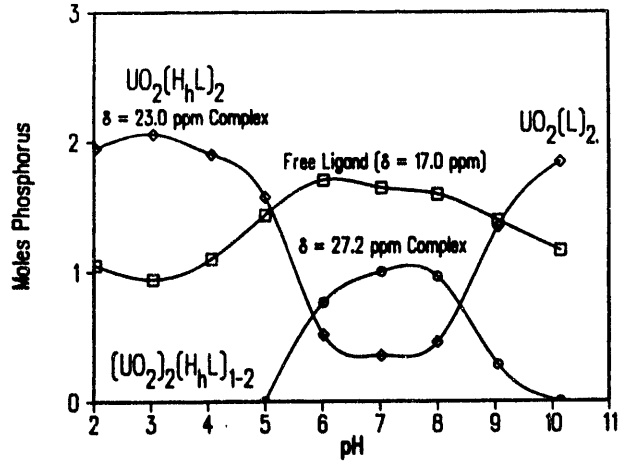

Figure X-3. Distribution of phosphonate species in the uranyl-MDPA system from pH 2-11 (0.005 M total ligand concentration) as deduced from ^{31}P NMR spectroscopy.

To gain further insight and to aid in identification and confirmation of the species present in the system, enthalpy titrations were performed. Solutions of 1:2 mole ratios of uranyl:MDPA were prepared at high pH and back titrated with standard $HClO_4$. Because overlapping reactions contribute to the observed heats, more extensive titrations are required than we have completed. The predicted speciation for these titrations and the results are shown in Figure X-4.

These results indicate that the 1:2 complexes previously identified as dominant at pH < 2 actually represent the major uranyl-MDPA species up to the pH 4-5 region. Above this pH, coincident with the loss of the third hydrogen ion of MDPA, polynuclear complexes, probably involving MDPA ligands bridging two metal ions, become the dominant species. The potentiometric and NMR data suggest complexes having the general form shown in Figure X-5.

The 23.0 ppm phosphorus environment probably includes both the ligands in the mononuclear 1:2 complexes (at both low and high pH) and "capping" ligands bound to the open ends of the bridged uranyl cations. It is conceivable that more than one bridging ligand could be present in a given polynuclear

complex, but the NMR results require that any such arrangement must be one of high symmetry to account for the relative paucity of phosphorus environments. The line broadening in the ^{23}Na NMR results strongly suggests the existence of ternary complexes at high pH.

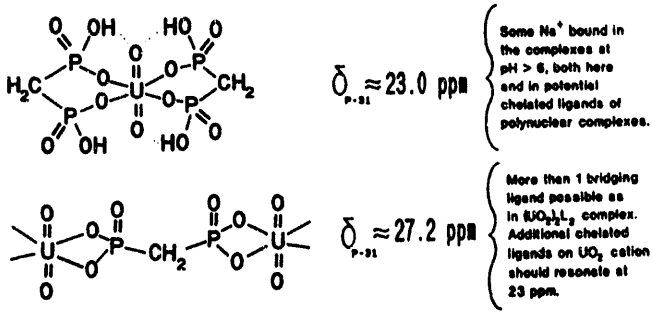

Figure X-4. Probable structures for uranyl-MDPA complexes in the pH 2-11 range. (Free ligand resonance at ≈17.0 ppm.)

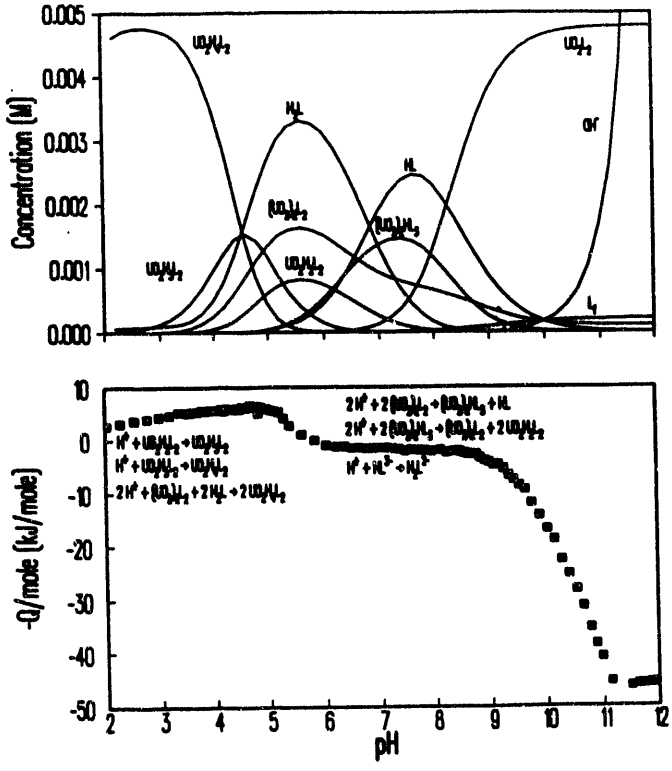

Figure X-5. Top: species-distribution curve for enthalpy titration experiments at 0.005 M uranyl, 0.01 M MDPA; bottom: observed heats per mole of uranyl with probable contributing reactions.

D. Kinetics of Uranyl-Diphosphonate Complexation in Acidic Solutions

J. C. Sullivan, K. L. Nash

There are a few reports of the kinetics of complexation of f elements for a number of ligand systems, but insufficient results have been reported to permit much systematic analysis of the data. To complement our studies of complexation thermodynamics, we have also attempted to investigate the kinetics of metal-ion complexation reactions for amenable systems.

One system moderately well characterized with respect to species and stability is the complexation of uranyl by 1,1-, and 1,2-diphosphonic acids in acidic solutions. Complexation reactions of the f elements occur with millisecond lifetimes suitable for stopped-flow spectrophotometry. Our investigation of the uranyl diphosphonate system was accomplished using arsenazo(III) (2,2'-(1,8-dihydroxy-3,6-disulfonapthalene-2,7-bisazo)bisbenzenearsonic acid) as a competing ligand. Arsenazo(III) forms colored complexes with uranyl in acidic solutions, and forms complexes comparable in stability to the diphosphonates.

The experiments were conducted by mixing uranyl-arsenazo(III) solutions with diphosphonate solutions of varying concentrations and monitoring the disappearance of the uranyl-arsenazo(III) complex(es). The kinetic data were interpreted in terms of a first order approach to equilibrium:

$$UO_2^{2+} + H_3L^- \underset{k_r}{\overset{k_f}{\rightleftharpoons}} UO_2H_2L + H^+, \qquad (8)$$

where H_3L^- is the dominant form of the free diphosphonate ligand. The overall rate equation has the form:

$$R = k_f[UO_2^{2+}][H_3L^-] - k_d[H^+][UO_2H_2L]. \qquad (9)$$

Determination of both forward and reverse rate constants was accomplished as a function of temperature. The complete data set permits elucidation of not only rate and activation parameters, but also equilibrium and thermodynamic parameters. The activation entropies for both complex formation and acid-promoted dissociation reactions are negative, consistent with an associative mechanism. The thermodynamic parameters derived from the kinetic data are unique, as they proved inaccessible to more conventional determination. They are, however, consistent with earlier data for related complexes.

E. Molecular Mechanics Calculations for f Element Complexes

K. L. Nash

Computer modeling can be of great utility in facilitating our ability to design new complexants for lanthanide and actinide metal ions. Previous investigations have established the utility of such analyses, for example, in the explanation of the complex stability of various europium-polycarboxylate complexes. For calculations involving the f elements, the parameters incorporated in programs like *Alchemy*™ are not adequate for modeling their coordination chemistry. In solution, f elements typically demonstrate coordination numbers of 8-10 and are strongly hydrated. The penta- and hexavalent actinides exist in most solutions as the linear dioxocations (e.g., O-U-O^{2+} for uranyl(VI)). These physical constraints require the modification of the data tables used by the program.

Fortunately, molecular mechanics programs provide for the opportunity to alter or supplement the parameters required for the minimization routine. We have introduced appropriate coordination geometries, new atom types, and the appropriate constraints for europium and uranyl as representative trivalent and hexavalent f elements for *Alchemy*™ modeling studies. Testing and adjustment of the parameters are being done by comparing the results from energy minimization with known crystal structures, but relevant data for dimensions in aqueous solutions are also considered. Work is underway to correlate molecular mechanics with thermodynamic data to further establish the foundation of this work.

F. Thermal/Oxidative Instability of Complexants/Complexes

K. L. Nash, E. H. Appelman, P. G. Rickert

Though metal ion complexants serve a useful function in a variety of areas, many of the most common complexants persist long after their usefulness is ended. This resistance to degradation in the environment has contributed to significant waste-disposal problems and even to potential safety hazards both within and outside of the DOE complex. It is toward the fundamental chemistry of such problems that the next aspect of this program is directed.

Several Class A thermally unstable complexants, based on gem-diphosphonic acids, have been prepared and tested for their thermal instability. We have observed that the relative ease of decomposition of the diphosphonates is (in order of increasing ease of decomposition):

MDPA < HEDPA < VDPA < DHEDPA << CHMDPA,

(DHEDPA: 1,2-dihydroxyethane-1,1-diphosphonic acid; CHMDPA: carboxyhydroxymethane-1,1-diphosphonic acid). These ligands require, respectively, 4, 4, 4, 3, and 1 equivalents per carbon atom for complete oxidation to CO_2 and H_3PO_3. VDPA, DHEDPA, and CHMDPA decompose spontaneously in acidic solutions at room temperature, though at different rates, whereas HEDPA and MDPA are resistant to oxidation. Clearly, the observed differences in persistence depend upon both kinetic and thermodynamic factors.

The objective of this subtask is to determine the rates and mechanism of the decomposition reactions of representative ligands, to correlate structural characteristics of the complexants with their ease of oxidation, and to develop generic procedures for homogeneous decomposition of chelating agents and their metal complexes. We seek to establish the basic chemistry so that two goals can be realized: (1) to devise oxidation procedures that are inherently clean, that is, they do not exacerbate existing waste-disposal problems or create new ones, and (2) to enhance our ability to design controllable instability into useful complexants.

1. Nitric Acid Oxidation of Vinylidene-1,1-diphosphonic Acid

P. G. Rickert, K. L. Nash

We have completed an investigation of the decomposition kinetics of VDPA by HNO_3 at elevated temperature. The progress of the reaction has been monitored by NMR spectroscopy (^1H, ^{31}P, and ^{13}C, as necessary) whereas the gaseous products (CO_2, CO, N_2O, NO, etc.) were identified by collection of the reaction gases for mass spectrometric analysis. Several important intermediates (carboxylic acids and phosphonic acids) have been identified, and

some details of the complex decomposition pathway elucidated.

In the range of 60-80 °C and 6.0-8.0 M nitric acid, VDPA is quantitatively decomposed in less than 24 hrs by a complex reaction pathway. For the first half-life, VDPA is converted to a second diphosphonic acid via a first-order process. ^1H NMR spectroscopy establishes that this intermediate is apparently a simple hydrolysis product of VDPA, 2-hydroxyethane-1,1-diphosphonic acid. The activation energy (E_a) for the first-order hydrolysis reaction is 19 kcal/mol. The reaction is second order in [HNO_3].

After the first half conversion is complete, the rate of disappearance of VDPA from the solution continues by a zero-order process that is more rapid than the original reaction. Gaseous reaction products CO_2, CO, NO, N_2O, and N_2 are produced in the second stage of the conversion reaction. No gaseous products are observed in the first stage of the reaction. Simultaneously with the evolution of gaseous decomposition products, the first evidence for H_3PO_4 is seen in the NMR spectrum. Both VDPA and the hydrolysis product are decomposed in this stage of the reaction sequence. The oxidation of VDPA can be induced without the first-order induction period by the introduction of ethanol, $NaNO_2$, and NO_2 or NO gases.

2. Vanadium-catalyzed Oxidation of 1-Hydroxyethane-1,1-diphosphonic Acid (HEDPA) by Hydrogen Peroxide

E. H. Appelman, A. W. Jache

As a potential TUCS reagent, HEDPA represents a more difficult case. Though its complexes with the f elements are generally stronger, it is much more difficult to decompose. It is resistant to oxidation by HNO_3, having served the role of internal standard in the previous investigation of VDPA decomposition kinetics. Earlier research has established that HEDPA can be decomposed under relatively mild conditions by hydrogen peroxide. Pursuant to our continuing studies of practical means of oxidatively degrading diphosphonic acid chelating agents, we have begun to examine the kinetic details of the reaction of hydrogen peroxide with HEDPA.

HEDPA is one of the present TUCS compounds less readily degradable, as its structure provides no easy point of attack for an oxidant. Preliminary results reported previously indicated that HEDPA could be oxidized at elevated temperatures by hydrogen peroxide in the presence of catalytic quantities of vanadium compounds. We have recently begun to examine the reaction in greater detail, with the goal of obtaining an in-depth understanding of the reaction mechanism.

A preliminary survey of iron, selenium, osmium, molybdenum, tungsten, and vanadium as potential catalysts indicated that only the last was particularly effective. In a typical reaction of 0.3 M HEDPA with 0.1 M H_2O_2 at 50 °C in 1 M $HClO_4$ with 0.001 M VO_2ClO_4 present as a catalyst, the reaction proceeded with an initial half-time of about 40 min. One mole of phosphoric acid was produced for every two moles of hydrogen peroxide consumed. The immediate direct attack on the phosphonate functionality is in contrast with the nitric acid oxidation of VDPA.

The reaction order with respect to H_2O_2 was intermediate between 0 and 1. The course of individual reactions was fit by the following model:

$$VO_2^+ + H_2O_2 \xrightarrow{\text{fast}} VO(O_2)^+ + 2H^+, \quad (10)$$

$$VO(O_2)^+ + H_2O_2 \overset{K}{\rightleftharpoons} VO(O_2)_2^- + 2H^+, \quad (11)$$

$$VO(O_2)_2^- + \text{HEDPA} \xrightarrow{k} \text{products} + VO_2^+. \quad (12)$$

However, analysis of multiple experiments does not quantitatively fit the model. The dependence of reaction rate on vanadium concentration is greater than predicted, whereas the dependence on [HEDPA] and [H^+] is substantially less than predicted. Further refinement of the model will obviously be required.

It is also apparent from changes in the visible absorption spectra of the solutions that the vanadium ions are not simple aquo species, but are being complexed by the HEDPA. Speciation of the VO_2^+-HEDPA system has not been investigated. Further development of this kinetic study may include attempts to "lock in" the form of the vanadium species by introducing the vanadium as a preformed complex with a strongly binding or substitution-inert ligand.

PUBLICATIONS

KINETICS OF COMPLEXATION AND REDOX REACTIONS OF THE LANTHANIDES IN AQUEOUS SOLUTIONS (review)

K. L. Nash and J. C. Sullivan

Handbook for the Physics and Chemistry of the Rare Earths, K. Gschneidner and L. Eyring, Eds., 1991, pp. 347-391

THE EFFECT OF LIGAND RIGIDITY ON THE STABILITY OF EUROPIUM COMPLEXES WITH SUBSTITUTED DIGLYCOLIC ACIDS

K. L. Nash, E. P. Horwitz, R. C. Gatrone, and P. G. Rickert

J. Alloys Compds. 180, 375-381 (1992)

TUCS: A NEW CLASS OF AQUEOUS COMPLEXING AGENTS FOR USE IN SOLVENT EXTRACTION PROCESSES

E. P. Horwitz, H. Diamond, R. C. Gatrone, K. L. Nash, and P. G. Rickert

Solvent Extraction 1990, T. Sekine, Ed., 1990, pp. 357-362

CALORIMETRIC STUDIES OF NEPTUNIUM(V) COMPLEXATION BY POLYCARBOXYLATE LIGANDS

G. R. Choppin*, L. F. Rao*, E. N. Rizkalla*, and J. C. Sullivan

Radiochim. Acta 55, 0000 (1992)

KINETICS OF URANIUM(VI) REDUCTION IN AQUEOUS POLYELECTROLYTE SYSTEMS

C. G. Pippin*, J. C. Sullivan, D. Meisel, and G. R. Choppin*

Radiochim. Acta 55, 0000 (1992)

KINETIC AND STRUCTURAL STUDIES ON THE OXOTETRACYANOTECHNETATE(V) CORE: PROTONATION AND LIGATION OF DIOXOTETRACYANOTECHNETATE(V) IONS AND CRYSTAL STRUCTURE OF 2,2'-BIPYRIDINIUM TRANS-OXOTHIOCYANATOTECHNETATE(V)

A. Roodt*, J. G. Leipoldt*, E. A. Deutsch*, and J. C. Sullivan

Inorg. Chem. 31, 1080-1085 (1992)

ELECTRON TRANSFER REACTIONS OF TECHNETIUM AND RHENIUM COMPLEXES. 3. PULSE RADIOLYSIS STUDIES ON TRANS-$[M(III)X_2(DMPE)_2]^+$ AND $[M(I)(DMPE)_3]^+$ COMPLEXES IN AQUEOUS AND AQUEOUS SURFACTANT MEDIA, WHERE M = Tc OR Re, X = Cl OR Br, AND DMPE = 1,2-BIS(DIMETHYLPHOSPHINO)ETHANE

A. Roodt*, J. C. Sullivan, D. Meisel, and E. Deutsch*

Inorg. Chem. 30, 4545-4549 (1991)

THE CHEMISTRY OF URANIUM (VI), NEPTUNIUM (VI), AND PLUTONIUM (VI) IN AQUEOUS CARBONATE SOLUTIONS

B. E. Stout*, G. R. Choppin*, and J. C. Sullivan

Transuranium Elements: A Half Century, Chapter 23, L. R. Morss and J. Fuger, Eds., 1991

SUBMISSIONS

THERMALLY UNSTABLE COMPLEXANTS: STABILITY OF LANTHANIDE/ACTINIDE COMPLEXES, THERMAL INSTABILITY OF THE LIGANDS, AND APPLICATIONS IN ACTINIDE SEPARATIONS

K. L. Nash and P. G. Rickert

Separation Sci. Tech. (in press)

---

*Not affiliated with the Chemistry Division or affiliated on a temporary basis.

SEPARATION CHEMISTRY FOR LANTHANIDES AND TRIVALENT ACTINIDES (review)
K. L. Nash
Handbook for the Physics and Chemistry of the Rare Earths (in press)

STABILITY AND STOICHIOMETRY OF URANYL PHOSPHONATE COORDINATION COMPOUNDS IN ACIDIC AQUEOUS SOLUTIONS
K. L. Nash
Radiochim. Acta (1992)

A KINETIC STUDY OF THE REDUCTION OF Np(VI) AND Pu(VI) IN CARBONATE MEDIA BY TRIS [1,2-BIS(DIMETHYLPHOSPHINO)ETHANE] COMPLEXES OF Tc(I) AND Re(I)
C. J. Anderson*, M. Woods*, E. Deutsch*, K. Deutsch*, and J. C. Sullivan
Radiochim. Acta (1992)

THE HYDROLYSIS OF Pu(VI) AND TIME DEPENDENT POLYMERIZATION REACTIONS
I. Pashilidis*, J. I. Kim*, Ch. Lierse*, and J. C. Sullivan
Radiochim. Acta (1992)

COLLABORATIONS

G. R. Choppin, Florida State University, Tallahassee
The thermodynamics of complex formation reactions of lanthanide and actinide metal ions with chelating agents that form strong complexes in acidic solutions are investigated by calorimetry and laser fluorescence. The results of such studies provide insights into the coordination geometries of the complexes and aid in the design of more efficient chelating agents.

D. D. Ensor and E. Lisic, Tennessee Technological University, Cookeville
Synthesis of new chelating agents designed to enhance complex strength and solubility are prepared, and the ability of these complexants for sequestering transition metals are evaluated. These studies directly impact our ability to prepare new compounds and to test for their complexation efficiency throughout the periodic table.

J. L. Kim, Institute of Radiochemistry, Technical University of Munich, Germany
A collaborative program on the chemistry and physics of actinide elements, primarily in solution, under conditions relevant to environmental and radioactive waste storage is being pursued. Emphasis is currently placed on the behavior of Np, Pu, and Am.

---

*Not affiliated with the Chemistry Division or affiliated on a temporary basis.

XI. HEAVY ELEMENTS PHOTOPHYSICS AND PHOTOCHEMISTRY

J. V. Beitz, G. K. Liu, C. W. Williams, L. R. Morss, W. T. Carnall

Outside Collaborators: *H. F. Brito, R. T. Brundage, J. Huang*

The excited electronic state properties of actinide ions are the central focus of this effort. We carry out complementary experimental and theoretical investigations that strive to achieve a predictive understanding of the consequences of f-state excitation. We examine a variety of excited state processes such as luminescence and nonradiative decay to lattice phonons, but emphasize unusual or novel processes such as photoinduced site distortion and excitation line narrowing. Present emphasis is on the photophysics of excited 5f-electron states in crystalline and amorphous fluoride-containing phases. These phases are being probed using laser-based methods and theoretical modeling while concurrent spectroscopic investigations are being pursued across the actinide series. Our research impacts nuclear waste management efforts and addresses such fundamental areas of f-element science as dynamical aspects of structural inhomogeneity, ion-ligand and ion-ion interactions, and nonlinear excited state dynamics.

A. Photophysics of 4+ Actinide Ions in CeF_4

G. K. Liu, J. V. Beitz, C. W. Williams, W. T. Carnall, J. Huang

Inhomogeneous broadening in the solid state spectroscopy of dilute ions in solid phases is generally attributed to variation in the local environment around a given ion. Due to the resulting increased linewidth, inhomogeneous broadening has usually been considered an impediment to detailed energy level structure or homogeneous linewidth determinations. A variety of techniques have been developed to minimize or eliminate the static effects of inhomogeneous broadening, but application of these methods has given rise to new questions with respect to the effects of structural inhomogeneity on the excited state dynamics of ions in solids. Consequently, attention has focused on the microscopic nature of inhomogeneous broadening.

The relatively localized nature of 5f states of actinide ions and the wide range of ionic radii of such ions provide a unique opportunity for investigating the nature of inhomogeneous broadening. We are exploiting this opportunity in systematic experiments involving tetravalent actinide ions. We employ photoexcitation to perturb as well as probe the actinide dopant ion and its interaction with surrounding ions. Our working hypothesis is that differences between the ionic radius of the actinide dopant ion and the host metal ion influence the stability of the dopant ion and its local environment. Support for this hypothesis is found in the relationship of the widths of 5f-5f transitions that we have observed with literature values for the ionic radii of 4+ actinide ions: decreasing ionic radius correlates with increasing linewidth. Our current work has focused on investigation of an unusual phenomenon, excitation line narrowing, in 5f-state transitions of Cf^{4+} doped into CeF_4, and on related nonresonant fluorescence line narrowing and spectral hole burning studies.

We use the term excitation line narrowing (ELN) to denote observation of reduced excitation linewidths when selectively monitoring fluorescence emission. This effect previously had been reported only for organic molecules in glassy hosts where the wide range of local environments precluded detailed analysis. An example of ELN observed in Cf^{4+} in CeF_4 is shown in Figure XI-1. A linear relation was observed between the excitation energies of crystal field states of the $^5G_4$ manifold of Cf^{4+} and the fluorescence wavelengths of the lower lying $^5G_6$ state. Analysis of these results by means of our extension of a microscopic theory of inhomogeneous broadening by Laird and Skinner has provided insights into the structural properties of Cf^{4+} in CeF_4. For example, determination that the ratio of measured excitation linewidth

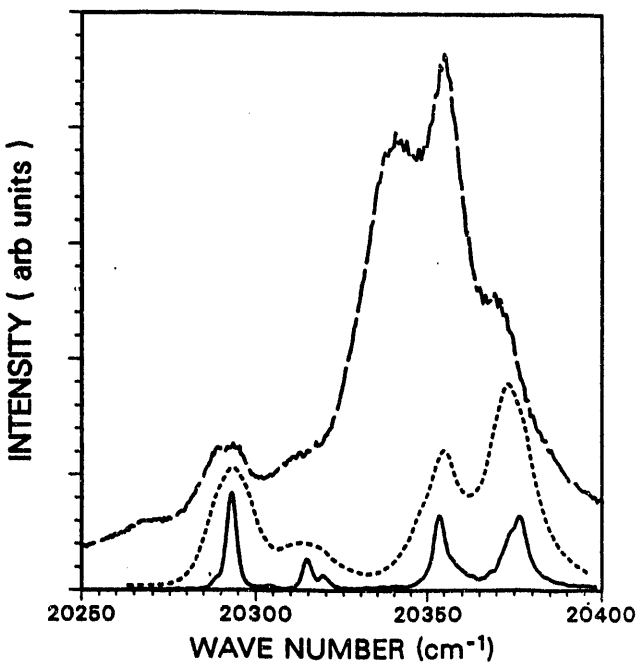

Figure XI-1. Excitation spectra of the lowest lying components of the $^5G_4$ state of Cf^{4+} in CeF_4 at 12 K. The broken curve is the spectrum with site resolution. The dashed curve shows the spectrum of Cf^{4+} on the C_2 site and the solid curve is the corresponding excitation line narrowed spectrum.

and the slope of the line shift is a constant equal to the linewidth of the emission line not only provides evidence that the perturbation of the energies of the two states is linearly correlated but also corresponds to one limit of the microscopic theory.

Persistent spectral holes, readily evident in Figure XI-2, were burned in inhomogeneously broadened 5f-5f transitions of Cf^{4+}. In addition to a resonant hole, satellite holes were observed in transitions to different electronic states. The presence of satellite holes provides definitive evidence of correlation between energy levels of Cf^{4+} in an inhomogeneous environment. Analysis of these spectral holes established the homogeneous linewidth of several crystal field transitions of Cf^{4+} and evidence was obtained for the contribution of spectral diffusion to the observed linewidths. Observation of persistent spectral holes is attributed to photoinduced site distortion (i.e., a change in the local environment surrounding Cf^{4+} following optical excitation). The photoinduced site distortion was stable below 80 K and was reversed at higher temperature by thermal activation.

We first observed photoinduced site distortion in 5f electronic states of Cm^{4+} in CeF_4 and subsequently found evidence of this effect in Bk^{4+} in CeF_4. Our observations to date are consistent with the hypothesis that the ionic radius of the dopant ion relative to that of the host metal ion in CeF_4 influences the stability of the dopant ion and its local environment. We have begun optical studies on Am^{3+} in a hydroxide phase to test the applicability of these methods to materials such as synthetic waste forms and mineralized phases likely to form as actinides migrate in the geosphere.

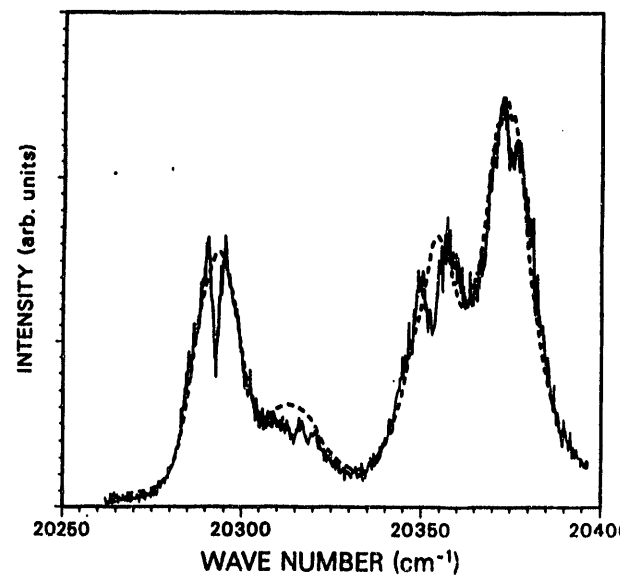

Figure XI-2. Fluorescence excitation spectra showing spectral holes burnt in the $^5G_4$ state bands of Cf^{4+} in CeF_4 at 12 K. The dashed curve is the spectrum before high-intensity laser excitation at 20293 cm^{-1}; the solid line curve is the spectrum after such excitation.

B. Spectra and Dynamics of Trivalent Actinide Ions in Fluoride Phases

J. V. Beitz, G. K. Liu, C. W. Williams, L. R. Morss, W. T. Carnall, R. T. Brundage

Much interest currently exists concerning the properties of 4f electronic states of trivalent lanthanides (Ln^{3+}) in heavy metal fluoride glasses (HMFG) containing LaF_3. This interest arises from the high degree to which such glasses suppress 4f state nonradiative decay, demonstrated technical

methods of drawing optical fibers from such glasses, and observation of optical gain at near-infrared wavelengths of interest in telecommunication. In principle, trivalent actinide (An^{3+}) ions can provide distinct advantages over Ln^{3+}-doped HMFG due to the generally more open energy level structure of low-lying f states of An^{3+} ions and the typically order-of-magnitude-larger absorption cross-sections of An^{3+} ions. An additional motivation for this work comes from the large amounts of radioactively contaminated waste containing metal fluorides at DOE production facilities. If such waste is converted to heavy metal fluoride glass for storage, the spectroscopic and photophysical information gained in our current work will prove of considerable value in waste form characterization.

We are collaborating with R. Brundage (Macalester College) in studies of An^{3+}-doped HMFG. This effort has provided the first evidence that nonradiative decay of 5f states of An^{3+} ions in HMFG is suppressed to much the same degree as is the case for 4f states of Ln^{3+} in HMFG. However, the comparatively broad 5f-state absorption and fluorescence bands of An^{3+} ions in HMFG prevented accurate determination of 5f-state energy-level structure. To provide benchmark data for An^{3+} ions in fluoride phases, we have undertaken the first detailed study of the 5f-state energy-level structure of a trivalent actinide ion in crystalline LaF_3. In addition to being a component of most heavy metal fluoride glasses of current interest, LaF_3 has long been used as a carrier in radiochemical separations and has served as the host for Nd^{3+} lasing in the vacuum ultraviolet. Our study involved a few micrograms of ^{253}Es and necessarily involved rapid sample preparation and data collection due to the 20.47 day half-life of ^{253}Es.

Time- and wavelength-resolved laser-induced fluorescence methods were employed in resolving the ground state splitting of Es^{3+} in LaF_3 and determination of the energies of crystal field components of six of its excited 5f states. Lifetimes ranging from 1.6 to 2.5 ms were observed when fitting the long time portion of the observed fluorescence decay of the $^5F_5$ state of Es^{3+} in LaF_3 to a single exponential decay. These values are in good agreement with the 2.4 ms purely radiative lifetime of the $^5F_5$ state of aquo Es^{3+} calculated from Judd-Ofelt theory. A preliminary crystal field analysis of the observed bands has been carried out (see Figure XI-3). As might be expected from comparison of the energy-level structure of 4f states of trivalent lanthanide ions in $LaCl_3$ and LaF_3, the centers of gravity of 5f states of Es^{3+} are relatively insensitive to the host ($LaCl_3$ or LaF_3), but larger crystal field splitting is found in LaF_3. These results provide a firm basis for future systematic investigation of the energy-level structure of An^{3+} ions in LaF_3. In addition, this work and recent systematic investigations of the 5f states of An^{3+} ions in $LaCl_3$ will aid in estimating the energy-level structure of lighter An^{3+} ions doped into LaF_3 and heavy metal fluoride glasses containing LaF_3.

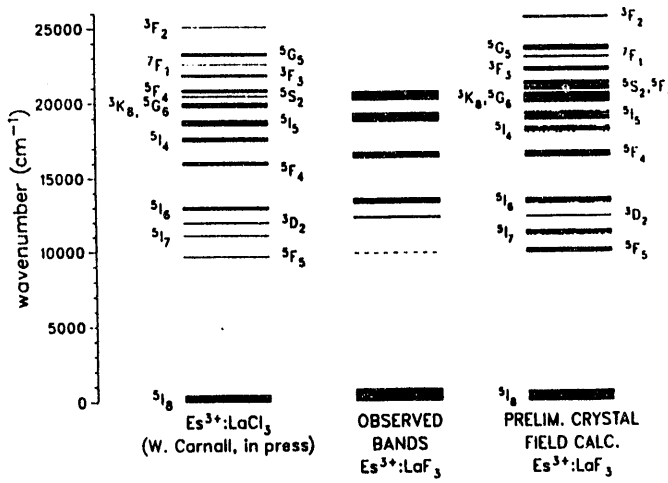

Figure XI-3. Comparison of the 5f-state crystal field levels of Es^{3+} in $LaCl_3$, the extent of observed purely electronic bands of Es^{3+} in LaF_3, and a preliminary calculation of the crystal field levels of Es^{3+} in LaF_3.

PUBLICATIONS

ANALYSIS OF THE CRYSTAL-FIELD SPECTRA OF THE ACTINIDE TETRAFLUORIDES. I UF_4, NPF_4, AND PUF_4

W. T. Carnall* , G. K. Liu, C. W. Williams, and M F. Reid*

J. Chem. Phys. 95, 7194-7203 (1991)

*Not affiliated with the Chemistry Division or affiliated on a temporary basis.

LASER-INDUCED FLUORESCENCE STUDIES OF TERBIUM TRISCYCLOPENTADIENIDE
G. K. Liu, J. V. Beitz, and B. Kanellakopulos*
J. Alloys Compds 180, 157-163 (1992)

5f STATE LUMINESCENCE FROM Am^{3+} AT MODERATE LOADING IN A HEAVY METAL FLUORIDE GLASS
J. V. Beitz and R. T. Brundage*
J. Alloys Compds 181, 49-56 (1992)

PHOTOCHEMICAL REMOVAL OF NpF_6 AND PuF_6 FROM UF_6 GAS STREAMS
J. V. Beitz and C. W. Williams
Transuranium Elements: A Half Century, L. R. Morss and J. Fuger, Eds., American Chemical Society, Washington, D. C., 1992, Chapter 17, pp. 168-180

VIBRONIC INTERACTION AND CRYSTAL STRUCTURE DISTORTION IN Cm^{4+}:CeF_4
G. K. Liu, J. V. Beitz, and W. T. Carnall*
Transuranium Elements: A Half Century, L. R. Morss and J. Fuger, Eds., American Chemical Society, Washington, D. C., 1992, Chapter 18, pp. 181-186

ION-ION INTERACTION AND ENERGY TRANSFER OF 4+ TRANSURANIUM IONS IN CERIUM TETRAFLUORIDE
G. K. Liu and J. V. Beitz
Transuranium Elements: A Half Century, L. R. Morss and J. Fuger, Eds., American Chemical Society, Washington, D. C., 1992, Chapter 19, pp. 187-194

SUBMISSION

MICROSCOPIC NATURE OF INHOMOGENEOUS LINE BROADENING: ANALYSIS OF THE HOLE BURNING AND EXCITATION LINE NARROWING SPECTRA OF Cf^{4+} IN CeF_4
G. K. Liu, J. Huang*, and J. V. Beitz
Phys. Rev. B (1992)

COLLABORATIONS

J. Huang, University of Wisconsin at Eau Claire
Spectra and dynamics of 5f states of actinide ions in solid phases are being determined using time- and wavelength-resolved laser-induced fluorescence. Current emphasis is on studies of trivalent actinide ions on sites of moderate symmetry.

H. F. Brito, Universidate de Sao Paulo, Brazil
A collaborative study on the spectroscopy of actinide and lanthanide ions is being made to define crystal field parameters. The molar enthalpies of selected lanthanide sesquioxides are being determined in calorimetric studies.

R. T. Brundage, Macalester College, St. Paul, MN
Investigation of the optical properties of actinide-doped amorphous phases is in progress. Static and dynamic optical properties of these materials are being probed using laser-based methods to determine the effects of systematic variation of glass composition, temperature, and dopant concentration.

*Not affiliated with the Chemistry Division or affiliated on a temporary basis.

XII. f-ELECTRON INTERACTIONS

L. Soderholm, C. W. Williams, J. S. Xue

Outside Collaborators: *C.-K. Loong**, M. M. Abraham, L. A. Boatner, N. M. Edelstein, G. L. Goodman**, J. E. Greedan, S. Kauzlarich, S. Kern, G. Lander, K. L. Lykke*, F. W. Lytle, H. Radousky, U. Welp***

The emphasis of this program is on the exploitation of the unique electronic and bonding characteristics of f electrons to further an understanding of basic properties of the heavy elements important to energy-related processes in such diverse fields as waste management and superconductivity. Details of the electronic structure of f ions in a solid, such as their oxidation states, energy-level splittings, and bonding characteristics, can have a profound influence on the physical properties exhibited by the materials that contain them. The 4f electrons are generally well localized, and provide a good experimental test for single-ion theories. The electronic and bonding properties of 5f electrons are intermediate between the valence electrons of transition-metal ions and the localized 4f-lanthanide electrons. This intermediate behavior is much harder to model, but provides an important bridge for furthering an understanding of subtle bonding effects.

The characteristics that the 5f electrons provide for exploitation include a variety of accessible oxidation states, large angular momentum of the valence electrons, and a radial distribution of the 5f-valence orbitals that makes them behave sometimes as localized and sometimes as delocalized. Although not well understood, it is this latter feature that manifests itself in some of the unusual bulk properties that have been observed, such as anomalously large electronic effective masses, lattice instabilities, electronically driven phase transitions, superconductivity, and unusual magnetic properties. The f-electron elements have, therefore, been the focus of wide recent interest because of the need to understand the fundamental mechanisms responsible for several potentially technologically important applications. The ultimate goal of this work is a fundamental and predictive understanding of the role of an f element in determining properties of solids, along with an ability to tailor compounds to specific applications. Toward this end, we have focused our efforts on the projects listed below.

A. The Electronic Properties of Rare-Earth Ions in High-T_c Superconductors

L. Soderholm, C.-K. Loong, C. W. Williams, J. S. Xue

The new families of high-T_c superconducting oxides afford the first opportunities to study the magnetic properties of systems in which the interatomic magnetic interactions are much smaller than those responsible for superconductivity. It is important to understand the magnetic properties of f elements in the presence of superconductivity for several reasons, in particular because some of the mechanisms recently suggested to account for the CuO conduction-hole superconductivity invoke magnetic interactions to account for Cooper-pair formation. From a more experimental standpoint, we are interested in determining if there is any observable effect of superconductivity on the magnetic properties of the rare-earth ions, and also to see if the standard single-ion theories used to account for the magnetic properties of insulators can be used to characterize these materials.

Unfortunately, the CuO sublattice renders these samples opaque to visible light. Attempts to probe the localized rare-earth f-energy levels by using UV-visible techniques have not succeeded because of the overwhelming absorption of light by the CuO states.

*Collaborator from another ANL Chemistry Division group.
**Collaborator from another ANL division.

We have overcome this problem by utilizing inelastic neutron scattering (INS) to probe the localized f states. Unlike light, neutrons are scattered by an interaction of their magnetic moment with the local moment on the rare earth. By measuring the energy lost (or gained) as a neutron passes through the sample, information is obtained about both the energy of the localized states and the transition matrix elements connecting them. Unfortunately, for technical reasons, INS is limited to energy transfers of less than about 250 meV, so that for the systems under study here we can obtain information only about the crystal-field splitting of the Russell-Saunders ground multiplet. Depending on the magnetic transition strengths connecting the various states within the ground multiplet, this restriction can severely limit the data available for analysis. It should be noted, however, that in terms of understanding the cooperative behavior of the superconducting system, it is the low-temperature electronic behavior of the f element that is of most interest to us here.

Although INS provides information about the energy-level spacing within the Russell-Saunders ground term, there are often insufficient data to uniquely determine the electronic properties of the rare-earth ion. To determine the correct crystal-field scheme from the limited data, we have developed software programs based on the superpositioning modeling ideas suggested several years ago by Newman. These programs permit the determination of intrinsic crystal-field parameters, obtained from a well-characterized series of rare-earth garnets, and their subsequent transference to a rare earth in a site of interest. These calculated values are then used as starting parameters for a fit to the available data by using our modification of the computer programs developed by Crosswhite at ANL. This modeling has worked very well for oxide systems, as demonstrated by the examples listed in Table XII-1. Also included in Table XII-1 is an example of the modeling applied to our work on phosphates, where the agreement is poor. Clearly, more work on the intrinsic parameter determination is necessary before we have a good basis for predicting the crystal-field influence on a rare earth in a variety of environments.

We have used this modeling procedure to provide a set of starting crystal-field parameters for the superconducting materials $R_{2-x}Ce_xCuO_4$ (R = Pr, Nd; x = 0, 0.15). Using these parameters, and the limited data available from our INS experiments, we have

Table XII-1. A comparison of the crystal-field parameters estimated from our superposition modeling and our best fit to INS data. The model is a good approximation for a variety of oxides that we have studied, but does not well estimate experimental results in the orthophosphates, indicating further work is necessary.

	$ErBa_2Cu_3O_7$		$ErPO_4$	
	SP Model	Experiment	SP Model	Experiment
B^4_0	-1852	-1942	614	390
B^4_2	123	-4		
B^4_4	1039	1338	1657	1114
B^6_0	595	458	-581	-696
B^6_2	-1	-56		
B^6_4	1254	1237	45	-62
B^6_6	2	0		

successfully accounted for all the INS data, as well as calculating the magnetic susceptibility and the electronic specific heat arising from the rare-earth sublattice. These calculated quantities agree well with data available in the literature, and provide helpful insight into the interpretation of these bulk properties. The observed crystal-field transitions in the superconductor $Pr_{1.85}Ce_{.15}CuO_4$ shift to slightly lower energies and are broadened relative to the parent, nonsuperconducting material. These changes can be adequately understood in terms of the chemical disordering about the rare-earth site as a result of Ce^{4+} doping. This work clearly demonstrates that the electronic behavior of the rare-earth sublattice can be understood in terms of a simple, single-ion model. There is no evidence that the superconductivity of the CuO sublattice is interfering with the magnetic response of the rare-earth sublattice.

There is no evidence of broadening of the Pr^{3+} crystal-field transitions as a result of interactions of f-electron delocalization, or the localized Pr f states with the CuO conduction states, as observed for Pr in the nonsuperconductor $PrB_2Cu_3O_7$. We understand this difference, together with the very different influence of Pr on the superconductivity in the two series $RBa_2Cu_3O_7$ and $R_{1.85}Ce_{.15}CuO_4$, as arising from the different crystal-field environments of the two series. In the former case, the Pr^{3+} has a pseudo-triplet ground state, whereas Pr in Pr_2CuO_4 has an isolated singlet ground state. The isolated nature of the singlet ground state does not permit any spin-flip interactions with the CuO conduction electrons within kT, whereas this spin-flipping appears to occur in $PrBa_2Cu_3O_7$, and we suggest that it suppresses superconductivity.

The work on understanding the role select f ions play in the suppression of superconductivity is continuing. We are examining the rare-earth electronic properties in a variety of other superconducting systems, including the $Pb_2Sr_2RCu_3O_8$ series. This effort is providing information necessary to the overall understanding of the electronic behavior of rare-earth-containing, high-T_c superconductors.

B. The Electronic and Magnetic Properties of RPO_4: $TmPO_4$

L. Soderholm, C.-K. Loong, M. M. Abraham, L. A. Boatner, N. M. Edelstein

The rare-earth orthophosphates, RPO_4, have been extensively studied as possible ceramic hosts for radioactive-waste storage. During the course of these studies, it became clear that there are several basic aspects of the electronic behavior of these materials that make them unusually interesting. For example, the lattice provides a good host for studying and modeling the magnetic interactions that lead to long-range ordering. Also, the rare-earth luminescence properties in this host make them potential phosphors or laser materials. With the outstanding need for new phosphors for detector technology, we decided to focus some attention on the study of the rare-earth electronic properties in these phosphate hosts. This project fits in well with our overall program because it provides a new opportunity to test some of the methodology that we developed for the high-T_c oxide materials. The rare earths in the phosphates still have oxygens as near-neighbors, but the PO_4^{3-} anions provide bonding different enough that our modeling ideas will have to be expanded, as shown by the example in Table XII-1.

We decided to begin this program by investigating the energy levels of Tm in $TmPO_4$. There are extensive optical, Raman, and resonance Raman data available in the literature to aid in our initial studies. We collected INS data at two temperatures, and several incident energies, in order to get an overall picture of the magnetic response of the Tm. We were able to resolve all of the possible 13 states of the $^3H_6$ Russell-Saunders ground multiplet. Symmetries were assigned to the observed transitions with the aid of published parameters, in part because our attempts at superposition modeling did not provide us with a good enough estimate to proceed. Surprisingly, the optical and Raman data provided only a poor model of our INS data as well, and fitting the parameters to our data resulted in an agreement better than any of those previously reported. This improvement in fit over the fit to the optical and Raman data can be explained in part by the heavy weighting that is usually given to the higher energy states when fitting optical data. INS probes only the low-lying states at energies less than about 4000 cm^{-1}, whereas optical spectroscopy is optimized for measurements of the high-energy levels with good resolution. It is well known that fits to optical data often do not well reproduce low-temperature properties, such as magnetic susceptibility. There has been some question as to whether there is some fundamental difference between optical data and other, lower energy techniques such as INS. For example, some expansion in the radial part of the wavefunction is to be expected with increasing energy of the excited state. Also, there should be more admixture of higher energy configurations into the higher energy states. Neither of these effects are directly included when fitting the optical data. Our method of fitting the INS data weighs more heavily the lower energy transitions, and the fact that the overall fit is better than previously reported shows that, at least in this case, there is no need to invoke any other contributions, such as f-electron delocalization, to the fitting of the crystal-field parameters. The eigenfunctions and energy levels obtained by this method well reproduce both the average magnetic susceptibility and the low-temperature heat capacity. We are not aware of any experimental data for the susceptibility of single-crystal $TmPO_4$ in the literature, but there are reports on large anisotropic magnetic interactions in $TmPO_4$ at low temperatures that may be responsible for the anomalies in the observed EPR spectrum and the measured elastic constants.

There are some very interesting discrepancies between our INS results and the data obtained by resonance Raman spectroscopy. The absence of the expected transitions around 250 cm^{-1} in electronic Raman scattering for both diluted Tm^{3+} in $LuPO_4$ and pure $TmPO_4$ is in contradiction to the strong intensities predicted for these transitions by the Judd-Ofelt theory. Electronic Raman scattering for rare-earth ions in solids involves transitions from an initial

$|4f^n,m\rangle$ to a final $|4f^n,n\rangle$ state via excited intermediate states $|4f^{n-1},\beta\rangle$. The scattering amplitude given by second-order perturbation theory involves an intractable sum over the complex intermediate states. The Judd-Ofelt approximation employs a closure relation to perform a piecewise summation over subgroups of *noninteracting* intermediate states, usually assumed to be states of the $4f^{n-1}5d$ configuration. A serious inconsistency exists between the observed and expected symmetry ratios of all three lowest Γ_5 transition lines that has been used as reason to argue that intermediate states of the type $4f^{n-1}g$ should also be included in the summation. Our results clearly demonstrate that the positions and intensities of the states at about 250 cm^{-1} are in agreement with a simple crystal-field model that utilizes only contributions from an f^n configuration. This agreement implies that the problem in understanding Raman intensities does not involve the ground-state wavefunctions, but rather contributions from the virtual excited states.

We have demonstrated here for the first time the benefit of considering simultaneously both neutron and optical data in a crystal-field analysis. We will continue to analyze the rare-earth magnetic excitations in RPO_4 using inelastic neutron scattering, combined with other optical data, with the expectation of furthering our knowledge about crystal-field modeling and low-temperature thermodynamic behaviors of f electrons in a variety of environments.

PUBLICATIONS

THE SUPERCONDUCTOR-RELATED OXIDES Cm_2CuO_4 AND $Cm_{1.83}Th_{0.17}CuO_4$
L. Soderholm, C. W. Williams, and U. Welp*
Physica C 179, 440-446 (1991)

CURIUM (Z=96) AS A PROBE FOR STUDYING HIGH T_c SUPERCONDUCTIVITY
L. Soderholm
J. Alloys Cmpds 181, 13-22 (1992)

A CRYSTAL FIELD ANALYSIS OF THE ENERGY LEVEL SPLITTINGS FOR ERBIUM IN $ErBa_2Cu_3O_7$
L. Soderholm, C.-K. Loong*, and S. Kern*
J. Alloys Compds 181, 225-231 (1992)

CRYSTAL FIELD EXCITATIONS IN RE_2CuO_4 (RE = Pr, Nd)
C.-K. Loong* and L. Soderholm
J. Alloys Compds 181, 241-247 (1992)

INELASTIC-NEUTRON-SCATTERING STUDY OF THE Er^{3+} ENERGY LEVELS IN $ErBa_2Cu_3O_7$
L. Soderholm, C.-K. Loong*, and S. Kern*
Phys. Rev. B 45, 10,062-10,070 (1992)

SUBMISSIONS

THE INFLUENCE OF Pr AND Cm ON THE SUPERCONDUCTING PROPERTIES OF HIGH-T_c OXIDES
L. Soderholm, C.-K. Loong*, and C. W. Williams
High Temperature Superconductors, S. K. Malik and S. S. Shah, Eds., Nova Science Publishers (1991)

RARE EARTH MAGNETISM AND SUPERCONDUCTIVITY IN $Pr_{2-x}Ce_xCuO_4$ AND $Y_{1-x}Pr_xBa_2Cu_3O_7$: A NEUTRON SCATTERING STUDY
C.-K. Loong* and L. Soderholm
High Temperature Superconductors, S. K. Malik and S. S. Shah, Eds., Nova Science Publishers (1991)

*Not affiliated with the Chemistry Division or affiliated on a temporary basis.

SUPERCONDUCTIVITY AND RARE-EARTH PARAMAGNETISM IN $Pr_{1.85}Ce_{0.15}CuO_4$
C.-K. Loong* and L. Soderholm
J. Alloys Compds (1992)

Pr AND Cm IN SUPERCONDUCTOR-RELATED OXIDES
L. Soderholm and C.-K. Loong*
J. Alloys Compds (1992)

PREPARATION, CHEMICAL REACTIONS, AND SOME PHYSICAL PROPERTIES OF NEPTUNIUM PENTAFLUORIDE
J. G. Malm*, C. W. Williams, L. Soderholm, and L. R. Morss
J. Alloys Compds (1992)

AN EXAFS STUDY OF THE METALLOFULLERENE YC_{82}: IS THE YTTRIUM INSIDE THE CAGE?
L. Soderholm, P. Wurz*, K. Lykke, D. H. Parker*, and F. W. Lytle*
J. Phys. Chem. (1992)

THE ELECTRONIC AND MAGNETIC PROPERTIES OF Ho IN $Pb_2Sr_2HoCu_3O_{9-x}$
L. Soderholm, C.-K. Loong*, J. P. Hammonds*, J. S. Xue*, M. Maric*, and J. E. Greedan*
J. Appl. Phys. (1992)

RARE EARTH ENERGY LEVELS IN Nd_2CuO_4, Pr_2CuO_4 AND THE ELECTRON SUPERCONDUCTOR $Pr_{1.85}Ce_{0.15}CuO_4$
C.-K. Loong* and L. Soderholm
Phys. Rev. B (1992)

NEUTRON STUDY OF CRYSTAL FIELD TRANSITIONS IN $ErPO_4$
C.-K. Loong*, L. Soderholm, J. P. Hammonds*, M. M. Abrahams*, L. A. Boatner*, and N. M. Edelstein*
J. Appl. Phys. (1992)

CRYSTAL FIELD EXCITATIONS AND MAGNETIC PROPERTIES OF $TmPO_4$
C.-K. Loong*, L. Soderholm, M. M. Abrahams*, L. A. Boatner*, and N. M. Edelstein*
J. Appl. Phys. (1992)

COLLABORATIONS

M. M. Abraham and L. A. Boatner, Oak Ridge National Laboratory
The study of the electronic and thermodynamic behavior of the rare-earth orthophosphates is relying on the expertise in large-scale sample preparation of the group at Oak Ridge.

N. M. Edelstein, Lawrence Berkeley Laboratory
Magnetic and electronic properties of RPO_4 are being studied to further the understanding of electronic-phonon coupling.

G. L. Goodman, Materials Science Division, Argonne National Laboratory
Mutual interests in the modeling of electronic properties of f electrons are pursued in an ongoing collaboration.

J. E. Greedan, Institute of Materials Research, McMaster University, Hamilton, Ontario, Canada
The focus of this collaborative effort is to further the understanding of the effects of magnetic rare-earth ions on the superconducting properties of materials in which they are contained.

---

*Not affiliated with the Chemistry Division or affiliated on a temporary basis.

S. Kauslarich, University of California, Davis
We are beginning a collaboration directed toward mutual interests in electronic, superconducting, and magnetic properties of pnictides. Kauslarich will visit ANL on sabbatical in the fall of 1992.

S. Kern, Physics Department, Colorado State University, Fort Collins
Energy-level splittings in a variety of oxides and fluorides are under investigation with particular emphasis on obtaining an understanding of the informatio provided by a variety of experimental techniques.

G. H. Lander, European Institute for Transuranium Elements, Karlsruhe, Germany
Energy-level splittings in a variety of oxides and fluorides are under investigation with particular emphasis on obtaining an understanding of the information provided by a variety of experimental techniques, including X-ray resonant magnetic scattering.

F. W. Lytle, The Boeing Co., Seattle, WA
Problems of mutual interest are being investigated using X-ray absorption spectroscopy, in an effort to develop a synchrotron-based program.

H. Radousky, Lawrence Livermore National Laboratory
The focus of this collaborative effort is to further an understanding of the effects of magnetic rare-earth ions on the superconducting properties of materials in which they are contained.

U. Welp, Materials Science Division, Argonne National Laboratory
Magnetic susceptibility studies on a variety of oxides are being performed to ascertain the interactions of f electrons with their environment.

XIII. RADIATION CHEMISTRY OF HIGH-LEVEL WASTES
ANL/CHM TASK FORCE ON GAS GENERATION IN WASTE TANKS

D. Meisel, C. D. Jonah, M. S. Matheson, M. C. Sauer, F. Barnabas, E. Cerny, Y. Cheng, Y. Wojta

The accumulation of radioactive high-level liquid wastes in tanks at temporary storage facilities of the Department of Energy poses some risks that are of much concern to the public in general and to DOE in particular. Some of these mixed wastes were found to generate mixtures of gases (primarily H_2, N_2O) that may spontaneously ignite under certain conditions. The Chemistry Division was requested to identify the role of radiation in the production of hydrogen and other gases in waste tanks, and to develop a mechanistic understanding of the buildup of hydrogen, nitrous oxide, and other, undesirable, gases in waste tanks. To address this problem of national concern, the Division organized a task force composed of experts, mostly in the fields of radiation chemistry, colloid chemistry, and electron transfer; all are staff from established groups within the Division, reinforced with technical assistance specifically recruited for this task. The task force has been in operation for nearly two years and is expected to complete its studies early in 1993.

The program undertaken by the task force was divided into two main subtasks, the nature of which was dictated by the milestones and goals of the sponsors of the project. The goal of the first subtask was to determine the yields of gases produced upon the radiolysis of simulated waste solutions and slurries, and to propose mechanisms for the generation of these gases. The objective of the second subtask is to conduct computer modeling of predictive capabilities of the radiation and thermal chemistry of the complex waste mixtures. The activities of these two subtasks are described below. The problem of retention of gases by the slurry particles has also been studied by the task force, but will not be discussed here.

A. Radiolytic and Thermal Generation of Gases

1. Radiolytic Yields

The goal of this subtask component is to experimentally determine the identity and quantity of the gases generated radiolytically or by radiolytically induced reactions in simulated waste. Together with the other subtask, this effort is expected to result in the formulation of a quantitative mechanistic understanding of the processes that lead to the generation of the gases. When needed, quantitative information concerning the parameters that control the mechanisms (e.g., rate constants, initial yields of radicals, etc.) are determined and are then utilized as input parameters to the computations described below.

Simulated waste solutions were irradiated in several radiation sources available in the Chemistry Division, and the yields (expressed as G values in units of molecules per 100 eV) of gases determined gas-chromatographically. A standard waste solution has been devised (2.27 M NaOH, 0.86 M $NaAlO_2$, 2.22 M $NaNO_2$, and 2.79 M $NaNO_3$ and organic chelators) to mimic the actual solutions in the waste tanks.

It was found that the intensity of irradiation (dose rate) has no effect on the yield of any of the gases except N_2O. Two mechanisms for the radiolytic generation of H_2 were identified: (a) H_2 is produced by direct absorption of the radiation by water and intra- or interspur radical-radical reactions, and (b) H_2 is produced by hydrogen abstraction, reaction 1, from the

$$H + RH \rightarrow H_2 + R \qquad (1)$$

organic constituents of the waste. The first mechanism accounts for $G(H_2) = 0.031$. The second source, notably reaction 1, may account for up to $G(H_2) = 0.1$, depending on concentration and identity of the organic compounds in the wastes. Both the identity and concentrations of most of the organic compounds in the tanks are presently unknown. Rate constants

for reaction 1 for several likely organic constituents in the waste solutions under conditions relevant to the actual waste have been determined and are summarized in Table XIII-1. Comparison with literature values (last column, Table XIII-1) shows that the rate constants are strongly dependent on the pH of the solution. With these rate constants, and utilizing radiation chemical models for the radiolysis of water, one can compute the yields of H_2 expected under various scenarios.

Table XIII-1: Rate constants for hydrogen abstraction (reaction 1) at 30 and 60 °C[a]

RH	$10^{-9} \times k_1$ at 30 °C $M^{-1} s^{-1}$	$10^{-9} \times k_1$ at 60 °C $M^{-1} s^{-1}$	E_a kcal M^{-1}	$10^{-9} \times k_1$ at 25 °C and at pH 1 (literature value)
EDTA	1.2	2.7	5.4	0.065
HEDTA	1.4	1.6	0.9	
NTA	0.6	1.3	5.2	0.0075
IDA	0.55	0.85	2.9	0.00040
Glycolate		0.14		
Citrate	≈0.007	≈0.02	7.1	0.00043
OH^-[a]	0.033	0.13	9.2	

[a]All reaction rate constants in the table were measured using the competition method following yields of H_2 relative to the reaction of H with OH^-. Solutions contained 0.1 M NaOH, 1 mM $NaNO_3$, and 1 M NaCl.

In the presence of the organic substrates, given in Table XIII-1, production of O_2 (produced by the direct absorption of radiation by NO_3^-) is completely inhibited. In fact, O_2 is destroyed with $G(-O_2) = 7.0$, by reactions with the organic radicals that are formed. This important observation implies that O_2 is absent from the gases generated or retained in the waste tanks and, therefore, need not be of concern in the construction of flammability diagrams. However, N_2O, which is produced radiolytically and thermally, is an effective oxidant and can sustain H_2 burning.

The effect of temperature (the temperature in the waste tanks reaches 60 °C) on the yields of gases has been measured. In most cases, the yields of both H_2 and N_2O increase upon increasing the temperature. In slurries (nominally containing 2.3 M NaOH, 2.2 M $NaAlO_2$, 3.7 M $NaNO_3$, 3.2 M $NaNO_2$, and 0.6 M Na_2CO_3 and the organic chelators), which simulate some waste compositions, the yields at 30 °C are decreased to ca. half their values in the corresponding homogeneous simulant. This is due to partial trapping of the radiolytically produced species within the solid particles. Raising the temperature of the slurry to 60 °C restores the yield to nearly the same level as in the homogeneous solution. At higher temperature, the solubility of many of the slurry components increases and trapping in the solids decreases.

2. Radiolytic Degradation of Organics

The composition of the organic compounds in the waste tanks is presently unknown. The organics that were fed into the tanks were mostly organic chelators (EDTA, HEDTA, etc.). In an attempt to identify the fate and consequences of long-term storage of these organic compounds under the irradiation field, the yield of their destruction has been determined. A yield of $G(-RH) \geq 2.9$ has been determined for EDTA and HEDTA (at 0.065 M each) whereas a yield of $G(-RH) \leq 0.3$ was determined for citrate (at 0.1 M). Thus, only a negligible amount of the original chelators should remain in a tank after a few years of storage. Analysis of tank core samples, specifically designed to check this point, confirmed our prediction. More importantly, the products of the radiolytic degradation were found to be more efficient in thermally producing H_2 and N_2O than the original chelators. The dependence of the rate of thermal generation of H_2 on the dose of preirradiation is shown in Figure XIII-1. Given that the rate declines with storage times in excess of a few years, Figure XIII-1 suggests that radiolytic destruction of the organic matter may provide a remediation strategy for the gas generation.

3. The Formaldehyde Reaction

The results discussed in the previous section show that a relatively long-lived intermediate (hours) is generated by radiolytic degradation of the chelators. This intermediate efficiently generates H_2, and efforts to determine its identity were undertaken. Formaldehyde and glyoxalate are known degradation products of the chelators and were prime candidates for this intermediate. We find that formaldehyde indeed generates H_2 very efficiently in highly alkaline solutions. The rate and yield of H_2 generation from formaldehyde at several $[OH^-]$ are shown in Figure XIII-2. Both the rate and yield increase upon increasing the hydroxide concentration. The rate also increases on increasing

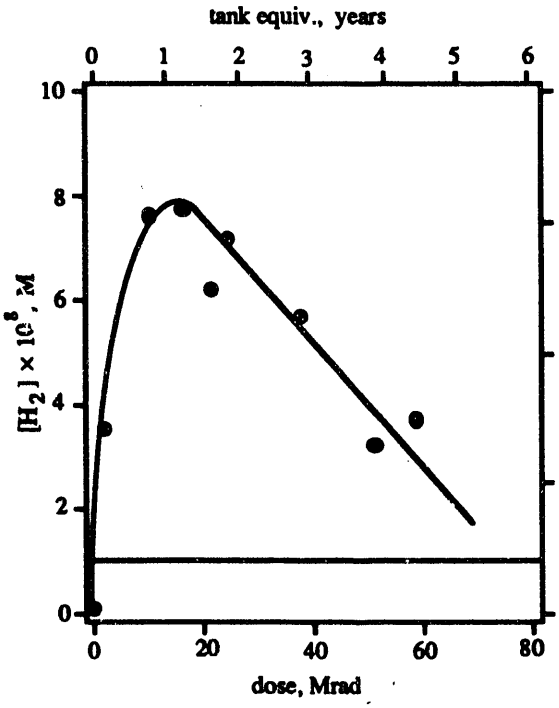

Figure XIII-1. Rate of thermal generation of H_2 at 60 °C as a function of dose of preirradiation. The dashed line indicates the rate in the tank. Standard waste simulant containing 0.065 M HEDTA, EDTA, and 0.1 M citrate.

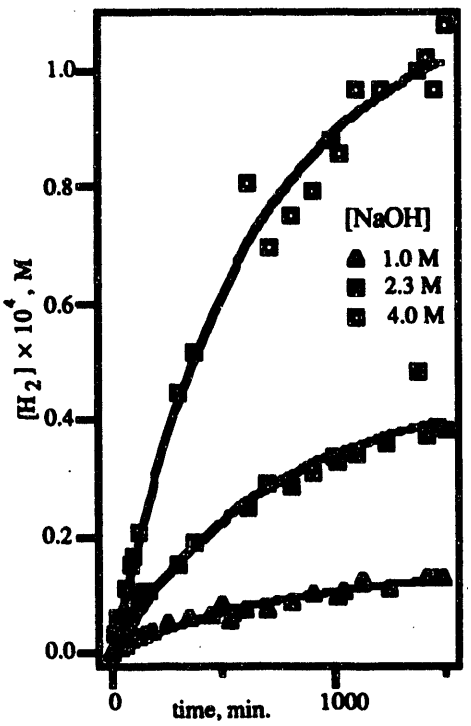

Figure XIII-2. H_2 generation from 5 mM formaldehyde solutions containing 1.0 M (triangles), 2.3 M (solid squares), or 4.0 M (open squares) NaOH at 60 °C.

the formaldehyde concentration but the yield, then, decreases. This is an indication that the H_2 generation reaction competes with the well-known Cannizzaro reaction, which is second order in the aldehyde concentration. In all cases studied, the rate and yield of H_2 generation also increase on increasing the temperature. Addition of aluminate, nitrate, and nitrite has only a minor effect on the reaction. Glyoxalate reacts similarly to formaldehyde, and it is likely that other aldehydes that do not contain hydrogen in the α position to the carbonyl will react in a similar fashion. The detailed mechanism of the H_2 production reaction is presently under investigation; we speculate that hydride transfer, similar to the Cannizzaro reaction, is involved.

4. Mechanisms of N_2O Generation

In all cases studied, $G(N_2O)$ is nearly an order of magnitude larger than $G(H_2)$. This contrasts with the situation in the waste tanks, where the ratio $G(H_2)/G(N_2O)$ is approximately unity. One possible explanation is that the concentration of N_2O in the tanks is much higher than in our experiments, leading to some destruction of N_2O by secondary reactions. So far, we have observed that: (a) organic substrates are necessary for the production of N_2O; (b) the organic compounds do not necessarily have to contain nitrogen moieties (e.g., glycolate); (c) the yield of N_2O is nearly independent of [RH]; and (d) based on isotopic ^{15}N labeling experiments, none of the nitrogen atoms in N_2O come from the organic substrate. There are many possible pathways from nitrite to nitrous oxide under the radiolytic conditions (e.g., we verified that hydroxylamine will efficiently generate N_2O in the waste simulants), but identifying the exact mechanism will probably not be possible within the lifetime of this project.

B. Computer Modeling of Simulated Waste Solutions

1. Computation of H_2 Yields

Because of the great variability in composition of the waste in various tanks, a computer model of predictive capabilities was developed. The model will allow rapid evaluation of the effect of various parameters on radiolytic gas generation. A diffusion model, developed in the past to simulate the radiation chemistry of relatively dilute solutions, has been modified to encompass the highly concentrated solutions encountered in the waste under consideration by the task force. This model simulates the three different types of processes that occur immediately (10^{-13} s and later) following the absorption of radiation by a solution: (a) recombination reactions among radiolysis fragments within spurs, (b) scavenging of these fragments by solutes, and (c) diffusion of the fragments out of the spurs. Pertinent to the chemistry in the tanks are reactions 1-4, which lead to the generation of H_2.

$$H + H \rightarrow H_2 \qquad (2)$$

$$e^-_{aq} + e^-_{aq} \xrightarrow{H_2O} H_2 \qquad (3)$$

$$e^-_{aq} + H \xrightarrow{H_2O} H_2 \qquad (3)$$

$$RH + H \rightarrow H_2 + R^{\bullet} \qquad (1)$$

A much larger set of reactions, which better represent the processes in the tanks, was included in the actual calculations. Figure XIII-3 shows the calculated yield of H_2 as a function of organic solutes, RH, in the standard simulant. The effect of RH is presented in this figure as $k_1 \times [RH]$ in units of s^{-1}. As the concentration of RH (or the rate constant) increases, the formation (yield and rate) of H_2 increases, due to the increased contribution from reaction 1. From the values of k_1 (e.g., Table XIII-1) one can calculate the expected $G(H_2)$, provided the identity of the chelators and their concentrations are known.

2. Computation of the NO_x System

The NO_x system is very complicated because several stable, but reactive, intermediates are formed during radiolysis. Even in the absence of organic compounds, the reaction scheme includes 18 reactions. The rate equations were solved using a conventional Gear-type integrator. The scheme does not address reactions in the presence of organics because they are unknown, but it does describe the relevant chemistry in their absence. Results from such calculations are shown in Figure XIII-4. For all cases studied, the steady-state concentration of the various NO_x radical species will be in the 10^{-8} M range and the N_2O_x concentrations will be in the 10^{-12} M range. No result is presented for N_2O in the figure because none was obtained in the calculations. The depletion in NO_3^- and increase in NO_2^- concentration will be small and <10% of the initial concentration of NO_3^- could have been depleted during the two decades of storage in the tanks. The absence of N_2O gas in the absence of organic compounds was verified experimentally (see section B.4) and tank core samples show, indeed, that the nitrate and nitrite concentrations have not significantly changed over the years.

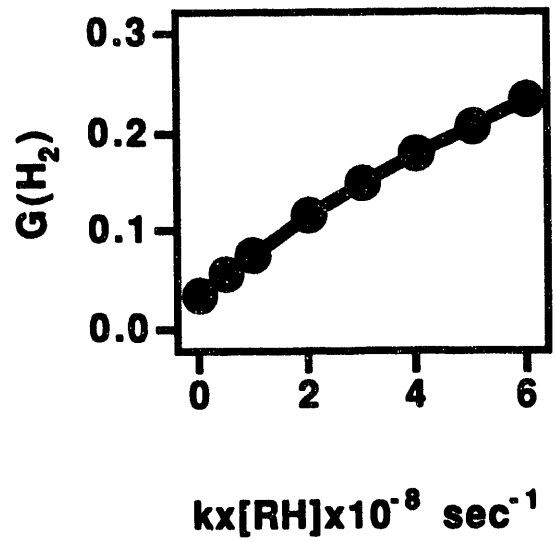

Figure XIII-3. Yield of H_2 as a function of rate for the H-atom abstraction reaction from the organic solute. All concentrations of the inorganic solute are the same as in the standard simulant.

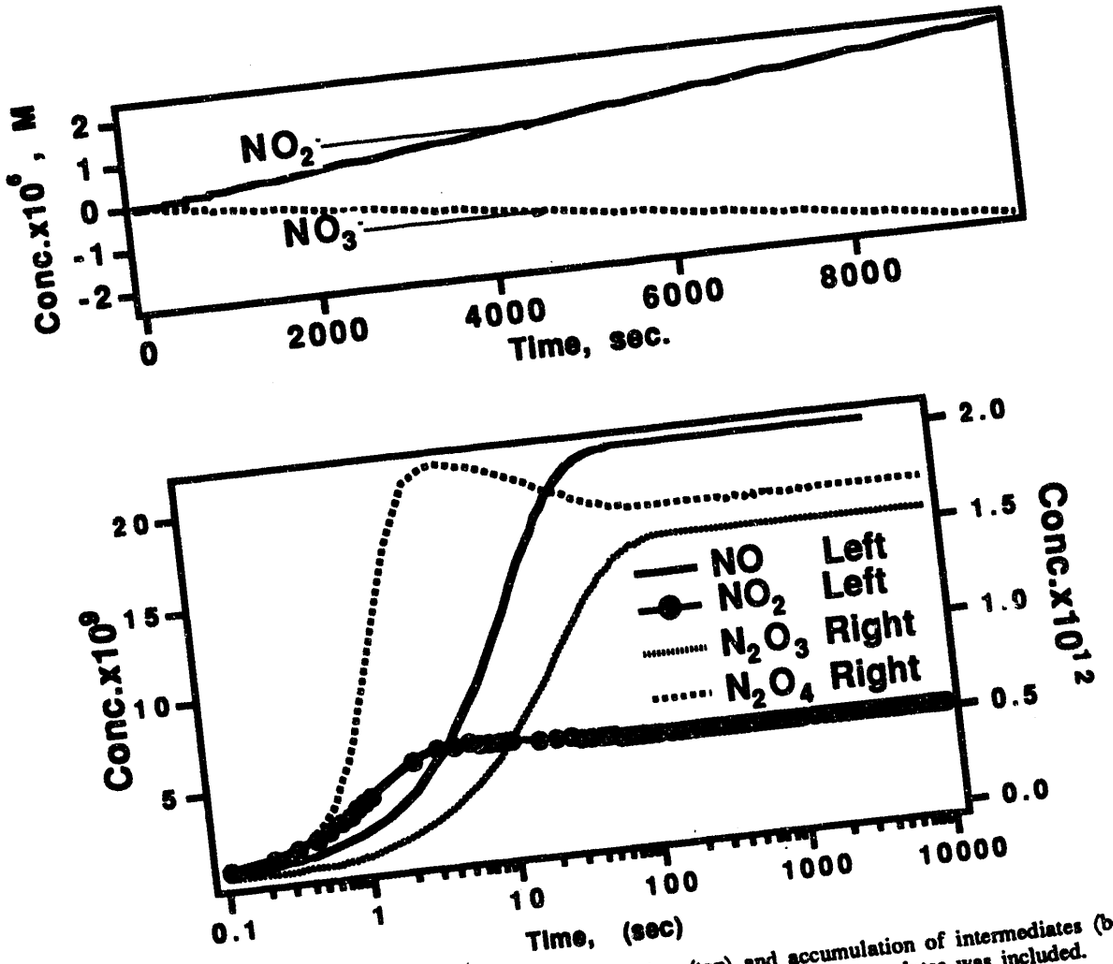

Figure XIII-4. Changes in the nitrate and nitrite concentration (top) and accumulation of intermediates (bottom) as a result of radiolysis (0.025 krad/min; same as in the tank). No reaction with organic solutes was included.

C. Conclusions

The ANL/CHM task force on gas generation in high-level liquid wastes during its short period of operation has been able to identify two major sources for the gases generated in waste tanks at the Hanford site:

1. Significant amounts of the dihydrogen may be attributed to radiolytic processes. A large fraction of this dihydrogen arises from hydrogen atom abstraction from organic additives by free hydrogen atoms. Once rate parameters for this reaction are collected and accurate analysis of the composition of the waste is performed, modeling calculations will allow the determination of the yields of H_2 from radiolysis under various scenarios. Such a computational approach will, however, require analysis of the organic constituents and their concentration in the tank.

2. Thermal processes, in particular the reaction of formaldehyde with hydroxide, also contribute significant amounts to the generation of dihydrogen. This essentially unstudied reaction needs to be studied in detail and its mechanism identified before any recommendations could be made.

In considering remediation strategies, several approaches may be envisioned: Removal of the radionuclide (^{137}Cs) responsible for most of the radiolysis will, of course, eliminate all of the radiolytic sources for H_2. It will not eliminate the portion generated thermally because degradation products have already accumulated in the tanks. Removal of the organic components will eliminate most of the radiolytic production of H_2 as well as that due to thermal generation. However, approximately 10% from direct

radiolysis of water will still remain. Addition of chemicals to minimize generation of H_2 (or to minimize gas retention in the tanks) should be carefully thought out and tested prior to execution in the field. Addition of organic scavengers (at concentrations above the few mM level) is not attractive due to their deleterious effects (in particular, their effect on gas retention by slurry particles).

PUBLICATIONS

RADIOLYTIC AND RADIOLYTICALLY INDUCED GENERATION OF GASES IN SIMULATED MIXED WASTE SOLUTIONS
D. Meisel, H. Diamond, C. D. Jonah, M. C. Sauer, Jr., J. C. Sullivan, F. Barnabas*, E. Cerny*, and Y. D. Cheng*
"Waste Management 92", R. G. Post and M. E. Wacks, Eds., Am. Nuc. Soc. & IAEA, Vol. 1, 1992, pp. 859-865

NITROUS OXIDE PRODUCTION FROM RADIOLYSIS OF SIMULATED HIGH-LEVEL NUCLEAR WASTE SOLUTIONS
D. D. Walker*, D. T. Hobbs*, J. B. Tiffany*, N. E. Bibler*, and D. Meisel
"Waste Management 92", R. G. Post and M. E. Wacks, Eds., Am. Nuc. Soc. & IAEA, Vol. 1, 1992, pp. 855-858

EVALUATION OF GENERATION AND RELEASE OF FLAMMABLE GASES IN TANK 241-SY-101
H. Babad*, G. D. Johnson*, J. A. Lechelt*, D. A. Reynolds*, L. R. Pederson*, D. M. Strachan*, D. Meisel, C. Jonah, and E. C. Ashby*
Westinghouse Hanford Company Report WHC-EP-0517 (1991)

RADIATION CHEMISTRY OF SYNTHETIC WASTE
D. Meisel, H. Diamond, E. P. Horwitz, C. D. Jonah, M. S. Matheson*, M. C. Sauer, Jr., and J. C. Sullivan
Argonne National Laboratory Report 91/40 (1991)

RADIOLYTIC GENERATION OF GASES FROM SYNTHETIC WASTE
D. Meisel, H. Diamond, E. P. Horwitz, C. D. Jonah, M. S. Matheson*, M. C. Sauer, Jr., J. C. Sullivan, F. Barnabas*, E. Cerny*, and Y. D. Cheng*
Argonne National Laboratory Report 91/41 (1991)

SUBMISSIONS

ON THE GENERATION OF H_2 FROM FORMALDEHYDE IN BASIC AQUEOUS SOLUTIONS
S. Kapoor*, F. Barnabas*, C. D. Jonah, M. C. Sauer, Jr., and D. Meisel
J. Am. Chem. Soc. (1992)

GAS GENERATION AND RETENTION IN TANK 101-SY: A SUMMARY OF LABORATORY STUDIES, TANK DATA AND INFORMATION NEEDS
D. Meisel, C. D. Jonah, E. C. Ashby*, L. R. Pederson*, and D. M. Strachan*
Pacific Northwest Laboratory Report (1992)

*Not affiliated with the Chemistry Division or affiliated on a temporary basis.

XIV. ULTRAFAST MOLECULAR ELECTRONIC DEVICES

M. R. Wasielewski, D. Gosztola, S. R. Greenfield, S. Watanabe

A. Background

The development of molecular electronic devices is a rapidly growing enterprise that seeks to use molecules as electronic switches, wires, microsensors for chemical analysis, and optoelectronic components in optical computing. The principal advantages of using molecules in these applications are high component density, increased response speed, and high-energy efficiency. The design and production of energy-efficient, state-of-the-art electronic devices depend increasingly on the ability to produce ever-higher densities of circuit elements within integrated circuits. Continuing improvements in microfabrication techniques have made 1 μm component sizes possible in semiconductor materials. These sizes result in 4 Mbit cm^{-2} data-storage densities. There has been a great deal of discussion regarding the possibility of increasing the data-storage density to as much as 10^{18} bits cm^{-2} using molecular switches. However, such massive size reduction will most likely be limited by quantum statistical considerations, if reasonable data-error rates are to be maintained. Nevertheless, if light is used to control molecular devices, the resultant advantages more than compensate for the statistical limitations on size reduction. Because energy- and electron-transfer processes within molecules can take place on a picosecond time scale, it is possible to produce devices that respond very rapidly. Although the wavelength of light limits the spot size that can be addressed by a light beam, even for visible light this represents data densities of 2.5×10^9 bits cm^{-2}. Recent results suggest that three dimensional addressing and the use of excitonic waveguides could greatly increase this resolution. Another advantage of using light-driven molecular devices is the ability to perform optical multiplexing, whereby light of specific frequencies is used to selectively address molecular devices. Finally, employing high-quantum efficiency, fast photodriven processes will decrease the heat load produced by molecular devices. This results in a much more energy-efficient and reliable system. These latter advantages readily make up for the size considerations mentioned above and should result in economically viable molecular electronic devices.

Recent successful approaches to molecular electronic devices have concentrated primarily on molecular wires, chemical sensors, and nonlinear optical (NLO) polymers for switching and modulation. Molecular wire research has focused mainly on conductive polymers, such as polyacetylene, polypyrrole, and polythiophene. These-low dimensional materials can be doped to make them highly conductive. Films of these materials are finding application as organic batteries and electrochromic devices. Because the conductivity of these materials is very sensitive to chemical doping, electron donor-acceptor molecules have been attached to these polymers to modulate their dopant level and thereby change their conductivity. In addition, there is a significant literature on polyarene ladder polymers and conductive polyimides that are finding application both as conductive materials and as (NLO) materials.

Chemical sensors have been developed that interface crown ethers and other molecules with molecular-recognition properties to electronic devices such as field-effect transistors. The ability of one molecule to selectively recognize another is providing the basis for developing practical molecular sensors. Optical multiplexing has been demonstrated using two-color photon-gated hole burning in electron donor-acceptor molecules. In this work, narrow-frequency lasers are used to write and address information in a matrix of donor-acceptor molecules at low temperature.

Molecule-based optical switching research has focused intensively on the preparation of polymers with NLO properties. Nonlinear optical response can be imparted to a polymer either by its intrinsic chemical structure or by appending organic molecules with known NLO properties to preformed polymer backbones. These polymers are finding application in frequency conversion of light through second- and third-order nonlinear processes. Using these materials in practical devices depends to a large extent on finding ways to deal with materials problems such as low solubilities and poor mechanical properties.

Although there are a number of theoretical discussions in the literature that strongly suggest that electron-transfer reactions can form the basis for a molecular switch, the design, synthesis, and demonstration of such switches has not been forthcoming. We have developed an approach to a practical molecular switch that makes use of high quantum yield, picosecond time scale electron-transfer processes to store information and to recover it.

Our fundamental approach to achieving efficient, long-lived photoinitiated charge separation is to produce arrays of electron-donor molecules in which the redox partners are rigidly attached in specific spatial arrangements relative to one another. Thus, photoexcitation of a donor or acceptor will result in vectorial electron transport to the redox partners attached to the photoexcited molecule, provided that the free energies of the electron-transfer reactions taking place within them are optimized. These are fundamental requirements for any electron donor-acceptor molecule that forms the basis of a molecular electronic device.

B. Concepts and Designs of Molecular Switches

Three distinct types of molecular switch are being developed. The first type of molecular switch uses two electron donors that can each transfer an electron to a common two-electron acceptor. This donor-acceptor-donor (DAD) switch undergoes a single electron-transfer reaction when the donor is excited by a laser pulse to yield D^+-A^--D. Increasing the light intensity of the excitation light pulse results in absorption of a photon by the remaining uncharged donor molecule. This results in transfer of a second electron to yield D^+-A^{-2}-D^+. The light-intensity-dependent switching between production of A^- and A^{-2} results in large photochromic changes to the A molecule. These photochromic changes can be used to modulate light beams of different colors depending on the ability of the initial laser pulse to switch the DAD molecule between the two reduced states of A.

The second type is a bistable electron-transfer array (BETA) switch. The basic design employs either one or two chromophores in a triad electron-transfer array, donor-acceptor(1)-acceptor(2). An energy-level scheme for this array is given in Figure XIV-1. In the first variation, Figure XIV-1, which uses a single chromophore, photoexcitation of acceptor(1) with visible light results in picosecond electron transfer from the donor to acceptor(1) to yield donor$^+$-acceptor(1)$^-$-acceptor(2). Subsequent dark electron transfer yields donor$^+$-acceptor(1)-acceptor(2)$^-$. The resultant long-lived (about 1 ms) donor$^+$-acceptor(1)-acceptor(2)$^-$ ion pair is the bit set "1" state of the switch. This state decays naturally to its original neutral, bit "0" state on a millisecond time scale in much the same fashion as does semiconductor memory. However, the unique feature of this switch is the intrinsic photoactive nature of acceptor(1). Optical excitation of acceptor(1) with a second light pulse greatly accelerates ion-pair recombination, thereby switching the charge separated, "1" state of the molecule back to its original "0" state on a 10-ps time scale. This defines *a color-sensitive molecular switch that uses visible light with a switching time of about 10 ps or 100 GHz.* The second variation of the BETA switch is more versatile because it makes use of different colors to set the "1" and "0" states. This switch requires the lowest excited singlet state of the donor molecule to be below that of acceptor(1). Excitation of the donor with color 1 once again results in two sequential electron-transfer steps producing donor$^+$-acceptor(1)-acceptor(2)$^-$. A second light pulse with color 2 excites acceptor(1) resulting in accelerated ion-pair recombination.

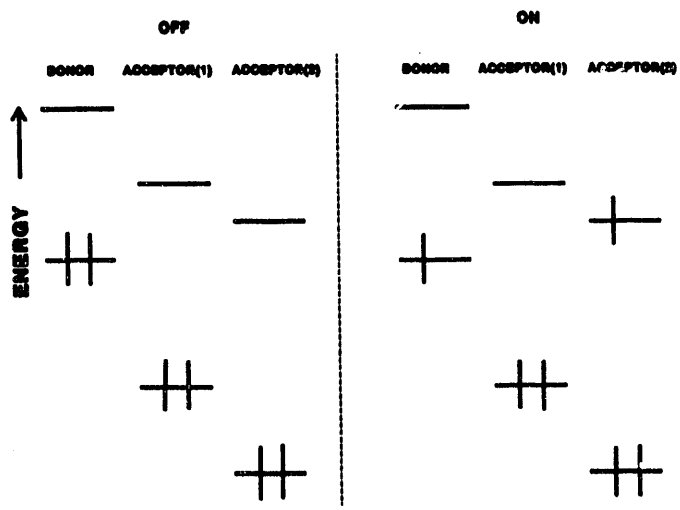

Figure XIV-1. Energy-level diagram of the BETA switch showing the highest occupied and lowest unoccupied molecular orbitals of the donor and acceptors.

A third type of molecular switch that we will develop is a field-effect donor-acceptor (FEDA) switch, Figure XIV-2. The FEDA switch consists of a donor(1)-acceptor(1)-donor(2)-acceptor(2) array. Excitation of donor(1) with color 1 results in rapid production of donor(1)$^+$-acceptor(1)$^-$-donor(2)-acceptor(2). The energetics of electron transfer within the donor(2)-acceptor(2) pair is designed so that rapid electron transfer is inhibited in solid state. However, the charge-separated pair donor(1)$^+$-acceptor(1)$^-$ creates a 10^6-10^7 V cm^{-1} electric field. This electric field is oriented vectorially to stabilize the ion pair state donor(2)$^+$-acceptor(2)$^-$. The added stabilization provided by the field makes electron transfer within the donor(2)-acceptor(2) pair energetically favorable. Thus, if during the lifetime of donor(1)$^+$-acceptor(1)$^-$, donor(2) is excited with color 2, a second electron transfer occurs within donor(2)-acceptor(2) to yield donor(1)$^+$-acceptor(1)$^-$-donor(2)$^+$-acceptor(2)$^-$. The two donor-acceptor pairs are sufficiently isolated electronically that electron transfer between pairs is not kinetically competitive with the desired processes. This arrangement constitutes a molecular AND gate that depends on two colors to determine its logical state.

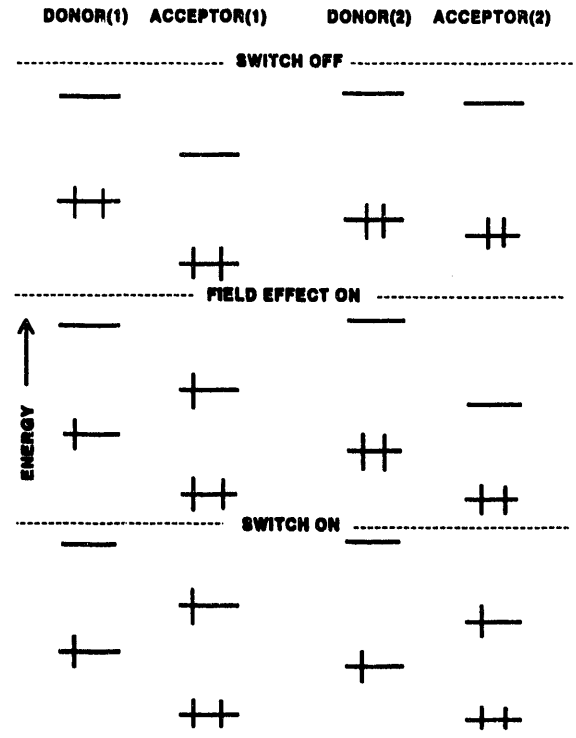

Figure XIV-2. Energy-level diagram of the FEDA switch showing the highest occupied and lowest unoccupied molecular orbitals of the donors and acceptors.

C. Development of an Electron Donor-Acceptor-Donor Molecular Switch

We have designed and prepared an electron donor-acceptor-donor molecule, 1, Figure XIV-3, consisting of two free-base *meso*-tripentylmonophenylporphyrins (HP) rigidly attached to N,N'-diphenyl-3,4,9,10-perylenebis(dicarboximide) (PBDCI) that exhibits light-intensity-dependent optical switching by means of two ultrafast electron-transfer reactions. A corresponding reference molecule, 2, Figure XIV-3, possessing only a single porphyrin donor was also prepared. PBDCI is an excellent, photostable electron acceptor that has been employed in dyes, electrophotography, and liquid-crystal displays.

PBDCI derivatives 1 and 2 can be reversibly reduced with either one or two electrons at thermodynamic half-wave potentials $E_{1/2}^- = -0.50$ V and $E_{1/2}^{-2} = -0.73$ V vs. SCE in pyridine, whereas $E_{1/2}^+$ for one-electron oxidation of the porphyrin is 0.92 V. These data show that PBDCI is an excellent electron acceptor with reduction potentials similar to those of benzoquinone. The PBDCI$^-$ and PBDCI^{-2} ions possess characteristic intense ($\varepsilon \approx 10^5$ M^{-1} cm^{-1}) optical absorptions at 713 nm and 546 nm, respectively. This opens up the possibility that rapid, photoinduced

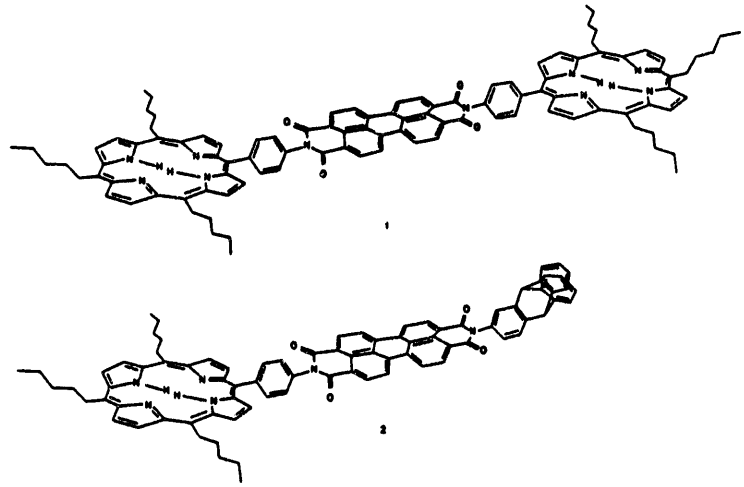

Figure XIV-3. Structures of compounds 1 and 2.

electron transfers from donor molecules may be used to selectively reduce PBDCI with either one or two electrons. The resultant photochromic changes in absorption from 713 nm to 546 nm could form the basis for molecular switches based on optimized molecular absorption characteristics. Molecule 1 is designed to test this hypothesis.

Photoinduced reduction of PBDCI by the lowest excited singlet state of HP can be detected readily with transient optical absorption spectroscopy. Time-resolved transient absorption spectra (160-fs time resolution), Figure XIV-4, show that single-photon excitation of both 1 and 2 results in formation of HP^+-$PBDCI^-$, as characterized by the intense absorption of $PBDCI^-$ at 713 nm. The rate constant for HP^+-$PBDCI^-$ formation at low light intensities in both 1 and 2 is $1.1 \times 0.2 \times 10^{11}$ s^{-1}. The inset to Figure XIV-4 shows a typical kinetic trace for the formation and decay of HP^+-$PBDCI^-$ in 1.

The lifetime of HP^+-$PBDCI^-$ in both 1 and 2 was measured as a function of laser-excitation intensity up to 20 photons per molecule, Figure XIV-5. The lifetime of the HP^+-$PBDCI^-$ ion-pair in 2 is independent of excitation intensity, whereas the lifetime of the same ion-pair in 1 decreases as the laser intensity increases, reaching a value that saturates at about half the lifetime of the ion-pair in 2. In addition, at high light intensities the rate constant for formation of HP^+-$PBDCI^-$ within 1 increases to $2.0 \pm 0.2 \times 10^{11}$ s^{-1}, whereas that for 2 remains constant.

Because we are monitoring the population of $PBDCI^-$ at 713 nm, it is clear that another process that is competitive with HP^+-$PBDCI^-$ ion-pair recombination is depleting the $PBDCI^-$ population in 1 at high light intensities. At these intensities, the 160-fs duration of the excitation flash ensures that both porphyrins within 1 are excited simultaneously.

Two-photon excitation of 1 yields HP^{1*}-PBDCI-HP^{1*}, which has the 3.8-eV total energy of two HP lowest excited singlet states available to perform further reactions. Rapid electron transfer follows in both mechanisms to yield HP^+-$PBDCI^-$-HP^{1*} with a free energy of formation of -0.5 eV. The $2.0 \pm 0.2 \times 10^{11}$ s^{-1} rate constant observed for this process is consistent with rate versus free-energy relationships for porphyrin-acceptor molecules that we have observed previously. The fact that the rate constant for the initial electron transfer at high light intensity in 1 is twice that for electron transfer following single-photon excitation in either 1 or 2 is a consequence of the twofold increase in concentration of $^{1*}HP$ within HP^{1*}-PBDCI-HP^{1*}.

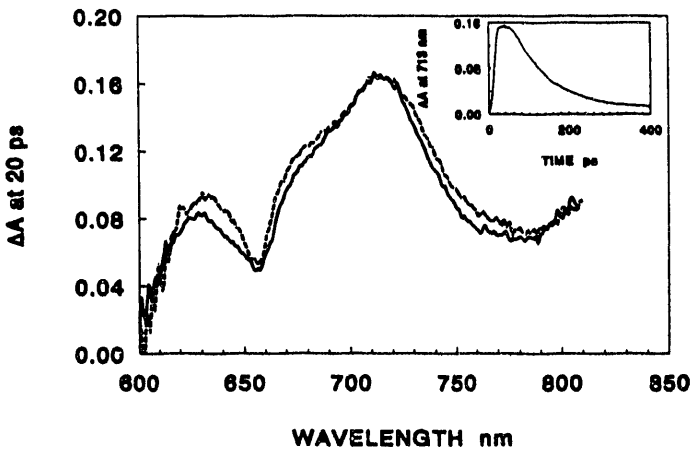

Figure XIV-4. Transient absorption spectra of 1 (—) and 2 (----) obtained 10 ps following a 160-fs laser flash. Inset: recovery kinetics at 713-nm for 1.

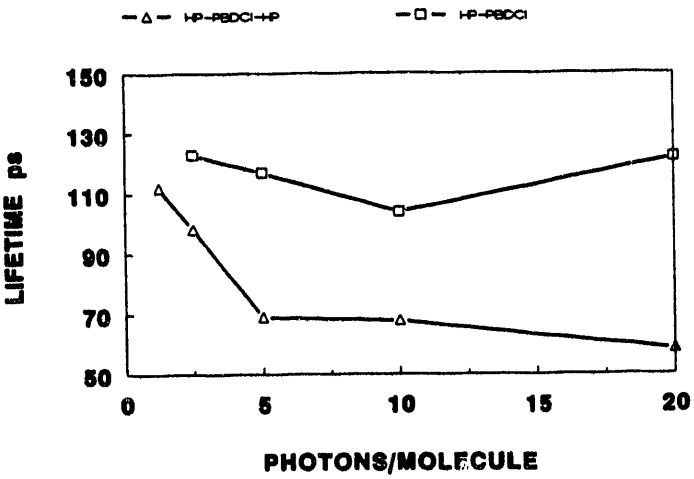

Figure XIV-5. Light intensity dependence of absorption changes at 713 nm in 1 and 2.

A 546-nm absorption band, which is characteristic of $PBDCI^{-2}$, appears at high light intensities in 1, but not in 2, Figure XIV-6. The positive absorbance change observed for 1 at 546 nm, Figure XIV-6, suggests that mechanism shown in equation 1 is primarily responsible for the increased rate constant of $PBDCI^-$ decay at high light intensities. The laser-power density required to switch molecule 1 from being a 713 nm absorber to being a 546-nm absorber is 2.5×10^9 W/cm^2 (5 photons/molecule, Figure XIV-4). This compares favorably with other two-

$$\begin{array}{ccccc} & \Delta G = -0.5 \text{ eV} & & \Delta G = -0.3 \text{ eV} & \\ {}^{1*}HP\text{-}PBDCI\text{-}HP^{1*} & \rightarrow & HP^+\text{-}PBDCI^-\text{-}HP^{1*} & \rightarrow & HP^+\text{-}PBDCI^{-2}\text{-}HP^+ \\ 3.8 \text{ eV} & & 3.3 \text{ eV} & & 3.0 \text{ eV} \end{array} \quad (1)$$

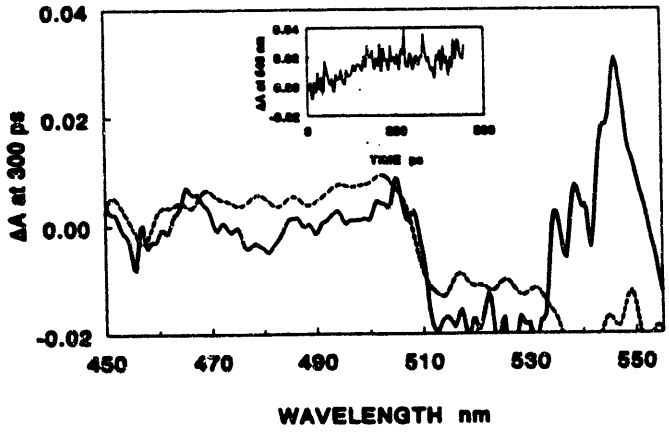

Figure XIV-6. Transient absorption changes at 200 ps following a high-intensity, 160-fs laser flash for 1 and 2. Inset: appearance for 546-nm feature in 1.

photon photochromic systems, and can be improved even further by a simple change in excitation wavelength. Nearly quantitative (>95%) two-photon turnover of 1 to yield HP^+-$PBDCI^{-2}$-HP^+ should be able to be accomplished by adjusting the concentration of 1 *downward* to give an optical density of 1 at the 410-nm Soret band ($\varepsilon = 4 \times 10^5\ M^{-1}\ cm^{-1}$) of HP and exciting the sample at this wavelength. The power-density requirement to effect this change will drop to about 10^8 W/cm^2. Mode-locked diode laser technology should be able to provide the pulses necessary to switch molecules such as 1.

The photophysical behavior of 1 constitutes a light-intensity-dependent optical switch. As the light intensity is increased, 1 switches from being a strong transient absorber at 713 nm to one in which the transient absorption occurs at 546 nm. Such molecules could be used to modulate two light beams at different colors on a picosecond time scale. Moreover, 1 should be able to switch using two different excitation wavelengths. Becaue the PBDCI molecule absorbs strongly at 526 nm ($\varepsilon = 10^5\ M^{-1}\ cm^{-1}$) and possesses a 2.3-eV lowest excited singlet state, excitation of PBDCI will initiate the first electron transfer to produce HP^+-$PBDCI^-$-HP. The second electron transfer may be initiated by application of a second photon, for example, at 585 nm, that is absorbed principally by the remaining ground-state porphyrin. Thus, this molecule should be able to perform logic operations. This opens up the possibility of developing molecular electronic devices based solely on electron motion within donor-acceptor complexes.

PUBLICATION

PICOSECOND OPTICAL SWITCHING BASED ON BIPHOTONIC EXCITATION OF AN ELECTRON DONOR-ACCEPTOR-DONOR MOLECULE.

M. P. O'Neil*, G. L. Gaines, III*, M. P. Niemczyk*, W. A. Svec, D. Gosztola, and M. R. Wasielewski
Science 257, 63-65 (1992)

SUBMISSION

NONLINEAR OPTICAL PARAMETERS OF 7',7'-DICYANO-7'-APO-β-CAROTENE IN HEXANE BY SELF-ACTION TECHNIQUES

H. A. Abdeldayem, W. Sheng*, P. Venkateswarlu*, W. K. Witherow*, D. O. Frazier*, P. Chandra Sekhar*, M. C. George*, L. Kispert*, and M. R. Wasielewski
Optics Comm. (in press)

*Not affiliated with the Chemistry Division or affiliated on a temporary basis.

XV. NUCLEAR MEDICINE

R. W. Atcher, J. J. Hines, G. L. Cox, B. Shafii, R. F. Barnes, A. C. Youngs, E. P. Horwitz, M. L. Dietz**

Outside Collaborators: *S. J. Adelstein, V. Alvarez, C. Black, M. J. Blend, M. W. Brechbiel, G. Chen, D. Colcher, T. K. DasGupta, E. R. DeSombre, D. Elmaleh, A. Fritzberg, O. A. Gansow, S. J. Gatley, T. Goffman, D. J. Grdina, J. A. Greager, S. W. Hadley, R. Hanson, P. V. Harper, E. Harvey, R. V. Hay, D. Hayes, A. C. Herbst, J. Holt, C. Jones, A. Kassis, D. Kufe, V. Langmuir, P. Leichner, R. M. Macklis, J. B. Mitchell, C. Pelizzari, J. Roeske, J. R. Rotmensch, A. Russo, J. W. Ryan, J. Schlom, J. L. Schwartz**, A. Shachter, B. Shafii, M. Strand, F. Stuart, C. Waldren, R. Weichselbaum, D. S. Wilbur, Z. Steplewski*

The nuclear medicine research program focuses on the development of radiopharmaceuticals for use in the diagnosis and treatment of disease. Our program includes the production of radionuclides; the synthesis and testing of drugs with potential use in imaging, particularly those well suited to tomographic techniques; the synthesis and testing of drugs with potential uses in the diagnosis and therapy of receptor-positive tumors; the radiolabeling of monoclonal antibodies for diagnosis and treatment of disease; and the development and testing of particle-emitting radiopharmaceuticals for therapy. The aims of these investigations include determination of the parameters in optimal radionuclide production; the stability of the radiopharmaceuticals in vitro and in vivo; the toxicity of the radiopharmaceuticals in vitro and in vivo; structure-activity relationships; the biologic effect of the therapeutic compounds and how this can be mediated to improve the outcome of treatment. Many of these aims are only possible through the excellent collaborations which we have established over the years.

A. Production of Alpha Emitters for Use in Therapy

R. W. Atcher, J. J. Hines, R. F. Barnes, D. S. Wilbur

Our research group has been involved for 18 years in the production of alpha emitters for therapy. Early work focused on the use of ^{211}At, an alpha emitter with a 7-hr half-life, because it was presumed that it would behave in a manner substantially similar to iodine. In fact, its behavior was dissimilar enough that the attention of the group was refocused on other radionuclides. Another drawback of astatine was that it is only produced in high radionuclidic purity by two reactions: ^{209}Bi(^{4}He,2n)^{211}At and ^{209}Bi(^{6}Li,4n)^{211}Rn $\xrightarrow{e.c.}$ ^{211}At. Neither of these reactions is within the capability of the cyclotrons commonly used to produce positron emitters for diagnostic purposes. The production of astatine is only within the realm of the research cyclotrons.

Despite this production problem, astatine offers a significant advantage over the radiometals that emit alpha particles. It can be bound to small molecules without the use of chelates. The larger halogens are of the same size as a methyl group. To offer an example, compounds that can bind to receptors on cancer cells, which are described in more detail in section D, have a molecular weight of about 300-500. The chelates, which are used in this work, have molecular weights on the order of 1000. Thus, chelation of the hormone will increase the molecular weight substantially. Furthermore, the chelates such as a derivative of diethylenetriaminepentaacetic acid (DTPA) will also introduce a net negative charge on the molecule that will impede its movement across cell membranes.

*Collaborator from another ANL Chemistry Division group.
**Collaborator from another ANL division.

Work on the production of ^{211}At has proceeded slowly, however. Our collaborators have not had the funding to vigorously pursue work with this radionuclide. We have been turning our thoughts to facilities in which we could test the production of the precursor, ^{211}Rn. To date, we have not located a facility that is capable of accelerating a Li-7 beam with currents high enough to test this reaction in batch as well as continuous processing mode.

Our work with the ^{224}Ra generator has continued. This radioisotope is still the workhorse of our group. Most of the biological studies are done with this system and are described in detail later.

The current focus on ensuring that the utmost care is taken in observing environmental, safety, and health (ESH) concerns has required the modification of the ^{224}Ra generators and the production facility. Because there is a short-lived radon daughter in the decay scheme, this has the potential for significant undesirable emission of daughter products. We have been progressively simplifying the separation system while simultaneously introducing as many barriers as possible to minimize any ESH insults. This has proceeded quite well; emissions from our system have been reduced by nearly a factor of 10. We have proceeded with another set of improvements to improve the flexibility of the hot cell that is used for the separation, to minimize the waste generated in the process by recycling nearly all of the waste, and to eliminate the need for the operator to enter the hot cell to make repairs by instituting a system with parts that can be replaced remotely. In addition, the separation system is enclosed in a box that is sealed for most of the operation, minimizing the efflux of radon and daughter radionuclides from the cell. This facility has been in operation for over a year and has been quite successful.

We have received several shipments of several hundred millicuries of ^{232}U, which is the source of the ^{228}Th, which is, in turn, the source of the ^{224}Ra. We designed a separation system for U-Th that can be operated remotely. In fact, we use the same hot cell for this work as we use for the ^{224}Ra production. This separation is done by using ion-exchange chromatography developed in the Chemistry Division. The yields and breakthrough of ^{232}U in the ^{228}Th have not been evident. This has enabled us to deliver larger generators as the user community is moving toward preclinical testing in large animals.

Finally, we have begun preliminary investigations into the production of a different radionuclide that produces alpha particles. Actinium-225 has a half-life of 10 days and decays by several short-lived alpha particle emitters to ^{209}Bi. One of the criticisms of the ^{211}At and the ^{212}Pb is that the half-life is too short to deliver the necessary dose via the biomolecules currently used for tumor targeting. We have begun testing the separation chemistry of ^{225}Ac from its parent, ^{229}Th. These studies have shown that we can produce the Ac free of Th using similar chemistry to the Th-Ra system. We also are removing the intermediate ^{225}Ra to insure quick recovery of the parent generator. In addition, ^{225}Ac decays through a ^{213}Bi, which has a 47-min half-life. Thus, we can use the same chemical techniques for conjugation of this isotope as we do for ^{212}Bi.

B. Development of Alpha-Emitting Radiopharmaceuticals for Therapy

R. W. Atcher, J. J. Hines, D. J. Grdina, J. R. Rotmensch, J. L. Schwartz, F. Stuart, R. Weichselbaum, O. A. Gansow, M. Strand, D. S. Wilbur, R. M. Macklis, B. Shafii

The majority of the work in this project has focused on the use of ^{212}Pb. We have continued to refine the use of the radiocolloids with this isotope. Collaborators have begun to test the ability to bind it to biomolecules using chelates. And we have begun animal tests that will examine the use of the ^{212}Bi conjugated to monoclonal antibodies. In addition, we have reported on the stability of a ^{211}At conjugate compared to its iodinated form in tumor-bearing animals.

The effectiveness of a colloid in treating cancer might be improved by injecting a dose of radioactivity several times, or fractionating. This has two benefits. The first is to increase the potential for normal tissue to recover from the radiation. The second is for the cells killed by the prior treatment to be sloughed off and expose new tumor cells for treatment. In order to test this hypothesis, we injected 100,000 cells into mice and treated them a day later. We waited up to one week to give the second dose of activity. In this treatment protocol, all of the control animals died,

whereas those receiving the fractionated doses survived. This was excellent proof of the value of such a protocol.

Our collaborators at Harvard have taken a different approach to this problem. Instead of injecting the isotope several times, they incorporated the ^{212}Pb into a slow release polymer that would degrade over the lifetime of the isotope. This protects it from leakage from the body cavity while maintaining a constant supply to the tumor bed. As an extra measure, they have injected the animal with antibodies that are conjugated to a ligand that binds ^{212}Bi. This enhances the targeting to the tumor by chemically binding the ^{212}Bi to the tumor surface. The preliminary studies of this approach have shown lower toxicity to critical organs than were seen with systemic therapy.

Finally, we have continued to pursue the ^{211}At conjugates for therapy. This work demonstrated that ^{211}At could be stably bound to an antibody and that it would achieve nearly identical biodistribution in tumor-bearing animals as that seen with the iodinated counterpart. In earlier studies, we had observed some striking differences between the iodinated and astatinated antibodies. We are beginning to think that this was due not to the chemistry of astatine, but to the biological processing of that particular antibody in vivo.

C. Monoclonal Antibodies for Diagnosis and Therapy

R. W. Atcher, D. Colcher, O. A. Gansow, J. R. Rotmensch, M. J. Blend, T. K. DasGupta, J. A. Greager, D. Kufe, D. Hayes, R. M. Macklis, M. Strand, G. Chen, J. Roeske, D. S. Wilbur, S. W. Hadley, A. Fritzberg, V. Alvarez, C. Pelizzari, J. Schlom, R. Weichselbaum, Z. Steplewski

The use of monoclonal antibodies (MoAbs) for diagnosis and therapy of cancer has created a great deal of excitement. Our work in this area is done largely through collaborations with a number of investigators throughout the country. In general, we have provided the expertise in radionuclide production and labeling chemistry, and they have provided the system in which the therapy is developed.

We have increased our success in treating a tumor in the mouse with a specific antibody labeled with ^{212}Bi. The nonspecific antibody treatment resulted in some life-lengthening but no cures. This was quite exciting inasmuch as ^{212}Bi has such a short half-life. An additional finding in these studies was that the chelate used is stable in vivo. Thus, there is less nontarget tissue toxicity than we saw with earlier generation chelates. In particular, the marrow toxicity was less than that expected from other studies with beta emitters.

We anticipate that the NCI investigators will begin toxicity tests in the next year in order to demonstrate the stability of the ^{212}Bi conjugate. These studies will be used to obtain approval from the appropriate regulatory agencies for approval of ^{212}Bi in humans.

One of the antibodies that has been widely used clinically is B72.3, a mouse MoAb that recognizes a high-molecular-weight mucinous antigen that is present on many epithelial tumors including ovarian, breast, and colon. Our interest in this antibody is for the diagnosis and treatment of ovarian cancer, which we are pursuing in collaboration with Schlom at NCI. We are in the process of obtaining approval for the use of this antibody with ^{90}Y for therapy. We have begun labeling studies with this conjugate to determine its ability to bind ^{90}Y, which is produced at ANL. Once the approvals are obtained, we will begin patient trials in ovarian cancer at the University of Chicago.

If necessary, we may use ^{87}Y produced at the ANL cyclotron to perform imaging studies in humans. These studies will focus on the biodistribution of the radioyttrium so that we may determine the anticipated dose to the bone and bone marrow from this conjugate. We are in the process of obtaining approval for this work at the University of Chicago as well.

We spent a significant amount of time in the past year developing the production and purification of ^{87}Y for this purpose. Sterling Drug approached us about this isotope when it became apparent that other widely used radionuclides would not bind to their chelate. This work is now in the preclinical testing stages. More details on the isotope production are provided below.

In an effort to improve the application of halogens to immunoconjugates, Shafii has improved the synthesis of the para- and meta-substituted tri-butyl

tin N-hydroxy succinimidyl esters of benzoic acid. These syntheses are both faster and higher in yield. This will enable us to make these compounds while minimizing the waste in the process.

Finally, we have devoted a part of our efforts to improving the ability to use imaging data from patients to predict the dose to tumors and to normal tissues. This work resulted in a Ph.D. dissertation by Roeske at the University of Chicago. We utilized several experiments performed by us to test the assumptions and the calculations associated with this model. Most of them turned out to be correct. We are now going to use this image-based treatment planning in our patient studies.

D. Hormone Receptor Binding Drugs for Diagnosis and Treatment of Malignancy

R. W. Atcher, B. Shafii, E. R. DeSombre, J. R. Rotmensch, J. L. Schwartz, R. Weichselbaum, R. Hanson, P. V. Harper, A. C. Herbst

Our work is based on the following fact: tumor heterogeneity dictates that at any time, a significant percentage of the cells are devoid of hormone (estrogen, androgen, or progestin) receptors. Because the presence of the hormone receptor usually correlates with a good response to therapy, this is an important parameter. Chemotherapy, which is infused over a period of time, has a higher likelihood of killing these cells as they progress through the cell cycle and present the receptors. However, radionuclide therapy is delivered in a bolus and, as such, some cells will not receive the therapeutic agent if it is delivered by using a biomolecule targeted to a receptor. We can overcome this problem if we use a particle emitter that has a range greater than one cell diameter. The alpha particle fits this requirement.

Our work on this project has focused primarily on the estrogen receptor. We have utilized two different compounds for this purpose. The first is an antiestrogen; this will bind to the receptor but will not have any biological effect. The other is an estrogen-like substance. The former compound has the advantage of not having any physiologic effect. We have found that this compound also has some superior characteristics when used in humans.

During the past year, we have improved the synthesis of this triphenylethylene compound. We have succeeded in developing a synthesis that is more efficient and uses less steps. This has the added advantage of requiring fewer purification steps.

In addition, we have completed our research on a novel system for halogenation. We have determined the conditions under which halogenation is optimized using nitric acid as the oxidizing agent, rather than a mixture of acetic acid and hydrogen peroxide. The disadvantage of the latter system is that it also oxidizes chloride and bromide. These can also react with the precursor compound, diluting our radiolabeled substance with other halogenated derivatives. If nitric acid is used, the oxidation potential is below that for chlorine and bromine, so we do not form these compounds. The added advantage of this system is that it will work with astatine as well.

Another avenue of research has been to examine precursor compounds other than the tributyl tin compounds as leaving groups for the halogen displacement reaction. This is a rather labile bond at room temperature, making these compounds susceptible to degradation. Secondly, this bulky group impedes the approach of the larger halogen molecules in the displacement reaction.

We have synthesized trimethylgermanium and dihydroxygallium derivatives in order to overcome the limitation of the tributyl tin compounds. Both of these compounds form more stable precursors while being a smaller, less sterically hindering moiety for displacement. Early tests of this Ge derivative have shown it to behave as anticipated.

E. Cyclotron Production of Radionuclides for Research

R. W. Atcher, J. J. Hines, G. L. Cox, A. C. Youngs, O. A. Gansow, D. S. Wilbur, E. Harvey, P. Leichner

As mentioned above, we have pursued the production of ^{87}Y using the ANL cyclotron. This work focused primarily on the $^{85}Rb(^{4}He,2n)$ reaction. Our cyclotron is also capable of making this isotope via

the ^{87}Sr(p,n) and Sr(d,xn) reaction. These reactions would require the use of an isotopically enriched target, which is not financially feasible currently.

We developed a target that is composed of rubidium chloride as a pressed powder. This target can withstand the heat load deposited by the beam, while maintaining its physical form. An added advantage is that it can be dissolved in water. This provides a means of minimizing dissolution of the target backing. The ^{87}Y and other multivalent cations are isolated on a cation-exchange resin, separated from the rubidium, stripped, and switched to a different ion-exchange resin to minimize other +3 cations from the product. Finally, the ^{87}Y is stripped from the column and converted to a dilute acid form.

We have found that the radionuclide can be produced in sufficient purity to bind to the most demanding ligand systems. This has been a major focus of our work with cyclotron-produced isotopes during the last year. We are currently testing this isotope in animals to determine its suitability for use in tomographic imaging systems.

This has not been the sole isotope of utility, however. As interest in the environmental fate of ^{99}Tc has increased, the need for an intermediate-lived Tc isotope that emits gamma rays has increased as well. We have had several inquiries from investigators in waste management as well as the nuclear medicine field regarding this isotope. Our earlier work with ^{95m}Tc has enabled us to meet this sporadic, but critical, need.

Our work with radioisotopes of lead for therapy has also alerted us to the need for an isotope of Pb that can be used in biodistribution studies as well as human imaging studies. We have focused our attention on the use of ^{203}Pb. This isotope has a 52-hr half-life and emits a single photon at 280 keV. This is ideal for use in cancer imaging; the half-life is long enough to be used with monoclonal antibodies and the energy is high enough to not be attenuated during imaging of deep structures.

We plan to begin production trials to determine the best reaction path to produce this isotope. Radiochemical purity and high specific activity are essential if this isotope is to be used for labeling monoclonal antibodies.

In addition, we have had several inquiries from environmental researchers regarding the production of isotopes of Pu and Np for use in isotope dilution studies as well as radiotracer studies. Plutonium-237, ^{236}Pu, and ^{236}Np have all been produced on our cyclotron and potentially could be produced again.

Finally, we have had requests from the nuclear physics community for two radionuclides, ^{56}Co and ^{207}Bi, to be used in gamma-spectrometry experiments. We have produced ^{56}Co for ANL researchers. We are investigating the potential of producing ^{207}Bi for these investigators as well.

F. Large-scale Production of ^{90}Y for Use in Radionuclide Therapy

R. W. Atcher, J. J. Hines, R. F. Barnes, E. P. Horwitz, M. L. Dietz

The use of ^{90}Y as a therapeutic isotope has been expanding gradually over the past few years as the technology for conjugating proteins with chelates has improved. This element is a bone seeker as is its parent, ^{90}Sr. The consequence is that the stable conjugation of ^{90}Y to the protein is crucial to the success of the therapy. As new, more stable chelates have been developed, the requirements for higher purity of the ^{90}Y have become evident. In view of this need, we have developed a new production process for ^{90}Y.

There are three major criteria to be met in producing ^{90}Y: (1) Low breakthrough of the ^{90}Sr parent, (2) high yield of the ^{90}Y daughter, and (3) high radiochemical purity as measured by the amount of ionic Y present as well as the minimization of cold metal contamination. On this last point, our collaborators at NCI (Gansow, Brechbiel, Pippin) have been valuable in defining what elements are problematic for the "state of the art" chelates that bind ^{90}Y stably to the proteins. This includes derivatives of DTPA as well as other macrocyclic chelates that are just beginning to be tested preclinically and clinically.

Using a process originally defined by the separations science group at ANL, we developed new methods of removing ^{90}Sr from the daughter products, including ^{90}Y. This technology has been reported at the ACS meeting as well as in a published paper. Because this separation is to be done on a scale that presents significant radiation hazards, the separation is performed remotely in hot cells. This technique introduces constraints on how the extraction can be done. We have focused on column technology. The

extractant is adsorbed on an inert support. The capacity of these columns is clearly less than a batch extraction, but it is easier to perform the separation remotely.

We originally modeled this system in a glove box operation. The separation was cumbersome, but proved to be an excellent source of ^{90}Y. The decontamination factor from ^{90}Sr was at least 10^{10}. In addition, the yield was good and the process did not suffer from repetitive operations.

When this system was scaled up to multicurie levels, several problems became obvious. The first is that the columns required to retain the ^{90}Sr and other cold Sr are quite large. This results in large volumes of liquid to be handled. The final analysis of this system was that the volume of liquid was too large to be efficiently managed. A second consideration was to try to keep the volume of liquid small enough that one could use columns in series, rather than evaporating the solutions to reduce the volume for downstream operations. Finally, we wanted to use the same solutions for both the ^{90}Sr and the ^{90}Y extraction.

The solution to this problem was to begin the separation by a precipitation step. The ^{90}Sr is precipitated, which removes 99.9+% of the material. This reduces the volume of solution that is passed through the column and reduces the need for large ion-exchange columns to retain all of the Sr in the generator. The second modification that we used was to back-wash the columns to insure that ^{90}Sr never passed through them. This had the advantage of extending column life and reducing ^{90}Sr breakthrough. The smaller volumes also enabled us to utilize the same process stream for the ^{90}Sr extraction and the ^{90}Y extraction. As an added bonus, we also have cut the processing time by one day.

We have produced from millicurie to two curie quantities of ^{90}Y for tests by several scientists. Eventually, this material will be used in trials of radiolabeled monoclonal antibodies for therapy as well as in some other trials of ^{90}Y in therapy.

PUBLICATIONS

ASTATINE-211 LABELING OF AN ANTI-MELANOMA ANTIBODY AND IT'S FAB FRAGMENT USING N-SUCCINIMIDYL PARA-ASTATOBENZOATE: COMPARISONS IN VIVO WITH THE PARA-[^{125}I] IODOBENZOYL CONJUGATE

S. W. Hadley*, D. S. Wilbur*, M. A. Gray*, and R. W. Atcher
Bioconjugate Chem. 2, 171-179 (1991)

INCREASED NUCLEAR DAMAGE BY HIGH LINEAR ENERGY TRANSFER RADIOISOTOPES APPLICABLE FOR RADIODIRECTED THERAPY AGAINST RADIOLOGIC MALIGNANCIES

J. Rotmensch*, J. L. Schwartz*, R. W. Atcher, P. V. Harper*, and E. DeSombre*
Gynecol. Obstet. Invest 32, 180-184 (1991)

ASSESSMENT OF DOSIMETRY AND EARLY RENAL RADIOTOXICITY AFTER TREATMENT WITH AN ALPHA PARTICLE EMITTING RADIOPHARMACEUTICAL

M. T. Speidel*, J. Humm*, M. R. Bellerive*, R. Mulkern*, R. W. Atcher, J. J. Hines, and R. M. Macklis*
Antibody, Immunoconjugates, and Radiopharmaceuticals 4, 681-692 (1991)

DIFFERENTIAL LOCUS SENSITIVITY TO MUTATION INDUCTION BY IONIZING RADIATIONS OF DIFFERENT LETS IN CHINESE HAMSTER OVARY K1 CELLS

J. L. Schwartz*, C. R. Ashman*, R. W. Atcher, B. A. Sedita*, J. D. Shadley*, J. Tang*, J. L. Whitlock*, and J. Rotmensch*
Carcinogenesis 12, 1721-1726 (1991)

*Not affiliated with the Chemistry Division or affiliated on a temporary basis.

BIODISTRIBUTION PARAMETERS AND RADIATION ABSORBED DOSE ESTIMATES FOR RADIO-LABELED HUMAN LOW DENSITY LIPOPROTEIN

R. V. Hay*, J. W. Ryan*, K. A. Williams*, R. W. Atcher, M. W. Brechbiel*, O. A. Gansow*, R. M. Fleming*, V. J. Stark*, K. A. Lathrop*, and P. V. Harper*

Proceedings, 5th International Radiopharm. Dos. Symposium, Conf-910529, pp. 256-273 (1992)

INTERLABORATORY COMPARISON OF DIFFERENT ALPHA-PARTICLE AND RADON SOURCES: CELL SURVIVAL AND RELATIVE BIOLOGICAL EFFECTIVENESS

J. L. Schwartz*, J. Rotmensch*, R. W. Atcher, R. F. Jostes*, F. T. Cross*, T. E. Hui*, D. Chen*, S. Carpenter*, H. H. Evans*, J. Mencl*, G. Bakale*, and P. S. Rao*

Health Phys. 62, 458-461 (1992)

ANALYSIS OF ASCITES FROM PATIENTS WITH OVARIAN CARCINOMA BY CELL FLOW CYTOMETRY

J. R. Rotmensch*, R. W. Atcher, J. L. Schwartz*, and D. J. Grdina*

Gynec. Oncol. 44, 10-12 (1992)

SUBMISSIONS

ALPHA RADIATION-INDUCED G2M ARREST IN MURINE LYMPHOMA CELLS

S. T. Palayoor*, R. W. Atcher, J. J. Hines, and R. M. Macklis*

Int. J. of Rad. Biol.

LOCALIZATION OF SARCOMA XENOGRAFTS IN NUDE MICE WITH INDIUM-111 LABELED MONOCLONAL ANTIBODIES

T. C. Chao*, M. J. Blend*, A. D. Lopes*, R. W. Atcher, T. K. DasGupta*, and J. A. Greager*

J. Surg. Oncol.

INDUCTION OF MUTATIONS BY BISMUTH-212 ALPHA PARTICLES AT TWO GENETIC LOCI IN HUMAN B-LYMPHOBLASTS

N. F. Metting*, S. T. Palayoor*, R. M. Macklis*, R. W. Atcher, H. L. Liber*, and J. B. Little*

Rad. Res.

AN IMPROVED AND FACILE METHOD FOR THE SYNTHESIS OF 1,1-BIS(4-HYDROXYPHENYL)-2-PHENYLETHYLENE AND ITS DERIVATIVES

B. Shafii*, R. W. Atcher, and E. R. DeSombre*

Nucl. Med. Biol.

MURINE HEMATOPOIETIC ABLATION BY ALPHA-PARTICLE-EMITTING RADIOPHARMACEUTICALS. TRANSPLANTATION

R. M. Macklis*, B. A. Beresford*, J. Y. Lin*, R. W. Atcher, and J. L. Humm*

Appl. Radiat. Isot.

AN IMPROVED METHOD FOR IODINATION OF BIOMOLECULES

B. Shafii*, R. W. Atcher, and E. R. DeSombre*

Bioconjugate Chem. (1992)

---

*Not affiliated with the Chemistry Division or affiliated on a temporary basis.

COLLABORATIONS

J. Rotmensch and R. Weichselbaum, The University of Chicago
We are currently investigating the use of colloids of ^{212}Pb and ^{90}Y as radiotherapeutic agents in treating ovarian cancer. Studies with ^{203}Pb show that there is a difference in whole-body clearance between different preparations, which may be attributable to size and also to chemical state. Toxicity studies of these radiopharmaceuticals are underway in order to better understand the results of the biodistribution studies. Studies of these compounds to treat a tumor in animals are also underway.

F. Stuart and D. Smith, The University of Chicago
Our groups are working on methods to label cells and antibodies to be used in the selective suppression of the immune system. Because the alpha emitters offer the potential of cell-selective cytotoxicity, they are optimal for use in temporarily suppressing a particular subset of lymphocytes to facilitate the successful transplant of organs. To date, the work has focused on improved methods of labeling cells with ^{212}Pb, which is then used to immunize mice for later transplant. If successful, this could improve the chances of graft survival and would free the constraint of extremely closely matched donor and recipient.

R. Hanson, Northeastern University, Boston, MA
We are collaborating on a study of estrogen-receptor-binding compounds for use in the diagnosis and therapy of gynecologic malignancy. These studies include Br-76 for PET imaging, Br-77, I-123, and At-211 for therapy.

E. Harvey and A. Vessey, Sterling Drug, Sharon Hill, PA
Sterling Drug has developed a chelate that is specific for yttrium (and presumably the rare earth radionuclides as well). We have been collaborating with them to develop a radionuclide that can be used for biodistribution studies in humans as well as to supply them with ^{90}Y for their therapy studies.

O. A. Gansow, M. Brechbiel, and G. Pippin, National Cancer Institute, Bethesda, MD
Our groups are working on the development of chelates that will bind lead and bismuth-212 to proteins in order to use these radionuclides effectively in vivo. Generator-produced bismuth has been complexed to antibodies with derivatives of diethylenetriaminepentaacetic acid. These complexes have been shown to have little or no effect on the function of the antibodies. Testing of the radium-224 generator is also an ongoing project.

M. Strand, Johns Hopkins University, Baltimore, MD
Our groups have been testing ^{212}Bi-labeled antibodies for therapy in a leukemia model in mice. The results of the work thus far have been promising, although the expected cure of the tumor has been somewhat difficult to achieve. In vivo tests of the chelates developed at the National Cancer Institute are also being conducted here using ^{206}Bi to model the pharmacokinetics of the label.

V. Alvarez, Cytogen Corp., Princeton, NJ
Our groups have been testing bismuth-labeling procedures by applying a unique chelate system developed at Cytogen. This chelate, which binds to the carbohydrate moiety of the immunoglobulin molecule, enables us to maintain the integrity of the binding part of the molecule while making these modifications.

D. Grdina, Biological and Medical Research Division, Argonne National Laboratory
We are examining the use of radioprotectors, specifically WR2721, which is an alkylaminothiol, to be used in vivo to protect normal tissue when radionuclidic therapy is being used. In the past, gastrointestinal and marrow toxicity have been the dose-limiting factors in these forms of therapy. If the use of radioprotectors enables us to use higher doses of alpha or beta emitters, then we will have made this form of therapy much more valuable in the clinic. Similarly, these compounds may also be valuable in reducing the mutagenic properties of radionuclide therapy.

A. C. Herbst and E. DeSombre, The University of Chicago
We are investigating the use of radiolabeled estrogen-receptor-binding radiopharmaceuticals to diagnose and treat gynecologic malignancies that express the estrogen receptor. Ultimately, we would like to treat patients with Auger electron emitting radionuclides, which are bound to the estrogen receptor and internalized by the cells.

J. Schwartz and R. Weichselbaum, Biological and Medical Research Division, Argonne National Laboratory and The University of Chicago
We are currently testing the radiosensitivity of alpha emitters of those human tumor cells that are resistant to either radiation, chemotherapy, or both. The theory of high-LET radiation suggests that there should be no cell that is "resistant" to the high-LET radiation. If this premise is borne out, the implications for treatment of resistant tumors with alpha emitters are enormous. In addition, we are examining the mutagenic potential of alpha emitters in terms of their use in therapy and the dangers associated with environmental radon.

T. DasGupta and J. Greager, University of Illinois Medical Center, Chicago
We are undertaking a study of an antibody that was developed in the university laboratory that recognizes soft-tissue sarcomas. Although these tumors have reasonable response to surgery, an adjuvant therapy that utilizes this antibody would enable the clinician to eliminate the microfoci missed in surgery by labeling the antibody with a cytotoxic radionuclide.

M. Blend and R. Seevers, Michael Reese Hospital, Chicago, IL
We are investigating the use of radiolabeled antibodies to determine in patients the presence of tumors that are not detected by other methods. Improved techniques for labeling and administering the antibodies are under development. These antibody-imaging tests can be used also to predict the dose to target tissue and nontarget tissue if the antibodies are to be used for therapy when labeled with a particle-emitting isotope.

A. Fritzberg, S. Wilbur, and S. Hadley, NeoRx Corp., Seattle, WA and The University of Washington, Seattle
We are collaborating in the development of a procedure to halogenate antibodies with astatine for therapy and with positron emitters for diagnosis. These are complementary techniques that could provide valuable information for treatment planning with radionuclides.

D. Hayes and D. Kufe, Harvard Medical School, Boston, MA
We are collaborating on the use of DF3, a monoclonal antibody that recognizes a cell-surface antigen present on gynecological cancers. This work is ongoing in cell culture tests; if these tests are promising, we will begin an imaging trial with this antibody with the aim of using it for therapy.

D. Colcher, University of Nebraska
J. Schlom, National Cancer Institute, Bethesda, MD
We are collaborating on an imaging trial of the antibody B72.3 for ovarian cancer. These studies will be used to obtain permission from the Food and Drug Administration to use this antibody for radionuclide therapy, initially with Y-90.

C. Black and A. Russo, National Cancer Institute, Bethesda, MD
We are collaborating on the use of ESR to determine the chemical species produced in treating cancer with alpha and beta emitters. The data derived from this study will be used to assess the value of a variety of radiosensitizers for tumor cells.

C. Chen and C. Pelizzari, The University of Chicago
We have been collaborating with these investigators on techniques for correlating images obtained by using nuclear medicine techniques with those obtained from X-ray computerized axial tomography and magnetic resonance imaging. This correlation allows one to judge the anatomical site of uptake of radiopharmaceuticals in humans.

J. B. Mitchell, National Cancer Institute, Bethesda, MD
We are collaborating on a study of the fundamental radiobiology of radionuclide therapy. Aspects of this study include tissue oxygenation, rate of dose deposition, cell cycle, growth kinetics, and high- and low-LET emitters as the toxic agent.

D. Elmaleh, Massachusetts General Hospital, Boston
We are collaborating with Elmaleh on the use of positron emitters for diagnostic purposes. These include Br-76 and I-124 for labeling antibodies and receptor-binding drugs for neurologic imaging.

S. J. Adelstein, A. Kassis, and R. Macklis, Harvard Medical School, Boston, MA

We are investigating the use of the alpha-emitting isotopes to treat bone marrow in vitro to eliminate any diseased cells before injection back into the patient. The selectivity of the alpha emitters, especially when attached to a monoclonal antibody that is directed against the target cells, is optimal for this application. Bismuth-212 with a 1-hr half-life is particularly well suited to this application. This work would enable the patients to receive their own marrow in transplant procedures where the disease has spread to the marrow.

XVI. ACCELERATOR ACTIVITIES

C. D. Jonah, B. E. Clifft, G. L. Cox, D. T. Ficht, R. H. Lowers, A. C. Youngs, D. Werst, R. W. Atcher

A. 20-MeV Linac *C. D. Jonah, B. E. Clifft, G. L. Cox, D. T. Ficht*

The safety systems of the linac have been upgraded in both hardware and documentation during the past year. All radiation detectors in user-occupied areas have been replaced with "fail-safe"-type detectors that are suitable for high-peak-pulse machines. In addition, a failure analysis for the interlock systems was done, new operating procedures were written, and new safety systems were installed. The results will appear in the Safety Analysis Report for the linac.

This linac was built in the late 1960s for radiation chemical studies. It is uniquely suited to radiation chemical experiments because both short pulses and high powers are available. The current in the picosecond pulse was increased approximately fourfold in 1978 by modifying the subharmonic bunching to work on the 12th harmonic instead of the sixth harmonic. In the late 1980s, a pulse-compression technique was devised that compressed the electron pulse to 5 ps from 30 ps with the same beam current. Studies are possible ranging over a 5-ps pulse with 6 nC of charge to a 30-ps pulse with 40 nC of charge to a 9-μsec pulse with 10 μC of charge. The energy of the beam, 20-MeV transient mode or 15-MeV steady-state mode, is sufficiently high to easily penetrate a reaction cell or even an oven, but not so high that nuclear activation is a major problem. The machine is currently being used to study the pathways by which kinetic energy is transformed into chemical potential energy, to study electron-transfer reactions, to create and study unusual oxidation states of lanthanides and actinides, and to study unusual short-lived molecules. In addition, scientists from the Advanced Photon Source are using the linac to characterize the impedance of the waveguides and chambers that will make up the light source. These experiments are critical to the design of the APS because the eddy currents induced by the positron beam going through the cavities and chambers of the machine can defocus the positron beam.

B. 3-MeV Van de Graaff Accelerator *R. H. Lowers, A. C. Youngs, D. Werst*

The 3-MeV Van de Graaff accelerator supports the magnetic resonance studies of the Radiation Chemistry and Photochemistry Group. The machine can provide 1-ns to 10-μs pulses of electrons or protons. The low noise of the machine makes it ideal for studying radical processes by using magnetic resonance and optical-magnetic resonance techniques. Such studies are described above.

This year, considerable time has been spent reviewing control and safety systems with the goal of documenting the safety of the system. The activities are very similar to those outlined for the linac. One major study was a maximum credible incident analysis for a gas spill from the Van de Graaff tank.

C. 60-Inch Cyclotron *G. L. Cox, A. C. Youngs, R. W. Atcher*

The cyclotron is a fixed-frequency machine capable of accelerating protons, deuterons, ^{3}He, and ^{4}He ions to 11, 21, 34, and 43 MeV, respectively.

The major use of the cyclotron has been radionuclide production for the nuclear medicine research program. Radionuclides produced for this program and for other ANL groups and for external investigators include ^{87}Y, $^{206,5}Bi$, ^{95}Tc, ^{198}Au, ^{139}Ce, and ^{56}Co.

XVII. COMPUTER SYSTEM AND NETWORK SERVICES

R. E. VanBuskirk, J. M. Kolenko

The Computer Services Group is responsible for designing, implementing, and maintaining the Chemistry Division's in-house central computer systems and networks. The in-house central computing needs are supported by nine networked MicroVAX computers and two IBM RS/6000 computers. In addition to the centralized computers, the network consists of eight DEC LSI-11 microcomputers, 11 UNIX computers of various types, and over 120 personal computers. The many internal and external network connections extend this central network worldwide.

The central VAX and Unix systems provide the computational power for general computation and various graphics activities. The LSI-11 systems are used for experiment control, data acquisition, and data analysis. Eleven of the 13 UNIX systems are used mostly for theoretical and graphical activities. The other two are used to control data acquisition systems. The personal computers are used for word processing, spreadsheets, data bases, graphics, communications, experiment control, data acquisition, and data analysis.

A. Networking Computers

The Chemistry Division's computer network continues to grow. A seventh FastPath 4 bridge has been added to the network to provide the occupants of Building 211 with direct access to the Chemistry network. Like the Building 200 Macintosh computers, the Building 211 Macintosh computers can now communicate directly with any computer system that supports TCP/IP. This permits easier access to the Chemistry Division's central computers and facilitates the use of electronic mail between the two buildings.

The Chemistry computer network is in the process of being connected to the Laboratorywide Fiber Distributed Data Interface (FDDI) network. Currently, there are only a few nodes on the FDDI network. In September and October of 1992, fiber optic cables will be pulled to most of the buildings on site. This will permit the Local Area Networks in these buildings to connect to the 100 Mbit per second FDDI network. This is 100 times the transfer rate of the existing PBX-Ethernet sitewide network currently in use.

In addition to connecting the Chemistry Computer Network to the FDDI, a CISCO router/bridge will be used to segment the Building 200 Ethernet backbone. The four segments will isolate some of the existing traffic. There will be a VAX cluster segment, workstation subnet segment, PC network segment, and a separate segment for the theoretical chemists. Currently, all messages are transmitted on the backbone Ethernet. The segmentation of the backbone Ethernet will improve performance by restricting some of the communication protocols to a single segment.

B. Experiment Control and Data Acquisition

The group continues to maintain the data acquisition systems that are running on the LSI-11 computer systems. However, new applications are no longer being developed for the outdated LSI-11 computers. Instead, IBM PCs and Apple Macintoshs are the hardware platforms of choice.

Currently, the group is planning for the conversion of one of the data acquisition systems. This conversion will move the system from a LSI-11 computer to a new VAXstation 4000 computer. Of the several options, this was considered the most cost effective. This new data acquisition system will be easily modifiable and extendible.

C. RISC UNIX Computers

The IBM RS/6000 series provides an excellent range of computers to serve the computing needs of the Chemistry Division. The Workstation network began with the installation of two IBM RS/6000 model 530 computers. These computers have proven themselves to be reliable and well suited to the computational needs of the Chemistry Division. They have been so well accepted that the workstation network has been augmented with two RS/6000 model 220, two model 320H, and three model 350 systems.

One of the RS/6000 systems purchased, a model 530, has been configured as a server for other RS/6000 systems. The two model 220 systems, having no local disk drives, are supported by the server as diskless workstations. The other systems are provided varying degrees of service from the server.

All of these RISC workstations are on an Ethernet segment isolated from the Chemistry Division's backbone Ethernet. This isolation is provided by a MicroVAX II with two Ethernet hardware interfaces. To improve performance and reliability, the MicroVAX II routing function will be replaced by the soon-to-be-installed CISCO router/bridge.

END

DATE FILMED

1/12/93